FACULTAD DE CIENCIAS

DEPARTAMENTO DE FÍSICA APLICADA

Contribution to the Development of Electronic Devices Based on Zn_3N_2 Thin Films, and ZnO and GaAs Nanowires

by

Carlos García Núñez

Madrid, July 2015

Contribution to the Development of Electronic Devices Based on Zn_3N_2 Thin Films, and ZnO and GaAs Nanowires

A dissertation presented to the

Applied Physics Department,

Universidad Autónoma de Madrid

In partial fulfillment

of the requirements

for the degree

Doctor of Philosophy in Physics

by

Carlos García Núñez

Advisors:

Prof. Jose Luis Pau Vizcaíno

Prof. Basilio Javier García Carretero

Madrid, July 2015

“Estudia mucho, trabaja mucho y aprende mucho”

−F.G.M.−

A Esther

Acknowledgement

En primer lugar, y como no podría ser de otra manera, me gustaría dar las gracias a los profesores José L. Pau y Basilio J. García por la oportunidad que me han brindado de realizar esta tesis doctoral con ellos. Agradecerles la gran confianza que han depositado en mí desde el principio y por toda su dedicación, sus enseñanzas y su paciencia. También me gustaría agradecer su impecable labor de edición llevada a cabo en este texto, no solo en el campo científico, sino también en el lingüístico; sin vosotros esta tesis no hubiera sido posible. De nuevo, mis más sinceros agradecimientos.

José Luis, en primer lugar me gustaría agradecerte la oportunidad que me diste de participar en tu proyecto de investigación y que me ha permitido no solo desarrollar la mayoría del trabajo presentado en esta tesis, sino también realizar dos estancias en el extranjero que nunca olvidaré. Gracias por mostrarme la visión más aplicada de la física, enseñándome a investigar sobre aplicaciones que cubran necesidades cotidianas. Te estoy agradecido por infinidad de cosas pero me gustaría destacar el ánimo y apoyo que en todo momento me has dado. Siempre recordaré los buenos ratos que hemos pasado en los congresos, en la estancia en Alemania bebiendo "*Weissbier*" y comiendo "*Weisswurst*", y por su puesto en la pista de pádel, donde somos todavía la pareja invicta del torneo "*interminable*". Siempre te estaré agradecido por todo ello.

Basilio, quiero agradecerte en primer lugar que me animaras a hacer el doctorado; creo que es una de las mejores decisiones que he tomado en mi vida. También quiero darte las gracias por haberme ayudado y dedicado tu tiempo, en ocasiones, hasta altas horas de la madrugada, incluso cuando nos separaban miles de kilómetros de distancia. Me gustaría darte las gracias por todo lo que me has enseñado y en especial por haberme instruido en el manejo del sistema CBE. Aunque en ocasiones hemos tenido ideas contrarias, siempre has dejado abierta una ventana a la discusión y al diálogo, y eso es de valorar. Siempre recordaré los buenos momentos que hemos pasado en los congresos Euro-MBE, y lo mucho que he disfrutado de tus lecciones bianuales de esquí. Por todo ello, mil gracias.

Quiero dedicar mis más sinceros agradecimientos al profesor Juan Piqueras. Me siento un privilegiado por haber podido investigar junto a ti durante gran parte de esta tesis doctoral. Gracias por haberme dado la oportunidad de iniciarme en el mundo de la investigación y por todo el conocimiento que me has trasmitido durante todos estos años. Siempre te estaré agradecido.

Me gustaría dar las gracias a mis compañeros del Grupo de Electrónica y Semiconductores de la Universidad Autónoma de Madrid (UAM): Pepe, Alejandro, Antonio, Manolo, Marichu, Andrés, y Nair, y también a Daniel que ahora está a muchos kilómetros de distancia pasando frío en su Rumanía natal. Gracias por haber creado un ambiente de trabajo agradable, positivo y enriquecedor, en el que trabajar cada día ha sido un verdadero placer. Quiero dar las gracias en especial a mis "compis" Andrés y Nair, que aunque lleváis poco tiempo con nosotros, es increíble lo bien que hemos sintonizado desde el principio; gracias por vuestros consejos, por vuestra compañía, y sobre todo por vuestros ánimos en el tramo final de esta tesis; os doy las gracias de corazón.

Si de algo estoy especialmente orgulloso, es del increíble equipo técnico que tenemos en el grupo, formado por Tomás, Pedro y Edu. Gracias por vuestro esfuerzo y dedicación, que han permitido tener los equipos del laboratorio a punto en todo momento. Edu, quiero agradecerte en particular la paciencia y cercanía con la que me has trasmitido todos los secretos relacionados con la fabricación de dispositivos electrónicos en la sala blanca. Contigo he experimentado una verdadera progresión, abarcando desde el clivaje de una oblea de Si(111) en "quesitos" perfectos, hasta la fabricación de un TFT de tamaño micrométrico. Gran parte de esta tesis ha sido posible gracias a ti. Como recompensa, yo creo que ahora nos podríamos hacer un viajecito de los tuyos, no?!

Part of the results presented in this thesis work was developed during a three months stay at the University of Alabama. I would like to thank professor Patrick Kung and professor Seongsin M. Kim to accept me in their research group. Thank you for the excellent supervision, all the helpful conversations and guidance that sustained my interest until the very end of the stay. Honestly, I can say that I enjoyed my stay and work in your group; this is mainly thanks to the great people I had the enormous privilege to work with. Specially, I would particularly like to thank Gang and Shawn for their much appreciated and valuable contributions and fruitful collaboration. Joe, Eli, Nabil, Nick, Soner, Mohammad, Elmer and my roommate Josh, I am very thankful for your friendship and hospitality during my stay in Alabama and I can say that I greatly enjoyed our time inside and outside the laboratory. I wish you all the best in your future!

I want to thank professor Jose A. Garrido the opportunity to research during three months in his group at the Walter Schottky Institut (WSI). I really enjoyed and learned a lot from this stay. I am thankful for your excellent supervision, constant motivation, and also the innumerable discussions we had. Thank you also for your very warm hospitality inside and outside the laboratory; I will always remember your "liquid-solid" paella Valencia; I known you did your best! I wish also to express my thanks to Benno for supervising me during the device fabrication and Matthias for helping me and introducing me to the XPS, AFM, CPD, and functionalization subjects; I want to thank you for our fruitful discussions and collaborations. I would like to thank my friend Julian Treu for keeping me in shape and in very pleasant company during my stay in and outside the WSI. Vielen Dank!

Me gustaría agradecer al departamento de Física Aplicada de la UAM por la formación recibida durante el máster de Materiales Avanzados y Nanotecnología, a la UAM por las labores administrativas y de gestión (en especial a nuestra secretaria Beatriz por su impecable labor), a la Comunidad de Madrid por el contrato en el proyecto AVANSENS (S2009/PPQ-1642), y al Ministerio de Economía y Competitividad por la beca FPI (TEC2010-20796).

Muchas de las medidas presentadas en esta tesis se han realizado en el Servicio Interdepartamental de Investigación (SIdI) y en el Centro de Micro-Análisis de Materiales (CMAM). Quiero dar las gracias al gran equipo de profesionales de ambos centros y en especial a Isi por las imágenes de SEM, Noemi por las medidas de XRD y al profesor David Martín por las medidas de RBS.

En ésta tesis también se presentan resultados obtenidos en colaboración con la Universidad Rey Juan Carlos. Querría agradecer al profesor Ángel L. Álvarez, a la profesora Carmen Coya, y al profesor Juan Jiménez, por haberme introducido en el apasionante mundo de la litografía por descargas eléctricas. Gracias por el entusiasmo e interés mostrado durante toda la colaboración, y por poner a nuestra disposición en todo momento vuestros equipos y conocimientos.

Fuera de los muros del laboratorio cuento con un ejército de amigos que me han demostrado su cariño y apoyo durante toda esta larga travesía. "MS-team" y los "Willy", aunque llevo una temporada desconectado del mundo social, quiero daros las gracias por ayudarme a recargar las pilas en nuestras "comilonas" y "viajecitos"; creerme si os digo que sois también culpables de que haya llegado hasta aquí.

Gracias a mi familia por estar a mi lado en los momentos buenos y en los menos buenos. Querría dar las gracias a mi madre por enseñarme que la constancia es el fruto del éxito; a mi hermano "Paul" por los ratos increíbles que pasamos juntos, que me hacen reponer las pilas al 200%; estoy seguro de que algún día ganaremos "la liga de oro de pádel". Como dice el dicho "*no entiendes algo a menos que seas capaz de explicárselo a tu padre*"; gracias papá por escucharme hablar sobre semiconductores y crecimientos epitaxiales durante horas sin fingir ni pizca de aburrimiento, y por enseñarme que la mejor forma de solucionar un problema grande, es resolver problemas pequeños. Gracias por todo vuestro cariño.

Por último, pero no menos importante, me gustaría dar las gracias a Esther, por arroparme durante todos estos años. Gracias por tus consejos, por tu comprensión, por tu eterna sonrisa, por trasmitirme tu energía y aportarme tanto cada día. Gracias por escucharme y ayudarme a preparar todas las presentaciones sobre "enanohilos" como tú los llamas. Jamás podré agradecerte todo lo que me has ayudado y apoyado durante todos estos años. Por todo ello, esta tesis te la dedico a ti.

Abstract

The main scope of this thesis work is the design, fabrication and characterization of electronic devices based on advanced materials. Advanced materials refer to all materials that represent advances over traditional materials. On the other hand, novel structures such as nanowires (NWs) based on traditional materials are also considered advanced materials due to they have exceptional properties such as low dimensionality and special mechanisms that can improve the existing technology based on thin film and bulk materials.

Zinc nitride (Zn_3N_2) is an advanced material used in this work for the development of high performance thin film transistors (TFTs) due to its high electrical mobility and conductivity at large carrier concentrations. In addition, Zn_3N_2 based photo-transistors have been fabricated and characterized. The growth of Zn_3N_2 layers has been carried out by radio-frequency magnetron sputtering from a Zn target and using a N_2/Ar plasma. Rutherford backscattering spectrometry (RBS) measurements performed on layers grown at high growth rates (r_g) above 50 nm/min, show a stoichiometric Zn_3N_2 composition. X-ray diffraction and scanning electron microscopy analysis (SEM), showing the formation of polycrystalline Zn_3N_2 layers. The grain size and its preferential orientation depend on the substrate temperature (T_s), observing an improvement of the crystalline orientation, and a reduction of the grain size as T_s decreases. In addition, the reduction of the r_g (4.44 nm/min) leads to a less definition of grain boundaries, improving the electrical conduction between grains, and showing Hall mobility values of 100 $cm^2/V{\cdot}s$ for carrier concentrations of $3.2{\times}10^{18}$ cm^{-3}. From SEM images and Hall results, one can conclude that the electrical transport through Zn_3N_2 is mainly limited by the grain boundaries and the ionized impurity scattering. Optical transmission measurements confirm a direct band gap semiconductor behaviour of Zn_3N_2, and an absorption edge blue-shift with T_s. On the other hand, Zn_3N_2 surface oxidation (metastability) has been demonstrated by spectroscopic ellipsometry and RBS. Surface oxidation rate is estimated between 20 and 36 nm/day, depending on the T_s; after sufficient time, Zn_3N_2 layers are completely transformed into transparent ZnO. In this work, it is shown a novel procedure to obtain sub-micron crystals of ZnO from the rapid transformation of Zn_3N_2 layers using electric arcs to accelerate the oxidation process. On the other hand, the oxidation of Zn_3N_2 can be prevented depositing a ZnO capping layer thereafter the deposition of Zn_3N_2 in vacuum conditions and in the same run. The research about Zn_3N_2 was part of works carried out in the AVANSENS (S2009/PPQ-1642) Spanish project, funded by the Comunidad Autónoma de Madrid. During that time, TFTs and photo-transistors were designed, fabricated and characterized using Zn_3N_2 as channel layer. The electrical characterization of TFTs shows transistor characteristics in n-channel enhancement-mode (threshold voltage of 6 V) without need of annealing process. Zn_3N_2 based TFTs and photo-transistors present high sensitivity to the visible (VIS) light, demonstrating the potential of Zn_3N_2 compound for VIS photodetectors (PDs).

Zinc oxide (ZnO) NWs based PDs present one of the highest photoconductive gain values among all the structures and materials with ultraviolet (UV) photosensitivity. In this work, UV PDs based on ZnO NWs have been designed, fabricated and characterized. Vertically aligned ZnO NWs have been grown by chemical

vapor transport on Si(100) crystalline substrates, and using a thin film of Zn as seed layer. The optical characterization of these NWs shows high absorption in the UV spectral range. Optimizing growth conditions, ZnO NWs have been obtained with an excellent aspect ratio, high crystalline quality, radii below 50 nm, and lengths above 10 μm, simplifying their integration in electronic devices. NW integration has been carried out by using alternating electric fields applied between conductive electrodes, being separated distances below the NW length. This cost-effective technique enables to trap and to align NWs at specific sites, controlling the number of assembled NWs with some selective properties on the NW size, and allowing for their electrical characterization. Electric current measured through a single NW strongly depends on its diameter; O adsorption around ZnO NW surface leads to trap free charge along the NW surface, reducing the conductive volume in the NW and then lowering the current measured in dark ambient conditions. Since the NW is illuminated with UV light, photogenerated holes desorb surface O, releasing surface trapped electrons towards the conductive bulk. Then, the O adsorption/desorption mechanisms along NW surface modulate the space charge region of the NW. NW photoresponsivity (R_{photo}) steadily increases as the NW radius reduces, confirming the important role of surface in the PD photoresponse, and yielding R_{photo} of 10^8 A/W ($\lambda = 370$ nm, and 5 V) in NWs with a radius below 50 nm. In addition, transient photoresponse studies show that NWs with lower radii have longer rise times and shorter decay times mainly due to the mentioned surface trapping effects. ZnO NW surface properties and electrical characteristics have been also analyzed after different surface treatments, including hydroxylation and silanization.

GaAs NWs have been grown by Ga-assisted chemical beam epitaxy (CBE). SEM images demonstrate the formation of Ga droplets on oxidized Si(111) substrates at T_s of 580 ºC; Ga droplet formation is mainly due to: i) thermal cracking of the Ga metalorganic precursor on the oxide surface layer; ii) diffusion of Ga atoms along the oxide surface layer; iii) reaction of Ga with oxide at those regions where oxide is thinner (pinholes), enabling the nucleation in contact with the Si surface. The preparation of the Si(111) substrate surface is therefore crucial for the successful NW growth in CBE. For oxide thicknesses around 0.5 nm, Ga droplet formation is possible, allowing for the growth of GaAs NWs by means of the vapor-liquid-solid (VLS) mechanism. However, the use of thinner or thicker oxides promotes the growth of GaAs polycrystalline layer or inhibits the GaAs growth, respectively. The incubation time refers to the time at which NW growth starts, being ranged between 30 and 200 s, depending on the initial droplet size. For growths performed at $T_s = 580$ ºC and V/III = 0.8, a $r_g = 5.4$ μm/h is observed. Reflection high-energy electron diffraction (RHEED) and transmission electron microscopy (TEM) confirm the formation of vertically aligned GaAs NWs along the direction [111]B with pure zinc blende structure; TEM measurements also show that the whole NW body is free of twins. The RHEED spotty pattern characteristic of NW growth consists of horizontal bars whose length is related to the NW diameter, and which are formed from electrons scattered through the NW facets, demonstrating the NW hexagonal footprint *in-situ*. GaAs NWs have been also aligned between conductive electrodes using the same method utilized for ZnO NWs. Electrical characteristics of a single GaAs NW show dark currents in the nA range and sensitivity to the VIS light through a decrease of its resistivity. Nano-contacts formed between the Ga droplet and the GaAs NW facets during the VLS process are the main responsible for

the device conductivity as demonstrated by the characterization of similar devices based on GaAs NWs without droplet. Most of the work has been carried out in the TEC2010-20796 project, funded by the Spanish Ministerio de Economía y Competitividad (MINECO). This project aims to design UV and VIS PDs based on ZnO and GaAs NWs, respectively. Results obtained during the research have confirmed the use of ZnO and GaAs NWs as active structures in the realization of UV and VIS PDs, improving the sensitivity, and enabling the integration of different semiconductor technologies at the microscale.

Resumen

El objetivo principal de esta tesis doctoral es el diseño, fabricación y caracterización de dispositivos electrónicos basados en materiales avanzados. Los materiales avanzados son aquellos que presentan propiedades avanzadas con respecto a los materiales tradicionales. Por otro lado, nuevas estructuras como los nanohilos basados en materiales tradicionales, también son considerados materiales avanzados; propiedades excepcionales como su baja dimensionalidad y mecanismos especiales pueden mejorar la tecnología existente basada en lámina delgada y materiales volumétricos.

El nitruro de zinc (Zn_3N_2) es un material avanzado utilizado en este trabajo para la fabricación de transistores de lámina delgada (*Thin Film Transistors*, TFTs) de alto rendimiento debido a su alta movilidad y conductividad eléctrica para concentraciones de carga altas. También se han fabricado y caracterizado foto-transistores basados en Zn_3N_2. El crecimiento de láminas delgadas de Zn_3N_2 se ha llevado a cabo mediante la técnica de pulverización catódica de radio frecuencia, a partir de un blanco de Zn y utilizando un plasma de N_2/Ar. Las medidas de espectrometría de retrodispersión Rutherford (*Rutherford Backscattering Spectrometry*, RBS) realizadas en capas crecidas a velocidades superiores a 50 nm/min, muestran una composición estequiométrica Zn_3N_2. Los estudios de difracción de rayos-X y de microscopía de barrido electrónico (*Scanning Electron Microscopy*, SEM) muestran la formación de capas policristalinas de Zn_3N_2. El tamaño de los cristales y su orientación preferencial dependen de la temperatura del sustrato, observándose una mejora de la orientación cristalina y una reducción del tamaño de cristal a medida que la temperatura del sustrato disminuye. Además, la reducción de la velocidad de crecimiento (4.44 nm/min) produce una menor definición de las fronteras de grano ayudando a mejorar la conducción eléctrica entre granos, y mostrando valores de movilidad Hall de 100 $cm^2/V{\cdot}s$ y concentraciones de carga de 3.2×10^{18} cm^{-3}. A partir de los resultados obtenidos por SEM y las medidas de efecto Hall, podemos concluir que el transporte eléctrico a través de una lámina delgada de Zn_3N_2 está limitado fundamentalmente por las fronteras de grano y la dispersión por impurezas ionizadas. Las medidas de transmisión óptica realizadas en capas de Zn_3N_2 confirman un comportamiento semiconductor de tipo directo, así como un corrimiento hacia el azul del borde de absorción con el aumento de T_s. Por otro lado, la oxidación superficial del Zn_3N_2 (metaestabilidad) ha sido demostrada por elipsometría espectroscópica y RBS. A partir de estos estudios, se han determinado ritmos de oxidación superficial entre 20 y 36 nm/día dependiendo de la temperatura del sustrato usada durante el crecimiento; la capa de Zn_3N_2 puede llegar a transformarse completamente en una capa transparente de ZnO, después de una exposición al aire un tiempo suficiente, que dependerá del espesor inicial de la capa de Zn_3N_2 y de su ritmo de oxidación. En este trabajo se muestra un procedimiento novedoso que permite transformar una capa de Zn_3N_2 en cristales de ZnO de tamaño sub-micrométrico utilizando arcos eléctricos para acelerar el ritmo de oxidación. Por otro lado, también se ha desarrollado un método para inhibir la oxidación del Zn_3N_2 utilizando una capa protectora de ZnO depositada en un ambiente de vacío inmediatamente después del depósito de la capa de Zn_3N_2. El trabajo de investigación llevado a cabo sobre el Zn_3N_2, se desarrolló en el marco del proyecto

nacional AVANSENS (S2009/PPQ-1642), financiado por la Comunidad Autónoma de Madrid. Durante la investigación, se ha llevado a cabo con éxito el diseño, fabricación y caracterización de TFTs y foto-transistores utilizando Zn_3N_2 como capa canal. La caracterización eléctrica de los TFTs muestra características de transistor, un comportamiento tipo-n en modo enriquecimiento (voltaje umbral de 6 V), y sin necesidad de aplicar tratamientos térmicos. Tanto los TFTs como los foto-transistores muestran una alta sensibilidad a la luz visible, demostrando el potencial del Zn_3N_2 para el desarrollo de fotodetectores de luz visible.

Los fotodetectores basados en nanohilos de óxido de zinc (ZnO) presentan una de las mayores ganancias fotoconductoras sobre el resto de estructuras y materiales con fotosensibilidad a la luz ultravioleta. En este trabajo se han diseñado, fabricado y caracterizado fotodetectores de luz ultravioleta basados en nanohilos de ZnO. Para ello, se han sintetizado nanohilos de ZnO verticalmente alineados sobre sustratos de Si(100) mediante la técnica conocida como transporte en fase vapor, utilizando una lámina delgada semilla de Zn. La caracterización óptica de estos nanohilos muestra una alta absorción a la luz ultravioleta. Optimizando las condiciones de crecimiento, se han crecido nanohilos con una excelente relación de aspecto, alta calidad cristalina, radios menores de 50 nm y longitudes superiores a 10 μm, facilitando su integración en dispositivos electrónicos; dicha integración se ha llevado a cabo mediante el uso de campos eléctricos alternos aplicados entre dos electrodos conductores separados una distancia inferior a la longitud del nanohilo. Esta técnica permite atrapar y alinear nanohilos en sitios específicos, controlando el número de nanohilos atrapados, teniendo cierta selectividad sobre el tamaño del nanohilo atrapado, y permitiendo su posterior caracterización eléctrica. Las corrientes eléctricas medidas a través de un único nanohilo dependen fuertemente de su diámetro. Además, parte de la carga existente en el volumen del nanohilo puede verse atrapada en la superficie mediante la adsorción de O alrededor de la superficie del nanohilo; este fenómeno reduce el volumen conductivo en el nanohilo, y afecta de manera diferente a los mecanismos de conducción en nanohilos con diferentes diámetros. Cuando el nanohilo es iluminado con luz ultravioleta, los huecos fotogenerados desorben el oxígeno superficial, liberando electrones atrapados en la superficie hacia el volumen conductor. Por lo tanto, los mecanismos de adsorción/desorción de O sobre la superficie del nanohilo modulan su región de carga espacial, mejorando su fotoresponsividad (R_{photo}) a la luz ultravioleta. Los valores de R_{photo} incrementan a medida que el radio del nanohilo disminuye, confirmando la importancia del papel que juega la superficie del nanohilo en la R_{photo} del fotodetector; en este trabajo, se han diseñado fotodetectores basados en nanohilos con diámetros inferiores a 50 nm alcanzándose R_{photo} de 10^8 A/W. Además, estudios del tiempo de respuesta de estos dispositivos muestran que los nanohilos con el menor radio tienen una respuesta a la iluminación UV más rápida que los nanohilos de mayor radio, sin embargo, presentan tiempos de relajación mucho mayores. En este trabajo también se han estudiado las propiedades superficiales y características eléctricas de nanohilos de ZnO después de diferentes tratamientos superficies como son la hidroxilación y la silanización.

En este trabajo se han crecido nanohilos de arseniuro de galio (GaAs) mediante epitaxia de haces químicos (*Chemical Beam Epitaxy*, CBE) asistida por Ga. Las imágenes de SEM demuestran la formación de gotas de Ga sobre una superficie oxidada de Si(111) a T_s de 580 ºC; la formación de gotas de Ga es debida fundamentalmente a: i) la descomposición térmica de la molécula metalorgánica de Ga sobre el óxido; ii) la

difusión de átomos de Ga sobre el óxido; iii) la reacción del Ga con el óxido en zonas de menor espesor (*pinholes*), donde se produce la nucleación en contacto con la superficie del Si. La preparación de los sustratos de Si(111) es por lo tanto crucial para el crecimiento de nanohilos de GaAs en CBE. Para espesores de óxido alrededor de los 0.5 nm la formación de gotas de Ga es posible, permitiendo el crecimiento de nanohilos de GaAs mediante el mecanismo conocido como vapor-líquido-sólido. El uso de menores o mayores espesores promueve la formación de una capa policristalina de GaAs o inhibe la nucleación de GaAs, respectivamente. El tiempo necesario para que los nanohilos nucleen sobre la superficie del sustrato se define como tiempo de incubación; este tiempo oscila entre los 30 y 200 s dependiendo del tamaño inicial de la gota de Ga. Utilizando una temperatura de sustrato de 580 ºC y una relación de flujos V/III de 0.8 se observan ritmos de crecimiento de 5.4 μm/h, indicando que los nanohilos de GaAs crecen aproximadamente un factor 11 más rápido que una lámina delgada de GaAs sobre un sustrato de GaAs(100) utilizando los mismos flujos. Medidas de reflexión/difracción de electrones de alta energía (*Reflection High-Energy Electron Diffraction*, RHEED) y de microscopía de transmisión electrónica (*Transmission Electron Microscopy*, TEM) confirman la formación de nanohilos de GaAs verticalmente alineados a lo largo de la dirección [111]B con una fase zinc blenda; además, las medidas de TEM muestran que los nanohilos están libres de defectos rotacionales a lo largo de toda su estructura. El diagrama de puntos observado en RHEED durante el crecimiento de los nanohilos, está compuesto por barras horizontales cuya longitud depende del diámetro de los nanohilos, y que están formadas por la dispersión de electrones a través las facetas de los nanohilos lo que demuestra *in-situ* que su sección es hexagonal. Una vez los nanohilos de GaAs han sido crecidos, estos son alineados entre electrodos conductores utilizando el mismo procedimiento usado para alinear nanohilos de ZnO. Las características eléctricas de un único nanohilo de GaAs muestran una corriente en oscuridad en el rango de los nA y sensibilidad a la luz visible a través de la bajada de su resistencia. La formación de nano-contactos entre la gota de Ga y el nanohilo de GaAs durante el crecimiento es el principal responsable de la conductividad eléctrica mostrada por el dispositivo, tal y como se demostró durante la caracterización de dispositivos similares basados en nanohilos de GaAs sin gota de Ga. La mayor parte del trabajo se ha desarrollado en el marco del proyecto nacional TEC2010-20796, financiado por el Ministerio de Economía y Competitividad (MINECO). El principal objetivo de este proyecto es el diseño de fotodetectores de luz ultravioleta y visible basados en nanohilos de ZnO y de GaAs, respetivamente. Los resultados obtenidos durante la investigación confirman el uso de nanohilos de ZnO y de GaAs como estructuras activas en la realización de fotodetectores de luz ultravioleta y visible, mejorando la sensibilidad y permitiendo la integración de diferentes tecnologías semiconductoras en la micro-escala.

Index

Acknowledgement i

Abstract v

Abbreviations xix

1. Introduction 1

1.1. Zinc Nitride ... 1

1.1.1. Zinc Nitride Properties ... 1

1.1.2. Thin Film Transistors ... 2

1.1.3. Transparent Electronics ... 2

1.2. Zinc Oxide Nanowires ... 4

1.2.1. Ultraviolet Photodetection ... 4

1.2.2. ZnO NW UV PDs ... 6

1.2.3. Other Applications of ZnO NWs ... 8

1.3. Gallium Arsenide Nanowires ... 9

1.3.1. GaAs NW Growth ... 9

1.3.2. GaAs NW VIS PDs ... 10

1.3.3. Other Applications of GaAs NWs ... 11

1.4. Nanowire Integration in Electronics ... 12

1.4.1. Dielectrophoresis ... 12

1.4.2. Drop-Casting on Electrodes ... 12

1.4.3. Fluidic Alignment ... 13

1.4.4. Nanomanipulation ... 13

1.4.5. Roll Transfer Printing ... 13

1.4.6. Langmuir-Blodgett Film Technique ... 14

1.4.7. NW Growth on Electrodes ... 14

1.4.8. Bottom-up Growth 15

1.5. Work Place 16

1.6. Thesis Motivation and Scopes 18

1.6.1. Motivation 18

1.6.2. Scopes 20

1.7. Thesis Content 22

References 24

2. Materials 33

2.1. Zinc Nitride 33

2.1.1. Growth Techniques 33

2.1.2. Structural Properties 33

2.1.3. Electrical Properties 34

2.1.4. Optical Properties 35

2.1.5. Metastability 36

2.2. Zinc Oxide Nanowires 37

2.2.1. Growth Techniques 37

2.2.2. Photoconductivity of ZnO NWs 40

2.2.3. Other Properties of ZnO NWs 43

2.3. Gallium Arsenide Nanowires 47

2.3.1. Growth Techniques 47

2.3.2. Properties of GaAs NWs 51

References 53

3. Growth Techniques 61

3.1. Magnetron Sputtering 61

3.1.1. Gas Lines and Control System 62

3.1.2. Vacuum System 64

3.1.3. Targets and Substrate Holders 65

3.1.4. Calibration Curves....... 66

3.2. Chemical Vapor Transport 68

3.2.1. Temperature Profile 70

3.3. Chemical Beam Epitaxy....... 72

3.3.1. Metalorganic Precursors 73

3.3.2. Gas Flow Controller 74

3.3.3. Vacuum System....... 76

4. Analysis Techniques 79

4.1. Ion Beam Analysis 79

4.1.1. Ion Backscattering Spectrometry....... 79

4.1.2. Non-Rutherford Backscattering 86

4.1.3. Nuclear Reaction Analysis 87

4.1.4. Simulation of the Experimental Data 90

4.2. SEM and EDAX 92

4.3. Transmission Electron Microscopy....... 94

4.4. Electro-Optical Characterization....... 98

4.4.1. Four-Probe Van der Pauw Method....... 98

4.4.2. CPD and SPV 104

4.4.3. Photoresponsivity Measurements 106

4.5. X-ray Diffraction 108

4.6. Reflection High-Energy Electron Diffraction 110

4.6.1. RHEED Technique Applications....... 112

4.7. Mass Spectrometry....... 117

4.7.1. Metalorganic Precursor Decomposition....... 118

4.8. Optical Spectroscopy....... 122

4.8.1. Spectroscopic Ellipsometry 122

4.8.2. Raman Spectroscopy 128

4.8.3. Photoluminescence 131

4.8.4. Spectrophotometry 133

4.8.5. X-ray Photoelectron Spectroscopy 136

References 138

5. Zinc Nitride Thin Films 141

5.1. Zinc Nitride Properties 142

5.1.1. Growth Conditions 142

5.1.2. Compositional Study 144

5.1.3. Morphological Study 148

5.1.4. Structural Study 151

5.1.5. Optical Study 152

5.1.6. Electrical Study 160

5.2. Oxidation Mechanism of Zinc Nitride Layers 164

5.2.1. Compositional Study 164

5.2.2. Optical Study 167

5.2.3. Electrical Study 170

5.2.4. Structural Study 171

5.2.5. Rapid Oxidation of Zinc Nitride Induced by Electric Arcs 172

5.3. Transistors Based on Zinc Nitride as Channel Layer 180

5.3.1. Bottom-Gate Thin Film Transistor 180

5.3.2. Photo-Transistor 184

Conclusions 186

References 188

6. Zinc Oxide Nanowires 191

6.1. Synthesis of ZnO NWs by CVT 192

6.1.1. Growth of ZnO TPs 192

6.1.2. Growth of Vertically Aligned ZnO NWs 195

6.1.3. Growth of ZnO NWs with Al/ZnO/C Powder 198

6.2. Characterization of ZnO NWs 199

6.2.1. Optical Analysis 199

6.2.2. Compositional Analysis 202

6.2.3. Structural Analysis 210

6.3. Integration of ZnO NWs in Optoelectronics 213

6.3.1. NW Suspension Preparation 213

6.3.2. Drop-Casting 214

6.3.3. Dielectrophoresis 214

6.4. ZnO NW Based PDs 226

6.4.1. *I-V* Characteristics 226

6.5. Chemical Modification of ZnO NW Surface 235

6.5.1. Hydroxylation and Silanization of ZnO NWs 235

6.5.2. Characterization of ZnO NW Surfaces 236

Conclusions 244

References 246

7. Gallium Arsenide Nanowires 251

7.1. Growth of GaAs NWs by Ga-assisted CBE 252

7.1.1. Si(111) Substrate Preparation 252

7.1.2. Principles of Ga-Assisted GaAs NW Growth 256

7.1.3. Study of GaAs NW Growth 260

7.2. Characterization of GaAs NW Properties 274

7.2.1. Morphological Analysis 274

7.2.2. Structural Analysis 276

7.3. Integration of GaAs NWs in Optoelectronics 293

7.3.1. GaAs NW Assembled by DEP..293

7.3.2. GaAs NW Photoconductivity 299

Conclusions 302

References 304

8. Conclusions and Future Work 307

8.1. Conclusions 307

8.1.1. Zn_3N_2 Thin Films 307

8.1.2. ZnO NWs 309

8.1.3. GaAs NWs 310

8.2. Future Work 312

8.2.1. Zn_3N_2 Thin Films 312

8.2.2. ZnO NWs 312

8.2.3. GaAs NWs 314

8.2.4. Integration of Nanostructures 315

8.3. Conclusiones 317

8.3.1. Láminas Delgadas de Zn_3N_2 317

8.3.2. Nanohilos de ZnO 319

8.3.3. Nanohilos de GaAs 321

8.4. Trabajo Futuro 323

8.4.1. Láminas Delgadas de Zn_3N_2 323

8.4.2. Nanohilos de ZnO 324

8.4.3. Nanohilos de GaAs 326

8.4.4. Integración de Nanoestructuras 327

Appendix A: Publications and Conference Contributions 329

Abbreviations

a	Lattice constant
AC	Alternating current
AES	Auger electron spectroscopy
AFM	Atomic force microscopy
amu	Atomic mass units
APDEMS	Amino-propyldiethoxymethylsilane
ATR	Attenuated total reflectance
AZO	Aluminum doped zinc oxide
B	Magnetic field
BZ	Brillouin zone
BEP	Beam equivalent pressure
CBE	Chemical beam epitaxy
CMAM	Center for material microanalysis
CNT	Carbon nanotube
CTA	Conventional thermal annealing
CVD	Chemical vapor deposition
CVT	Chemical vapor transport
d	Layer thickness
DC	Direct current
DEP	Dielectrophoresis
d_{hkl}	Distance between crystal planes
DI	Deionized
E	Electric field
E_C	Conduction band energy level
ECR	Electron cyclotron resonance
ED	Electron diffraction
EDM	Electrical discharge machining
EDAX	Energy dispersive X-ray spectroscopy
E_C	Conductive band energy level
E_F	Fermi energy level
E_g	Band gap energy
E_{ion}	Incident ion energy
EMA	Effective medium approximation
E_{opt}	Optical band gap
ERDA	Elastic recoil detection analysis
E_{ss}	Surface states energy level
EtOH	Ethanol
E_V	Valence band energy level

E_{vac}	Vacuum energy level
f	Frequency
f_{cm}	Clausius-Mossotti factor
F_{DEP}	Dielectrophoretic force
FET	Field effect transistor
FFT	Fast Fourier transform
FTIR	Fourier transform infrared
FWHM	Full width at half-maximum
GIXRD	Grazing incidence X-ray diffraction
G_{photo}	Photoconductive gain
GaAs	Gallium arsenide
GCF	Gas correction factor
hcp	Hexagonal close-packed
HRTEM	High-resolution transmission electron microscopy
HT	Hydrothermal
I	Electrical current
ICDD	International centre for diffraction data
I_D	Drain current
I_{dark}	Dark current
I_{light}	Light current
I_{photo}	Photo current
IR	Infrared
ITO	Indium tin oxide
IBA	Ion beam analysis
IBS	Ion backscattering spectrometry
J	Current density
JCPD	Joint committee on powder diffraction
k	Extinction coefficient
K	Kinematic factor
LED	Light emitting diode
LO	Longitudinal optical phonon
LP	Low pass filter
L_{NW}	Nanowire length
MBE	Molecular beam epitaxy
MFC	Mass flow controller
MOCVD	Metalorganic chemical vapor deposition
MOVPE	Metalorganic vapor phase epitaxy
n	Refractive index (in optical characterization)
n	Carrier density (in electrical characterization)
ND	Neutral density filter
n_e	Electron carrier density

n_h	Hole carrier density
n_{Hall}	Carrier density measured by Hall effect
NP	Nanoparticle
NRA	Nuclear resonance analysis
NW	Nanowire
OD	Optical density
p	Dipolar moment
PCM	Phonon confinement model
PD	Photodetector
PID	Proportional-integral-derivative
PIXE	Proton-induced X-ray emission
PLD	Pulsed laser deposition
PRC	Pressure regulated control
P_{res}	Residual pressure
Q	Dose
Q_{ex}	Excess of kinetic energy
QMA	Quadrupole mass analyzer
QMS	Quadrupole mass spectrometer
QW	Quantum well
R	Optical reflectance
RBS	Rutherford backscattering spectrometry
rf	Radio-frequency
r_g	Growth rate
RHEED	Reflection high-energy electron diffraction
r_{NW}	Nanowire radius
R_{NW}	NW electrical resistance
R_{photo}	Photoresponse
R_s	Sheet resistance
RT	Room-temperature
SAM	Self-assembled monolayer
SCR	Surface charge region
SNR	Signal-to-noise ratio
SE	Spectroscopic ellipsometry
SEM	Scanning electron microscopy
SNR	Signal-to-noise ratio
sr	Steradian
T	Optical transmission
t	Layer thickness
TBAs	Tertiarybuthylarsine
TEGa	Triethylgallium
TEM	Transmission electron microscopy

TP	Tetrapod
TFT	Thin film transistor
TO	Transversal optical phonon
T_s	Substrate temperature
u	Atomic mass units
UAM	Universidad Autónoma de Madrid
UV	Ultraviolet
V_{DS}	Drain-source voltage
V_{GS}	Gate-source voltage
V_H	Hall voltage
VIS	Visible
VLS	Vapor-liquid-solid
V_p	Peak voltage (amplitude)
VPT	Vapor phase transport
V_{rms}	Root-mean-square voltage
V_{th}	Threshold voltage
W/L	Width-to-length ratio
WZ	Wurtzite
XRD	X-ray diffraction
ZB	Zinc blende
Zn_3N_2	Zinc nitride
ZnO	Zinc oxide
ZnON	Zinc oxynitride
1D	One-dimensional
2D	Two-dimensional
α	Absorption coefficient
$\Delta\omega$	Raman shift
ε	Stopping cross-section
ε_0	Vacuum permittivity
ρ	Electrical resistivity
μ	Hall mobility
μ_{FE}	Field Effect mobility
λ	Wavelength
λ_c	Cut-off wavelength
θ	Scattering angle (in IBS)
Θ	Surface coverage
Φ	Work function
Φ_O	Surface dipole potential
Φ_S	Surface band bending

1. Introduction

1.1. Zinc Nitride

1.1.1. Zinc Nitride Properties

Zinc nitride (Zn_3N_2) was firstly synthesized at the mid-20th century by Juza and Hahn [1], and remained uncharacterized until the end-20th century [2]. Since 1993, few relevant works have investigated Zn_3N_2 properties [2-10]; those works analyze properties of Zn_3N_2 films synthesized by different techniques such as direct reaction between ammonia (NH_3) and Zn films [2], radio-frequency (rf) pulsed laser deposition (PLD) [3], rf-magnetron sputtering [4, 5, 9, 10], molten salt electrochemical process [6], rf-molecular beam epitaxy (rf-MBE) or metalorganic chemical vapor deposition (MOCVD) [7]. Zn_3N_2 films are typically polycrystalline and present a cubic anti-bixbyite structure [2, 4]. There are evidences that recognize Zn_3N_2 as a n-type semiconductor material [4] attributed to N vacancies into the nitride sub-lattice [8]. However, its band gap type (direct or indirect) and energy (E_g) are still unknown. Several studies about the optical properties of this semiconductor material show that its band gap is strongly influenced by the growth conditions, and deposition technique; resultant characterization studies show both direct [2-7] and indirect [9, 10] band gap types, and E_g values between 1.01 eV [5, 6] and 3.2 eV [2, 3]. In 1993, Kuriyama et al. [2] prepared Zn_3N_2 films by direct reaction between NH_3 and Zn films, and they reported the band gap was direct and around 3.2 eV. In 1998, Futsuhara et al. prepared Zn_3N_2 films by rf-magnetron sputtering and the films had a direct band gap of 1.23 eV. Yang et al. [5] and Toyoura et al. [6] prepared Zn_3N_2 films by rf-magnetron sputtering and molten salt electrochemical process, respectively, reporting both a band gap of 1.01 eV. In 2006, the band gap of Zn_3N_2 was reported to be direct and 1.06 eV by Suda et al. [7], and indirect and 2.12 by Zong et al. [9] and Du et al. [10]. In 2010, Zn_3N_2 was determined to be a n-type semiconductor with a direct band gap of 3.2 eV by Ayouchi

et al. [3]. Such a wide range of E_g values is unusual in other semiconductors, so the origin of the discrepancy is still under debate.

There are some relevant works reported in the literature showing that Zn_3N_2 tends to oxidize in air ambient conditions [2, 4]; in addition, the high reactivity of O with respect to N, allows to the incorporation of O atoms into the Zn_3N_2 sublattice, even during growths carried out under high vacuum conditions [7], hampering the synthesis of pure Zn_3N_2 films. Both effects (surface oxidation and O structural impurities) could therefore hinder the characterization of electrical and optical properties of this material. In this regard, although optical constants of Zn_3N_2, including refractive index (n) and extinction coefficient (k), have been studied in the past [3, 7], the impact of structural defects and surface effects such as roughness or the formation of native oxide on the calculated parameters has not been discussed yet.

Since 2009, potential applications based on Zn_3N_2 have been demonstrated in the literature, including thin film transistor (TFT) displays [11], and transparent electronics [12]. The latter has attracted the attention of research community because of the possibility to obtain p-type ZnO by thermal annealing treatments of Zn_3N_2 thin films in an oxidizing ambient [13-16].

1.1.2. Thin Film Transistors

TFTs are essential devices in active-matrix liquid crystal and organic light emitting diode (OLED) displays. Although hydrogenated amorphous silicon (a-Si) is usually the material of choice for the TFT channel, this technology presents some issues such as the low mobility, and the poor levels of stability [17, 18]. Nowadays, polycrystalline silicon (p-Si) is also used as channel layer in TFTs, exhibiting an important enhancement of the field effect mobility in comparison with those based on a-Si; however, the randomly distributed grain boundaries in a high area can hinder the fabrication process yield [19]. Alternatively, different organic and inorganic materials are being investigated as potential substitutes of Si. A promising candidate is Zn_3N_2 because of its high electron mobilities (156 $cm^2/V{\cdot}s$) [7] and low resistivities (4×10^{-3} $\Omega{\cdot}cm$) [20], as well as, the low cost of its constituting materials and fabrication procedure.

Aperathitis et al. [11] designed, fabricated and characterized the first transparent bottom-gate TFT, using Zn_3N_2 as the channel layer. However, that TFT only showed output characteristics after an annealing treatment at temperatures between 300 and 400 ºC, converting the initial Zn_3N_2 layer into a transparent zinc oxide (ZnO) based compound. The transistor worked in enhancement mode (normally off), showing a reduction of the threshold voltage (V_{th} is the required gate voltage for the channel to start conducting) as the annealing temperature increases.

1.1.3. Transparent Electronics

It is well known that undoped ZnO is naturally n-type because of the presence of intrinsic defects, such as O vacancies, Zn interstitials or even H atoms incorporated during the growth process, that contribute to increase density of majority carriers (electrons) [21]; the existence of a high density of these donor-like defects

in ZnO hinders to obtain p-type ZnO mainly due to the difficulty to incorporate a foreign acceptor-like dopant into the ZnO structure to compensate the electron concentration. Therefore, there is an important challenge to find a promising method to fabricate low resistance and high mobility p-type ZnO thin films that enables the development of advanced transparent optoelectronics.

Several groups have postulated the use of V group elements such as P [22], As [23] and N [24] as possible acceptor elements for p-type doping of ZnO. The latter is suggested to be the most promising material because its ionic size is similar to O. Although, there are theoretical studies predicting that N would produce a shallow acceptor level in ZnO [25], to our knowledge, there are no works reported in the literature confirming a reliable and reproducible way to obtain p-type ZnO.

Kambilafka et al. [12] fabricated a p-n diode in a single deposition run, consisting of a p-type ZnO:N and a n-type Zn_3N_2; resultant device exhibited rectifying behaviour and a turn-on voltage of around 2 V. The growth of those layers was carried out in a sputtering system from a zinc nitride target and at room-temperature (RT), using different Ar/O_2 gas ratios, allowing to tune not only the resultant layer composition (Zn_3N_2, ZnO or ZnO:N) but also the semiconductor type (n or p).

Alternatively, thermal annealing treatment of Zn_3N_2 thin films performed in ambient air is a rapid and easy of developing technique to obtain p-type ZnO [13-16]; in addition, this process takes advantage of the Zn element which is a constituent in both Zn_3N_2 and ZnO, and therefore could be advantageous to fabricate p-n junctions using the same deposition technique and through a single deposition run. In this regard, Li et al. [13] demonstrated the conversion of n-type Zn_3N_2 into p-type ZnO thin films through thermal annealing performed for 1 h at substrate temperatures (T_s) between 500 and 800 ºC. This kind of thermal treatment makes Zn_3N_2 suitable for the development of transparent electronics, including applications such as LEDs.

1.2. Zinc Oxide Nanowires

1.2.1. Ultraviolet Photodetection

The ultraviolet (UV) light is an electromagnetic radiation with wavelengths (λ) ranged between 400 nm (visible, VIS) and 10 nm (X-ray); this light can be divided in four different spectral regions: UVA (400-320 nm), UVB (320-280 nm), UVC (280-200 nm), and Far UV (200-10 nm) as described in figure 1.1.

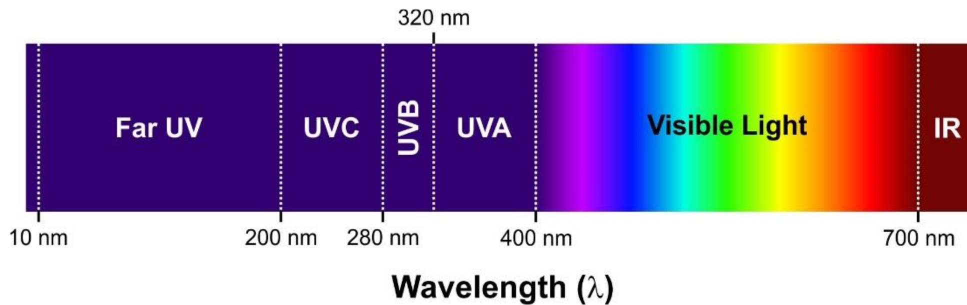

Figure 1.1. Electromagnetic spectrum.

There are many applications based on the UV photodetection, including UV optoelectronic devices in civil and military applications such as missile launching detection, flame sensing (fire alarms, missile warning or combustion monitoring), UV radiation calibration and monitoring (instrumentation and UV lithography), chemical and biological analysis, space research, environmental monitoring (ozone, pollutants, ...), optical communications (inter-satellite communications) and astronomical studies. For these applications, fast response time, fast reset time, high selectivity, high responsivity, and good signal-to-noise ratio are desired characteristics [26, 27].

Last years, a new generation of UV photodetectors (PDs) based on advanced materials has emerged, involving wide band gap ($E_g > 3.0$ eV) semiconductor materials such as gallium nitride (GaN), silicon carbide (SiC), diamond and ZnO [28, 29]. In that respect, GaN and ZnO based structures, including thin films and nanowires (NWs), are highlighted over the rest of mentioned materials mainly due to their high photoresponsivity (R_{photo}) and photoconductive gain (G_{photo}) in the UV spectral range.

GaN UV PDs

GaN is a III-V semiconductor material with a wide E_g of 3.4 eV, matching the whole UV photon energy region, and then is promising for the development of UV PDs [30, 31]. Muñoz et al. [30] fabricated UV PDs based on GaN thin films, obtaining high R_{photo} of 10^3 A/W, and G_{photo} between 1 and 10^5 at excitation power densities (P) between 3×10^3 and 5×10^{-3} W/m^2, respectively. These devices show a decrease of G_{photo} with both temperature, and the excitation power, exhibiting a non-exponential conductance decay as the excitation source is turned off. Gain mechanisms of these PDs were proposed to be governed by the modulation of the conductive volume through changes of the space charge region (SCR) width (w_{SCR}) at the GaN surface

caused by excitation/relaxation charge carrier mechanisms. In addition, it was observed that G_{photo} depends on ~ P^{-k}, k being 0.9 for measurements taken at RT in the P range detailed above.

GaN based nanostructures such as NWs have been found to reveal higher G_{photo} than those obtained in the thin film counterparts. Chen et al. [32] fabricated UV photoconductors based on GaN NWs with diameters between 40 and 135 nm, obtaining G_{photo} values of 1.9×10^5 which are three other of magnitude higher than those obtained in the thin film counterparts (at the same power density of 10 W/m^2) [30, 33]. In addition, GaN NW PDs showed a dependence of G_{photo} with ~ $P^{-0.9}$ which further proves that the high gain presented by these photoconductors is mainly dominated by the surface states.

ZnO UV PDs

ZnO is a promising semiconductor material for the development of UV PDs mainly because its wide band gap energy (E_g = 3.4 eV) and low VIS absorption make this material highly sensitive and selective to UV light. In ZnO bulk and thin film based PDs, charge trapping effects at surface states and grain boundaries lead to long generation-recombination times (long electron lifetimes) which yield very high G_{photo} at the expense of slowing down the optical response. In this regard, the photoresponse of ZnO to the UV light exposure is mainly governed by two different processes during and after UV illumination [34]:

i) During UV illumination, a rapid and reproducible photon absorption process along which electron-hole pairs are generated [$h\nu \rightarrow e^- + h^+$], and a slow O_2 desorption from the ZnO surface caused by the recombination of photogenerated holes with surface trapped electrons [$O_2^-(ad) + h^+ \rightarrow O_2(g)$], releasing electrons towards the ZnO bulk. Both, photogenerated electrons in the ZnO bulk and released electrons from the ZnO surface contribute to increase the conductivity.

ii) After UV illumination, a rapid decrease of the free charge carrier density, and a slow and uncontrolled process, involving O_2 re-adsorption along ZnO surface defects by trapping electrons [$O_2(g) + e^- \rightarrow O_2^-(ad)$] contribute to reduce the current down to the initial dark current (I_{dark}) level.

ZnO slow photoresponse induced by the O_2 adsorption/desorption processes, is observed to be dominant in polycrystalline ZnO thin films [35]. This is mainly because of the slow adsorption rate of O_2 at the ZnO surface defects and grain boundaries. Therefore, the fast photoresponse becomes dominant with the crystalline quality improvement of the ZnO films, which greatly reduces the grain boundaries, and the density of defects. In this regard, UV PDs based on high crystal quality ZnO thin films show high R_{photo} around 400 A/W at $300 < \lambda < 373$ nm under a bias voltage of 5 V [34].

Thanks to the enhancement of the surface-to-volume ratio, ZnO NW PDs present one of the highest G_{photo} values (~ 10^8 A/W) among all the structures and materials with UV photosensitivity [36, 37]. This is also possible due to the high crystal quality of ZnO NWs, which in comparison to polycrystalline ZnO films,

enhances carrier mobility along the NW body, and reduces scattering mechanisms in absence of grain boundaries. In addition, their cost-effective and easy of manufacturing procedure, excellent mechanical properties, and possible integration into Si technology have fostered the investigation of ZnO NWs for high performance UV PDs.

1.2.2. ZnO NW UV PDs

Properties of ZnO NWs such as high conductivity, high crystalline quality and high surface-to-volume ratio, and advantages such as the low cost of their constituting elements and fabrication procedure, make ZnO NWs attractive to the semiconductor industry. Moreover, ZnO NWs are highly sensitive to UV light in the whole UV spectrum (from Far UV to UVA) due to the ZnO wide band gap, and VIS-blindness. For all these reasons, ZnO NWs are promising structures for the development of advanced UV PDs in highly integrated optical systems [36-50].

Metal-NW Contact

UV detection in ZnO NW devices is based on the change of the NW electrical conductivity under UV illumination. ZnO NW PDs are commonly built from the fabrication of two metallic contacts on the NW ends. Depending on the electrode material and also the technique to deposit the electrodes, the characteristic behaviour of the contact could change. Since the performance of these devices critically depends on the quality of the contacts, the development of low-resistance contacts has attracted significant attention.

In general, ohmic contacts formed on ZnO NWs can be obtained defining metal electrodes on top of both NW ends. Different metal electrodes defined by techniques such as lithography or focus ion beam (FIB) have demonstrated to form ohmic contacts on ZnO NWs, including Au/Ti [36], Au [38], Pt-Ga [39], and Pt [37]. In contrast, the direct [38] or controlled [40] dispersion of ZnO NWs on pre-patterned Au electrodes typically shows non-linear current-voltage (I/V) characteristics. For some specific applications, ZnO NW devices have been fabricated using a combination of both linear and non-linear contacts. Accordingly, Hu et al. [39] disperse ZnO NWs on pre-patterned Pt contacts, evaporating a Pt-Ga contact at one of the NW ends to make an ohmic contact, forming the other NW end a non-linear contact. Furthermore, electrodes based on graphene have been also defined on ZnO NWs, resulting in non-linear contacts [41, 42].

ZnO NW Gain Mechanisms

During UV illumination, the recombination mechanism of photogenerated holes at electron-trap states located at ZnO NW surface prevents charge-carrier recombination in the NW conductive volume. This mechanism prolongs the photocarrier lifetime, and then enhances the G_{photo} of these UV PDs. Furthermore, the NW short length reduces the electron transient time, contributing to the G_{photo} enhancement. One of the best performance obtained in UV PDs, was obtained by Soci et al. [36] and He et al. [37], showing high internal $G_{\mathrm{photo}} \sim 10^{8}$; this giant G_{photo} and the low power consumption of the resultant devices are considered interesting advantages for the development of a new generation of phototransistors with potential applications in fields

such as photodetection, sensing, imaging, and intrachip optical interconnections. The analysis of G_{photo} as a function of P, concluded that $G_{photo} \sim P^{-0.9}$ (as in the case of GaN) which suggests that the gain mechanisms are dominated by charge trapping along the ZnO NW surface. Table 1.1 summarizes R_{photo} and G_{photo} obtained in UV PDs based on different structures of semiconductor materials.

Table 1.1. R_{photo} and G_{photo} of UV PDs based on different structures of semiconductor materials.

Material [REF]	**Structure**	$\boldsymbol{\lambda}$ **(nm)**	$\boldsymbol{P}$ **(W/m^2)**	$\boldsymbol{R_{photo}}$ **(A/W)**	$\boldsymbol{G_{photo}}$
GaN [30]	Thin film	325	5×10^{-3}	1×10^{3}	1.6×10^{5}
GaN [32]	NW	325	1×10^{1}	1.2×10^{3}	1.9×10^{5}
ZnO [34]	Thin film	380		4×10^{2}	6×10^{2}
ZnO [36]	NW	375	1×10^{2}	1×10^{8}	2×10^{8}

The long recovery times of ZnO NW UV PDs is a limiting factor for practical applications. The recovery time of these devices depends on the re-adsorption of O species along the NW surface which lowers the current down to the initial level. This re-adsorption process is much slower than the desorption process observed during illumination and is strongly influenced by the ambient conditions (humidity, pressure, …). In this regard, previous research on ZnO NW UV PDs has been focused on improving the sensitivity, response time, and recovery time, comprising the fabrication of Schottky barrier (SB) type devices [43], the surface functionalization by polymers with UV absorption [44], or the coating with Ag and Au nanoparticles (NPs) [45, 46].

Effects of ZnO NW Diameter on the Conductivity

The growth of ZnO NWs has been explored by using various methods and mechanisms such as the chemical vapor transport (CVT) [51], chemical vapor deposition (CVD) [52], and PLD [53] by using vapor-solid (VS) or vapor-liquid-solid (VLS) mechanisms. VS and VLS mechanisms are commonly linked to the use of a seed buffer layer or particles to promote and assist the longitudinal growth of ZnO NWs along a preferential direction fixed by the substrate orientation. Moreover, the size of the resultant NW diameter (d_{NW}) can be adjusted by the seed layer thickness or the seed particle diameter [54, 55]. The growth of ZnO NWs with different d_{NW} allows to analyze the effects of d_{NW} on their optoelectronic properties.

The resistivity (ρ) of the ZnO NWs measured in air ambient conditions is demonstrated to increase by decreasing d_{NW} [56]; this effect might be a consequence of the formation of O_2^- from surface-adsorbed O_2 at surface defects such as O vacancies [57] that capture free electrons from the conductive volume [58], depleting

the surface electron states [59]. This mechanism might contribute to decrease free charge carrier density in the NW bulk, increasing the NW resistance in a manner that becomes more effective for narrower NWs because of the increasing surface-to-volume ratio. However, the effects of d_{NW} on the ZnO NW photoconductivity and response time were still unclear at the onset of this work and needed to be further investigated.

1.2.3. Other Applications of ZnO NWs

ZnO NWs are promising structures for the development of biosensors mainly due to interesting properties, involving nontoxicity, biosafety, biocompatibility, high electron transfer rates and combination with immobilized enzymes [60]. The high electrostatic interactions formed between organic molecules with ZnO NW surface, make these structures potential platforms for the immobilization of organic molecules such as acidic proteins or DNA with a high bonding stability [61]; in addition, ZnO NWs are promising for the detection of low concentrations of biomolecules such as glucose [62], and penicillin [63].

ZnO is a good candidate for UV laser applications because its high exciton binding energy (60 meV), which is much larger than that observed in other wide band gap materials such as ZnSe (22 meV) or GaN (25 meV). In this regard, UV lasing at RT was firstly demonstrated in ZnO NWs by Huang et al. [64].

Nowadays, there is a strong interest in the development of high sensitivity lightweight-gas sensors capable to operate in the subpart per million (ppm) sensitivity range. The high chemical reactivity of ZnO surface, as well as, the high surface-to-volume ratio of ZnO NWs have a tremendous potential for the detection of lightweight gases [65-71].

Properties such as piezoelectricity (coming from the non-centrosymmetric symmetry of its wurtzite (WZ) structure), high melting point (~ 2000 ºC), high stability under an O environment, and photocatalytic behaviour, make ZnO NWs attractive for the development of applications such as nanogenerators [72, 73], field emission devices [74, 75], field effect transistors (FETs) [76, 77], and photocatalysis [78, 79].

1.3. Gallium Arsenide Nanowires

Gallium arsenide (GaAs) NWs are promising semiconductor nanostructures as building blocks for the development of a new generation of electronic, optoelectronic, photonic and photovoltaic applications mainly because of their excellent electronic transport properties and light-coupling effects. The small footprint of these NWs combined with the direct band gap of GaAs, make GaAs NWs excellent candidates for their integration in high performance optoelectronics based on Si technology.

1.3.1. GaAs NW Growth

The growth of GaAs NWs has been commonly carried out by techniques such as solid source molecular beam epitaxy (SS-MBE) [80, 81], gas source molecular beam epitaxy (GS-MBE) [82, 83], metalorganic vapor phase epitaxy (MOVPE) [84, 85], MOCVD [86], and chemical beam epitaxy (CBE) [87, 88]. These growths are usually performed on Si substrates due to some important advantages:

i) Si native oxide (SiO_x) has a high density of pinholes along its surface where Ga atoms could preferentially form droplets and react with the Si substrate surface;

ii) the use of Si substrates allows for the integration with advanced Si processing technology;

iii) the low GaAs-Si mismatch (~ 4%) increases the critical GaAs NW diameter up to 110 nm, which means NWs with d_{NW} below 110 nm can be coherently grown due to the efficient relaxation of elastic stress on the facets sidewalls [89];

iv) Si(111) allows for the growth of GaAs NWs perpendicularly aligned to substrate surface.

GaAs NWs are usually grown by a VLS mechanism whose fundamental principle is the use of a metal catalyst to assist NW growth along preferential directions determined by the substrate orientation [90]. During the growth process, the catalyst forms a liquid alloy with at least one of the materials that will constitute the NW; when the alloy becomes supersaturated of that constituent, there is a solid precipitation towards the alloy/substrate interface. This solid phase accumulates enough strain underneath the liquid alloy, allowing for the coherent growth of a vertical nanostructure with a small footprint [91]. The d_{NW} is then limited by seed size (minimum d_{NW}) and substrate lattice mismatch (critical d_{NW}).

Although Au is extensively used as catalyst to assist the VLS growth of GaAs NWs [81, 83, 85, 88], its unintentional incorporation into the GaAs NW structure during the growth might hinder GaAs electrical properties [92], inherently limiting the performance of NW-based optoelectronic devices [93]. In order to overcome this drawback, Ga is suggested as a potential substitute of Au in catalyst-assisted VLS growths.

Ga-assisted process resembles a liquid phase epitaxial growth in which As and Ga atoms are incorporated at the surface of the initial Ga droplet. As the As concentration increases, the As solubility limit can be achieved in the droplet, leading to the GaAs epitaxial growth at the liquid-solid interface. Ga-assisted VLS growth of GaAs NWs has been carried out by different techniques [80, 82, 84, 87]. The characterization of resultant GaAs NW structure carried out by techniques such as transmission electron microscopy (TEM)

shows an important reduction of the phase polytypisms along the NW body, which are typically observed in Au-assisted growths [94]. This phase uniformity might improve the device performance.

1.3.2. GaAs NW VIS PDs

Once the most common techniques and methods to synthesize GaAs NWs have been reviewed, now we illustrate a few examples to demonstrate their potential applications. The use of GaAs NWs in PDs has not been extensively studied and the clear evidence of this statement is found in the reduced number of publications about GaAs NW photoconductivity. The growth of GaAs NWs with high crystalline quality and lengths (L_{NW}) above the micron is still nowadays an important challenge. This issue limits their integration between electrodes defined by optical lithography, forcing to utilize sophisticate and expensive techniques such as FIB to define electrodes covering both NW ends. Therefore, the research about GaAs NW nanodevices should be focused on the development of new assembling techniques, allowing for the manipulation and integration of short NWs between electrodes gap, and new experimental procedures to extend the maximum L_{NW} during growth processes.

The integration of GaAs NWs in electronics involves to make electric contacts in order to connect NW ends and electrodes. During a VLS growth of these NWs, precursor atoms are diffused through the metal catalyst forming a metal/semiconductor interface; in that respect, chemical bonds formed at this interface result in nanoscale metal/NW contacts which might minimize interfacial states. These contacts differ from bulk contacts with a weak physical interaction between post-growth deposited metal electrodes and NWs. Nanoscale contacts have been used to fabricate NW based devices, forming a SB contact at one of the NW ends [95, 96].

The use of GaAs NWs in PDs has been scarcely published in the literature. However, these devices have crucial advantages to foster the improvement of the existing PD technology. First, the formation of metal-semiconductor-metal structures can play an important role in the PD performance. These SB contacts control the sensitivity of the PD because of the SB height strongly depends on the carrier generation and transport [97, 98]. Secondly, the high surface-to-volume ratio of the NWs, contributing to their high photosensitivity and the reduced dimensions of the effective conductive channel, produces both high speed and high G_{photo}.

Thunich et al. [99] studied the optoelectronic properties of PDs based on single *p*-doped GaAs NW grown by Ga-assisted MBE. That NW was suspended between a pair of Au electrodes, i.e. the NW electrically connects both electrodes; thereafter, the attachment of the NW to both electrodes was ensured, depositing two carbon sheets at the NW ends by FIB. Resultant *I-V* characteristics are non-linear and symmetric with respect to the bias voltage, indicating the formation of two SB contacts at both NW ends. Under this stable configuration, it was carried out the optical excitation of different regions along the GaAs NW, observing changes in the device optoelectronic properties. On one hand, there is a photocurrent generated at the SB contacts formed between the GaAs NW and the Au electrodes. Electron-hole pairs generated in the p-type GaAs NW are separated by the local built-in electric field at the SB contacts, resulting in a maximum or a

minimum photocurrent signals when the SB contacts are reverse- or forward-biased, respectively. On the other hand, those regions of the NW located far away the SB contacts are predominantly governed by photoconductance effects. Briefly, the photoconductance observed in the GaAs NW is mainly attributed to the separation of charged carriers. Since the electron-hole pairs are generated, electrons can drift towards the NW surface, creating a surface negative gate, increasing the hole density in the NW bulk, and then widening the conductive volume of the GaAs NW.

Wang [100] fabricated PDs based on a single un-doped GaAs NW, using FIB to contact both NW ends with Pt. The characterization of these devices under a monochromatic laser excitation (λ = 522 nm) shows high G_{photo} of 2×10^3 at a P of 3000 W/m^2; G_{photo} was found to be related to P through an inverse power law $G_{\text{photo}} \sim P^{-k}$, k taking values between 0.65 and 0.89 for biases between 2 and 4 V, respectively. The increase of k with bias indicated that surface defects contribute more to carrier transportation; in addition, k values close to 0.9 confirmed that gain mechanism in the GaAs NW is mainly dominated by the surface. The G_{photo} could be even higher for excitation power intensities even lower, suggesting that GaAs NW based PDs could present higher G_{photo} than those giant values (~10^8) obtained in ZnO NW PDs for P of 0.1 W/m^2 [36].

1.3.3. Other Applications of GaAs NWs

The use of epitaxial techniques allows to synthesize complex structures based on NWs, controlling accurately the composition of the NW. As an example, Gudiksen et al. [101] have successfully grown GaAs/GaP NW superlattices. The direct and indirect band gaps of GaAs and GaP, respectively, make GaAs/GaP NW heterostructure very attractive for the development of nano-photonic applications such as labels for imaging (nano-barcodes). Haraguchi et al. [102] fabricated LEDs based on p-n junction GaAs NWs, showing infrared (IR) light emission. Svensson et al. [103] fabricated GaAs/InGaP core/shell NWs, resulting in nanoscale light sources that might be integrated directly on a Si based platform, playing a major role in future nano-photonics and on-chip optical communications.

The use of GaAs NWs for the development of photovoltaic devices is attractive in terms of lower cost and greater energy conversion efficiency compared to conventional thin film devices. An important advantage of GaAs NWs compared to other nanostructured semiconductors such as Si NWs, is the possibility to tune its band gap in order to better match the solar spectrum. Of particular interest are coaxial structures in which a doped NW core is surrounded by a shell of opposite doping type, forming a core-shell p-n junction [95, 104]. A coaxial p-n junction allows for the carrier extraction across the NW radius (r_{NW}), while a long axial length of the NWs enables high optical absorption.

NW based FETs are fundamental elements for the development of a new generation of nano-electronics. Of particular interest is the ability to control the atomic composition of NW channels; especially, the modulation between p- and n-type conduction is high attractive for enabling the NW complementary metal oxide-semiconductor (CMOS) technology. In this regard, Han et al. [50] fabricated p-n switches based on GaAs NWs, tailoring transport properties of GaAs NWs with different d_{NW}.

1.4. Nanowire Integration in Electronics

While significant advances have been made in synthesis and characterization of NWs, post-growth manipulation and placement of these nanostructures are still a considerable challenge, hindering to realize large-scale complex systems based on NWs. Processing of NWs in optoelectronic and electronic devices is still a key issue, limiting the fabrication yield of commercial devices. The main issue lies within the assembly of NWs between conductive electrodes to form functional structures. Different assembling methods have been developed to manipulate NWs, including dielectrophoresis (DEP) [105-110], drop-casting [100, 111], fluidic alignment [112], nanomanipulation [113, 114], roll contact printing [115, 116], and Langmuir-Blodgett (LB) film technique [117]. Fluidic alignment, roll contact printing transfer, and LB techniques, all offer the ability to align NWs in parallel but do not allow for precise NW placement in functional systems.

1.4.1. Dielectrophoresis

DEP is defined as the kinetic motion of a dielectric material in a non-uniform electric field. DEP is currently an active area of research for manipulation of biological materials such as cells, bacteria, and DNA [118]. During a DEP process, a polarized material is driven towards (positive DEP) or away from (negative DEP) the high electric field region, depending on the complex dielectric permittivity of the particle and its surrounding medium. This technique relies on alternating-current (AC) electric fields to align structures in a given solution at specific sites over large areas, at RT, and without need of expensive tools. In this regard, DEP offers an alternative method to attract NWs onto predefined electrodes.

The manipulation of nanostructures using electric fields has been recognized as a useful technique for separation, alignment and positioning of NPs [119], carbon nanotubes (CNTs) [107], semiconductor NWs [108, 110, 120] and metallic NWs [109]. DEP can be tailored to work with NWs of various conductivities and materials, allowing for integration upon arbitrary substrates, including those that require low temperature processing such as flexible substrates. Since NWs are assembled on predefined electrodes, identifying their final location, integrating them with a larger system becomes straightforward. DEP also enables to integrate NWs of different types into one system, performing a hierarchical series of DEP processes [121].

1.4.2. Drop-Casting on Electrodes

Drop-casting is a low-cost procedure that has been used to integrate rapidly NWs in electronic devices [100, 111]. This method consists in the random deposition of NWs on a sample with pre-fabricated electrodes. For that purpose, NWs are firstly solved in a liquid solvent (typically an organic solvent), sonicated for a few seconds (in order to prevent the formation of clusters), and then a droplet extracted from that solution is casted on the sample with electrodes. Once the solvent is evaporated, some NWs might connect the electrodes. This technique is not time-consuming, however, the fabrication yield is very low and stochastic mainly because of the uncontrolled NW suspension concentration and deposition conditions. In addition, this technique

commonly requires the use of complementary techniques such as FIB or optical lithography in order to improve the stability of the resultant contacts [100].

1.4.3. Fluidic Alignment

The alignment of NWs have been demonstrated using fluidic approach whereby NWs are aligned along the flow direction, controlling not only the NW density but also the separation between NWs [112]. The degree of alignment of NWs can be controlled by the flow rate, observing that higher flow rates produce larger shear forces in the fluid and hence lead to better NW alignment. In addition, the density and spacing between NWs can be tuned by means of the flow duration and are strongly affected by the surface chemical functionality of the substrate.

The use of complementary chemical interactions between chemically patterned substrates and NWs during the assembling process can extend ordering NW arrays over millimeter-scale areas. This approach can be potentially used for organizing NWs into highly integrated device arrays, and thus offers a general pathway for new electronic nano-systems.

1.4.4. Nanomanipulation

The nanomanipulation technique allows to manipulate nanostructures, placing and aligning them at specific positions. This procedure is commonly carried out using an atomic force microscopy (AFM) cantilever to interact with the nanostructures by applying lateral forces of the appropriate magnitude (typically in the pN range) in order to prevent nanostructure harassment [113]. Then, the manipulation process is developed using the AFM system in contact mode. It is interesting to notice that the effect of the tip over the nanostructure might produce irreversible damages, depending on the nanostructure elastic properties, and also the substrate surface properties.

Another example of nanomanipulation was carried out by Peng et al. [114]. They manipulate both CNTs, and Au NWs using the end of a FIB-refined tungsten tip. This tip is capable to contact a single CNT, and to pull it out from the substrate by means of Van der Walls forces. However, this force is insufficient to pick up a Au NW, being necessary to carry out a nano-weld of the Au NW to the tip end; once the NW is separated from the substrate and moved to the new position, the NW and the tip can be separated by FIB cut.

1.4.5. Roll Transfer Printing

Roll transfer printing is suggested as a potential technique to carry out a large-area ordered assembly of NWs with controlled orientation and density. The method consists in the growth of vertically aligned NWs on a donor substrate, and using a roller, NWs are transferred from the donor substrate to a stamp. Finally, NWs are transferred from the stamp to the received substrate with horizontal alignment.

The advantages of this method include high transfer speed, compatibility with the roll-to-roll processes and the ability to work in atmospheric conditions, without the requirement of using extreme expensive and large-scale vacuum systems.

Bai et al. [115] fabricated ZnO NW based UV PDs in large-scale by integrating multiple ZnO NWs connected in parallel via the contact printing method. Chang et al. [116] successfully fabricated a FET based on ZnO NWs using roll transfer printing to assemble the NWs. The excellent characteristics presented by these devices suggest that the roll-transfer printing method, has a good potential for the high-speed fabrication of large-area NW based transistors for the development of high performance flexible devices and flat panel displays.

1.4.6. Langmuir-Blodgett Film Technique

LB film technique is a solution-based approach for organizing NW building blocks over large areas. In this technique, NWs are aligned with controlled nanometer to micrometer scale using the LB film technique [122]; firstly, NWs are suspended in a non-polar solvent, then the suspension is spread on the surface of the aqueous phase in a LB trough and compressed. During compression, NWs become aligned along their long axes with the average spacing (center-to-center distance) controlled by the compression process. Parallel NWs are transferred to planar substrates in a layer-by-layer process to form parallel and even crossed NW structures over centimeter length scales [123]. Since the NWs are transferred to the substrate, photolithography can be used to define patterns into repeating arrays of controlled dimensions [124]. Nanoelectronic devices can be fabricated from these hierarchical NW arrays by using complementary technique such as FIB to define series of parallel finger electrodes, contacting NWs in each of the arrays [117].

Summarizing, this solution-based method offers a flexible pathway for bottom-up assembly of NW materials into integrated and hierarchically organized structures.

1.4.7. NW Growth on Electrodes

Post-growth manipulation techniques described above, show different ways to “pick and place” NWs into electronic circuits. However, some of those techniques might produce NW harassment. In order to prevent NW damages, the integration of NWs in devices has been carried out growing NWs directly on the electrodes, aiming to build a bridge of multiple NWs, connecting a pair of electrodes [47-49]. This procedure prevents NW damage due to the absence of post-growth manipulation, and in general facilities the fabrication steps. However, this method does not allow to control over the resultant number of NWs connecting the electrodes, and has a poor reproducibility due to the random connection formed between NWs.

1.4.8. Bottom-up Growth

The growth of vertically aligned ZnO NWs on crystalline substrates opens the possibility of creating patterned close-packed nanostructures which would give a surface area much larger than that of a flat thin film, and equivalent to the roughness factor typically achieved with NP based films [125]. These unique characteristics are attractive for the development of applications such as sensor arrays, piezoelectric antenna arrays, optoelectronic devices, and interconnects.

Since vertically aligned NWs are successfully grown on a substrate [126, 127], which is typically the bottom electrical contact of the device, different methods are used to form the counter electrode. One possibility consists in the evaporation a metal film on top of a rigid substrate surface. The metal face of that substrate is directly contacted with NWs ends, pressing with clips to ensure the connection between them [125]. However, depending on the NW nature, this device architecture could be fragile, impeding the use of pressure to make a direct contact on top of the NW ends. In order to overcome these inconveniences, ZnO NWs can be conformally surrounded and encapsulated with an insulator layer, ensuring the separation between NWs, and giving both stability and resistance to the total device structure [128]. Thereafter, a chemical/mechanical polishing step is performed to planarize and partially expose the NW ends. Finally, the counter metallic electrode can be evaporated on the NWs ends connecting the whole structure.

Therefore, bottom-up growth allows to integrate NWs in vertical channel devices, using the NW integrated platform for direct device fabrication.

1.5. Work Place

Almost the thesis work was developed in the Microelectronics Laboratory and the Electronics and Semiconductors Laboratory both located in the Applied Physics Department of Universidad Autónoma de Madrid (UAM).

Microelectronics Laboratory has a class 10000 cleanroom divided in three different rooms. Central room is equipped with a:

i) rf-magnetron sputtering system to carry out the growth of Zn_3N_2, ZnO, Zn, Al, Al doped ZnO (AZO), and Cr thin films;

ii) Tempress furnace for the synthesis of ZnO NWs;

iii) Joule evaporator to deposit metal layers, including Al and Au.

The other two rooms are class 1000 and correspond to the lithography and chemical rooms. The latter has some class 100 zones where the cleaning of the substrates (typically Si wafers) is carried out in a high pure ambient. Outside the cleanroom, the Microelectronics Laboratory has a characterization room with some of the systems used in this work:

i) Scanning electron microscopy (SEM)

ii) Karl Suss probe-station

iii) LCR meter

iv) Ellipsometer

v) DEP system

The Electronics and Semiconductor Laboratory has a class 100000 cleanroom where the CBE is located. This cleanroom also has a class 1000 zones to carry out the preparation of the substrates before their transfer to the CBE system. This system is equipped with reflective high-energy electron diffraction (RHEED) and a mass spectrometer, and is used to grow GaAs NWs. Outside the cleanroom, there is a characterization room equipped with some of the techniques used in this work:

i) UV/VIS spectrophotometer

ii) Hall effect measurements (Van der Pauw method)

Other characterization techniques utilized in this work are described below aside with their corresponding institution and location.

Servicio Interdepartamental de Investigación (SIDI, UAM)

i) X-ray diffraction (XRD) analysis

ii) SEM

iii) Energy dispersive X-ray (EDAX) spectroscopy

iv) Attenuated total reflection (ATR)

v) Fourier transform infrared (FTIR) spectroscopy

Centro de Microanálisis de Materiales (CMAM, UAM)

i) Ion beam analysis (IBA): Rutherford backscattering spectrometry (RBS), non-Rutherford backscattering spectrometry (non-RBS), and nuclear reaction analysis (NRA).

The University of Alabama (United States of America, USA)

During a three months stay in The University of Alabama, GaAs NWs grown in the CBE-UAM were characterized by different techniques, including:

i) TEM
ii) EDAX
iii) Raman spectroscopy
iv) Photoluminescence (PL)

Walter Schottky Institute (WSI, Germany)

During a three months stay in the WSI, ZnO NWs grown in the CVT-UAM were characterized by different techniques, including:

i) X-ray photoemission spectroscopy (XPS)
ii) Atomic force microscopy (AFM)
iii) Contact angle measurements
iv) Contact potential difference (CPD)
v) Surface photovoltage (SPV)

1.6. Thesis Motivation and Scopes

1.6.1. Motivation

The main motivation of this thesis work is to investigate new advanced materials such as Zn_3N_2 thin films, ZnO NWs and GaAs NWs, and to integrate them in optoelectronic devices, aiming to improve the existing technology.

Zn_3N_2 Thin Films

Zn_3N_2 properties are strongly affected by the growth conditions, and growth techniques. In this regard, it is still a big challenge to grow Zn_3N_2 layers in a reproducible way. In order to clarify this point, this work thoroughly analyzes resultant properties of Zn_3N_2 layers grown under different conditions in a rf-magnetron sputtering system.

Although optical properties of Zn_3N_2 have been studied in the past, one can find in the literature a wide range of E_g values associated to this material ($1.01 < E_g < 3.2$ eV). The origin of these controversial E_g is still unclear and then needs to be further investigated. It is worth noting that the metastability of Zn_3N_2 in ambient air can hinder the determination of not only the E_g but also other intrinsic properties such as semiconductor type (direct or indirect), optical constants (n, k, …), and electrical properties (mobility, resistivity, …). In this respect, the oxidation rates of Zn_3N_2 films, and the effects of Zn_3N_2 degradation over its properties are still unclear and should be analyzed in depth. In addition, it is an important challenge to find an effective way to prevent the oxidation of Zn_3N_2, ensuring its stability in ambient air.

The high mobility of Zn_3N_2 makes this material a promising substitute for a-Si and poly-Si for the development of high performance TFT displays. This work shows the successful design, fabrication and characterization of a TFT based on Zn_3N_2 as channel layer.

ZnO NWs

Optical response of ZnO NWs has been previously analyzed [36, 38, 43, 129]; however, the relationship between the G_{photo}, cut-off wavelength, response time, and the NW dimensions has not been studied in detail. For that reason, the effects of ZnO NW diameter on the optoelectronic properties of the UV PDs are analyzed in this work. Aside the dimensions, the electrical conductivity of ZnO NWs is strongly influenced by the surface states [36]; adsorption/desorption mechanisms of oxygen species are reported to be the main factors, governing the conductive volume of these NWs. In this regard, chemical surface properties of the ZnO NWs are expected to have a strong impact on their conductivity. This work shows different physical (hydroxylation) and chemical (silanization) treatments to create a stable surface coverage of ZnO NWs; electrical and surface properties of NWs are analyzed after each surface treatment.

GaAs NWs

GaAs NWs have been successfully grown by Ga-assisted VLS using different techniques [80, 82, 84, 87]; however, this kind of growth is still unclear in CBE. For that reason, we analyze resultant properties of GaAs NWs grown by Ga-assisted CBE as a function of growth conditions. Ga-assisted growths are commonly linked to the use of crystalline substrates covered with surface oxide because of both: i) the good diffusion of Ga over the oxide layer, and ii) the existence of pinholes where Ga droplets can nucleate. The formation of Ga droplets is mandatory for the successful growth of GaAs NWs through VLS mechanism. In MBE, the oxide nature and critical thickness that allow for the Ga droplet formation have been studied in depth [130]. In CBE, the low cracking efficiency of metalorganic gas precursors on oxidized surfaces is an important challenge that hinders the formation of Ga droplets. In that respect, this work analyzes different methods to prepare Si(111) substrates in order to enable the growth of GaAs NWs with high aspect ratio and crystal quality.

NW Integration in Devices

The nanometric size of NWs hinders their integration in devices. The control over the number of assembled NWs is still an important challenge that makes difficult the characterization of a single NW. The integration of NWs in devices is commonly linked to the use of expensive, time-consuming or complex techniques such as FIB, or nanomanipulation with AFM cantilevers. Other techniques such as contact printing, fluidic alignment and DEP are emerging as a low-cost and easy of developing alternatives for the integration of NWs in devices. DEP is highlighted among all of these techniques because allows to trap, and to align rapidly NWs at specific sites.

This work investigates the integration of ZnO and GaAs NWs between conductive electrodes using DEP. The assembling efficiency of DEP is studied as a function of geometries and width of the inter-electrode pitch, and DEP parameters (AC frequency and amplitude). Since the DEP attractive force (positive DEP conditions) depends on the electrical properties of both NW and surrounding medium, the study of both ZnO and GaAs NW alignment as a function of DEP conditions needs to be further clarified and understood. The selectivity of DEP to NWs with different dimensions, is also addressed in this work.

Photodetection

This work investigates new ways to overcome existing limitations for the development of PDs. Advanced materials such as ZnO and GaAs NWs are proposed as active elements in UV and VIS PDs, respectively. Their excellent optoelectronic properties are expected to improve R_{photo}, G_{photo}, recovery times, selectivity, and power consumption of existing PDs. In addition, the fabrication of PDs with high detection in both UV/VIS ranges could be possible by integrating different materials with high sensitivity in each spectral range. Although the reduction of the material size allows a higher integration in portable nano-chips, the manipulation of nanostructures such as NWs is still a challenge that needs to be further investigated.

1.6.2. Scopes

Briefly, this work aims to characterize properties of Zn_3N_2 films grown by rf-magnetron sputtering, ZnO NWs grown by CVT, and GaAs NWs grown by CBE.

The research carried out about Zn_3N_2 thin films aims to optimize nitride electrical properties in order to fabricate high mobility TFTs.

The research carried out about ZnO and GaAs NWs aims to develop a reproducible method to grow high aspect ratio NWs, facilitating their later integration in devices.

This work aims to develop a technique to integrate NWs between conductive electrodes that allows to control not only the number of assembled NWs but also the dimensions of trapped NWs.

This work also aims to study the photoconductivity of single ZnO and GaAs NWs as a function of the NW dimensions. In the case of ZnO NWs, the electrical conductivity is also expected to be analyzed after different physical and chemical treatments, involving hydroxylation and silanization.

For the sake of clarity, the scopes of this thesis work are further described below:

Zn_3N_2 Thin Films

- The growth Zn_3N_2 thin films by rf-magnetron sputtering deposited under different conditions (substrate temperature, gas flux composition, rf-power, …).
- The characterization of the Zn_3N_2 thin films properties (morphology, electrical conductivity, optical response, crystalline structure, chemical composition, …).
- The determination of Zn_3N_2 thin films properties such as energy band gap, semiconductor type, and optical constants.
- The optimization of Zn_3N_2 thin film electron mobility through the growth conditions.
- The study of the Zn_3N_2 metastability in air ambient conditions over time, including the determination of the oxidation rate, and the development of a prevention method to inhibit Zn_3N_2 oxidation.
- The study of different procedures to force the rapid transformation of Zn_3N_2 into ZnO.
- The design, fabrication and characterization of TFTs based on Zn_3N_2.

ZnO NWs

- The growth of high aspect ratio ZnO NWs by CVT.
- The control over the resultant ZnO NW aspect ratio as a function of the growth conditions.
- The characterization of the ZnO NW properties (morphology, electrical conductivity, crystal structure, chemical composition, …).
- The characterization of ZnO NW surface and electrical properties after physical and chemical surface treatments, involving hydroxylation and silanization.
- The integration of ZnO NWs between conductive electrodes by different techniques, including DEP, and drop-casting.

- The study of DEP efficiency as a function of DEP conditions (AC frequency and amplitude, electrode material and geometry, …).
- The optimization of DEP procedure (NW solution concentration and DEP conditions) in order to assemble a single ZnO NW between a pair of conductive electrodes.
- The characterization of the optoelectronic properties of a single ZnO NW, including *I*/*V* characteristics measured in dark, R_{photo}, G_{photo}, response time, cut-off wavelength, … as a function of the NW dimensions.

GaAs NWs

- The growth of high aspect ratio GaAs NWs by Ga-assisted CBE on oxidized Si(111) substrates.
- The development of a preparation procedure for Si(111) substrates that allows the reproducible and feasible growth of GaAs NWs in CBE.
- The control over the resultant NW aspect ratio through the growth conditions (substrate temperature, V/III flux ratio, …).
- The optimization of both substrate preparation and growth conditions in order to prevent the nucleation of parasitic GaAs nanocrystals and nanotraces, promoting the only growth of GaAs NWs.
- The optimization of growth conditions, aiming to obtain pure zinc blende (ZB) phase GaAs NWs.
- The characterization of the GaAs NWs main properties (morphology, electrical conductivity, optical response, crystal structure, chemical composition,…).
- The integration of a single GaAs NW between a pair of conductive electrodes.
- The study a single GaAs NW photoconductivity.

1.7. Thesis Content

This thesis work is divided in 8 chapters, including an introduction about the state of the art of existing applications based on Zn_3N_2 thin films, ZnO NWs, and GaAs NWs, the thesis motivation and scopes of this research (Chapter 1).

Chapter 2 is divided in 3 sections: Zn_3N_2 (section 2.1), ZnO (section 2.2) and GaAs (section 2.3).

Section 2.1 contains the most relevant information about growth procedures of Zn_3N_2 thin films, including studies about Zn_3N_2 properties (crystalline structure, electrical conductivity, metastability, etc.).

Section 2.2 describes different growth mechanisms of ZnO NWs based on vapor phase procedures, and includes ZnO NW properties analyzed by different characterization techniques.

Section 2.3 shows common growth mechanisms of NWs based on the bottom-up approach; the section also presents the most extended techniques to grow GaAs NWs, as well as, characterization studies that show main properties of GaAs NWs.

Chapter 3 describes the growth techniques used in this work: magnetron sputtering (section 3.1), CVT (section 3.2), and CBE (section 3.3) to synthesize Zn_3N_2 thin films, ZnO NWs, and GaAs NWs, respectively.

Chapter 4 describes the characterization techniques used in this work, including IBA (section 4.1), SEM, and EDAX (section 4.2), TEM (section 4.3), resistivity, Hall effect, CPD, SPV, and spectral response measurements (section 4.4), XRD (section 4.5), RHEED (section 4.6), mass spectrometry (section 4.7), SE, Raman spectroscopy, PL, spectrophotometry, and XPS (section 4.8).

Chapter 5 contains the main results obtained in this work about the growth and characterization of Zn_3N_2 thin films and their use in optoelectronic applications. The chapter is divided in three sections: zinc nitride properties (section 5.1), oxidation mechanism of zinc nitride layers (section 5.2) and transistors based on zinc nitride as channel layer (section 5.3).

Section 5.1 describes the experimental growth produce (5.1.1) and characterization of Zn_3N_2 layers, including compositional (5.1.2), morphological (5.1.3), structural (5.1.4), optical (5.1.5) and electrical (5.1.6) analysis as function of the growth conditions.

Section 5.2 presents a thorough study of zinc nitride oxidation mechanism when is storage in air ambient conditions. Properties such as chemical composition (5.2.1), optical constants (5.2.2), electrical conduction (5.2.3), crystalline structure (5.2.4) are analyzed overtime. In the subsection 5.2.5, it is described a cost-effective and novel method to carry out a rapid and localized transformation of Zn_3N_2 compound into ZnO by using electric arcs applied through a micrometric metallic tip.

Section 5.3 shows the design, fabrication and characterization of TFTs (5.3.1) and photo-transistors (5.3.2) based on zinc nitride as channel layer.

Chapter 6 describes the growth and characterization of ZnO NWs and their integration in UV PDs. The chapter is divided in five sections: synthesis of ZnO NWs by CVT (section 6.1), their characterization (section 6.2), their integration in optoelectronics (section 6.3), characterization of ZnO NW based UV PDs (section 6.4), and characterization of ZnO NWs after different surface treatments (section 6.5).

Section 6.1 describes the experimental procedure to grow both ZnO tetrapods (TPs) (6.1.1) and NWs (6.1.2). Both subsections present SEM-morphological characterization of resultant nanostructures grown at different conditions (temperature, gas flux, substrates, …).

Section 6.2 presents the main results about the optical (6.2.1), compositional (6.2.2) and structural (6.2.3) characterization of ZnO NWs.

Section 6.3 shows different integration procedures of ZnO NWs between conductive electrodes, allowing for their electrical characterization. This section includes a description of the NW suspension preparation (6.3.1), and two methods to assemble NWs between conductive electrodes: drop-casting (6.3.2) and DEP (6.3.3). In the case of DEP, the assembling theory is further explained, showing the strong influence of factors such as electrode composition and geometry, solvent electrical properties, and DEP conditions (AC frequency and amplitude), on the resultant assembling efficiency.

Section 6.4 presents the electro-optical characterization of ZnO NW PDs fabricated by DEP, including electrical characteristics, R_{photo}, G_{photo}, and response time.

Section 6.5 describes hydroxylation and silanization of ZnO NW surface (6.5.1), and their effects on ZnO NW surface properties (6.5.2), involving changes on the surface band bending, surface wettability, ...

Chapter 7 describes the growth of GaAs NWs by CBE. The chapter is device in three sections: growth of GaAs NWs by Ga-assisted CBE (section 7.1), characterization of GaAs NW properties (section 7.2), and integration of GaAs NWs in PDs (section 7.3).

Section 7.1 explains the growth of GaAs NWs under a bottom-up approach through the Ga-assisted VLS mechanism in CBE. This section includes a description of different protocols developed in this work to prepare Si(111) substrates using different buffer solutions to etch substrate surface, as well as, a characterization of the resultant surface oxide (7.1.1). Subsection 7.1.2 describes in general terms a standard growth of GaAs NWs by Ga-assisted CBE. Subsection 7.1.3 analyze the effects of substrate preparation and growth parameters such as substrate annealing, T_s, V/III flux ratio, … on the GaAs NW morphological and structural properties.

Section 7.2 studies the resultant GaAs NW properties, including the analysis of NW morphology by SEM (7.2.1), chemical composition by EDAX, and crystalline structure by RHEED, TEM, and Raman (7.2.2).

Section 7.3 describes the integration of GaAs NWs between conductive electrodes using DEP. In this section, it is included different studies about the assembling efficiency of GaAs NWs between electrodes as a function of the DEP conditions, i.e. magnitude and frequency of the AC electric field (7.3.1). Electrical characteristics of resultant devices were measured in dark and under illumination, showing important differences between GaAs NWs ended with a Ga droplet and those NWs without a Ga droplet (7.3.2).

Chapter 8 shows the general conclusions of this work, summarizing most relevant results obtained around the growth and characterization of Zn_3N_2 thin films, ZnO NWs and GaAs NWs, as well as their integration in optoelectronic devices. The chapter also includes future work around these materials.

Finally, appendix A presents publications and conference contributions resulting from this work.

REFERENCES

[1] R. Juza and H. Hahn, "Über die Kristallstrukturen von Zn3N2, Cd3N2 und Ge3N4. Metallamide und Metallnitride. IX. Mitteilung," *Zeitschrift für anorganische und allgemeine Chemie,* vol. 244, pp. 125-132, 1940.

[2] K. Kuriyama, Y. Takahashi, and F. Sunohara, "Optical band gap of Zn 3 N 2 films," *Physical Review B,* vol. 48, p. 2781, 1993.

[3] R. Ayouchi, C. Casteleiro, L. Santos, and R. Schwarz, "RF-plasma assisted PLD growth of Zn3N2 thin films," *physica status solidi (c),* vol. 7, pp. 2294-2297, 2010.

[4] M. Futsuhara, K. Yoshioka, and O. Takai, "Structural, electrical and optical properties of zinc nitride thin films prepared by reactive rf magnetron sputtering," *Thin Solid Films,* vol. 322, pp. 274-281, 1998.

[5] T. Yang, Z. Zhang, Y. Li, M. Lv, S. Song, Z. Wu*, et al.*, "Structural and optical properties of zinc nitride films prepared by rf magnetron sputtering," *Applied Surface Science,* vol. 255, pp. 3544-3547, 2009.

[6] K. Toyoura, H. Tsujimura, T. Goto, K. Hachiya, R. Hagiwara, and Y. Ito, "Optical properties of zinc nitride formed by molten salt electrochemical process," *Thin Solid Films,* vol. 492, pp. 88-92, 2005.

[7] T. Suda and K. Kakishita, "Band-gap energy and electron effective mass of polycrystalline Zn3N2," *Journal of Applied Physics,* vol. 99, p. 076101, 2006.

[8] R. Long, Y. Dai, L. Yu, B. Huang, and S. Han, "Atomic geometry and electronic structure of defects in Zn 3 N 2," *Thin Solid Films,* vol. 516, pp. 1297-1301, 2008.

[9] F. Zong, H. Ma, W. Du, J. Ma, X. Zhang, H. Xiao*, et al.*, "Optical band gap of zinc nitride films prepared on quartz substrates from a zinc nitride target by reactive rf magnetron sputtering," *Applied surface science,* vol. 252, pp. 7983-7986, 2006.

[10] W. Du, F. Zong, H. Ma, J. Ma, M. Zhang, X. Feng*, et al.*, "Optical band gap of zinc nitride films prepared by reactive rf magnetron sputtering," *Crystal Research and Technology,* vol. 41, pp. 889-892, 2006.

[11] E. Aperathitis, V. Kambilafka, and M. Modreanu, "Properties of n-type ZnN thin films as channel for transparent thin film transistors," *Thin Solid Films,* vol. 518, pp. 1036-1039, 2009.

[12] V. Kambilafka, A. Kostopoulos, M. Androulidaki, K. Tsagaraki, M. Modreanu, and E. Aperathitis, "Transparent p/n diode device from a single zinc nitride sputtering target," *Thin Solid Films,* vol. 520, pp. 1202-1206, 2011.

[13] B. Li, Y. Liu, Z. Zhi, D. Shen, Y. Lu, J. Zhang*, et al.*, "Optical properties and electrical characterization of p-type ZnO thin films prepared by thermally oxiding Zn3N2 thin films," *Journal of materials research,* vol. 18, pp. 8-13, 2003.

[14] C. Wang, Z. Ji, K. Liu, Y. Xiang, and Z. Ye, "p-Type ZnO thin films prepared by oxidation of Zn 3 N 2 thin films deposited by DC magnetron sputtering," *Journal of Crystal Growth,* vol. 259, pp. 279-281, 2003.

[15] E. Kaminska, A. Piotrowska, J. Kossut, A. Barcz, R. Butkute, W. Dobrowolski*, et al.*, "Transparent p-type ZnO films obtained by oxidation of sputter-deposited Zn 3 N 2," *Solid state communications,* vol. 135, pp. 11-15, 2005.

[16] V. Kambilafka, P. Voulgaropoulou, S. Dounis, E. Iliopoulos, M. Androulidaki, V. Šály*, et al.*, "Thermal oxidation of n-type ZnN films made by rf-sputtering from a zinc nitride target, and their conversion into p-type films," *Superlattices and Microstructures,* vol. 42, pp. 55-61, 2007.

[17] P. F. Carcia, R. S. McLean, M. H. Reilly, and G. Nunes, "Transparent ZnO thin-film transistor fabricated by rf magnetron sputtering," *Applied Physics Letters,* vol. 82, pp. 1117-1119, 2003.

[18] R. B. Wehrspohn, M. J. Powell, and S. C. Deane, "Kinetics of defect creation in amorphous silicon thin film transistors," *Journal of Applied Physics,* vol. 93, pp. 5780-5788, 2003.

[19] A. Corradetti, R. Leoni, R. Carluccio, G. Fortunato, C. Reita, F. Plais*, et al.*, "Evidence of carrier number fluctuation as origin of 1/f noise in polycrystalline silicon thin film transistors," *Applied Physics Letters,* vol. 67, pp. 1730-1732, 1995.

[20] C. García Núñez, J. L. Pau, M. J. Hernández, M. Cervera, E. Ruiz, and J. Piqueras, "On the zinc nitride properties and the unintentional incorporation of oxygen," *Thin Solid Films,* vol. 520, pp. 1924-1929, 2012.

[21] D. C. Look, G. C. Farlow, P. Reunchan, S. Limpijumnong, S. Zhang, and K. Nordlund, "Evidence for native-defect donors in n-type ZnO," *Physical review letters,* vol. 95, p. 225502, 2005.

[22] B. Xiang, P. Wang, X. Zhang, S. A. Dayeh, D. P. R. Aplin, C. Soci*, et al.*, "Rational Synthesis of p-Type Zinc Oxide Nanowire Arrays Using Simple Chemical Vapor Deposition," *Nano Letters,* vol. 7, pp. 323-328, 2007/02/01 2007.

[23] W. Lee, M.-C. Jeong, and J.-M. Myoung, "Optical characteristics of arsenic-doped ZnO nanowires," *Applied Physics Letters,* vol. 85, pp. 6167-6169, 2004.

[24] X. Yang, A. Wolcott, G. Wang, A. Sobo, R. C. Fitzmorris, F. Qian*, et al.*, "Nitrogen-Doped ZnO Nanowire Arrays for Photoelectrochemical Water Splitting," *Nano Letters,* vol. 9, pp. 2331-2336, 2009/06/10 2009.

[25] A. Kobayashi, O. F. Sankey, and J. D. Dow, "Deep energy levels of defects in the wurtzite semiconductors AlN, CdS, CdSe, ZnS, and ZnO," *Physical Review B,* vol. 28, p. 946, 1983.

[26] Ü. Özgür, Y. I. Alivov, C. Liu, A. Teke, M. A. Reshchikov, S. Doğan*, et al.*, "A comprehensive review of ZnO materials and devices," *Journal of Applied Physics,* vol. 98, p. 041301, 2005.

[27] E. Monroy, F. Omnès, and F. Calle, "Wide-bandgap semiconductor ultraviolet photodetectors," *Semiconductor Science and Technology,* vol. 18, p. R33, 2003.

[28] F. Omnès, E. Monroy, E. Muñoz, and J.-L. Reverchon, "Wide bandgap UV photodetectors: A short review of devices and applications," in *Integrated Optoelectronic Devices 2007*, 2007, pp. 64730E-64730E-15.

[29] M. Razeghi and A. Rogalski, "Semiconductor ultraviolet detectors," *Journal of Applied Physics,* vol. 79, pp. 7433-7473, 1996.

[30] E. Munoz, E. Monroy, J. Garrido, I. Izpura, F. Sanchez, M. Sánchez-Garcıa*, et al.*, "Photoconductor gain mechanisms in GaN ultraviolet detectors," *Applied physics letters,* vol. 71, pp. 870-872, 1997.

[31] M. A. Khan, J. N. Kuznia, D. T. Olson, J. M. Van Hove, M. Blasingame, and L. F. Reitz, "High-responsivity photoconductive ultraviolet sensors based on insulating single-crystal GaN epilayers," *Applied Physics Letters,* vol. 60, pp. 2917-2919, 1992.

[32] R.-S. Chen, H.-Y. Chen, C.-Y. Lu, K.-H. Chen, C.-P. Chen, L.-C. Chen*, et al.*, "Ultrahigh photocurrent gain in m-axial GaN nanowires," *Applied Physics Letters,* vol. 91, p. 223106, 2007.

[33] B. Shen, K. Yang, L. Zang, Z.-z. Chen, P. Chen, R. Zhang*, et al.*, "Study of photocurrent properties of GaN ultraviolet photoconductor grown on 6H-SiC substrate," *Japanese journal of applied physics,* vol. 38, p. 767, 1999.

[34] Y. Liu, C. Gorla, S. Liang, N. Emanetoglu, Y. Lu, H. Shen*, et al.*, "Ultraviolet detectors based on epitaxial ZnO films grown by MOCVD," *Journal of Electronic Materials,* vol. 29, pp. 69-74, 2000.

[35] D. Zhang and D. Brodie, "Photoresponse of polycrystalline ZnO films deposited by rf bias sputtering," *Thin Solid Films,* vol. 261, pp. 334-339, 1995.

[36] C. Soci, A. Zhang, B. Xiang, S. A. Dayeh, D. Aplin, J. Park*, et al.*, "ZnO nanowire UV photodetectors with high internal gain," *Nano letters,* vol. 7, pp. 1003-1009, 2007.

[37] J. He, P. Chang, C. Chen, and K. Tsai, "Electrical and optoelectronic characterization of a ZnO nanowire contacted by focused-ion-beam-deposited Pt," *Nanotechnology,* vol. 20, p. 135701, 2009.

[38] H. Kind, H. Yan, B. Messer, M. Law, and P. Yang, "Nanowire ultraviolet photodetectors and optical switches," *Advanced materials,* vol. 14, p. 158, 2002.

[39] Y. Hu, J. Zhou, P. H. Yeh, Z. Li, T. Y. Wei, and Z. L. Wang, "Supersensitive, Fast-Response Nanowire Sensors by Using Schottky Contacts," *Advanced Materials,* vol. 22, pp. 3327-3332, 2010.

[40] G. Cheng, X. Wu, B. Liu, B. Li, X. Zhang, and Z. Du, "ZnO nanowire Schottky barrier ultraviolet photodetector with high sensitivity and fast recovery speed," *Applied Physics Letters,* vol. 99, p. 203105, 2011.

[41] H. Chang, Z. Sun, K. Y.-F. Ho, X. Tao, F. Yan, W.-M. Kwok*, et al.*, "A highly sensitive ultraviolet sensor based on a facile in situ solution-grown ZnO nanorod/graphene heterostructure," *Nanoscale,* vol. 3, pp. 258-264, 2011.

[42] X.-W. Fu, Z.-M. Liao, Y.-B. Zhou, H.-C. Wu, Y.-Q. Bie, J. Xu*, et al.*, "Graphene/ZnO nanowire/graphene vertical structure based fast-response ultraviolet photodetector," *Applied Physics Letters,* vol. 100, p. 223114, 2012.

[43] J. Zhou, Y. Gu, Y. Hu, W. Mai, P.-H. Yeh, G. Bao*, et al.*, "Gigantic enhancement in response and reset time of ZnO UV nanosensor by utilizing Schottky contact and surface functionalization," *Applied Physics Letters,* vol. 94, p. 191103, 2009.

[44] C. S. Lao, M.-C. Park, Q. Kuang, Y. Deng, A. K. Sood, D. L. Polla, *et al.*, "Giant enhancement in UV response of ZnO nanobelts by polymer surface-functionalization," *Journal of the American Chemical Society,* vol. 129, pp. 12096-12097, 2007.

[45] D. Lin, H. Wu, W. Zhang, H. Li, and W. Pan, "Enhanced UV photoresponse from heterostructured Ag–ZnO nanowires," *Applied Physics Letters,* vol. 94, p. 172103, 2009.

[46] K. Liu, M. Sakurai, M. Liao, and M. Aono, "Giant improvement of the performance of ZnO nanowire photodetectors by Au nanoparticles," *The Journal of Physical Chemistry C,* vol. 114, pp. 19835-19839, 2010.

[47] K. Keem, H. Kim, G.-T. Kim, J. S. Lee, B. Min, K. Cho, *et al.*, "Photocurrent in ZnO nanowires grown from Au electrodes," *Applied Physics Letters,* vol. 84, pp. 4376-4378, 2004.

[48] Y. Li, F. Della Valle, M. Simonnet, I. Yamada, and J.-J. Delaunay, "High-performance UV detector made of ultra-long ZnO bridging nanowires," *Nanotechnology,* vol. 20, p. 045501, 2009.

[49] P.-Y. Yang, J.-L. Wang, W.-C. Tsai, S.-J. Wang, J.-C. Lin, I.-C. Lee, *et al.*, "Photoresponse of hydrothermally grown lateral ZnO nanowires," *Thin Solid Films,* vol. 518, pp. 7328-7332, 2010.

[50] L. Guo, H. Zhang, D. Zhao, B. Li, Z. Zhang, M. Jiang, *et al.*, "High responsivity ZnO nanowires based UV detector fabricated by the dielectrophoresis method," *Sensors and Actuators B: Chemical,* vol. 166, pp. 12-16, 2012.

[51] Z. Zhu, T.-L. Chen, Y. Gu, J. Warren, and R. M. Osgood, "Zinc oxide nanowires grown by vapor-phase transport using selected metal catalysts: a comparative study," *Chemistry of materials,* vol. 17, pp. 4227-4234, 2005.

[52] S.-W. Kim, S. Fujita, and S. Fujita, "ZnO nanowires with high aspect ratios grown by metalorganic chemical vapor deposition using gold nanoparticles," *Applied Physics Letters,* vol. 86, p. 153119, 2005.

[53] R. Guo, J. Nishimura, M. Matsumoto, D. Nakamura, and T. Okada, "Catalyst-free synthesis of vertically-aligned ZnO nanowires by nanoparticle-assisted pulsed laser deposition," *Applied Physics A,* vol. 93, pp. 843-847, 2008.

[54] M. H. Huang, Y. Wu, H. Feick, N. Tran, E. Weber, and P. Yang, "Catalytic growth of zinc oxide nanowires by vapor transport," *Advanced Materials,* vol. 13, pp. 113-116, 2001.

[55] L. S. Yeol, "Controllability of threshold voltage of ZnO nanowire field effect transistors by manipulating nanowire diameter by varying the catalyst thickness," *Transactions on Electrical and Electronic Materials,* vol. 14, pp. 156-159, 2013.

[56] J. Li, Q. Zhang, H. Peng, H. O. Everitt, L. Qin, and J. Liu, "Diameter-Controlled Vapor− Solid Epitaxial Growth and Properties of Aligned ZnO Nanowire Arrays," *The Journal of Physical Chemistry C,* vol. 113, pp. 3950-3954, 2009.

[57] Y. Zhang, A. Kolmakov, S. Chretien, H. Metiu, and M. Moskovits, "Control of catalytic reactions at the surface of a metal oxide nanowire by manipulating electron density inside it," *Nano Letters,* vol. 4, pp. 403-407, 2004.

[58] F. Chaabouni, M. Abaab, and B. Rezig, "Metrological characteristics of ZnO oxygen sensor at room temperature," *Sensors and Actuators B: chemical,* vol. 100, pp. 200-204, 2004.

[59] Z. Fan, D. Wang, P.-C. Chang, W.-Y. Tseng, and J. G. Lu, "ZnO nanowire field-effect transistor and oxygen sensing property," *Applied Physics Letters,* vol. 85, pp. 5923-5925, 2004.

[60] A. Fulati, S. M. U. Ali, M. H. Asif, M. Willander, C. Brännmark, P. Strålfors*, et al.*, "An intracellular glucose biosensor based on nanoflake ZnO," *Sensors and Actuators B: Chemical,* vol. 150, pp. 673-680, 2010.

[61] S. M. Usman Ali, O. Nur, M. Willander, and B. Danielsson, "Glucose detection with a commercial MOSFET using a ZnO nanowires extended gate," *Nanotechnology, IEEE Transactions on,* vol. 8, pp. 678-683, 2009.

[62] X. Liu, Q. Hu, Q. Wu, W. Zhang, Z. Fang, and Q. Xie, "Aligned ZnO nanorods: a useful film to fabricate amperometric glucose biosensor," *Colloids and Surfaces B: Biointerfaces,* vol. 74, pp. 154-158, 2009.

[63] Z. H. Ibupoto, S. M. U. Ali, K. Khun, C. O. Chey, O. Nur, and M. Willander, "ZnO nanorods based enzymatic biosensor for selective determination of penicillin," *Biosensors,* vol. 1, pp. 153-163, 2011.

[64] J. C. Johnson, H. Yan, P. Yang, and R. J. Saykally, "Optical cavity effects in ZnO nanowire lasers and waveguides," *The Journal of Physical Chemistry B,* vol. 107, pp. 8816-8828, 2003.

[65] P.-S. Cho, K.-W. Kim, and J.-H. Lee, "NO2 sensing characteristics of ZnO nanorods prepared by hydrothermal method," *Journal of electroceramics,* vol. 17, pp. 975-978, 2006.

[66] Z. Fan and J. G. Lu, "Gate-refreshable nanowire chemical sensors," *Applied Physics Letters,* vol. 86, p. 123510, 2005.

[67] O. Lupan, V. Ursaki, G. Chai, L. Chow, G. Emelchenko, I. Tiginyanu*, et al.*, "Selective hydrogen gas nanosensor using individual ZnO nanowire with fast response at room temperature," *Sensors and Actuators B: Chemical,* vol. 144, pp. 56-66, 2010.

[68] H.-T. Wang, B. Kang, F. Ren, L. Tien, P. Sadik, D. Norton*, et al.*, "Hydrogen-selective sensing at room temperature with ZnO nanorods," *Applied Physics Letters,* vol. 86, p. 243503, 2005.

[69] X.-H. Wang, Y.-F. Ding, J. Zhang, Z.-Q. Zhu, S.-Z. You, S.-Q. Chen*, et al.*, "Humidity sensitive properties of ZnO nanotetrapods investigated by a quartz crystal microbalance," *Sensors and Actuators B: Chemical,* vol. 115, pp. 421-427, 2006.

[70] C. Wang, X. Chu, and M. Wu, "Detection of H 2 S down to ppb levels at room temperature using sensors based on ZnO nanorods," *Sensors and Actuators B: Chemical,* vol. 113, pp. 320-323, 2006.

[71] J. Yi, J. M. Lee, and W. I. Park, "Vertically aligned ZnO nanorods and graphene hybrid architectures for high-sensitive flexible gas sensors," *Sensors and Actuators B: Chemical,* vol. 155, pp. 264-269, 2011.

[72] Z. L. Wang and J. Song, "Piezoelectric nanogenerators based on zinc oxide nanowire arrays," *Science,* vol. 312, pp. 242-246, 2006.

[73] S. N. Cha, J. S. Seo, S. M. Kim, H. J. Kim, Y. J. Park, S. W. Kim*, et al.*, "Sound-Driven Piezoelectric Nanowire-Based Nanogenerators," *Advanced materials,* vol. 22, pp. 4726-4730, 2010.

[74] J. O. Hwang, D. H. Lee, J. Y. Kim, T. H. Han, B. H. Kim, M. Park, *et al.*, "Vertical ZnO nanowires/graphene hybrids for transparent and flexible field emission," *Journal of Materials Chemistry,* vol. 21, pp. 3432-3437, 2011.

[75] Q. Zhao, C.-K. Huang, R. Zhu, J. Xu, L. Chen, and D. Yu, "2D planar field emission devices based on individual ZnO nanowires," *Solid State Communications,* vol. 151, pp. 1650-1653, 2011.

[76] X. Wang, J. Zhou, J. Song, J. Liu, N. Xu, and Z. L. Wang, "Piezoelectric field effect transistor and nanoforce sensor based on a single ZnO nanowire," *Nano letters,* vol. 6, pp. 2768-2772, 2006.

[77] S. S. Kwon, W. K. Hong, G. Jo, J. Maeng, T. W. Kim, S. Song, *et al.*, "Piezoelectric Effect on the Electronic Transport Characteristics of ZnO Nanowire Field-Effect Transistors on Bent Flexible Substrates," *Advanced Materials,* vol. 20, pp. 4557-4562, 2008.

[78] C. Ma, Z. Zhou, H. Wei, Z. Yang, Z. Wang, and Y. Zhang, "Rapid large-scale preparation of ZnO nanowires for photocatalytic application," *Nanoscale research letters,* vol. 6, pp. 1-5, 2011.

[79] T.-J. Kuo, C.-N. Lin, C.-L. Kuo, and M. H. Huang, "Growth of ultralong ZnO nanowires on silicon substrates by vapor transport and their use as recyclable photocatalysts," *Chemistry of Materials,* vol. 19, pp. 5143-5147, 2007.

[80] C. Colombo, D. Spirkoska, M. Frimmer, G. Abstreiter, and A. F. i Morral, "Ga-assisted catalyst-free growth mechanism of GaAs nanowires by molecular beam epitaxy," *Physical Review B,* vol. 77, p. 155326, 2008.

[81] J. Harmand, M. Tchernycheva, G. Patriarche, L. Travers, F. Glas, and G. Cirlin, "GaAs nanowires formed by Au-assisted molecular beam epitaxy: Effect of growth temperature," *Journal of Crystal Growth,* vol. 301, pp. 853-856, 2007.

[82] M. Plante and R. LaPierre, "Control of GaAs nanowire morphology and crystal structure," *Nanotechnology,* vol. 19, p. 495603, 2008.

[83] M. Plante and R. LaPierre, "Au-assisted growth of GaAs nanowires by gas source molecular beam epitaxy: Tapering, sidewall faceting and crystal structure," *Journal of Crystal Growth,* vol. 310, pp. 356-363, 2008.

[84] J. Noborisaka, J. Motohisa, and T. Fukui, "Catalyst-free growth of GaAs nanowires by selective-area metalorganic vapor-phase epitaxy," *Applied Physics Letters,* vol. 86, p. 213102, 2005.

[85] A. Bouravleuv, N. Sibirev, G. Statkute, G. Cirlin, H. Lipsanen, and V. Dubrovskii, "Influence of substrate temperature on the shape of GaAs nanowires grown by Au-assisted MOVPE," *Journal of Crystal Growth,* vol. 312, pp. 1676-1682, 2010.

[86] H. J. Joyce, Q. Gao, H. H. Tan, C. Jagadish, Y. Kim, X. Zhang, *et al.*, "Twin-free uniform epitaxial GaAs nanowires grown by a two-temperature process," *Nano letters,* vol. 7, pp. 921-926, 2007.

[87] C. García Núñez, A. F. Braña, J. L. Pau, D. Ghita, B. J. García, G. Shen, *et al.*, "Pure zincblende GaAs nanowires grown by Ga-assisted chemical beam epitaxy," *Journal of Crystal Growth,* vol. 372, pp. 205-212, 2013.

[88] B. Ohlsson, M. Björk, M. Magnusson, K. Deppert, L. Samuelson, and L. Wallenberg, "Size-, shape-, and position-controlled GaAs nano-whiskers," *Applied Physics Letters,* vol. 79, pp. 3335-3337, 2001.

[89] G. E. Cirlin, V. G. Dubrovskii, I. P. Soshnikov, N. V. Sibirev, Y. B. Samsonenko, A. D. Bouravleuv*, et al.*, "Critical diameters and temperature domains for MBE growth of III–V nanowires on lattice mismatched substrates," *physica status solidi (RRL) – Rapid Research Letters,* vol. 3, pp. 112-114, 2009.

[90] R. S. Wagner and W. C. Ellis, "VAPOR-LIQUID-SOLID MECHANISM OF SINGLE CRYSTAL GROWTH," *Applied Physics Letters,* vol. 4, pp. 89-90, 1964.

[91] F. Glas, "Critical dimensions for the plastic relaxation of strained axial heterostructures in free-standing nanowires," *Physical Review B,* vol. 74, p. 121302, 2006.

[92] D. E. Perea, J. E. Allen, S. J. May, B. W. Wessels, D. N. Seidman, and L. J. Lauhon, "Three-dimensional nanoscale composition mapping of semiconductor nanowires," *Nano letters,* vol. 6, pp. 181-185, 2006.

[93] S. Breuer, C. Pfüller, T. Flissikowski, O. Brandt, H. T. Grahn, L. Geelhaar*, et al.*, "Suitability of Au-and self-assisted GaAs nanowires for optoelectronic applications," *Nano letters,* vol. 11, pp. 1276-1279, 2011.

[94] H. Shtrikman, R. Popovitz-Biro, A. Kretinin, L. Houben, M. Heiblum, M. Bukała*, et al.*, "Method for suppression of stacking faults in wurtzite III− V nanowires," *Nano letters,* vol. 9, pp. 1506-1510, 2009.

[95] N. Han, F. Wang, S. Yip, J. J. Hou, F. Xiu, X. Shi*, et al.*, "GaAs nanowire Schottky barrier photovoltaics utilizing Au–Ga alloy catalytic tips," *Applied Physics Letters,* vol. 101, p. 013105, 2012.

[96] M. Fang, N. Han, F. Wang, Z.-x. Yang, S. Yip, G. Dong*, et al.*, "III–V Nanowires: Synthesis, Property Manipulations, and Device Applications," *Journal of Nanomaterials,* vol. 2014, 2014.

[97] Z. Zhang, K. Yao, Y. Liu, C. Jin, X. Liang, Q. Chen*, et al.*, "Quantitative Analysis of Current–Voltage Characteristics of Semiconducting Nanowires: Decoupling of Contact Effects," *Advanced Functional Materials,* vol. 17, pp. 2478-2489, 2007.

[98] C.-J. Kim, H.-S. Lee, Y.-J. Cho, K. Kang, and M.-H. Jo, "Diameter-Dependent Internal Gain in Ohmic Ge Nanowire Photodetectors," *Nano Letters,* vol. 10, pp. 2043-2048, 2010/06/09 2010.

[99] S. Thunich, L. Prechtel, D. Spirkoska, G. Abstreiter, A. Fontcuberta i Morral, and A. W. Holleitner, "Photocurrent and photoconductance properties of a GaAs nanowire," *Applied Physics Letters,* vol. 95, p. 083111, 2009.

[100] H. Wang, "High gain single GaAs nanowire photodetector," *Applied Physics Letters,* vol. 103, p. 093101, 2013.

[101] M. S. Gudiksen, L. J. Lauhon, J. Wang, D. C. Smith, and C. M. Lieber, "Growth of nanowire superlattice structures for nanoscale photonics and electronics," *Nature,* vol. 415, pp. 617-620, 2002.

[102] K. Haraguchi, T. Katsuyama, and K. Hiruma, "Polarization dependence of light emitted from GaAs p-n junctions in quantum wire crystals," *Journal of Applied Physics,* vol. 75, pp. 4220-4225, 1994.

[103] C. P. T. Svensson, T. Mårtensson, J. Trägårdh, C. Larsson, M. Rask, D. Hessman*, et al.*, "Monolithic GaAs/InGaP nanowire light emitting diodes on silicon," *Nanotechnology,* vol. 19, p. 305201, 2008.

[104] J. A. Czaban, D. A. Thompson, and R. R. LaPierre, "GaAs core− shell nanowires for photovoltaic applications," *Nano Letters,* vol. 9, pp. 148-154, 2008.

[105] D. Wang, R. Zhu, Z. Zhou, and X. Ye, "Controlled assembly of zinc oxide nanowires using dielectrophoresis," *Applied Physics Letters,* vol. 90, p. 103110, 2007.

[106] R. Krupke, F. Hennrich, H. B. Weber, M. M. Kappes, and H. v. Löhneysen, "Simultaneous Deposition of Metallic Bundles of Single-walled Carbon Nanotubes Using Ac-dielectrophoresis," *Nano Letters,* vol. 3, pp. 1019-1023, 2003/08/01 2003.

[107] J. Li, Q. Zhang, N. Peng, and Q. Zhu, "Manipulation of carbon nanotubes using AC dielectrophoresis," *Applied Physics Letters,* vol. 86, p. 153116, 2005.

[108] J. Suehiro, N. Nakagawa, S.-i. Hidaka, M. Ueda, K. Imasaka, M. Higashihata*, et al.*, "Dielectrophoretic fabrication and characterization of a ZnO nanowire-based UV photosensor," *Nanotechnology,* vol. 17, p. 2567, 2006.

[109] J. Boote and S. Evans, "Dielectrophoretic manipulation and electrical characterization of gold nanowires," *Nanotechnology,* vol. 16, p. 1500, 2005.

[110] S. Raychaudhuri, S. A. Dayeh, D. Wang, and E. T. Yu, "Precise Semiconductor Nanowire Placement Through Dielectrophoresis," *Nano Letters,* vol. 9, pp. 2260-2266, 2009/06/10 2009.

[111] N. Ramgir, S. Sen, M. Kaur, S. K. Mishra, V. Rikka, R. Choukikar*, et al.*, "Investigation of SnO2 nanowire based gas sensors," 2010.

[112] Y. Huang, X. Duan, Q. Wei, and C. M. Lieber, "Directed Assembly of One-Dimensional Nanostructures into Functional Networks," *Science,* vol. 291, pp. 630-633, January 26, 2001 2001.

[113] P. Avouris, T. Hertel, R. Martel, T. Schmidt, H. R. Shea, and R. E. Walkup, "Carbon nanotubes: nanomechanics, manipulation, and electronic devices," *Applied Surface Science,* vol. 141, pp. 201-209, 3// 1999.

[114] Y. Peng, I. Luxmoore, M. Forster, A. Cullis, and B. Inkson, "Nanomanipulation and electrical behaviour of a single gold nanowire using in-situ SEM-FIB-nanomanipulators," in *Journal of Physics: Conference Series*, 2008, p. 012031.

[115] S. Bai, W. Wu, Y. Qin, N. Cui, D. J. Bayerl, and X. Wang, "High-Performance Integrated ZnO Nanowire UV Sensors on Rigid and Flexible Substrates," *Advanced Functional Materials,* vol. 21, pp. 4464-4469, 2011.

[116] Y.-K. Chang and F. C.-N. Hong, "The fabrication of ZnO nanowire field-effect transistors by roll-transfer printing," *Nanotechnology,* vol. 20, p. 195302, 2009.

[117] D. Whang, S. Jin, Y. Wu, and C. M. Lieber, "Large-Scale Hierarchical Organization of Nanowire Arrays for Integrated Nanosystems," *Nano Letters,* vol. 3, pp. 1255-1259, 2003/09/01 2003.

[118] M. P. Hughes, "AC electrokinetics: applications for nanotechnology," *Nanotechnology,* vol. 11, p. 124, 2000.

[119] R. J. Barsotti, M. D. Vahey, R. Wartena, Y.-M. Chiang, J. Voldman, and F. Stellacci, "Assembly of Metal Nanoparticles into Nanogaps," *Small,* vol. 3, pp. 488-499, 2007.

[120] O. Harnack, C. Pacholski, H. Weller, A. Yasuda, and J. M. Wessels, "Rectifying Behavior of Electrically Aligned ZnO Nanorods," *Nano Letters,* vol. 3, pp. 1097-1101, 2003/08/01 2003.

[121] X. Duan, Y. Huang, Y. Cui, J. Wang, and C. M. Lieber, "Indium phosphide nanowires as building blocks for nanoscale electronic and optoelectronic devices," *Nature,* vol. 409, pp. 66-69, 01/04/print 2001.

[122] A. Ulman, *An Introduction to Ultrathin Organic Films: From Langmuir--Blodgett to Self--Assembly*: Academic press, 2013.

[123] O. Albrecht, H. Matsuda, K. Eguchi, and T. Nakagiri, "Construction and use of LB deposition machines for pilot production," *Thin Solid Films,* vol. 284, pp. 152-156, 1996.

[124] D. Whang, S. Jin, and C. M. Lieber, "Nanolithography Using Hierarchically Assembled Nanowire Masks," *Nano Letters,* vol. 3, pp. 951-954, 2003/07/01 2003.

[125] J. B. Baxter and E. S. Aydil, "Nanowire-based dye-sensitized solar cells," *Applied Physics Letters,* vol. 86, p. 053114, 2005.

[126] H. T. Ng, B. Chen, J. Li, J. Han, M. Meyyappan, J. Wu*, et al.*, "Optical properties of single-crystalline ZnO nanowires on m-sapphire," *Applied Physics Letters,* vol. 82, pp. 2023-2025, 2003.

[127] P. X. Gao, Y. Ding, and Z. L. Wang, "Crystallographic Orientation-Aligned ZnO Nanorods Grown by a Tin Catalyst," *Nano Letters,* vol. 3, pp. 1315-1320, 2003/09/01 2003.

[128] H. T. Ng, J. Han, T. Yamada, P. Nguyen, Y. P. Chen, and M. Meyyappan, "Single crystal nanowire vertical surround-gate field-effect transistor," *Nano Letters,* vol. 4, pp. 1247-1252, 2004.

[129] Z. Fan, P.-c. Chang, J. G. Lu, E. C. Walter, R. M. Penner, C.-h. Lin*, et al.*, "Photoluminescence and polarized photodetection of single ZnO nanowires," *Applied Physics Letters,* vol. 85, pp. 6128-6130, 2004.

[130] A. Fontcuberta i Morral, C. Colombo, G. Abstreiter, J. Arbiol, and J. Morante, "Nucleation mechanism of gallium-assisted molecular beam epitaxy growth of gallium arsenide nanowires," *Applied Physics Letters,* vol. 92, pp. 063112-063112-3, 2008.

2. Materials

2.1. Zinc Nitride

2.1.1. Growth Techniques

At the beginning of 20th century, the abundance of Zn in the nature fostered the investigation of Zn alloys in order to increase the presence of Zn in the industry. In 1920, Bentley and Sterm investigated the synthesis of Zn_3N_2 powder from the ammonization of Zn, consisting in the reaction between Zn dust and NH_3 in a furnace at temperatures of around 600 ºC [1]. Twenty years later, Juza and Hahn reported the first work about the synthesis of Zn_3N_2 powder [2]. This material remained relatively unstudied until 1993 when Kuriyama et al. reported the growth of Zn_3N_2 films by the direct reaction of NH_3 and Zn [3]. In that work, N source is obtained from NH_3 rather than from N_2 molecules, presenting more thermal stability. However, the extremely high substrate temperature necessary to dissociate NH_3 molecules hinders the control over the resultant film properties. In 1998, Futsuhara et al. published for the first time, the preparation of polycrystalline Zn_3N_2 thin films by using plasma methods [4]. The use of plasma allows to carry out growths at lower substrate temperatures because active N is directly obtained from the plasma. Many years later, Zn_3N_2 was successfully synthesized by using alternative methods such as electrochemical processes [5], rf-MBE, MOCVD [6], and PLD [7].

2.1.2. Structural Properties

Crystalline structure of Zn_3N_2 powder was firstly studied by Juza and Hahn [2], and further analyzed by Partin et al. [8], obtaining that Zn_3N_2 crystallizes with a cubic *anti*-bixbyite structure. In this structure, Zn

atoms are in tetrahedral sites of an approximately cubic close packed array of N atoms (figure 2.1(a)). Accordingly, Zn atoms are in general positions 48*e* of the space group $Ia\bar{3}$, whereas there are two different types of N atoms: N(1) and N(2), which are in positions 8*b* (1/4,1/4,1/4; …) and 24*d* (x,0,1/4; …), respectively (figure 2.1(b)). Partin et al. experimentally demonstrated that Zn_3N_2 lattice constant is 9.769 Å, and Zn-N bond lengths are: Zn-N(1) 2.133 Å, Zn-N(2) 1.996 Å, Zn-N(2) 2.068 Å, and Zn-N(2) 2.262 Å (figure 2.1(b)). These results were later confirmed by theoretical works carried out by Long et al. [9].

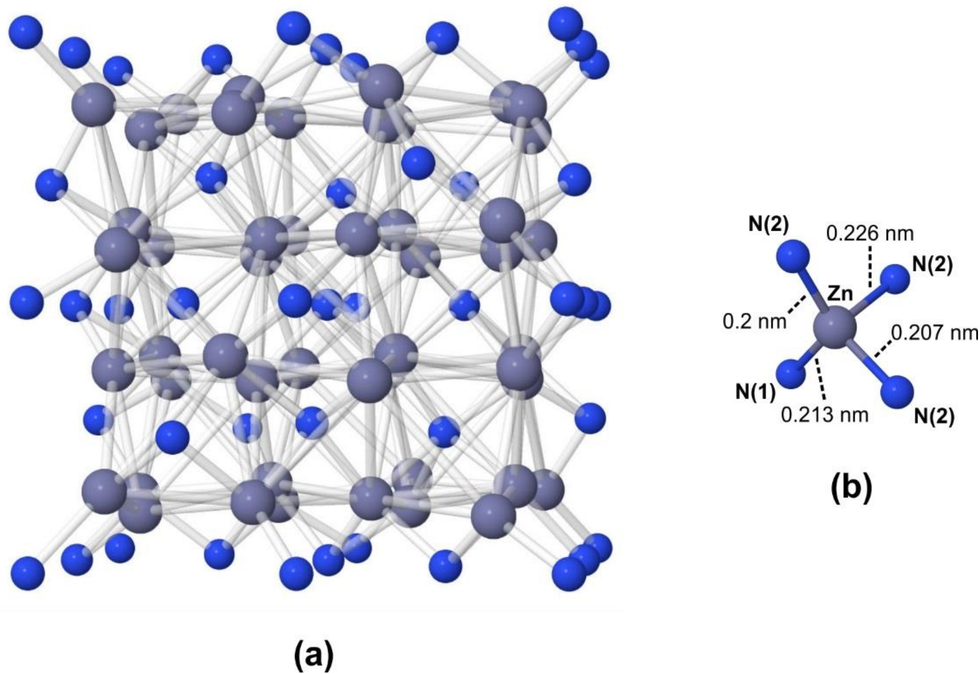

Figure 2.1. (a) Molecule of Zn_3N_2 consisting of 96 atoms; (b) Zn-N(1) and Zn-N(2) bond lengths.

Zn_3N_2 films deposited by rf-magnetron sputtering were characterized by Futsuhara et al. [4] showing polycrystalline structures. The orientation of crystallites is observed to be strongly dependent on the N_2 content in the plasma during the sputtering growth. The use of pure N_2 ambient promotes the formation of a random oriented polycrystal, whereas the addition of Ar to the processing gas benefits the orientation of crystallites. These results were later confirmed by Yang et al. [10] in sputtered Zn_3N_2 thin films, obtaining polycrystalline structures with a preferential orientation of (400).

2.1.3. Electrical Properties

Hall effect measurements of sputtered Zn_3N_2 thin films show n-type semiconductor behaviour [4]. The origin of this conduction character is associated to the existence of N vacancies in the Zn_3N_2 sublattice [9]. Zn_3N_2 films present different electrical conductivities depending on the growth conditions and technique. Zn_3N_2 films grown by rf-magnetron sputtering show ρ_{Hall} between 1.4×10^{-3} and 1×10^{-2} Ω·cm, and carrier concentrations (n_{Hall}) between 1.2×10^{20} and 6×10^{18} cm^{-3}, respectively [4]. Accordingly, the increase ρ_{Hall} is attributed to the decrease of n_{Hall}. In addition, the decrease of n_{Hall} from 1.2×10^{20} to 6×10^{18} cm^{-3} shows an

increase of the electron mobility (μ_{Hall}) from 40 to 100 cm^2/V·s, suggesting that the μ_{Hall} in Zn_3N_2 films is mainly dominated ionized impurity scattering.

Suda et al. [6] characterized Zn_3N_2 films grown by MOCVD and rf-MBE techniques. MOCVD films present an increase of μ_{Hall} from 86 to 118 cm^2/V·s as n_{Hall} decreases from 1.6×10^{20} to 1.5×10^{19} cm^{-3}. In good agreement with this trend, MBE films show an increase of μ_{Hall} from 24 to 156 cm^2/V·s as n_{Hall} decreases from 1.6×10^{20} to 1×10^{20} cm^{-3}. These results indicate that μ_{Hall} continuously increases as the n_{Hall} decreases, suggesting that the scattering by ionized impurities becomes less effective.

It is worth noting that the use of techniques such as magnetron sputtering enables to grow high quality Zn_3N_2 films with excellent optoelectronic properties, presenting μ_{Hall} close to those obtained in epitaxial techniques.

2.1.4. Optical Properties

Zn_3N_2 films grown by different techniques exhibit E_{g} of 1.01 [5, 10], 1.06 [6], 1.23 [4], 2.1 [11, 12], and 3.2 eV [3, 13]. Long et al. [9] suggested that different defective Zn_3N_2 structures may cause energy shifts or band gap changes, which would explain different E_{g} found in Zn_3N_2. In addition, the unintentional incorporation of O into the Zn_3N_2 sublattice during the growth [6], may also lead to change its E_{g} [14].

As mentioned, Zn_3N_2 presents high n_{Hall} (10^{18}-10^{20} cm^{-3}) which may lead to a Burstein-Moss energy shift (ΔE) of the E_{g} [15, 16]. The Burstein-Moss effect is the phenomenon of which the apparent band gap of a semiconductor is increased as the absorption edge is pushed to higher energies as a result of all states close to the conduction band are populated. As the n_{Hall} becomes larger, the Fermi level can move into the conduction band, shifting the apparent band gap towards higher values, hindering the accurate determination of E_{g}. In order to calculate the intrinsic band gap energy of Zn_3N_2, one can subtract ΔE from the apparent band gap energy or also called optical band gap energy (E_{opt}). As the latter can be measured by spectrophotometry, E_{g} can be therefore extracted from the following expression

$$E_{\mathrm{g}} = E_{\mathrm{opt}} - \Delta E \qquad (2.1)$$

where ΔE is proportional to the n_{Hall} and depends on the semiconductor type (direct or indirect).

The semiconductor type of Zn_3N_2 is also unclear, showing both direct [3-6, 10, 13], and indirect [11, 12] behaviour. In spite of this controversy, Zn_3N_2 films typically exhibit absorption coefficients (α) of around 10^4 cm^{-1}, which are similar than those presented by direct band gap semiconductors [17].

2.1.5. Metastability

Optoelectronic properties of Zn_3N_2 presented above, are subjected to the uncontrolled oxidation mechanisms experimented by this material when is exposed to the ambient air. In that respect, the characterization of Zn_3N_2 is still a big challenge. The unclear oxidation rate of Zn_3N_2 may hinder the determination of magnitudes such as E_g, and optical constants (n and k).

Futsuhara et al. analyzed surface chemical states of Zn_3N_2 films exposure to the ambient air by XPS [4]. Resultant spectra show the existence of Zn-N, Zn-O, O-H, and N-H bonds in the analyzed Zn_3N_2 film which are associated to the hydrolysis of Zn_3N_2. This reaction is suggested to occur along the Zn_3N_2 surface and can be written as

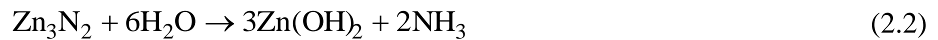

$$Zn_3N_2 + 6H_2O \rightarrow 3Zn(OH)_2 + 2NH_3 \quad (2.2)$$

However, this result only shows a surface reaction, and it does not clarify the oxidation mechanisms of Zn_3N_2 bulk structure.

On the other hand, the oxidation of Zn_3N_2 can be accelerated by thermal treatments which are usually carried out at T_s above 300 ºC [18]. Kambilafka et al. [18] carried out annealing processes at T_s between 300 and 550 ºC in Zn-rich and stoichiometric Zn_3N_2 films, observing the formation of ZnO and ZnO:N phases, respectively. In the case of Zn-rich Zn_3N_2 films, this rapid transformation of Zn_3N_2 into ZnO is based on the direct reaction between O and the excess of Zn which promotes the formation of both ZnO and ZnO_2 phases. In contrast, the thermal oxidation of stoichiometric Zn_3N_2 results in the formation of ZnO:N, whose p-type characteristics are confirmed by Hall effect measurements, indicating that N is acting as an acceptor defect. In both processes, external O tends to substitute N into the Zn_3N_2 sublattice.

2.2. Zinc Oxide Nanowires

2.2.1. Growth Techniques

The growth of ZnO NWs has been carried out using diverse techniques, including vapor phase transport (VPT) [19-22], MOVPE [23], physical vapor deposition (PVD) [24], solvothermal method [25], CVD [26], direct thermal evaporation [27], and PLD [28], and on different substrates, such as Si(100) [19], Ga-doped ZnO/Si_3N_4/SiO_2/Si [20], ZnO/Si(100) [22], and sapphire [23].

Vapor phase (VP) growth is probably one of the most extensively used methods to grow nanostructures such as NWs. VP growth is based on the principle that a solid powder source is thermally evaporated, resulting in a gas which is condensed under specific conditions (temperature, pressure, ambient, substrate, …) on a substrate surface, where the nucleation of the nanostructure takes place. VP allows to control the resultant NW aspect ratio (L_{NW} and d_{NW}), and crystallinity. The VP growth of ZnO NWs can be carried out through either VS or VLS mechanisms.

VS Mechanism

Figure 2.2 describes the VS mechanism for the specific case of ZnO NW growth. Zn solid source is evaporated under high temperature (T_e) conditions in the evaporation region; then, Zn vapor phase is carried towards the condensation region where the temperature is lower than in the evaporation region ($T_c < T_e$). Zn(g) and O_2(g) react to form ZnO molecules or cluster that crystalize on the substrate surface in the condensation region. The initial ZnO crystals will act as preferential nucleation sites, promoting the formation of ZnO nanostructures.

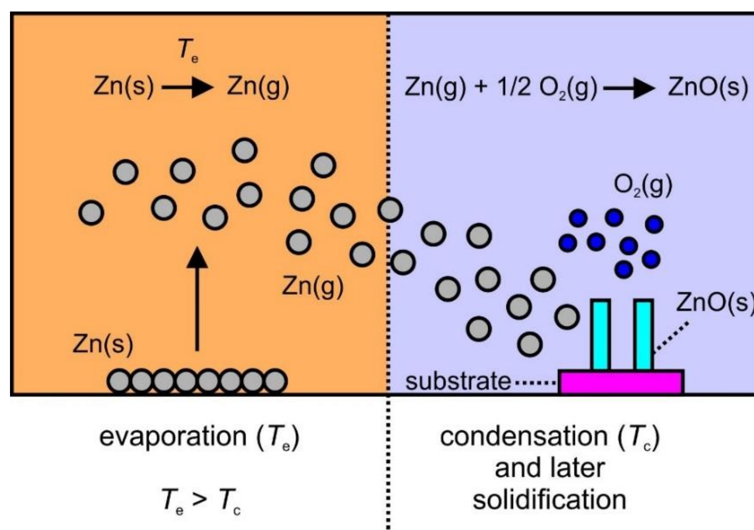

Figure 2.2. Schematic of the VS mechanism in ZnO NWs.

In VS growths, ZnO [29, 30] and Zn [31] seed layers pre-deposited on the substrate surface are commonly used to help the adsorption of Zn and O gases at the surface crystal grains. These grains have two main roles: i) to act as a nucleation site and ii) to guide the NW growth along the <0001> direction of the ZnO WZ structure. Under optimized conditions of temperature, total gas flux, gas flux composition, … Zn and O atoms tend to be adsorbed to the {0001} surface, resulting in the growth of ZnO along the <0001> faster than in other directions [32]. This is the main reason for the anisotropic growth of ZnO NWs [33]. VS is therefore a self-assisted growth because is not necessary the use of foreign catalyst such as Au to assist the NW growth.

Depending on the growth conditions (temperature, pressure, substrate, …) the product resultant from a VS growth is observed in different morphologies such as NWs [34], nanobelts [35], nanobridges, nanonails [36], nanoshells [37], and TPs [38].

VLS Mechanism

VLS mechanism was firstly proposed by Wagner and Ellis to explain the growth of Si NWs using Au as a seed particle [39]. VLS mechanism uses a seed particle to act as a sink for the vapor growth species, and to guide the NW growth along a direction determined by the substrate preferential orientation. The growth was carried out utilizing a Au seed particle to trap Si vapor, forming an Au-Si liquid alloy (figure 2.3(a)). Then, the supersaturation of that alloy leads to a solid precipitation of Si towards the liquid/solid interface formed between the alloy and the Si(111) substrate surface (figure 2.3(b)). Once the solid phase accumulates enough strain in two dimensions, it is observed the coherent growth of a Si NW underneath the Au seed with a small footprint. The Au seed is also called catalyst because it guides the NW growth along a direction fixed by the preferential orientation of the substrate (epitaxial growth).

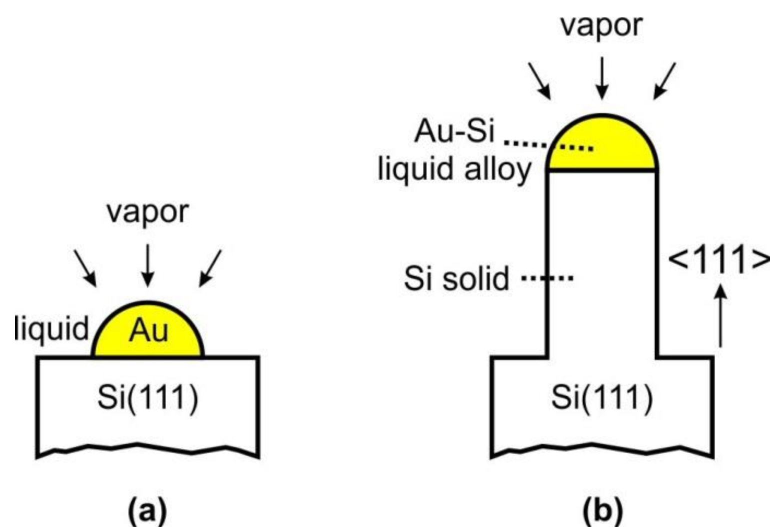

Figure 2.3. Illustration of the VLS mechanism for Si NWs.

Au is commonly chosen as seed because the advantage to form liquid alloys with NW constituents at moderate temperatures, and the possibility to form nanodroplets on the substrate surface from Au thin films [40].

Figure 2.4 shows a schematic of the Au-assisted VLS growth sequence of ZnO NWs. Firstly, Au nanodroplets are pre-deposited on the substrate surface (figure 2.4(1)). Zn(g) and O_2(g) are dissolved in these nanodroplets forming liquid alloys (figure 2.4(2)). When a nanodroplet is supersaturated of (Zn,O), there is a precipitation of these elements towards the droplet/substrate interface, forming a ZnO solid crystal (figure 2.4(3)). Once the crystal underneath the droplet accumulates enough strain, the crystal grows forming a "NW-like" structure that keeps a sharp boundary with the liquid droplet (figure 2.4(4)). In that respect, each Au droplet act as a nucleation site for the growth of an individual NW. As the NW growth occurs at the droplet/NW interface, the growth species (Zn,O) can be incorporated to NW by the diffusion of Zn and O atoms: i) through the Au droplet, and ii) along the substrate surface, and the NW sidewalls (figure 2.4(4)).

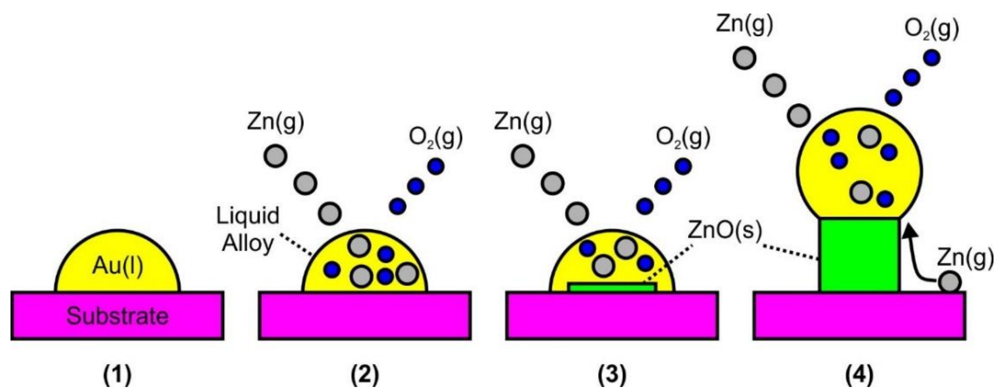

Figure 2.4. Schematic of the VLS mechanism in ZnO NWs.

The Au droplet size remains essentially unchanged during the NW growth. In this regard, the droplet size limits the axial growth of the NW, while the longitudinal growth rate is promoted.

Zn Vapor Source

Zn gas source is commonly obtained from a: i) direct thermal evaporation of Zn powder and ii) carbo-thermal reduction of ZnO powder by using a carbon source such as graphite. While the direct evaporation of Zn is carried out a temperatures as low as 450 ºC due to the low vapor pressure of the Zn element [24], carbo-thermal reduction of ZnO powder needs temperatures above 900 ºC [41] to promote the formation of an oxidizing gas mixture. Carbo-thermal reduction of ZnO powder is expressed as

$$\mathrm{ZnO(s)+C(s) \rightarrow Zn(g)+CO(g)} \tag{2.3}$$

$$\mathrm{ZnO(s)+CO(g) \rightarrow Zn(g)+CO_2(g)} \tag{2.4}$$

Accordingly, the growth of ZnO NWs using ZnO/C powder as Zn source occurs from the reaction between Zn(g) and different O species, including CO(g) and CO_2(g) obtained from reactions (2.3) and (2.4), and O_2(g) contains in the O-rich atmosphere. These reactions can be written as

$$\mathrm{Zn(g)+CO(g)\rightarrow ZnO(s)+C(s)} \quad (2.5)$$

$$\mathrm{2Zn(g)+CO_2(g)\rightarrow 2ZnO(s)+C(s)} \quad (2.6)$$

$$\mathrm{2Zn(g)+O_2(g)\rightarrow 2ZnO(s)} \quad (2.7)$$

2.2.2. Photoconductivity of ZnO NWs

ZnO NW Photoconductor

ZnO is a II-VI semiconductor material with a direct band gap and wide band gap energy (E_g = 3.37 eV), which has been drawing increased attention in the last years, due to its suitable properties for the development of transparent electronic and optoelectronic devices [42, 43]. This compound is considered a promising candidate for high-performance optoelectronic applications such as PDs because of the possibility to tailor its E_g in the UV/VIS spectral range by forming ZnCdO [44] or ZnMgO [45] ternary alloys. In addition, it is chemically and thermally stable, having important advantages for high temperature and low consumption operation.

Although the UV R_{photo} of ZnO was firstly observed by Mollow [46], the research of ZnO based UV photoconductors started gradually forty years later in the 1980s [47]. In figure 2.5, it is shown a schematic of a basic ZnO photoconductor, where the load resistance (R_{load}) is typically much smaller than the ZnO

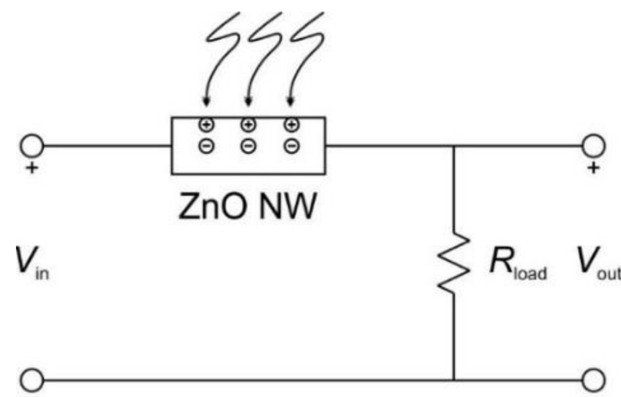

Figure 2.5. Schematic of a simple ZnO NW based photoconductor.

resistance. When ZnO is illuminated with UV light, photons can be absorbed in ZnO, producing electron-hole pairs, and increasing the total free charge in the ZnO bulk, which leads to the reduction of its resistance. The large resistance variation of these devices enables the measurement of the R_{photo} without using any amplifying subsystem. However, this kind of devices is strongly dependent on the power density of the exciting light source and it is affected by negative effects such as persistent photoconductivity which slows down device time response.

The origin of the slow decay time (also called recovery time) observed in ZnO NW photoconductors is mainly associated to the re-adsorption of O species along the NW surface. It is known, that surface defects of metal oxides, such as O vacancies, create empty surface states, functioning as adsorption sites [48]. O species such as O_2 molecules can be adsorbed at these sites, acting as electron acceptors, and forming O_2^- at room temperature [49]. Accordingly, ZnO NW surface is highly reactive to the O species in the ambient, having a strong influence on the resultant electrical properties of ZnO NWs.

When ZnO NW is exposed to the ambient, O gas species such as O_2 molecules tend to adsorb along the NW surface by capturing free electrons from the bulk, and forming O_2^- anions (dark conditions in figure 2.6). These free electrons in the NW bulk become trapped at the surface, reducing the effective free charge density, and therefore increasing the internal resistance of the ZnO NW. That means, the diffusion of free electrons from the NW bulk towards the surface produces an effective reduction of the conductive volume by creating a SCR at the surface whose electrical conductivity is very low due to its low carrier concentration. Therefore, the internal resistance of ZnO NW in dark conditions is strongly influenced by these surface states.

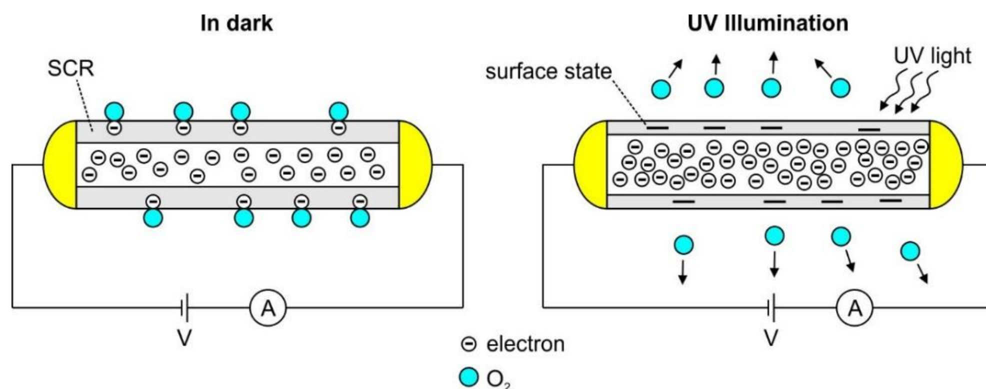

Figure 2.6. Schematics of ZnO NW photoconductor electrical conduction in dark and under UV illumination conditions.

The increase of the current when ZnO NW is illuminated with UV light (UV illumination conditions in figure 2.6), is governed by two main mechanisms: i) photo-generated carriers produced by the absorption of UV photons (faster process) and ii) electrons released from the surface traps (slower process). The photogenerated holes in the NW bulk are drifted towards surface states, or also called surface traps, by the electric field in the SCR; those photoholes recombine with trapped electrons, desorbing O species to the ambient and releasing electrons towards NW bulk. This process contributes to increase G_{photo} of ZnO NW photoconductors by increasing the lifetime of electrons in the NW bulk.

After the illumination of ZnO NW photoconductor, current tends to recover the initial dark level. As mentioned, this process takes a lot of time due to persistent photoconductivity of ZnO. The signal relaxation comprises two components: i) a fast decay related to band-to-band recombination, and ii) a slower decay associated to the re-adsorption of O species along the ZnO NW surface and subsequent electron trapping.

The optoelectronic properties of ZnO NWs has been improved by the functionalization of the NW surface [50], the coverage of the NW surface with metallic NPs [51], and the fabrication of SB contacts [50]. The latter is the most extended method due to the effective improvement of the photoresponse speed (at expense of the G_{photo}) and its principles are described below.

Metal-NW-Metal Photodiode

The development of SB contacts in ZnO NWs can be also influenced by the existence of surface states. In order to understand this point, a basic electronic band diagram of n-type ZnO NW is represented in figure 2.7, including the energy levels corresponding to the valence band (E_V), the conductance band (E_C), the Fermi level (E_F), the surface states (E_{ss}), and the vacuum level (E_{vac}). The work function (Φ) can be changed due to the accumulation of negative charge along the ZnO NW surface. This work function is given by the sum of the ZnO work function (Φ_{ZnO}), the surface band bending (Φ_S) and the surface dipole (Φ_O) created by the adsorbed species along the ZnO NW surface. Moreover, different surface treatments such as functionalization or surface passivation can be used to change the work function of ZnO NW before the deposition of a metal electrodes in order to modify the contact characteristics [52].

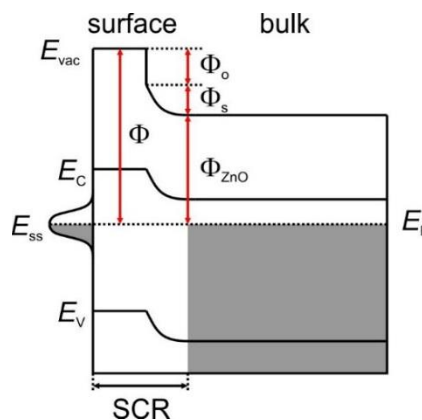

Figure 2.7. Electronic band structure of ZnO NW.

In dark conditions, ZnO NW photodiodes based on SB contacts present a potential barrier formed at the interface between the metal electrode and NW (figure 2.8). O species such as O_2 can be adsorbed along the NW surface and at the SB interface by capturing free electrons from the NW bulk. As in the case of ohmic contacts described in figure 2.6, a low conductivity SCR is created at the ZnO NW surface.

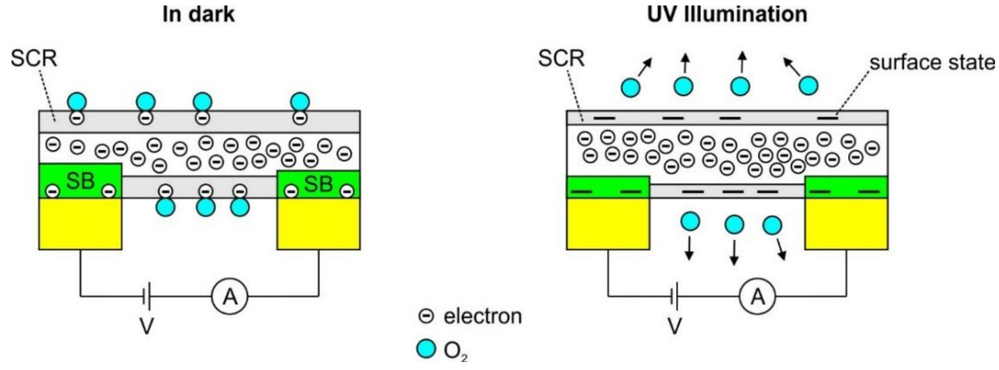

Figure 2.8. Schematic of a ZnO NW SB photodiode in dark and under UV illumination conditions.

The SB height is strongly dependent on the trapped/released electrons at the surface states. In this scenario, the potential barrier height is independent on the difference between ZnO and metal work functions mainly because of the Fermi level pining at surface states [53]. The SB height (φ) is expressed as:

$$\varphi = \psi_{bi} + \xi = \frac{Q_S^2}{2q N_{SCR} \varepsilon_S A^2} + \xi \ , \qquad (2.8)$$

where ψ_{bi} is the built-in potential of the depletion layer, ξ is the potential difference between E_C and E_F in the bulk, Q_S is the surface charge density in the SB interface, N_{SCR} is the charge concentration in the SCR, ε_S is the dielectric constant and A is the contact area of the SB.

Under UV illumination, electro-hole pairs are photogenerated and separated by the electric field created in the SB region (figure 2.8); photogenerated holes are then drifted to the SB interface where can be recombined with trapped electrons, neutralizing the negative charge of O_2^- anions, and producing desorption of O_2 molecules from the SB interface [54]. Therefore, the generation of holes and desorption of O_2^- at the SB interface reduce Q_S, and then φ is also reduced, according to expression (2.8), resulting in an increase of the photocurrent ($I_{photo} = I_{light} - I_{dark}$, where I_{light} is the current under UV illumination).

After UV illumination, ZnO NW photodiodes follow a recovery process based on the re-adsorption of O_2 at the SB interface and the subsequent refilling of the surface states. This mechanism contributes to sharply reduce the current. In addition, the current flow helps to fill faster the empty states in the SB interface between the NW and the contact than in the rest of the surface [55].

2.2.3. Other Properties of ZnO NWs

Structural Properties

Under ambient conditions, the thermodynamically stable phase observed in ZnO is that of WZ. ZnO can be also crystalized in ZB or rocksalt structures but only when it is grown on cubic substrates or under high

pressure conditions, respectively. ZnO WZ hexagonal structure belongs to the *P63mc* space group in the Hermann-Mauguin notation; the lattice parameters are $a = b = 3.25$ Å, $c = 5.21$ Å and $c/a = 1.633$ ($\alpha = \beta = \gamma = 90º$) [56]. A reduced cell of ZnO is shown in figure 2.9, consisting of a tetrahedrally coordinated O^{-2} (small blue balls) and Zn^{+2} ions (big gray balls) stacked alternately along the *c*-axis, corresponding to the <0001> direction. Each sublattice includes four atoms per unit cell and each anion (O^{-2}) is surrounded by four cations (Zn^{+2}) located at the corners of a tetrahedron, and vice versa. ZnO WZ structure can be also understood as the interpenetration of two hexagonal close-packed (hcp) sublattices formed by one type of atom displaced between each other an amount of $u = 3/8$ along the threefold *c*-axis. The tetrahedral coordination of ZnO results in a non-central symmetric structure, which is responsible for the piezoelectric and pyroelectric properties of ZnO.

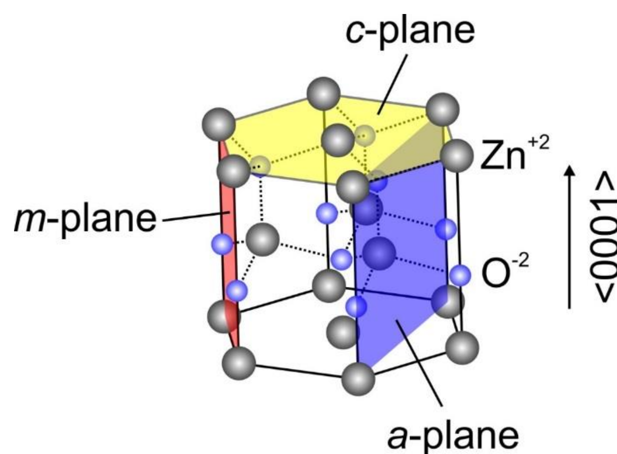

Figure 2.9. ZnO WZ hexagonal crystal structure; this figure shows *a*, *m* and *c* principal planes in ZnO.

WZ ZnO lacks of inversion plane perpendicular to the *c*-axis, that means, ZnO surface can be either positively charged which corresponds to Zn-terminated surface whose designation is (0001) or (0001)A, or negatively charged which corresponds to O-terminated surface and whose designation is $(000\bar{1})$ or (0001)B. Both surface terminations are therefore polar surfaces. On the other hand, ZnO also has two stable non-polar surfaces which correspond to $\{10\bar{1}0\}$ and $\{1\bar{2}10\}$; these planes contain the same number of Zn and O atoms and therefore are electrically neutral.

ZnO grows preferentially along three different crystalline directions: $<10\bar{1}0>$, $<1\bar{2}10>$ and <0001>, which correspond to minimum energy directions. While ZnO structures grown along $<10\bar{1}0>$ and $<1\bar{2}10>$ result in belt-like shape, structures synthesized along <0001> direction result in hexagonal wires whose facets and edges correspond to $\{10\bar{1}0\}$ or *m*-planes, and $\{1\bar{2}10\}$ or *a*-planes, respectively (figure 2.9).

A single-crystalline ZnO has eight sets of optical phonon modes at the center of the Brillouin zone (Γ point), classified as $A_1+E_1+2E_2$ modes (Raman active), $2B_1$ modes (Raman silent), and A_1+E_1 modes (infrared active). Moreover, both A_1 and E_1 modes split into longitudinal optical (LO) and transversal optical (TO) components. Raman spectroscopy measurements of vertically aligned ZnO NWs performed in backscattering

configuration, i.e. the incident light is aligned with the NWs (*c*-axis), only exhibit E_2 and A_1(LO) modes around the energies of 438 and 581 cm^{-1}, respectively [57]. At this configuration, A_1(TO) and E_1(TO) modes are forbidden by the Raman selection rules. In this regard, the absence of the TO modes in the Raman spectrum of ZnO NWs (under the described conditions) confirms the orientation of the NWs along the *c*-axis. On the other hand, the existence of A_1(LO) mode in the Raman spectrum is characteristic of nanostructures based on ZnO such as NWs and NPs [58] but not in bulk ZnO [59].

Electrical Conductivity

The electrical conductivity of a single ZnO NW has been measured by different methods. Chang et al. [26] deposited Ti/Au electrodes covering both ZnO NW edges, allowing to measure the electrical current along a single ZnO NW. Due to the similar work functions of Ti (4.33 eV) and ZnO (4.3 eV) the ohmic contact between both materials enables the characterization of the NW resistivity. Assuming that the entire potential supplied between source and drain electrodes is dropping across the ZnO NW, a ZnO NW with diameter of 60 nm and a length of 7.6 μm exhibits a resistivity of around 0.12 Ω·cm, a carrier concentration of 2.5×10^{18} cm^{-3} and mobility of 21.7 cm^2/V·s.

Electrical properties of ZnO NWs are strongly influenced by the growth system and conditions. Park et al. [60] grew ZnO NWs by MOVPE, obtaining carrier mobilities up to 75 cm^2/V·s. Soci et al. [54] synthesized ZnO NWs by CVD, enhancing the carrier mobility up to 270 cm^2/V·s. Comparing to the mobilities obtained in ZnO thin films (0.01-10 cm^2/V·s), ZnO NWs exhibit higher mobilities mainly because of the absence of grain boundaries causes a strong impact on the electric transport by reducing the scattering mechanisms.

Mechanical Properties

Direct measurement of the mechanical behavior of individual nanostructures is rather challenging since the traditional methods for bulk materials cannot be applied. Song et al. [61] designed a method to measure the elastic modulus of individual NWs aligned on a solid substrate using AFM. Following that method, the elastic modulus of a single ZnO NW could be obtained without destructing or manipulating the NW sample. Results showed that ZnO NWs grown on a sapphire substrate and with an average diameter of 45 nm presented an elastic modulus of 29 GPa. Huang et al. [62] demonstrated that ZnO NW elastic modulus can be enhanced up to 487 GPa by doping ZnO structure with In. Therefore, ZnO NWs are promising for the development of nanoresonators and nanocantilevers mainly because their small size may improve the sensitivity of conventional cantilevers.

Piezoelectricity

The lack of a center of symmetry in ZnO WZ structure combined with a large electromechanical coupling, resulting in large piezoelectricity and pyroelectricity coefficients of ZnO, making ZnO suitable to be employed in mechanical actuators, piezoelectric sensors and surface acoustic wave devices [63-66].

Although electrical and mechanical properties of ZnO NWs have been analyzed in the past, the electromechanical coupling and its potential size-effects have not been accurately addressed. This is mainly because in NWs there are some experimental challenges, including difficulties i) to manipulate NWs, ii) to make appropriate electrical contacts on NWs, iii) to measure currents and voltages with enough resolution. Fan et al. [67] used piezoresponse force microscopy to determine the piezoelectric coefficient of ZnO NWs with diameters between 150 and 500 nm, obtaining values of 4.41 and 7.5 pm/V, respectively. On the other hand, Zhu et al. [68] obtained higher values around 12000 pm/V, measuring ZnO NWs with average diameters of 230 nm by resonance shift method. Both results showed piezoelectric coefficients much higher than those obtained in ZnO bulk (12.4 pm/V) [69].

Surface Properties

In terms of surface sensitivity, ZnO NWs are expected to be superior to its thin film counterpart [70]. Due to the large surface-to-volume ratio and the Debye length (30 nm) comparable to the NW diameter [71], ZnO NWs show superior surface chemical processes, and the surface effects become more prominent in charge carrier dynamics [72]. In this regard, the chemisorption of species along the NW surface induces that surface states affect the electronic structure of the entire NW, enhancing the sensitivity of NWs.

Fan et al. [73, 74] fabricated a ZnO NW FET for the detection of NO_2 and NH_3 at RT. Due to a Debye screening length comparable to the NW diameter, the electric field applied over the back gate electrode is found to significantly affect the sensitivity of the NW as it modulates the carrier concentration. In this regard, ZnO NW based chemical sensors have demonstrated to have high sensitivity and selectivity to the ambient gas concentration and composition.

Photoluminescence

ZnO NWs present a strong and sharp UV emission peak at around 380 nm (~ 3.26 eV) and a broad blue-green emission band between 485 and 510 nm [75]. The UV peak can be attributed to the UV near-band edge emission [76], whereas the VIS broad band can be attributed to singly ionized O vacancies in the ZnO NWs [77]. Observing that the stronger the intensity of the green luminescence, the more singly ionized O vacancies there are.

2.3. Gallium Arsenide Nanowires

2.3.1. Growth Techniques

GaAs NWs have been successfully grown by different techniques such as MBE [78-88], CVD [89-91], and CBE [92-94]. Epitaxial techniques such as MBE, and CBE are highlighted over the rest mainly because of the resultant high-quality NWs, and the thorough control over the growth parameters, allowing to tailor NW resultant properties. It is worth noticing that these techniques enable to develop different growth mechanisms due to the high vacuum conditions and the accurate control over the gas source fluxes, allowing to carry out reproducible growths. NW growth methods in a bottom-up approach [95], can be divided in two different groups: particle assisted growth (PAG), or non-particle assisted growth (non-PAG). The main difference between both methods is related to the use of a seed metal particle to assist the NW growth. In the case of non-PAG, the lack of that particle involves the use of lithographed substrates to promote the formation NWs.

Non-PAG

The non-PAG method consists in the suppression of the axial growth in two directions, while the longitudinal growth along the third direction is promoted. Two different examples of non-PAG are selective area epitaxy (SAE) [96] and oxide-assisted growth (OAG) [97].

In SAE, a mask with nanometric openings is previously defined on the substrate surface. These openings are commonly defined by electronic lithography on a surface oxide layer deposited on crystalline substrates (figure 2.10(a)). At the beginning of the growth, axial crystal growth is limited by the dimension of the nanometric openings (figure 2.10(b)). Once the NW length overcomes the opening height, the growth proceeds along the direction normal to the substrate surface, showing longitudinal growth rates much higher than axial growth rates (figure 2.10(c)).

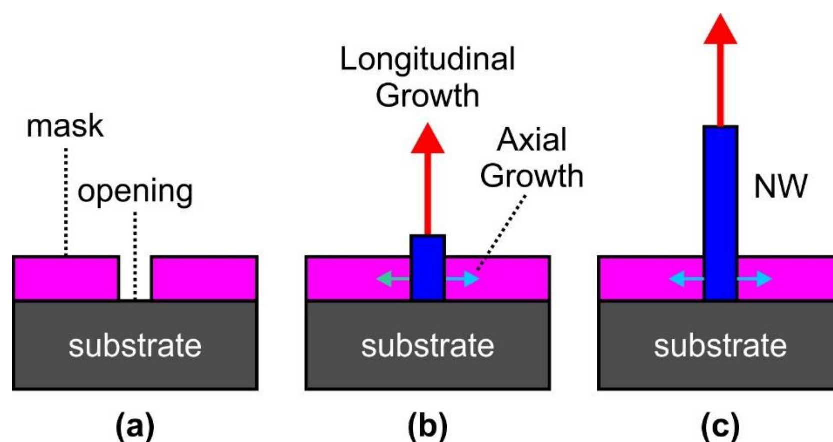

Figure 2.10. Schematic of SAE mechanism.

In OAG, the phase separation between semiconductor and oxide leads to the formation of a semiconductor NW (figure 2.11). For the sake of clarity, we analyze the growth of Si NWs on a Si substrate by OAG. First, Si sub-oxide clusters are deposited on a Si substrate surface (figure 2.11(a)); these clusters become strongly bonded to Si atoms which limit their lateral motion. Once the Si NW growth starts, the incorporation of new Si atoms to the NW structure might expel O atoms towards the NW edges, forming an oxide shell (figure 2.11(b)) that inhibits the lateral growth (figure 2.11(c)).

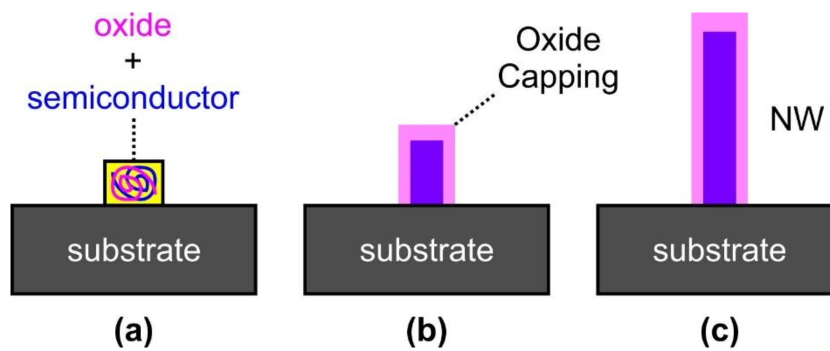

Figure 2.11. Schematic of the OAG mechanism.

PAG

PAG can be divided in two different sub-groups, depending on the particle composition. When the particle is composed by a NW constituent, the mechanism is called homo-PAG or self-PAG (figure 2.12(a)) [98]; whereas, if the particle is composed by a foreign material the mechanism is known as hetero-PAG (figure 2.12(b)) [99].

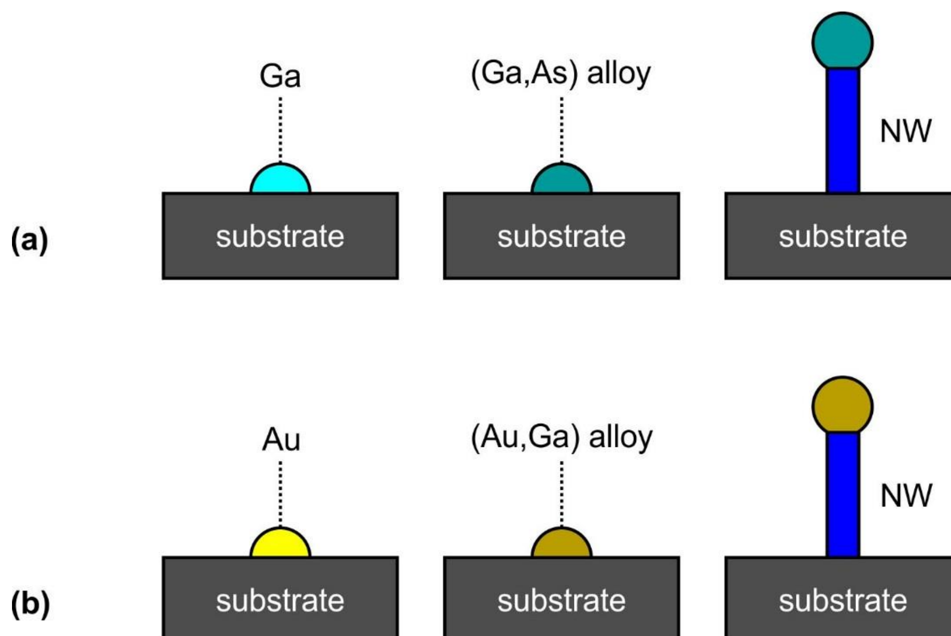

Figure 2.12. (a) homo-PAG and (b) hetero-PAG of GaAs NWs, using Ga and Au particles, respectively.

Since 1975, GaAs NWs have been grown by hetero-PAG using Au seed particles [100]. Twenty years later, Hiruma et al. reported one of the most relevant works about the hetero-PAG of GaAs NWs using a thin film of Au as seed layer [101]. Prior to the NW growth, the Au layer is pre-evaporated on the substrate surface and later annealed in order to form Au NPs with diameters around 40 nm that will act as catalysts of the NW growth.

Au is commonly used in hetero-PAG of GaAs NWs mainly due to the (Au,Ga) eutectic alloy reduces the initial melting temperature of Au below temperatures commonly used in NW epitaxial growths. However, the unintentional incorporation of Au into the GaAs structure could hinder its properties [102]. In addition, hetero-PAG assisted by Au particles has been observed to produce the formation of different crystal phases in GaAs NW structure, comprising cubic ZB and hexagonal WZ structures. In that respect, Au is suggested to be responsible for the growth of ZB/WZ polytypisms along the GaAs NW body during VLS growths [87]. In order to overcome this drawback, alternative metals such as Al [103], Ti [104], and Ga [105, 106] have been proposed as an alternative for Au.

GaAs NWs have been grown by homo-PAG in MBE [106] and CBE (chapter 7); this kind of growth is also called Ga-assisted. Among all possible substrates, Si is widely used for Ga-assisted GaAs NW growths because of many advantages (see chapter 1, section 1.3.1). In that respect, homo-PAG GaAs NWs have been grown on both Si(100) and Si(111) substrates, resulting in NWs which are forming angles of 34.5º and 90º with respect to the substrate surface, respectively. These results confirm the epitaxial growth of these NWs along the preferential direction fixed by the substrate crystal orientation.

Figure 2.13 shows a schematic of GaAs NWs grown by Ga-assisted method on oxidized Si substrates. Since both Ga and As elements are directly supplied to the NW growth, this schematic could explain a typical growth carried out in MBE through VLS mechanism. Although VLS mechanism was firstly developed to explain the growth of Si NWs using Au particles (hetero-PAG) (figure 2.3), it has been demonstrated to be also valid for homo-PAG processes.

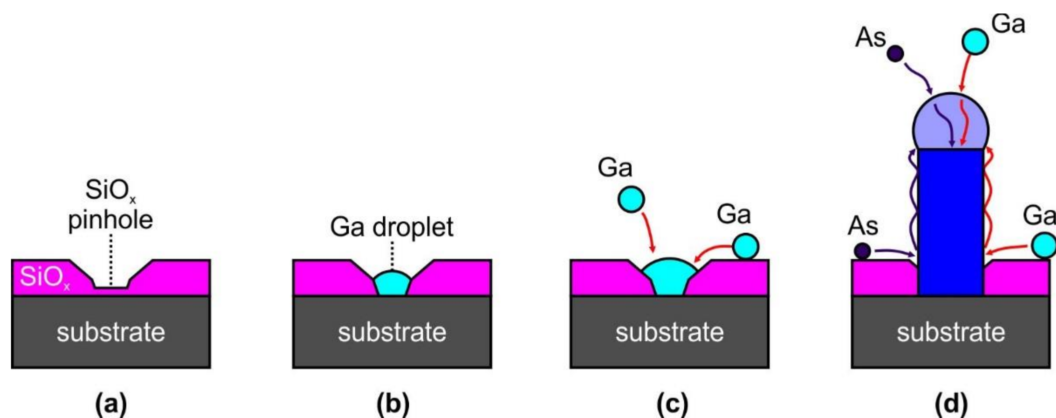

Figure 2.13. Schematic of a Ga-assisted GaAs NWs grown in MBE.

Prior to the growth, a hydrofluoric acid (HF) etching of the substrate surface oxide (SiO_x) is carried out in order to open pinholes in the oxide layer, exposing the underlying Si substrate (figure 2.13(a)) [107]. The pinholes are anticipated to serve as nucleation sites for GaAs since the sticking coefficient of Ga adatoms on Si is much higher than on SiO_x. After that, Ga flux is opened, allowing for Ga atoms to form Ga droplets at the oxide pinholes (figure 2.13(b)). In that respect, Ga atoms react with the SiO_x at the pinhole, producing oxidized Ga droplets and deoxidizing the Si surface:

$$\mathrm{Ga(g) + SiO_x(s) \rightarrow GaO_x(l) + Si(s)} \tag{2.9}$$

Ga droplets formed in this stage are therefore in contact with the Si surface and then are chemically immobilized. In addition, this contact between droplet and substrate surface will allow the growth of the NW along the preferential direction fixed by the substrate orientation. However, the increase of the initial SiO_x layer thickness in the range of 6 to 20 nm is confirmed to hinder the preferential orientation of NWs. A further increase of the oxide thickness (> 30 nm) can even inhibit the NW growth [106].

At temperatures above 530 °C, the oxide capping layer of the Ga droplets tends to be desorbed:

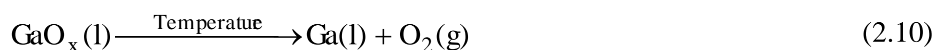

$$\mathrm{GaO_x(l) \xrightarrow{Temperatue} Ga(l) + O_2(g)} \tag{2.10}$$

During the pre-deposition of Ga, Ga droplet size can be changed due to the rearrangement of liquid droplets or the incorporation of Ga atoms from the gas flux (figure 2.13(c)). Since both Ga and As fluxes are opened, both As and Ga atoms are incorporated at the surface of the initial Ga droplet. As the concentration of As in the droplet increases, the As solubility limit can be achieved in the droplet, leading to the GaAs epitaxial growth at the liquid-solid interface (figure 2.13(d)). When the GaAs solid phase underneath the droplet accumulates enough strain the NW growth is observed.

During the NW growth, Ga atoms have two different ways to be incorporated to the Ga droplet: i) the direct incorporation from the Ga gas flux, and ii) the diffusion of Ga atoms from the base of the NW along the NW facet (figure 2.13(d)). The mobility of Ga species over the SiO_x surface layer is very high, which means, Ga atoms remain mobile until they are desorbed by effect of the temperature or are incorporated to the Ga droplet. Since the absorbed/consumed ratio of Ga atoms at the droplet is preserved, the droplet keeps its sizes, and promotes the growth of the NW along a preferential direction, resulting in a high-aspect ratio free-standing NW. The aspect ratio of the NW can be also affected by changes in the average NW length. The formation of Ga droplets may also occur during the nucleation of GaAs NWs, i.e. Ga and As fluxes are opened, which means the growth of NWs can start at different moments, resulting in NWs with different lengths.

The mechanisms that govern the homo-PAG of GaAs NWs in a CBE system are different to the MBE technique mainly because the use of metalorganic sources rather than pure form gas sources. In this regard, this work aims to understand the growth kinetics of GaAs NWs by means of homo-PAG CBE (chapter 7).

2.3.2. Properties of GaAs NWs

Photoconductivity

Thunich et al. [108] studied optoelectronic properties of a single p-doped GaAs NW freely suspended between two Au electrodes acting as drain/source electrodes. Since the NW is illuminated, the current through the NW is enhanced mainly due to two different mechanisms:

i) the photocurrent generated at the SB contacts between the NW and metal source-drain electrodes [109].

ii) the photoconductance generated at illuminated NW regions away from the contacts.

The photoconductance effect is related to the surface BB produced by the surface states along the NW. Separated charge carriers can contribute two-fold to the photoconductance of the NWs. Since the NW is illuminated: 1) photogenerated electrons tend to be trapped along the NW surface, acting as a negative gating voltage on the p-doped NW (photo-gating effect) and then increasing the conductive bulk; 2) photoholes density increases within the NW (photo-doping effect). Both photocurrent and photoconductance of a GaAs NW are demonstrated to be dependent on the polarization of the incident light. The photocurrent and photoconductance vary 35% and 15%, respectively, for a photon polarization parallel and perpendicular to the NW axis. Furthermore, the time response of a GaAs NW is obtained to be faster than 200 μs.

Structural Properties

Due to the large surface-to-volume ratio of NWs, they may crystallize in structures that are not stable in the bulk form. In the case of GaAs NWs, it is very common to find polytypisms between WZ and ZB phases along the NW structure [86]. It is worth noting that WZ is not stable in the bulk form of GaAs. From the thermodynamic point of view, the surface energy of {1100} WZ planes should be lower than the {110}, and {111}A/B of ZB [110]. In that respect, for small radii NWs the WZ phase should be more stable than the ZB. In the case of GaAs, the critical radius under which WZ is expected to be the most stable phase has been predicted to lie between 5 and 26 nm [86].

GaAs NW structure has been analyzed by TEM, showing that GaAs NWs grow perpendicularly on GaAs(111) and Si(111) [86, 111] substrates whereas NWs appear at 35º to the surface of GaAs(100) substrates [112]. The growth direction thus coincides with one of the <111> directions of the underlying substrate [113]. The low growth rate of GaAs NW facets $\{0\bar{1}1\}$ in comparison to the {111} surface improves the diffusion of Ga species along the NW facets towards the growth region, promoting the preferential growth of the NW along the <111> direction.

Different structural defects, including twins and staking faults, are observed during VLS growth of GaAs NWs. The formation of twins, i.e. structural rotations conserving the phase, has been observed in both hetero- and homo-PAG of GaAs NWs. In the case of hetero-PAG, the use of a foreign particle such as Au can induce the formation of ZB/WZ intermixing along the NW stem through stacking faults in the {111} planes

[92, 101]. In the case of homo-PAG, NWs grown along the $[\bar{1}\,\bar{1}\,\bar{1}]$B growth direction exhibit a high density of stacking faults perpendicularly aligned to the growth direction, whereas, NWs grown along the [111]A direction present lack of stacking faults [114]. However, [111]A NWs present significant tapering and their growth orientation is less well-controlled than the NWs grown along the $[\bar{1}\,\bar{1}\,\bar{1}]$B.

Zardo et al. [86] analyzed GaAs NWs with different contents of ZB and WZ phases by Raman spectroscopy. Each crystalline phase is demonstrated to be more sensitive to a specific configuration of the polarization of the incident/analyzed beams with respect to the NW axis. The intensity of the Raman peaks associated to the ZB or WZ phases is observed to be enhanced using incident/analyzed beams polarized parallel or perpendicular to the NW axis, respectively. The presence of both crystalline phases along the GaAs NWs and, in particular, the existing strain between both phases leads to a relative shift of TO phonons E_1 (267 cm^{-1}) and E_2^H (255 cm^{-1}), which are related to the ZB and WZ phases, respectively. Raman spectra also show the existence of a third peak located between LO and TO which is associated to the surface optical (SO) phonon. The existence of this peak means the presence of roughness along the {110} facets.

Photoluminescence

Novikov et al. [115] analyzed the PL of GaAs NWs at 5 K. GaAs NWs with predominant ZB or WZ phases present a PL peak at 1.519 eV or 1.478 eV, respectively. Both peaks correspond to a free exciton emission from ZB and WZ crystal phases. The polarization of the emission is observed to be characteristic of the crystalline phase; ZB and WZ NWs exhibit emission polarized parallel and perpendicular to the NW axis, respectively. On the other hand, ZB NWs with an average diameter of 40 nm show a slight blue-shift of the PL peak of around 5 meV with respect to the PL peak of GaAs bulk, which is related to a quantum confinement effect in narrow NWs.

Thermal Conductivity

Soini et al. [116] estimated the thermal conductivity (κ) of a freely suspended GaAs NW. The method is based on the laser heating of the NW and the measurement of the local temperature by micro-Raman spectroscopy. In this regard, the local temperature is estimated from the shift of the TO peak. κ values of a GaAs NW with a diameter of 160 nm lie in the range of 8 (300 K) and 36 (400 K) W/m·K; being lower than those results obtained in GaAs bulk (54 W/m·K) [117]. These results are in good agreement with predicted values published by Martin et al. [118].

REFERENCES

[1] W. J. Bentley and P. L. Sterm, "The preparation of zinc nitride and its alloy with zinc," *Armour Institute of Technology,* 1920.

[2] R. Juza and H. Hahn, "Über die Kristallstrukturen von Zn3N2, Cd3N2 und Ge3N4. Metallamide und Metallnitride. IX. Mitteilung," *Zeitschrift für anorganische und allgemeine Chemie,* vol. 244, pp. 125-132, 1940.

[3] K. Kuriyama, Y. Takahashi, and F. Sunohara, "Optical band gap of Zn 3 N 2 films," *Physical Review B,* vol. 48, p. 2781, 1993.

[4] M. Futsuhara, K. Yoshioka, and O. Takai, "Structural, electrical and optical properties of zinc nitride thin films prepared by reactive rf magnetron sputtering," *Thin Solid Films,* vol. 322, pp. 274-281, 1998.

[5] K. Toyoura, H. Tsujimura, T. Goto, K. Hachiya, R. Hagiwara, and Y. Ito, "Optical properties of zinc nitride formed by molten salt electrochemical process," *Thin Solid Films,* vol. 492, pp. 88-92, 2005.

[6] T. Suda and K. Kakishita, "Band-gap energy and electron effective mass of polycrystalline Zn3N2," *Journal of Applied Physics,* vol. 99, p. 076101, 2006.

[7] S. Simi, I. Navas, R. Vinodkumar, S. Chalana, M. Gangrade, V. Ganesan*, et al.*, "Pulsed laser ablation of zinc selenide in nitrogen ambience: Formation of zinc nitride films," *Applied Surface Science,* vol. 257, pp. 9269-9276, 2011.

[8] D. Partin, D. Williams, and M. O'Keeffe, "The Crystal Structures of Mg 3 N 2 and Zn 3 N 2," *Journal of Solid State Chemistry,* vol. 132, pp. 56-59, 1997.

[9] R. Long, Y. Dai, L. Yu, B. Huang, and S. Han, "Atomic geometry and electronic structure of defects in Zn 3 N 2," *Thin Solid Films,* vol. 516, pp. 1297-1301, 2008.

[10] T. Yang, Z. Zhang, Y. Li, M. Lv, S. Song, Z. Wu*, et al.*, "Structural and optical properties of zinc nitride films prepared by rf magnetron sputtering," *Applied Surface Science,* vol. 255, pp. 3544-3547, 2009.

[11] W. Du, F. Zong, H. Ma, J. Ma, M. Zhang, X. Feng*, et al.*, "Optical band gap of zinc nitride films prepared by reactive rf magnetron sputtering," *Crystal Research and Technology,* vol. 41, pp. 889-892, 2006.

[12] F. Zong, H. Ma, W. Du, J. Ma, X. Zhang, H. Xiao*, et al.*, "Optical band gap of zinc nitride films prepared on quartz substrates from a zinc nitride target by reactive rf magnetron sputtering," *Applied surface science,* vol. 252, pp. 7983-7986, 2006.

[13] R. Ayouchi, C. Casteleiro, L. Santos, and R. Schwarz, "RF-plasma assisted PLD growth of Zn3N2 thin films," *physica status solidi (c),* vol. 7, pp. 2294-2297, 2010.

[14] R. Long, Y. Dai, L. Yu, M. Guo, and B. Huang, "Structural, electronic, and optical properties of oxygen defects in Zn3N2," *The Journal of Physical Chemistry B,* vol. 111, pp. 3379-3383, 2007.

[15] E. Burstein, "Anomalous optical absorption limit in InSb," *Physical Review,* vol. 93, p. 632, 1954.

[16] T. S. Moss, *Proc. Phys. Soc. London,* vol. B67, p. 775, 1954.

[17] J. Wu, W. Walukiewicz, K. Yu, J. W. Ager, E. Haller, H. Lu*, et al.*, "Small band gap bowing in In 1-x Ga x N alloys," *Applied Physics Letters,* vol. 80, pp. 4741-4743, 2002.

[18] V. Kambilafka, P. Voulgaropoulou, S. Dounis, E. Iliopoulos, M. Androulidaki, V. Šály, *et al.*, "Thermal oxidation of n-type ZnN films made by rf-sputtering from a zinc nitride target, and their conversion into p-type films," *Superlattices and Microstructures,* vol. 42, pp. 55-61, 2007.

[19] C. Geng, Y. Jiang, Y. Yao, X. Meng, J. A. Zapien, C. S. Lee, *et al.*, "Well-Aligned ZnO Nanowire Arrays Fabricated on Silicon Substrates," *Advanced Functional Materials,* vol. 14, pp. 589-594, 2004.

[20] Y. K. Tseng, C. J. Huang, H. M. Cheng, I. N. Lin, K. S. Liu, and I. C. Chen, "Characterization and Field-Emission Properties of Needle-like Zinc Oxide Nanowires Grown Vertically on Conductive Zinc Oxide Films," *Advanced functional materials,* vol. 13, pp. 811-814, 2003.

[21] J. Jie, G. Wang, Y. Chen, X. Han, Q. Wang, B. Xu, *et al.*, "Synthesis and optical properties of well-aligned ZnO nanorod array on an undoped ZnO film," *Applied Physics Letters,* vol. 86, p. 031909, 2005.

[22] C. Li, G. Fang, Q. Fu, F. Su, G. Li, X. Wu, *et al.*, "Effect of substrate temperature on the growth and photoluminescence properties of vertically aligned ZnO nanostructures," *Journal of crystal growth,* vol. 292, pp. 19-25, 2006.

[23] W. I. Park, D. H. Kim, S.-W. Jung, and G.-C. Yi, "Metalorganic vapor-phase epitaxial growth of vertically well-aligned ZnO nanorods," *Applied Physics Letters,* vol. 80, pp. 4232-4234, 2002.

[24] S. C. Lyu, Y. Zhang, C. J. Lee, H. Ruh, and H. J. Lee, "Low-temperature growth of ZnO nanowire array by a simple physical vapor-deposition method," *Chemistry of materials,* vol. 15, pp. 3294-3299, 2003.

[25] L. Vayssieres, "Growth of arrayed nanorods and nanowires of ZnO from aqueous solutions," *Advanced Materials,* vol. 15, pp. 464-466, 2003.

[26] P.-C. Chang, Z. Fan, D. Wang, W.-Y. Tseng, W.-A. Chiou, J. Hong, *et al.*, "ZnO nanowires synthesized by vapor trapping CVD method," *Chemistry of materials,* vol. 16, pp. 5133-5137, 2004.

[27] Z. R. Dai, Z. W. Pan, and Z. L. Wang, "Novel nanostructures of functional oxides synthesized by thermal evaporation," *Advanced Functional Materials,* vol. 13, pp. 9-24, 2003.

[28] H. J. Son, K. A. Jeon, C. E. Kim, J. H. Kim, K. H. Yoo, and S. Y. Lee, "Synthesis of ZnO nanowires by pulsed laser deposition in furnace," *Applied surface science,* vol. 253, pp. 7848-7850, 2007.

[29] J. Conley Jr, L. Stecker, and Y. Ono, "Directed assembly of ZnO nanowires on a Si substrate without a metal catalyst using a patterned ZnO seed layer," *Nanotechnology,* vol. 16, p. 292, 2005.

[30] L.-W. Ji, S.-M. Peng, J.-S. Wu, W.-S. Shih, C.-Z. Wu, and I.-T. Tang, "Effect of seed layer on the growth of well-aligned ZnO nanowires," *Journal of Physics and Chemistry of Solids,* vol. 70, pp. 1359-1362, 2009.

[31] K. P. Musselman, A. Wisnet, D. C. Iza, H. C. Hesse, C. Scheu, J. L. MacManus-Driscoll, *et al.*, "Strong Efficiency Improvements in Ultra-low-Cost Inorganic Nanowire Solar Cells," *Advanced Materials,* vol. 22, pp. E254-E258, 2010.

[32] Y. Tong, Y. Liu, C. Shao, and R. Mu, "Structural and optical properties of ZnO nanotower bundles," *Applied physics letters,* vol. 88, p. 123111, 2006.

[33] S. L. Brock, "Nanostructures and Nanomaterials: Synthesis, Properties and Applications By Guozhang Cao (University of Washington). Imperial College Press (distributed by World Scientific): London.

2004. xiv+ 434 pp. $78.00. ISBN 1-86094-415-9," *Journal of the American Chemical Society,* vol. 126, pp. 14679-14679, 2004.

[34] S. Rackauskas, A. G. Nasibulin, H. Jiang, Y. Tian, G. Statkute, S. D. Shandakov, *et al.*, "Mechanistic investigation of ZnO nanowire growth," *Applied Physics Letters,* vol. 95, p. 183114, 2009.

[35] Z. W. Pan, Z. R. Dai, and Z. L. Wang, "Nanobelts of semiconducting oxides," *Science,* vol. 291, pp. 1947-1949, 2001.

[36] J. Lao, J. Huang, D. Wang, and Z. Ren, "ZnO nanobridges and nanonails," *Nano Letters,* vol. 3, pp. 235-238, 2003.

[37] Y. Leung, K. Tam, A. Djurišić, M. Xie, W. Chan, D. Lu, *et al.*, "Zno nanoshells: Synthesis, structure, and optical properties," *Journal of crystal growth,* vol. 283, pp. 134-140, 2005.

[38] S. Rackauskas, K. Mustonen, T. Järvinen, M. Mattila, O. Klimova, H. Jiang, *et al.*, "Synthesis of ZnO tetrapods for flexible and transparent UV sensors," *Nanotechnology,* vol. 23, p. 095502, 2012.

[39] R. S. Wagner and W. C. Ellis, "VAPOR-LIQUID-SOLID MECHANISM OF SINGLE CRYSTAL GROWTH," *Applied Physics Letters,* vol. 4, pp. 89-90, 1964.

[40] P. Yang, H. Yan, S. Mao, R. Russo, J. Johnson, R. Saykally, *et al.*, "Controlled growth of ZnO nanowires and their optical properties," *Advanced Functional Materials,* vol. 12, p. 323, 2002.

[41] P. Kung, A. Mohanta, J. G. Simmons, H. O. Everitt, G. Shen, J. Waters, *et al.*, "Synthesis and Optical Properties of Undoped and Aluminum Doped ZnO Nanowires for Optoelectronic Nanodevice Applications," in *Photonics Society Summer Topical Meeting Series, 2014 IEEE*, 2014, pp. 198-199.

[42] Ü. Özgür, Y. I. Alivov, C. Liu, A. Teke, M. A. Reshchikov, S. Doğan, *et al.*, "A comprehensive review of ZnO materials and devices," *Journal of Applied Physics,* vol. 98, p. 041301, 2005.

[43] S. Pearton, D. Norton, K. Ip, Y. Heo, and T. Steiner, "Recent advances in processing of ZnO," *Journal of Vacuum Science & Technology B,* vol. 22, pp. 932-948, 2004.

[44] F. Z. Wang, Z. Z. Ye, D. W. Ma, L. P. Zhu, F. Zhuge, and H. P. He, "Synthesis and characterization of quasi-aligned ZnCdO nanorods," *Applied Physics Letters,* vol. 87, p. 143101, 2005.

[45] M. Zhi, L. Zhu, Z. Ye, F. Wang, and B. Zhao, "Preparation and Properties of Ternary ZnMgO Nanowires," *The Journal of Physical Chemistry B,* vol. 109, pp. 23930-23934, 2005/12/01 2005.

[46] E. Mollow, *Proceedings of the Photoconductivity Conference,* pp. 509-512, 1954.

[47] H. Fabricius, T. Skettrup, and P. Bisgaard, "Ultraviolet detectors in thin sputtered ZnO films," *Applied optics,* vol. 25, pp. 2764-2767, 1986.

[48] Y. Zhang, A. Kolmakov, S. Chretien, H. Metiu, and M. Moskovits, "Control of catalytic reactions at the surface of a metal oxide nanowire by manipulating electron density inside it," *Nano Letters,* vol. 4, pp. 403-407, 2004.

[49] F. Chaabouni, M. Abaab, and B. Rezig, "Metrological characteristics of ZnO oxygen sensor at room temperature," *Sensors and Actuators B: chemical,* vol. 100, pp. 200-204, 2004.

[50] J. Zhou, Y. Gu, Y. Hu, W. Mai, P.-H. Yeh, G. Bao, *et al.*, "Gigantic enhancement in response and reset time of ZnO UV nanosensor by utilizing Schottky contact and surface functionalization," *Applied Physics Letters,* vol. 94, p. 191103, 2009.

[51] D. Lin, H. Wu, W. Zhang, H. Li, and W. Pan, "Enhanced UV photoresponse from heterostructured Ag–ZnO nanowires," *Applied Physics Letters,* vol. 94, p. 172103, 2009.

[52] C. Lao, Y. Li, C. Wong, and Z. Wang, "Enhancing the electrical and optoelectronic performance of nanobelt devices by molecular surface functionalization," *Nano letters,* vol. 7, pp. 1323-1328, 2007.

[53] G. Cheng, S. Wang, K. Cheng, X. Jiang, L. Wang, L. Li, *et al.*, "The current image of a single CuO nanowire studied by conductive atomic force microscopy," *Applied Physics Letters,* vol. 92, p. 223116, 2008.

[54] C. Soci, A. Zhang, B. Xiang, S. A. Dayeh, D. Aplin, J. Park, *et al.*, "ZnO nanowire UV photodetectors with high internal gain," *Nano letters,* vol. 7, pp. 1003-1009, 2007.

[55] G. Cheng, X. Wu, B. Liu, B. Li, X. Zhang, and Z. Du, "ZnO nanowire Schottky barrier ultraviolet photodetector with high sensitivity and fast recovery speed," *Applied Physics Letters,* vol. 99, p. 203105, 2011.

[56] J. Albertsson, S. Abrahams, and Å. Kvick, "Atomic displacement, anharmonic thermal vibration, expansivity and pyroelectric coefficient thermal dependences in ZnO," *Acta Crystallographica Section B: Structural Science,* vol. 45, pp. 34-40, 1989.

[57] Y. Zhang, H. Jia, R. Wang, C. Chen, X. Luo, D. Yu, *et al.*, "Low-temperature growth and Raman scattering study of vertically aligned ZnO nanowires on Si substrate," *Applied physics letters,* vol. 83, pp. 4631-4633, 2003.

[58] M. Rajalakshmi, A. K. Arora, B. Bendre, and S. Mahamuni, "Optical phonon confinement in zinc oxide nanoparticles," *Journal of Applied Physics,* vol. 87, pp. 2445-2448, 2000.

[59] J. Scott, "UV resonant Raman scattering in ZnO," *Physical Review B,* vol. 2, p. 1209, 1970.

[60] W. I. Park, J. S. Kim, G.-C. Yi, M. Bae, and H.-J. Lee, "Fabrication and electrical characteristics of high-performance ZnO nanorod field-effect transistors," *Applied Physics Letters,* vol. 85, pp. 5052-5054, 2004.

[61] J. Song, X. Wang, E. Riedo, and Z. L. Wang, "Elastic property of vertically aligned nanowires," *Nano Letters,* vol. 5, pp. 1954-1958, 2005.

[62] Y. Huang, Y. Zhang, X. Wang, X. Bai, Y. Gu, X. Yan, *et al.*, "Size independence and doping dependence of bending modulus in ZnO nanowires," *Crystal Growth and Design,* vol. 9, pp. 1640-1642, 2009.

[63] Z. L. Wang, "Zinc oxide nanostructures: growth, properties and applications," *Journal of Physics: Condensed Matter,* vol. 16, p. R829, 2004.

[64] J.-H. Lee, K.-H. Ko, and B.-O. Park, "Electrical and optical properties of ZnO transparent conducting films by the sol–gel method," *Journal of Crystal Growth,* vol. 247, pp. 119-125, 2003.

[65] D. Bao, H. Gu, and A. Kuang, "Sol-gel-derived c-axis oriented ZnO thin films," *Thin solid films,* vol. 312, pp. 37-39, 1998.

[66] T. Kawano and H. Imai, "Characteristically shaped ZnO particles produced by periodic precipitation in organic gel media," *Journal of crystal growth,* vol. 283, pp. 490-499, 2005.

[67] H. J. Fan, W. Lee, R. Hauschild, M. Alexe, G. Le Rhun, R. Scholz, *et al.*, "Template-Assisted Large-Scale Ordered Arrays of ZnO Pillars for Optical and Piezoelectric Applications," *Small,* vol. 2, pp. 561-568, 2006.

[68] R. Zhu, D. Wang, S. Xiang, Z. Zhou, and X. Ye, "Piezoelectric characterization of a single zinc oxide nanowire using a nanoelectromechanical oscillator," *Nanotechnology,* vol. 19, p. 285712, 2008.

[69] J. Christman, H. Maiwa, S.-H. Kim, A. Kingon, and R. Nemanich, "Piezoelectric measurements with atomic force microscopy," in *MRS Proceedings*, 1998, p. 617.

[70] A. Kolmakov and M. Moskovits, "Chemical sensing and catalysis by one-dimensional metal-oxide nanostructures," *Annu. Rev. Mater. Res.,* vol. 34, pp. 151-180, 2004.

[71] J. Jose and M. A. Khadar, "Impedance spectroscopic analysis of AC response of nanophase ZnO and ZnO-Al 2 O 3 nanocomposites," *Nanostructured materials,* vol. 11, pp. 1091-1099, 1999.

[72] J. G. Lu, P. Chang, and Z. Fan, "Quasi-one-dimensional metal oxide materials—synthesis, properties and applications," *Materials Science and Engineering: R: Reports,* vol. 52, pp. 49-91, 2006.

[73] Z. Fan and J. G. Lu, "Gate-refreshable nanowire chemical sensors," *Applied Physics Letters,* vol. 86, p. 123510, 2005.

[74] Z. Fan, D. Wang, P.-C. Chang, W.-Y. Tseng, and J. G. Lu, "ZnO nanowire field-effect transistor and oxygen sensing property," *Applied Physics Letters,* vol. 85, pp. 5923-5925, 2004.

[75] H. T. Ng, B. Chen, J. Li, J. Han, M. Meyyappan, J. Wu, *et al.*, "Optical properties of single-crystalline ZnO nanowires on m-sapphire," *Applied Physics Letters,* vol. 82, pp. 2023-2025, 2003.

[76] M. H. Huang, Y. Wu, H. Feick, N. Tran, E. Weber, and P. Yang, "Catalytic growth of zinc oxide nanowires by vapor transport," *Advanced Materials,* vol. 13, pp. 113-116, 2001.

[77] S. Bethke, H. Pan, and B. W. Wessels, "Luminescence of heteroepitaxial zinc oxide," *Applied Physics Letters,* vol. 52, pp. 138-140, 1988.

[78] G. Cirlin, V. Dubrovskii, Y. B. Samsonenko, A. Bouravleuv, K. Durose, Y. Y. Proskuryakov, *et al.*, "Self-catalyzed, pure zincblende GaAs nanowires grown on Si (111) by molecular beam epitaxy," *Physical Review B,* vol. 82, p. 035302, 2010.

[79] G. E. Cirlin, V. G. Dubrovskii, I. P. Soshnikov, N. V. Sibirev, Y. B. Samsonenko, A. D. Bouravleuv, *et al.*, "Critical diameters and temperature domains for MBE growth of III–V nanowires on lattice mismatched substrates," *physica status solidi (RRL) – Rapid Research Letters,* vol. 3, pp. 112-114, 2009.

[80] S.-G. Ihn, J.-I. Song, T.-W. Kim, D.-S. Leem, T. Lee, S.-G. Lee, *et al.*, "Morphology-and orientation-controlled gallium arsenide nanowires on silicon substrates," *Nano letters,* vol. 7, pp. 39-44, 2007.

[81] V. Dubrovskii, G. Cirlin, N. Sibirev, F. Jabeen, J. Harmand, and P. Werner, "New mode of vapor− liquid− solid nanowire growth," *Nano letters,* vol. 11, pp. 1247-1253, 2011.

[82] F. Glas, "Critical dimensions for the plastic relaxation of strained axial heterostructures in free-standing nanowires," *Physical Review B,* vol. 74, p. 121302, 2006.

[83] Y. H. Kim, D. W. Park, and S. J. Lee, "Gallium-droplet behaviors of self-catalyzed GaAs nanowires: A transmission electron microscopy study," *Applied Physics Letters,* vol. 100, p. 033117, 2012.

[84] S. Plissard, K. A. Dick, G. Larrieu, S. Godey, A. Addad, X. Wallart*, et al.*, "Gold-free growth of GaAs nanowires on silicon: arrays and polytypism," *Nanotechnology,* vol. 21, p. 385602, 2010.

[85] S. Breuer, M. Hilse, A. Trampert, L. Geelhaar, and H. Riechert, "Vapor-liquid-solid nucleation of GaAs on Si (111): Growth evolution from traces to nanowires," *Physical Review B,* vol. 82, p. 075406, 2010.

[86] I. Zardo, S. Conesa-Boj, F. Peiro, J. Morante, J. Arbiol, E. Uccelli*, et al.*, "Raman spectroscopy of wurtzite and zinc-blende GaAs nanowires: polarization dependence, selection rules, and strain effects," *Physical Review B,* vol. 80, p. 245324, 2009.

[87] H. Shtrikman, R. Popovitz-Biro, A. Kretinin, L. Houben, M. Heiblum, M. Bukała*, et al.*, "Method for suppression of stacking faults in wurtzite III− V nanowires," *Nano letters,* vol. 9, pp. 1506-1510, 2009.

[88] L. Ahtapodov, J. Todorovic, P. Olk, T. Mjåland, P. Slåttnes, D. L. Dheeraj*, et al.*, "A story told by a single nanowire: optical properties of wurtzite GaAs," *Nano letters,* vol. 12, pp. 6090-6095, 2012.

[89] H. Huang, X. Ren, X. Ye, J. Guo, Q. Wang, Y. Yang*, et al.*, "Growth of Stacking-Faults-Free Zinc Blende GaAs Nanowires on Si Substrate by Using AlGaAs/GaAs Buffer Layers," *Nano Letters,* vol. 10, pp. 64-68, 2010/01/13 2010.

[90] H. J. Joyce, Q. Gao, H. H. Tan, C. Jagadish, Y. Kim, M. A. Fickenscher*, et al.*, "High purity GaAs nanowires free of planar defects: growth and characterization," *Advanced Functional Materials,* vol. 18, pp. 3794-3800, 2008.

[91] S. Lehmann, D. Jacobsson, K. Deppert, and K. A. Dick, "High crystal quality wurtzite-zinc blende heterostructures in metal-organic vapor phase epitaxy-grown GaAs nanowires," *Nano Research,* vol. 5, pp. 470-476, 2012.

[92] A. I. Persson, M. W. Larsson, S. Stenström, B. J. Ohlsson, L. Samuelson, and L. R. Wallenberg, "Solid-phase diffusion mechanism for GaAs nanowire growth," *Nature materials,* vol. 3, pp. 677-681, 2004.

[93] B. Ohlsson, M. Björk, M. Magnusson, K. Deppert, L. Samuelson, and L. Wallenberg, "Size-, shape-, and position-controlled GaAs nano-whiskers," *Applied Physics Letters,* vol. 79, pp. 3335-3337, 2001.

[94] L. Samuelson, M. T. Björk, K. Deppert, M. Larsson, B. J. Ohlsson, N. Panev*, et al.*, "Semiconductor nanowires for novel one-dimensional devices," *Physica E: Low-dimensional Systems and Nanostructures,* vol. 21, pp. 560-567, 3// 2004.

[95] W. Lu and C. M. Lieber, "Nanoelectronics from the bottom up," *Nature materials,* vol. 6, pp. 841-850, 2007.

[96] K. Ikejiri, T. Sato, H. Yoshida, K. Hiruma, J. Motohisa, S. Hara*, et al.*, "Growth characteristics of GaAs nanowires obtained by selective area metal–organic vapour-phase epitaxy," *Nanotechnology,* vol. 19, p. 265604, 2008.

[97] R. Q. Zhang, Y. Lifshitz, and S. T. Lee, "Oxide-Assisted Growth of Semiconducting Nanowires," *Advanced Materials,* vol. 15, pp. 635-640, 2003.

[98] C. Colombo, D. Spirkoska, M. Frimmer, G. Abstreiter, and A. F. i Morral, "Ga-assisted catalyst-free growth mechanism of GaAs nanowires by molecular beam epitaxy," *Physical Review B,* vol. 77, p. 155326, 2008.

[99] J. Harmand, M. Tchernycheva, G. Patriarche, L. Travers, F. Glas, and G. Cirlin, "GaAs nanowires formed by Au-assisted molecular beam epitaxy: Effect of growth temperature," *Journal of Crystal Growth,* vol. 301, pp. 853-856, 2007.

[100] E. Givargizov, "Fundamental aspects of VLS growth," *Journal of Crystal Growth,* vol. 31, pp. 20-30, 1975.

[101] K. Hiruma, M. Yazawa, K. Haraguchi, K. Ogawa, T. Katsuyama, M. Koguchi, *et al.*, "GaAs free-standing quantum-size wires," *Journal of Applied Physics,* vol. 74, pp. 3162-3171, 1993.

[102] D. E. Perea, J. E. Allen, S. J. May, B. W. Wessels, D. N. Seidman, and L. J. Lauhon, "Three-dimensional nanoscale composition mapping of semiconductor nanowires," *Nano letters,* vol. 6, pp. 181-185, 2006.

[103] Y. Wang, V. Schmidt, S. Senz, and U. Gösele, "Epitaxial growth of silicon nanowires using an aluminium catalyst," *Nature nanotechnology,* vol. 1, pp. 186-189, 2006.

[104] T. Kamins, R. S. Williams, D. Basile, T. Hesjedal, and J. Harris, "Ti-catalyzed Si nanowires by chemical vapor deposition: Microscopy and growth mechanisms," *Journal of Applied Physics,* vol. 89, pp. 1008-1016, 2001.

[105] B. Mandl, J. Stangl, T. Mårtensson, A. Mikkelsen, J. Eriksson, L. S. Karlsson, *et al.*, "Au-free epitaxial growth of InAs nanowires," *Nano letters,* vol. 6, pp. 1817-1821, 2006.

[106] A. Fontcuberta i Morral, C. Colombo, G. Abstreiter, J. Arbiol, and J. Morante, "Nucleation mechanism of gallium-assisted molecular beam epitaxy growth of gallium arsenide nanowires," *Applied Physics Letters,* vol. 92, pp. 063112-063112-3, 2008.

[107] S. Hertenberger, "Growth and Properties of In(Ga)As Nanowires on Silicon," *Thesis Work,* vol. 978-3-941650-44-2, 2012.

[108] S. Thunich, L. Prechtel, D. Spirkoska, G. Abstreiter, A. Fontcuberta i Morral, and A. W. Holleitner, "Photocurrent and photoconductance properties of a GaAs nanowire," *Applied Physics Letters,* vol. 95, p. 083111, 2009.

[109] Y. Gu, E.-S. Kwak, J. Lensch, J. Allen, T. W. Odom, and L. J. Lauhon, "Near-field scanning photocurrent microscopy of a nanowire photodetector," *Applied Physics Letters,* vol. 87, p. 043111, 2005.

[110] F. Glas, J.-C. Harmand, and G. Patriarche, "Why does wurtzite form in nanowires of III-V zinc blende semiconductors?," *Physical review letters,* vol. 99, p. 146101, 2007.

[111] H. J. Joyce, Q. Gao, H. H. Tan, C. Jagadish, Y. Kim, X. Zhang, *et al.*, "Twin-free uniform epitaxial GaAs nanowires grown by a two-temperature process," *Nano letters,* vol. 7, pp. 921-926, 2007.

[112] A. Fontcuberta i Morral, D. Spirkoska, J. Arbiol, M. Heigoldt, J. R. Morante, and G. Abstreiter, "Prismatic Quantum Heterostructures Synthesized on Molecular-Beam Epitaxy GaAs Nanowires," *small,* vol. 4, pp. 899-903, 2008.

[113] K. Brunner, G. Abstreiter, G. Böhm, G. Tränkle, and G. Weimann, "Sharp-line photoluminescence and two-photon absorption of zero-dimensional biexcitons in a GaAs/AlGaAs structure," *Physical Review Letters,* vol. 73, p. 1138, 1994.

[114] B. A. Wacaser, K. Deppert, L. S. Karlsson, L. Samuelson, and W. Seifert, "Growth and characterization of defect free GaAs nanowires," *Journal of crystal growth,* vol. 287, pp. 504-508, 2006.

[115] B. Novikov, S. Y. Serov, N. Filosofov, I. Shtrom, V. Talalaev, O. Vyvenko*, et al.*, "Photoluminescence properties of GaAs nanowire ensembles with zincblende and wurtzite crystal structure," *physica status solidi (RRL)-Rapid Research Letters,* vol. 4, pp. 175-177, 2010.

[116] M. Soini, I. Zardo, E. Uccelli, S. Funk, G. Koblmüller, A. F. i Morral*, et al.*, "Thermal conductivity of GaAs nanowires studied by micro-Raman spectroscopy combined with laser heating," *Applied Physics Letters,* vol. 97, p. 263107, 2010.

[117] R. Carlson, G. Slack, and S. Silverman, "Thermal conductivity of GaAs and GaAs1− xPx laser semiconductors," *Journal of Applied Physics,* vol. 36, pp. 505-507, 1965.

[118] P. N. Martin, Z. Aksamija, E. Pop, and U. Ravaioli, "Reduced thermal conductivity in nanoengineered rough ge and gaas nanowires," *Nano letters,* vol. 10, pp. 1120-1124, 2010.

3. Growth Techniques

Growth systems described in this chapter have been used to synthesize materials analyzed in this work. These systems are available in the Microelectronics Laboratory and Electronic and Semiconductors Laboratory both located in the Applied Physics Department at UAM.

3.1. Magnetron Sputtering

Thin films of Zn-based semiconductor materials such as Zn_3N_2, ZnO and AZO as well as metal elements such as Al and Zn have been deposited using an Alcatel A450 magnetron sputtering system (figure 3.1) under controlled conditions of rf and direct current (DC) source powers, residual pressure (P_{res}), T_s, growth time, gas flow, and gas composition. In this system, gas reactive species are directly extracted from plasma, allowing for the growth of high quality polycrystalline layers due to the high vacuum ambient, and the use of T_s up to 573 K.

Figure 3.1. Magnetron sputtering system.

The sputtering process is based on particle-to-particle collisions, involving a momentum and energy transfer. During a sputtering process, ions either supplied from an ion gun or generated by exciting a neutral gas are accelerated towards a target by the applied electric field; as the ions are accelerated to impinge on the target surface, they extract target atoms and/or ions by energy exchange. The ejected atoms can arrive directly to the substrate and later absorb on its surface, thus growing a thin film of the same target

material (Al, Zn, and AZO cases). Ejected atoms can also react with plasma species such as N_2 or O_2 (reactive sputtering), composing a new material and then forming a thin film of this new material on the substrate (ZnO and Zn_3N_2 cases).

Our sputtering system uses a magnetron that utilizes strong electric and magnetic fields to confine charged plasma particles close to the surface of the sputter target. In a magnetic field, electrons follow magnetic field lines, promoting the increase of ionizing collisions with neutral gas near the target surface. In this regard, ions created as a result of these collisions lead to a higher deposition rate. Moreover, the sputtered atoms are neutrally charged and thus unaffected by the magnetic trap. The use of magnetron sputtering enables to the plasma formation and sustain even at lower pressures.

In this system, the growth process can be carried out by using either rf or DC power supplies. Charge build-up on insulating targets can be avoided with the use of rf-sputtering where the sign of the anode-cathode bias is varied at a high rate (commonly 13.56 MHz). On the other hand, the use of DC sputtering is therefore recommended only for conductive targets.

3.1.1. Gas Lines and Control System

Mass Flow Controller

The gas control system is responsible for the accurate and reproducible regulation of the gas fluxes which determine the growth rate, the composition, and the quality of the resulting layers. Our sputtering system uses a mass flow controller (MFC) to measure and to regulate gas fluxes.

Thermal MFCs are widely used to control gas flux in different applications; as its name implies, thermal MFC uses heat transfer to measure the gas flux by introducing a heat flux into the flow stream and measuring how much heat it dissipates using one or more temperature sensors. The heat leak rate from the sensor is dependent not only on the gas flux, but also on both the sensor design and the thermal properties of the gas species.

A precision power supply dissipates heat at the midpoint of a sensor tube carrying a constant fraction of the gas flow; on the same tube, resistance temperature measuring elements are placed equidistant upstream and downstream of the heating point. In absence of gas flow, the heat flux reaching each temperature sensing element is the same, and also the temperature increases at both sides, so no noticeable temperature difference is measured between them. Under gas flow conditions, the flow stream carries heat away from the upstream element to downstream element; an increasing temperature difference develops between both elements, this difference being proportional to the gas flux. A bridge measuring circuit senses the temperature difference which is then amplified to provide the analog signal output to the control electronics.

The gas flow can be determined by the MFC using basically two different methods based on the principle that higher velocity flow results in a greater cooling effect:

i) Constant differential temperature method. Mass flow rate is calculated based on the amount of electrical power required to maintain a constant difference in temperature between both temperature sensors.

ii) Constant current (power) method. Mass flow rate is calculated from the temperature difference reached on both temperature sensors while keeping constant current (power) on the heating element.

Once the gas flux is measured, the control electronics compares the set-point value to the measured gas flux, positioning a precision solenoid control valve in order to keep the gas flow at the fixed set-point, using an appropriate control algorithm, such as the proportional-integral-derivative (PID).

Working Gases

Figure 3.2 shows a schematic of the magnetron sputtering growth chamber during the synthesis of a Zn_3N_2 layer on a crystalline substrate. The working gases used in the sputtering system are Ar, O_2, and N_2 (all of them 99.999% purity). Ar gas is introduced into the growth chamber through a MFC, allowing for a maximum flow of 100 sccm, while O_2 and N_2 gases share the same MFC, which regulates the gas flux up to 50 sccm.

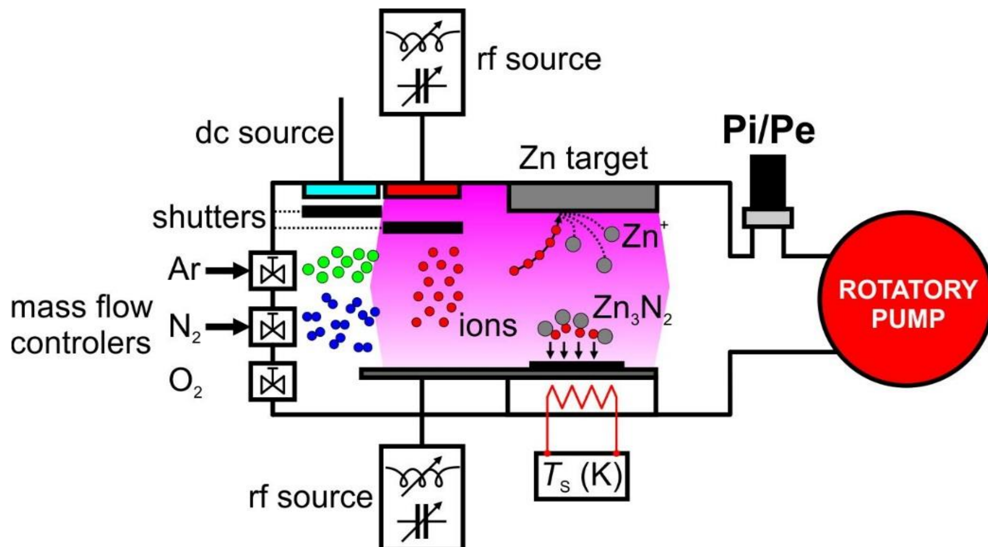

Figure 3.2. Schematic of the magnetron sputtering growth chamber.

As previously mentioned, the MFC reading depends on the properties of the gas species. Gas flow meters and controllers are usually calibrated for N_2; when used with gases different than N_2, a gas correction factor must be used (GCF). This factor is defined as the ratio between the gas fluxes of one specific gas and N_2 which will produce the same output signal in the same MFC; in this regard, GFC for N_2 is unity.

GCF is then dependent on specific heat, density, and molecular structure of the gases. The GCF for any other gas is determined by the following equation:

$$\mathrm{GCF_X} = \frac{0.3106 \cdot S}{d_\mathrm{X} \cdot C_\mathrm{pX}} \ , \tag{3.1}$$

where S is the molecular structure correction factor (S = 1.003 and S = 1 for monoatomic and diatomic gases, respectively), d_X is the density of the gas X expressed in g/l (under standard conditions, T = 0 ºC, P = 760 Torr), and C_{pX} is the specific heat of the gas X expressed in cal/g ºC. The GCF for Ar and O_2 gases was calculated using equation (3.1), resulting in S = 1.39, and S = 0.99, respectively.

3.1.2. Vacuum System

Figure 3.3 shows a schematic of the Alcatel A450 sputtering vacuum system used in this work; this system basically consists of two chambers: introduction and growth chambers, separated by the valve VM1.

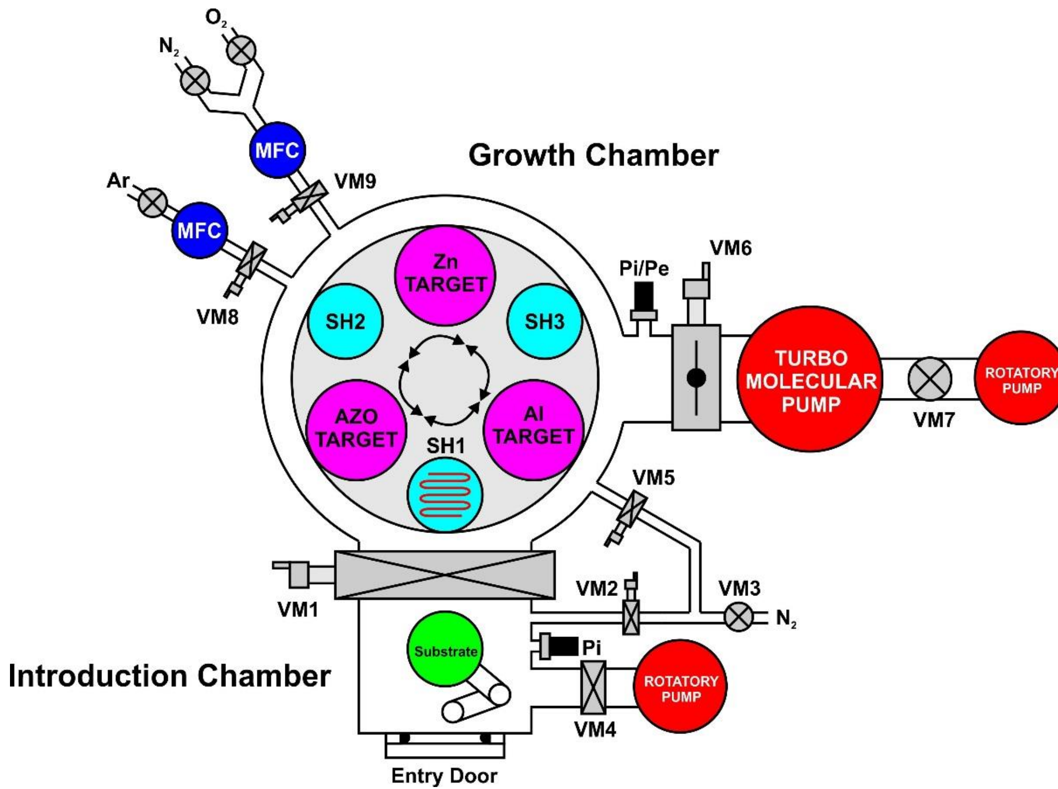

Figure 3.3. Schematic of the sputtering vacuum system.

The introduction chamber is used to load the samples into the system while preserving the high-vacuum conditions in the growth chamber. During sample introduction, both VM2 and VM3 valves are opened, while VM1, VM4 and VM5 are closed, in order to fill up the introduction chamber with a N_2 overpressure to prevent chamber contamination. The samples are loaded into the introduction chamber through an entry door. Once samples are loaded into the substrate holder, the N_2 purge is turned off by closing VM2 and VM3 valves; VM4 is then opened, pumping the introduction chamber down to 10^{-2} Torr, as

determined by a Pirani gauge located in this chamber, by the rotary pump (Alcatel 2004A, pumping rate 1 l/s). When the pressure in the introduction chamber reaches values close to 10^{-3} Torr, VM4 is now closed; growth and introduction chambers can then be connected by opening VM1, which allows for sample transfer from the introduction chamber to the growth chamber.

The growth chamber is pumped down using a turbo-molecular pump (Alcatel 5402CP, 380 l/s), assisted by a rotary pump (Alcatel 2033A, 10 l/s) by opening VM6 and VM7 valves. The residual pressure in the growth chamber reaches values around 10^{-6} Torr, as measured by a Penning gauge. When typical gas fluxes are introduced in the growth chamber, the turbo-molecular pump keeps the pressure in the 10^{-3} Torr range if the butterfly valve (VM6) is totally open. During a standard growth, VM6 is partly closed at around 80% of its full scale in order to increase the pressure in the growth chamber up to a 10^{-2} Torr value, which is necessary to allow for the formation of stable plasma.

Prior to the growth process, gas lines are evacuated through VM8 and VM9 (keeping Ar, N_2 and O_2 containers closed) while establishing the maximum set-point in the MFCs, until a 0 sccm reading is observed, at this moment gas lines can be considered completely evacuated.

VM5 is a manual valve that allows to supply a N_2 purge gas to the growth chamber, allowing overpressure and enabling to carry out system maintenance, either to target exchanging or periodic cleaning of the growth chamber inner sidewalls which tend to be covered by multilayers after several deposition processes.

3.1.3. Targets and Substrate Holders

Sputtering system used in this work has both rf and DC power supplies which have been used accordingly to the target material. If the target material is a good electrical conductor, a constant voltage can be used to accelerate the ions to the chosen energy; as these ions strike the target surface, the resulting charges can move freely along the material, preventing any charge build-up. However, in the case of an insulating material, not free charge movement is allowed; as the ions strike the target surface, their charge will remain localized over that surface, producing a charge build-up, screening and distorting the electric field distribution which makes the sputtering process difficult to proceed.

In our sputtering system, there are three different targets: Al, Zn, and AZO, enabling to deposit metals and semiconducting materials such as: Zn, Al, ZnO, Zn_3N_2, $Zn_xN_yO_z$, and AZO, by using O_2 and N_2 plasmas. While Al films are deposited using a DC-plasma, Zn based materials are deposited using rf-plasma; although Zn is metallic and therefore its electrical conductivity is very high, the use of rf-plasma promotes the reaction between plasma species (N_2 or O_2) with the ejected Zn atoms to grow Zn-based compounds (reactive sputtering process).

Film deposition can be carried out over three different substrate holders: SH1, SH2 and SH3 (figure 3.3). As SH1 can be heated up to 573 K, this substrate holder is used to grow AZO, ZnO and Zn_3N_2 layers at different T_s. On the other hand, growths performed using SH2 and SH3 are carried out at RT, and are utilized

to deposit Zn and Al based compounds, respectively. The use of different substrate holders for different elements/compounds also prevents sample contamination with materials originated from previous depositions.

Prior to the growth process both, substrate and target, are cleaned with an rf Ar plasma; this process is called here "pre-sputtering" and its main purpose (aside to reduce contamination) is to ensure the stability of the sputtering rate due to target cleaning. After the cleaning step, growth parameters such as T_s, P_{res}, and gas fluxes are set at their set-point levels.

3.1.4. Calibration Curves

Resultant thickness (*d*) of sputtered films is strongly dependent on plasma power (DC and rf), sputtering time, pressure, gas flux, and gas composition (in the case of using a carrier gas such as Ar), as well as on the material nature. In figure 3.4, calibration curves of Al, AZO, ZnO, and Zn_3N_2 thin films are shown, representing *d* as a function of the growth time, under standard conditions detailed in each graph legend. *d* is measured by profilometry and spectroscopic ellipsometry (SE). From curves represented in figure 3.4, it can be noticed that *d* obtained by sputtering technique for growth times below 1 h is

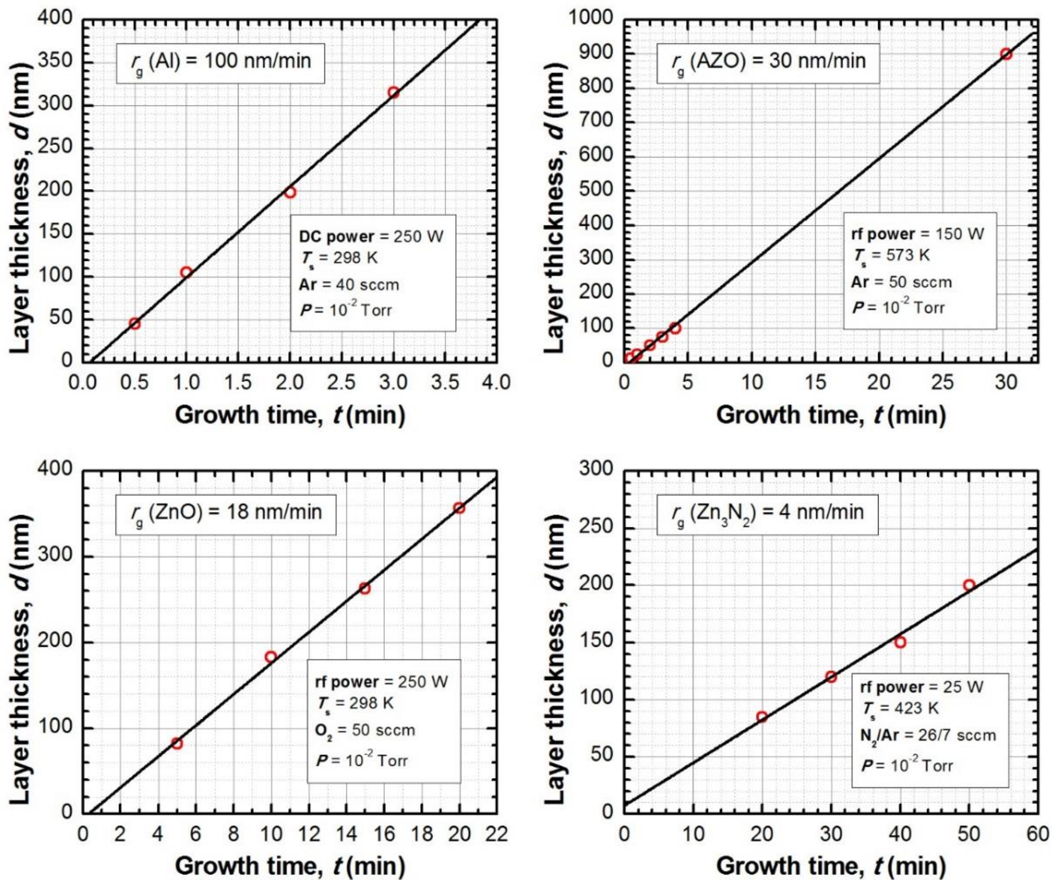

Figure 3.4. Calibration curves of sputtered films as a function of time.

proportional to the growth time. Figure 3.4 shows specific growth conditions, however, the growth rate (r_g) is observed to be strongly influenced by growth conditions as it will be observed later on (chapter 5).

3.2. Chemical Vapor Transport

The term CVT summarizes a process composed by three main stages: i) thermal evaporation of a solid precursor forming a vapor phase; ii) transport of the vapor phase by a carrier gas; iii) crystallization of the vapor phase at the condensation zone. The evaporation of the solid precursor occurs in the evaporation region, where the temperature is usually above the melting point of this material, while crystallization takes place at the condensation zone where temperature is lower than in the evaporation zone. For the transport of the vapor phase between both regions it is commonly used an element whose molecules are bigger in size than the transported material. The main role of this carrier gas is to ensure a laminar flux of the vapor phase, preventing the formation of turbulences, and leading to the formation of a uniform deposited layer in the condensation region.

Figure 3.5 shows a picture of the CVT system used in this work, where it can be distinguished a high temperature furnace with a long and narrow quartz tube inside, and three gas lines (Ar, O_2, and N_2) whose gas flow is individually controlled by an MFC. The quartz tube is 1 m long with a 4 cm diameter. The gas entrance is located on the right side of the tube, while the left side is connected to a rotary pump with a pumping rate of 0.5 l/s.

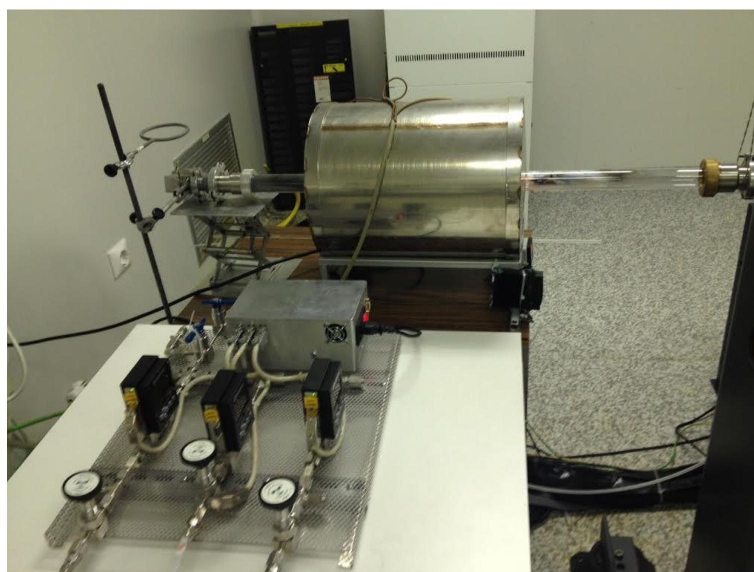

Figure 3.5. CVT system.

Prior to each synthesis process, the quartz tube is cleaned using an acid buffer solution of $HCl:H_2O$ (10:90) and later annealed at 200 ºC under a 100 sccm Ar flux for 1 h in order to desorb water molecules from the inner sidewalls of the tube.

Figure 3.6 shows the schematic of a CVT system, where the evaporation and condensation zones are pointed out.

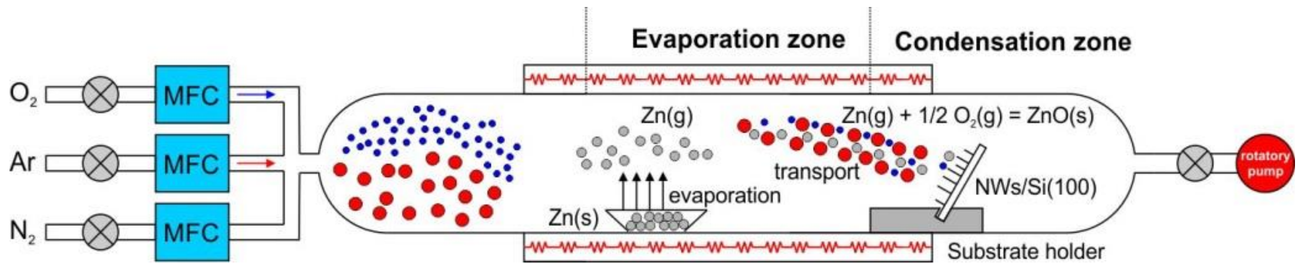

Figure 3.6. Schematic of the CVT system during the synthesis of ZnO NWs.

Solid metal precursor powder is transferred to a ceramic crucible located at the evaporation zone under a typical Ar flux of 100 sccm, in order to avoid metal oxidation. Two different Zn precursors have been utilized in this work: micro-sized Zn powder and nano-sized ZnO powder (both 99.999% purity).

In the case of Zn powder, Zn vapor can be directly obtained from pure Zn solid powder at relative low temperatures due to the low vapor pressure of this element. The CVT system can increase the temperature in the tube up to 1000 ºC, using an Omron (E5CSV) temperature controller. Since Zn powder is heated up to a temperature above the Zn melting point (400 ºC), Zn powder is transformed to liquid phase (see figure 3.7). Above that temperature, Zn liquid and vapor phases coexist, obtaining a Zn vapor pressure of 1 atm at the Zn boiling point (900 ºC).

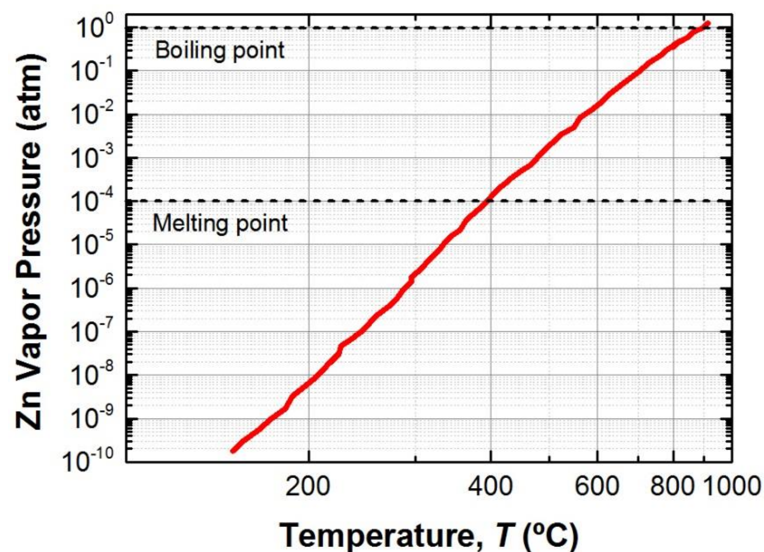

Figure 3.7. Zn vapor pressure measured at different temperatures.

In the case of ZnO powder, ZnO compound has an extremely high melting point, around 1975 ºC, meaning that our system maximum allowable temperature is insufficient to directly evaporate ZnO powder. For this reason, an alternative procedure is used, consisting in the carbo-thermal reduction of ZnO powder at moderate temperatures around 900 ºC. ZnO powder is reduced using graphite powder, producing Zn vapor such as described in reactions 2.3-2.7 (chapter 2).

The powder mixture is standardly made by adding 0.25 g of both ZnO and C powders to a recipient, resulting in a total mass of 0.5 g with a ZnO:C ratio of 1:1. In order to obtain a homogeneous distribution of C and ZnO powders, increasing the efficiency of carbo-thermal reaction, the resultant mixture is solved in ethanol and sonicated for 1 min. Thereafter, the solution is transferred to an oven where it is heated at 90 ºC for 1 hour, aiming to completely evaporate the organic solvent.

Both Zn and ZnO:C powders are spread in a ceramic crucible in order to maximize the ambient exposed area inside the tube, which is expected to improve the powder evaporation ratio. The ceramic crucible containing the powder is transferred to the quartz tube center at room temperature.

A special substrate holder is used to place the substrate nearly perpendicular to the gas flow, aiming to obtain a homogeneous deposition of ZnO NWs along the substrate surface, such as represented in figure 3.6. The quartz tube has graduation marks which allow to accurately determine the position of the sample relative to the source, as well as to know the temperatures at both source and sample regions, using the furnace temperature profile previously calibrated.

The CVT system allows the simultaneous introduction of Ar, O_2 and even N_2 gases inside the quartz tube. The flux of each gas, taking into account the GCF, is controlled by an individual MFC whose maximum allowed flux is 100 sccm (referenced to N_2 gas).

Prior to the temperature increase, Ar flux is turned on at 100 sccm during 30 min to evacuate the gas inside the tube (Ar flux evacuates the total volume inside the tube in approximately 10 min). Thereafter, the temperature is increased up to growth temperature (typically between 700 and 900 ºC), maintaining the Ar flux at 100 sccm during the whole heating process.

Once the temperature reaches the set-point level, the O_2 valve is opened while Ar carrier gas flux is maintained. As mentioned before, Zn vapor phase is created from: either by direct evaporation of Zn powder or by carbo-thermal reduction of ZnO:C mixed powder, which is transported by the Ar carrier gas, and finally reacts with O_2 ambient preferentially at the condensation zone, where temperature is about 100-200 ºC lower than in the evaporation zone. The product of the reaction tends to form nanostructured ZnO, which is preferentially grown on a crystalline substrate such as Si(100), forming vertically aligned NWs. At the same time, the inner sidewalls of the tube located in the condensation zone, are also covered with a whitish powder, consisting of ZnO based nanostructures such as TPs, nanosheets, NWs, etc.

3.2.1. Temperature Profile

Temperature profile inside the quartz tube has been measured using a thermocouple. The calibration has been carried out for five different temperatures between 500 and 900 ºC as shown in figure 3.8. All temperature profiles show a flat response (plateau) around the center of the quartz tube (evaporation zone), while outside this zone temperature reaches lower values (condensation zone); these conditions ensure the homogeneous evaporation of the solid source during the evaporation stage.

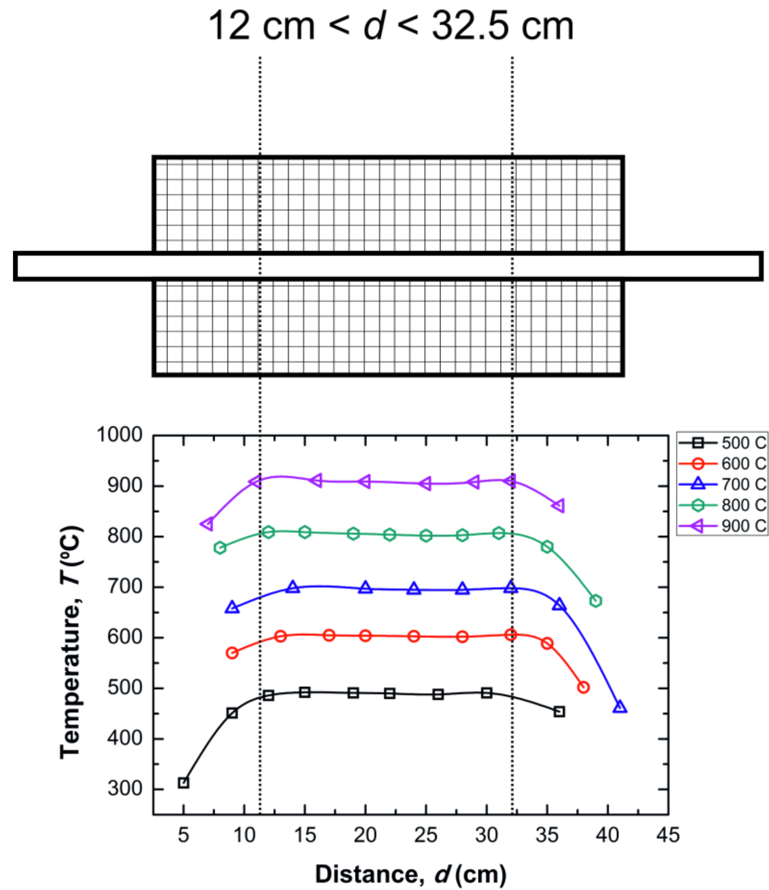

Figure 3.8. Temperature profile of the CVT system.

Looking at the 900 ºC curve, which is the temperature used to grow ZnO NWs using ZnO:C powder, it can be observed a flat region 20 cm long at the tube center; moving outside the central zone by 10 cm, the temperature decays to 800 ºC. This temperature reduction is the main factor promoting the preferential condensation of transported material over the rest hotter places of the system. For that reason, crystalline substrates are placed at regions with temperatures 100-200ºC below the temperature at the tube center.

3.3. Chemical Beam Epitaxy

The CBE system used in this work (figure 3.9) is a MBE system modified to use of gas sources.

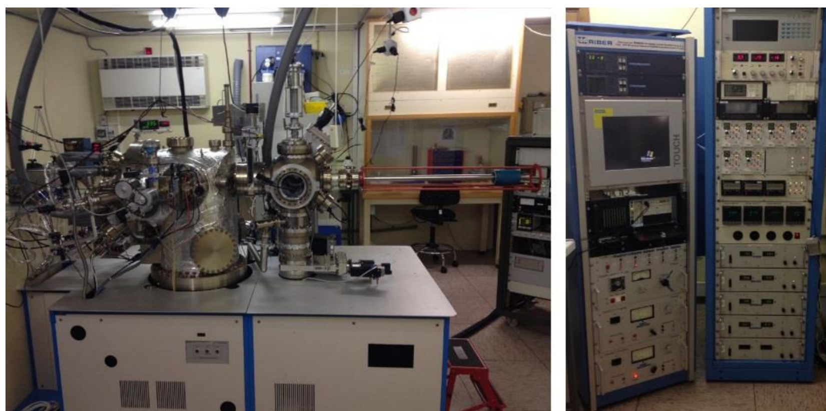

Figure 3.9. CBE system.

The schematic of the CBE system is drawn in figure 3.10, showing three different chambers: growth chamber, intermediate chamber, and introduction chamber. The system also includes a gas flow control system, pumping gas systems, a substrate temperature pyrometer and different characterization techniques such as RHEED and mass spectrometry.

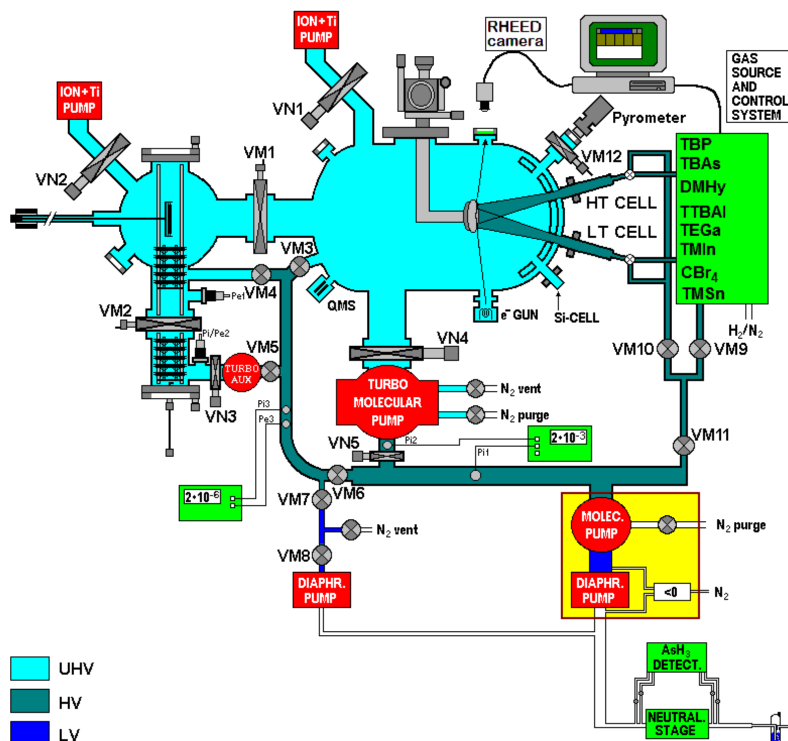

Figure 3.10. Schematic of the CBE system.

3.3.1. Metalorganic Precursors

The CBE system described above uses metalorganic gas precursors for both III and V elements. In this work, CBE system is used to grow GaAs NWs, being triethylgallium (TEGa) and tertiarybutylarsine (TBAs) the metalorganic precursors used for Ga and As, respectively. As both precursors are liquid at RT, the gas phase in equilibrium with the liquid phase is extracted from their containers to supply the gas flux during the growth process.

The TEGa molecule, as shown in figure 3.11, consists of three ethyl radicals bonded to a central Ga atom. During a standard CBE GaAs growth, uncracked TEGa is introduced to the growth chamber through a low temperature gas cell (T_{LT} = 80 ºC). The use of such a low temperature is necessary to prevent TEGa cracking inside the LT cell at higher temperatures (T_{LT} > 350 ºC); that cracking could cause a subsequent condensation of Ga in the inner sidewalls of the LT cell because of its high sticking coefficient and the cell temperature, much lower than an typical MBE effusion cell (T > 800 ºC); therefore, the cracking of TEGa could significantly reduce the effective gas flux towards the substrate surface due to liquid Ga accumulation. Summarizing, the utilization of a low T_{LT} mainly aims:

i) to prevent both TEGa cracking and subsequent Ga condensation inside the LT cell, which can be achieved using moderate temperatures ranged between 80 and 140 ºC;
ii) to produce a uniform and homogeneous TEGa flux towards the substrate surface, where TEGa will be thermally cracked at higher temperatures (400 ºC < T_s < 620 ºC).

TEGa molecule is thus thermally decomposed on a reactive substrate surface such as GaAs, which is heated up to a T_s typically in the 400 to 650 ºC range. In this process, ethyl bonds are broken either by pyrolysis, catalysis or a combination of both, liberating Ga atoms on the sample surface to incorporate them to the grown layer. In the case of a non-reactive substrate surface such as oxidized Si, the useful T_s window is much narrower when compared to reactive substrates, because TEGa cracking is just allowed only in regions either not covered by the oxide capping or with a very thin oxide, while it is inhibited in regions where the oxide is much thicker. The growth on oxidized patterned substrates is known as SAE and can be considered a potential procedure to grow nanostructured GaAs in a “bottom-up” approach as previously described in chapter 2 (figure 2.10).

Triethylgallium

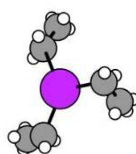

Tertiarybutylarsine

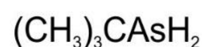

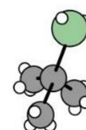

Figure 3.11. TEGa and TBAs precursors.

The precursor of As, TBAs, is formed by three methyl radicals (CH_3-) and an arsine radical (AsH_2-), bonded to a central C atom. Contrary to the TEGa, TBAs is introduced into the growth chamber through a high temperature (HT) cell, where it is pyrolytically cracked at the typical temperature of T_{HT} = 820 ºC, producing an As radical-rich gas flow directed to the substrate surface. The HT cell was firstly designed to pyrolytically crack hydrides of V elements such as AsH_3 or PH_3, working at temperatures up to 1200 ºC, but this cell can also be used with metalorganic precursors such as TBAs or TBP. As the analysis of TBAs cracking as a function of T_{HT} will demonstrate in chapter 4, our HT cell can be used at a moderate temperature (T_{HT} = 820 ºC) to efficiently crack TBAs prior to the precursor gas flux arrives to substrate surface, obtaining a flux of reactive As and AsH_x species. Although uncracked TBAs could be directed towards the substrate surface at typical T_s between 500 and 600 ºC, cracking efficiency is much lower than the previous cracking produced in the HT cell.

3.3.2. Gas Flow Controller

The gas flow controller system available in the CBE is an essential part of the system, which is responsible for the accurate growth of epitaxial layers, ensuring the reproducibility and the high quality of the resultant samples. In our CBE, the gas flux for each precursor is individually regulated by a pressure regulated control (PRC). Each gas line consists of an intermediate chamber (labeled as "P" in figure 3.12) whose pressure (P_{cam}) is controlled using a variable aperture solenoid valve, the gradual aperture of this valve being controlled by a PID controller reading its pressure by a capacitance manometer (baratron). There are some manual valves for system maintenance, plus four two-positions (ON/OFF) electro-pneumatic valves (V1, V3, V4, and V5) and a three-ways electro-pneumatic valve (V2) directing the gas flux either to the growth chamber or to the vacuum system (run/vent).

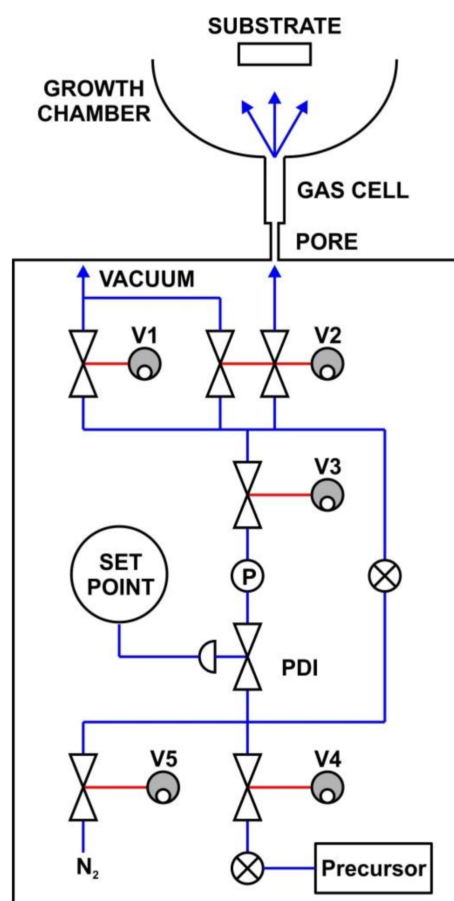

Figure 3.12. Schematic of a gas line.

Intermediate chambers are connected to the gas cell or injector through a small sized hole (diameter between 3 and 2 mm) located at the input of V2. The gas flow supplied to the growth chamber depends on the pressure difference between the intermediate chamber and cell input. However, due to the low pressure existent in the growth chamber under the ultra-high vacuum conditions (< 10^{-6} Torr), and the high gas conductance of the cells, the effective gas flux is practically only dependent on P_{cam}.

Whenever growth process does not take place, gas lines are cleaned by baking them under vacuum. This step is mandatory in order to preserve the system free of contaminants. For gas line cleaning, V1, V3, V4 and the by-pass valve (placed at the right side on the schematic, it is the direct way to connect both V3 and V4/V5 outputs) are opened, whereas the precursor reservoir manual valve (close to V4 input) is closed. The gas line is considered to be clean when its pressure is below 10^{-3} Torr.

During a standard growth, the valves V2, V3, V4, and the precursor bottle manual valve are opened. In this configuration, the precursor gas flows from the precursor reservoir to the intermediate chamber allowing its pressure to reach the set-point. The desired gas flux then leaks through the gas line hole and flows towards the gas cell and the growth chamber. When V2 is switched, the gas flux is directed to the vacuum system instead to the growth chamber; the conductance of both branches of the gas line, i.e. to the vacuum line and to the growth chamber, should be similar to avoid switching transients on fluxes due to pressure transients on the intermediate chamber.

The N_2 purge connected to the V5 valve is used for maintenance purposes or to pre-calibrate the flux of the gas line with a standard gas. All the electro-pneumatic valves presented above and the PID can be controlled either manually or remotely by a computer, allowing a thorough control over the gas flux and open/close switching times of each valve.

In CBE, it is not necessary to recalibrate the gas line flux periodically, because it is almost insensitive to source filling, as it is the case of MBE; only when the gas source is complete exhaust, the new reservoir is installed, and pumping is only needed in a small volume pipe, evacuating then both Ar or N_2 carrier gases (if present in the bottle) to guarantee the purity of the precursor source. This has a fundamental advantage when compared to the MBE. The gas cell is always in ultra-high vacuum conditions because the growth chamber is not opened, and therefore neither the cell nor the growth chamber have not be outgassed.

Beam Equivalent Pressure

The beam equivalent pressure (*BEP*) is an indirect way to measure the precursor gas flux in the growth chamber. *BEP* is measured using an ionization gauge placed at the same position than the sample during a growth process (by using an exchange mechanism). This pressure reading is dependent on the gas nature by means of its ionicity relative to N_2 (I) and mass (M), and also is dependent on the gas flux (F) and temperature (T). The gas kinetic theory establishes a relationship for the *BEP*, corresponding to a gas which is flowing unidirectionally:

$$BEP = 2.55 \times 10^{21} F \cdot I \sqrt{\frac{M}{T}} \tag{3.2}$$

The initial calibration of a gas line consists in the measurement of *BEP* as function of P_{cam}. Precursor gases TEGa and TBAs are directed to the growth chamber through the LT and HT cells, respectively, at a

low temperature ($T_{LT} = T_{HT} = 80$ ºC) to prevent precursor cracking and a possible condensation of the gas in the cell, as well as to minimize the effect of T on the BEP values. The resultant BEP measurements as function of P_{cam} for TEGa and TBAs are shown in figure 3.13.

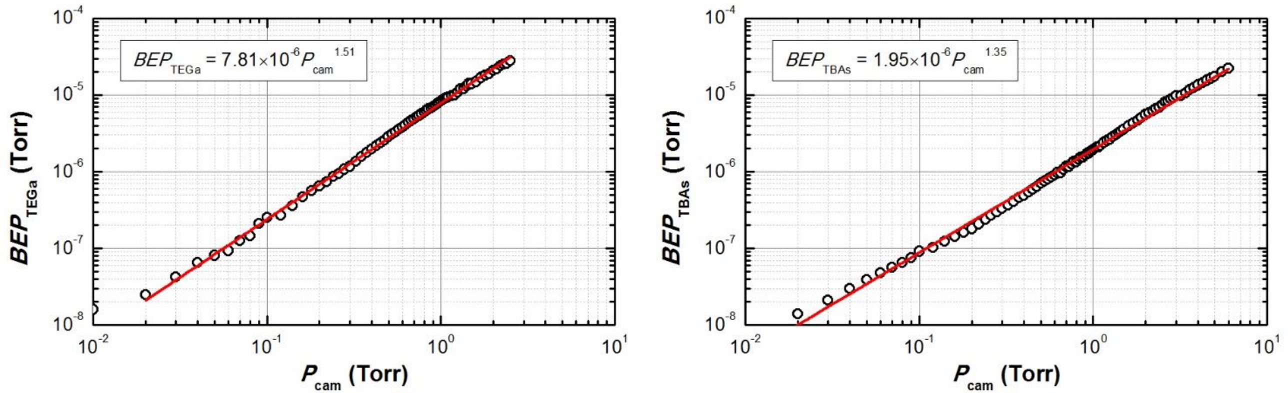

Figure 3.13. TEGa and TBAs gas lines calibration curves.

The F is expected to have a linear dependence on the pressure difference between P_{cam} and the pressure at the cell input (P_{cell}).

$$F = k\left(P_{cam} - P_{cell}\right)$$
$$F \approx k\,P_{cam} \Leftrightarrow P_{cam} >> P_{cell} \quad (3.3)$$

Where k is a constant that depends on both geometric factors (small pore and pipe conductance) and gas precursor nature. Because P_{cell} is much lower than P_{cam} due to the low conductance of the small pore located at V2 valve input, producing a large pressure drop. Experimental measurements show a non-linear dependence of F on P_{cam}, because it has been empirically obtained as a power dependence:

$$F = k\,P_{cam}^{n} \quad (3.4)$$

n being 1.5 and 1.3 for TEGa and TBAs, respectively.

Accordingly to equation (3.2), where BEP is proportional to F, BEP can be used to calibrate the dependence between F and P_{cam}, obtaining k value from another kind of measurement or technique such as RHEED as will be shown in chapter 4.

3.3.3. Vacuum System

Samples are loaded into the CBE system through the introduction chamber. During the sample introduction stage, this chamber is completely filled up with N_2 purge gas, obtaining an overpressure,

preventing the incorporation of contaminants from the atmosphere. Once the samples are loaded into the introduction chamber, the N_2 purge gas is turned off and the chamber is firstly pumped down to 10^{-2} Torr (as measured with a Pirani gauge) using a diaphragm pump, and then the pressure is lowered down to 10^{-5} Torr (as measured with a Penning gauge), utilizing either a molecular drag or a turbo-molecular pump. Thereafter, introduction and intermediate chambers are connected, and both chambers are pumped down to 10^{-7} Torr, using an ion pump assisted with a Ti sublimation pump. Although the samples in this work are commonly used the same day they were prepared, the intermediate chamber is a place for sample storage under high vacuum ambient, preventing sample degradation and contamination.

The growth chamber is pumped with a turbo molecular (Leybold MAG W2800, 2800 l/s), having the possibility to work with a N_2 purge; its high pumping rate allows to reach a residual pressure of 10^{-9} Torr with both HT and LT cells at their working temperatures (820 and 120 ºC, respectively). In addition, the growth chamber is equipped with liquid N_2 cooled cryopanels surrounding the CBE body, cells and manipulator, lowering the residual pressure down to 10^{-11} Torr range. The pressure in this chamber during a standard growth is the range of 10^{-7}-10^{-6} Torr (depending on TBAs and TEGa fluxes).

The turbo molecular pump in the growth chamber can be pumped by two different primary pumping systems, either an Alcatel Drytel 100 (27 l/s) consisting of a molecular drag pump with a final pressure of 10^{-6} Torr assisted by a diaphragm pump with a final pressure of 1 Torr, or a recently installed Adixen 100L (28 l/s) root pump with a final pressure of 5×10^{-3} Torr. Aside to assist the main turbo molecular pump, both primary pumping systems are also used to:

i) Pump the gas lines, opening valves V1, V3 and V4 while V2 is closed to the growth chamber (figure 3.12). This process is commonly carried out whenever no growth is taking place, to preserve the gas lines free of contaminants, and also evacuating the residual gas from previous processes.
ii) Pump the precursor flux when is not directed to the growth chamber (gas flux switching during run/vent operation of V2).
iii) Pump the introduction/intermediate chambers.

4. Analysis Techniques

4.1. Ion Beam Analysis

IBA is based on the atomic and nuclear interaction between high energy ions (1-10 MeV) and sample elements. When high energy ions are directed towards the sample and penetrate into its structure, they interact with electrons and nucleus into the target structure, partly losing energy and usually changing their trajectories. During this interaction, backscattered ions, new particles, and radiation can be emitted; the detection and later analysis of these emitted products can give relevant information about the chemical composition and structure of the analyzed material.

There are different IBA techniques, usually classified depending on the detection type (backscattered ions, atoms, protons, …), and analysis type. In this work, three different IBA techniques have been used: i) RBS, ii) non-RBS, and NRA. These techniques have been used to analyze chemical composition of both Zn_3N_2 and ZnO semiconductor materials with different structures (thin film and NW). Measurements were performed at the Center of Microanalysis of Materials (UAM).

4.1.1. Ion Backscattering Spectrometry

In a typical ion backscattering spectrometry (IBS) experiment, low-mass incident ions (typically $^4He^{2+}$ or also called α-particles) are accelerated at high energies ranged between 1 and 4 MeV, then penetrate into the sample structure, having a certain probability to be backscattered after suffering nuclear elastic collisions with heavier atoms in the target structure. Backscattered ions escape from the sample at the scattering angles (θ) larger than 90º with respect to the incident beam direction. A surface barrier semiconductor detector is placed at $\theta \sim 180º$ in order to detect backscattered particles. Analyzing the energy

of the backscattered ions, some relevant information about the target material such as the layer thickness and element molar fraction can be extracted.

The atomic concentration in the target structure can be determined from the analysis of the IBS peak intensity (or counts number) which is related to the scattering probability also called scattering cross-section, as will be explained below.

When the nuclear collision takes place below the sample surface, the incident ion loses energy gradually as it passes through the sample layer (or layers) due to interactions with sample electrons. Therefore, IBS can be also used to obtain a depth profile of the sample composition, because the energy of detected ions bring the signature of the elastic collision suffered plus the energy lost during the trajectory inside the sample. The use of a simulation software allows to address the above analysis.

The IBS experimental system used in this work was designed and constructed by High Voltage Engineering Europe (HVEE) and is available in the CMAM-UAM facility. Figure 4.1 shows a schematic of this IBS system. Basically, the system consists of an ion source (typically α-particles) whose produced ions are accelerated by a coaxial high current accelerator of 5 MV; then accelerated ions are focused, collimated and finally filtered in order to obtain a mono-energetic ion beam which is directed towards the target sample. Incident ions are backscattered along different θ, but only a small fraction impacts in a detector, covering a specific solid angle (Ω), and producing a peak signal which is later amplified, registered, and finally counted in a digital system.

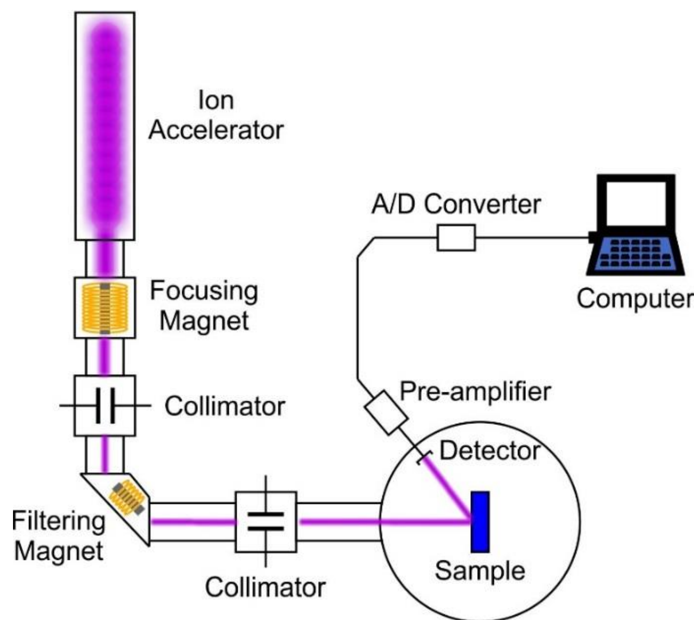

Figure 4.1. Schematic of the RBS experimental setup.

The complete ion beam path from the ion accelerator to the detector is under high vacuum conditions (< 10^{-5} Torr); this scenario guarantees a large mean free path for ions that prevents unintentional collisions

between ions and residual gas molecules, which could hinder beam collimation, and lead to both attenuate beam energy and spread energy distribution.

The ion detector consists of a Schottky diode that is capable to generate a cascade of carrier charge after the ion impact; in this regard, the current pulse generated after each impact is related to the ion incident energy and can be analyzed by a multichannel system after amplification and pulse conditioning. This procedure allows to account for the number of ions obtained at a specific energy interval during a given integration time.

Kinematic Factor (*K*)

Under low energy conditions, when the incident ion energy is much lower than the threshold needed to produce nuclear interactions, incident ions can be elastically scattered after colliding with target nuclei due to Coulomb interaction. When the scattering takes place at the sample surface, the only energy loss mechanism for these ions is due to a simple momentum and energy transfer to the target nuclei. These conditions were initially used by Rutherford in his original scattering experiment using α-particles and a thin Au foil as target [1]. In that experiment, Rutherford explains the scattering probability and energy distribution of scattered particles by using a classical mechanics model. Rutherford results are used in low energy conditions, giving rise to the technique known as RBS, a particular case of the IBS technique.

Figure 4.2 represents the elastic collision of an accelerated ion with an energy and a mass of E_0 and M_1, respectively, and a target atom of the analyzed sample with a mass of M_2. After colliding, backscattered ion escapes from the sample at $\theta > 90º$, and with lower energy (E_1) with respect to E_0. In this collision, the energy is conserved, which means $E_0 = E_1 + E_2$ (elastic collision), where E_2 is the energy of the recoil atom.

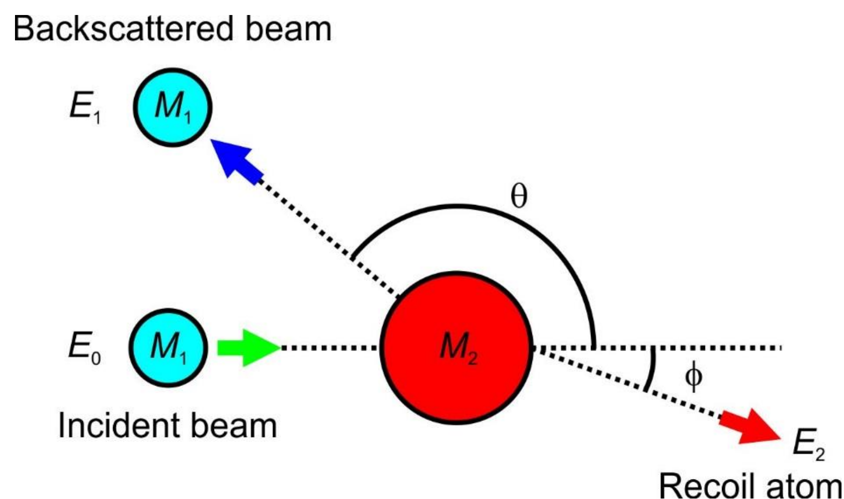

Figure 4.2. Elastic collision between an accelerated ion (E_0, M_1) and an atom in the target sample (M_2). θ and ϕ are the scattering angles of ion (E_1) and atom (E_2), respectively, after the collision.

The energy ratio between backscattered ions is defined as kinematic factor ($K = E_1/E_0$). Taking into account both energy and momentum conservation laws, K can be expressed as [2]:

$$K(\theta) = \frac{E_1}{E_0} = \left[\frac{\sqrt{1 - \left(\frac{M_1}{M_2}\right)^2 \sin^2\theta} + \frac{M_1}{M_2}\cos\theta}{1 + \frac{M_1}{M_2}} \right]^2 \tag{4.1}$$

In this equation, it can observe that K only depends on the ion/atom mass ratio (M_1/M_2) and on the θ. As K depends on atom mass (M_2) but not on its atomic number (Z_2), RBS allows to distinguish between different isotopes when the detection system has enough energy resolution. Figure 4.3 represents the dependence of K on the target nucleus mass, using some different incident ions.

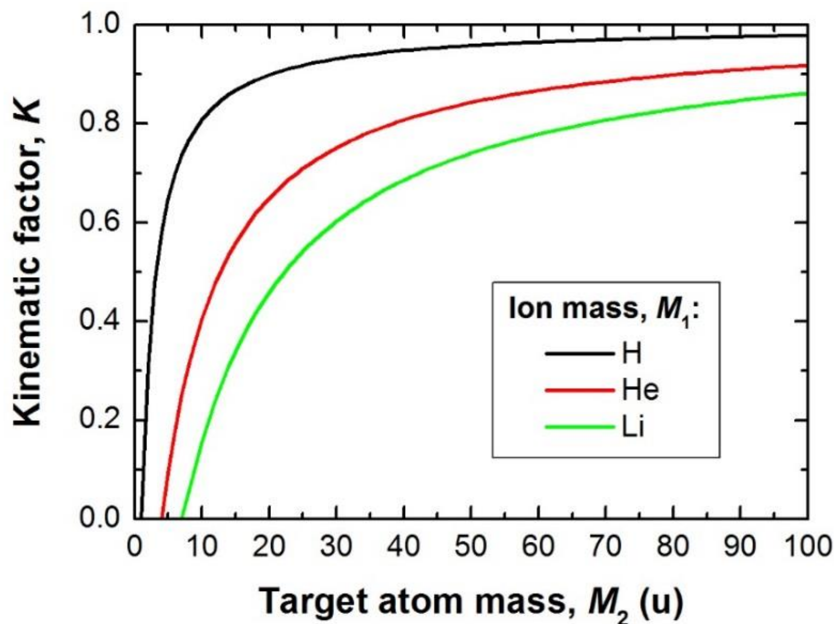

Figure 4.3. Kinematic factor calculated from equation (4.1), as a function of M_2 for different incident ions, and θ=165º.

For light incident ions, i.e. ions whose mass is much smaller than the mass of the atoms in the target sample ($M_1 \ll M_2$), K tends rapidly to the unity, hindering mass separation in the analyzed spectrum.

For light target atoms, K decreases rapidly, which means they are better resolved (better mass separation) in RBS. Moreover, figure 4.3 shows that the variation of K with M_2 is enhanced for lighter M_1. However, target atoms lighter than the incident ions ($M_2 < M_1$) cannot be detected, as these atoms will scatter at forward trajectories with significant energy.

Stopping Power, Energy Loss, and Energy Straggling

When an incident particle penetrates a material, it loses energy interacting with sample atoms. The interactions are usually divided into two separate processes, namely:

i) energy losses due to elastic collisions with sample atom nuclei (nuclear stopping power), and

ii) inelastic collisions with electrons (electronic stopping power).

In the energy range of 1 to 4 MeV, the energy loss is mainly due to interaction of the incident ions with the electrons in the material, ionizing target atoms. A particle backscattered from an element deep in a sample, has a significant less energy than the same particle when backscattered from the same element on the sample surface. The energy loss per unit path is known as stopping power of the target material for a penetrating ion.

By evaluating the stopping powers on inward and outward paths, the correlation between depth and energy of the scattered particle can be obtained. A good depth resolution requires not only a good detector energy resolution but also a well-defined energy of impinging particles. Depth resolution is also limited by the spread in energy loss on both paths in the target, which is termed as energy straggling and is caused by statistical fluctuations in the number and kind of encounters that an energetic particle undergoes when traveling in matter. For thin layers, the amount of energy straggling is considered to be proportional to the square of the energy loss, hence the depth resolution will deteriorate with increasing depth.

Energy of Particles Backscattered from a Target

Figure 4.4 shows an incident ion (Z_1, M_1, E_0) striking a target material (Z_2, M_2) with an incident angle θ_1, and two ions backscattered from the same element, either at the sample surface or at some depth (Δx) in the sample, whose energies are E_1 and E_1', respectively, and whose backscattered angle is θ_2.

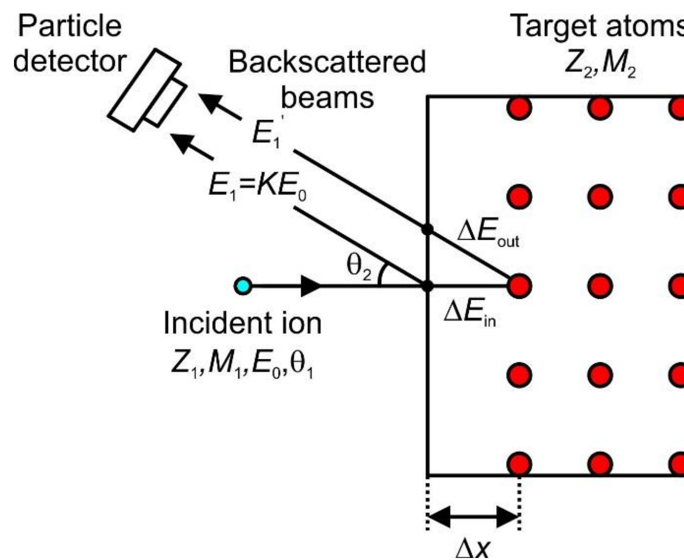

Figure 4.4. Schematic used for the derivation of formulas for energy loss of ions in a target material.

The energy of the scattered particle from a surface atom was previously given in equation (4.1). On the other hand, the energy of a particle (E_1') scattered from the innermost atom at a given depth Δx, can be obtained as a function of E_0, and the energy loss along both the incident (ΔE_{in}) and the backscattered (ΔE_{out}) paths of the ions in the material, resulting in:

$$E_1^{'} = K(E_0 - \Delta E_{\mathrm{in}}) - \Delta E_{\mathrm{out}} = KE_0 - \left[\frac{K}{\cos\theta_1}\left(\frac{\mathrm{d}E}{\mathrm{d}x}\right)_{\mathrm{in}} + \frac{1}{\cos\theta_2}\left(\frac{\mathrm{d}E}{\mathrm{d}x}\right)_{\mathrm{out}} \right] x \tag{4.2}$$

The energy loss factor (S) can be extracted from the derivative of equation (4.2) with respect to x; assuming a normal incident ($\theta_1 = 0$), the resultant equation can be written as:

$$S = K\left(\frac{\mathrm{d}E}{\mathrm{d}x}\right)_{\mathrm{in}} + \frac{1}{\cos\theta_2}\left(\frac{\mathrm{d}E}{\mathrm{d}x}\right)_{\mathrm{out}} \tag{4.3}$$

where dE/dx is the energy loss per unit length previously defined as stopping power. S takes into account an average over all possible energy dissipative processes activated by the incident ion on its way past a target atom.

In RBS, it is commonly used the so-called stopping power cross-section (ε) rather than dE/dx in order to take into account the atomic density of the target material (N):

$$\varepsilon(E) = \frac{dE}{dx}\frac{1}{N} \tag{4.4}$$

Differential Scattering Cross-Section

Since an ion such as a α-particle penetrates inside the target material, there is a finite probability of being scattered by a target atom at a given forward direction ($\theta < 90º$) or backward direction ($\theta > 90º$). The cross-section (σ, expressed in m^2 = barn) is indicative of the probability of such an interaction can occur; the larger the cross-section value, the greater the probability that an interaction will take place when a particle is incident on the target material.

Instead of σ, the differential cross section ($d\sigma/d\Omega$ expressed in m^2/sr, where sr is steradian) is commonly used, representing the probability of an incident ion to collide with an atom and then to be backscattered at an specific angle θ over a solid angle $d\Omega$ centered on that angle. The differential cross section can be expressed as a function of the total incident ion dose (Q), N, the effective layer thickness (t is expressed in atoms per cm^2), and the total number of detected particles per unit solid angle ($dQ/d\Omega$):

$$\frac{d\sigma}{d\Omega} = \frac{1}{N\,t\,Q}\frac{dQ}{d\Omega} \tag{4.5}$$

The value for the differential scattering cross-section can be deduced by assuming the following classical approaches:

i) nuclei are considered as point-like charges,
ii) Coulomb forces are the only allowed interaction,
iii) collisions are elastic, and
iv) target atoms do not recoil.

Then, $d\sigma/d\Omega$ is given by [3]:

$$\frac{d\sigma(E_0,\theta_2)}{d\Omega} = \left(\frac{Z_1 Z_2 e^2}{8\pi\varepsilon_0 E_0}\right)^2 \frac{1}{\sin^4\theta_2} \frac{\left[M_2\cos\theta_2 + \sqrt{M_2^2 - M_1^2\sin\theta_2}\right]^2}{M_2\sqrt{M_2^2 - M_1^2\sin^2\theta_2}} \tag{4.6}$$

where e is the elementary charge (1.602×10^{-19} C) and ε_0 is the vacuum electrical permittivity (8.85×10^{-12} F/m). It can be observed from equation (4.6) that the scattering probability $d\sigma/d\Omega$ increases with both Z_1 and Z_2 while it decreases for increasing E_0.

Therefore, RBS sensitivity (as number of scattered particles) is larger for heavier elements, because the cross-section increases with the target atomic mass (Z_2); however, RBS resolves better lighter elements (as energy separation), as above mentioned. For these reasons, RBS is sometimes complemented with additional techniques such as proton-induced X-ray emission (PIXE) or elastic recoil detection analysis (ERDA), allowing for the detection of lighter elements.

RBS Spectra for a Thin Film

In this work, Zn-based thin films and also NWs are analyzed by RBS using α-particles at 3.7 MeV and the detector placed at $\theta = 170º$, obtaining a large Zn scattering cross section. Figure 4.5 shows a typical RBS spectrum in the energy interval where incident particles are scattered by Zn atoms in a Zn_3N_2 thin film grown on a glass substrate. In this figure, the high energy edge (E_1) corresponds to backscattered ions from the surface Zn atoms, whereas the low energy edge (E_2) is associated to backscattered ions from the deepest Zn atoms in the Zn_3N_2 film, adjacent to the glass substrate. E_1 is described by the equation (4.1), whereas E_2 is described by the equation (4.2) due to the collision occurs inside the target material. The area under the curve showed in figure 4.5, is equivalent to the number of backscattered ions (dQ) that can be estimated from equation (4.5).

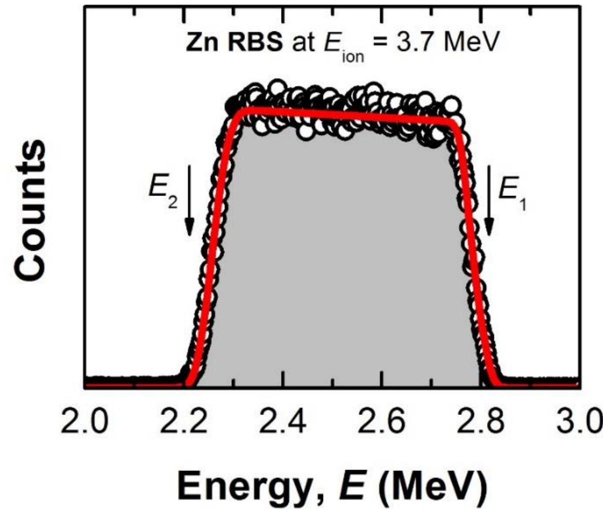

Figure 4.5. RBS spectrum measured at 3.7 MeV in a Zn_3N_2 layer, corresponding to backscattered ions from Zn atoms.

Magnitudes such as the energy offset (E_{offset}) and the energy per channel ($E_{channel}$) are necessary to be determined in order to fit both experimental and simulation results. Both magnitudes can be estimated by using the high energy edge (E_1) of a surface element; in the case of Zn_3N_2 layers, RBS signal of Zn can be used. RBS spectrum shows the effective energy ($E_{effective}$) of an element which depends on the channel ($N_{channel}$) in the multichannel counter, E_{offset} and $E_{channel}$ through the equation (4.7).

$$E_{effective} = E_{offset} + E_{channel} \cdot N_{channel} \tag{4.7}$$

Therefore, E_{offset} (keV) and $E_{channel}$ (keV per channel) are calibrated by fitting the high energy edge of Zn (E_1 or $E_{effective}$) in figure 4.5.

4.1.2. Non-Rutherford Backscattering

The classical Rutherford cross-section equation is no longer satisfied (non-Rutherford cross section) when nuclear interaction between the incident ion and the target atom becomes significantly important; this is observed when either high energy incident ions or high scattering angles are used, and target atoms with low atomic number are involved. For sufficient high energies, when the distance of closest approach between an incident ion and a target nuclei is reduced to the typical dimensions of nuclear size, the short-range nuclear forces begin to influence the scattering process and deviation from Rutherford cross-sections appear.

RBS measurements show that above a certain energy, a resonant structure appears (observed as sharp peaks on the scattering cross section); in the resonance region, there may exist several energy zones where the scattering cross-section presents an enhanced and smooth variation usually known as non-Rutherford cross-section. For light elements (typically $Z \leq 16$) non-Rutherford cross-section takes values from two or three times up to several orders of magnitude greater than Rutherford cross-section. As there is no general

theory for the calculation of non-Rutherford scattering cross-sections, usually experimental values have to be used.

The analysis of lighter elements such as N and O by RBS technique is difficult because its signal can be masked by the signal background produced by heavy elements contained in the substrate, as it is the case for Zn based oxides and nitrides {Kuriyama, 1993 #66}. The use of some characteristic ion energies at which backscattered signal due to light elements is enhanced, i.e. the element cross-section is increased by the resonance of α-particles (non-RBS), can increase the sensitivity for light atoms on the target.

A collision reaction is usually written as $T(p_i,p_{bs})P$, where T and P parameters represent the atom in the target before and after the collision, while p_i and p_{bs} are the incident and backscattered particles, respectively. Under non-RBS conditions, as no nuclear reactions take place, T = P and $p_i = p_{bs}$.

As an example, figure 4.6(a) and (b) show N and O non-RBS signals, respectively, measured in an oxidized Zn_3N_2 layer. In this scenario, a N resonance is found at 3.7 MeV, and is denoted as $^{14}N(\alpha,\alpha)^{14}N$ [4]; in the case of O, the reaction is written as $^{16}O(\alpha,\alpha)^{16}O$ and is excited at around 3.045 MeV [5]. In this regard, non-RBS allows us to detect low concentrations of light elements, such as the case of O which comes from the thin oxide layer formed on top of the zinc nitride.

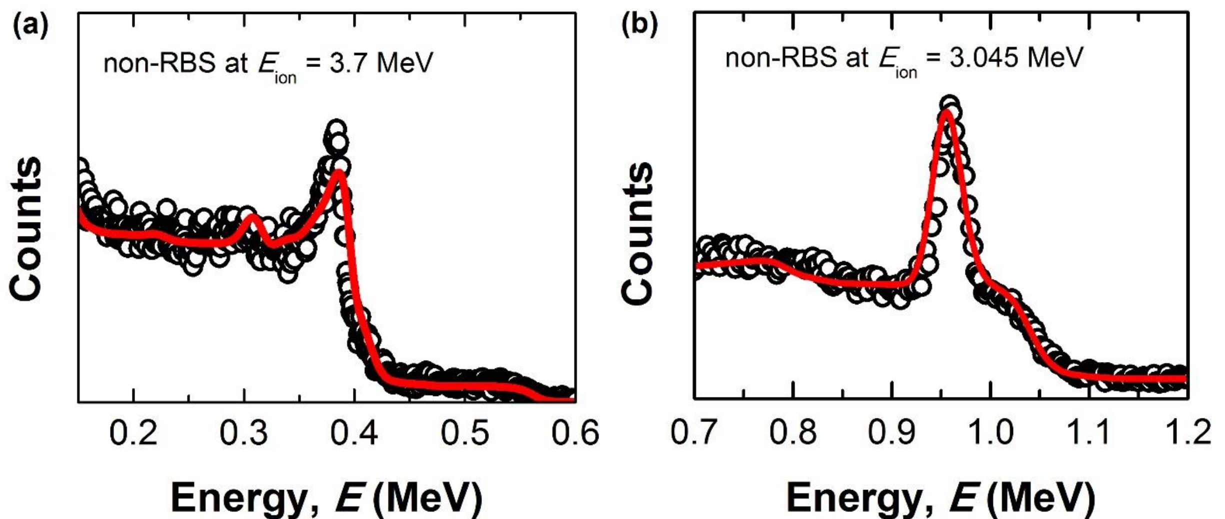

Figure 4.6. Non-RBS spectra of a oxidized Zn_3N_2 layer measured at (a) 3.7 and (b) 3.045 MeV, corresponding to $^{14}N(\alpha,\alpha)^{14}N$ and $^{16}O(\alpha,\alpha)^{16}O$ resonances, respectively.

4.1.3. Nuclear Reaction Analysis

NRA technique consists in the analysis of the nuclear reaction between light incident ions and heavier atoms in the target sample. This technique is useful to obtain the atomic concentration of light atoms on surface layers, usually hidden by heavier elements in the substrate. In this regard, the backscattered background signal due to collisions in the substrate (with higher cross-section) can mask the RBS signal due to lighter elements. Particles produced by the nuclear reaction are in general different from incident ones

(typically protons, neutrons, …), allowing to identify not only the nature of the atoms in the sample but also to obtain their concentration and depth distribution.

Considering an incident ion beam with a higher energy than the Coulomb barrier, impinging the target sample, highly energetic ions can induce nuclear reactions when colliding with target atoms by exciting their nuclei. Following the notation shown figure 4.7, a nuclear reaction can be expressed as

$$\mathrm{A} + \mathrm{B} \rightarrow \mathrm{B}^* \rightarrow \mathrm{C} + \mathrm{D} + \mathrm{n}\gamma \quad (4.8)$$

where A is the incident particle (with mass M_1 and an energy E_1) impinging on the target nucleus B (with mass M_2 and an energy E_2), producing a meta-stable compound nucleus B^* (with mass M_1+M_2). B^* tends to be spontaneously dissociated to an emitted particle C (with mass M_3 and an energy E_3) scattered along an angle θ, plus a nucleus D (with mass M_4 and an energy E_4) recoiled along the angle ϕ; γ-rays (γ) are also usually emitted after the des-excitation of the nucleus.

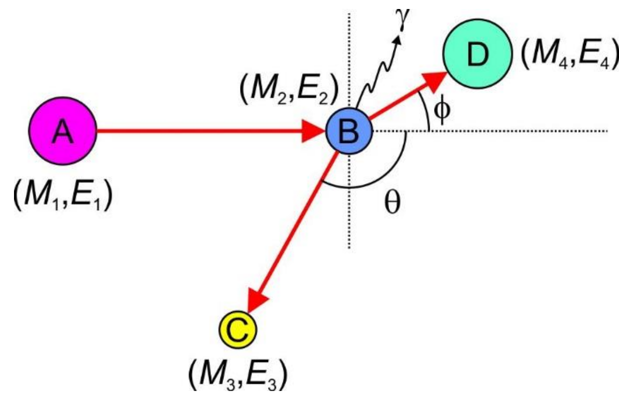

Figure 4.7. Schematic of the NRA principle.

The excess kinetic energy (Q_{ex}) resulting from the final NRA products is given by:

$$Q_{\mathrm{ex}} = E_3 + E_4 + E_\gamma - E_1 \quad (4.9)$$

where $Q_{\mathrm{ex}} > 0$ and $Q_{\mathrm{ex}} < 0$ correspond to an exothermic and endothermic reactions, respectively. Applying the conservation laws of both energy and momentum, and using the reaction kinematics shown in figure 4.7, the energy of the light (E_3) and heavy (E_4) products are given by [3]:

$$E_3 = A_{13}\left(\cos\theta \pm \sqrt{\frac{A_{24}}{A_{13}} - \sin^2\theta}\right)^2 E_{\mathrm{T}} \quad (4.10)$$

$$E_4 = A_{14}\left(\cos\phi \pm \sqrt{\frac{A_{23}}{A_{14}} - \sin^2\phi}\right)^2 E_{\mathrm{T}} \tag{4.11}$$

where E_{T} is the total final energy ($E_{\mathrm{T}} = Q_{\mathrm{ex}} + E_1$), and A_{13}, A_{14}, A_{23}, and A_{24} are constants defined as:

$$A_{13} = \frac{M_1 M_3}{(M_1 + M_2)(M_3 + M_4)} \frac{E_1}{E_{\mathrm{T}}} \tag{4.12}$$

$$A_{14} = \frac{M_1 M_4}{(M_1 + M_2)(M_3 + M_4)} \frac{E_1}{E_{\mathrm{T}}} \tag{4.13}$$

$$A_{23} = \frac{M_2 M_3}{(M_1 + M_2)(M_3 + M_4)}\left(1 + \frac{M_1}{M_2}\frac{Q_{\mathrm{ex}}}{E_{\mathrm{T}}}\right) \tag{4.14}$$

$$A_{23} = \frac{M_2 M_4}{(M_1 + M_2)(M_3 + M_4)}\left(1 + \frac{M_1}{M_2}\frac{Q_{\mathrm{ex}}}{E_{\mathrm{T}}}\right) \tag{4.15}$$

Resonant NRA

Resonant NRA occurs when the involved nuclear reaction presents a sharp maximum for the cross-section at a narrow energy range. For incident ions with the resonant energy, the resonance effect is restricted to the sample surface where incident ions excite the nuclear reaction at the specific resonant energy. Obviously, resonant NRA can be carried out with deeper atoms if the energy of incident ions is increased over the resonant energy, allowing for energy losses during the input path until the resonant energy is reached deep in the sample.

Examples of NRA

NRA has been used to detect N and to obtain the concentration of this element in the grown samples, using again α-particles at 3.7 MeV as incident ions; at this energy, the nuclear reaction $^{14}\mathrm{N}(\alpha,\mathrm{p})^{17}\mathrm{O}$ (Q = -1193 keV) presents a strong resonance due to the increase of the cross-section, as observed at $\theta \sim 165°$ [6]. However, at this incident energy there is an overlapping between NRA produced protons and scattered α-particles, both contributing to the detected signal. In order to overcome this drawback, a 13-μm thick Mylar foil was placed covering the detector. The goal of this filter is to slow down the α-particles (4 times heavier than protons) much more than protons, due to different stopping powers of protons and α-particles, allowing

to energetically separate both α-particles and proton signals. However, this method reduces the depth resolution due to the increase of the energy straggling produced by the Mylar foil.

In our experiments, two detectors are simultaneously used: the first one is located at θ = 170º and is used to obtain RBS and non-RBS signals from Zn, N and O elements; whereas the second one is located at θ = 165º, wears the Mylar foil cover, and is used to measured N NRA signal. This NRA signal is measured in a reference sample consisting of a GaN bulk layer with a well-known thickness and excellent stoichiometry. Resultant NRA spectrum is simulated and fitted using a software to accurately calibrate the total dose Q, i.e. the number of particles per sr (figure 4.8).

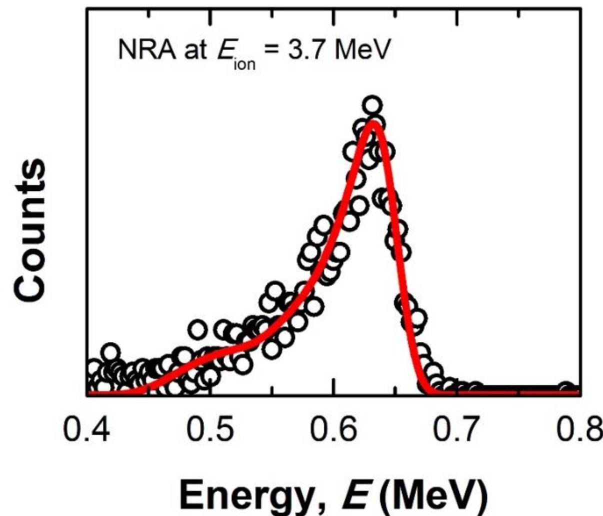

Figure 4.8. NRA spectrum of a GaN reference sample measured at 3.7 MeV and θ = 165º, corresponding to $^{14}N(\alpha,p)^{17}O$ nuclear reaction.

Then, Q is used to fit experimental data to the simulation, mainly influencing the height of the simulated spectrum. Due to Q is defined as the number of incident particles times the solid angle of the detector (particles·sr), it depends on the angle covered by the detector (or on both, sample to detector distance and detector area).

4.1.4. Simulation of the Experimental Data

The analysis of the resultant spectrum obtained from any of the described IBA techniques is performed by SIMNRA software [7]. This software allows to simulate RBS, non-RBS and also NRA spectra because it takes into account all the necessary parameters to both simulate and fit experimental data under specific experimental conditions (such as incident ion mass and energy, dose, detector geometry, etc.). In addition, this software has a complete database including cross-sections for the most common elements, either calculated or experimentally obtained, and reactions, which can be upgraded to include any particular data of interest from published experimental data. In this work, the standard database included with this software was used to simulate the majority of the IBA spectra; however, for some of the reactions new cross-

sections from the ion beam analysis nuclear data library (IBANDL) database [8], were imported to the software.

For particular cases, where the element cross-section is not available in a database, prior to the sample measurement it is necessary to carry out a system calibration using a reference sample. The reference sample should be uniform, stable in both air and vacuum conditions, and thin enough to prevent energy straggling effects. In addition, the element concentration in the reference sample and total layer thickness should be well-known.

Summarizing, SIMNRA software allows us:

i) to calibrate Q (particle · sr) using the NRA signal measured in a reference sample with a well-known thickness and excellent stoichiometry;
ii) to calibrate the E_{offset} and E_{channel} using the high $E_{\mathrm{effective}}$ edge of a surface element RBS signal.

Once Q, E_{offset}, and E_{channel} are determined, layer thickness, and composition can be univocally estimated. The layer thickness is typically given in atoms/cm^2 units. In this regard, this magnitude can be transformed into nm units through the equation (4.16):

$$t\,(\mathrm{nm}) = t\left(\frac{\mathrm{atoms}}{\mathrm{cm}^2}\right)\frac{m_{\mathrm{a}} N_{\mathrm{A}}}{d} \times 10^7 \qquad (4.16)$$

where m_{a} and d are the atomic mass and density, respectively, of the analyzed element, and N_{A} is the Avogadro number.

4.2. SEM and EDAX

SEM operates on the same basic principles as the light microscope but uses electrons instead of light. Because the wavelength of electrons is much smaller than that of light, the optimal resolution attainable for SEM images is many orders of magnitude better than that from a light microscope.

The FEI XL30-SFEG SEM system available in the inter-department research service (SIDI-UAM) facility has been extensively used during this work to characterize the morphology and composition of samples. SEM is considered a fundamental tool for the optimization of growth conditions, allowing to analyze the morphology of resultant structures with sizes from a few microns down to nanometers.

As shown in figure 4.9, during SEM measurements a primary electron beam is directed towards the sample surface, interacting with the material structure. Different signals can be obtained from this interaction, supplying some different information about the sample:

i) Secondary electrons, which are low energy electrons excited by the primary beam escaping from the sample. These electrons provide information about the sample morphology.

ii) Backscattered electrons, which are primary electrons suffering elastic collisions with sample atoms. In a similar way than in RBS experiments, backscattered electron energy is dependent on the sample element with which the primary electron collides, providing then information about sample chemical composition.

iii) Visible photons obtained after the recombination of electron-hole pairs produced by the primary beam. The associated technique is known as cathodoluminescence.

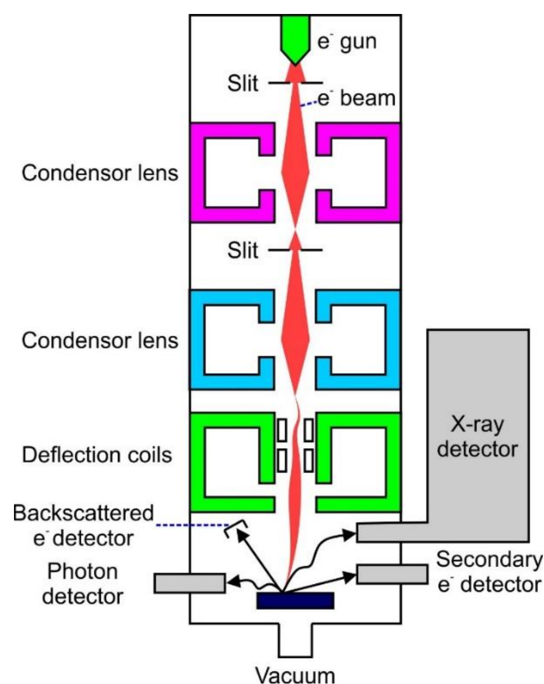

Figure 4.9. Schematic of a SEM/EDAX system.

iv) X-ray photons; primary beam irradiation may also excite sample atoms whose relaxation produce X-ray emission. The energy and intensity analysis of this X-ray emission is known as EDAX allowing to quantify sample chemical composition.

The primary beam is usually scanned over the sample surface following a TV frame scan, while a synchronous signal detection is performed to obtain an image of electrons, photons or X-rays emitted by the sample.

EDAX, or also called EDX, is a technique not only associated to SEM systems, which can be generally used after sample excitation by a high energy beam of charged particles such as electrons or protons, even a beam of X-rays. When the incident particle interacts with one atom in the target sample, it may excite an electron from its inner shell, sometimes with enough energy to release it from the atom, creating a hole at that energy level (figure 4.10). An electron from an outer higher-energy shell may relax to fill the hole, emitting one X-ray photon wearing the energy difference between both energy levels, which is characteristic for each chemical element. The number and energy of X-rays emitted from a specimen can be measured by an energy-dispersive spectrometer, obtaining the EDAX spectrum.

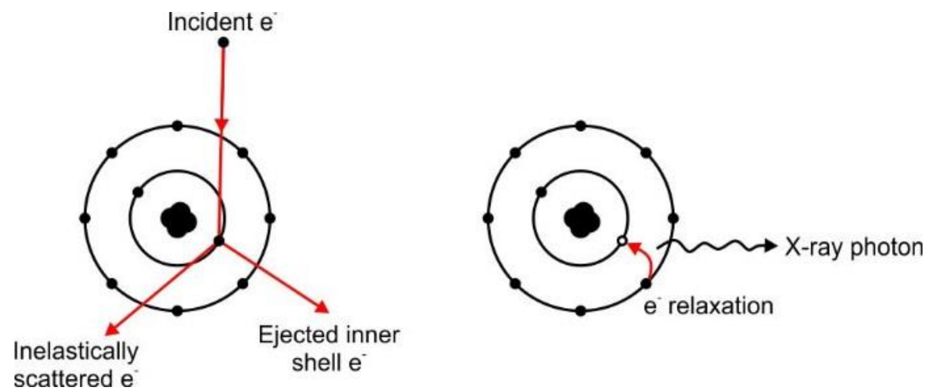

Figure 4.10. Schematic of the EDAX principle.

EDAX has been used in this work to identify the chemical composition of different samples. For the qualitative characterization of the sample, the analysis involves the identification of the lines in the spectrum, which is fairly straightforward owing to the simplicity of X-ray spectra. On the other hand, the quantitative analysis which means the determination of the concentrations of the elements present in the sample, involves measuring line intensities for each element in the sample and for the same elements in calibration standards of known composition (typically using some software with an element database).

4.3. Transmission Electron Microscopy

Transmission electron microscopy (TEM) technique allows to obtain a high resolution image of a thin specimen using a very high energy electron beam transmitted through its structure. Electrons pass through the specimen structure, interacting with atoms, and forming an image which is magnified and focused onto an imaging device such as a fluorescent screen, a photographic film, or detected by a CCD camera. When compared to SEM, as the wavelength of electrons used in TEM is much lower because of the larger energy of the primary beam, a better resolution is achieved.

TEM system used in this work is a FEI F20 model equipped with a CCD camera located at the central facilities of Alabama University. Different TEM techniques have been used, including high-resolution imaging (HRTEM), high angle annular dark field imaging (HAADF), scanning transmission electron microscopy imaging (STEM), selected area electron diffraction (SAED) and also EDAX. This section describes sample preparation, and shows a brief theoretical background of TEM techniques.

Prior to TEM measurements, samples were prepared as follow. In the first step, GaAs NW samples (1×1 cm^2) are dipped in ethanol, and sonicated for a few seconds to remove NWs from Si substrate, resulting in a GaAs NW suspension. After that, a micro-droplet is extracted from the suspension and deposited on a holey carbon copper grid that simplifies the localization of the NWs. Once the organic solvent is evaporated, the grid is transferred to the TEM system. As the NWs are dispersed on the grid, the electron beam impacts perpendicularly to the NW facets.

HRTEM imaging principle is shown in figure 4.11; this schematic presents atomic planes carefully oriented parallel to the incident electron beam, producing a strong transmitted beam and multiple beams

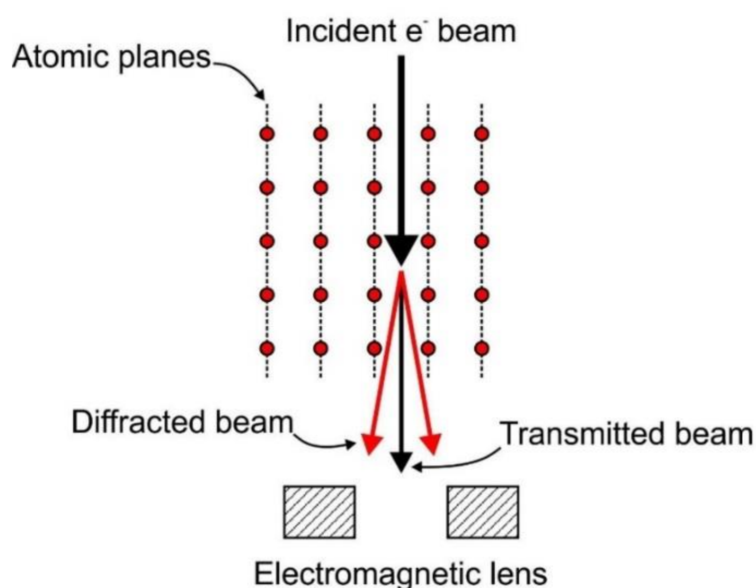

Figure 4.11. HRTEM imaging principle.

diffracted from these sets of atomic planes. In contrast to XRD, the high electron energy used in TEM (200 keV, i.e. very short wavelength) allows to simultaneously collect multiple diffraction spots from different atomic planes at low incidence angles. Multiple diffracted beams are then collected with electromagnetic lens; the interference of these beams creates an image which essentially reproduces the crystal lattice of the analyzed sample. Mathematically, the electromagnetic lens performs a Fourier transform (FT) that creates the diffraction pattern of the object in the back focal plane and an inverse FT that makes the interference of the diffracted beams back to a real space image in the image plane (also called lattice image).

Figure 4.12(a) shows a typical example of HRTEM image obtained from a GaAs NW. This image clearly exhibits the atomic planes of GaAs, where dark-holes can be interpreted as the position of individual atoms. This image has a very high quality over the large NW body area. Atomic planes can be identified through its relative orientation after determining the lattice spacing by using an imaging software. The analysis of these planes is performed on the HRTEM images following different steps. Since the area of interest is selected from the HRTEM image (figure 4.12(a)), then, the selected area image is filtered to subtract the diffuse background intensity, making the line intensity peaks (which can be interpreted as the positions of the atoms) more defined (figure 4.12(b)). Following the filtering step, intensity line scans can be generated along any direction chosen in the plane of the high resolution lattice image; resulting intensity profile shows a collection of peaks which corresponds to a sequence of atoms stacked along the analyzed direction (figure 4.12(c)). The distance between two consecutive peaks allows for the determination of the atomic spacing along the examined direction. In order to minimize the error of this calculation, the atomic spacing can be also obtained by multiple averaging, i.e. by dividing the distance between two non-consecutive atoms (aligned along the analyzed direction) by N+1, where N is the number of atoms between them.

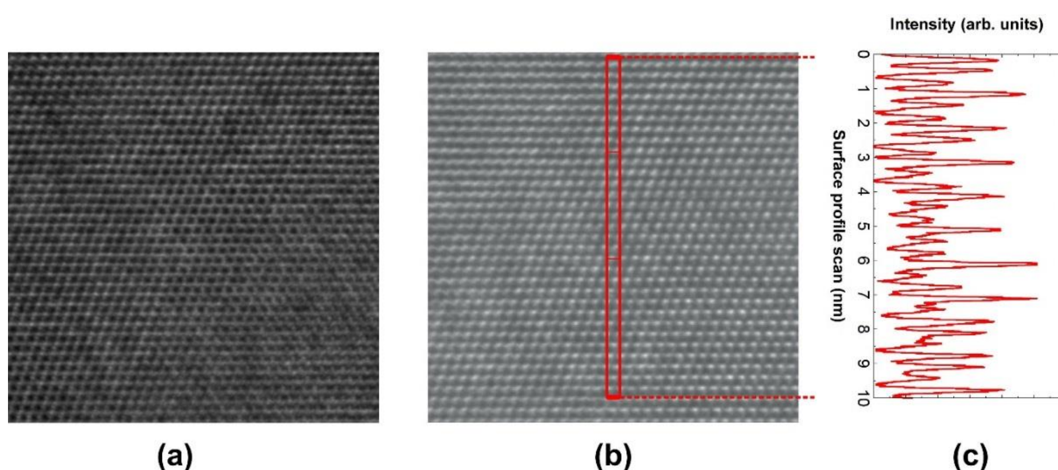

Figure 4.12. (a) Original and (b) post-filtered HRTEM images; (c) intensity profile across the image (b).

The identification of atomic planes and the determination of their spacing can be also carried out by SAED technique (also available in the TEM system) or performing a fast Fourier transform (FFT) in the

HRTEM image. In SAED, a diffraction pattern is made under broad and parallel electron illumination. An aperture in the image plane is used to select the section of the sample the user wishes to examine, giving site-selective diffraction analysis. SAED patterns such as the one shown in figure 4.13(a), are a projection of the reciprocal lattice, with lattice reflections showing as sharp diffraction spots. By tilting the sample to low-index zone axes, SAED patterns can be used to identify crystal structures and measure lattice parameters. SAED is essential for setting up dark field (DF) imaging conditions.

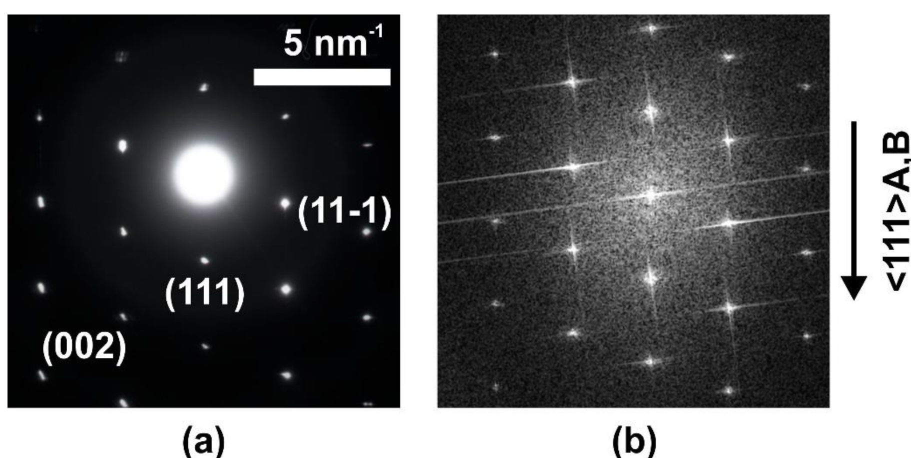

Figure 4.13. (a) ED diffractogram and (b) FFT of a GaAs NW.

Image processing in Fourier space is performed in a similar way as image formation in the TEM. First, the FFT of a HRTEM image is calculated; periodic structures in that image give rise to sharp spots in the resulting diffraction pattern (figure 4.13(b)).

TEM can also work as a high resolution SEM, which is called STEM mode. In STEM mode, electrons diffracted at high angles are collected for imaging, which generates a HAADF image. Since the ability of atoms to diffract electrons depends on their number of protons, the intensity contrast of HAADF STEM image generally tells the mass of the atoms in the sample with high resolution (figure 4.14).

As mentioned, EDAX technique is also available in the used system, and was used to study the composition of GaAs NWs. Since the STEM image of a single GaAs NW is focused (figure 4.14(a)), the electron beam scans the NW surface, leading to an emission of X-rays from NW which can be analyzed by an energy spectrometer. The system allows to drive and focus the electron beam along a specific path; in the case of figure 4.14(a), this measurement technique allows to study variations of the chemical composition over the scanned area. This technique has a lateral resolution which is limited by the smallest spot size achievable by the focused beam; for the microscope used in this work, the lateral resolution is estimated around 2 nm. Figure 4.14(b) shows an example of resulting chemical composition obtained from the analysis of the specific region of the GaAs NW marked with a red circle in figure 4.14(a). These results reveal that the NW is composed by both Ga and As; comparing the area under Ga and As peaks, one can estimate the stoichiometry of the material.

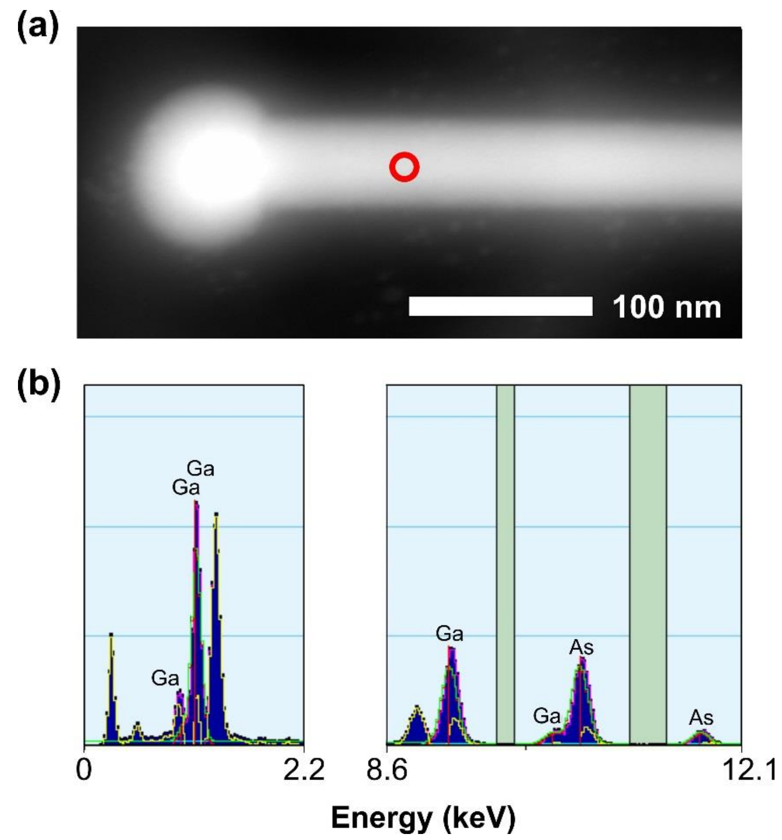

Figure 4.14. (a) STEM image of a GaAs NW with a Ga-rich droplet; (b) resulting chemical analysis of a GaAs NW region marked with a red circle in image (a).

4.4. Electro-Optical Characterization

4.4.1. Four-Probe Van der Pauw Method

Van der Pauw method allows to determine the resistivity (ρ), doping type (n- or p-type), and the majority carrier density (electron carrier density, n_e, or hole carrier density, n_h) and Hall mobility (μ_{Hall}) of a sample with an arbitrary shape [9]. This method needs to be carried out at specific conditions:

1) sample thickness should be constant and much thinner than sample width and length;
2) sample should be solid, homogeneous and isotropic, and should not be composed by pores;
3) electrodes should be defined on the sample perimeter;
4) the electrode contact size should be much lower than the distance between them (point-like contacts).

Resistivity Measurements

In order to reduce errors in the calculations of electrical magnitudes, it is better to use a symmetrical shaped sample. Measurements require four ohmic contacts typically defined at sample corners (figure 4.15).

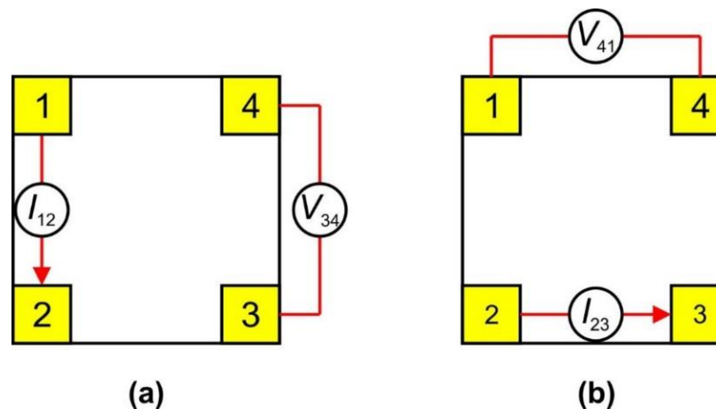

Figure 4.15. Schematic of the sample preparation for Van der Pauw measurements; (a) and (b) are two set of ρ measurements.

Resistivity can be calculated from two basic measurements:

1) An electrical current (I_{12}) is injected in the sample using two adjacent contacts (for example between electrodes 1 and 2), while the voltage drop between the remaining contact pair (V_{34}) is measured (figure 4.15(a)).
2) The same electrical current (I_{23}) is injected again using another pair of adjacent contacts (but not those located on the opposite sample edge than used before, for example between electrodes 2 and 3), while the voltage (V_{41}) is measured in the remaining contact pair (figure 4.15(b)).

From measured voltages and currents two equivalent resistances can be calculated as

$$R_{12,34} = \frac{V_{34}}{I_{12}} \tag{4.17}$$

$$R_{23,41} = \frac{V_{41}}{I_{23}} \tag{4.18}$$

The sheet resistance (R_s), defined as the resistance measured in a plane of one sheet aligned to the current direction, can be written in terms of both resistances as

$$\exp\left(-\pi \frac{R_{12,34}}{R_s}\right) + \exp\left(-\pi \frac{R_{23,41}}{R_s}\right) = 1 \tag{4.19}$$

When using a symmetrical sample and contacts of the same material, it can be assumed that $R_{12,34} \sim R_{23,41} = R$, equation (4.19) can then be simplified as

$$R_s = \frac{\pi}{\ln 2} R \tag{4.20}$$

From equation (4.20), the sample ρ can be calculated as

$$\rho = R_s\, t = \frac{\pi}{\ln 2} R\, t \tag{4.21}$$

where ρ is typically given in Ω·cm units, and t is defined as the layer thickness.

Hall Effect Measurements

Hall effect measurements can also be carried out using the above four-probe experimental setup. Hall effect is observed since a magnetic field ($\vec{B}$) is applied perpendicularly to the sample surface, and also to the electric current ($\vec{I}$) flowing through the sample [10]. The charge carriers moving in the $\vec{B}$ are subjected to a force ($\vec{F}_B$) expressed as

$$\vec{F}_B = q\left(\vec{v} \times \vec{B}\right) \tag{4.22}$$

where q is the carrier charge (± e), v is the drift velocity of a charge carrier subjected to the electric field applied along the y-axis in figure 4.16(a). $\vec{F}_B$ is perpendicular to both $\vec{I}$ (y-axis) and $\vec{B}$ (z-axis), and deviates the charge carrier from the initial current path followed in absence of $\vec{B}$ (figure 4.16(a)). This effect leads to form a bipolar distribution of charge in the layer, involving the separation of positive and negative charges along the x-axis (figure 4.16(b)); this charge accumulation creates an electric field ($\vec{E}$) whose associated force ($\vec{F}_E$) is parallel to $\vec{F}_B$ (y-axis).

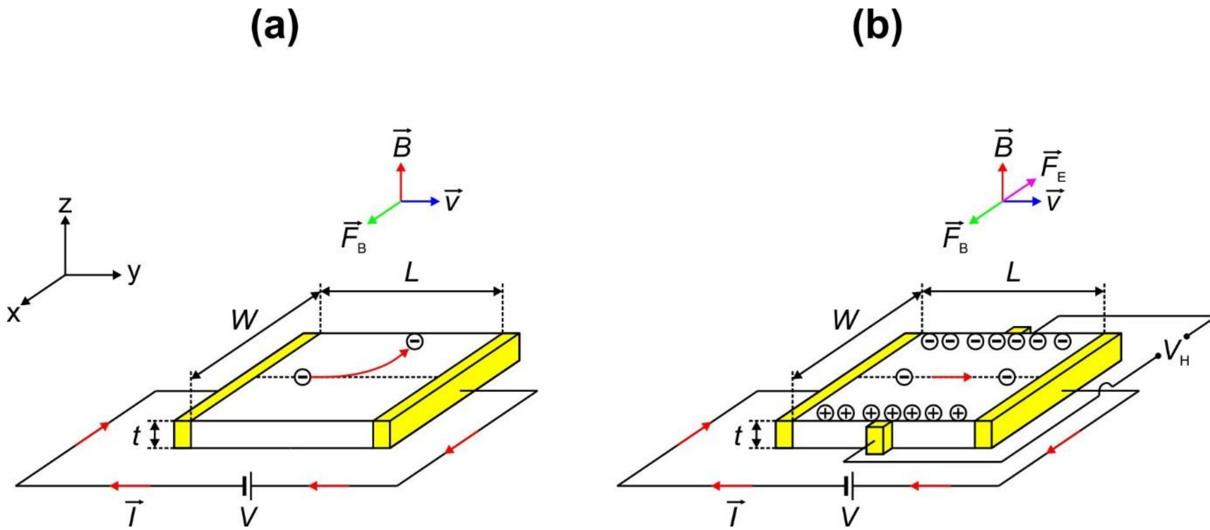

Figure 4.16. Schematic of Hall effect.

In this scenario, flowing charge carriers are subjected to an electro-magnetic field, experimenting the Lorentz force ($\vec{F}_L$) which is defined as

$$\vec{F}_L = q\left(\vec{E} + \vec{v} \times \vec{B}\right) \tag{4.23}$$

As the charge carriers are accumulated, $\vec{F}_E$ increases up to compensate $\vec{F}_B$; then, $\vec{F}_L$ becomes nullify, reaching a stationary state, and showing a voltage along the perpendicular direction to both $\vec{I}$ and $\vec{B}$ (x-axis) known as Hall voltage (V_H). The V_H depends on both $\vec{E}$ (electric field generated along the x-axis) and the sample width (W) through the following equation:

$$V_H = E \cdot W \tag{4.24}$$

In the stationary state ($\vec{F}_L = 0$), equation (4.23) can be expressed as

$$E = v\,B \rightarrow E = \frac{L}{T}B \tag{4.25}$$

where v is defined as the velocity of charge carriers flowing between two electrodes separated a distance L (figure 4.16); therefore, v can be expressed as $v = L / T$ (where T is the time).

The current (I) is defined as $I = Q / T$, where Q is the charge and can be expressed as

$$Q = n\,L\,W\,t\,q \tag{4.26}$$

n being the carrier density. Using equation (4.26), I can be redefined as

$$I = \frac{n\,L\,W\,t\,q}{T} \tag{4.27}$$

Combining equations (4.24), (4.25), and (4.27) the V_H can be re-defined as

$$V_H = \frac{B\;I}{q\,n\,t} \tag{4.28}$$

From the expression above, one can conclude that V_H is proportional to I and B, whereas is inversely proportional to t and n. The equation (4.28) can be also expressed as

$$\frac{V_H\,t}{B\,I} = \frac{1}{q\,n} = R_H \tag{4.29}$$

R_H being the Hall coefficient. Therefore, once V_H, t, I, and B are known, R_H can be calculated using equation (4.29); then, n can be univocally determined. In general terms, R_H magnitude is not exactly described in equation (4.29); a thorough study of this magnitude results in [11]:

$$R_H = r_H\,\frac{1}{q\,n} \tag{4.30}$$

where r_H is a pre-factor that depends on scattering mechanisms, hindering the carrier mobility in the solid; in this regard, r_H can be defined as:

$$r_H = \frac{< \tau_m^2 >}{< \tau_m >^2} \tag{4.31}$$

τ_m being the relaxation time between collisions. This factor takes values between 1 and 2, depending on the scattering mechanism:

i) Phonons, $r_H = 1.18$.

ii) Ionized impurities, $r_H = 1.93$.

iii) Neutral impurities $r_H = 1$.

In Hall measurements performed in a layer with two types of carrier charges (*p* and *n*) contributing to the V_H, the R_H is defined as

$$R_H = \frac{r_H}{e} \frac{p \mu_p^2 - n \mu_n^2}{(p \mu_p - n \mu_n)^2} \tag{4.32}$$

where R_H takes positive or negative sign depending on the dominant term $p\mu_p^2$ or $n\mu_n^2$, respectively. Therefore, from the sign of R_H one can deduce the semiconductor type of the layer (p-type: $R_H > 0$, and n-type: $R_H < 0$).

Finally, the μ can be calculated in terms of *n* and ρ:

$$\mu = q n \rho \tag{4.33}$$

Instead of μ, it is usually given the Hall mobility (μ_H) which is corrected by the r_H (equation (4.34)) and takes higher values than the real carrier charge mobilities.

$$\mu_H = r_H \mu \tag{4.34}$$

Under the four-probe configuration, the current is injected between two opposite electrodes such as 2-4 or 1-3 in figure 4.17(a,b) when $\vec{B}$ is perpendicular to the sample plane; the other electrode pair, i.e. 1-3 or 2-4, respectively, are used to measure V_H.

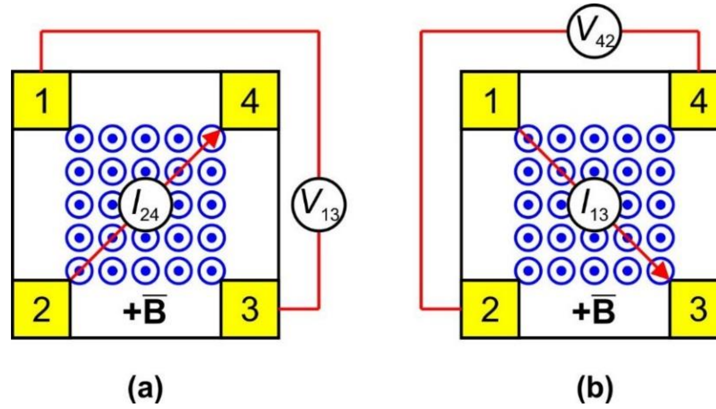

Figure 4.17. Two sets of Hall effect measurements using positive magnetic field.

Hall effect measurements need several sets of basic measurements in order to determine parameters such as the μ and n. Applying a magnetic field ($+\vec{B}$), current is firstly injected between contacts 2 and 4 ($I_{24}=I$) while measuring the lateral voltage drop between contacts 1 and 3 (V_{13}^{++}). Current source is then switched to contacts 1 and 3 ($I_{13}=I$), and lateral voltage drop between contacts 2 and 4 is then measured (V_{24}^{++}).

Ideally, by reversing the current polarity, the voltage sign should also change, but not its magnitude; however, non-ideal contact voltage drops could slightly distort voltage measurements by adding an extra offset to them. To avoid this pernicious effect, current polarity is reversed ($-I$) and the above measurements are repeated to obtain V_{13}^{+-} and V_{24}^{+-} values. The average quantities $V_{13}^{+} = (V_{13}^{++} - V_{13}^{+-})/2$ and $V_{24}^{+} = (V_{24}^{++} - V_{24}^{+-})/2$ are then obtained.

Following, the magnetic field is also reversed ($-\vec{B}$), repeating the above 4 voltage measurements under both current polarities and geometries to finally obtain the averaged V_{24}^{-} and V_{13}^{-} values.

It is worth noticing that the whole set of measurements must be carried out using the same module for $|\vec{B}|$ ($\pm\vec{B}$) and the same current absolute value ($\pm I$). The value of the V_H is obtained by averaging again as

$$V_H = \frac{\left(V_{13}^{+} - V_{13}^{-}\right) + \left(V_{42}^{+} - V_{42}^{-}\right)}{4} \tag{4.35}$$

Our experimental setup for both resistivity and Hall measurements is fully automatized, performing all the above measurements under current and voltage inversion. In addition, Hall measurements are usually done using thirteen different values for the magnetic field (-0.6 T $< B <$ 0.6 T, $\Delta B = 0.1$ T), checking the obtained values for both n and μ are magnetic field independent.

4.4.2. CPD and SPV

CPD Principles

CPD and SPV measurements were carried out using a Kelvin probe vibrating gold mesh electrode separated a small distance from the sample surface, and in ultra-high vacuum conditions. The basics of the CPD voltage measurement are described in figure 4.18.

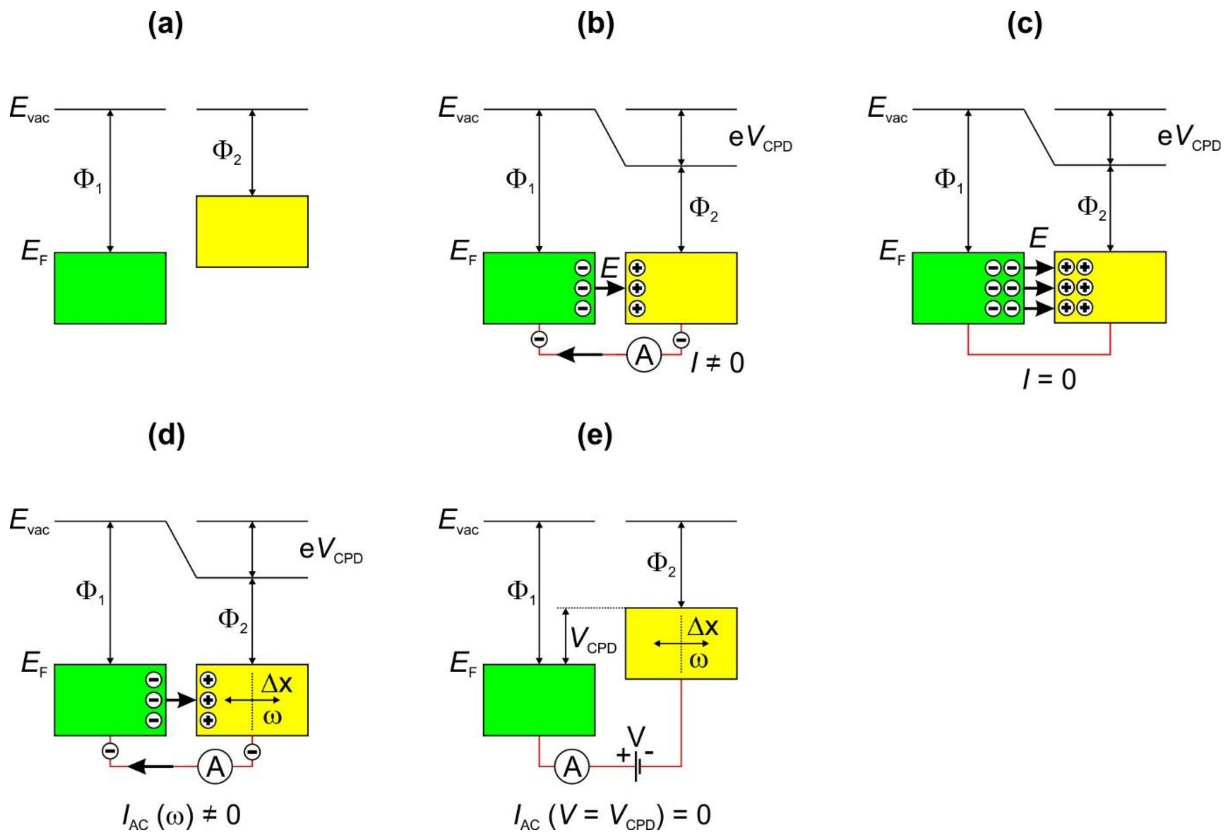

Figure 4.18. Schematic of the CPD principle.

In general, two metals in close proximity but without electrical contact between them, have their E_F at different energies with respect to the vacuum level (E_{vac}) (figure 4.18(a)). That energy is defined as the work function (Φ), and depends on the metal (Φ_1 and Φ_2, where $\Phi_1 > \Phi_2$). When both metals are connected through a wire (figure 4.18(b)), both Fermi levels become aligned, and subsequently the E_{vac} of that metal with lower work function (Φ_2) is lowered by an energy of eV_{CPD}. V_{CPD} is known as contact potential difference voltage. In this scenario, the electron current flows from the lower work function metal (Φ_2, yellow metal) to the higher one (Φ_1, green metal), creating a charge difference between electrodes. The higher work function metal becomes negatively charged, whereas the lower work function metal is positively charged. Accordingly, an electric field (E) is created between metals during the charge accumulation, nullifying the electron flow between electrodes (figure 4.18(c)).

The vibration of one of the electrodes with a frequency of ω, changes the distance (Δx) between both electrodes surfaces over time, producing a variation of E, and then generating an electric current flowing from the metal with the lower work function to the higher (figure 4.18(d)). Finally, a counter voltage (V) is applied in order to nullify this current (figure 4.18(d)). This voltage is equivalent to the V_{CPD}.

If the work function of one of the metals (for example Φ_2) is calibrated with another technique, the work function corresponding to the other metal (for example Φ_1) can be univocally determined using following equations:

$$V_{\mathrm{CPD}} > 0 \rightarrow \Phi_1 = \Phi_2 + V_{\mathrm{CPD}} \quad (4.36)$$

$$V_{\mathrm{CPD}} < 0 \rightarrow \Phi_1 = \Phi_2 - |V_{\mathrm{CPD}}| \quad (4.37)$$

SPV Principles

In the surface of a semiconductor, there are surface defects that lead to the formation of a SCR where the conduction band (CB) is bent away from the Fermi level (figure 4.19(a)). Under illumination with light above the energy band gap of the semiconductor, minority carriers such as holes or electrons in n-type or p-type semiconductors, respectively, are photo-generated and tend to screen the surface charges and then to flatten the bands (figure 4.19(b)).

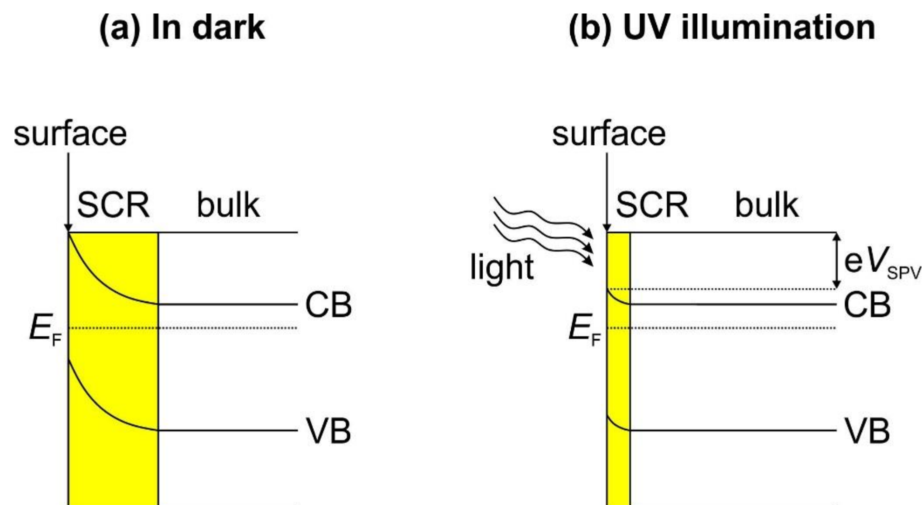

Figure 4.19 Schematic of the SPV principle.

The SPV corresponds to the change in the surface potential due to the illumination. If the light is sufficiently high comparing with the energy band gap of the material under study, then it is possible to flatten

the bands and to make an estimation of the BB. Therefore, the BB can be estimated from the difference between the V_{CPD} measured in dark (V_{CPD}^{dark}) and under illumination (V_{CPD}^{light}):

$$BB = V_{CPD}^{dark} - V_{CPD}^{light} \tag{4.38}$$

System Description

CPD and SPV measurements were obtained under ultra-high vacuum conditions using a Besocke Delta Phi Kelvin Probe S vibrating Au mesh electrode controlled by a Besocke Kelvin Control 07 unit from Besocke Delta Phi GmbH (Jülich, Germany). All the CPD voltages are referenced to the Au work function (Φ_{Au} = 4.7 eV). The study of the SPV was carried out by using a low pressure Hg lamp (Benda, Germany) to illuminate the sample with UV light at λ = 266 nm.

4.4.3. Photoresponsivity Measurements

This work includes the study of the photosensitivity of devices based on Zn_3N_2 thin films, ZnO NWs, and GaAs NWs. Figure 4.20 shows a schematic of the system used to characterize R_{photo}, G_{photo}, and response time of these devices.

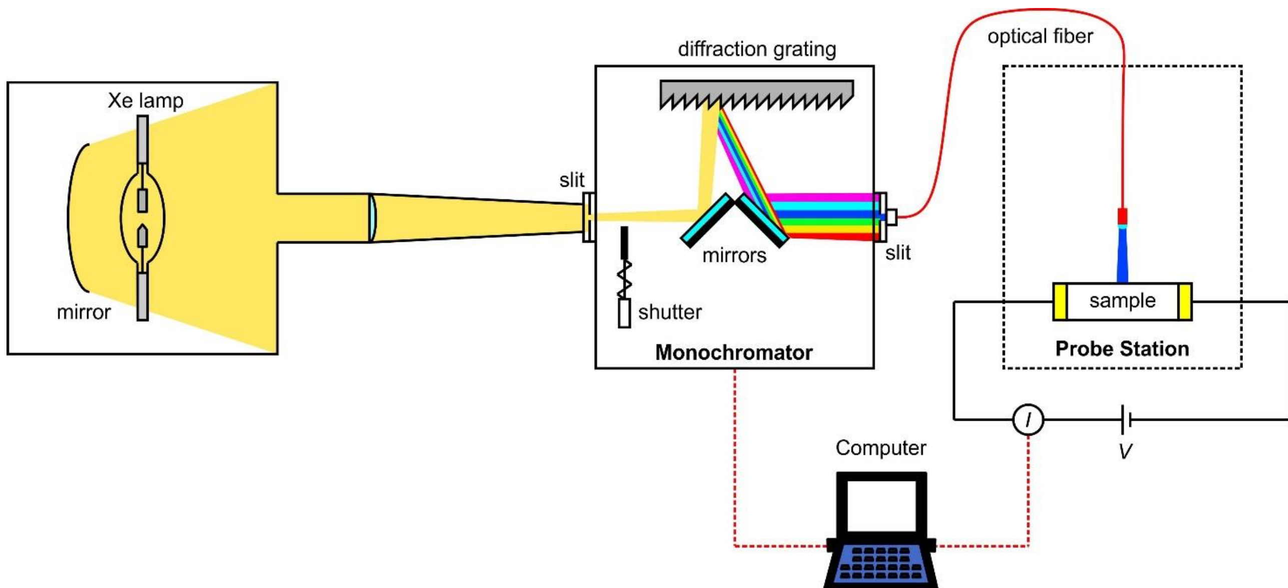

Figure 4.20. Schematic of the photoresponsivity system.

I-V characteristics are measured in a Karl suss probe station in dark and under illumination using a Xe lamp (150 W) coupled to a monochromator (Newport Oriel Instrument, 1/8m Cornerstone 130 Monochromator) through a 3×12 mm slit. The monochromator spectral range is between 250-2000 nm.

Monochromatic light is re-directed through an optical fiber coupled to the monochromator output towards the sample surface.

The R_{photo} as a function of λ can be expressed as

$$R_{photo}(\lambda) = \frac{I_{photo}(\lambda)}{P(\lambda)} \tag{4.39}$$

where I_{photo} is the photocurrent which is defined as the light current (I_{light}) minus the dark current (I_{dark}); P is the absorbed power by the irradiated sample and is calculated by

$$P = P^{*} \frac{A_{sample}}{A_{beam}} (1 - R)\left(1 - e^{-\alpha \cdot x}\right) \tag{4.40}$$

where P^{*} is the lamp power measured with a semiconductor power meter placed in the equivalent position of the sample, A_{beam} is the area of the circular spot produced by the optical fiber on the sample surface (~80mm^2), A_{sample} is the irradiated area of the sample, R is the sample reflectance, and α is the sample absorption coefficient.

4.5. X-Ray Diffraction

In a XRD experiment, a monochromatic incident X-ray beam is scattered by interacting with atoms in the crystal lattice; scattered X-rays interfere constructively only when their optical path difference is an integer multiple of their λ, as shown in figure 4.21.

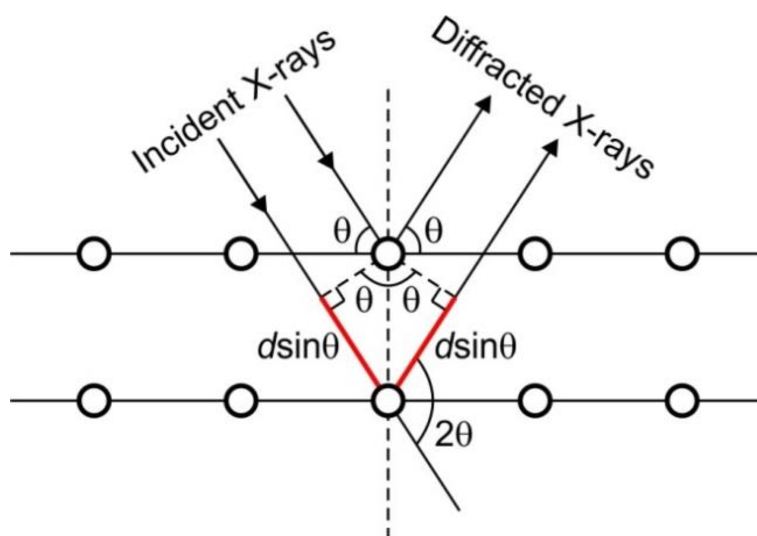

Figure 4.21. Schematic of the Bragg's law.

Constructive interference of scattered beams, also known as diffraction, is governed by the Bragg's law (figure 4.21), which accounts for the above phase difference:

$$2d_{\mathrm{hkl}} \sin\theta = n\lambda \qquad (4.41)$$

θ being the incidence angle at which the diffraction peak will be observed, d_{hkl} is the distance between crystal planes producing the diffraction effect usually identified by its Miller index (hkl). Each crystal structure has therefore its own set of diffraction peaks located at specific angles given by the above law. The relative intensity of those peaks is also a characteristic fingerprint of a material, which depends on structure and atomic scattering factors [12].

The identification of diffraction peaks observed during the analysis of a sample, is commonly carried out by comparing experimental data with powder diffraction files accurately compiled by the International Centre for Diffraction Data (ICDD) [13]. The ICDD maintains a database of powder diffraction patterns, the powder diffraction file (PDF), including the d-spacings (related to angle of diffraction, 2θ) and relative intensities (I) of observable diffraction peaks.

In this work, Zn_3N_2 and ZnO are the crystalline materials analyzed by XRD. The ICDD cards shown in tables below, are the three files used to characterize both Zn_3N_2 and ZnO based thin films and NWs.

Table 4.1. ZnO powder diffraction (Card no. 04-008-8197)

2θ	***d*(Å)**	***I***	**h**	**k**	**l**	**2θ**	***d*(Å)**	***I***	**h**	**k**	**l**	**2θ**	***d*(Å)**	***I***	**h**	**k**	**l**
31.77	2.81	575	1	0	0	72.57	1.30	16	0	0	4	107.43	0.96	7	2	0	4
34.42	2.60	414	0	0	2	76.96	1.24	33	2	0	2	110.38	0.94	28	3	0	0
36.25	2.48	999	1	0	1	81.38	1.18	16	1	0	4	116.27	0.91	68	2	1	3
47.54	1.91	214	1	0	2	89.61	1.09	66	2	0	3	121.55	0.88	36	3	0	2
56.59	1.62	307	1	1	0	92.79	1.06	23	2	1	0	125.16	0.87	5	0	0	6
62.86	1.48	264	1	0	3	95.30	1.04	65	2	1	1	133.91	0.84	29	2	0	5
66.37	1.41	40	2	0	0	98.62	1.02	33	1	1	4	136.53	0.83	6	1	0	6
67.95	1.38	217	1	1	2	102.93	0.98	25	2	1	2	138.51	0.82	9	2	1	4
69.08	1.36	105	2	0	1	104.13	0.98	43	1	0	5	142.91	0.81	21	2	2	0

Table 4.2. Zn_3N_2 powder diffraction (Card no. 00-035-0762)

2θ	***d*(Å)**	***I***	**h**	**k**	**l**	**2θ**	***d*(Å)**	***I***	**h**	**k**	**l**	**2θ**	***d*(Å)**	***I***	**h**	**k**	**l**
22.25	3.99	11	2	1	1	66.16	1.41	9	4	4	4	101.06	0.99	4	8	4	4
25.75	3.46	1	2	2	0	67.69	1.38	3	5	4	3	102.53	0.99	1	9	4	1
31.66	2.82	12	2	2	2	69.28	1.36	1	6	4	0	103.45	0.98	1			
34.28	2.61	100	3	2	1	70.74	1.33	26	7	2	1	105.45	0.97	3	10	1	1
36.73	2.44	89	4	0	0	72.25	1.31	1	6	4	2	108.42	0.95	1	9	4	3
39.05	2.30	1	4	1	1	76.68	1.24	18	6	5	1	111.45	0.93	5	10	3	1
41.27	2.19	1	4	2	0	78.14	1.22	4	8	0	0	116.12	0.91	1	10	4	0
43.37	2.08	63	3	3	2	79.61	1.20	1	7	4	1	117.71	0.9	1	9	6	1
45.41	1.99	1	4	2	2	81.01	1.19	1	6	4	4	124.36	0.87	4	10	5	1
47.37	1.92	3	4	3	1	83.91	1.15	1	6	6	0	126.09	0.86	1	8	8	0
51.12	1.79	7	5	2	1	85.30	1.14	1	7	4	3	131.58	0.84	4	9	7	2
52.92	1.73	67	4	4	0	86.75	1.12	1	6	6	2	133.51	0.84	1	10	6	0
56.41	1.63	2	6	0	0	88.18	1.11	5	7	5	2	135.50	0.83	1	11	4	1
58.11	1.57	4	6	1	1	89.60	1.09	4	8	4	0	139.70	0.82	1	9	6	5
59.78	1.55	1	6	2	0	93.88	1.05	6	9	2	1	144.32	0.81	1	9	8	1
61.40	1.51	1	5	4	1	95.31	1.04	1	6	6	4	149.57	0.80	3	10	7	1
63.01	1.47	2	6	2	2	96.73	1.03	1	8	5	1	152.50	0.79	1	12	2	2
64.62	1.44	4	6	3	1	99.61	1.01	3	9	3	2						

Table 4.3. Zn powder diffraction (Card no. 00-004-0831)

2θ	***d*(Å)**	***I***	**h**	**k**	**l**	**2θ**	***d*(A)**	***I***	**h**	**k**	**l**	**2θ**	***d*(A)**	***I***	**h**	**k**	**l**
36.29	2.47	53	0	0	2	82.10	1.17	23	1	1	2	116.39	0.91	11	1	1	4
38.99	2.31	40	1	0	0	83.77	1.15	5	2	0	0	124.05	0.87	5	2	1	0
43.23	2.09	100	1	0	1	86.56	1.12	17	2	0	1	127.49	0.86	9	2	1	1
54.34	1.69	28	1	0	2	89.92	1.09	3	1	0	4	131.84	0.84	2	2	0	4
70.06	1.34	25	1	0	3	94.90	1.05	5	2	0	2	138.21	0.82	1	0	0	6
70.66	1.33	21	1	1	0	109.13	0.95	8	2	0	3	138.95	0.82	9	2	1	2
77.03	1.24	2	0	0	4	115.79	0.91	6	1	0	5						

where 2θ is the diffraction angle, d is the spacing between crystal planes (hkl) producing the diffraction effect, and I is the relative intensity of observed diffraction peaks.

4.6. Reflection High-Energy Electron Diffraction

Davisson and Germer discovered the electron diffraction phenomenon in 1928 [14]. They employed a diffraction geometry which is basically a reflection electron diffraction geometry, and considered the reflected beam intensity as a function of the primary beam energy. Nowadays, the technique involves from their early experimental setup called low energy electron diffraction (LEED) to the RHEED. Although the great majority of known surface structures are determined by LEED [15], there are many reasons why RHEED is still an attractive technique for surface studies. On the one hand, the glancing incidence angle makes the technique extremely surface sensitive and ideal for combination with growth techniques such as MBE or CBE. On the other hand, the use of high energy electrons simplifies the theoretical treatment of diffraction processes [16].

RHEED is not only used to obtain static diffraction patterns, but also to the study of dynamic diffraction pattern changes during growth, estimating *in-situ* the surface coverage or 2D growth rate in monolayers per second.

Figure 4.22(a) shows a schematic of the RHEED standard configuration. Electrons with a high energy typically between 10 and 15 keV at a grazing incidence angle between 0.5º and 2º, are diffracted by atoms at the sample surface. Because of the very short penetration depth of electrons for this energy range [17], and also to the grazing incidence angle, electrons escaping from the sample only penetrate a few atomic layers under the sample surface, thus avoiding bulk diffraction when the sample surface is ideally flat. Only electrons diffracted by the 2D sample surface structure can constructively interfere at some specific angles (Bragg's condition described in equation (4.41)), according to the crystal structure, atomic spacing and associated λ of the incident electrons. Diffracted electrons are collected on a phosphorus screen placed in the electron path over a growth chamber window, where impacting beams induce the phosphorescent emission of green light, building the electron diffraction pattern. The RHEED geometry configuration allows

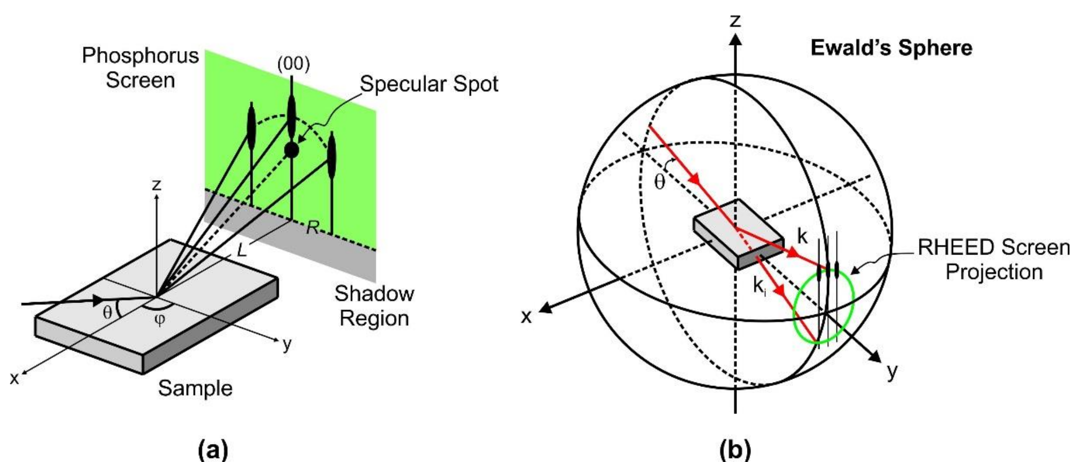

Figure 4.22. (a) Schematic of the RHEED geometry and (b) intersection of the reciprocal lattice with Ewald's sphere.

continuous monitoring of the sample surface during growth process, such as layer growth rate, planarity, surface reconstruction, etc.

RHEED pattern following Bragg's law can be interpreted by means of the Ewald's sphere (figure 4.22(b)). In the reciprocal space, incident electrons with a momentum given by $k_i = 2\pi/\lambda$ suffer elastic scattering processes without losing energy, scattered electron wave-functions interfere constructively (diffraction) at some scattering angles but they keep the same momentum modulus than incident electrons ($|k_f| = |k_i|$), which means both incident and diffracted electrons have the same wavelength in the real space. The vector resulting from the difference between both momentums is called scattering vector ($\Delta k = |k_i - k_f|$), which has to be a vector of the reciprocal space. Since k_i and k_f have the same modulus, both vectors must lie on the surface of a sphere with radius $k_i = 2\pi/\lambda$, which is known as Ewald's sphere.

The reciprocal lattice of a 2D lattice in the (x,y) plane is not a pure 2D lattice [12], but a 2D lattice with no z-axis restrictions, which is then formed by lines expanding perpendicularly to the sample surface. Thermal agitation and point defects relax the reciprocal lattice lines to rods, and the non-purely mono-energetic character of electron beam also relax the Ewald's sphere to a spherical crown with thickness δk_i. The diffraction conditions are then satisfied where reciprocal space rods intersect the Ewald's spherical crown (figure 4.22(b)), giving rise to a line pattern for a near perfect 2D sample surface structure.

Sample rotation allows to also rotate the reciprocal lattice, obtaining different oriented diffraction patterns. RHEED geometry is designed in such a way that only the low diffraction orders impinge on the phosphorus screen. The geometrical arrangement of diffraction spots corresponds to the interplanar spacing and the angles between crystal planes. For an (hkl) surface, the diffraction condition is

$$uh + vk + wl = 0 \tag{4.42}$$

<uvw> being the azimuth of the electron beam. Considering a cubic single-crystal, the observed azimuths are <010>, <110>, and <120> for the (001) surface, <100>, <01−1>, and <11−1> for the (011) surface and <1−10>, and <11−2> for the (111) surface. The observed spacing of the diffraction lines on the screen (R) is proportional to the product of the interplanar spacing (d_{hkl}) and the lattice period in the incident direction of the electron beam. Thus, the lattice constant in the real spacing can be calculated as [18]

$$d_{\mathrm{hkl}} = \frac{\sqrt{u^2 + v^2 + w^2}}{\sqrt{h^2 + k^2 + l^2}} \frac{\lambda L}{R} \tag{4.43}$$

where L is the distance from sample center position to screen.

The reciprocal lattice for a 2D lattice differs from a 3D lattice in which a 2D reciprocal lattice consists of rods (figure 4.23(a)), whereas a 3D lattice consists of a set of points (figure 4.23(b,c)).

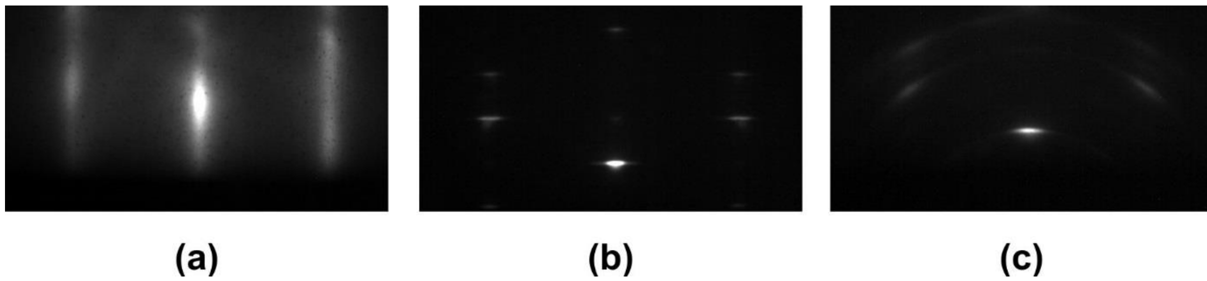

Figure 4.23. RHEED patterns of (a) Si(111) substrate, (b) GaAs NWs on Si(111) and (c) polycrystalline GaAs layer on Si(111), obtained at <1-10> azimuth.

In the case of 2D lattice, only the first few layers of the material contribute to the diffraction in the RHEED pattern (figure 4.23(a)). On the other hand, 3D diffraction (also called bulk diffraction) occurs when incident electrons are allowed to diffract through a rough surface without being absorbed; this scenario can be observed when the epitaxial layer surface is rough, instead specular, but with very small protuberances whose lateral dimensions are much lower than electron penetration depth, allowing electron diffraction under transmission conditions on that structures. Bulk diffraction is then easily identified as a spotty pattern rather than a streaky pattern. Figure 4.23(b,c) show two representative examples of RHEED spotty patterns obtained from diffraction through vertically aligned GaAs NWs (b) and polycrystalline GaAs layer (c), both grown on Si(111) substrates. These spots show horizontal spacing similar to the rod spacing observed in the Si substrate (figure 4.23(a)), meaning the lattice parameter of both GaAs NWs and GaAs polycrystalline layer match to the Si substrate (epitaxial growth).

4.6.1. RHEED Technique Applications

The specular spot has the highest intensity on the RHEED pattern of a flat surface, being superimposed to the central (00) bar (figure 4.22(a)). This spot is due to electrons whose waves are directly reflected on the sample surface at the same angle (θ) than incident electrons; the larger the surface planarity, more intense will the specular spot be.

RHEED oscillations were observed for the first time in 1981 during a MBE growth [19]; the oscillation period was found to be the same than the characteristic time to grow a monolayer on the substrate. This effect is explained on the basis of a periodic change of surface roughness during growth which also changes the constructive interference of waves on the specular spot. The best configuration to obtain large changes on the specular spot intensity is using off-Bragg conditions for the incidence angle [20]; for a given step height between surface terraces, destructive interference is enhanced at the middle position between two Bragg constructive interference angles. Under this condition, electron waves reflected from terraces differing by one monolayer step height arrive to the RHEED screen under phase inversion, thus subtracting their amplitudes. If we can imagine the sample surface covered by only two level terraces differing by one monolayer step height under off-Bragg incidence condition, the specular spot intensity cancellation would be

total when the surface is covered by 50% each, while the specular spot intensity would be maximum when only one kind of terrace is present on the sample surface.

Fluctuations of the specular spot intensity are then commonly used in ultra-high vacuum epitaxial systems to study the surface coverage (Θ) over time, which can be explained using Weeks-Gilmer's model [21]. Figure 4.24 shows an example of how the Θ changes during epitaxial growth, thus inducing a periodic specular spot intensity change.

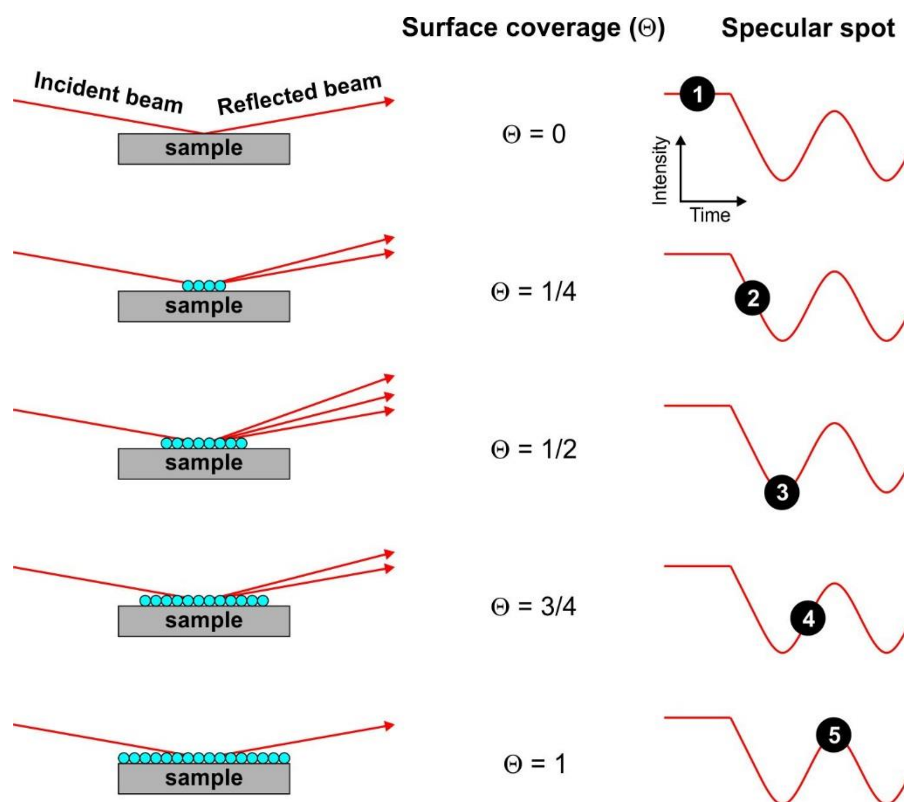

Figure 4.24. RHEED specular spot intensity fluctuations during an epitaxial growth.

Consider a crystalline substrate with an initial ideal flat and specular surface, exhibiting the maximum intensity of the specular when the surface coverage is zero (Θ = 0) before growth starts. Once the epitaxial growth starts, atoms arriving to the substrate surface tend to nucleate islands when colliding after diffusion. As step edges of these islands will act themselves as atomic sinks for surface physisorbed atoms, nucleated islands will grow laterally due to the incorporation of new atomic species after diffusion, increasing the surface terrace coverage, and then lowering the specular spot intensity.

Once half-monolayer is already grown (Θ = 1/2) the surface roughness is maximum, then producing the minimum value for the specular spot intensity. As the surface coverage further increases, surface roughness will decrease; the destructive interference in the reflected beam will also decrease, increasing the specular spot intensity. The specular spot intensity will reach again the initial maximum value since the first

monolayer is completed with a full surface coverage ($\Theta = 1$). The growth of one monolayer is then associated to one oscillation period in the RHEED specular spot intensity.

Experimental evidences show that the amplitude of the specular spot intensity oscillations tends to decrease progressively over time (figure 4.25). Some other factors such as random nucleation, atomic diffusion, and molecular beam inhomogeneity promote the formation of a new layer at some places on the surface while the previous layer is not yet completed in other positions; in this scenario, the surface roughness progressively increases as growth proceeds, attenuating the specular spot intensity over time.

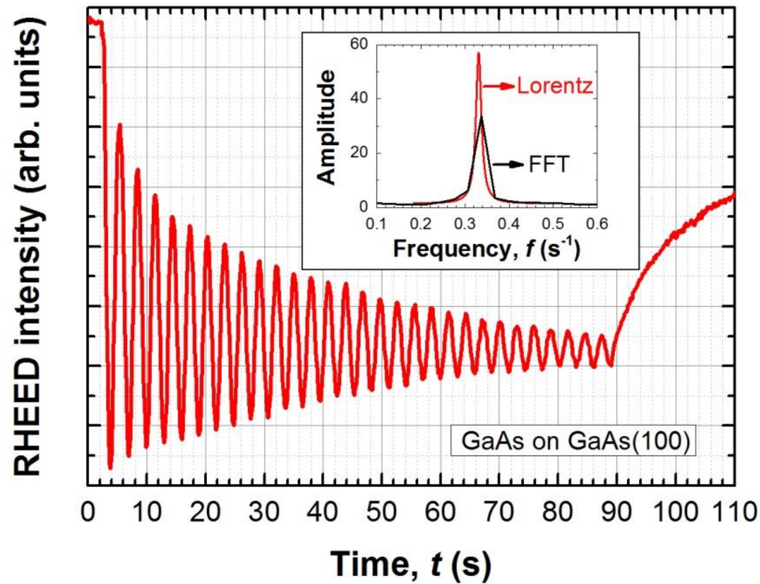

Figure 4.25. RHEED specular spot intensity oscillations obtained during the growth of GaAs on GaAs(100). Inset: Fast Fourier Transform (FFT) of the oscillations curve and its corresponding Lorentzian fitting.

2D-Layer Growth Rate

Figure 4.25 shows specular spot intensity oscillations measured during the growth of GaAs on GaAs(100) in our CBE system. According to this figure, the intensity oscillates periodically, being its characteristic frequency calculated from the intensity fast Fourier transform (FFT). Both intensity FFT and its corresponding Lorentzian fitting are shown in the inset of figure 4.25. This characteristic frequency (f) is the same than 2D-layer growth rate (ML/s). In addition, if the thickness (d) of a monolayer is known ($d = d_{200} = a/2$ for GaAs grown on the (100) surface), the growth rate (r_g) can be directly calculated (in nm/s or μm/h) as

$$r_g = d \cdot f \tag{4.44}$$

Ga Flux Calibration

As explained in chapter 3, gas flux can be univocally calibrated from *BEP* measurements as a function of the P_{cam} if using an additional technique such as RHEED to determine the effective atom flux incorporation (atoms/cm^2·s).

The growth of GaAs layers on GaAs(100) substrates is used to calibrate r_g of this compound using different TEGa and TBAs fluxes at different T_s, T_{HT} and T_{LT}. For this calibration, epi-ready GaAs(100) substrates are previously heated up to T_s = 580 ºC to desorb the surface oxide.

GaAs r_g is calibrated as a function of T_s and BEP_{TEGa}, because r_g is controlled only by Ga element flux under As excess flux conditions, and it can be obtained from the RHEED intensity oscillations as explained above.

During the growth of GaAs on GaAs(100) substrates under As excess conditions, RHEED pattern shows the presence of a (2×4) surface reconstruction. RHEED oscillations are usually measured using the specular spot under the direction of the 2-fold surface reconstruction.

Figure 4.26 shows the result obtained on the growth of GaAs layers at T_s = 600 ºC, using T_{HT} = 820ºC, T_{LT} = 80 ºC, under TBAs excess (P_{cam} = 0.72 Torr), where r_g values obtained from RHEED intensity oscillations are represented as a function of BEP_{TEGa}.

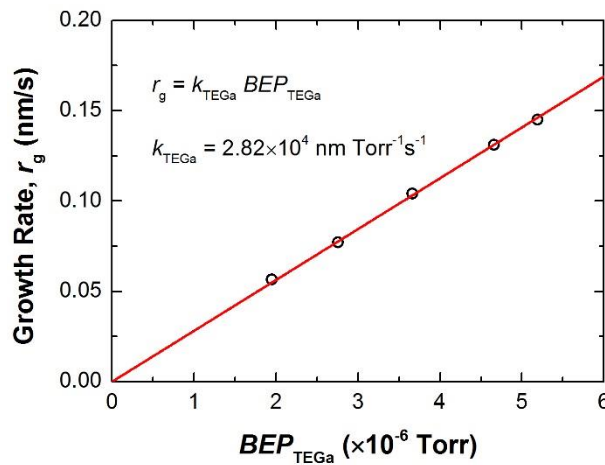

Figure 4.26. GaAs r_g as a function of BEP_{TEGa}.

It is clear the linear dependence observed in the above figure, the proportionality constant k_{TEGa} = 2.82×10^4 nm Torr^{-1}s^{-1}, being obtained by a linear fitting. The effective Ga flux incorporated to the growth (F_{Ga}) can be defined in terms of r_g and the Ga atomic surface density (N_s) on the growth surface ($N_s = N_{002} = 2/a^2_{GaAs}$ for ZB {001} surfaces):

$$F_{\mathrm{Ga}}\left[\frac{\mathrm{atoms}}{\mathrm{cm}^2\cdot\mathrm{s}}\right] = r_{\mathrm{g}} N_{\mathrm{s}} = k_{\mathrm{TEGa}} BEP_{\mathrm{TEGa}} \frac{2}{a_{\mathrm{GaAs}}^2} = 1.77\times10^{10}\cdot BEP_{\mathrm{TEGa}} \tag{4.45}$$

Since the BEP_{TEGa} depends on TEGa P_{cam}, as determined experimentally in chapter 3, F_{Ga} can be also expressed as a function of TEGa P_{cam}:

$$F_{\mathrm{Ga}}\left[\frac{\mathrm{atoms}}{\mathrm{cm}^2\cdot\mathrm{s}}\right] = 1.38\times10^{5} P_{\mathrm{cam}}^{1.51} \tag{4.46}$$

4.7. Mass Spectrometry

Mass spectrometry, also called mass spectroscopy, is a high sensitive instrumental technique for identifying the chemical composition of a substance by means of the separation of gaseous ions according to their differing mass and charge. This technique allows not only to identify the molecular mass of a compound, but also to detect and to determine the different molecular fragments formed after the ionization and further molecular breaking. The ionized species or sub-species are separated depending on their mass/charge ratio by means of an analyzer, acting as a filter and mass selector. Finally, a detector is conveniently placed at the analyzer output in order to quantify the selected ions concentrations.

In this work, mass spectra have been obtained by using of a quadrupole mass spectrometer (QMS) (Balzers QMS250) located in the growth chamber of the CBE, aligned with the aperture of the high temperature cell. This QMS has a display to analyze mass spectra, and also allows to download numerical data for their later analysis in a computer.

The mass spectrometry process is carried out in four different stages:

i) ionization of the sample,
ii) acceleration of ions by means of electric field,
iii) dispersion of ions depending on their mass/charge ratio, and
iv) detection of ions producing the resultant spectrum.

Figure 4.27 shows a schematic of a QMS where it can be distinguished three main parts: i) ionization stage, ii) quadrupole mass separator (ion analyzer), and iii) ion detector.

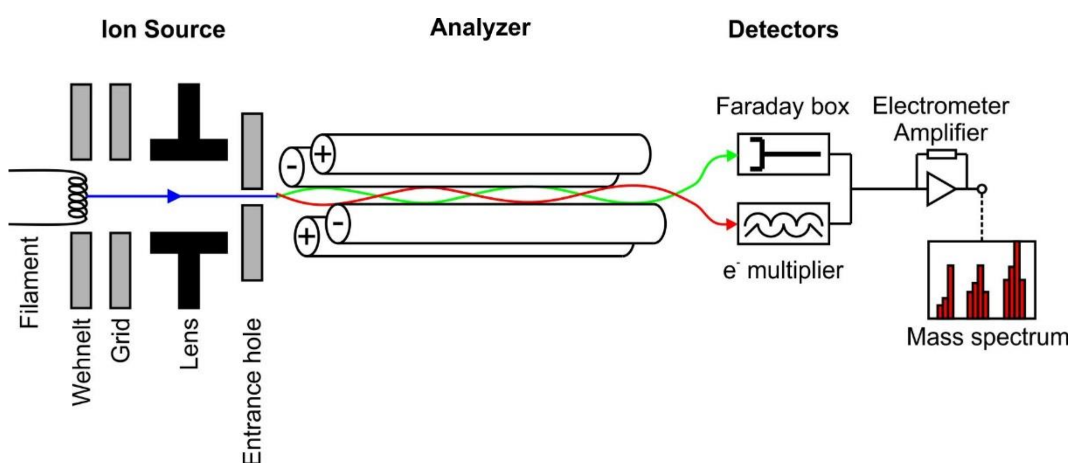

Figure 4.27. Schematic of the QMS available in the CBE.

During the ionization stage, electrons emitted from a heated filament are accelerated to low energies (around 100 eV) by an electric potential, bombarding gas molecules (M) and producing charged species (M^+) as described by the reaction:

$$M + e^- \rightarrow M^+ + 2e^- \qquad (4.47)$$

Commonly, M^+ consists of an excited state and then can be fragmented in two different ways:

$$M^+ \begin{cases} E^+ + R & (4.48)(a) \\ P^+ + N & (4.48)(b) \end{cases}$$

where R and N are a radical (with one or more unpaired electrons) and a molecule, respectively. In addition, E^+ and P^+ ions can be also fragmented.

Once the ions are formed in the ionization source, they are selected as a function of their mass/charge ratio and directed towards the detector by means of a mass analyzer. There are a wide variety of mass analyzers, including magnetic sector, time of flight, and quadrupole. Here, we thoroughly describe the latter because is the mass analyzer available in our CBE system.

The quadrupole mass analyzer (QMA) consists of four cylindrical parallel rods which are equidistant to the central edge (figure 4.27). An electrostatic potential ($U/2$) (typically ranged between 500 and 2000 V) is applied through a pair of opposite rods (+), whereas an electrostatic potential with the same magnitude but opposite sign is applied to the other pair of rods (-). Additionally, a rf alternating potential with amplitude ($V/2$) (ranged between 0 and 3000 V) is applied, resulting in a potential difference between each rod pair:

$$\phi(t) = (U + V\cos\omega t) \qquad (4.49)$$

In these conditions, ions can cross the QMA along oscillating trajectories, being repealed and attracted continuously by the rods. For pre-defined values of U and V, only ions with a specific mass/charge ratio will reach the detector, while the other ions will follow trajectories towards the rods. By keeping a constant U/V ratio but simultaneously changing their values, ions with different mass/charge ratios can reach the detector; the registered number of ions for a given integration time is recorded versus the calibrated U/V value, generating then a mass spectrum.

In our QMA the detector can be changed from the standard Faraday box to a secondary electron multiplier, in order to increase the QMA sensitivity for pressures below 10^{-8} Torr.

4.7.1. Metalorganic Precursor Decomposition

As described in chapter 3, the epitaxial growth of GaAs is carried out using metalorganic precursors of Ga and As. Prior to the Ga and As incorporation to the epitaxial layer, precursor molecules need to be

cracked in order to liberate Ga and As atoms. Cracking processes are usually pyrolytic and/or catalytic, and occur either at the sidewalls of the high temperature effusion cell or on the substrate surface.

In the case of element III precursors such as TEGa, the substrate temperature in the range between 400 and 600 ºC is enough to thermally decompose the molecule over a non-passivated substrate surface (partly catalytic), therefore being unnecessary to previously crack the molecule inside the gas cell.

In the case of element V precursors such as TBAs, the substrate temperature is not sufficiently high to thermally crack the TBAs molecule, being necessary to carry out a molecule pre-cracking using a high temperature cell, allowing for decomposition of the TBAs molecule, producing a molecular beam with As atoms and AsH_x radicals to the epitaxial growth.

Figure 4.28 shows the characteristic mass spectrum of TBAs acquired with the QMS, injecting the TBAs flux ($BEP_{TBAs} = 4.4\times10^{-7}$ Torr) in the CBE growth chamber through the HT cell at different T_{HT} of 50, 700 and 1050 ºC. These spectra have been acquired after the stationary regime is achieved, which means the intensity of every peak remains constant.

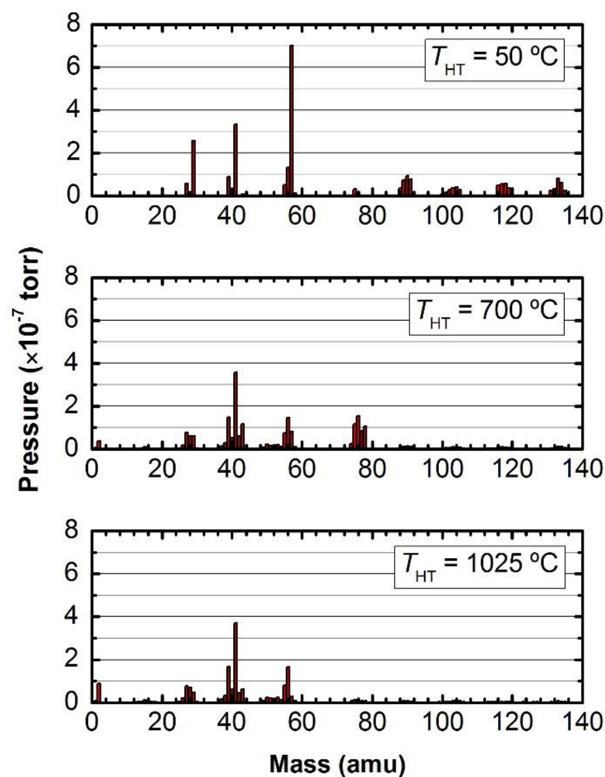

Figure 4.28. TBAs mass spectra measured at different T_{HT}.

At T_{HT} = 50ºC, it is observed the characteristic mass peaks of TBAs sub-products due to the ionization process inside the QMA, according to equations (4.47) and (4.48). At this temperature, it can be found the uncracked TBAs peak ($C_4H_{11}As$) at 134 amu. However, due to the low intensity of this peak, it is difficult to be used as a marker for uncracked TBAs detection. In order to overcome this issue, the peak at 57 amu, associated to the tertiarybuthyl radical (C_4H_9), resulting from TBAs dissociation into AsH_2 and C_4H_9

inside the QMA (equation (4.48)(a)), is a better candidate for uncracked TBAs marker. The spectrum acquired at T_{HT} = 50 ºC has been chosen as the characteristic mass spectrum of TBAs, and is called here standard TBAs spectrum.

For much higher T_{HT} (T_{HT} = 700 and 1025 ºC), the characteristic TBAs peak intensity (57 amu) decreases, suggesting that TBAs is being pyrolytically cracked. The main compounds obtained from the pyrolytic decomposition of TBAs are: isobutane (C_4H_{10}), isobutene (C_4H_8), ethane (C_2H_6), methane (CH_4), arsine (AsH_3), AsH_2, AsH, As, and H_2; their mass spectra were obtained from the NIST database [22], and have been used to simulate our TBAs spectra at different T_{HT}.

The simulation of the TBAs spectra has been carried out through our own software which allows to make a linear combination of standard library spectra (remembering that the standard TBAs spectrum corresponds to the mass spectrum measured at T_{HT} = 50 ºC) in order to reproduce experimental spectra. The coefficients used in such linear combination can be interpreted as partial pressures and are represented in figure 4.29 as a function of T_{HT}.

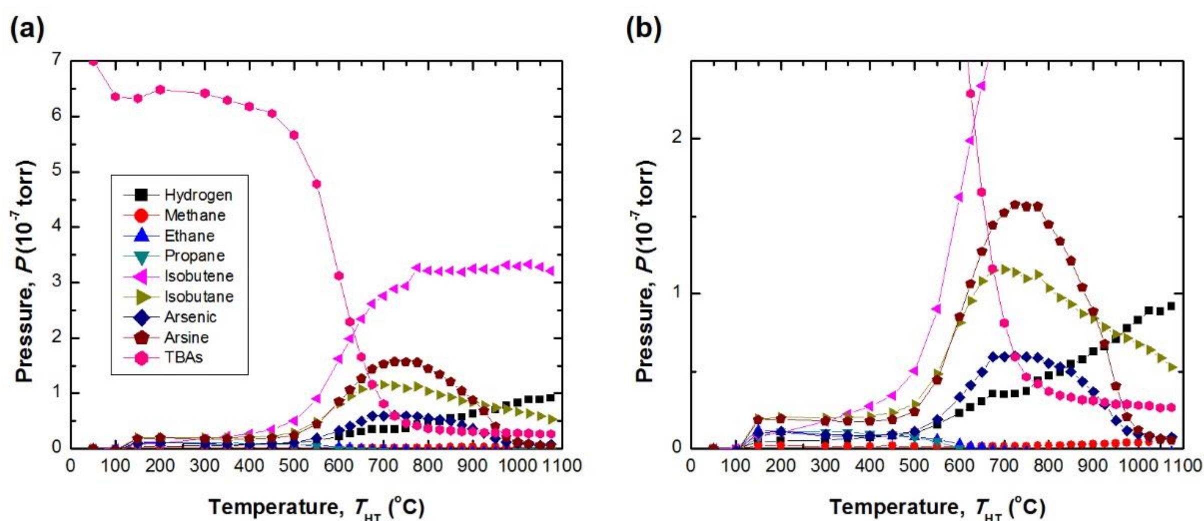

Figure 4.29. Products obtained from the TBAs decomposition at different T_{HT}; (b) is a zoom-in along P axis of (a).

For T_{HT} < 300 ºC, the mass spectrum is almost identical to uncracked TBAs. When T_{HT} is increased from 500 to 700 ºC, uncracked TBAs contribution suddenly decreases, remaining nearly constant for higher T_{HT} values; for T_{HT} values as high as 900 ºC, uncracked TBAs concentration in the molecular beam is low but not zero, which means the cell has reached its maximum decomposition efficiency for TBAs.

Isobutane, isobutene and arsine products can be obtained from two different reactions described below:

$$\begin{aligned} \text{TBAs} &\rightarrow C_4H_8 + AsH_3 \\ \text{TBAs} &\rightarrow C_4H_{10} + AsH \end{aligned} \quad (4.50)$$

Since T_{HT} takes values above 300 ºC, isobutene concentration increases, becoming saturated for T_{HT} > 650 ºC; isobutene saturation agrees with TBAs efficiency saturation as mentioned above. Both isobutane and arsine are also detected for T_{HT} > 500 ºC, isobutane showing lower concentrations than isobutene, with a tendency to decrease for higher T_{HT} after a maximum around 650 ºC; on the other hand, arsine reaches higher concentrations in the gas for T_{HT} between 700 and 800 ºC with an extinction tendency for T_{HT} larger than 1000 ºC.

Similar trend is observed for As, whose characteristic peak is found at 75 amu, but showing much lower concentrations than those observed for arsine. However, it could be possible that this peak be associated to an AsH radical instead of elemental As; the decomposition of AsH inside the QMS forming As and H cannot be followed in the spectra due to the H signal observed at T_{HT} > 550 ºC (see the slight increase of H with T_{HT} in figure 4.28), which is difficult to ascribe to a particular process.

Additionally, the group of peaks around 76 amu (associated to the arsine group) increases, showing a maximum around 700 ºC (figure 4.29), while at much higher temperatures (T_{HT} = 1025 ºC) arsine cracking also takes place.

Ethane and methane are also detected in the QMS spectra but in their concentrations are very low compared to other compounds.

The existence of AsH_3 and AsH as final species for growth using cracked TBAs can reduce C doping of epitaxial layers grown in CBE, when compared to layers grown with uncracked TBAs. From the above results, one can conclude that the optimum TBAs decomposition is reached for T_{HT} > 700 ºC.

4.8. Optical Spectroscopy

4.8.1. Spectroscopic Ellipsometry

SE is an optical measurement technique that characterizes light reflection (or transmission) from samples. The key feature of SE is that it measures the change in polarized light upon light reflection on a sample (or light transmission by a sample). SE is an effective and non-destructive tool to rapidly determine optical constants of a material. In addition, this technique allows to detect morphology and surface chemical modifications of materials over time [23].

In this work, SE is carried out in reflection mode, involving the reflection of light from the sample surface. To describe this reflection, we suppose an incident plane wave moving in the direction shown in figure 4.30, assuming that this wave is reflected by the sample surface. The plane of incidence is defined as the plane that contains the light beam ingoing and outgoing beams, i.e. light beam prior and after the reflection. In addition, the plane of incidence also contains the normal of the surface.

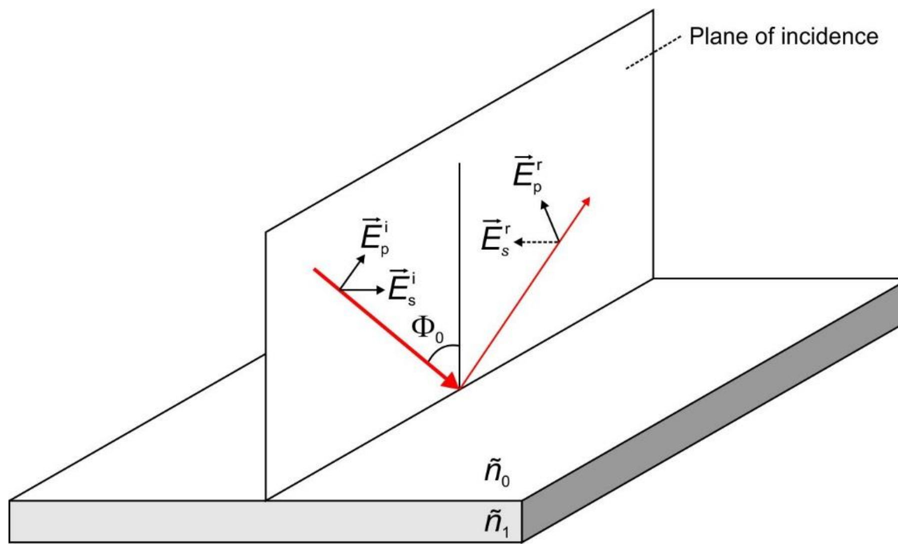

Figure 4.30. Schematic of SE working in reflection mode.

The electric field ($\vec{E}$) associated to a polarized plane wave can be decomposed in two orthogonal components parallel ($\vec{E}_p$) and perpendicular ($\vec{E}_s$) to the plane of incidence (figure 4.30). In this regard, the electric field of the incident and reflected plane waves are defined as $\vec{E}^i = (E_p^i, E_s^i)$, and $\vec{E}^r = (E_p^r, E_s^r)$, respectively. Plane wave changes its phase upon reflection, which means $\vec{E}_p^i$ and $\vec{E}_p^r$ have a phase difference of δ_p, whereas $\vec{E}_s^i$ and $\vec{E}_s^r$ have a phase difference of δ_s.

Components of $\vec{E}^i$ and $\vec{E}^r$ are related to the Fresnel reflection coefficients (r_p and r_s) through the following expressions:

$$E_{\mathrm{p}}^{\mathrm{r}} = r_{\mathrm{p}} \cdot E_{\mathrm{p}}^{\mathrm{i}} \tag{4.51}$$

$$E_{\mathrm{s}}^{\mathrm{r}} = r_{\mathrm{s}} \cdot E_{\mathrm{s}}^{\mathrm{i}} \tag{4.52}$$

r_{p} and r_{s} being complex functions of the optical constants of the mediums that define the reflection surface, the incident angle (Φ_0), and the wavelength (λ). The Fresnel coefficients provide information about changes in amplitude and phase of each electric field component upon reflection. From Fresnel coefficients, one can define a complex variable ρ as the ratio between Fresnel coefficients

$$\rho \equiv \frac{r_{\mathrm{p}}}{r_{\mathrm{s}}} \tag{4.53}$$

The ρ can be expressed in complex form as

$$\rho \equiv \tan\psi \cdot \mathrm{e}^{\,\mathrm{j}\Delta} \tag{4.54}$$

where Ψ and Δ are the ellipsometric variables, and determine changes in the amplitude and phase observed upon reflection

$$\psi = \tan^{-1}\left|\frac{r_{\mathrm{p}}}{r_{\mathrm{s}}}\right| \tag{4.55}$$

$$\Delta = \delta_{\mathrm{p}} - \delta_{\mathrm{s}} \tag{4.56}$$

Ψ is then the angle whose tangent is the ratio of the reflection coefficient magnitudes, and takes values ranged between 0 and 90º; whereas Δ is the change in phase difference that occurs upon reflection, and takes values between 0 and 360º.

Air/Substrate Structure

Figure 4.31 shows the case of an incident light beam propagating through a medium with complex refractive index: $\tilde{n}_1 = n_1 + \mathrm{j}k_1$, and later reflecting on the surface of a medium with a complex refractive index: $\tilde{n}_2 = n_2 + \mathrm{j}k_2$. The figure shows that some of the light is reflected and some is transmitted.

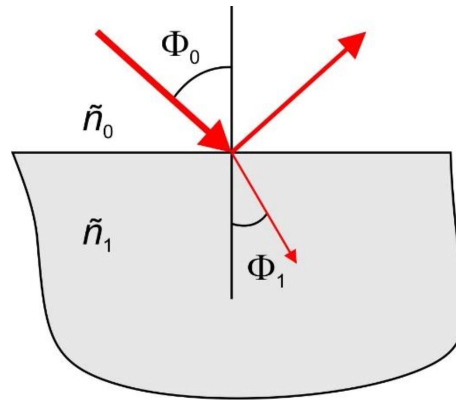

Figure 4.31. Schematic of light reflection and transmission at a single interface.

For the single interface case, Fresnel reflection coefficients are given by

$$r_{01}^{p} = \frac{\tilde{n}_1 \cos\Phi_0 - \tilde{n}_0 \cos\Phi_1}{\tilde{n}_1 \cos\Phi_0 + \tilde{n}_0 \cos\Phi_1} \tag{4.57}$$

$$r_{01}^{s} = \frac{\tilde{n}_0 \cos\Phi_0 - \tilde{n}_1 \cos\Phi_1}{\tilde{n}_0 \cos\Phi_0 + \tilde{n}_1 \cos\Phi_1} \tag{4.58}$$

where superscripts refer to the waves parallel or perpendicular to the plane of incidence, and subscripts refers to either medium (0) or medium (1).

Combining equations (4.53), (4.57), (4.58), and using the Snell law

$$\tilde{n}_0 \sin\Phi_0 = \tilde{n}_1 \sin\Phi_1 \ , \tag{4.59}$$

the complex refractive index of medium (1) can be written as

$$\tilde{n}_1 = \tilde{n}_0 \sin \Phi_0 \left(1 + \left(\frac{1-\rho}{1+\rho} \right) \tan^2 \Phi_0 \right)^{\frac{1}{2}} \tag{4.60}$$

Therefore, if the optical constants of medium (0) and Φ_0 are known, the optical constants of a medium (1) can be calculated from the measured ellipsometric variables Ψ and Δ using equation (4.60).

Air/Layer/Substrate Structure

Figure 4.32 shows a schematic of a plane wave reflected in an air/layer/substrate structure, where the thickness (d) and optical constants of the layer (n_1 and k_1) grown atop a substrate (n_2 and k_2) can be

determined using polarized light propagating through a medium (usually air or vacuum) with optical constants n_0 and k_0.

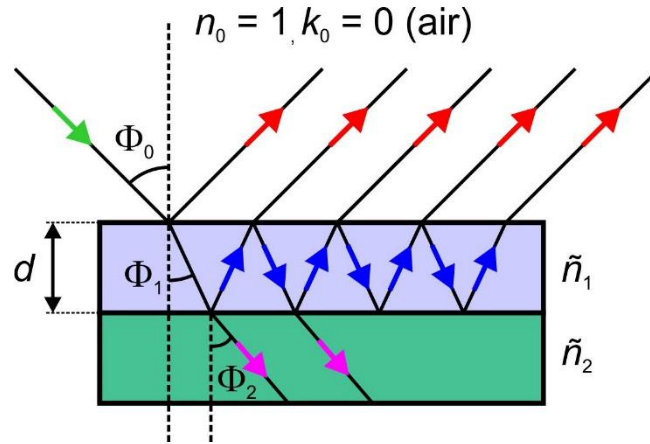

Figure 4.32. Plane wave reflection and transmission in air/layer/substrate structure.

Because reflected light accounts not only the direct reflection on the first air-layer interface but also the multiple and successive reflections at the interface the layer-substrate (blue arrows) and at the substrate-air interface, Fresnel reflection coefficients are not enough to solve the problem (transmitted light through the substrate will not be important for this study). In this regard, one should take into account the transmission coefficients between mediums (0) and (1) that are expressed as

$$t_{01}^{\mathrm{p}} = \frac{2\tilde{n}_0 \cos\Phi_0}{\tilde{n}_1 \cos\Phi_0 + \tilde{n}_0 \cos\Phi_1} \tag{4.61}$$

$$t_{01}^{\mathrm{s}} = \frac{2\tilde{n}_0 \cos\Phi_0}{\tilde{n}_0 \cos\Phi_0 + \tilde{n}_1 \cos\Phi_1} \tag{4.62}$$

and the reflection coefficients r_{01}^{p} (4.57), r_{01}^{s} (4.58), r_{12}^{p}, and r_{12}^{s}, where r_{12}^{p} and r_{12}^{s} are defined as

$$r_{12}^{\mathrm{p}} = \frac{\tilde{n}_2 \cos\Phi_1 - \tilde{n}_1 \cos\Phi_2}{\tilde{n}_2 \cos\Phi_1 + \tilde{n}_1 \cos\Phi_2} \tag{4.63}$$

$$r_{12}^{\mathrm{s}} = \frac{\tilde{n}_1 \cos\Phi_1 - \tilde{n}_2 \cos\Phi_2}{\tilde{n}_1 \cos\Phi_1 + \tilde{n}_2 \cos\Phi_2} \tag{4.64}$$

The total reflected plane wave consists of the direct reflection on the air-layer surface interface (red arrows in figure 4.32) and the multiple reflections inside the layer. Each contribution to the total reflected plane wave differs with respect to previous one an angle β determined as

$$\beta = 2\pi \frac{d}{\lambda}\left(\tilde{n}_1^2 - \tilde{n}_0^2 \sin^2\Phi_0\right)^{\frac{1}{2}} \tag{4.65}$$

The sum of contributions constituting the multiple reflected plane waves, gives a resultant reflected plane wave whose expressions are detailed below

$$R_p = \frac{r_{01}^p + r_{12}^p \, e^{-j2\beta}}{1 + r_{01}^p \, r_{12}^p \, e^{-j2\beta}} \tag{4.66}$$

$$R_s = \frac{r_{01}^s + r_{12}^s \, e^{-j2\beta}}{1 + r_{01}^s \, r_{12}^s \, e^{-j2\beta}} \tag{4.67}$$

Combining equation (4.53) (where r_p and r_s can be generalized as R_p and R_s), (4.66), and (4.67), the relationship between ellipsometric variables (Ψ and Δ) and optical constants of the air/layer/substrate structure ($\tilde{n}_0$, $\tilde{n}_1$, $\tilde{n}_2$, d, Φ_0 and λ) can be obtained for the case of:

$$\tan\Psi \, e^{j\Delta} = \rho = \frac{r_{01}^p + r_{12}^p \, e^{-j2\beta}}{1 + r_{01}^p \, r_{12}^p \, e^{-j2\beta}} \cdot \frac{1 + r_{01}^s \, r_{12}^s \, e^{-j2\beta}}{r_{01}^s + r_{12}^s \, e^{-j2\beta}} \tag{4.68}$$

In order to extract optical constants of the unknown medium (n_1 and k_1), Ψ and Δ are simulated as a function of λ using equation (4.68) for known values of n_0, k_0, n_2, k_2, Φ_0, Φ_1 and Φ_2, and different values of n_1 and k_1 in order to fit measured values of Ψ and Δ to simulated ones.

On the other hand, if the optical constants of medium (1) are already known, the thickness of this layer (d) can be determined by fitting the measured and simulated values of Ψ and Δ, using known values of n_0, k_0, n_1, k_1, n_2, k_2, Φ_0, Φ_1 and Φ_2 in equation (4.65).

Experimental System

The SE system used in this work is the Uvisel commercial ellipsometer shown in figure 4.33.

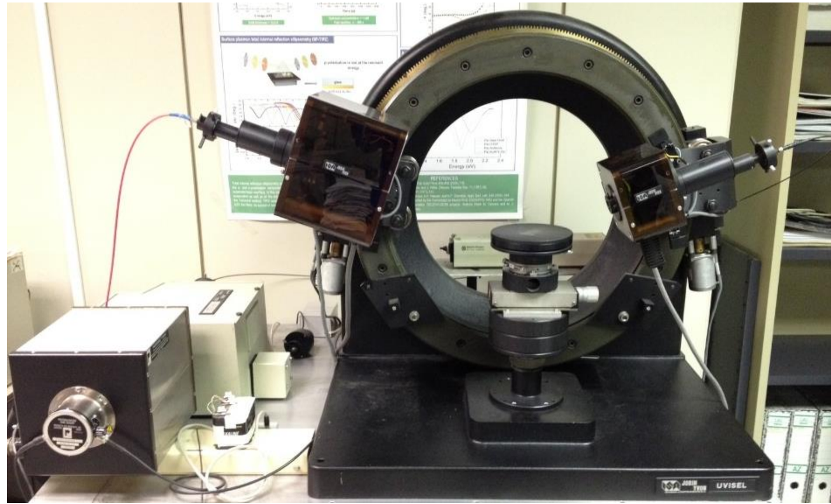

Figure 4.33. Uvisel commercial ellipsometer system.

Figure 4.36 shows a schematic of the Uvisel commercial ellipsometer system. The light source is a Xe-lamp that covers the UV/VIS spectral range. The emitted light beam is properly collimated, obtaining a near point-source. This light is then transmitted through an optical fiber which is coupled to a polarizer. Prior to the light incidence on the sample surface, a modulator regulates the light phase.

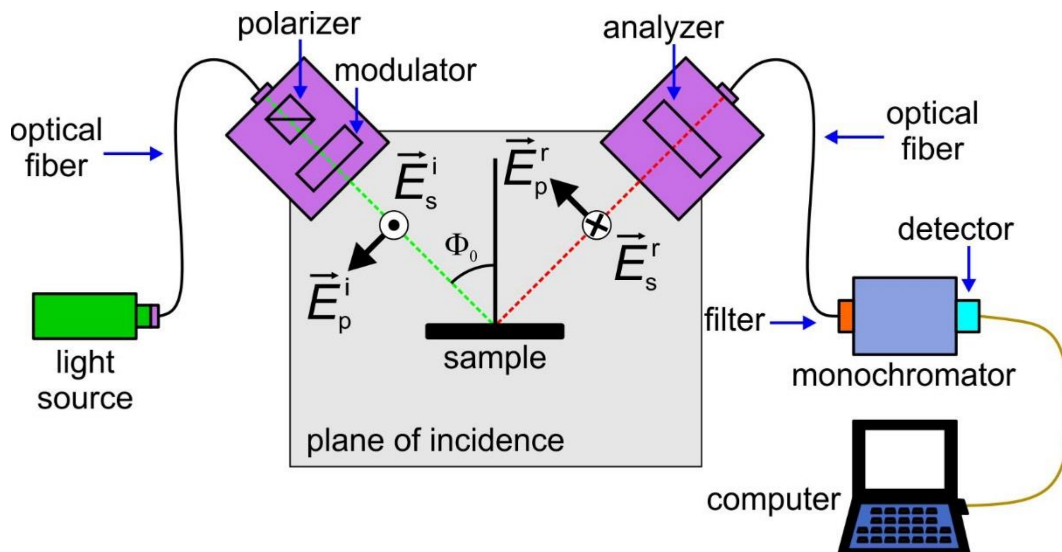

Figure 4.34. Schematic of the Uvisel commercial ellipsometer system.

Once the light is reflected on the sample surface, it reaches the analyzer. The optical edges of the polarizer, the modulator and the analyzer are forming angles of P, M and A referred to the plane of

incidence. In this work, measurements have been carried out using: M = 0º, A = +45º, P-M = +45º, and an incident angle of 70º.

After the analyzer stage, the light is coupled to an optical fiber, and transmitted to a monochromator (Jobin-Yvon, mod. HR-250) with a diffraction grating (1200 grooves/mm) and a spectral range of 240-850 nm. The output signal of the monochromator is detected by a photomultiplier (mod. R928S Hamamatsu), and finally is electronically treated and sent to an acquisition system.

4.8.2. Raman Spectroscopy

Raman scattering is an inelastic light scattering non-destructive technique, giving information on the structural properties of materials. Lattice dynamics, composition, strain, and in some cases phonon dispersion, phonon density of states, and electronic states of semiconductors can be studied by means of Raman spectroscopy.

Raman scattering involves the interaction between the electromagnetic radiation, and vibrational/rotational modes in a material. The scattering process comprises two packets of energy (also called quanta) simultaneously, and is usually described in two steps:

i) A photon with an energy of $h\nu_i$ and a wavevector of $\vec{k}_i$, is absorbed, exciting the system from the initial state to the excited state.

ii) The system emits a photon with an energy of $h\nu_s$ and a wavevector of $\vec{k}_s$ and relaxes from the excited state to the final state.

In the case where the final state is identical to the initial one, the incident and scattered light have the same energy ($h\nu_i = h\nu_s$). This process is called elastic or Rayleigh scattering. When the final state is different from the initial one, the scattering process is inelastic. In this case, the creation or the annihilation of an excited state of the system occurs, and the emitted photon has lost or gained energy. These processes are called respectively Stokes scattering and anti-Stokes Raman scattering. These scattering processes are summarized in figure 4.35.

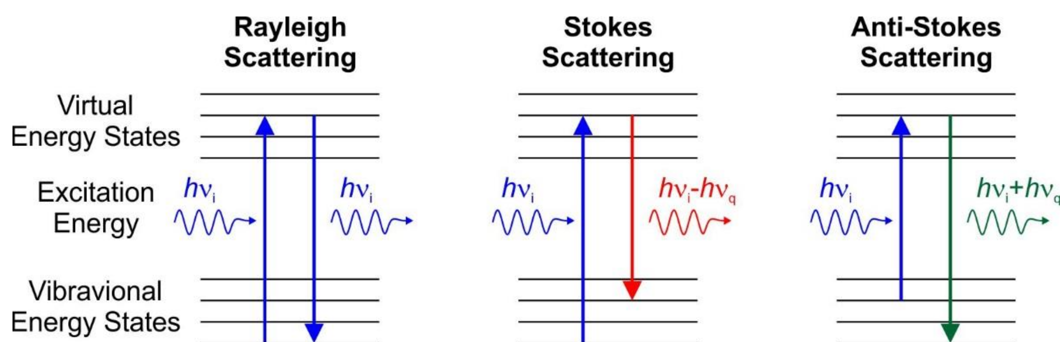

Figure 4.35. Schematic of transitions between vibrational energy states due to, from left to right, Rayleigh scattering, Stokes Raman scattering and anti-Stokes Raman scattering.

For the conservation of energy, the frequency of the scattered radiation is given by:

$$\nu_{\mathrm{s}} = \nu_{\mathrm{i}} \pm \frac{E_{\mathrm{i}}\text{-}E_{\mathrm{f}}}{h} = \nu_{\mathrm{i}} \pm \nu_{\mathrm{q}} \tag{4.69}$$

where ν_{i} and ν_{s} are defined as the frequency of the incoming and scattered photon, respectively; E_{i} and E_{f} are the initial and the final energy state of the system. The difference between the Raman scattering frequency ν_{s} and the excitation frequency ν_{i} is independent on the latter, and is equal to $\pm\nu_{\mathrm{q}}$. The Raman scattering is governed by the conservation of energy and by conservation of momentum, which implies that

$$\vec{k}_{\mathrm{s}} = \vec{k}_{\mathrm{i}} \pm \vec{q} \tag{4.70}$$

The consequence of the wavevector conservation is that one-phonon Raman scattering probes only phonons close to the center of the Brillouin zone ($\vec{q} = 0$). The orientation of the crystallographic axes with respect to the direction and polarization of the scattered light affects the Raman spectrum. In this respect, it is evident that Raman spectroscopy on single crystals gives information about the crystal symmetry.

The Raman intensity is calculated as follows

$$I_{\mathrm{s}} \sim \left| \vec{e}_{\mathrm{i}} \cdot \overleftrightarrow{R} \cdot \vec{e}_{\mathrm{s}} \right|^2 = \left| \hat{e}_{\mathrm{i}} \begin{pmatrix} R_{\mathrm{xx}} & R_{\mathrm{xy}} & R_{\mathrm{xz}} \\ R_{\mathrm{yx}} & R_{\mathrm{yy}} & R_{\mathrm{yz}} \\ R_{\mathrm{zx}} & R_{\mathrm{zy}} & R_{\mathrm{zz}} \end{pmatrix} \hat{e}_{\mathrm{s}} \right|^2 \tag{4.71}$$

where $\hat{e}_{\mathrm{i}}$ and $\hat{e}_{\mathrm{s}}$ are the unitary vectors of the incident and scattered light, and $\overleftrightarrow{R}$ is the scattering tensor. The use of a determined incident and analyzed polarization in the Raman scattering experiments results in the selection of certain elements of $\overleftrightarrow{R}$. In that respect, polarized Raman spectroscopy allows to determine Raman selection rules.

As an example, we consider ZB GaAs structure. The phonon dispersion is composed of six different branches: two transverse and on longitudinal acoustical modes (TA and LA) as well as two transverse and one longitudinal optical modes (TO and LO). The Raman tensors for ZB GaAs can be written in the base: x = <100>, y = <010>, and z = <001>, resulting in:

$$R(x) = \begin{pmatrix} 0 & 0 & 0 \\ 0 & 0 & 1 \\ 0 & 1 & 0 \end{pmatrix}, R(y) = \begin{pmatrix} 0 & 0 & 1 \\ 0 & 0 & 0 \\ 1 & 0 & 0 \end{pmatrix}, \text{and } R(z) = \begin{pmatrix} 0 & 1 & 0 \\ 1 & 0 & 0 \\ 0 & 0 & 0 \end{pmatrix} \tag{4.72}$$

However, the crystallographic axis of ZB GaAs <0-11>, <211>, and <-111> are commonly used as an alternative basis. Accordingly, the Raman selection rules are obtained transforming Raman tensors shown in (4.72), and expressing the polarization vectors ($\hat{e}_{\mathrm{i}}$ and $\hat{e}_{\mathrm{s}}$) into the new basis, and using equation (4.71). In this way, the Raman selection rules and the dependency of the intensity on the polarization direction can be calculated from different surfaces. For the sake of simplicity, experiments are commonly carried out in backscattering geometry where directions of excitation and collection are the same. In this scenario, both LO and TO phonon modes are observed from the (111)GaAs surfaces, while only TO is observed from (110)GaAs surfaces.

Experimental System

Figure 4.36 shows a schematic of the Raman system used in this work belonging to the University of Alabama (USA). This system can be used either with a VIS (λ = 532 nm) or UV (λ = 266 nm) laser for excitation. Each laser beam is re-directed using a specific full play-set of mirrors to minimize absorption losses, and can be gradually attenuated by a set of neutral density (ND) filters. Using a beam-splitter, the laser beam is re-directed to a microscope objective (×10 or ×100) where it is focused under normal incidence to the sample surface. The irradiated sample area is below 100×100 μm^2 when using the ×10 objective, while it could be reduced to around 10×10 μm^2 with the ×100 objective.

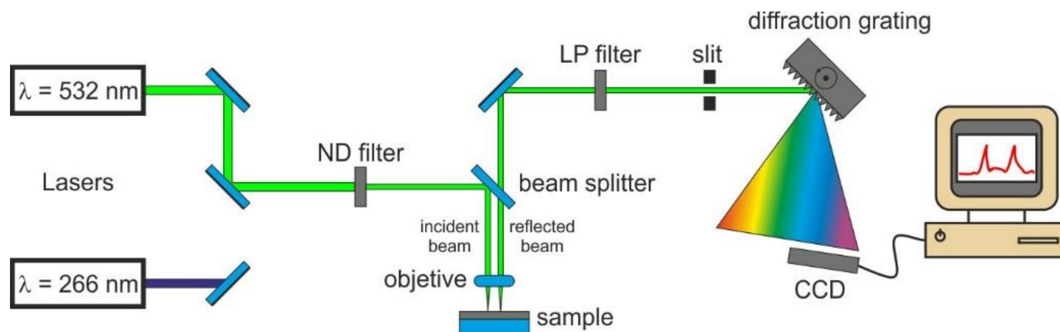

Figure 4.36. Schematic of the Micro-Raman and Micro-PL system.

Reflected beam is collected by the same objective (see figure 4.36), and continues its path to the charge-coupled device (CCD) detector through the beam splitter the low-pass (LP) filter removing the laser line, a 50 μm slit reducing the beam aperture, and the diffraction grating where it is finally dispersed.

The CCD collects in a single snapshot the specific range of wavelengths of interest for the Raman spectrum. As the diffraction grating can rotate, the CCD can collect a wide range of wavelengths overlapping several snapshots, whose exposure time can be selected in order to enhance system detectivity.

Measured Raman intensity is commonly represented as a function of the Raman shift (Δw), which is expressed in cm^{-1} units and can be calculated as:

$$\Delta w\,(\mathrm{cm}^{-1}) = \left(\frac{1}{\lambda_0} - \frac{1}{\lambda}\right) \times 10^7 \tag{4.73}$$

where λ_0 and λ are expressed in nm units and correspond to the excitation laser wavelength and the Raman wavelength, respectively.

Two different laser powers have been used during Raman measurements: 0.25 and 0.4 Watt and 5 different ND filters labeled as: 0, 1, 2, 3, and 4 (where 0 corresponds to the lowest attenuation and therefore 4 is the highest attenuation) for each laser power. The effective laser power irradiating the sample surface is measured as a function the ND filter for both laser powers (figure 4.37). The possibility to irradiate the sample with different laser powers allows to analyze thermal effects as will be thoroughly study during the characterization of GaAs NWs (chapter 7).

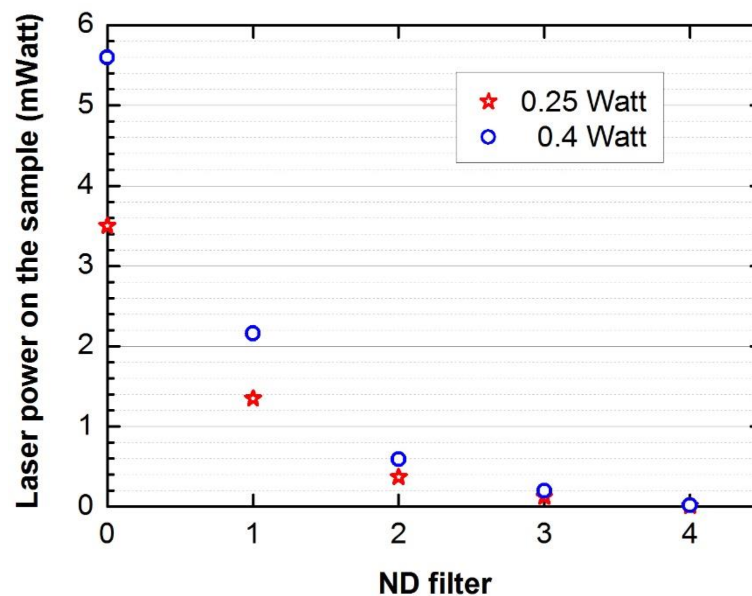

Figure 4.37. Calibration curves of laser powers measured on the sample surface vs ND filter.

4.8.3. Photoluminescence

PL technique allows to analyze optical transitions near the absorption edge such as free excitons and excitons bonded to impurity levels. In PL measurements the sample is irradiated by a monochromatic light

(typically a laser) with an energy above the band gap of the material under study ($h\nu_0$) in order to generate electron-hole pairs by means of the light absorption at the surface region (figure 4.38(a)). In this regard, the absorbed photons excite electrons from valence band (VB) to the conduction band (CB) forming electron-hole pairs (see mechanism (1) in figure 4.38(a)). The recombination of those charge carriers after their relaxation, and later diffusion can occur through radiative mechanisms which are dominant in direct band gap semiconductor materials. Assuming that photogenerated electrons are not at the center of the CB ($k = 0$) the recombination process can be understood in two steps:

i) firstly, photoelectrons become relaxed towards the center of the CB ($k = 0$), losing both energy and momentum (see mechanism (2) in figure 4.38(a));

ii) secondly, once the photoelectrons are at $k = 0$, they recombine radiatively to the VB emitting photons (see mechanism (3) in figure 4.38(a)).

The result is the emission of lower energy radiation; since this radiation escapes from the material, it can be analyzed, giving information of the material bands structure. In this regard, PL gives important information about properties of solids, and in particular, is especially useful for the study of epitaxial semiconductor films. PL allows to analyze material properties such as crystal quality, band gap energy, type of impurities (dopant or acceptors) and the transition energies involved in radiative recombinations.

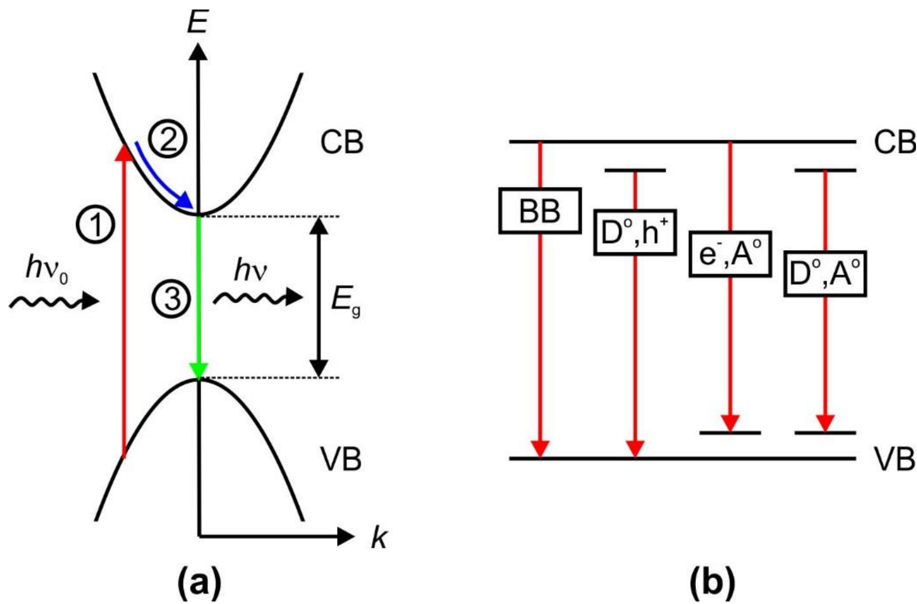

Figure 4.38. Schematic of (a) PL mechanism and (b) possible radiative recombinations.

Typical radiative recombination processes that can be observed in PL are shown in figure 4.38(b). Band-to-band transitions are represented as BB in the figure and correspond to radiative recombination of an electron in the CB with a hole in the VB. The energy of the emitted photon is equivalent to energy band gap of the material and therefore it is the most energetic radiative recombination.

Since an electron-hole pair is formed, both can be bonded by Coulomb forces as a hydrogen-like atom, which is known as exciton. Excitons can move freely by the crystal lattice or can be trapped by the

local field around some impurities. The energy emitted by an exciton recombination is equivalent to the energy band gap of the material minus the bonding energy of the exciton, which is only a few meV in most semiconductor materials.

One electron initially localized in a non-ionized donor level (D^o) can relax to an unoccupied VB state, emitting a photon with the energy difference; this transition is identified as (D^o,h^+). The photon energy for this transition can be calculated by subtracting the donor binding energy (some meV below the CB) to the energy band gap of the material.

Electrons can also recombine from the CB to a neutral acceptor level (e^-,A^o). This kind of recombination process can lead to the emission of a LO phonon (phonon replica) which can also be analyzed by Raman spectroscopy measurements.

Finally, the lowest energetic transitions are associated to electrons in a donor level recombined with the hole in a neighboring acceptor level (D^o,A^o). The energy of this transition can be calculated subtracting both donor and acceptor bonding energies to the energy band gap of the material; the Coulomb attraction must be added to the energetic balance, which is significant as the donor-acceptor pair distance is reduced. However, this kind of transition is only possible in materials which are highly compensated, including both kinds of impurities (donor and acceptors).

PL measurements were carried out using the same system previously described for Raman spectroscopy analysis (figure 4.36).

4.8.4. Spectrophotometry

Transmission and reflection spectrophotometry are used in this work to determine optical constants such as transmittance (T), reflectance (R), and absorbance (A) of semiconductor thin films deposited on transparent substrates such as glass or quartz. Figure 4.39 shows a schematic the UV/VIS/IR spectrophotometer used in this work configured in transmission mode. This system belongs to the Department of Physics of Materials (UAM). In transmission mode, polychromatic light from either UV or VIS lamps is directed to a diffraction grating. A near-monochromatic light beam is selected by using a slit and later split into two light beams by a beam splitter, which are transmitted through the sample and the reference such as described in the schematic shown in figure 4.39. The intensity of both transmitted beams is measured with a photodetector, resulting in I and I_0 for the sample and the reference beams, respectively.

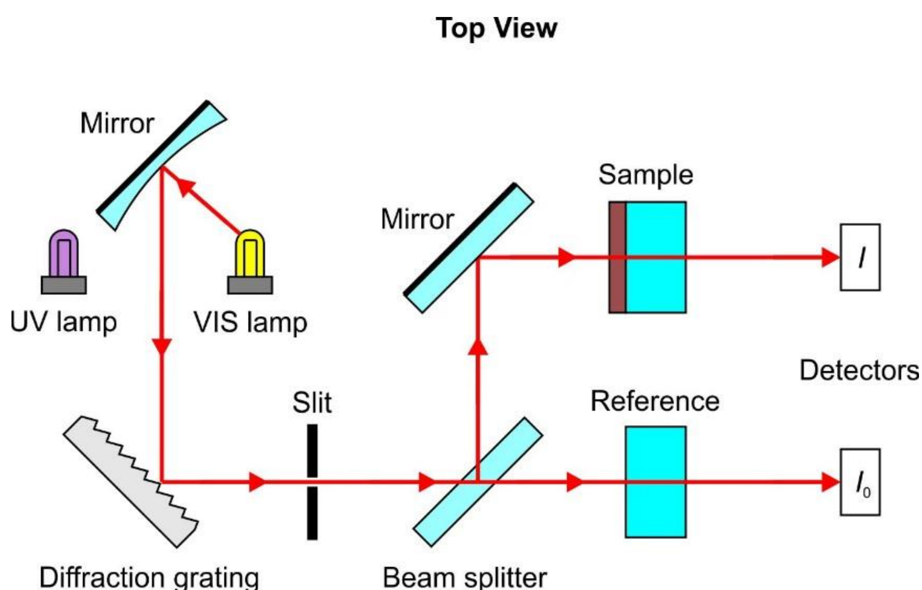

Figure 4.39. Schematic of the UV/VIS/IR spectrophotometer working in transmission mode.

Optical spectrophotometers work in different modes to measure optical density (*OD*), *A*, or *T*. These magnitudes are defined as a function of I and I_0 as follow [24]

$$OD = \log_{10}\left(\frac{I}{I_0}\right) \tag{4.74}$$

$$A = 1 - \frac{I}{I_0} \tag{4.75}$$

$$T = \frac{I}{I_0} \tag{4.76}$$

Nevertheless, it is important to emphasize here the advantage of measuring *OD* spectra over *A* or *T* spectra. *OD* spectra are more sensitive, as they provide a higher contrast than *A* or *T* spectra [24].

The light beam becomes attenuated after passing through a material. The beam intensity attenuation ($\mathrm{d}I$) after traversing a differential thickness ($\mathrm{d}x$) can be written as

$$\mathrm{d}I = \alpha\, I\, \mathrm{d}x \;, \tag{4.77}$$

where I is the light intensity at a distance x into the medium and α accounts for the amount of reduction due to the constitution of the material. In the case of negligible scattering, α is called the absorption coefficient of the material. Upon integration of equation (4.77), the I can be expressed as

$$I = I_0 \, e^{-\alpha \cdot x} \, , \tag{4.78}$$

which gives an exponential attenuation law relating the incoming light intensity I_0 to the thickness x. This law is known as the Lambert-Beer law. According to equations (4.74) and (4.78), the absorption coefficient is determined by

$$\alpha = \frac{2.303 OD}{x} \tag{4.79}$$

The spectrophotometer used in this work also allows to measure the R of a sample using the reflection mode shown in figure 4.40. Under this configuration, a monochromatic light beam is directed into an integrating sphere. Sample is positioned at the reflectance port of the sphere; the sample normal surface is slightly tilted away from the incident beam direction in order to prevent the direct beam reflection escaping through the same sphere entrance, preventing then the interference between incident and reflected beams. Once the incident beam is reflected onto the sample surface, multiple reflections occur along the inner sidewalls of the high reflective integrating sphere until all reflected beam intensity (I_R) is collected and integrated by the photodetector located at the center of the sphere.

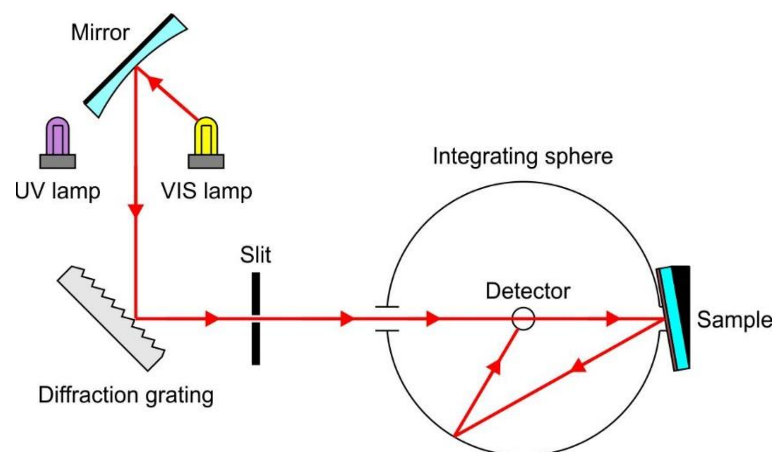

Figure 4.40. Schematic diagram of the UV/VIS/IR spectrophotometer working in reflection mode.

The same experiment is repeated substituting the sample by a standard high reflective reference, then obtaining the I_0. The OD is calculated from the ratio between both intensities

$$OD = \log\left(\frac{I_0}{I_R}\right) \, , \tag{4.80}$$

and the R is given by

$$R = 10^{-OD} = \frac{I_R}{I_0} \tag{4.81}$$

The relationship between $R(\lambda)$ and $\alpha(\lambda)$ can be obtained from the so-called Kramers-Krönig relations [25].

4.8.5. X-ray Photoelectron Spectroscopy

Basic Principles

XPS is a surface-sensitive and quantitative spectroscopic technique that measures the elemental composition (at the parts per thousand range), empirical formula, chemical state, and electronic state of the elements that exist within a material. XPS spectra are obtained by irradiating a material with a beam of X-rays while simultaneously measuring the kinetic energy (KE) and number of electrons that escape from the top thickness (< 10 nm) of the analyzed material (figure 4.41(a)).

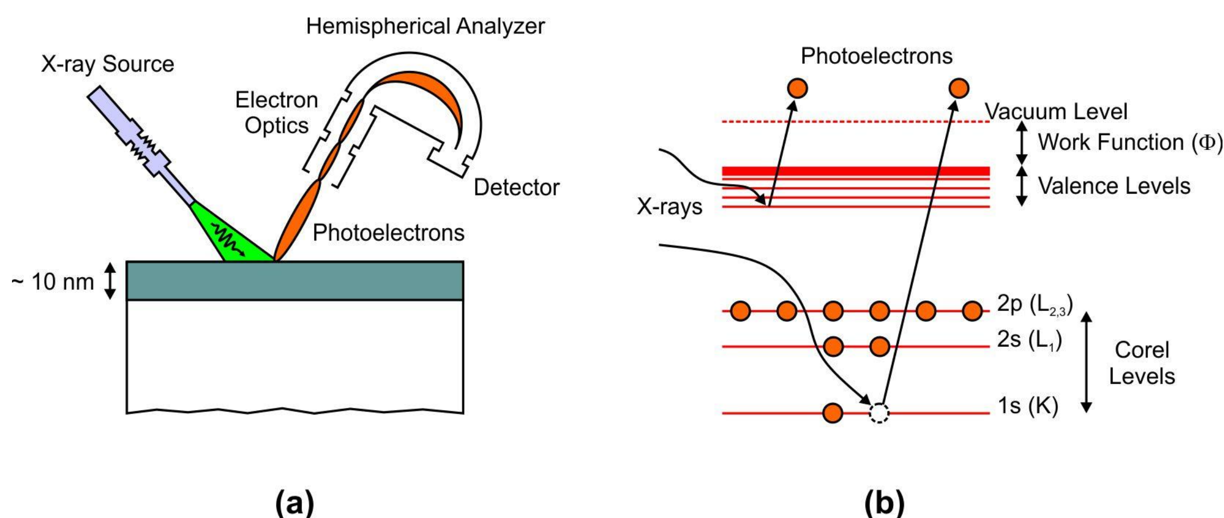

Figure 4.41. Schematic of (a) XPS system, and (b) XPS principles.

XPS basic principle consists in the photoemission of electrons from core levels (K, L_1, $L_{2,3}$, …) or valence levels by using a X-ray source (figure 4.41(b)). Because the energy of this X-ray with a particular wavelength is known (for Mg KE_α X-rays, E_{photon} = 1253.6 eV), and the KE of emitted electrons is measured, the electron binding energy (BE) of each of the emitted electrons can be determined by using an equation that is based on the work of Ernest Rutherford [26]:

$$\mathrm{BE} = E_{\mathrm{photon}} - (\mathrm{KE} + \Phi) \tag{4.82}$$

where Φ is the work function of the material. Above expression is essentially a conservation of energy equation.

A typical XPS spectrum is a plot of the number of detected electrons versus the BE of these electrons. Each element produces a characteristic set of XPS peaks at characteristic BE values that identify each element that exists in the analyzed material surface. These characteristic peaks correspond to the electron configuration of the electrons within the atoms, i.e. 1s, 2s, 2p, 3s, etc. The number of detected electrons in each of the characteristic peaks is directly related to the element concentration in the sample.

System Description

In this work XPS measurements are carried out in an ultrahigh vacuum system equipped with a SPECS XR-50 Mg-Anode X-ray source (KE_{α} = 1253.6 eV) and a SPECS Phoibos 100 hemispherical analyzer with an MCD-5 detector. Experimental data are acquired using a pass energy of 25 eV at a takeoff angle of 0º relative to the surface normal. The examined area is adjusted to about 7 mm^2 using a combination of a mechanical aperture, entrance and exit slits, and electron optics of the analyzer.

For analysis, the raw data are processed by subtraction of linear or Shirley backgrounds and fitted with a Gaussian-Lorentzian mixed function, also called quasi-Voigt function, using the software CasaXPS provided by SPECS GmbH (Berlin, Germany) [27]. For the analytical estimation of the relative element molar fraction, first the background accounting for the secondary electrons is removed using a Shirley function, then element peak is fitted using a Gaussian-Lorentzian mixed function. The integral of the peak is divided by a relative sensitivity factor (R.S.F.) which is characteristic of each element. The R.S.F. for N 1s, C 1s, Zn 2p3/2 and O 1s are 0.42 and 0.25, 4.8 and 0.66, respectively [27]. Finally, the resultant signal is normalized over all of the detected elements.

REFERENCES

[1] E. Rutherford, "LXXIX. The scattering of α and β particles by matter and the structure of the atom," *The London, Edinburgh, and Dublin Philosophical Magazine and Journal of Science,* vol. 21, pp. 669-688, 1911.

[2] H. Goldstein, *Mecánica clásica*: Reverté, 1996.

[3] "Rutherford Backscattering Spectroscopy," in *Atomic and Nuclear Analytical Methods*, ed: Springer Berlin Heidelberg, 2007, pp. 91-141.

[4] D. Furong, D. Shekui, and D. Weizhong, "Measurement of N in high Z substrate using non-rutherford backscattering," *Chinese Physics Letters,* vol. 9, p. 176, 1992.

[5] C. Ji, "Relativistic effects in electron capture of ion-atom collision at high energies," *Chinese Physics Letters,* vol. 10, p. 286, 1993.

[6] G. Terwagne, G. Genard, M. Yedji, and G. Ross, "Cross-section measurements of the 14 N (α, p) 17 O and 14 N (α, α) 14 N reactions between 3.5 and 6 MeV," *Journal of Applied Physics,* vol. 104, pp. 084909-084909-8, 2008.

[7] M. Mayer, "SIMNRA user's guide," 1997.

[8] "Ion Beam Analysis Nuclear Data Library, https://www-nds.iaea.org/exfor/ibandl.htm."

[9] L. Van der Pauw, "A method of measuring the resistivity and Hall coefficient on lamellae of arbitrary shape," *Philips technical review,* vol. 20, pp. 220-224, 1958.

[10] E. H. Hall, "On a new action of the magnet on electric currents," *American Journal of Mathematics,* vol. 2, pp. 287-292, 1879.

[11] N. W. Ashcroft and N. D. Mermin, "Solid State Physics (Saunders College, Philadelphia, 1976)," *Appendix N,* 2010.

[12] C. Kittel, "Introduction to Solid State Physics," *8th ed (John Wiley & Sons Inc),* 2005.

[13] I. C. f. D. Data, "http://www.icdd.com/index.htm."

[14] C. J. Davisson, "The diffraction of electrons by a crystal of nickel," *Bell System Technical Journal,* vol. 7, pp. 90-105, 1928.

[15] G. Held, "Low-energy electron diffraction," 1974.

[16] A. Ichimiya and P. I. Cohen, *Reflection high-energy electron diffraction*: Cambridge University Press, 2004.

[17] H. J. Fitting, H. Glaefeke, and W. Wild, "Electron penetration and energy transfer in solid targets," *Physica status solidi (a),* vol. 43, pp. 185-190, 1977.

[18] X. Wei, Y. Li, J. Zhu, Y. Zhang, Z. Liang, and W. Huang, "In situ analysis of lattice relaxation by reflection high-energy electron diffraction," *Journal of Physics D: Applied Physics,* vol. 38, p. 4222, 2005.

[19] J. Harris, B. A. Joyce, and P. Dobson, "Oscillations in the surface structure of Sn-doped GaAs during growth by MBE," *Surface Science,* vol. 103, pp. L90-L96, 1981.

[20] J. Van Hove, C. Lent, P. Pukite, and P. Cohen, "Damped oscillations in reflection high energy electron diffraction during GaAs MBE," *Journal of Vacuum Science & Technology B,* vol. 1, pp. 741-746, 1983.

[21] J. D. Weeks and G. H. Gilmer, "Dynamics of crystal growth," *Adv. Chem. Phys,* vol. 40, pp. 157-227, 1979.

[22] v. The NIST Mass Spectral Search Program for the NIST/EPA/NIH Mass Spectral Library, 2002.

[23] F. Nelson, V. Kamineni, T. Zhang, E. Comfort, J. Lee, and A. Diebold, "Optical properties of large-area polycrystalline chemical vapor deposited graphene by spectroscopic ellipsometry," *Applied Physics Letters,* vol. 97, p. 253110, 2010.

[24] J. Solé, L. Bausa, and D. Jaque, *An introduction to the optical spectroscopy of inorganic solids*: John Wiley & Sons, 2005.

[25] A. M. Fox and M. Fox, *Optical properties of solids* vol. 2010: Oxford university press New York, 2001.

[26] E. Rutherford, "LVII. The structure of the atom," *The London, Edinburgh, and Dublin Philosophical Magazine and Journal of Science,* vol. 27, pp. 488-498, 1914.

[27] N. Fairley, "CasaXPS: Spectrum Processing Software for XPS, AES and SIMS (Version 2. 3. 13)," *Casa Software Ltd., Cheshire,* 2006.

5. Zinc Nitride Thin Films

Zinc nitride is a n-type semiconductor material whose E_g and semiconductor behaviour (direct or indirect) are still unknown. One possible reason for that uncertainty is the metastable behaviour characteristic of this material, which induces the formation of an oxide layer on top of the nitride surface, hindering the study of its intrinsic properties. This work demonstrates the formation of this surface oxide layer by techniques such as IBA, SE, and spectrophotometry, analyzing the oxidation mechanisms, and determining the oxidation rate as a function of the zinc nitride properties [1]. Furthermore, it is also shown a cost-effective technique to accelerate this oxidation rate using localized arc-discharges [2].

Taking into account this oxidation mechanism, true optical constants of zinc nitride, including refractive index (*n*) and extinction coefficient (*k*) can be estimated by SE as confirmed by spectrophotometry [3].

Growth system and conditions have a strong impact on the resultant properties of zinc nitride. In this work, electrical, morphological, compositional, and structural properties have been thoroughly studied as a function of the growth conditions in a rf-magnetron sputtering [4]. This work demonstrates that O can be unintentionally incorporated into the Zn_3N_2 sublattice during the growth, affecting to its intrinsic properties [4].

In this work, zinc nitride has been used as channel layer for the development of TFTs, and photo-transistors [5]. Growth conditions of zinc nitride layers have been optimized in order to enhance the Hall mobility of TFTs. On the other hand, zinc nitride based photo-transistors showed sensitivity to the VIS light exposure.

5.1. Zinc Nitride Properties

5.1.1. Growth Conditions

In this work, zinc nitride layers are synthesized by means of rf-magnetron sputtering whose description can be seen in chapter 3 (section 3.1). These layers are grown using a Zn (99.995% purity) target and a mixture of N_2 (99.999% purity) and Ar (99.995% purity) as working gases, and at a constant pressure of 1 Pa in the growth chamber. In order to analyze the effects of growth conditions on resultant zinc nitride properties, layers are grown at different substrate temperatures ($298 < T_s < 523$ K), rf-powers (25 to 200 W), total gas flows (10 to 35 sccm) and N_2/Ar gas concentrations (10 to 100%). As these layers are characterized by different techniques, they are deposited on different substrates, including glass, quartz, Si(100), and SiO_2(300 nm)/Si(100).

Prior to each growth, substrates are cleaned in bubbling trichloroethylene for 5 min, later dipped in bubbling acetone for 5 min, rinsed in bubbling ethanol, and finally dried in N_2 flow. This standard procedure removes possible contamination of the substrate surface.

After the chemical cleaning, substrates are transferred to the sputtering system where they are sputtered for 1 min using an Ar flow of 100 sccm and a rf-plasma power of 50 W. Thereafter, growth parameters such as T_s, N_2 and Ar flows, residual pressure and rf-plasma power are established. Once the plasma is formed, the growth time of the zinc nitride layer and, therefore, the resultant layer thickness are controlled by a mechanical shutter.

The growth parameters (T_s, rf-power, …) have a strong influence on the layer growth rate (r_g). The r_g expressed in nm/min is estimated from the layer thickness (d is measured by profilometry) and the growth time through the expression: $r_g = d/t$. We now show r_g estimated during the growth of zinc nitride layers carried out at different growth conditions.

For zinc nitride layers grown for 30 min, using a rf-power of 200 W and a N_2 flow of 30 sccm, the r_g is fairly stable up to $T_s = 450$ ºC, showing values between 50 and 60 nm/min (figure 5.1(a)). Growths carried out at higher T_s show a strong decrease of r_g down to 20 nm/min, mainly due to the re-evaporation of both Zn and N species from the substrate surface.

On the other hand, r_g is also strongly affected by the rf-power, exhibiting an increase of r_g with rf-power from 4 nm/min at 25 W up to 50 nm/min at 150 W (figure 5.1(b)). The r_g tends to saturate for values larger than 150 W.

The growth of zinc nitride thin films at low powers (25 W) presents a constant r_g of 16 nm/min for growth times up to 30 min, exhibiting a slight reduction of r_g down to 12 nm/min for longer growths (50 min) (figure 5.1(c)). This constant r_g allows to carry out growth processes with high reproducibility in terms of layer thickness and surface morphology.

Finally, the r_g of the zinc nitride layers is observed to be also dependent on the gas composition (figure 5.1(d)). Using different concentrations of N_2/Ar in the working gas, it was observed a sharp enhancement of

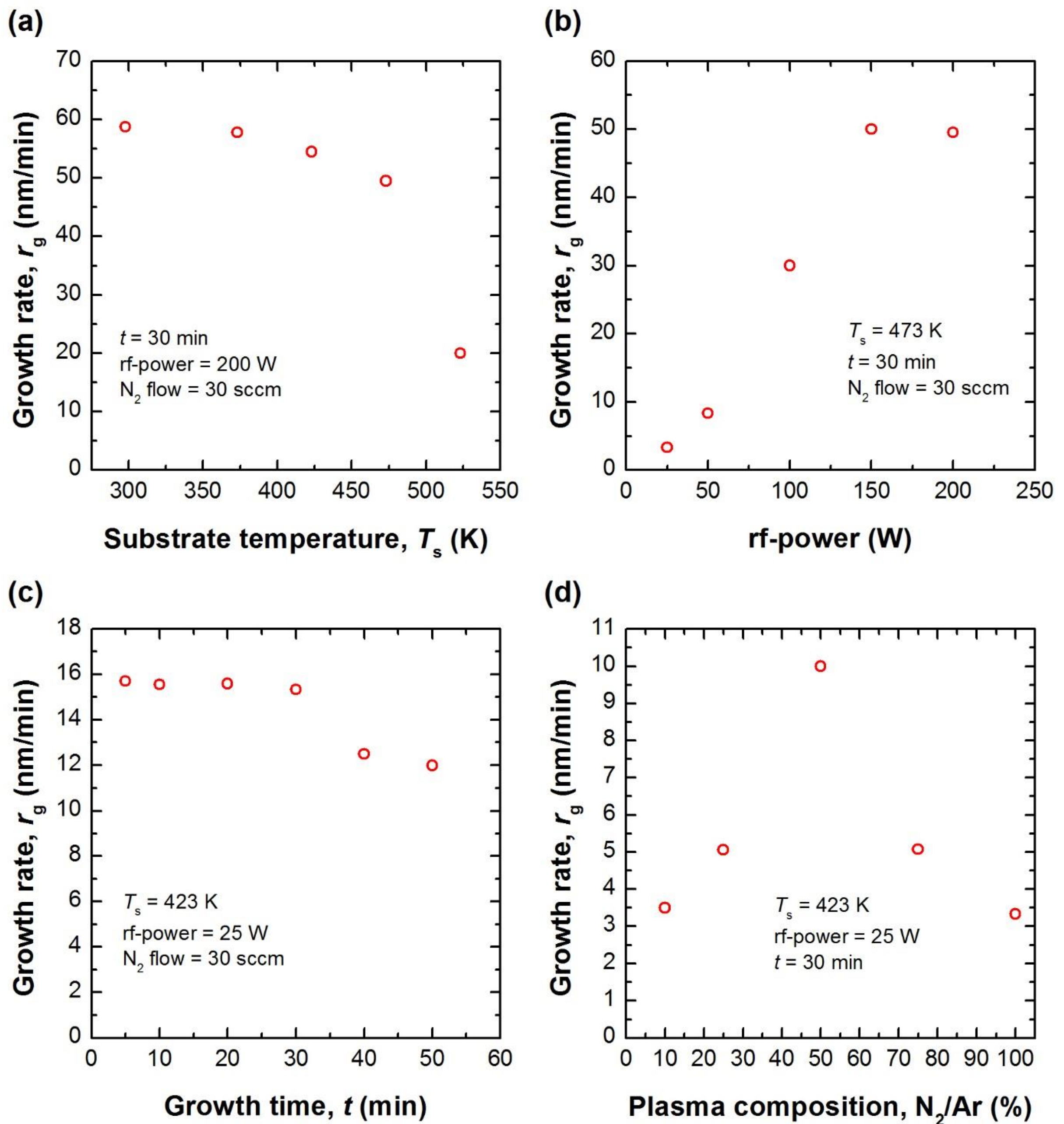

Figure 5.1. Zinc nitride r_g as a function of: (a) T_s, (b) rf-power, (c) growth time, and (d) plasma composition.

r_g around 50% mainly because the contribution of Ar to increase of the target sputtering rate. However, higher Ar concentrations in the working gas reduce the r_g because of the low concentration of N_2 in the plasma could hinder the reaction probability between Zn and N_2.

Once the growth conditions and r_g of zinc nitride layers have been described and determined, we now analyze the effects of these growth conditions on zinc nitride resultant properties by means of different techniques such as IBA, SEM, XRD, spectrophotometry and Hall effect measurements.

5.1.2. Compositional Study

The thickness and stoichiometry of zinc nitride (Zn_xN_y) layers can be obtained by using a combination of IBA techniques: RBS, non-RBS and NRA, through the use of the SIMNRA software (chapter 4, section 4.1.). This software allows to simulate the spectra from the experimental conditions (projectile nature and energy, system geometry, etc.), and the sample characteristics (layer stacking sequence and composition, etc.).

The backscattered signal from Zn atoms is described by the RBS collision $^{64}Zn(\alpha,\alpha)^{64}Zn$. The α-particles backscattered from Zn atoms can be easily identified at the high energy range of the spectra measured at both E_{ion} of 3.7 and 3.045 MeV as observed in figure 5.2(a) and (b), respectively. The good resolution not only in the peak intensity but also in energy is enhanced because of the collision between a light α-particle and a heavy element (Zn). On the other hand, at E_{ion} = 3.7 MeV the nuclear reaction $^{14}N(\alpha,p_0)^{17}O$ is also observed (figure 5.2(a)).

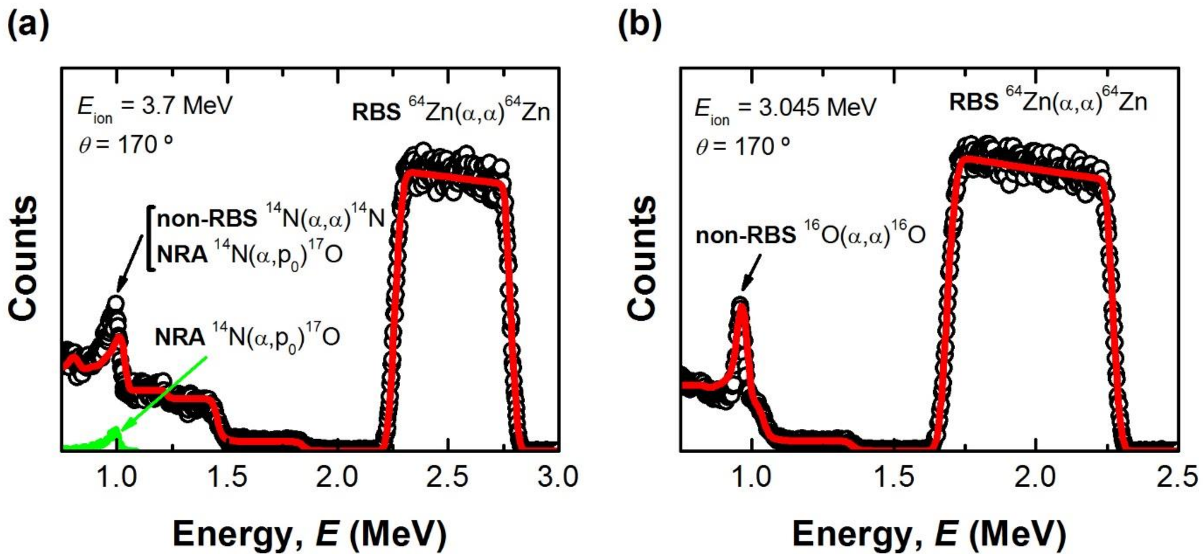

Figure 5.2. Experimental (open black dots) and simulated (red line) IBA data extracted from a Zn_xN_y/glass sample (where x=3 and y=2) at E_{ion} of (a) 3.7 MeV and (b) 3.045 MeV.

Firstly, $E_{channel}$ and E_{offset} are determined from the high energy edge of Zn RBS signal at any E_{ion}, resulting in 2.62 keV/channel and 114 keV, respectively. In addition, simulating the NRA signal of N, the dose (Q), i.e. the number of particles per sr, can be also estimated and depends on the detector angle. Once these parameters are determined, the molar fraction of the different elements and the total layer thickness can be directly obtained from the analysis of the RBS and non-RBS signals.

The IBA spectra shown in figure 5.2 correspond to a zinc nitride film grown during 30 min, using a rf-power of 100 W, a T_s of 473 K, and a N_2 flow of 30 sccm. The signal bandwidth accounts for the thickness of the zinc nitride film being in good agreement with the r_g of 30 nm/min estimated from profilometry measurements (figure 5.1(b)).

To accurately determine the intensity of ions backscattered from N atoms, we can use two different methods:

i) by subtracting proton contribution from the total signal at around 1 MeV; signals coming from both the nuclear reaction $^{14}N(\alpha,p_0)^{17}O$ and the non-RBS collision $^{14}N(\alpha,\alpha)^{14}N$ are overlapped at around 1 MeV (figure 5.2(a));
ii) by adding the $^{14}N(\alpha,p_0)^{17}O$ nuclear reaction cross-section to the simulation model in SIMNRA software.

Both methods are valid and show similar results in terms of zinc nitride composition. Therefore, after the contribution of the nuclear reaction is taken into account, the analysis can provide accurate results on both Zn and N molar fractions.

As mentioned, O is a highly reactive element which could be incorporated into the zinc nitride structure. Thus, IBA measurements are carried out at E_{ion} = 3.045 MeV (figure 5.2(b)), which corresponds to the ion energy for what incident ions are resonantly backscattered from O atoms ($^{16}O(\alpha,\alpha)^{16}O$); in those conditions, the cross-section associated to the collision between α-particles and O atoms is strongly increased (non-RBS), making easier the detection of the O incorporated into the zinc nitride sublattice, and therefore enabling the determination of the corresponding O molar fraction.

Influence of the Growth Rate

In a first study, we analyze the influence of r_g on the stoichiometry of zinc nitride layers. For that purpose, different r_g are established by changing the rf-power to vary the density of active species in the plasma. Thus, zinc nitride layers are grown on glass substrates under different rf-powers between 25 and 150 W, keeping a constant T_s and a N_2 gas flow of 473 K and 30 sccm, respectively.

Figure 5.3(a) and (b) show RBS and NRA signals obtained at E_{ion} = 3.045 and 3.7 MeV, respectively, and represented along with their corresponding best fitting. Analysing qualitatively figure 5.3(a), one can derive some interesting conclusions:

i) the increase of the Zn RBS peak bandwidth with the rf-power, which is attributed to the layer thickness increase;
ii) the increase of the O non-RBS peak intensity as the rf-power decreases, which is related to the enhancement of the O unintentional incorporation as the r_g is reduced, hindering the effective incorporation of N into the zinc nitride sublattice.

From the NRA signal of N shown in figure 5.3(b), the N molar fraction is observed to decrease with the rf-power which confirms that lowering r_g leads to a reduction of the N effective incorporation into the zinc nitride sublattice. This result might indicate that for low r_g, the O concentration in zinc nitride layers increases at expense of the N concentration decrease.

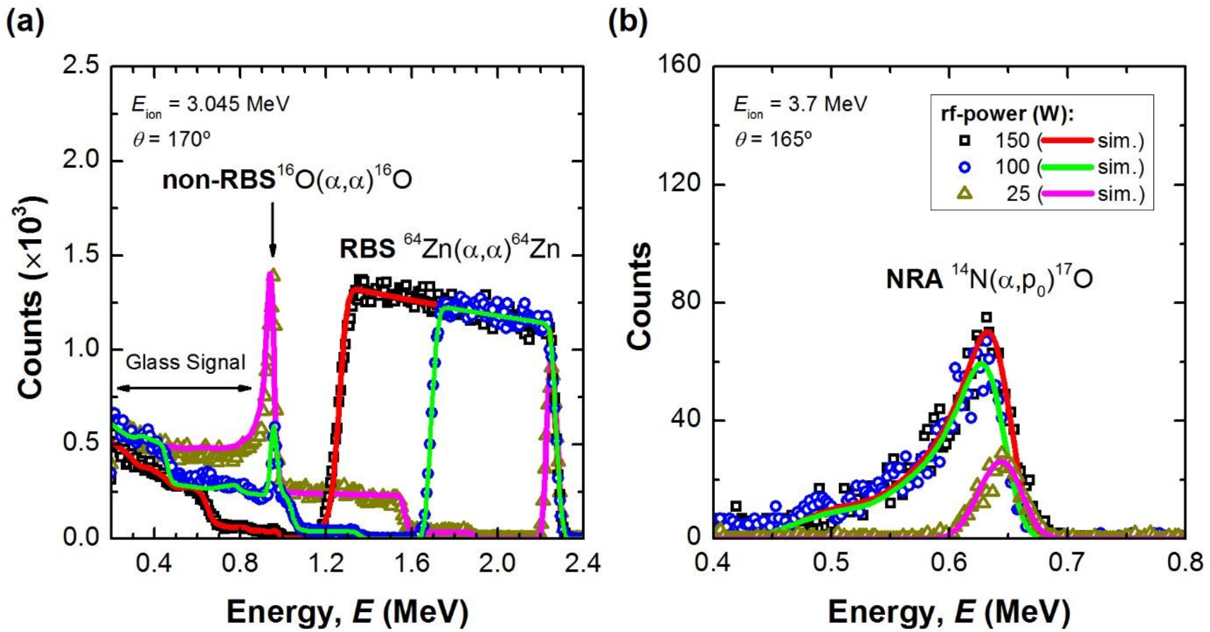

Figure 5.3. (a) Zn RBS and O non-RBS signals taken at 3.045 MeV, and (b) N NRA signal measured at 3.7 MeV in zinc nitride layers grown under different rf-powers.

Given the high ionicity of Zn-O bond compared to Zn-N bond, the effective incorporation of O species into the zinc nitride sublattice can occur during the layer growth in the sputtering system (*in-situ*) or after the growth (*ex-situ*). Potential contamination sources for both processes are:

i) (*in-situ*) outgassed O coming from sputtering system parts such as the inner walls of the growth chamber or the substrate holder. This outgassing process is strongly influenced by the plasma power and substrate holder temperature. Then, the O coming from previous depositions can be effectively gettered at the substrate surface during the growth of zinc nitride films. In addition, O might be provided by the N source. Although, prior to the deposition gas lines are completely purged and N source is composed of ultra-pure N element, we cannot discard possible O contamination coming from the plasma;

ii) (*ex-situ*) O_2 or H_2O molecules in ambient air. This oxidation of zinc nitride is difficult to be avoided because of the high concentration of those species in ambient air.

To take into account the O incorporation into the nitride layers after exposure to ambient air, the model used to fit the experimental data consists of a ZnO layer atop a $Zn_xN_yO_{y-1}$ in order to consider both *ex-situ* and *in-situ* O incorporation mechanisms. Resultant calculations of N and O molar fractions, assuming a constant Zn molar fraction of 60%, are extracted from the best fitting between simulation and experimental data (table 5.1).

Table 5.1. Zinc nitride layer composition as a function of the rf-power used during growth.

rf-power (W)	Thickness (μm)	r_g (nm/min)	Molar fraction (%)	
			N	O
150	1.5	50	39	1
100	0.9	30	36	4
50	0.3	8	30	10
25	0.1	3	24	16

From the previous table, we can conclude that the decrease of r_g, reducing the rf-power, leads to an increase of O contamination into the zinc nitride sublattice, showing maxima O molar fractions of 16% for minima r_g of around 3 nm/min (rf-power = 25 W). In addition, this increase of the O molar fraction is observed to occur at expense of the N molar fraction.

Therefore, the high O content observed in some of the nitride layers grown at lower r_g confirms the strong reactivity between Zn and O ions in the presence of N and alerts on the importance of measuring the O content in the Zn_3N_2 layers prior to their characterization.

Influence of the Substrate Temperature

Aside the rf-power, zinc nitride composition might be also affected by T_s; thus, the effects of two different T_s (298 and 473 K) on the chemical composition of the zinc nitride layers are analyzed (figure 5.4). Layers under study are grown on Si(100) substrates at a r_g = 55 nm/min (rf-power of 200 W and N_2 gas flow of 30 sccm) during 30 min, resulting in a total thickness of around 1.7 μm at both T_s. The layer thickness was measured by profilometry, confirming that the high r_g obtained at these specific growth conditions is almost independent on T_s (figure 5.1(a)). From the conclusions extracted in the rf-power study (table 5.1), nitride layers are expected to be stoichiometric because the use of a high r_g inhibits the incorporation of O into the Zn_3N_2 sublattice.

Figure 5.4(a) and (b) show IBA spectra measured at 3.045 MeV in zinc nitride layers grown at T_s of 473 and 298 K respectively. The experimental data obtained for the layer grown at T_s = 473 K are simulated using an ideal single layer model, consisting of a Zn_xN_y layer on top of a Si substrate. The best fitting is represented in figure 5.4(a), and it is achieved by introducing molar coefficients of x = 3 and y = 2 as expected for a stoichiometric zinc nitride film.

At a T_s = 298 K, a two layer model, consisting of a ZnO layer atop Zn_3N_2 layer, is required to simulate the experimental curve. In figure 5.4(b), stoichiometric deviations are also observed at the sample surface related to:

i) the reduction of the Zn signal intensity at high ion energies due to the lower molar fraction of Zn in the ZnO compound compared to that in Zn_3N_2, and
ii) the existence of a peak obtained from the resonant backscattered signal in O atoms at ~ 1 MeV.

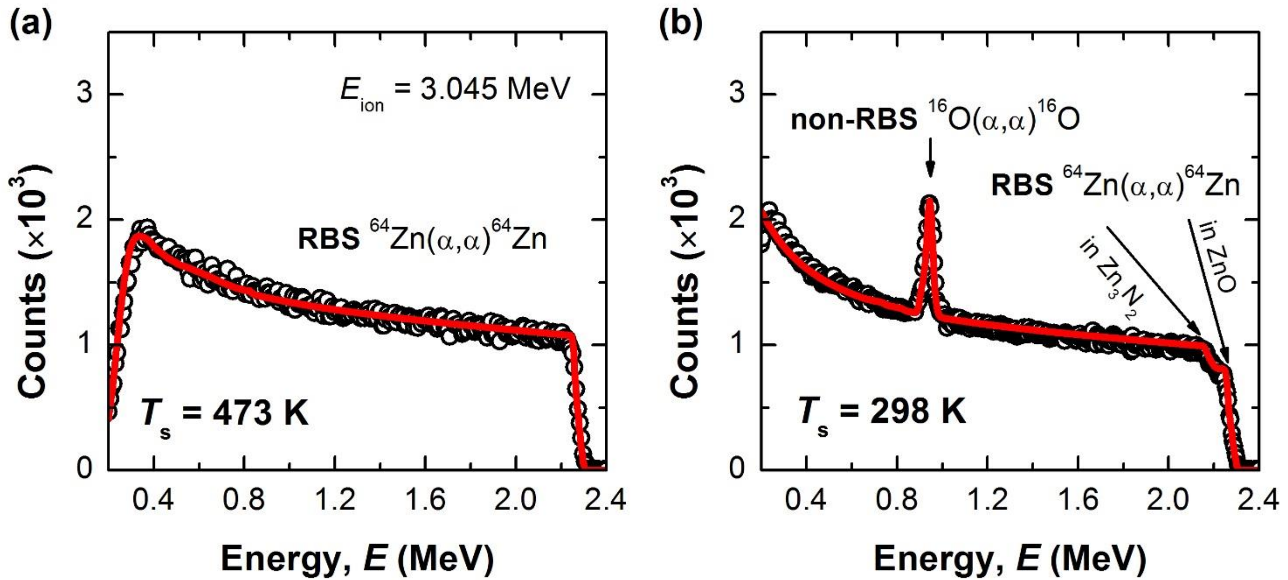

Figure 5.4. Experimental (open black dots) and simulated (red line) IBA data for Zn_xN_y/Si(100) sample (where x=3 and y=2) at (a) T_s=473K and (b) T_s=298K, and 3.045 MeV being the E_{ion}.

The origin of this ZnO layer is caused by the exposure of the zinc nitride sample to the ambient air for 1 week as will be discussed in depth in section 5.2. Therefore, the high r_g used during these two experiments did not show any difference between both T_s from the point of view of the O incorporation into the Zn_3N_2 bulk sublattice during growth [4]; however, the experiment evidences relevant differences in the surface layer composition.

5.1.3. Morphological Study

Surface morphology of zinc nitride layers grown at different T_s has been analyzed by SEM. Figure 5.5 shows a summary of five zinc nitride layers grown at different T_s between 298 and 523 K. These layers have been grown on glass substrates at a rf-power of 200 W, a N_2 flow of 30 sccm, and during 30 min. In addition, SEM images were taken at two different magnifications (×100k left column, and ×200k right column). From figure 5.5 one can observe that the resultant surface morphology of zinc nitride is strongly influenced by T_s, presenting an increase of the grain size, definition of the grain boundaries and polycrystalline characteristics with T_s. Furthermore, independently on the magnification, viewgraphs present surface porosity, showing nanometric pores which are covering the whole polycrystal surface. Since zinc nitride is stored in air ambient conditions, these nano-pores can act as nucleation centers for O species from which the degradation of zinc nitride is promoted and is further extended to the rest of bulk material (see section 5.2).

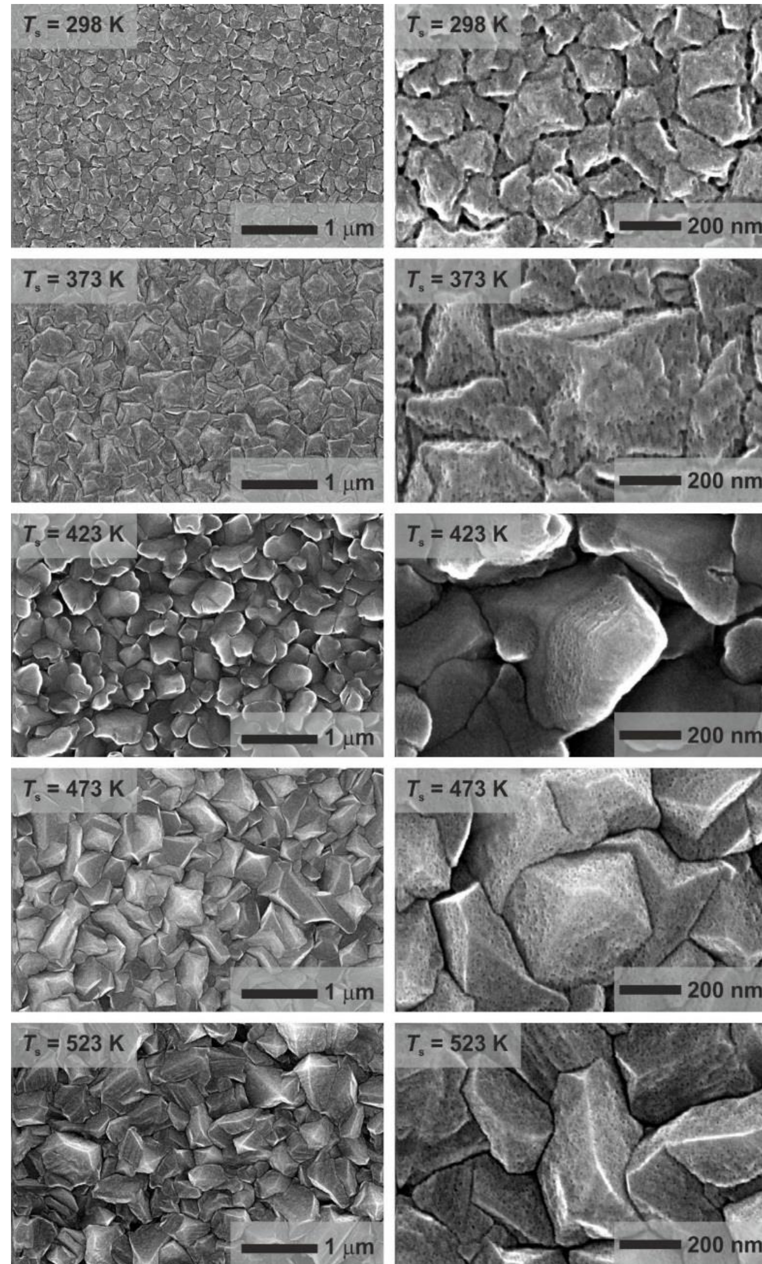

Figure 5.5. SEM images of zinc nitride layers grown at different T_s.

Influence of the Substrate Temperature

We now analyze in depth two of the layers shown in figure 5.5, which are grown at T_s = 298 K (figure 5.6(a)) and 473 K (figure 5.6(b)). Both layers show relevant differences in the surface morphology, indicating that the growth kinetics of zinc nitride is strongly influenced by T_s.

Zinc nitride layer grown at T_s = 298 K shows small grains with an average size of around 0.02 μm^2 (estimated from figure 5.6(a)) whereas the layer grown at T_s = 473 K presents larger grains with an average size of around 0.16 μm^2.

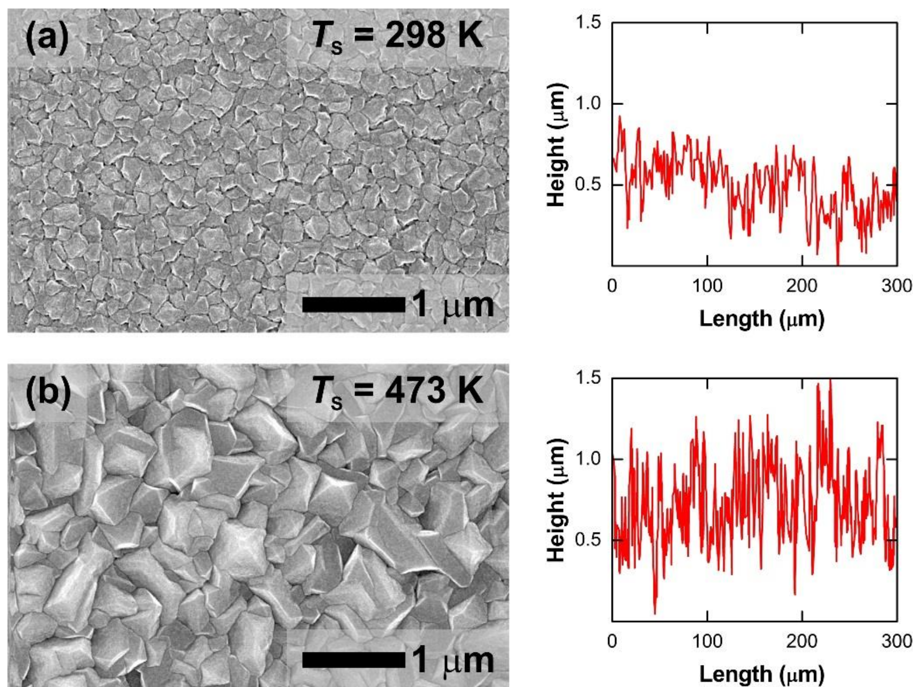

Figure 5.6. SEM images (and their corresponding linear scans obtained with a stylus profilometer) of Zn_3N_2 layers grown using a rf-power of 200 W, a N_2 flow of 30 sccm, and a T_s of (a) 298 K and (b) 473 K.

Surface roughness of both samples were measured by profilometry (see insets in figure 5.6), revealing an increase of surface roughness with the T_s used during the growth.

Influence of the Growth Rate

Surface morphology of resultant zinc nitride layers is also investigated as a function of r_g. Figure 5.7 shows a comparison between two zinc nitride layers grown at the same T_s = 423 K but at different r_g: 4.5 nm/min (figure 5.7(a)) and 43.3 nm/min (figure 5.7(b)). According to these images, the layer grown at slower r_g shows grain boundaries less defined than the layer grown at faster r_g.

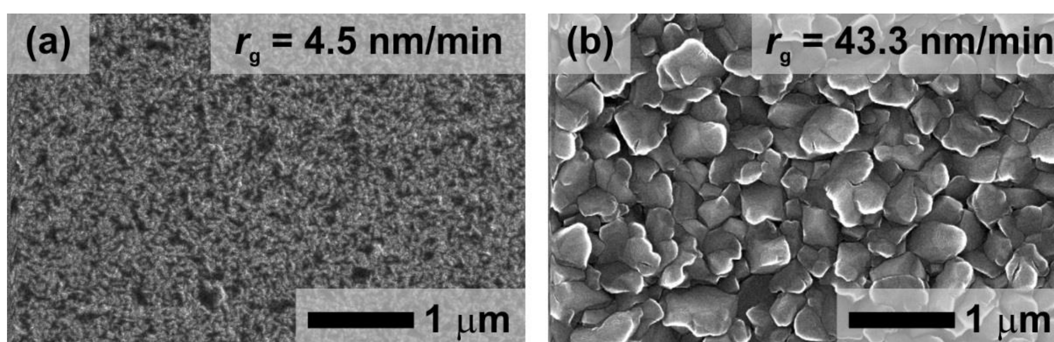

Figure 5.7. SEM images of Zn_3N_2 layers grown at different r_g of (a) 4.5 and (b) 43.3 nm/min.

The grain size and grain boundaries are one of the main mechanisms limiting the electrical conduction through a polycrystalline layer; in section 5.1.6, it will be discussed in depth the electrical properties showed by zinc nitride layers grown at different conditions.

5.1.4. Structural Study

Crystalline structure of zinc nitride has been reported by other groups. Sputtered zinc nitride films showed polycrystalline characteristics with a dominant <400> [6, 7], or <321> and <442> [8] diffraction peaks, depending on the growth conditions. Suda et al. [9] reported the growth of zinc nitride films by rf-MBE, resulting in films with a dominant diffraction peaks <400> or <440>, depending on T_s. On the other hand, zinc nitride films prepared by a molten salt electrochemical process showed many diffraction peaks typically observed in zinc nitride powder, which were considered to be mainly due to the phase mixture formed between zinc nitride and metal Zn [10]. From results reported in the literature, one can conclude that the crystalline structure of zinc nitride is strongly influenced by the growth technique and conditions, and therefore needs to be further investigated.

Since zinc nitride is stored in ambient air, this compound presents a metastable behaviour, hindering its characterization. For that reason, the crystalline structure of zinc nitride layers grown in this work, is analyzed by XRD right after its deposition, minimizing exposure time to the ambient air.

Figure 5.8 shows XRD diffractograms taken from as-grown zinc nitride layers deposited at different T_s. All peaks presented in these patterns are identified within the Zn_3N_2 cubic phase (see table 4.2); furthermore, there are not evidences of Zn and ZnO peaks within the detection limit of the system.

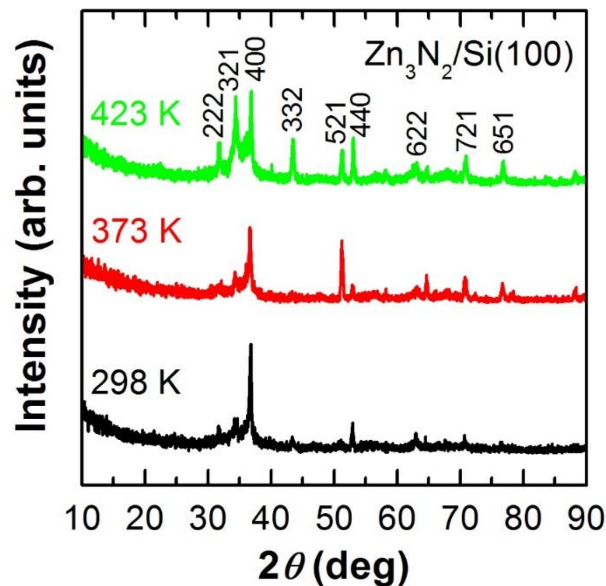

Figure 5.8. XRD patterns of samples grown at different T_s. Each peak was labeled using crystalline orientations extracted from the JCPD card Nr. 35-0762 for Zn_3N_2.

From patterns showed in figure 5.8, one can conclude that resultant layers are polycrystalline and their crystal grains are better aligned along the <400> direction ($2\theta = 36.7º$) for low T_s, and become disoriented as T_s increases. This result is in good agreement with the structural characterization of sputtered zinc nitride layers carried out by Futsuhara et al. [7].

The increase of the crystal disorientation in our zinc nitride layers with T_s confirms the morphology trend observed by SEM (figure 5.5) and is in good agreement with results reported by Xing et al. [11]. From those results, one can notice that T_s has a remarkable effect on the resultant crystalline structure of zinc nitride. We assume that at low T_s the kinetic energy of the Zn and N elements along the substrate surface can be insufficient to foster atomic diffusion. As the formation rate of Zn-N bonds is limited by the thermal dissociation, there is an optimum T_s for the growth of stoichiometric Zn_3N_2 films. Increasing T_s over that optimum temperature, makes the r_g collapse as shown before (figure 5.1(a)).

The lattice constant (a) of resultant layers presented in figure 5.8 is calculated from the diffraction angles for (400) or (440) planes and the Bragg's equation [12]. The position of those peaks varies with respect to the JCPD values as T_s increases. In particular, layers grown at lower temperatures (T_s = 298 K) show values close to those recorded in the JCPD database, while as T_s increases up to 473 K, the peak position shifts towards higher angles which can be interpreted as a reduction of a (figure 5.9). Then, calculated lattice constants are a = 0.978 and 0.973 nm for T_s = 298 and 473 K, respectively, which are in good agreement with the theoretical a of 0.9769 nm [13].

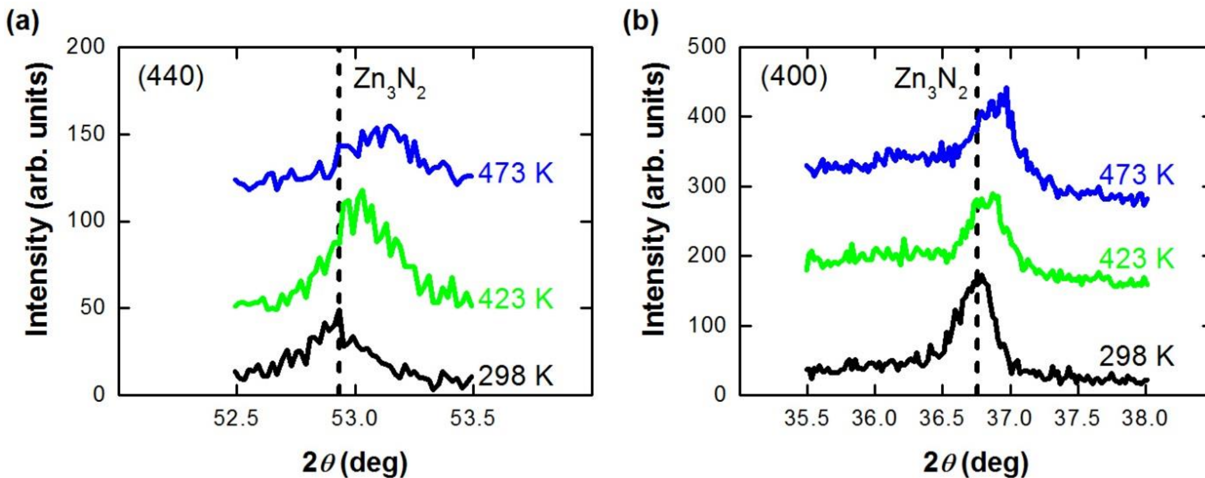

Figure 5.9. (440) and (400) reflection peaks as a function of T_s. Dashed line: position of the Zn_3N_2 peaks extracted from the JCPD card Nr. 35-0762.

The reduction of a with T_s is mainly attributed to the mismatch between the thermal expansion coefficient of the Si substrate and the nitride film, which produces a residual strain in the deposited layer during cooling down.

5.1.5. Optical Study

Although the optical properties of the zinc nitride have been studied in the past, its E_g and semiconductor type (direct or indirect) are still unknown and need to be further investigated. For zinc nitride layers grown by magnetron sputtering, Yang and Futsuhara reported E_g values of 1.01 [6] and 1.21-1.41 eV [7], respectively. In good agreement with them, Toyoura et al. reported a value of 1.01 eV for zinc nitride layers grown from a molten salt electrochemical process [10]. On the other hand, Suda et al. obtained E_g values

between 1.1 and 1.6 eV in zinc nitride layers grown by MOCVD and rf-MBE techniques [9], attributing the variation of the E_g to different O concentrations in the layers. In this regard, even wider E_g values have been observed in zinc nitride layers which are expected to be composed by a high concentration of O [14]. Therefore, crystalline structure and composition of Zn_3N_2 films might have a strong influence on their E_g value, being still necessary to carry out a further investigation to clarify these controversial results.

The synthesis of ternary compounds, consisting of zinc based semiconductors with an intermediate composition between Zn_3N_2 and ZnO, i.e. a zinc oxynitride ($Zn_xN_yO_z$), would allow to tune E_g from 1.01 eV (pure Zn_3N_2) towards 3.2 eV (pure ZnO) which can be a promising tool for the development of hybrids PDs capable to absorb light in a wide range of the electromagnetic spectrum (from NIR to UV). In this regard, Futsuhara et al. [7] showed the possibility to tune E_g of ZnO from 3.2 eV to 2.3 eV by introducing up to 10% of N into the ZnO sublattice and without altering the initial crystalline structure of ZnO. That decrease of E_g can be associated to a different ionicity of Zn-N and Zn-O bonds.

In this work, it has been demonstrated by IBA techniques (table 5.1), the opposite way to obtain intermediate compounds (zinc oxynitride) from pure Zn_3N_2, through the unintentional incorporation of O into the zinc nitride sublattice during the growth process [4] or rapidly transforming zinc nitride by using electric arc-discharges as will be shown in section 5.2.5 [2].

Figure 5.10 compares the absorption coefficient (α) of two zinc nitride layers grown in this work at T_s = 423 and 473 K. The graph also includes the absorption curves of other semiconductor materials with high absorption in the UV (Si and ZnO), and IR ($GaAs_{1-x}N_x$ and Zn_3N_2) spectral range, and which are typically used

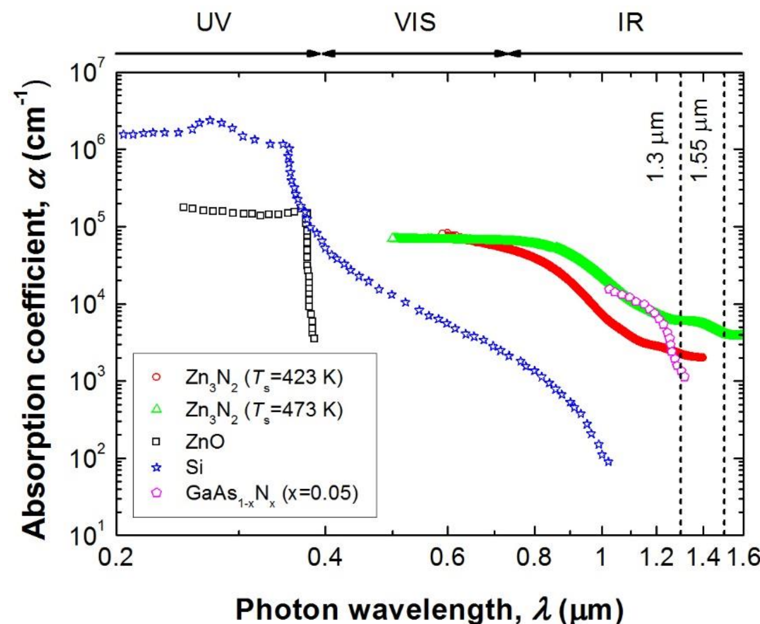

Figure 5.10. α of different semiconductor materials as a function of λ. Red circles and green triangles show two examples of Zn_3N_2 layers grown in this work at different T_s, showing a variation of the absorption edge.

as PDs. From this figure one can observe an absorption edge shift, comparing both zinc nitride layers, allowing to tune the E_g in the NIR range.

Due to the strong variations of E_g found in the literature during the characterization of zinc nitride layers, depending on the utilized growth technique and growth conditions, a deeper study of zinc nitride optical properties is still a matter of interest. In order to clarify this point, this section pursues to study the optical properties of sputtered zinc nitride layers grown at high r_g, minimizing the unintentional incorporation of O into the zinc nitride sublattice. In this regard, optical properties of stoichiometric Zn_3N_2 layers are analyzed by means of spectrophotometry (transmission and reflection modes), and SE.

Band Gap Energy and Type

The E_g of zinc nitride layers has been determined by transmission spectrophotometry. Samples under study consist of zinc nitride layers grown on glass substrates at a rf-power of 200 W, a N_2 gas flow of 30 sccm, and different T_s between 298 and 473 K. Depositions are carried out for 30 min at different r_g between 50 (T_s = 473 K) and 60 nm/min (T_s = 298 K), resulting in stoichiometric Zn_3N_2 layers (table 5.1) with a thickness between 1.5 and 1.8 μm, respectively (figure 5.1(a)).

As thoroughly described in chapter 4 (section 4.7.4), NIR/VIS/UV spectrophotometer used in this work allows to measure the *OD* of zinc nitride films as a function of the photon energy ($h\nu$) in both transmission and reflection modes. In transmission mode, the incident light is transmitted through the sample (zinc nitride layer and glassy substrate), losing intensity. Combining equations (4.74) and (4.76), one can deduce the relationship between *OD* and *T* as a function of $h\nu$, resulting in

$$T(h\nu) = 10^{-OD(h\nu)} \tag{5.1}$$

In addition, once the layer thickness is estimated by another technique, for example profilometry, the α can be calculated using equation (4.79).

Resultant T and α are represented in figure 5.11(a) and (b), respectively, showing absorption and transmission edges shift towards lower energies as T_s increases. Analysing in detail figure 5.11(b), one can find that values of α measured just above the absorption edge are near 10^4 cm^{-1}, which are typical values obtained in direct band gap semiconductors.

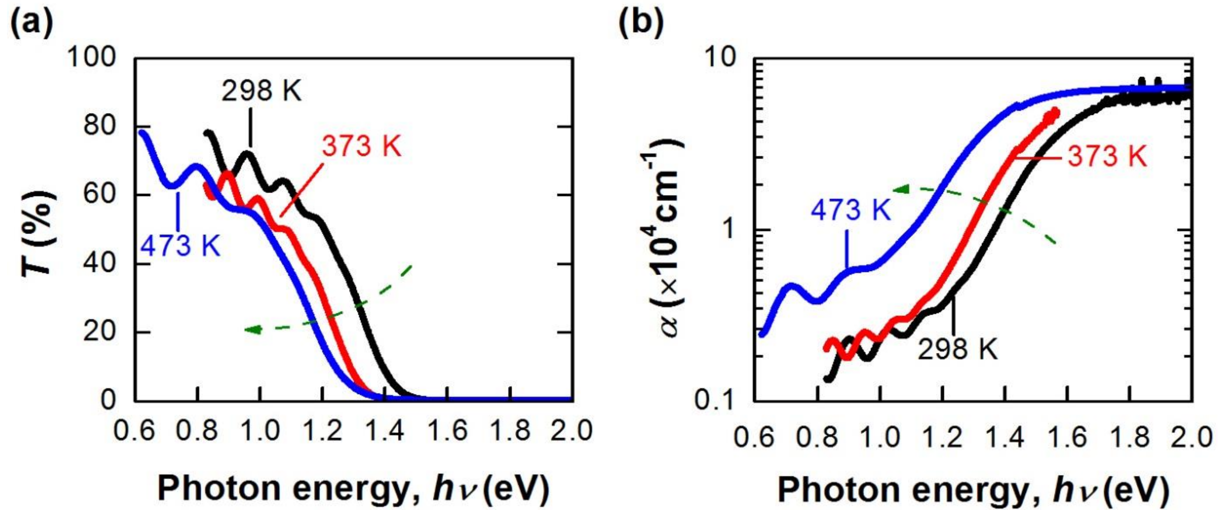

Figure 5.11. (a) T and (b) α of zinc nitride layers grown at different T_s represented as a function of $h\nu$.

For samples grown at different T_s, we determined the E_g value using Tauc's [15] and Davis-Mott's [8] models for direct and indirect polycrystalline semiconductors, respectively. Using Tauc's model, E_g shows a shift from 1.46 to 1.25 eV as T_s increases from 298 to 473 K (figure 5.12). On the other hand, E_g values calculated from Davis-Mott's model also present that trend (inset of figure 5.12); however, Tauc's model shows a better fitting to the experimental data than Davis-Mott's model.

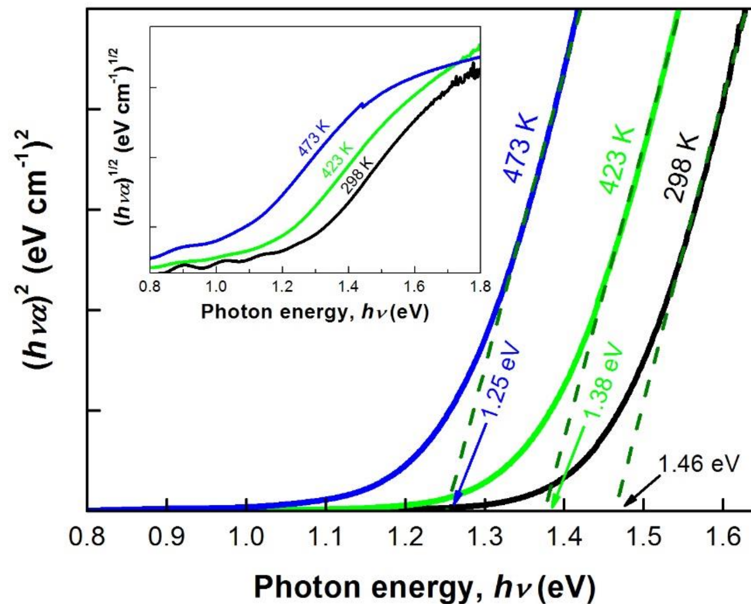

Figure 5.12. Optical band gap values calculated using Tauc's model (direct band gap) in three samples grown at different T_s. Inset: results obtained from Davis-Mott's model (indirect band gap).

Zinc nitride layers grown in this work at low temperatures (T_s = 298 K) whose crystal grains are highly oriented along the <400> direction, show an E_g = 1.46 eV. On the other hand, at high growth temperatures (T_s = 473 K), resultant zinc nitride layers consist of randomly oriented polycrystals and show E_g = 1.25 eV. Both

results match to the E_g values observed in highly oriented (E_g = 1.41 eV) and randomly oriented (E_g = 1.21 eV) zinc nitride polycrystalline layers obtained by different methods [7].

As a conclusion of these results, zinc nitride layers grown in this work at different T_s are expected to be direct band gap type, showing E_g values in the range of 1.25-1.46 eV, depending on the T_s [4]. Structural changes observed by SEM and XRD techniques in previous sections (5.1.3 and 5.1.4) are assumed to be the main responsible for the variation of the zinc nitride optical absorption edge.

Determination of *n* and *k*

Optical constants such as *n* and *k* of zinc nitride layers have been determined in the past [9, 16]. Suda et al. characterized zinc nitride layers grown by rf-MBE, obtaining *n* values around 2.3 at $\lambda = 700$ nm. Ayouchi et al. grown zinc nitride layers by rf-PLD whose *n* values were estimated to be ranged between 1.7 and 2.4. However, these nitride layers have an unintentional contamination of O that hinders the determination of true optical constants belonging to zinc nitride. Therefore, the impact of surface effects such as surface roughness or the formation of native oxide, as well as composition of zinc nitride layers, on the calculated optical constants of zinc nitride is still not clear.

In this section, *n* and *k* values belonging to stoichiometric Zn_3N_2 layers grown at different T_s between 298 and 523 K are analyzed in depth by means of SE and spectrophotometry (reflectance mode). Four samples are grown for 30 min, using a rf-power of 200 W, and a N_2 gas flow of 30 sccm, on Si(100) substrates. Resultant layer thickness is ranged between 1.8 and 0.6 μm, depending on T_s (figure 5.1(a)).

Values of *n* and *k* are obtained as a function of $h\nu$ in the range of 1.5-4.5 eV (chapter 4, section 4.7.1) for Zn_3N_2 layers grown at four different T_s. Experimental measurements of the ellipsometric parameters Ψ and Δ show a strong dependence with T_s. In particular, zinc nitride layers grown at higher T_s (423-523 K) exhibit higher Ψ (figure 5.13(a)), and lower Δ values (figure 5.13(b)), than those layers grown at lower T_s (298-373 K).

From figure 5.13(c) and (d), one can conclude that *n* and *k* parameters also exhibit relevant differences between *n* and *k* values measured in samples grown at high and low T_s. Furthermore, nitride layers grown at low T_s present a significant variation of the *k* curve. These differences observed between layers might be attributed to the surface roughness increase with T_s as analyzed by SEM (section 5.1.3).

To further investigate this point, a three-phase model, comprising three Zn_3N_2 phases with different thicknesses and densities of voids is used to fit experimental data corresponding to those samples grown at higher T_s in order to simulate the surface roughness effect on the ellipsometric parameters. The bottom phase is considered homogeneous, compact and semi-infinite and its Ψ and Δ values correspond to those measured in a sample with a smooth surface such as the nitride layer grown at T_s = 373 K. The other two phases atop that used the same Ψ and Δ values but different void density, which is introduced using the Bruggeman's EMA [17].

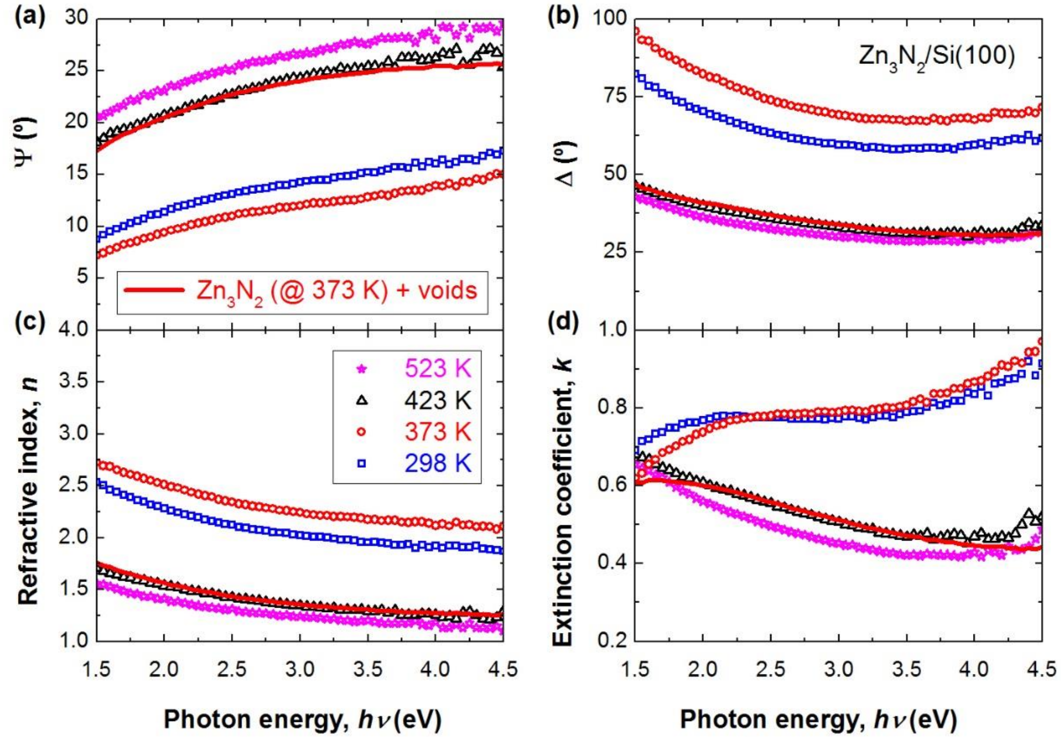

Figure 5.13. (a) Ψ, (b) Δ, (c) *n* and (d) *k* values of layers grown at different T_s vs. $h\nu$. Lines represent best fitting curves using the three-phase model.

Figure 5.13 shows that the best fitting (minimum chi square error, $\chi^2 = 0.03$) obtained for the Ψ and Δ values in the sample grown at $T_s = 423$ K is achieved using the following Zn_3N_2 phases from top to bottom:

i) a 48-nm thick layer with 50% void density,
ii) a 220-nm thick layer with 30% void density, and
iii) a 2.3-µm thick layer with 0% void density.

The effect of voids distributed in two top phases produces an increase of Ψ and a decrease of Δ values. The good agreement between the simulation works and the experimental data confirms that surface roughness may explain the deviation of the ellipsometric angles at high T_s.

One of the main conclusions extracted from resultant simulations of ellipsometric parameters is that nitride layers grown at lower T_s (298 and 373 K) present smoother surfaces. This result is in good agreement with previous observations obtained in the morphological study presented in figure 5.6. Therefore, the determination of true optical constants belonging to zinc nitride should be carried out in layers grown at lower T_s in order to avoid the contribution of surface roughness.

Aside the surface roughness, the metastable behaviour and the composition of zinc nitride can also hinder the characterization of properties such as its true optical constants. Therefore, the prompt characterization of stoichiometric Zn_3N_2 layers is required in order to prevent the generation of ZnO atop the nitride surface which also hinders the interpretation of results extracted from SE and spectrophotometry measurements.

As deduced from IBA results, zinc nitride layers grown at $r_g > 50$ nm/min are stoichiometric Zn_3N_2 (table 5.1). In addition, as will be confirmed in section 5.2 zinc nitride layers grown at low temperature (T_s = 298-373 K) present higher stability to the oxidation mechanisms. Therefore, ellipsometric angles (Ψ and Δ) of a zinc nitride layer grown at high $r_g > 50$ nm/min and at T_s = 373 K are used to calculate true values of n and k; results show n values between 2.8 and 2.0 and k values between 0.6 and 1.0, for $h\nu$ between 1.5 and 4.5 eV [3]. Those values of n and k might be considered the most realistic values among all the analyzed samples mainly because of:

i) ellipsometric measurements are carried out right after the deposition of the zinc nitride layer, preventing the formation of a ZnO surface layer;
ii) the nitride layer is deposited at low T_s which means that the resultant layer surface is smoother and its surface oxidation rate is slower (see section 5.2);
iii) the nitride layer is deposited using a high r_g of 60 nm/min, hindering the unintentional incorporation of O during the growth (table 5.1).

Results obtained from SE characterization can be used to calculate the optical reflectance (R) for a zinc nitride layers, aiming to compare to the R measured by means of spectrophotometry.

As described in the schematic of figure 5.14, we assume a simple structure, consisting of a zinc nitride layer (n_1 and k_1) with a thickness of d, on top of a glass substrate (n_2 = 1.5 and k_2 ~ 0), and in air ambient conditions (n_0 = 1 and k_0 ~ 0).

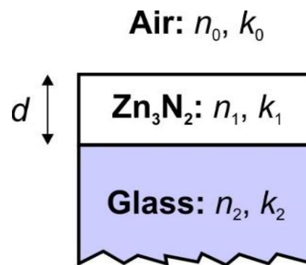

Figure 5.14. Schematic of the layer stacking sequence analyzed by spectrophotometry.

Assuming the conditions described in figure 5.14, and following Heavens' formulae [18], R can be estimated from the n and k values determined by SE. Heavens equations are shown below:

$$R = \frac{\left(g_1^2 + h_1^2\right)\exp(2\alpha_1) + \left(g_2^2 + h_2^2\right)\exp(-2\alpha_1) + A\cos 2\gamma_1 + B\sin 2\gamma_1}{\exp(2\alpha_1) + \left(g_1^2 + h_1^2\right)\left(g_2^2 + h_2^2\right)\exp(-2\alpha_1) + C\cos 2\gamma_1 + D\sin 2\gamma_1} \tag{5.2}$$

where

$$g_1 = \frac{n_0^2 - n_1^2 - k_1^2}{(n_0 + n_1)^2 + k_1^2}, \qquad h_1 = \frac{2n_0 k_1}{(n_0 + n_1)^2 + k_1^2},$$

$$g_2 = \frac{n_1^2 - n_2^2 + k_1^2 - k_2^2}{(n_1 + n_2)^2 + (k_1^2 + k_2^2)^2}, \qquad h_2 = \frac{2(n_1 k_2 - n_2 k_1)}{(n_1 + n_2)^2 + (k_1^2 + k_2^2)^2} \tag{5.3}$$

$$A = 2(g_1 g_2 + h_1 h_2), \quad B = 2(g_1 h_2 - g_2 h_1), \quad C = 2(g_1 g_2 - h_1 h_2), \quad D = 2(g_1 h_2 + g_2 h_1) \tag{5.4}$$

$$\alpha_1 = \frac{2\pi\, k_1 d}{\lambda} \quad \text{and} \quad \gamma_1 = \frac{2\pi\, n_1 d}{\lambda} \tag{5.5}$$

R is calculated using equation (5.2), and n and k values extracted from SE measurements carried out in two zinc nitride layers grown at T_s = 373 and 423 K, whose thicknesses are 190 and 2200 nm, respectively. Resultant calculations are represented in figure 5.15 with red (T_s = 373 K) and blue (T_s = 423 K) lines.

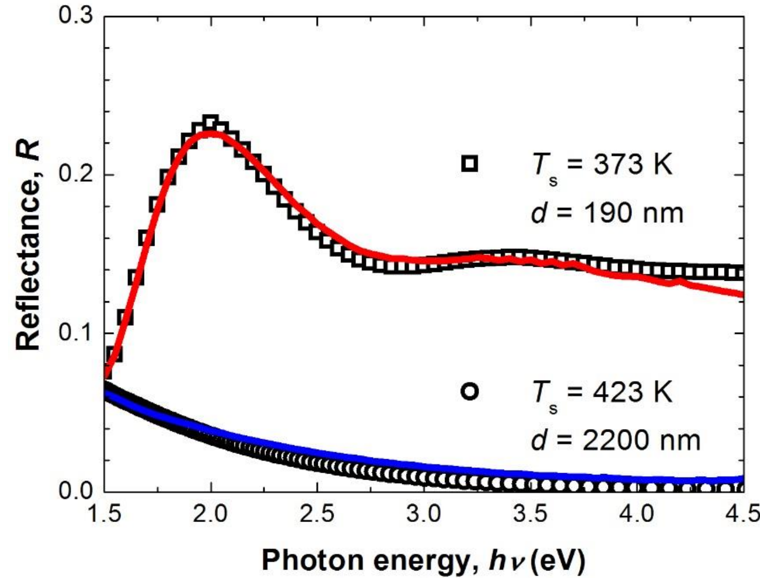

Figure 5.15. R measured in two Zn_3N_2 films grown at T_s = 373 K (squares) and 423 K (circles); R calculated from n and k values obtained by SE (red and blue lines).

The same samples are characterized by means of spectrophotometry, in reflection mode, aiming to obtain their R as a function of $h\nu$. The experimental results are also included in figure 5.15, representing with squares and circles R values measured in layers grown at T_s = 373 and 423 K, respectively.

From figure 5.15, one can observe the good agreement between *R* values calculated from *n* and *k*, and those directly measured by spectrophotometry, confirming the true optical constants (*n* and *k*) of zinc nitride obtained by SE.

5.1.6. Electrical Study

Resistivity and Hall Effect measurements are carried out at RT by means of Van der Pauw's method [19]. The electrical magnitudes of resistivity (ρ), carrier density (n_{Hall}) and mobility (μ) are obtained following the method described in chapter 4 (section 4.3.1). The analysis and optimization of zinc nitride electrical properties will be crucial for the development of high quality electronic devices based on zinc nitride as the active layer.

Influence of the Substrate Temperature

Electrical properties of zinc nitride layers are studied as function of T_s, using a rf-power of 200 W (figure 5.16). Analysing figure 5.16, one can deduce that μ presents a maximum (34 $cm^2/V{\cdot}s$), whereas ρ shows a minimum around $1{\times}10^{-3}$ $\Omega{\cdot}cm$ at $T_s = 423$ K; the latter being one of the lowest ρ values ever reported in the literature for this material [4].

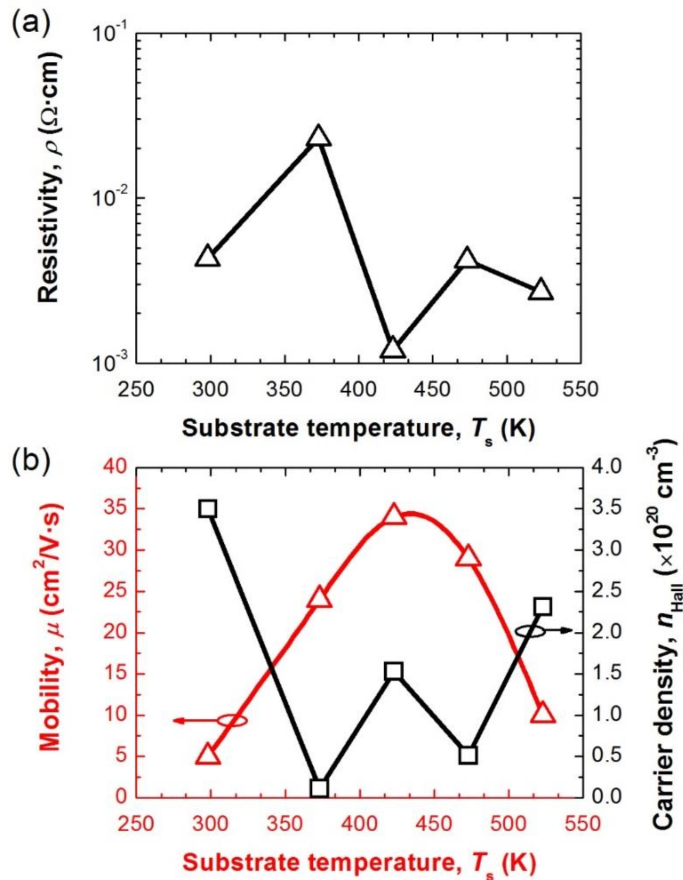

Figure 5.16. (a) ρ, and (b) μ and n_{Hall} of Zn_3N_2 films grown at different T_s.

These variations of the electrical parameters with T_s are related to those changes observed in the analysis of the surface morphology and crystalline structure. SEM images presented in figure 5.6 show polycrystalline morphologies with grain domains whose size has been demonstrated to be strongly influenced by the T_s used during the growth. Indeed, the reduction of T_s can provoke the decrease of the grain size.

In terms of electrical conductivity, Hall mobility could be limited by the grain-to-grain transport. This behaviour has been observed in zinc nitride layers grown by rf-MBE and MOCVD, presenting slight higher μ values due to the larger grain sizes (3-3.5 μm) obtained by those techniques [9].

Therefore, since T_s is lower than 423 K the reduction of μ depicted in figure 5.16(b) could be associated to the grain size reduction (figure 5.6); whereas for T_s higher than 423 K, the μ is hindered by the effect of grain-to-grain disorientation observed by XRD (figure 5.8).

Influence of the Growth Rate

In the second study, we examine the influence of r_g on the electrical properties of zinc nitride. Zinc nitride layers are grown at different r_g by controlling the rf-power which is ranged between 50 and 200 W. All the samples are grown at the optimized temperature (in terms of mobility) of T_s = 423 K obtained in the previous study (figure 5.16).

In figure 5.17, electrical magnitudes of ρ, n_{Hall} (a), and μ (b) are represented as function of the rf-power. The main results obtained from figure 5.17 are recorded in table 5.2. In that table, one can notice that ρ increases from 4×10^{-3} to 50×10^{-3} Ω·cm and n_{Hall} decreases from 52×10^{18} to 3×10^{18} cm^{-3} as the used rf-power decreases from 200 to 50 W (figure 5.17(a)). On the other hand, μ shows an increase up to 42 cm^2/V·s as the rf-power is reduced down to 50 W (figure 5.17(b)). A further reduction of the r_g using even lower rf-powers of 25 W (not shown in figure 5.17), shows μ values even higher (62 cm^2/V·s).

Table 5.2. Electrical properties of Zn_3N_2 layers grown using different rf-powers.

rf-power (W)	**Resistivity, ρ ($\times10^{-3}$ Ω·cm)**	**Carrier density, n ($\times10^{18}$ cm^{-3})**	**Mobility, μ (cm^2/V·s)**
50	50	3	42
100	10	17	36
150	5	39	32
200	4	52	30

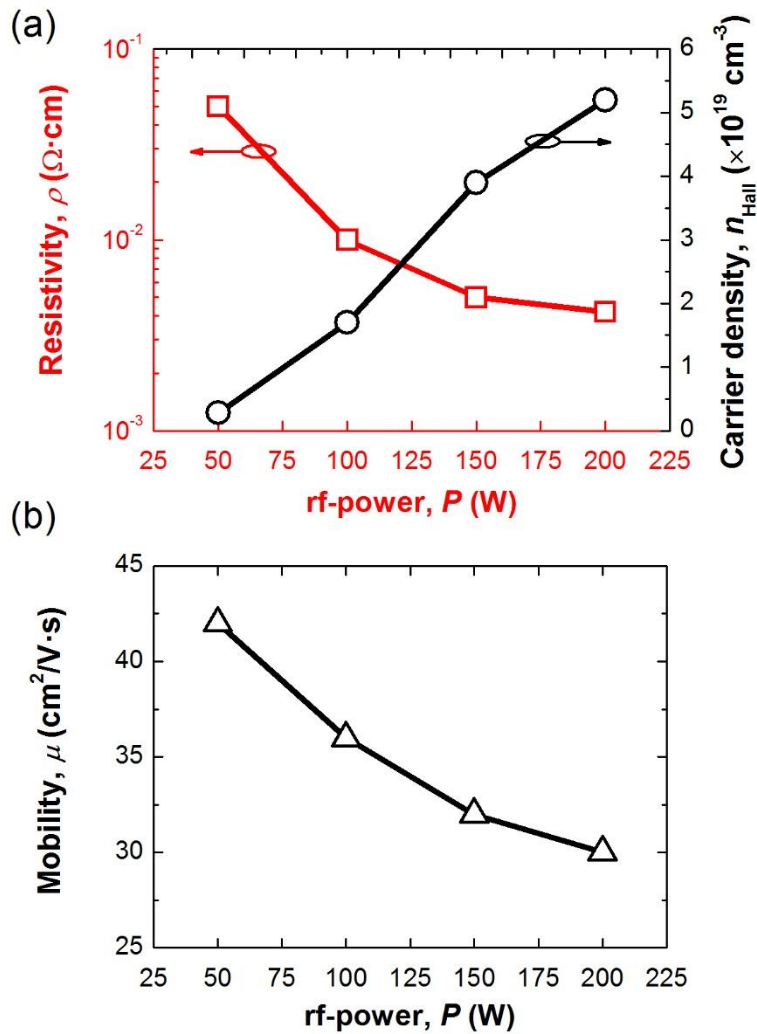

Figure 5.17. (a) ρ and n_{Hall} for Zn_3N_2 films grown at different rf-powers; (b) μ for the same samples.

The reduction of r_g promotes the incorporation of O into the zinc nitride sublattice (table 5.1). A higher concentration of O in zinc nitride could be responsible for the exhibited resistivity increase. Furthermore, the mobility might be improved due to the less defined grain boundaries characteristic of zinc nitride layers grown at low r_g (figure 5.7(a)).

Influence of the Working Gas Flux

Taking advantage of these results, the r_g is further lowered by diminishing the working gas flux in order to further improve μ in zinc nitride layers. For that purpose, three different total gas fluxes are used: 10, 20 and 30 sccm, keeping constant the growth chamber pressure at 1 Pa. Layers are grown at a rf-power of 25 W and T_s of 423 K (slow r_g) which are optimized parameters to obtain high mobility zinc nitride. At this low gas flux and rf-power, it is necessary to add a low concentration of Ar (N_2/Ar ~ 73%) to the working gas in order to ensure the stability of the plasma.

Results of the ρ and Hall measurements are shown in table 5.3.

Table 5.3. Electrical properties of Zn_3N_2 layers grown using different working gas fluxes.

Gas flux (sccm)	**Resistivity, ρ ($\times 10^{-3}$ Ω·cm)**	**Carrier density, n_{Hall} ($\times 10^{18}$ cm^{-3})**	**Mobility, μ (cm^2/V·s)**
10	20	3	100
20	10	7	94
30	5	21	62

From this table, it is observed that μ of the resultant layers tends to increase as the working gas flux decreases, reaching record values of around 100 cm^2/V·s at 10 sccm. That result confirms that lowering the r_g, as previously observed in the rf-power study (table 5.2), affects to the nucleation process positively, allowing to obtain higher μ values. Comparing samples in table 5.3 that present the highest (100 cm^2/V·s) and the lowest (62 cm^2/V·s) μ values, one can observe that n_{Hall} decreases from 21×10^{18} to 3×10^{18} cm^{-3}.

On the other hand, the ρ of zinc nitride layers tends to increase as the gas flux decreases. This behaviour is in good agreement with a higher unintentional incorporation of O into zinc nitride during slow growth processes, leading to increase zinc nitride resistivity.

Zinc nitride layers grown in this work show μ values which are in the same range (at the same doping levels) than those observed in materials commonly used in optoelectronic devices such as p-Si, as well as other materials with potential applications in optoelectronics such as ZnO (figure 5.18(a)). In addition, μ values in our Zn_3N_2 layers grown by sputtering are close to those obtained by techniques such as rf-MBE and MOCVD (figure 5.18(b)).

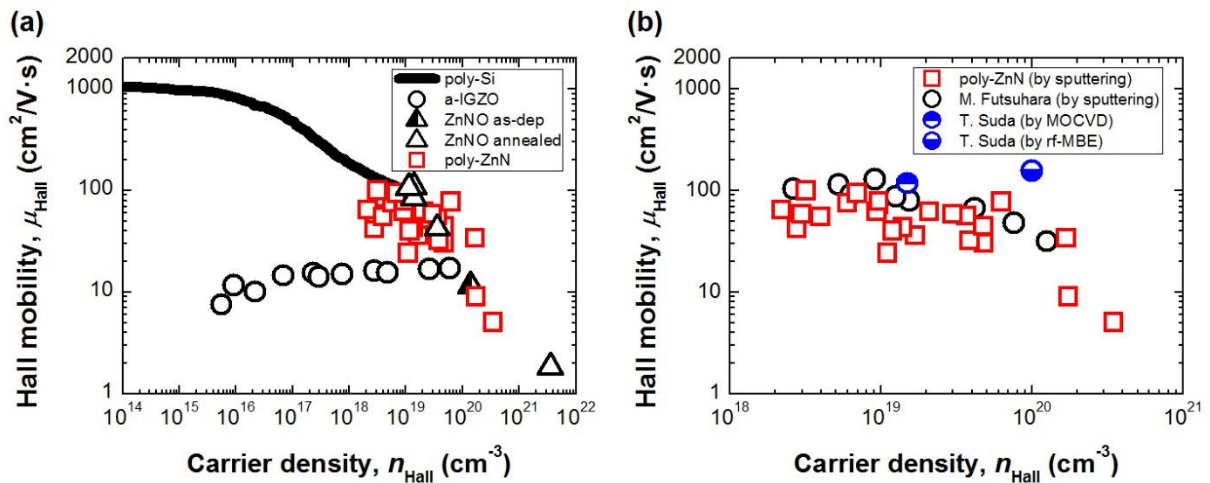

Figure 5.18. (a) Comparison of μ_{Hall} in different materials, including the Zn_3N_2 grown in this work as a function of n_{Hall}; (b) μ_{Hall} values for Zn_3N_2 grown by different techniques as a function of n_{Hall}.

5.2. Oxidation Mechanism of Zinc Nitride Layers

As mentioned, O is one of the most common impurities in zinc nitride compound due to its high reactivity in comparison to N, which limits the formation of pure and stoichiometric Zn_3N_2. During sputtering processes this issue can be minimized using high purity gas sources and metal targets, and high vacuum environments, resulting in pure Zn_3N_2 with a content of O below 1% as demonstrated in section 5.1.2.

After growth, Zn_3N_2 compound is highly sensitive to the storage conditions. In this section, it will be shown the effects of storage in ambient air, and how O can get incorporated into the Zn_3N_2 film forming an unsaturated surface layer of ZnO. This metastable behavior has been also observed in other metal nitrides such as Sn_3N_4 and Cu_3N [20]. Although, a few works have investigated this phenomenon, analysing surface properties of Zn_3N_2 by means of techniques such as Auger electron spectroscopy (AES) and XPS [6, 7], the composition and thickness of the oxidized Zn_3N_2 layers and the effect of the growth conditions on the oxidation rate are still unclear.

5.2.1. Compositional Study

Chemical composition of 2.3-μm thick Zn_3N_2 layers grown on Si(100) substrates at T_s = 298 and 473 K, and later stored in ambient air, is analyzed over time by a combination of IBA techniques: RBS, non-RBS and NRA.

Figure 5.19 shows O non-RBS signal obtained at a E_{ion} = 3.045 MeV for both samples, where, black triangle and red circle symbols represent 1 week and 1 month, respectively, after growth.

After 1 week, the experimental data corresponding to the sample grown at T_s = 473 K are fitted using a single-layer model, consisting of a Zn_xN_y layer atop Si substrate. Resultant fitting shows the stoichiometric coefficients for Zn and N of x = 3 and y = 2, respectively (figure 5.19(a)). That result confirms that layers grown at T_s = 473 K are still stoichiometric after 1 week.

On the other hand, after 1 week layers grown at T_s = 298 K show a variation of the Zn concentration near the surface (figure 5.19(b)), as it has been pointed out with a vertical dot line at around E ~ 2.2 MeV. This decrease of the Zn signal is justified because of the lower Zn content in the ZnO sublattice comparing to the Zn_3N_2. In order to simulate the experimental data, now a two-layer model is utilized. That model consists of a $Zn_{x'}O_{y'}$ layer on top of the Zn_3N_2 film, in which x' and y' result to be 1 and its thickness is around 290 nm. RBS gives the layer thickness in atoms per cm^2; this magnitude can be easily expressed in nm units, using ZnO molar mass (81.38 g/mol) and density (5.61 g/cm^3) through equation (4.16).

Figure 5.19 includes experimental data represented along with their corresponding simulations. The good agreement between both experimental and simulated data (using the two-layer model), corroborates that the oxidation process is evident after 1 week in samples grown at 298 K, producing a ZnO layer atop Zn_3N_2 surface with a hundreds of nm in depth.

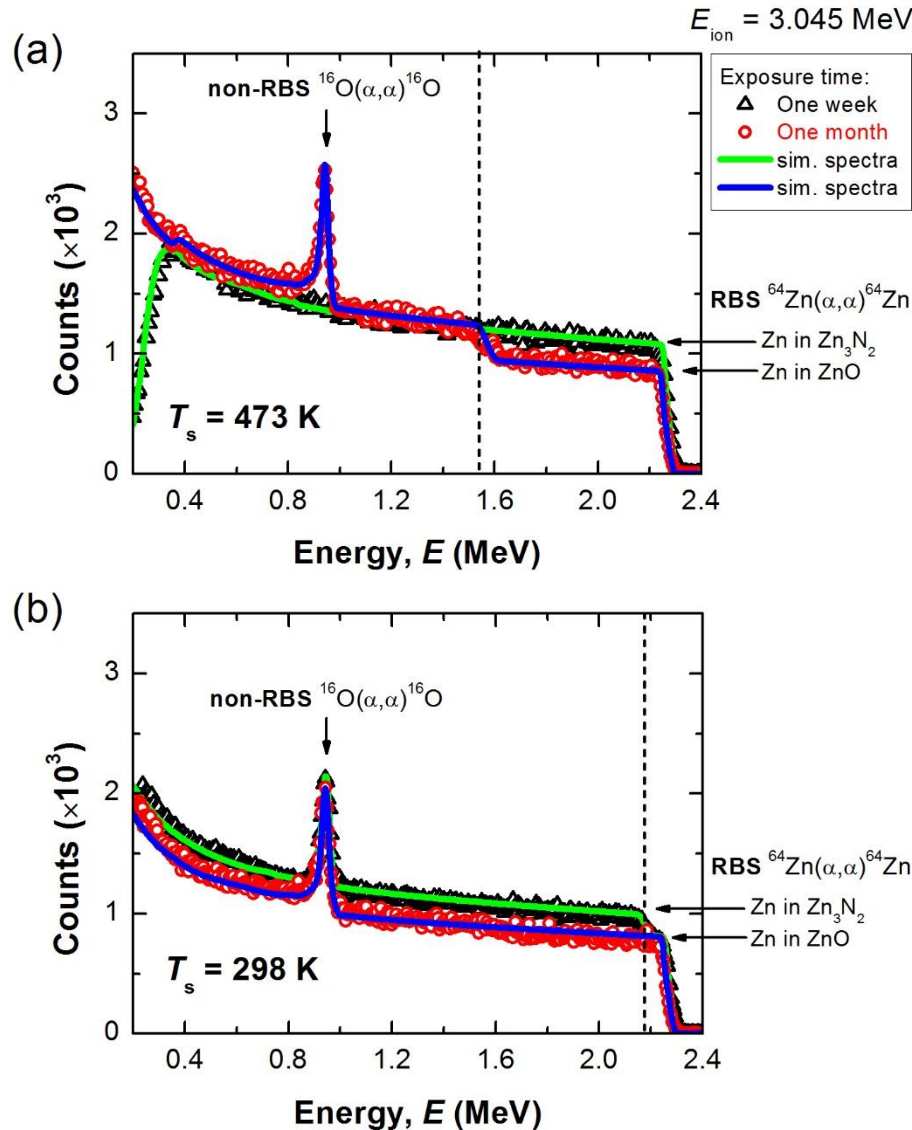

Figure 5.19. IBA spectra of Zn_3N_2/Si(100) samples grown at (a) T_s = 473 K and (b) T_s = 298 K and exposed to ambient air for 1 week (black triangles) and 1 month (red circles). Solid lines represent simulated spectra, whereas dot lines guide eyes to distinguish the Zn stoichiometry changes.

Therefore, samples grown at T_s = 473 K are more stable over time, exhibiting a slower oxidation rate, and showing no effects of oxidation after 1 week since their growth. After 1 month, Zn signal shows a step due to the formation of surface ZnO (figure 5.19(a)). The ZnO thickness increases over time and is calculated to be 0.72 μm after 1 month. In addition, the smooth transition observed between ZnO and Zn_3N_2 regions (figure 5.19(a), see dot line at E ~ 1.55 eV) suggests that the interface between both layers might be composed by a ternary compositional gradient ($Zn_xN_yO_z$).

In contrast, experimental data obtained from sample grown at T_s = 298 K was fitted using a single-layer of ZnO, which indicates that the initial compound was nearly completely transformed into ZnO, showing a lower Zn signal in the whole spectrum (figure 5.19(b)). The N content in this layer was lower than 6%, confirming the severe transformation of the layer composition.

For comparison with the oxidized layers, a heterostructure formed by $ZnO/Zn_3N_2/Si(100)$ was also analyzed by IBA techniques in order to confirm results observed in figure 5.19. That heterostructure was grown in the same sputtering system using the conditions described below:

i) ZnO: T_s = 298 K, rf-power = 250 W and O_2 flux = 50 sccm
ii) Zn_3N_2: T_s = 373 K, rf-power = 200 W and N_2 flux = 30 sccm

The thickness of the ZnO and Zn_3N_2 layers was determined by profilometry in two calibration samples grown separately on Si(100) substrates under described conditions; the measured thickness was 0.72 nm and 2.2 μm for ZnO and Zn_3N_2 layers, respectively. For the calculation of Zn_3N_2 thickness in nm from atoms per cm^2, it is use a molar mass of 224.15 g/mol and a density 6.22 of g/cm^3.

Results extracted at E_{ion} = 3.045 MeV are shown in figure 5.20 along with the best fitting curve from the two-layer model (ZnO/Zn_3N_2) applied to the heterostructure. From that simulation curve, ZnO and Zn_3N_2 layer thicknesses were estimated to be 0.72 and 2.1 μm, respectively. Analyzing the spectrum shape, it can be also observed the characteristic step associated to the change in the Zn molar fraction, as well as the resonance peak related to the O.

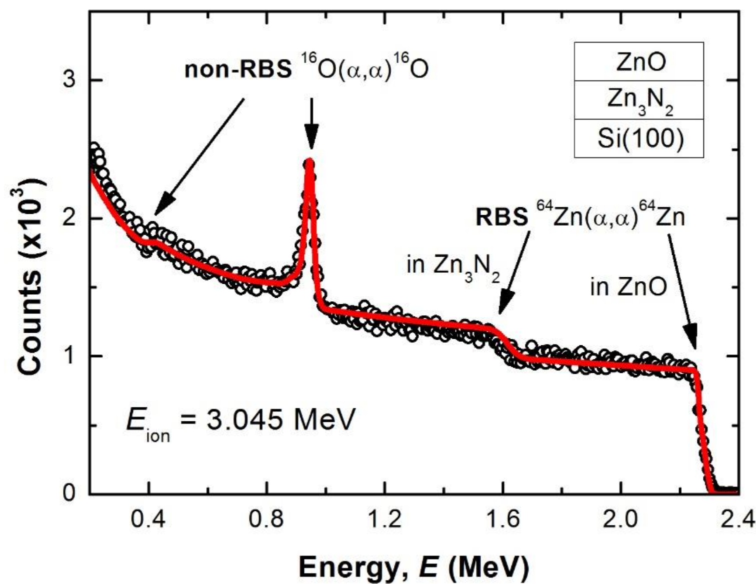

Figure 5.20. IBA spectrum of $ZnO/Zn_3N_2/Si(100)$ heterostructure. Line represents best fitting curve of the two-layer model. Inset: schematic of the layer sequence.

Therefore, the analysis of this heterostructure corroborates the validity of the suggested two-layer model, allowing for the simulation of IBA spectra measured in zinc nitride layers exposed to the ambient air for different periods of time.

5.2.2. Optical Study

The optical appearance to the naked eye of an as-grown stoichiometric Zn_3N_2 sample is black opaque. As a ZnO surface layer is formed on top of Zn_3N_2, light interferences are observed due to the coexistence of a two-layer structure formed by ZnO/Zn_3N_2. When Zn_3N_2 is completely transformed into ZnO, the sample colour changes to whitish transparent.

The study of zinc nitride metastability is addressed by thoroughly analyzing its optical properties at different oxidation stages. For this purpose, we use techniques such as SE and spectrophotometry.

Spectroscopic Ellipsometry

The oxidation rate of the Zn_3N_2 thin films was analyzed in depth by means of SE [1]. The ellipsometric angles Ψ and Δ of two different samples grown at T_s = 298 and 473 K were measured every two days during 1 month.

A brief collection of measurements corresponding to the zinc nitride layer grown at 473 K are recorded in figure 5.21(a,b). From these curves one can deduce that after two days, both Ψ and Δ show oscillations (also in the spectra extracted from sample grown at T_s = 298 K), whose number increases over time. These oscillations occur in a spectral range in which ZnO is transparent but Zn_3N_2 absorbs most of the light. In that scenario, constructive and destructive interferences occur between incident and reflected beams as a result of reflections in the top oxidized surface and the ZnO-Zn_3N_2 interface (see inset figure 5.21).

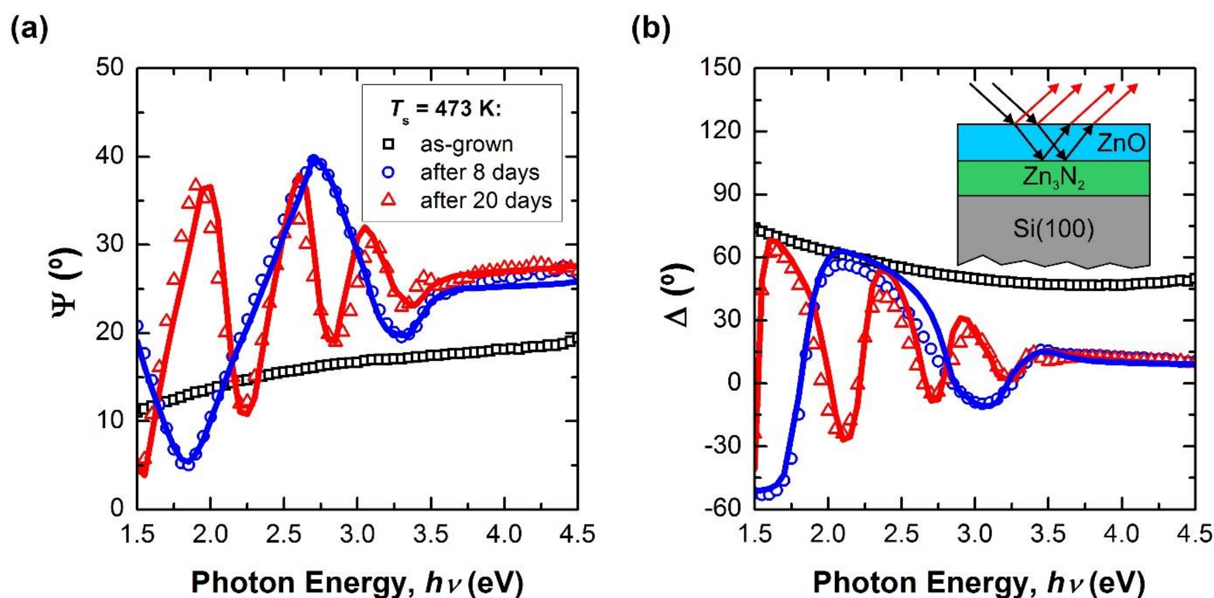

Figure 5.21. Ellipsometric angles (a) Ψ and (b) Δ measured over time in a Zn_3N_2 layer grown at 473 K. Lines represent the best fitting curves of the two-phase model described in the inset.

The two-phase model used to simulate experimental data is shown in the inset of figure 5.21(b). The fitting between the measured and the simulated angles show $\chi^2 < 0.01$ in all the examined samples; in addition,

the model used to simulate that layer structure takes into account surface roughness of samples grown at T_s = 298 and 473 K, allowing us to determine the average ZnO thickness (t_{ZnO}) as a function of time (figure 5.22). ZnO thickness presents a linear growth with time, showing rates of 36 nm/day and 20 nm/day for samples grown at T_s = 298 and 473 K, respectively. The result indicates that samples grown at higher T_s tend to get oxidized at lower rates than the ones grown at lower T_s [1].

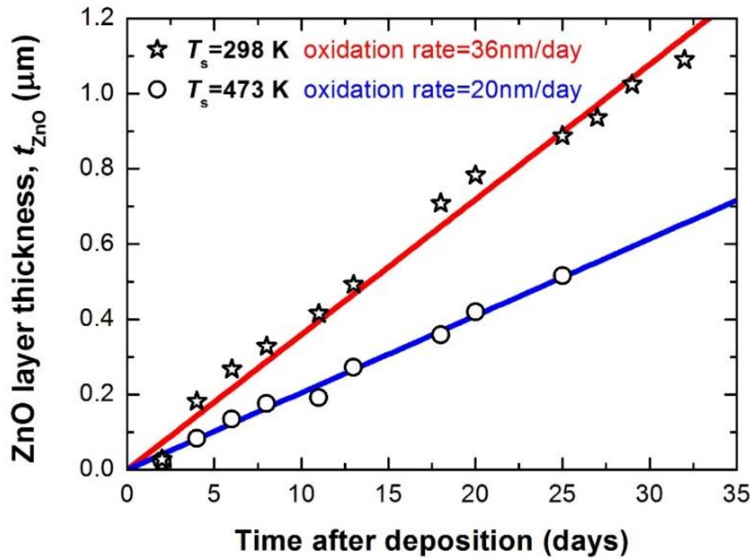

Figure 5.22. Oxidation rates of Zn_3N_2 layers grown at T_s = 298 and 473 K.

From the fabrication point of view, this fact is useful to improve the stability of Zn_3N_2 in electronic and optoelectronic devices. But despite the improvement, the optimization of the growth conditions seems to be insufficient to prevent oxidation. For that reason, the addition of a ZnO cap layer is proposed in this work to eliminate the high intrinsic surface reactivity of Zn_3N_2.

After the deposition of the zinc nitride layer at T_s = 473 K, a 10-nm thick ZnO layer is deposited on top of the nitride layer (in the same deposition run). This process prevents the exposure of the zinc nitride surface to the ambient air prior to the ZnO deposition.

Figure 5.23 shows different measurements of Ψ and Δ carried out periodically over time. All curves shown in that figure, corresponding to measurements performed as-grown, after 8 and 20 days in ambient air, are fitted using the same layer structure (ZnO/Zn_3N_2/Si) and layer thicknesses, indicating that oxidation of zinc nitride can be prevented by using a thin ZnO capping layer of around 10 nm.

The study continued for several months, showing similar results in the ellipsometric fittings, which is a good indication that this method successfully prevents the oxidation of the nitride over time, overcoming the metastability of this material. Furthermore, the analysis of the appearance to the naked eyes of the zinc nitride layers capped with ZnO, shows the opaque colour characteristic of zinc nitride after one year. In contrast, zinc nitride layer without capping layer becomes transparent after a few weeks.

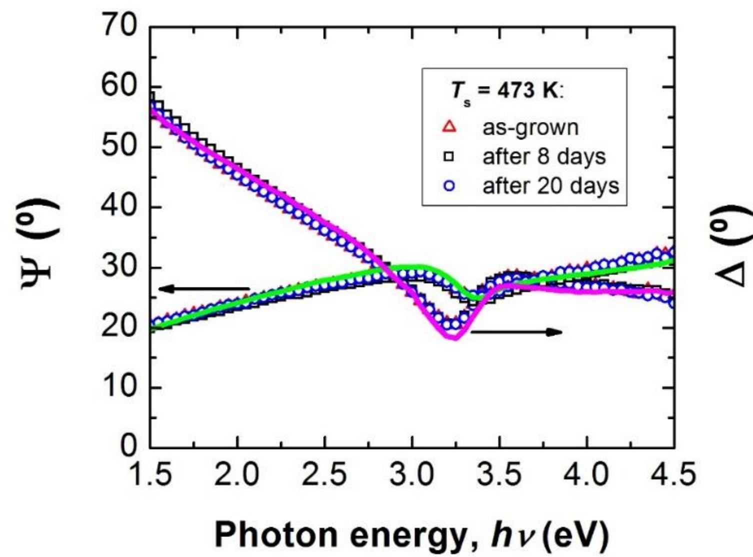

Figure 5.23. Zn_3N_2 layer capped with ZnO thin film, preserving nitride surface oxidation over time.

Transmission Spectrophotometry

The presence of an oxide layer on top of the surface can also be detected by transmission spectrophotometry, analysing transmission spectra of zinc nitride layers exposure to the ambient air over time (figure 5.24).

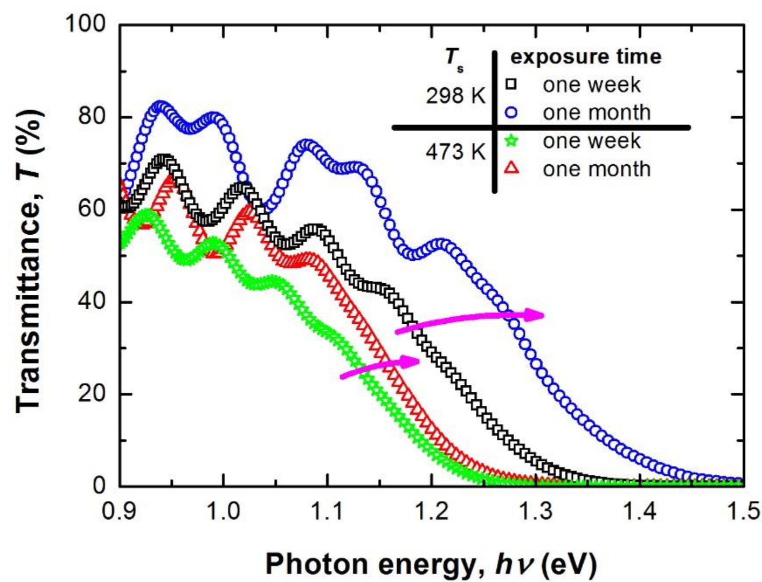

Figure 5.24. Transmittance as a function of $h\nu$ and oxidation time for nitride layers grown at T_s = 298 and 473 K.

Transmission experiments are carried out at $h\nu$ below 1.5 eV, where ZnO is totally transparent. In figure 5.24, T is represented as a function of $h\nu$ for two zinc nitride layers grown on quartz substrates at T_s = 298 and 473 K and analyzed one week and one month after their growth. As zinc nitride layers are grown at

r_g > 50 nm/min, the stoichiometry of as-grown layers is assumed to be Zn_3N_2. Therefore, different effects observed in figure 5.24 such as a transmission edge shift and the existence of oscillations above the transmission edge, are expected to be related with the oxidation of Zn_3N_2.

Comparing samples grown at different T_s but exposed to the ambient air for one week (black squares and green stars in figure 5.24), there is a red shift of the transmission edge as T_s increases. This change is not attributed to the surface oxidation but is mainly due to the morphological and structural changes observed by SEM (figure 5.5) and XRD (figure 5.8).

On the other hand, comparing samples grown at the same T_s but exposed during different times to the ambient air, it is found: i) a transmission edge blue shift, and ii) an increase of the transmission level above the transmission edge, both as the exposure time increases.

RBS studies shown in figure 5.19 that the transition between ZnO surface layer towards Zn_3N_2 bulk layer occurs through a region of intermediate composition ($Zn_xO_yN_z$). This region might be responsible for the blue shift of the transmission edge due to its high O content. On the other hand, the increase of the transmission in the Zn_3N_2 sub-band gap energy region where the ZnO is transparent can be associated to the decrease of the Zn_3N_2 layer thickness.

Figure 5.24 also shows oscillations in the transmission region of zinc nitride. These oscillations are originated by constructive and destructive interferences of incident light beam transmitted through the ZnO/Zn_3N_2/quartz structure. For longer exposure times (1 month), transmission region exhibits high frequency oscillations between the main oscillations; the formation of a complex multilayer structure, comprising ZnO, Zn_3N_2 and a layer with an intermediate composition ($Zn_xO_yN_z$) is suggested to be responsible of this behaviour.

5.2.3. Electrical Study

The electrical conductivity of a zinc nitride layer is analyzed as a function of the time after its growth. For this study, a zinc nitride layer is deposited on a glass substrate at T_s of 298 K, a rf-power of 200 W, a N_2 flux of 30 sccm, and during 2 min; the layer thickness results 120 nm as determined by profilometry. Once the nitride layer is grown, a pair of Ag electrodes separated 1.2 cm is deposited on top of its surface such as represented in the layer schematic of figure 5.25(a).

I/*V* characteristics of the nitride layer are measured over time in a probe station in dark conditions, and at voltages between -10 and 10 V (figure 5.25(b)). Resultant curves show a conduction of 0.3 µA at 10 V in as-grown samples. However, the current decreases sharply down to 1 nA at 10 V after one day, and tends to decrease progressively over time. After four days, current shows values around 10 pA at 10 V, exhibiting the same values after several months.

From those results, one can conclude that the oxidation of Zn_3N_2 lowers the conduction through the nitride bulk mainly because the formation of a resistive ZnO surface layer. The thickness of this oxide layer is demonstrated by SE to increase at around 36 nm/day for the used growth conditions. Therefore, after four days

of air exposure, zinc nitride layer is expected to be completely transformed into ZnO, showing then the lowest currents.

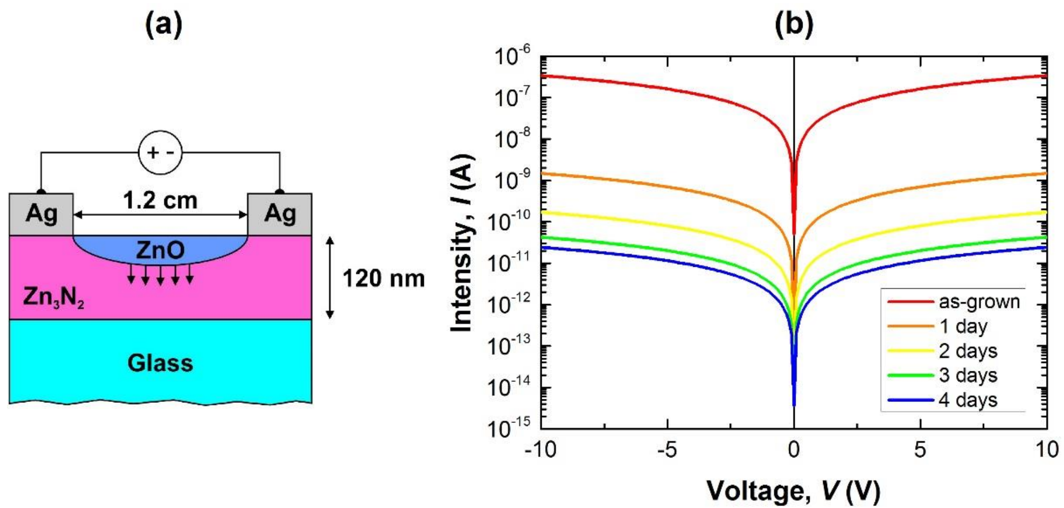

Figure 5.25. (a) Schematic of *I*/*V* measurements performed in a zinc nitride layer; (b) resultant *I*/*V* characteristics measured over time.

5.2.4. Structural Study

Comparing the crystalline structure of a Zn_3N_2 layer right after its deposition and after 1 month in ambient air (figure 5.26), one can conclude that the total oxidation of zinc nitride yields a compound whose crystalline structure shows diffraction peaks that can be identified within the WZ structure of ZnO; therefore, the oxidation of zinc nitride leads, not only to a change in the composition of the material, but also to a change in the crystalline structure from cubic anti-bixbyte, in Zn_3N_2, to hexagonal WZ, in ZnO.

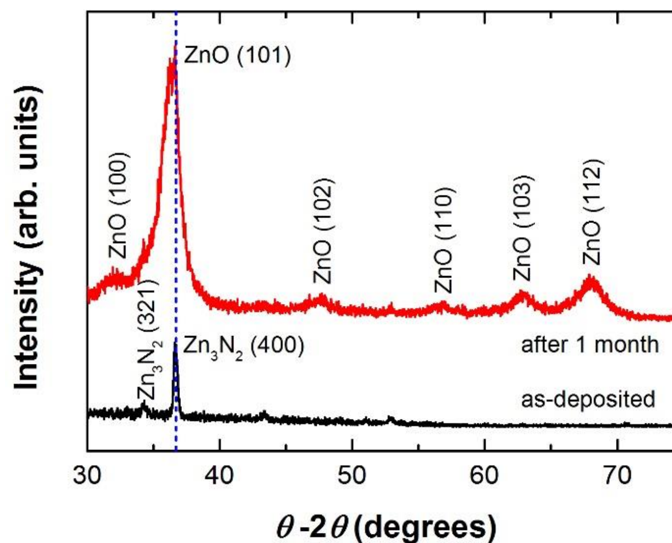

Figure 5.26. XRD pattern of a Zn_3N_2 layer measured as-deposited and after 1 month of air exposure.

5.2.5. Rapid Oxidation of Zinc Nitride Induced by Electric Arcs

In this subsection, it is presented a novel way to obtain ZnO submicron crystals from the rapid transformation of Zn_3N_2 layers using electric arcs to accelerate the oxidation procedure of Zn_3N_2 [2]. Due to the high increase of the local temperature at the sample surface, the oxidation rate of zinc nitride is extremely enhanced. In that respect, we investigate the effects of microscale electric arcs on Zn_3N_2 films.

The high energy density provided by an electric arc to conductive electrodes has been widely used in the industry to machine metal work pieces, in the so called electrical discharge machining (EDM). In general this technique employs high voltage pulses (from tens to hundreds of volts during microseconds) and use to work under immersion in a dielectric liquid (deionized (DI) water, kerosene, etc.). The usual working gap distance between electrode and metal bulk ranges from tens to thousands microns. Electrical discharges have not been used exclusively for material removal but also to modify metal surfaces [21-23]. In most cases, this is performed by taking advantage of the strong thermal shock accompanying the arc [24]. Occasionally, traces of chemical reduction [25] and oxidation [2] of materials due to electron irradiation have been found. It should be noted that at RT and atmospheric air pressure, low voltage (< 20 V) electrical discharges in very close gap spacing (below one micron) have received considerably less attention than electrical discharges in long air gaps (> 1 mm) [26, 27]. In fact, the electrical discharge mechanisms in such conditions are beyond those considered in the Paschem's Law and are still under discussion [28].

System Details

The system, developed by Dr. Álvarez et al. at Universidad Rey Juan Carlos, consists of a home-made assembly of micro- and nano-positioners electronically controlled via software, which allows accurate approach to the sample surface and horizontal scan of an electrically-biased micrometric probe at the nanoscale. In contrast to conventional EDM, we apply low DC voltages (< 20 V) to generate sparks at submicron scales, so we can perform electrical discharge lithography on semiconductor thin films. The probe includes a spring (350 ± 20% N/m spring constant) to damp mechanical force against the sample. The spring is squeezed just a few microns in normal operation. The home-made design allows surface scanning at speeds up to 15 mm/s with high pattern definition over working areas of 10×10 cm^2. This setup has been previously used to define patterns on different thin films, including semiconductor materials such as indium tin oxide (ITO) and metals such as Au/Cr and Al [29].

For this study, 1.5-μm thick polycrystalline Zn_3N_2 films are synthesized during 30 minutes either on Si(100) or glass substrates by rf-magnetron sputtering at a T_s of 473 K, a rf-power of 150 W, a N_2 gas flow of 30 sccm, and a residual pressure of 1 Pa, yielding a r_g of 50 nm/min. RT electrical discharge lithography is performed along the surface of that Zn_3N_2 film using the described experimental system. A low DC voltage is applied between a tungsten spring probe (with 50 μm of tip diameter) and the conductive sample surface (figure 5.27(a)). The counter electrode, identified as GND in the schematic, is thermally evaporated on the Zn_3N_2 surface and consisted of a gold pad with ohmic characteristics. A computer assisted system consisting of an assembly of electromechanical and piezoelectric steppers for accurate probe positioning along the xyz axis

yields a relative horizontal accuracy and absolute reproducibility of 0.1 and 1 μm, respectively, as well as a vertical accuracy and reproducibility below 1 nm. Prior to start scanning, the biased probe is smoothly approached to the Zn_3N_2 surface. At very short distance (< 1 μm), the gap distance is electrically short-circuited by an electron current likely built up as a result of field emission, in a scenario in which Paschen's law is unable to predict the breakdown voltage because of the low voltages and short distances between electrodes [30, 31]. These electrons contribute:

i) to raise the temperature and the charge of the thin film area underneath the probe by impacting its surface at high speeds, and
ii) to ionize the gas molecules contained in the air gap.

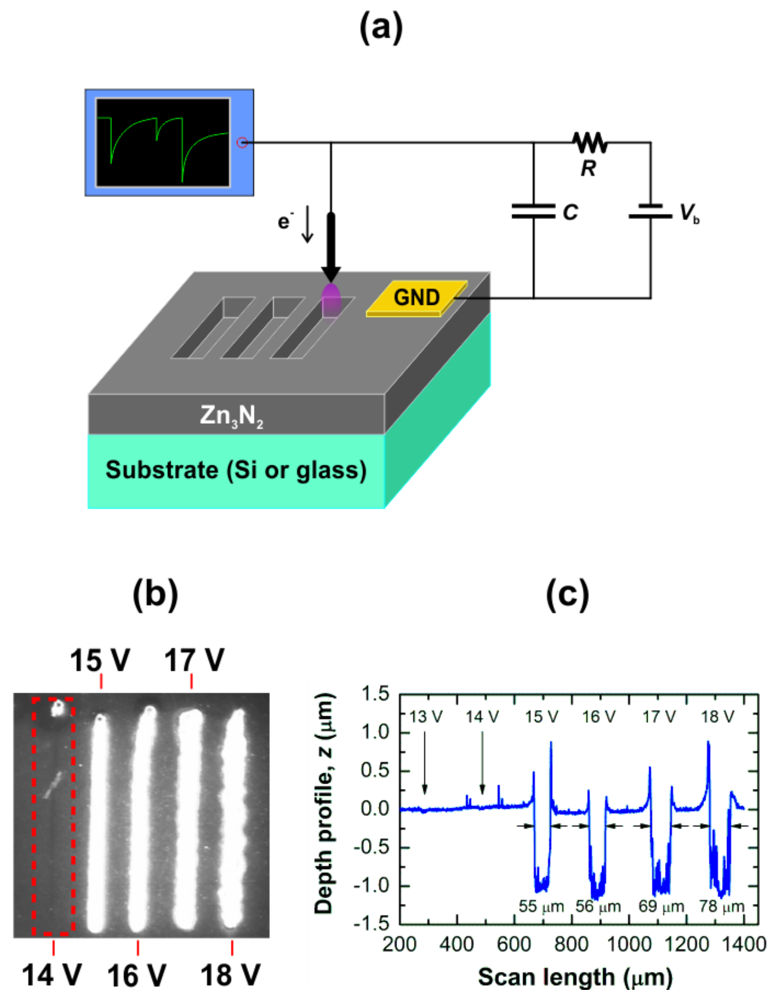

Figure 5.27. (a) Schematic of the experimental setup used for arc discharge lithography; (b) linear scans performed at different bias voltages between 14 and 18 V on Zn_3N_2/Si samples; (c) depth profile analysis for the different bias voltages.

These conditions finally lead to reach air breakdown. At that moment, the temperature rockets propelled by the electric arc, and defines a pattern in the Zn_3N_2 layer whose dimensions (depth and lateral size)

depend on the applied voltage and tip diameter. A shunt capacitor provides charge to keep the arc until the thin film material is removed or gets insulating. During that time, resistivity drops and a current pulse of a few amps and several microseconds duration is monitored in an oscilloscope. Once the tip is in contact with the electrically isolated region, the DC power supply enables capacitor recharge. Then, the probe sweeps over the xy plane in order to define different patterns by modifying the Zn_3N_2 layer properties. During the scan, the sample is kept on a ceramic stage in ambient air without refrigeration. Several regions are defined at different DC voltages and scanning speeds ranging between 0 and 20 V, and between 0.1 and 3 mm/s, respectively.

Profilometric Study

In order to study the effect of the electrical discharge lithography on Zn_3N_2/Si and Zn_3N_2/glass samples, 1-mm long linear scans are defined using different DC voltages ranging between 0 and 20 V. Figure 5.27(b) shows an optical microscope image of five 1-mm long linear scans defined using different DC voltages ranging between 13 and 18 V on Zn_3N_2/Si samples. The morphology of the sample surface is analyzed after these five scans by stylus profiler as presented in figure 5.27(c). Silicon substrates, whose thermal conductivity is 149 W $m^{-1}K^{-1}$, prevent charge accumulation under the tip area and give rise to the arc formation at bias voltages larger than 14 V. On the other hand, glass substrates whose thermal conductivity is much lower than Si (~1 W $m^{-1}K^{-1}$) enable formation and sustainability of the electric arc at voltages above 6 V. Therefore, there is a threshold voltage to produce arc discharges during the tip approach, which is mainly dependent on the tip material and diameter, and sample material. After overcoming the threshold voltage of 14 V, the arc produces severe modification of the layer properties. In particular, profilometry results indicate that the arc discharge yields a deep trench in the scanned areas whose width increases with the bias voltage. The trench, whose depth is about 1.1 μm, quite independently of the bias voltage, is the result of the partial sublimation of the nitride layer. The sharp upward edges obtained in the profilometry scan (figure 5.27(c)) suggest that residues of the process accumulate at the borders of the scanned area as typically occurs in arc erosion processes.

Two-dimensional simulation of the electric potential between the probe and the sample surface shows how the electric field rapidly attenuates because the region out of the 2.5 μm gap has higher spacing between electric field lines (figure 5.28). Since field emission exponentially decays with the electric field strength, it is expected to have an electron beam out of the tip limited to its closest edge and perpendicularly oriented to the sample surface. In that scenario, it seems logical to find a pattern, whose width reproduces the tip diameter [2, 32].

The broadening of the line width with bias voltage would be provoked by stronger heating effects as higher energy electrons hit the sample surface. The power enhancement will also expand the lateral limits of the thermal profile, thus producing wider affected areas.

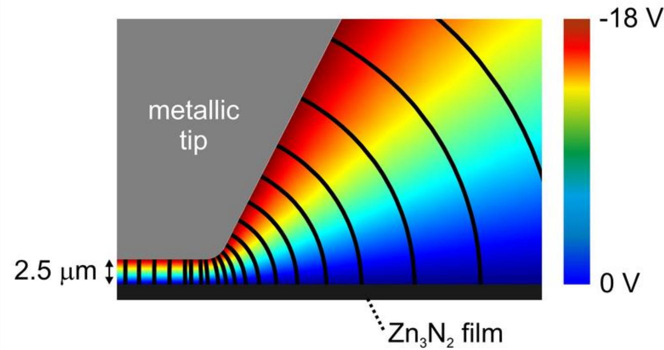

Figure 5.28. Two-dimensional simulation of the electric potential (surfaces) and the electric field (lines) in the air gap between the tip and the sample for a distance of 2.5 μm.

Electrical Properties

At values below the threshold voltages, the scan produces a shallow fingerprint on the sample surface. This fingerprint is attributed to the native oxide removal on top of the nitride layer. As this oxide usually presents higher resistivity than the nitride layer, its removal should lead to a reduction of the resistivity of the scanned area. To further investigate this point, 1×3 mm^2 areas are defined using voltages between 0 and 15 V on Zn_3N_2/glass samples, and later, these areas are analyzed by means of four-probe resistivity measurements (figure 5.29). The result shows that ρ diminishes from 7.3×10^{-3} $\Omega\cdot$cm down to 5.9×10^{-3} $\Omega\cdot$cm as the bias voltage increases from 0 to 4 V. These values are among the best values obtained for this material. It is worth noticing that ρ at zero volts is near the value found in non-scanned Zn_3N_2 areas. The resistivity reduction is attributed to the local heating produced by the tunneling current through the tip toward the nitride layer once in contact with the surface, which induces the electrical break down of the oxide layer on top of the nitride.

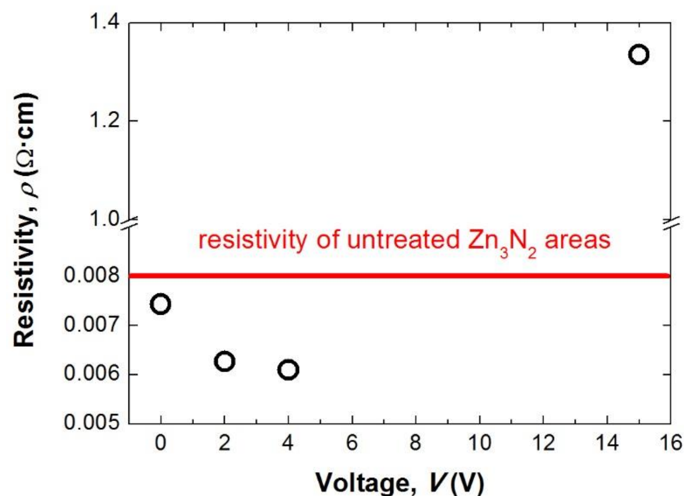

Figure 5.29. Electrical resistivity as a function of the tip voltages measured in 1×3 mm^2 defined areas of 1.5 μm thick Zn_3N_2 films deposited on glass substrates.

This heating effect promoted at low voltages would explain the resistivity improvement as the voltage increases. On the other hand, as electric arc does not occur at these voltages, the tip pressure on the surface during the scan could provoke mechanical polishing/planarization of the native oxide.

Above the threshold voltage for arc ignition, the resistivity measured in scanned areas increases drastically. At 15 V, it becomes at least two orders of magnitude higher than those values found at low voltages. Further increase of the bias voltage leads to resistivities much higher than the maximum limit of the setup measurable range (10^5 Ω·cm).

From those results, it is important to notice that arc discharge lithography would allow electrical insulation of TFTs fabricated on Zn_3N_2 layers with a channel length and resolution that would be determined by the tip size. At intermediate voltages (4-15 V), the surface becomes too rough with peak-to-valley amplitudes larger than 1 μm, hindering the measurement of the resistivity due to the poor current uniformity.

SEM and EDAX Studies

SEM observations indicate that the material tend to lift-off in sheets parallel to the scan line, keeping a separation between them of 15-20 μm. Figure 5.30(a-c) includes the SEM viewgraphs taken at the edge of the scanned area under arc discharge. The images show a well-defined border between treated and untreated regions over large distances. In addition, ordered arrangements of micro-droplets are observed around the trench with a linear density of 0.23 μm^{-1}. This density seems scarcely dependent on the substrate, scan speed and bias voltage used. Droplet size uniformity improves with the scan rate. Compositional studies carried out by EDAX indicate that the droplets are mainly formed by Zn. A close view of the droplet surface reveals circular areas likely related to its partial oxidation (figure 5.30(c)). These Zn-rich droplets are residues of the process, which have their origin in the decomposition of Zn_3N_2. Whereas N leaves the structure in molecular form during material sublimation, part of the Zn remains at the edges. The high density and order of micro-

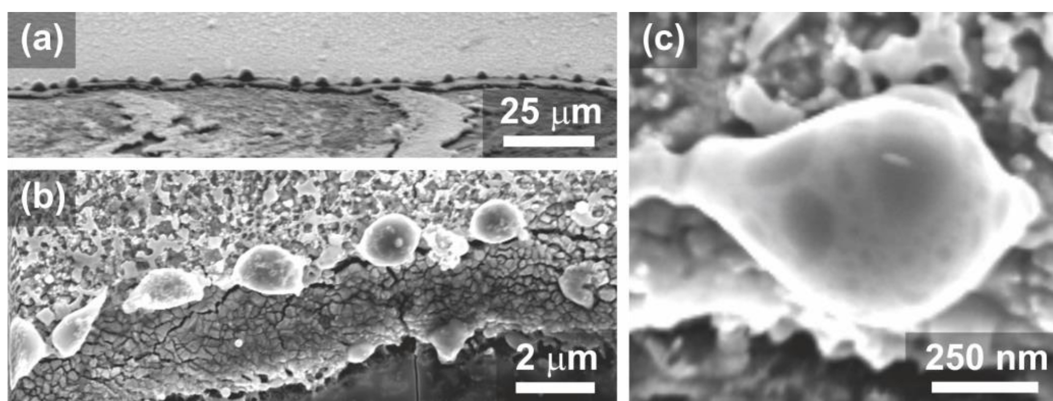

Figure 5.30. SEM viewgraphs of the Zn_3N_2 surface after arc discharge lithography. (a) Scan edge obtained at 15 V and 3 mm/s scan speed on a glass substrate. (b) Zn micro-droplets obtained as a residue of a 16 V and 0.1 mm/s scan on a Si substrate. (c) Zoom-in of one of the Zn droplets.

droplets along the contour of the trench suggest a potential method to synthesize seeds for the growth of Zn-based nanostructures such as ZnO NWs.

The central region of the scan presents a different morphology as a result of the arc discharge. Figure 5.31 compares the surface of the as-grown films (figure 5.31(a)) with the surface of the regions under treatments of 17 V (figure 5.31(b)) and 18 V (figure 5.31(c)).

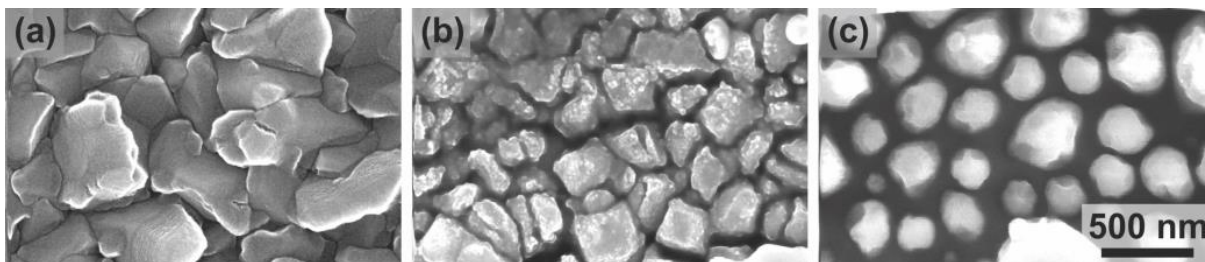

Figure 5.31. SEM viewgraphs of (a) the as-grown Zn_3N_2 film on Si, and two areas underneath the probe after arc discharge treatments carried out at (b) 17 V and (c) 18 V.

As the voltage increases, a characteristic structure formed by small facetted crystallites with sizes between 50 and 500 nm shows up. These crystallites account for the 30% volume of the layer that it is not sublimated and it is shown at the bottom part of the groove in the profilometry study. The surface density of these crystallites on the Si substrate is in good agreement with the typical grain density in polycrystalline Zn_3N_2 grown at 473 K, as shown in figure 5.31(a-c). As compared with Zn_3N_2 layers, grains become more separated as the tip voltage increases and tend to show marked facets. A reasonable explanation for the formation of these crystals could be a recrystallization process induced by the high temperatures reached in the presence of plasma, which is fed by ambient air, and is rich in O active species that can easily trigger the oxidation of the nitride grains.

Compositional Study

A thorough study about the resultant composition of those areas defined in Zn_3N_2 films under different DC voltages is carried out using IBA. Figure 5.32 shows the experimental results on regions scanned at tip voltages of 0, 15 and 20 V on a Zn_3N_2/glass sample, along with their best fitting spectra obtained from SIMNRA software. The simulation model comprises a $Zn_xN_yO_z$ layer (x, y and z are Zn, N and O molar fractions, respectively) on top of a glass substrate.

From the analysis of Zn RBS and O non-RBS signals (figure 5.32(a)), a Q of 1.26×10^{11} particles· sr is estimated for a detection angle of 170º. That value is consistent for all the samples studied here. On the other hand, N NRA signal is measured with a detector located at 165º (figure 5.32(b)). Due to the different detection angle, the Q value in N NRA signal must be corrected by a scaling factor proportional to the relationship between the detector solid angles at 170º and 165º ($\Omega_{170º}/\Omega_{165º} = 2.2$), yielding a value of 2.81×10^{11} particles· sr at 165º.

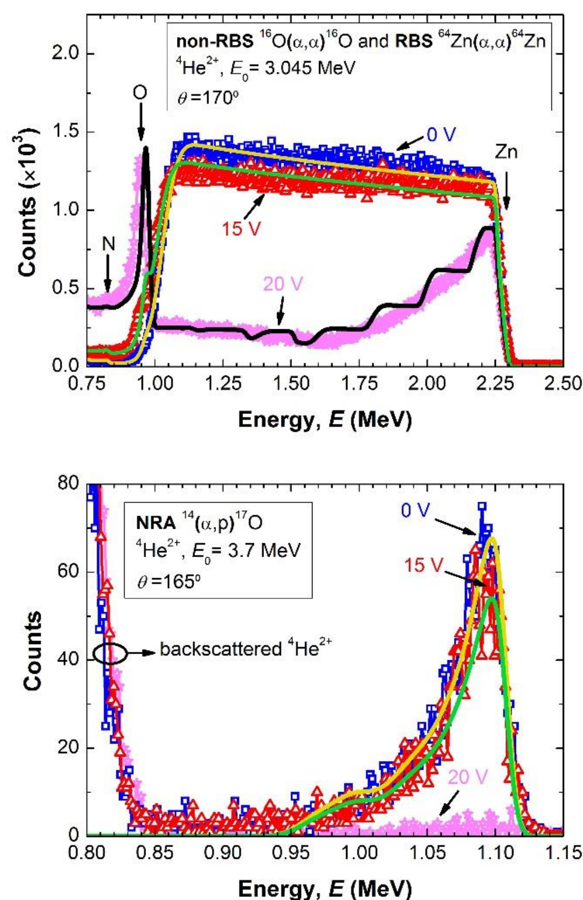

Figure 5.32. (a) Zn RBS, and O non-RBS signals measured at 3.045 MeV, and (b) N NRA signal extracted at 3.7 MeV from Zn_3N_2 treated at different tip voltages.

The N molar fraction is used as a fitting parameter for the three curves in figure 5.32(b); whereas the O molar fraction is obtained from the fitting of the non-RBS signals measured at 3.045 MeV in areas scanned at 0, 15 and 20 V. Resultant calculations are summarized in table 5.4. From these calculations, it is concluded that the O molar fraction increases with the bias voltage from 0.03 (at 0 V) to 0.48 (at 20 V), whereas the N molar fraction decreases from 0.39 (at 0 V) to 0.02 (at 20 V). The resultant Zn molar fraction obtained from the RBS fitting shifts from values near the stoichiometric molar fraction in Zn_3N_2 (x=0.58, y=0.39, and z=0.03) to stoichiometric values in ZnO (x=0.50, y=0.02, and z=0.48); revealing that ZnO crystals still retain up to 2% of N inside. This result confirms the successful transformation of Zn_3N_2 into ZnO submicron crystals under arc discharge treatment [2].

Table 5.4. Zn, N and O molar fractions (x, y and z) calculated by RBS, NRA, and non-RBS respectively, for Zn_3N_2 layers treated at different tip voltages.

Voltage	Molar fraction ($Zn_xN_yO_z$)		
	x	y	z
0	0.58	0.39	0.03
15	0.56	0.34	0.10
20	0.50	0.02	0.48

The control and precision of this method allow to define accurate patterns on metastable materials which can be very useful for the fabrication of devices, preventing the use of photolithography. The rapid transformation observed in Zn_3N_2 films, as well as the possibility to control the resultant composition of the ternary $Zn_xN_yO_z$ is expected to enable the fabrication, not only of sensors whose absorption edge can be tuned from VIS to UV ranges, but also the design of p-n heterostructures composed by Zn_3N_2/ZnO with potential applications in LEDs.

5.3. Transistors Based on Zinc Nitride as Channel Layer

In this section, transistors based on zinc nitride as channel layer are designed, fabricated and characterized [5]. Two different structures of transistors based on zinc nitride are fabricated: i) bottom-gate TFT and ii) photo-transistor. The latter consists in a transistor whose channel layer is modulated by light, taking advantage of the zinc nitride sensitivity to VIS light (section 5.1.5).

5.3.1. Bottom-Gate Thin Film Transistor

TFT Fabrication Steps

Bottom-gate TFTs based on zinc nitride are fabricated using mechanical masking and photolithography. A cross-sectional schematic of the fabricated TFT is shown in figure 5.33. In that figure, the layer stacking sequence is detailed along with the corresponding thickness of each layer.

The Si(100) substrate is previously cleaned with ethanol, rinsed in DI water, and blow-dried with N_2. The surface area of the Si(100) substrate is around 5 cm^2. A 140-nm thick Cr layer is deposited as the gate electrode by rf-magnetron sputtering (figure 5.33(1)). Half of the area is covered by a mechanical mask, while the remaining area is covered by a 200-nm thick SiO_2 layer at RT by electron cyclotron resonance (ECR) to form the dielectric layer (figure 5.33(2)). A 182-nm thick Zn_3N_2 thin film is grown as the channel layer on top of the dielectric layer by rf-magnetron sputtering using the following conditions (figure 5.33(3)): a T_s of 298 K, a total N_2 gas flow of 30 sccm, a rf-power of 200 W, and a growth chamber residual pressure of 1 Pa. The

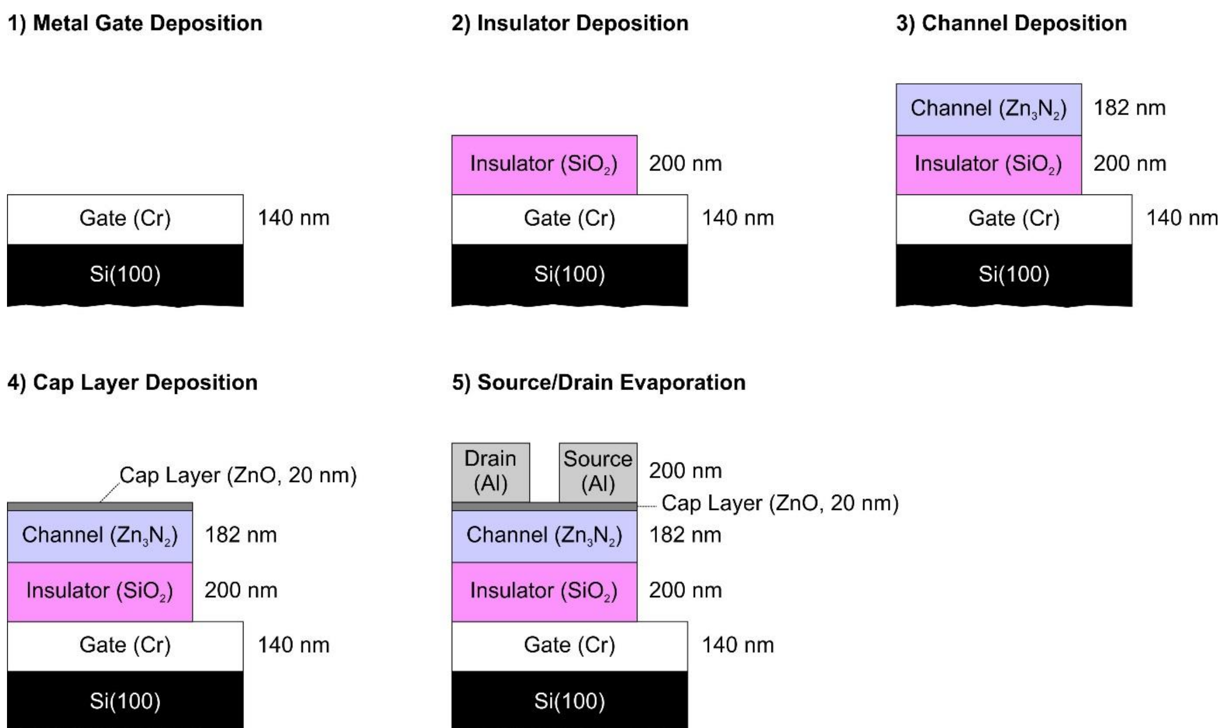

Figure 5.33. Schematic of the fabrication steps of a Zn_3N_2 based bottom-gate TFT.

electrical properties of the resultant Zn_3N_2 layer are analyzed by Hall effect measurements, showing a μ, ρ and n_{Hall} of 5 cm^2/V·s, 4.3×10^{-3} Ω·cm, and 3.5×10^{20} cm^{-3}, respectively.

The channel layer is covered with a 20-nm thick ZnO cap layer (figure 5.33(4)). Channel and cap layers are grown one after each other to prevent surface degradation due to the ambient exposure. Finally, a 200-nm thick Al layer is evaporated and patterned by photolithography and lift-off processes to form pairs of drain/source electrodes with different channel lengths L = 2-20 μm (figure 5.33(5)). The width-to-length (W/L) ratio ranged between 250 and 2500.

TFT Characterization

Output characteristics (I_D/V_{DS}) of bottom-gate TFTs are measured under different gate-source voltages (V_{GS}) at room temperature in a four-probe system (Karl Suss Probe Station). These measurements are obtained in dark and under VIS light illumination. Results for a transistor with a L of 2 μm are shown in figure 5.34.

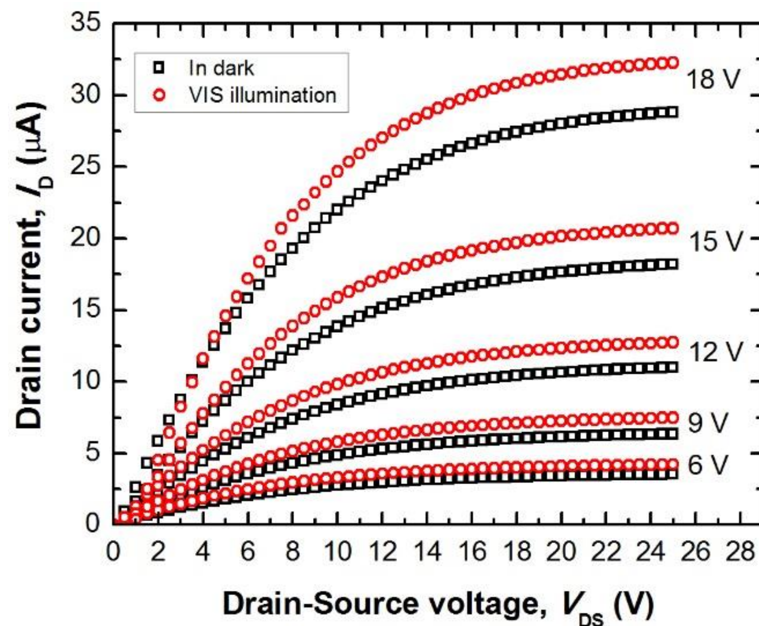

Figure 5.34. Bottom-gate I_D/V_{DS} characteristics in dark and under VIS light illumination as a function of V_{GS}.

The TFT is in the off-state at V_{GS} = 0 V and needs a V_{GS} voltage higher than 6 V to drive current (figure 5.35(a)). Therefore, the transistor operates as a n-channel enhancement mode FET, which is preferable to depletion-mode behaviour since device design is easier and power dissipation is reduced. Positive V_{GS} above the threshold voltage (V_{th} = 6V) is necessary to attract free electrons towards the gate and form the conductive channel in the Zn_3N_2 layer (figure 5.35(b)). A further increase of V_{GS} above the V_{th} increases the charge density in the channel so I_D increases. Saturation voltage and saturation drain current ($I_{D,sat}$) also increase with V_{GS}. It is noticeable that despite the high charge concentration and the low resistivities measured in the thin films grown on glass substrates, the device is in the off-state at V_{GS} = 0 V. This behaviour is believed to be caused

by a charge trapping effect in the SiO_2 layer and/or along zinc nitride grain boundaries since similar zinc nitride layer thickness provided much lower resistivity.

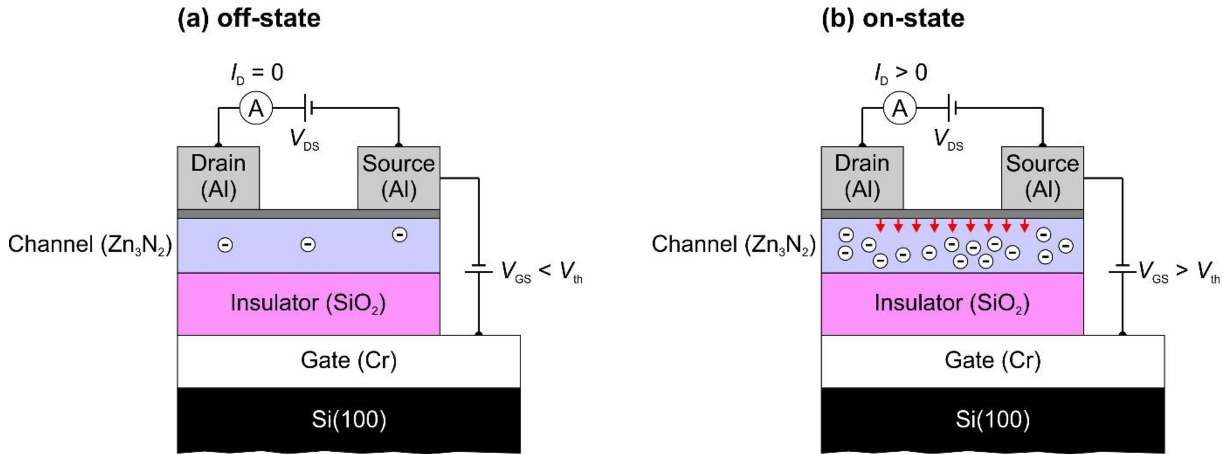

Figure 5.35. Schematic of TFT operating in n-type channel enhancement mode; (a) off-state at $V_{GS} < V_{th}$ and (b) on-state at $V_{GS} > V_{th}$ (for $V_{th} > 0$).

The field effect mobility (μ_{FE}) is estimated by using

$$I_{D,sat} = \frac{W}{L}\mu_{FE}C_{SiO_2}\frac{(V_{GS} - V_{th})^2}{2} \tag{5.6}$$

where C_{SiO_2} is the capacitance of the SiO_2 per unit area. $I_{D,sat}$ is represented as a function of V_{GS} at $V_{DS} = 25$ V (saturation region) and using the slope of that function, μ_{FE} is calculated to be 0.02 $cm^2/V{\cdot}s$. This value agrees well with that reported in the literature before [33] and is still low in comparison with those obtained in TFTs based on other materials such as amorphous-ZnO (25 cm^2/V s) [34] or GaN (1 cm^2/V s) [35]. This can be associated to the high dimensions of the bottom-gate devices which yield a high current leakage from the gate through the dielectric layer, reducing the effective current between drain and source.

The illumination of the channel with VIS light ($\lambda = 500$ nm and a power density of $P = 500$ W/m^2) leads to an increase of I_D as a result of the charge density increase which reduces the channel resistivity (see red circle curves in figure 5.34). Figure 5.36 shows the drain photocurrent (I_{photo}), defined as the difference between drain current measured under VIS light (I_{DL}) and in dark (I_{DD}) conditions, represented as a function of V_{GS}. It is worth noting that the I_{photo} increases with V_{GS}^2.

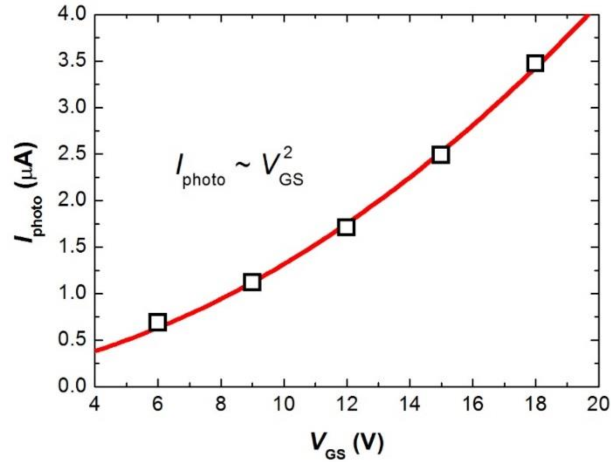

Figure 5.36. I_{photo} vs V_{GS}.

The R_{photo} of the TFTs has been calculated through the following expression

$$R_{photo} = \frac{I_{photo}}{P \cdot A_{sample}} , \tag{5.7}$$

where A_{sample} is the area of the sample irradiated by the light, and is equivalent to $W \cdot L = 10^{-4}$ cm^2. Accordingly, figure 5.37 shows the R_{photo} represented as a function of V_{DS} for different V_{GS}. From that figure one can extract some relevant conclusions:

i) R_{photo} tends to increase up to saturate with V_{DS}.

ii) The saturation level of R_{photo} increases with V_{GS}.

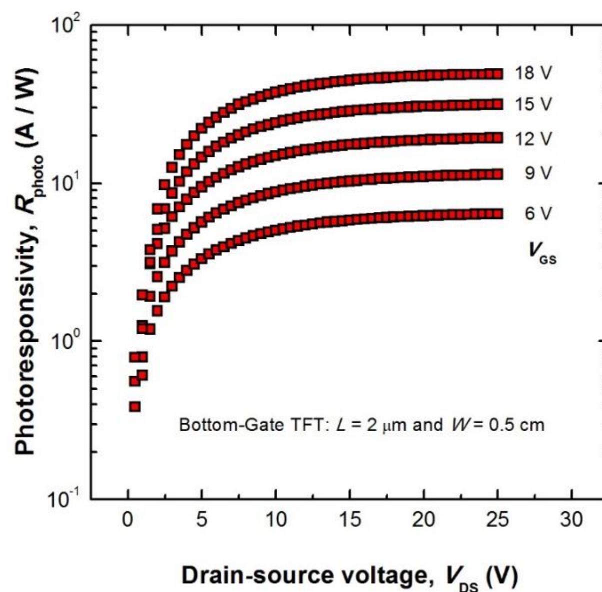

Figure 5.37. Bottom-gate TFT R_{photo} vs V_{DS} measured at different V_{GS}.

5.3.2. Photo-Transistor

Photo-Transistor Fabrication Steps

Photo-transistors are fully fabricated by optical lithography and chemical etching processes. The cross-sectional schematic and the top-view image of one of the resultant transistors are shown in figure 5.38. Drain and source pair of electrodes are directly evaporated (200-nm thick film) and patterned by photolithography and chemical etching processes on top of an oxidized Si(100) wafer substrate (figure 5.38(a)).

The conductive channel consists of a Zn_3N_2 layer grown by rf-magnetron sputtering (figure 5.38(b)). Zn_3N_2 layer is grown at a T_s of 423 K, a r_g of 4.5 nm/min, and a working gas composed by 73% of N_2 in Ar, in order to improve μ (~ 100 cm^2/V·s). During the same sputtering process, a 20-nm thick ZnO cap-layer is deposited atop the Zn_3N_2 layer in order to prevent surface oxidation (figure 5.38(c)). The channel layer is patterned by photolithography and chemical etching to open a window on the source and drain contacts. The *W* is 124 μm whereas *W*/*L* ratios equal to 7.75, 15.5, 31, and 62 are defined by varying *L*. A top-view image of the resultant device is shown in figure 5.38(d).

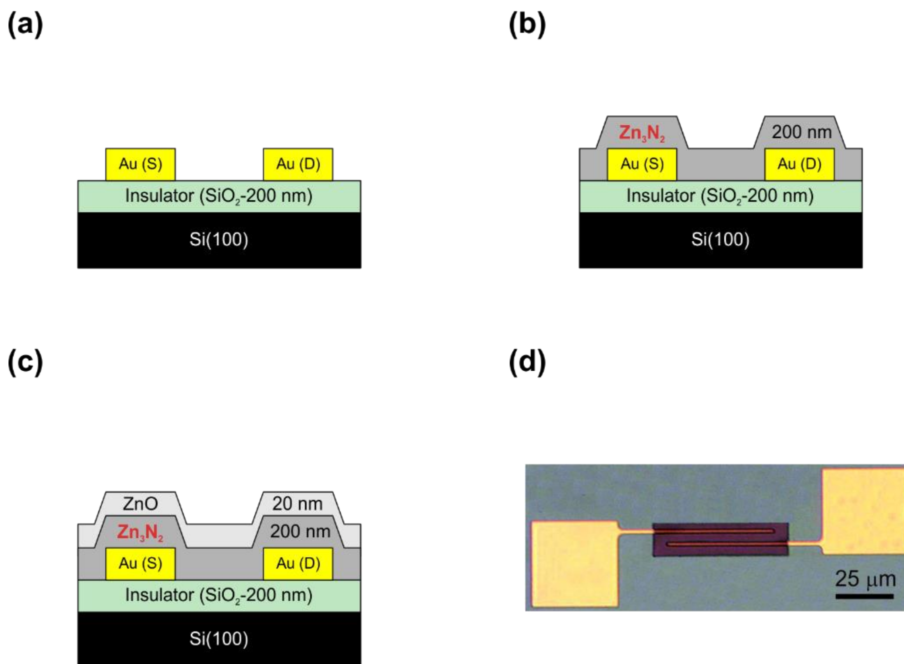

Figure 5.38. (a-c) Fabrication steps of the photo-transistor; (d) optical microscope top-view image.

Device Characterization

I_D/V_{DS} characteristics of a photo-transistor with a *L* of 16 μm measured in dark and VIS light illumination are shown in figure 5.39(a). The study shows linear regions at negative and positive biased voltages, indicating the low resistance of both Au drain/source contacts as a result of the high carrier concentration in zinc nitride layers which enhances the formation of good ohmic contacts and reduces the current crowding effect.

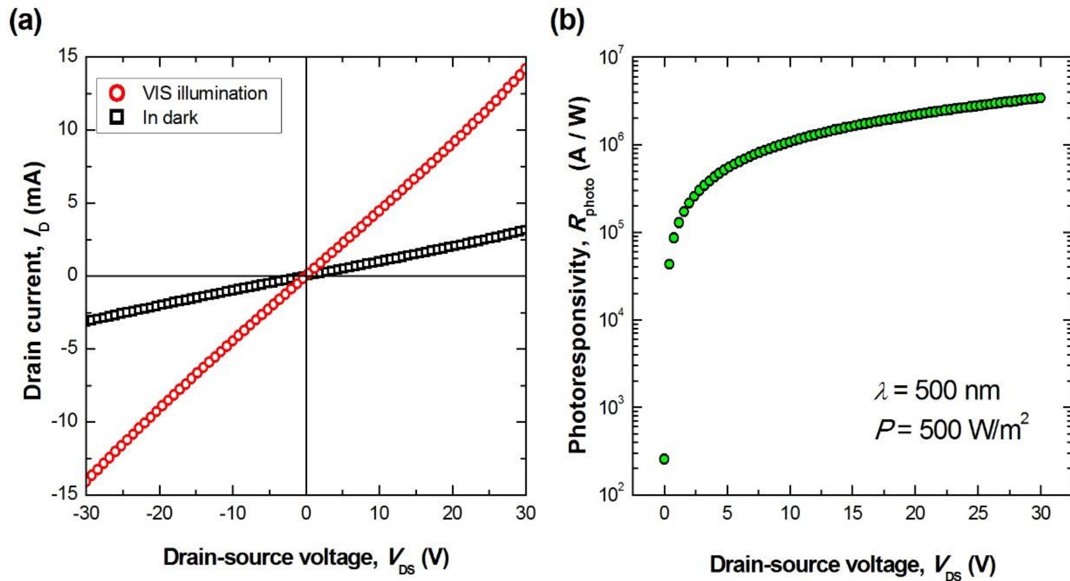

Figure 5.39. (a) I_D/V_{DS} characteristics of zinc nitride photo-transistor measured in dark and under VIS illumination; (b) photo-transistor R_{photo} vs V_{DS}.

Under VIS light illumination (λ = 500 nm and P = 500 W/m^2), I_D increases by a factor of six with respect to the dark level. The R_{photo} is calculated using equation (5.7) and represented as a function of V_{DS} (figure 5.39(b)). From that figure, one can observe an increase of R_{photo} with V_{DS} up to saturate. At high V_{DS} of 30 V, R_{photo} reaches values around 3.5×10^6 A/W, improving the R_{photo} shown by bottom-gate TFTs at similar V_{DS} (figure 5.37). This enhancement of the R_{photo} can be originated by two main factors:

i) the reduction of the transistor dimensions, leading to the reduction of device active area;

ii) the growth of zinc nitride under optimized conditions, leading to the increase of the I_{photo}.

CONCLUSIONS

In this work, zinc nitride layers have been grown by means of rf-magnetron sputtering system using a Zn target and N_2 as working gas. Nitride layers were grown under different conditions of T_s (298-523 K), rf-power (25-200 W), total gas flow (10-30 sccm), and N_2/Ar gas concentration (10 and 100%). Resultant properties of zinc nitride layers were analyzed as a function of these growth parameters by techniques such as IBA, SEM, XRD, spectrophotometry, SE, and Hall effect measurements.

The compositional study of zinc nitride layers grown under different r_g shows the successful growth of stoichiometric Zn_3N_2 for $r_g > 50$ nm/min which are obtained using rf-powers of 200 W at any T_s. RBS analysis also demonstrates the formation of a ZnO surface layer on top of the Zn_3N_2 whose thickness increases over time. In addition, RBS spectra show a smooth transition between ZnO and Zn_3N_2 RBS signals, revealing an intermediate ternary composition ($Zn_xN_yO_z$) along the region between both compounds.

Morphological study of zinc nitride layers grown at different T_s shows an increase of both the grain and grain-to-grain disorientation with T_s, which are suggested to be the main factors limiting the electrical conduction through the layer. XRD study confirms that resultant zinc nitride layers are polycrystalline and also shows that Zn_3N_2 crystallizes in a cubic antibixbyte structure. Their grains seem to be vertically oriented at low T_s, showing a preferential orientation along the <400> direction. In addition, it was observed a reduction of the resultant lattice constant as T_s increases which is mainly attributed to the mismatch between the thermal expansion coefficient of the substrate and the nitride film. The metastable behavior of Zn_3N_2 stored in ambient air leads to its complete oxidation, forming a ZnO layer whose structure was analyzed by XRD, showing polycrystalline structure and no evidences of Zn_3N_2 traces.

The E_g of zinc nitride layers grown at different T_s was analyzed by transmission spectrophotometry. Results show direct band gap type and a transmission edge that shifts towards lower energies as T_s increases; the latter is associated to changes in the resultant crystalline structure obtained using different T_s. Furthermore, the oxidation of the nitride layer when it is exposed to ambient air can also shift the absorption edge towards higher energies mainly due to the formation of regions with an intermediate ternary composition ($Zn_xN_yO_z$).

Optical constants n and k of zinc nitride were calculated to be 2.4±0.4 and 0.8±0.2, respectively, by SE. These measurements detect the formation of ZnO atop the Zn_3N_2 and allow us to estimate oxidation rates of 36 and 20 nm/min for nitride samples grown at T_s = 298 and 473 K, respectively.

Electrical properties of zinc nitride layers were analyzed by Hall measurements. Results showed maximum μ and ρ minimum values for nitride samples grown at T_s = 423 K. It was observed that lower T_s result in lower μ mainly due to the grain size reduction; on the other hand, higher T_s also show lower μ because of the effect of grain-to-grain disorientation. Furthermore, the value of ρ obtained at T_s = 423 K is around 10^{-3} Ω·cm which is the lowest value ever reported in the literature for zinc nitride layers. Measured values of ρ and μ increase whereas n_{Hall} decreases as r_g decreases. These results can be related to the unintentional incorporation of O for low r_g, leading to changes in the crystalline structure. The lowest r_g produces the

enhancement of μ up to record values of 100 $cm^2/V \cdot s$. These μ values are in the same range than those observed in materials commonly used in optoelectronic devices such as p-Si.

Zn_3N_2 layers were patterned using electrical discharge lithography through a micrometric tip. The study reveals that areas scanned at low voltages present a lower resistivity due to the removal of the native oxide. At larger voltages, arc discharge produces deep trenches with high electrical resistance properties. Periodic Zn-rich micro-droplets are obtained at the scan edges as residues of the sublimation process. Through the compositional study using IBA techniques, it is concluded that the treatment also induces strong compositional changes at the central part of the scan yielding ZnO:N submicron structures from the Zn_3N_2 crystal grains. These properties make the technique a useful tool for the reduction of contact resistivity in Zn_3N_2 surfaces, the insulation of Zn_3N_2 TFTs in two-dimensional arrays, and its use in the preparation of advanced ZnO nanostructures for optoelectronic applications. From the optical point of view, the transformation process is also attractive as optical data storage technique since it enables the definition of VIS transparent ZnO windows in opaque Zn_3N_2 layers.

In this work, bottom-gate TFTs and photo-transistors based on Zn_3N_2 as channel layer were successfully designed, fabricated by photolithography. Bottom-gate TFT output characteristics showed transistors characteristics in n-channel enhancement mode without need of annealing process. In addition, the drain current was sensitive to the IR/VIS light illumination, showing increasing photosensitivity with V_{GS}. Photo-transistors were fully fabricated by photolithography; resultant transistors presented high R_{photo} up to 3.5×10^6 A/W at V_{DS} = 30 V.

REFERENCES

[1] C. García Núñez, J. L. Pau, M. J. Hernández, M. Cervera, E. Ruíz, and J. Piqueras, "Influence of air exposure on the compositional nature of Zn 3 N 2 thin films," *Thin Solid Films,* vol. 522, pp. 208-211, 2012.

[2] C. García Núñez, J. Jiménez-Trillo, M. García Vélez, J. Piqueras, J. L. Pau, C. Coya*, et al.*, "Sub-micron ZnO: N particles fabricated by low voltage electrical discharge lithography on Zn 3 N 2 sputtered films," *Applied Surface Science,* vol. 285, pp. 783-788, 2013.

[3] C. García Núñez, J. L. Pau, M. J. Hernández, M. Cervera, and J. Piqueras, "On the true optical properties of zinc nitride," *Applied Physics Letters,* vol. 99, p. 232112, 2011.

[4] C. García Núñez, J. L. Pau, M. J. Hernández, M. Cervera, E. Ruiz, and J. Piqueras, "On the zinc nitride properties and the unintentional incorporation of oxygen," *Thin Solid Films,* vol. 520, pp. 1924-1929, 2012.

[5] C. García Núñez, J. L. Pau, E. Ruíz, and J. Piqueras, "Thin film transistors based on zinc nitride as a channel layer for optoelectronic devices," *Applied Physics Letters,* vol. 101, p. 253501, 2012.

[6] T. Yang, Z. Zhang, Y. Li, M. Lv, S. Song, Z. Wu*, et al.*, "Structural and optical properties of zinc nitride films prepared by rf magnetron sputtering," *Applied Surface Science,* vol. 255, pp. 3544-3547, 2009.

[7] M. Futsuhara, K. Yoshioka, and O. Takai, "Structural, electrical and optical properties of zinc nitride thin films prepared by reactive rf magnetron sputtering," *Thin Solid Films,* vol. 322, pp. 274-281, 1998.

[8] F. Zong, H. Ma, W. Du, J. Ma, X. Zhang, H. Xiao*, et al.*, "Optical band gap of zinc nitride films prepared on quartz substrates from a zinc nitride target by reactive rf magnetron sputtering," *Applied surface science,* vol. 252, pp. 7983-7986, 2006.

[9] T. Suda and K. Kakishita, "Band-gap energy and electron effective mass of polycrystalline Zn3N2," *Journal of Applied Physics,* vol. 99, p. 076101, 2006.

[10] K. Toyoura, H. Tsujimura, T. Goto, K. Hachiya, R. Hagiwara, and Y. Ito, "Optical properties of zinc nitride formed by molten salt electrochemical process," *Thin Solid Films,* vol. 492, pp. 88-92, 2005.

[11] G. Xing, D. Wang, B. Yao, L. Qune, T. Yang, Q. He*, et al.*, "Structural and electrical characteristics of high quality (100) orientated-Zn 3 N 2 thin films grown by radio-frequency magnetron sputtering," *Journal of Applied Physics,* vol. 108, pp. 083710-083710-5, 2010.

[12] W. L. Bragg, *The Crystalline State,* vol. 1, p. 189, 1946.

[13] R. Long, Y. Dai, L. Yu, M. Guo, and B. Huang, "Structural, electronic, and optical properties of oxygen defects in Zn3N2," *The Journal of Physical Chemistry B,* vol. 111, pp. 3379-3383, 2007.

[14] K. Kuriyama, Y. Takahashi, and F. Sunohara, "Optical band gap of Zn 3 N 2 films," *Physical Review B,* vol. 48, p. 2781, 1993.

[15] J. Tauc, "Optical properties of amorphous semiconductors," in *Amorphous and Liquid Semiconductors*, ed: Springer, 1974, pp. 159-220.

[16] R. Ayouchi, C. Casteleiro, L. Santos, and R. Schwarz, "RF-plasma assisted PLD growth of Zn3N2 thin films," *physica status solidi (c),* vol. 7, pp. 2294-2297, 2010.

[17] D. A. G. Bruggeman, *Ann. Phys.,* vol. 24, p. 636, 1935.

[18] O. S. Heavens, *Optical properties of thin solid films*: Courier Corporation, 1991.

[19] L. van der PAUYV, "A method of measuring specific resistivity and Hall effect of discs of arbitrary shape," *Philips Res. Rep.,* vol. 13, pp. 1-9, 1958.

[20] C. M. Caskey, R. M. Richards, D. S. Ginley, and A. Zakutayev, "Thin film synthesis and properties of copper nitride, a metastable semiconductor," *Materials Horizons,* vol. 1, pp. 424-430, 2014.

[21] A. Gangadhar, M. Shunmugam, and P. Philip, "Surface modification in electrodischarge processing with a powder compact tool electrode," *Wear,* vol. 143, pp. 45-55, 1991.

[22] Y. Tsunekawa, M. Okumiya, N. Mohri, and I. Takahashi, "Surface modification of aluminum by electrical discharge alloying," *Materials Science and Engineering: A,* vol. 174, pp. 193-198, 1994.

[23] Y.-F. Chen, H.-M. Chow, Y.-C. Lin, and C.-T. Lin, "Surface modification using semi-sintered electrodes on electrical discharge machining," *The International Journal of Advanced Manufacturing Technology,* vol. 36, pp. 490-500, 2008.

[24] S. Kumar, R. Singh, T. Singh, and B. Sethi, "Surface modification by electrical discharge machining: A review," *Journal of Materials Processing Technology,* vol. 209, pp. 3675-3687, 2009.

[25] J. M. Mativetsky, E. Treossi, E. Orgiu, M. Melucci, G. P. Veronese, P. Samorì*, et al.*, "Local current mapping and patterning of reduced graphene oxide," *Journal of the American Chemical Society,* vol. 132, pp. 14130-14136, 2010.

[26] P. G. Slade and E. D. Taylor, "Electrical breakdown in atmospheric air between closely spaced (0.2 μm-40 μm) electrical contacts," *Components and Packaging Technologies, IEEE Transactions on,* vol. 25, pp. 390-396, 2002.

[27] P. Muzykov, X. Ma, and T. Sudarshan, "Prebreakdown and breakdown investigation of needle-plane vacuum gaps in the micron/submicron regime," *Journal of Vacuum Science & Technology B,* vol. 18, pp. 1222-1226, 2000.

[28] D. B. Go and D. A. Pohlman, "A mathematical model of the modified Paschen's curve for breakdown in microscale gaps," *Journal of Applied physics,* vol. 107, p. 103303, 2010.

[29] J. Jiménez-Trillo, A. L. Alvarez, C. Coya, E. Céspedes, and A. Espinosa, "The use of arc-erosion as a patterning technique for transparent conductive materials," *Thin Solid Films,* vol. 520, pp. 1318-1322, 2011.

[30] E. Hourdakis, B. J. Simonds, and N. M. Zimmerman, "Submicron gap capacitor for measurement of breakdown voltage in air," *Review of scientific instruments,* vol. 77, pp. 034702-034702-4, 2006.

[31] M. Radmilović-Radjenović and B. Radjenović, "An analytical relation describing the dramatic reduction of the breakdown voltage for the microgap devices," *EPL (Europhysics Letters),* vol. 83, p. 25001, 2008.

[32] J. Jiménez-Trillo, Á. L. Álvarez, and C. Coya, "Solution-processed organic devices developed by a novel cost-effective patterning technique based on electrical erosion," *Proceeding 8th Spanish Conference on Electron Devices,* vol. 5744162, 2011.

[33] E. Aperathitis, V. Kambilafka, and M. Modreanu, "Properties of n-type ZnN thin films as channel for transparent thin film transistors," *Thin Solid Films,* vol. 518, pp. 1036-1039, 2009.

[34] H.-H. Hsieh and C.-C. Wu, "Amorphous ZnO transparent thin-film transistors fabricated by fully lithographic and etching processes," *Applied physics letters,* vol. 91, p. 013502, 2007.

[35] R. Chen, W. Zhou, and H. S. Kwok, "Top-gate thin-film transistors based on GaN channel layer," *Applied Physics Letters,* vol. 100, p. 022111, 2012.

6. Zinc Oxide Nanowires

Growth kinetics of ZnO NWs synthesized by CVT are studied as a function of the growth conditions (temperature, gas flux, gas composition, etc.). The growth of these NWs has been carried out in the CVT system available in the Microelectronics Laboratory (UAM). Resultant NWs are characterized by different techniques such as SEM, XRD, spectrophotometry, and PL [1]. Additionally, vertically aligned ZnO NWs grown on sapphire substrates in the CVT system belonging to The University of Alabama, have been analyzed, in that university, by different techniques such as SEM, Raman spectroscopy, and PL, and in the CMAM and SIDI facilities (UAM) by techniques such as XRD and IBA techniques; the latter allowing to obtain magnitudes such as NW tilt angle and surface density [1].

Different methods are developed here to integrate ZnO NWs in devices [2]. DEP is highlighted among all the assembling techniques used in this work because it allows to assemble ZnO NWs, connecting a pair of conductive electrodes. The assembling efficiency, and the control over the number and dimensions of assembled NWs, are analyzed as function of the DEP conditions [3].

The possibility to grow ZnO NWs with different aspect ratios in CVT, along with the effective manipulation of NWs by DEP, make possible the study of the optoelectronic properties (I/V characteristics, R_{photo}, time response, etc.) of single ZnO NWs as a function of their diameter [3].

Surface properties and electrical characteristics of ZnO NWs are also studied by different techniques (XPS, contact angle measurements, CPD, SPV, AFM, and photoresponse measurements) after surface treatments, including hydroxylation and silanization [4]. The functionalization process and characterization of the ZnO NWs have been carried out at the Walter Schottky Institute (Munich).

6.1. Synthesis of ZnO NWs by CVT

In this work, ZnO NWs are grown by using a CVT system which consists of a Tempress furnace with a quartz tube inside (see a thorough description of the CVT system in chapter 3, section 3.2). Briefly, the growth of ZnO NWs by CVT consists in the evaporation of a Zn solid source at high temperatures (typically above 450 ºC, depending on the Zn source), forming a Zn(g) which is transported by means of a carrier gas towards a condensation region (where the temperature is lower than the evaporation region). In the condensation region, Zn(g) is condensed forming Zn(l), and reacting with the oxidizing ambient, forming ZnO(s). Resultant solid product can form different nanostructures, including NWs [5], nanobelts [6], and TPs [7].

During a CVT process, the reaction can also occur in the gas ambient, i.e. $Zn(g)+1/2O_2(g)\rightarrow ZnO(s)$, and a good proof of that is the whitish product obtained not only on the substrate surface but also covering the inner sidewalls of the quartz tube.

Different Zn based powders have been used in this research: 1) micro-sized Zn powder and 2) nano-sized ZnO powder, both powders having a purity of 99.999%. The temperature of the evaporation region necessary to obtain Zn(g) strongly depends on the powder used namely, dimension and composition. In the case of Zn powder, direct thermal evaporation occurs at temperatures above 450 ºC (figure 3.7); in this work, CVT process carried out with Zn powder is typically performed at temperatures ranged between 700 and 900 ºC, in order to ensure enough Zn vapor pressure (figure 3.7). On the other hand, carbo-thermal reduction of ZnO powder using carbon (equations 2.3-2.7) is successfully carried out at temperatures above 900 ºC.

CVT allows to control NW morphology (length and diameter), NW surface density (also called NW surface coverage) and NW tilt angle by means of growth parameters such as temperature, total gas flux, gas composition, ZnO/C powder ratio, and type of substrate. In this regard, ZnO characteristics (morphology, crystalline structure, composition, …) were analyzed as function of the growth conditions. Results obtained from these characterizations are recorded in section 6.2.

6.1.1. Growth of ZnO TPs

ZnO obtained from a self-assisted process commonly tends to form TPs [7, 8]. It is believed that ZnO TPs growth is governed by the VS mechanism (figure 2.2) rather than VLS (figure 2.4) because their growth is not assisted by foreign liquid elements.

The nucleation and growth mechanism of ZnO TPs is still unclear. All existing models describe the growth mechanism of the ZnO TPs out of a seed nucleus [9-11]. The main difference between these models is the shape, geometry, and crystallographic structure of the nuclei which are subsequently overgrown during the growth process along fast growing planes. Although these TPs are ideally symmetric, some studies present SEM images [9], pointing out differences for angles formed between each two TP legs. These angles take values around 110º and are strongly influenced by the growth rate of each TP leg which can change during the growth process.

In this work, the growth of ZnO TPs is carried out using pure Zn solid powder as Zn source. A total powder mass of 0.5 g is transferred to a ceramic crucible, placed at the evaporation zone of the CVT system, while a Si(100) substrate is loaded at the substrate holder placed in the condensation region (see system description in chapter 3, section 3.2). This substrate is previously deoxidized in HF-ethanol (10% in volume) for 5 min, rinsed in ethanol and dried in N_2 gas flow, ensuring the full removal of the SiO_x native oxide and possible surface contamination. Once the substrate is transferred to the middle of the furnace, the temperature in that region (evaporation zone) is increased up to values ranged between 700 and 900 ºC, under an Ar flow of 100 sccm in order to prevent the oxidation of Zn powder. After the growth temperature is reached, the O_2 valve is opened for different times (30-180 min), forming an Ar/O_2 gas mixture that reacts with the gaseous Zn species to produce the synthesis of ZnO nanostructures.

After the growth process, a whitish product covers the substrate surface (and also the inner sidewalls of the quartz tube), indicating the successful formation of ZnO nanostructures. Samples grown under different temperatures, Ar/O_2 flux ratios, and times are analyzed by SEM.

Temperature Study

The growth of ZnO TPs is carried out on Si(100) substrates using 100 sccm of Ar, 100 sccm of O_2 for 30 min, and at different temperatures ranged between 700 and 900 ºC. The distance between the Zn source and the Si(100) substrate was around 10 cm. The morphology of the resultant TPs is analyzed by SEM.

Figure 6.1 show three SEM images corresponding to ZnO TPs grown at 700 ºC (a), 800 ºC (b), and 900 ºC (c). From those images, one can extract some conclusions: i) nanostructured ZnO is obtained for temperatures above 700 ºC because growths performed at lower temperatures do not show TP nucleation; ii) the aspect ratio of the TP legs is improved (larger length and narrower diameter) as the temperature increases; iii) the ends of the TP legs reduce their cross-section, forming a tip-shaped end for high temperatures; iv) surface coverage tends to decrease as the temperature increases.

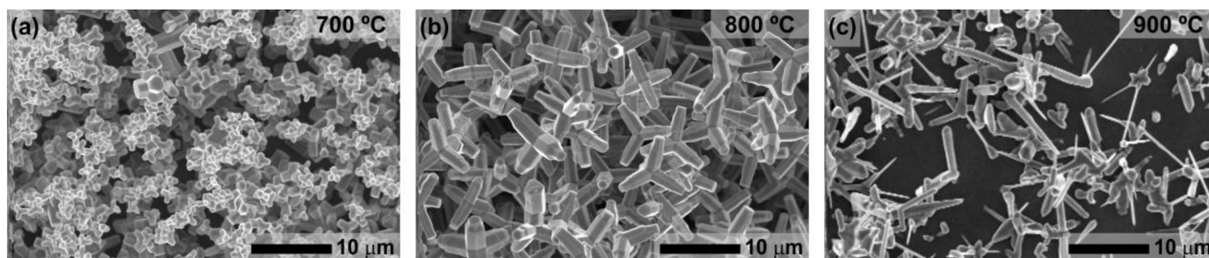

Figure 6.1. ZnO TPs grown at (a) 700, (b) 800, and (c) 900 ºC.

The increase of the growth temperature has been demonstrated to improve the aspect ratio of the TP legs; that has its origin in the increase of the Zn vapor pressure, which promotes the growth of TP legs along four preferential directions. The lack of Zn in the nucleation stage (low growth temperatures), leads to the axial growth of the TP legs.

On the other hand, the reduction of the TP surface coverage can be attributed to the increase of the Zn(g) and O_2(g) diffusion lengths, observing larger areas of the tube sidewalls covered with a lower density of TPs (figure 6.1(c)).

Working Gas Study

The morphology of resultant ZnO TPs is also analyzed as a function of the gas composition and total gas flux. Figure 6.2(a-d) show ZnO TPs grown at 900 ºC for 30 min and under different Ar/O_2 flux ratios. As in the previous study, the separation between the Zn source and the Si(100) substrates was around 10 cm. Using a low Ar flux of 10 sccm to enable the Zn(g) transport from the Zn source towards the Si(100) substrate, and in absence of O_2(g) flux (figure 6.2(a)), it is observed the growth of a high density of twisted and bent nanoneedles; these ZnO based nanostructures can be formed from the unintentional reaction of Zn(g) with O_2(g) impurities existent in the ambient. The low concentration of O_2(g) in the ambient leads to the formation of nanoneedles with a poor crystallinity and whose facets present high surface roughness.

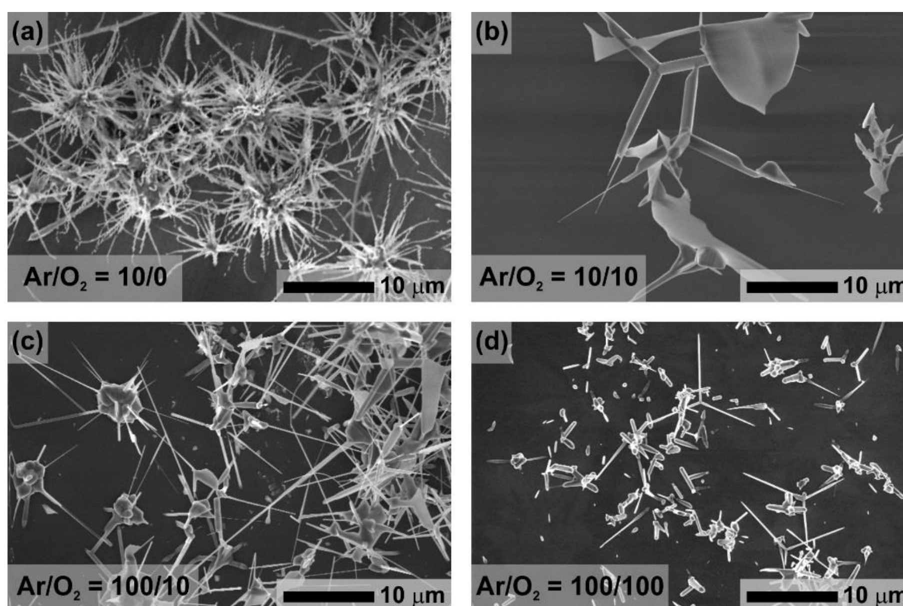

Figure 6.2. ZnO tetrapods grown at 900 ºC for 30 min and different Ar/O_2 flux ratios.

The increase of the total flux up to 20 sccm with an Ar/O_2 flux ratio around 1/1 shows a drastic change of the ZnO morphology (figure 6.2(b)). The SEM image shows the formation of TP-like nanostructures whose legs clearly exhibit two different parts. The base of the leg bonded to the TP cluster is a nanobelt, whereas the leg tip is a nanoneedle.

Increasing the Ar flux up to 100 sccm and using the same O_2 flux of 10 sccm, it is observed a reduction of the nanobelt length along the TP leg (figure 6.2(c)). Finally, for a total gas flux of 200 sccm with an Ar/O_2 flux ratio of 1/1, almost the entire TP legs are composed by nanoneedles.

Using the growth conditions described for figure 6.2(d), ZnO TPs are grown during different times ranged between 30 and 180 min. As shown in figure 6.3, the increase of the growth time leads to the increase both TP surface density and TP leg length, tending to form a TP network.

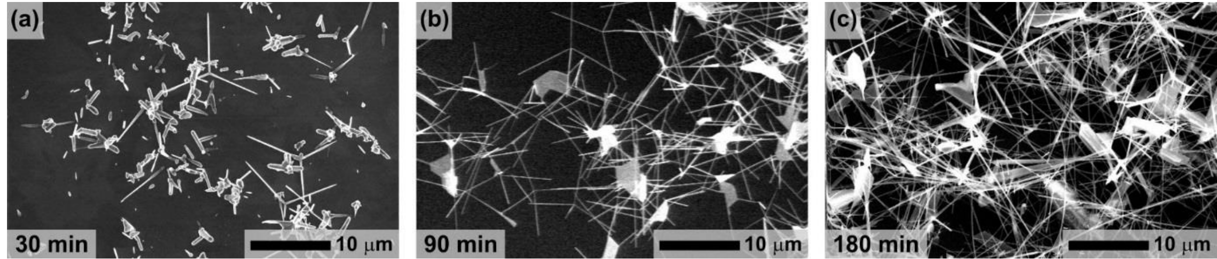

Figure 6.3. SEM images of ZnO TPs grown for (a) 30, (b) 90 and (c) 180 min, at 900 ºC and an Ar/O_2 flux ratio of 1/1.

6.1.2. Growth of Vertically Aligned ZnO NWs

Substrate Preparation

In this study, a Zn seed layer has been deposited on Si(100) substrates in order to assist the growth of ZnO NWs along the substrate normal direction during the CVT process. It is worth noting that the nucleation of ZnO NWs directly on a clean Si(100) substrate was not observed.

The seed layer consists of Zn thin film deposited on a clean Si(100) substrate by rf-magnetron sputtering for 15 s using a Zn target, an Ar flux of 40 sccm, and a rf-power of 25 W. The resultant thickness of the Zn layer was 7 nm as determined by SE.

The Zn/Si(100) substrate is transferred to the CVT system, and annealed at 900 ºC for 1 min in Ar ambient. Figure 6.4 show a top-view SEM image (a) and its corresponding view tilted 10º away the sample normal direction (b). From these SEM images, one can conclude that the annealing process leads to the transformation of the initial Zn layer into Zn nanocrystals with an average diameter of 15±5 nm, and an average separation between crystals around 10 nm. Assuming that each crystal acts as a NW nucleation site, the NW diameter and surface coverage are assumed to be limited by both the initial crystal size and crystal-to-crystal spacing.

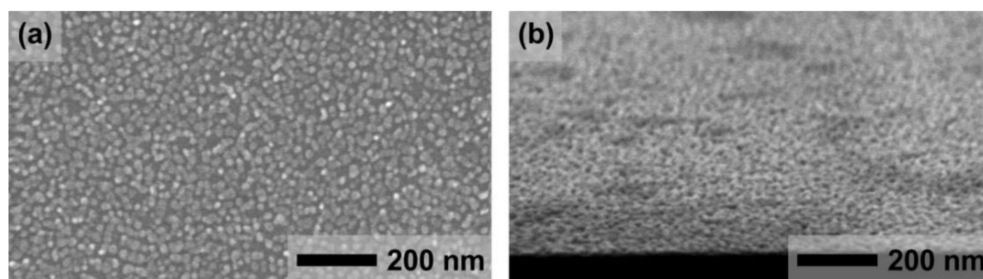

Figure 6.4. (a) top-view and (b) 10º tilted-view SEM images of Zn seed layer annealed at 900 ºC.

ZnO NW Mechanism

The growth of vertically aligned ZnO NWs has been carried out using a 7-nm thick Zn seed layer deposited on a Si(100) substrate. A total mass of 0.5 g of ZnO/C (1/1) powder is transferred to a ceramic crucible which is later placed in the middle of the furnace (evaporation region), while the Zn/Si(100) substrate is placed in the condensation region. The temperature at evaporation region is increased up to 900 °C under a Ar flux of 100 sccm in order to avoid the oxidation of compounds inside the tube, including the Zn layer. At those temperatures, Zn seed layer is transformed into Zn nanocrystals (figure 6.4) whose main role is to trap Zn and O species (preferential nucleation sites) and to assist the vertical NW growth.

After the annealing process, the O_2 valve is opened, supplying an O_2 gas flux of 100 sccm, keeping an Ar carrier gas flux of 100 sccm. NW growth is carried out for 30 minutes; after that, O_2 valve is turned off and furnace temperature is lowered down to RT under an Ar flux of 100 sccm.

Figure 6.5 show the morphological analysis carried out by SEM of resultant ZnO NWs. From these images, one can observe that NWs grow vertically following the (0001)-plane direction of the crystal (figure 6.5(a)), and exhibit diameters between 90 to 870 nm, and average lengths of 10.5 μm. The r_g is then estimated from figure 6.5(a), resulting in a r_g of 350 nm/min.

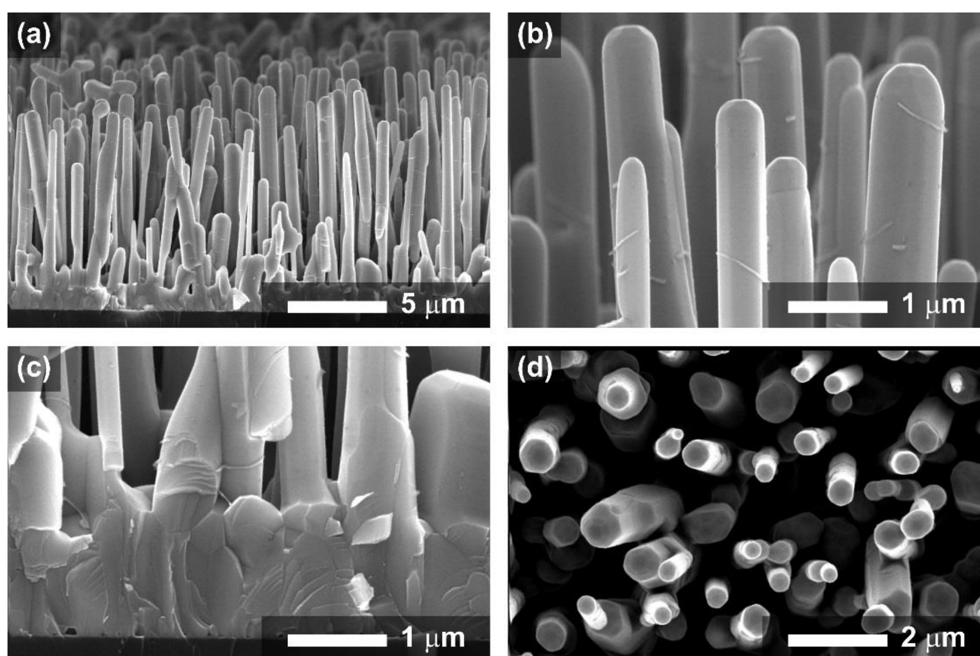

Figure 6.5. Cross sectional SEM images of ZnO NWs: (a) vertical growth, (b) NW ends, and (c) NW bases; (d) top view of a NW sample.

In a bottom-up approach, the growth of ZnO NWs can be explained by means of two different mechanisms: VLS [12] (figure 2.4) and VS [2] (figure 2.2). The former uses a metal seed particle to assist the growth along a preferential direction determined by the substrate crystal orientation; then, the best way to identify a VLS growth is to observe a metal particle on top of the NW end. Analysing our NW ends (figure 6.5(b)), the absence of that metal particle suggests that NWs have grown via VS mechanism rather than VLS.

VS growth mechanism of ZnO NWs consists in different steps described through the carbo-thermal equations 2.3-2.7. First, Zn(g) evaporated from the carbothermal-reduction of ZnO/C(s) powder, reacts with O_2(g), forming ZnO molecules or clusters, which will be deposited preferentially on the Zn nanocrystals pre-fabricated on the Si(100) substrate (figure 6.5(c)); comparing the initial density of Zn nanocrystals (figure 6.4) with the resultant ZnO NW surface density (figure 6.5(d)), one can conclude that approximately every Zn nanocrystal produces a ZnO NW. This top-view image also shows NWs with a hexagonal footprint.

In contrast to the NWs obtained from TPs, NWs grown from the Zn seed layer exhibit larger diameters and much lower aspect ratios (10-15). However, the morphology of vertically aligned NWs allows for the planarization procedure to their direct integration in nanodevices, taking advantage of the conductive substrate, such as previously carried out in the past [13].

Vertically aligned ZnO NWs were grown during different growth times under the same conditions described for NWs presented in figure 6.5. NWs grown for 1 h are still aligned vertically to the substrate surface (figure 6.6(a)), showing average NW lengths of around 20 μm, confirming the growth rate of 350 nm/min estimated from NWs grown during 30 min. The increase of the growth time (figure 6.6(b) and (c)) exhibits the formation of ZnO NWs networks, consisting of NWs totally disoriented and with giant lengths up to 100 μm and broad dispersion of the average NW diameter.

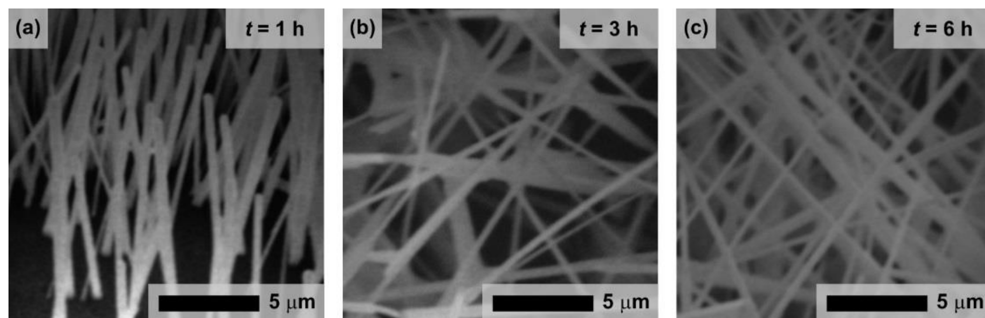

Figure 6.6. SEM images of ZnO NWs grown by CVT for different times. Images are tilted 45° away the substrate surface.

The Zn seed layer thickness has been observed to be critical for the successful growth of ZnO NWs. In this regard, the use of larger thicknesses was observed to inhibit the ZnO NW nucleation. Figure 6.7(a) shows a SEM image of resultant sample morphology after a CVT process carried out under the same conditions that those used in figure 6.5 sample. This seed layer leads to obtain polycrystalline morphologies. Similar results have been obtained using a seed layer of ZnO with a thickness of 9 nm (figure 6.7(b)).

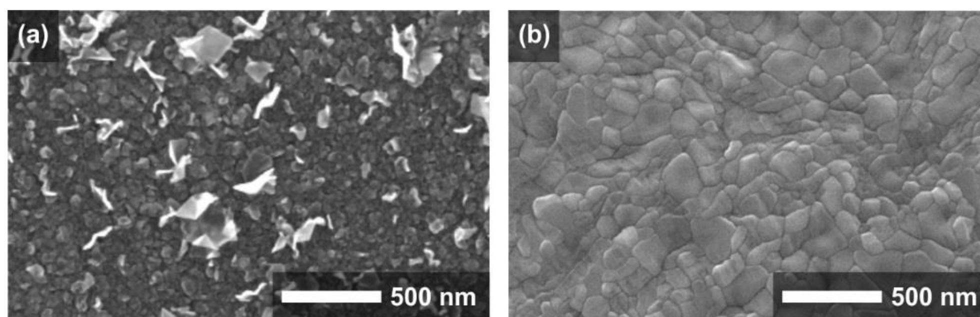

Figure 6.7. Top-view SEM images of (a) Zn (14 nm) and (b) ZnO (9 nm) seed layers annealed at 900 ºC.

6.1.3. Growth of ZnO NWs with Al/ZnO/C Powder

Figure 6.8 shows a comparison of the resultant NWs grown with a ZnO/C mass of 0.5 g (0.25/0.25), and Al masses of 0.01 (a), 0.03 (b), and 0.06 g (c). From these SEM images, the effect of Al on the growth kinetics of ZnO is demonstrated to have a strong influence on the resultant NW morphology.

The effect of the small amount of Al in the powder mixture (0.01 g) on the ZnO morphology, shows an improvement of the hexagonal-shape facets, reduces the NW diameter range (30-90 nm), keeps the same growth rate obtained in ZnO NWs (r_g = 355 nm/min), and exhibits similar surface coverages (figure 6.5(c)).

The use of Al mass above 0.01 g hinders the nucleation of NWs, showing a decrease of the NW longitudinal growth at expenses of promoting the lateral growth (figure 6.8(b) and (c)). In this scenario, Al might act as an O getter, reducing the effective incorporation of O to the growth process.

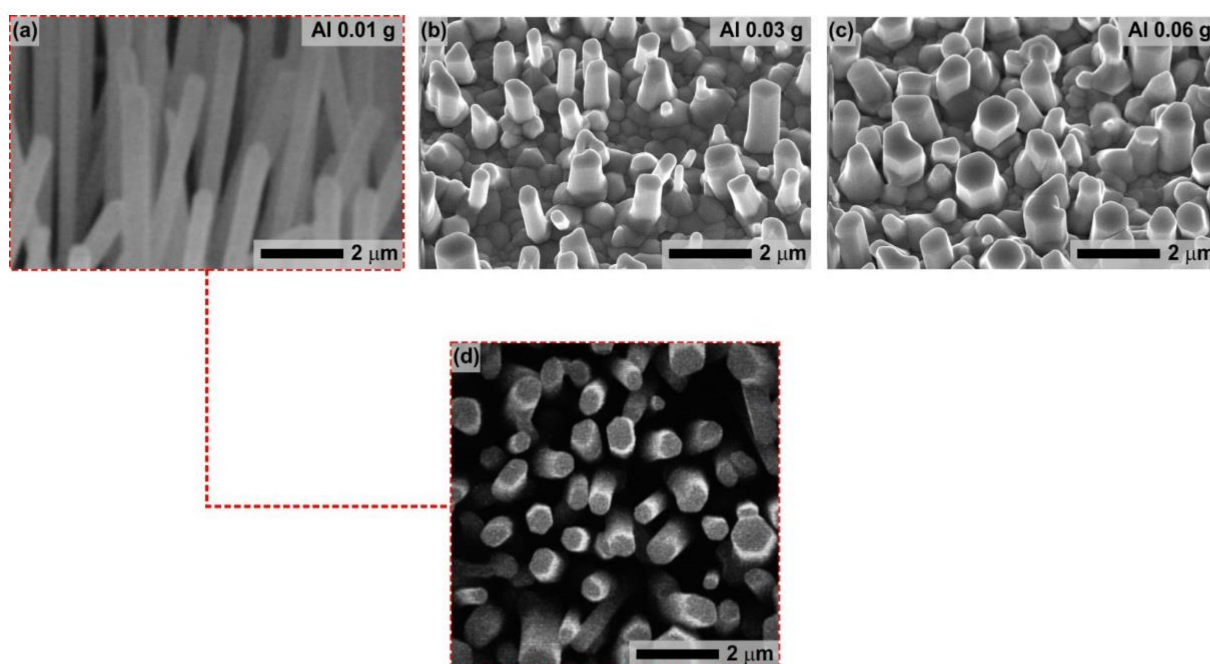

Figure 6.8. ZnO NWs grown by CVT using different Al powder masses.

6.2. Characterization of ZnO NWs

6.2.1. Optical Analysis

Transmission Spectrophotometry

Optical absorption of ZnO NWs is analyzed by means of transmission spectrophotometry. The sample with vertically aligned ZnO NWs described in section 6.1.2 is dipped in ethanol and sonicated for a few seconds to prepare a homogeneous suspension of NWs. Some droplets of the resultant NW solution are extracted and drop-casted on a clean quartz substrate rotating at 100 rpm in order to improve the uniformity of NW surface coverage along the quartz substrate surface.

Once the solvent is totally evaporated, optical absorption of this sample is measured in transmission mode. Figure 6.9 shows the optical absorbance of this sample as a function of the photon wavelength (λ), observing an abrupt absorption edge around a wavelength of 379 nm (E = 3.27 eV). This result points out the high absorption of ZnO NWs in the UV region and their VIS transparent properties. The transmission curve also shows a light absorption at $\lambda > 380$ nm which might be related to the light scattered from ZnO NWs.

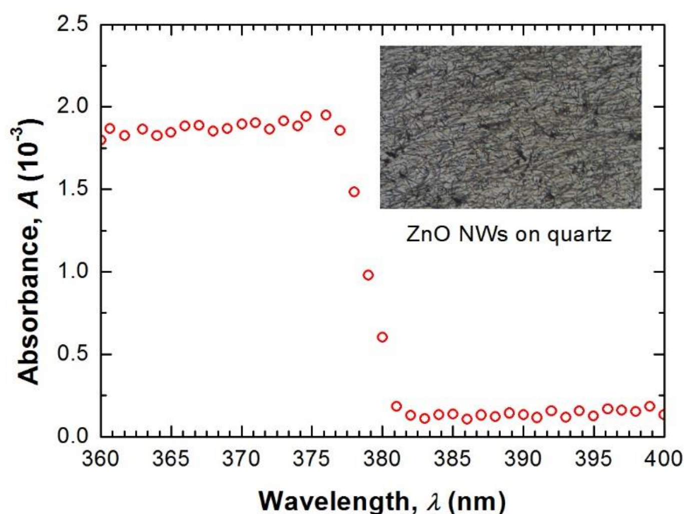

Figure 6.9. Optical absorbance of ZnO NWs dispersed on quartz. Inset: optical microscope image.

Photoluminescence

Characteristic emission peaks of as-grown ZnO NWs vertically aligned on the Si(100) substrate (section 6.2.2) are analyzed by means of micro- PL at RT. A laser power of 300 mW and a λ of 266 nm are used along with a monochromator, including a 2400 BLZ-HUV grating and an output slit width of 50 µm (see system description in chapter 4, section 4.7.3). During the measurement, the laser beam impinges perpendicularly to the sample surface, and parallel to the NW preferential orientation <0001>, through a

LMU(UV) 40× objective. PL peak intensity is analyzed as a function of the laser power, and the distance from the focal point of the laser beam to the substrate surface.

PL spectra of ZnO NWs measured at different excitation laser powers, exhibit an abrupt peak around $\lambda = 375$ nm and a broad band ranged between $425 < \lambda < 650$ nm (figure 6.10). The former is associated to a band-edge emission, while the latter is typically attributed to deep level emission [14-18]. The origin of the deep level emission is still unclear and has been associated to different defects formed in the ZnO structure during the growth process, comprising O antisites [14], O vacancies [15], Zn vacancies [16], interstitial Zn [17], and transitions between interstitial Zn and Zn vacancies [18]. From these articles, one may expect that various recombination centers can be involved in this emission of ZnO.

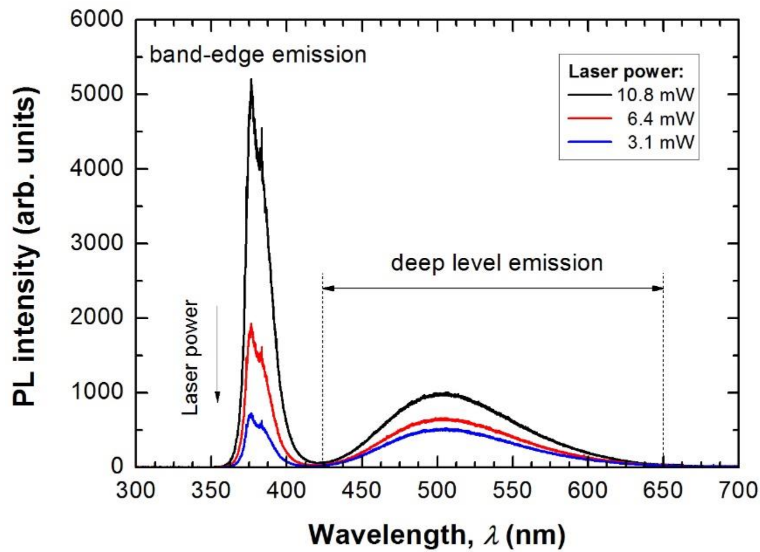

Figure 6.10. PL emission peaks of ZnO NWs measured at different laser powers.

It is well established that the PL intensity (I) increases with laser power (P) as [19, 20]:

$$I \sim P^k \tag{6.1}$$

According to the previous studies, if the excitation energy is higher than the band gap, the power factor k in equation (6.1) falls into one of the following ranges. It is in the range $1<k<2$ for the bound-exciton emission, and it is in the range $0<k<1$ for the free-to-bound radiative recombination.

The I calculated from the area under both peaks shown in figure 6.10, is represented as a function of the P (figure 6.11). From figure 6.11, one can observe that band-edge emission presents a superlinear behaviour, showing a k of 1.82 similar than that obtained in ZnO nanocrystals (k = 1.85) at $0.1<P<0.4$ mW [21]. From this result, the observed band-edge emission could be associated to a bound-exciton emission, however the low number of points used to fit to the equation (6.1) is not enough to confirm that recombination type.

Figure 6.11 also shows the dependence of I for the deep level emission as a function of P. Using equation (6.1), k is estimated to be 0.56, suggesting a sublinear behaviour. In this scenario, the number of defects could be insufficient to enable the recombination of excited electrons, showing a saturation of I. It is worth noting that the low number of points used to fit to equation (6.1) is insufficient to confirm the obtained value of k.

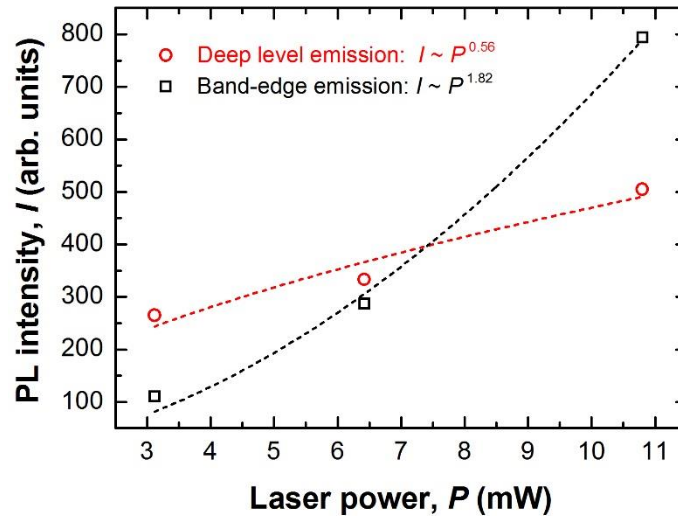

Figure 6.11. PL intensity of band-edge and deep level emission peaks vs. laser power.

Both emission peaks are also studied as a function of the distance from the focal point of the laser beam to the Si(100) surface (figure 6.12(a)). The microscope used to guide the laser beam towards the sample surface, has a camera which allows to observe the PL emission of the sample (figure 6.12(a)).

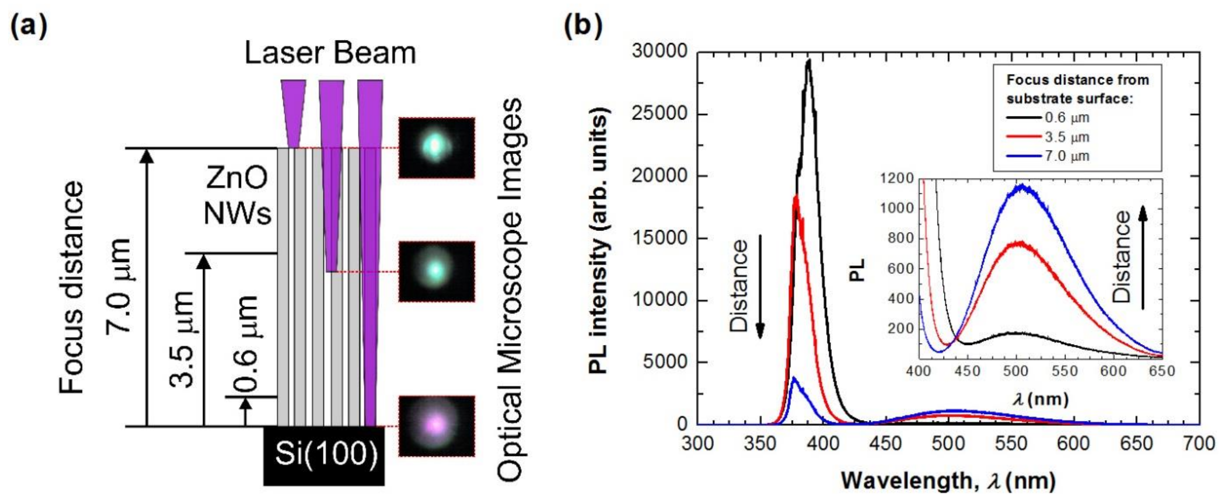

Figure 6.12. (a) Sketch of the experimental conditions used in the micro-PL studies and optical images taken from different regions excited along the NW body; (b) PL spectra measured at different focus distances from the Si(100) substrate.

The analysis is carried out by measuring the PL of the NWs at different heights. For that purpose, the sample is mounted in flat position on the platform of the microscope system, enabling to move the sample along x, y, and z directions with a spatial accuracy of 0.1 μm. The laser spot is initially focused on the Si(100) substrate surface, observing a pink color emission which cannot be associated to the ZnO compound. This pink emission is used as the reference height; then, the laser focus distance is increased using a z-axis micro-positioner, obtaining a uniform greenish emission, indicating that the laser is successfully irradiating NWs body. For further focus distances, the greenish emission exhibits brighter green spots when the laser is focused on top of the NW ends. This calibration procedure of the distance with respect to the Si(100) substrate surface, allows to study the PL intensity along the NW body.

Figure 6.12(b) contains the measurements performed at 0.6, 3.5 and 7.0 μm distances over the Si(100) surface. Vertical resolution associated to this technique is around 1 μm, which means photoemission is obtained from a region of 1-μm length around the focus height. From that figure, one can conclude that the band-edge emission peak located at the UV range increases as the distance to the substrate decreases. In contrast, the intensity of the deep-level band increases as the laser excite the top part of the NWs. This result suggests that the distribution of defects may not be uniform along the NWs.

6.2.2. Compositional Analysis

Growth Conditions

Vertically aligned ZnO NWs grown on sapphire substrates are characterized by means of a combination of IBA techniques. Samples were grown by Prof. Kung et al. [22] using the CVT system available at The University of Alabama.

Briefly, ZnO NWs growth is performed in a horizontal quartz tube furnace via a carbothermal reduction of ZnO powder and in an oxidizing ambient. Zn source consists of a ZnO/C powder mixture with a 1/2 mass ratio and a total mass of 1.5 g. The substrate is a *c*-plane sapphire covered with a ZnO seed layer; the specific deposition procedure of this ZnO layer is described elsewhere [23].

NWs are grown at different pressures of 0.67 and 1 atm, as measured by a pressure gauge placed at an equivalent sample position during a calibration stage. In this regard, NWs grown at 0.67 and 1 atm are identified here as low pressure (LP) and high pressure (HP), respectively. Both LP and HP processes are carried out under a constant Ar/O_2 gas flux of 46.86 sccm, consisting of only 2% of O_2 diluted in Ar.

Morphological Characterization

The use of different growth pressures allows to control resultant NW morphology; morphological characteristics of resultant NWs are analyzed by means of SEM (figure 6.13), including NW average diameter (d_{NW}) and length, NW density (defined as de number of NWs per area units).

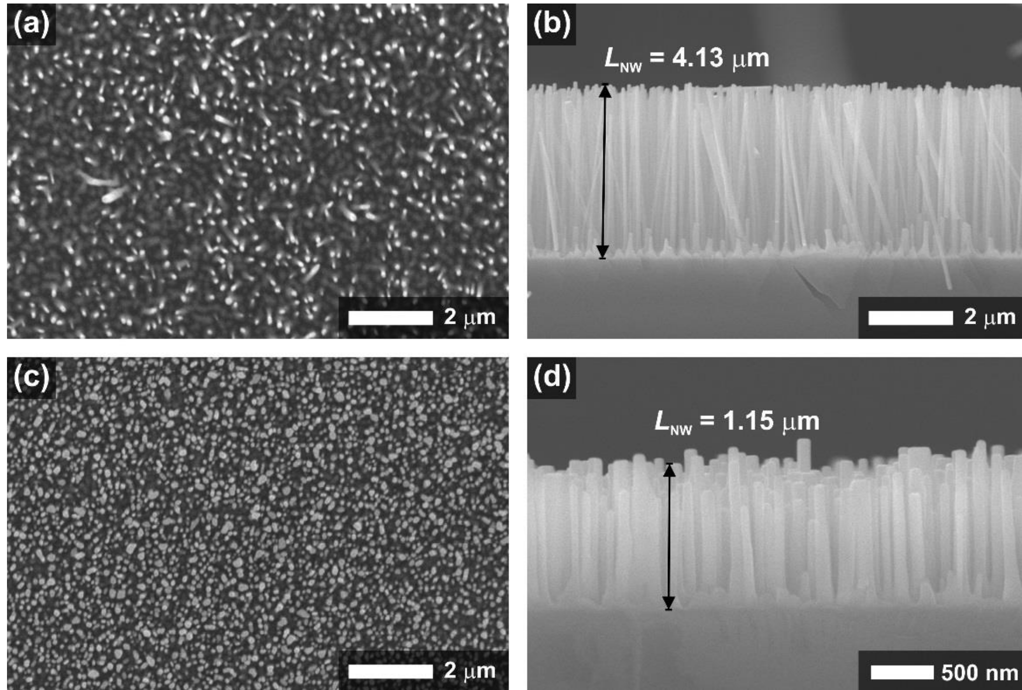

Figure 6.13. SEM images of (a,b) HP and (c,d) LP ZnO NW samples. (a,c) are top-views and (b,d) are cross-section views.

SEM images taken at 0º with respect to the sample surface (figure 6.13(a,c)), i.e. the electron beam is aligned to the NW edge, are used to estimate the average NW diameter and the surface coverage. The former is calculated taking into account the diameter of around 50 NWs, resulting an average diameter of 80 and 110 nm for sample grown under HP and LP conditions, respectively (figure 6.14).

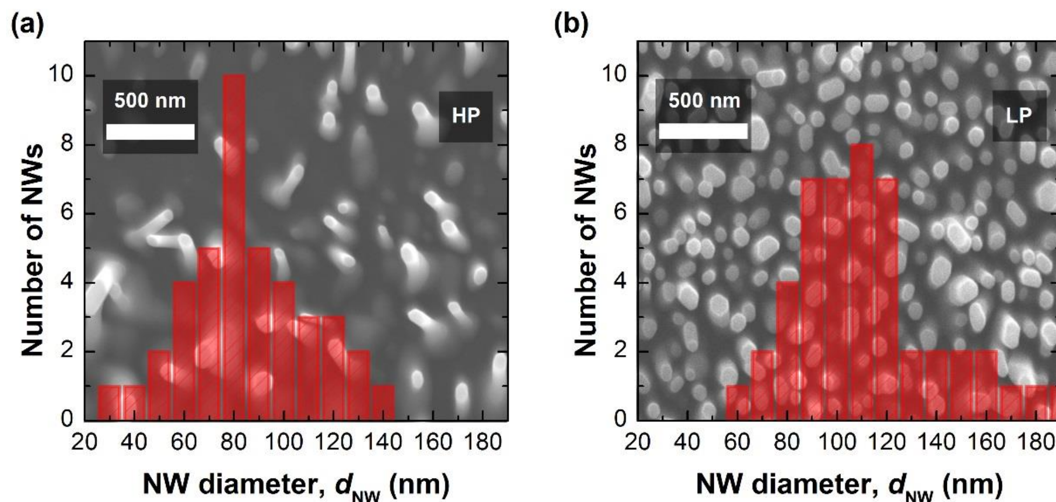

Figure 6.14. Estimation of the NW diameter distribution for NWs grown at (a) HP and (b) LP.

From figure 6.14, one can also extract the surface coverage, taking into account the number of NWs per area units, and the cross-sectional area of a single NW ($A_{NW} = \pi \cdot r_{NW}^2$, where r_{NW} is the NW radius). In the

HP sample, SEM image shows a NW surface density of around 7 NWs μm^{-2} (figure 6.14(a)); assuming an average A_{NW} ~ 5×10^{-3} μm^2 corresponding to a NW with a diameter of 80 nm, the surface coverage is about 3.5%. Following the same analysis for the LP sample, the obtained surface coverage is about 41.8%.

Figure 6.13(b) and (d) are SEM images taken at 90º with respect to the NW growth direction, allowing to estimate the average NW length; for HP and LP samples, the L_{NW} shows values around 4.13 and 1.15 μm, respectively.

Furthermore, figure 6.13(b) and (d) can be also used to extract information about the tilt angle of the NWs. The analysis shows a wide dispersion of values for NWs grown under HP conditions (figure 6.15(a)), whereas those NWs grown under LP conditions exhibit lower tilt angles and a more uniform vertical orientation (figure 6.15(b)).

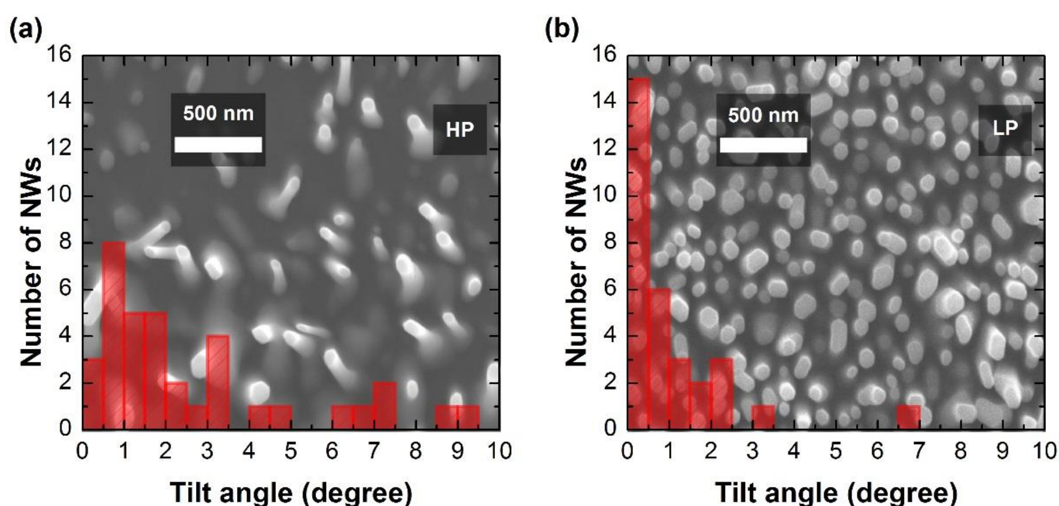

Figure 6.15. Estimation of the NW tilt angle distribution for NWs grown under (a) HP and (b) LP conditions.

Table 6.1 summarizes all the parameters extracted from the SEM characterization of ZnO NWs grown under both HP and LP conditions.

Table 6.1. Growth conditions of ZnO NWs grown on sapphire.

Growth pressure (atm)	Sample name	d_{NW} (nm)	L_{NW} (μm)	Surface coverage (%)	Maximum tilt angle (º)
1	HP	80	4.13	3.5	3.5º
0.67	LP	110	1.15	41.8	0.3º

Ion Beam Analysis

IBA techniques (RBS and non-RBS) allow to perform qualitative analysis of the L_{NW} distribution, as well as quantitative investigation of the NW atomic density and chemical composition, in the HP and LP

samples grown at the University of Alabama. The IBA measurements presented in this work were carried out at the CMAM (UAM).

For the IBA measurements, samples are mounted on a high-precision (0.01º) three axis goniometer in a vacuum chamber, so the orientation of the sample surface relative to the incident $^{4}He^{2+}$ beam can be precisely controlled. Backscattered ions are detected by a Si-barrier detector located at 170º with respect to the beam direction whose energy resolution is about 15 keV.

ZnO NWs grown at HP and LP conditions are expected to be composed of Zn and O elements. However, IBA spectra show contributions coming from both the NWs and the sapphire substrate. Therefore, it is essential to analyze IBA spectra with a software such as SIMNRA [24] to distinguish the origin of each contribution. In this regard, IBA spectra measured from ZnO NW samples show not only Zn and O elements from NWs but also a noticeable contribution of Al and O coming from the sapphire substrate.

In order to enhance the O signal, a $^{4}He^{2+}$ beam with a E_{ion} of 3.055 MeV is used to promote the resonance $^{16}O(\alpha,\alpha)^{16}O$. As Zn is a heavier element, its Rutherford cross section therefore provides a clean RBS signal at higher energies. A thorough description of the IBA technique used in this work has been included in chapter 4 (section 4.1).

Figure 6.16(a) shows the WZ structure of ZnO. The direction <0001> drawn in that figure corresponds to the NW preferential growth direction. The structural characterization of the NWs is performed at two different configurations: channeling and non-channeling, denoted as "<0001> aligned" and "random", respectively, represented in figure 6.16(b) and (c). For the <0001> aligned configuration, the incidence angle of the ion beam is kept constant and parallel to both the crystalline orientation of the substrate (*c*-plane sapphire) and the preferential growth direction of the NWs. On the other hand, random spectra are acquired by tilting the sample 20º off-axis to avoid channeling effects.

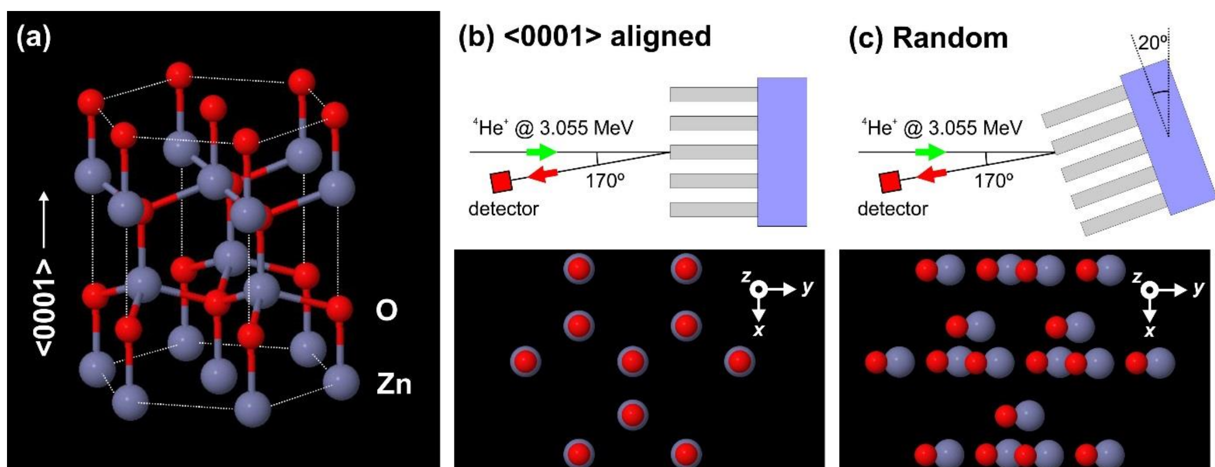

Figure 6.16. (a) Hexagonal cell of the WZ-ZnO structure. Schematics of RBS (b) <0001> aligned (channeling) and (c) random (non-channeling) configurations. (b) and (c) also include top-view, and 20º tilted away the top-view (along the y-axis) of WZ-ZnO structure, respectively.

As concluded from the SEM characterization, ZnO NWs grown under HP and LP conditions show relevant differences in terms of morphology, including d_{NW}, L_{NW}, surface coverage, and tilt angle (table 6.1). The existence of these noticeable differences might have a strong impact on the RBS spectra.

Random vs Channeling RBS

Among HP and LP samples, LP sample has been chosen for the comparison of channeling and random RBS spectra, mainly because of the good NW alignment observed in SEM (figure 6.15(b) and figure 6.17(c)). Spectra obtained at both <0001> aligned (channeling) and random (non-channeling) configurations from LP ZnO NWs are shown in figure 6.17(a).

IBA spectra measured at both configurations show two significant peaks around 0.95 and 2.2 MeV; the low energy peak is identified as the O resonance ($^{16}O(\alpha,\alpha)^{16}O$), whereas the high energy peak is associated to Zn atoms ($^{64}Zn(\alpha,\alpha)^{64}Zn$). The contribution of the Al coming from the sapphire substrate is also found between O and Zn peaks.

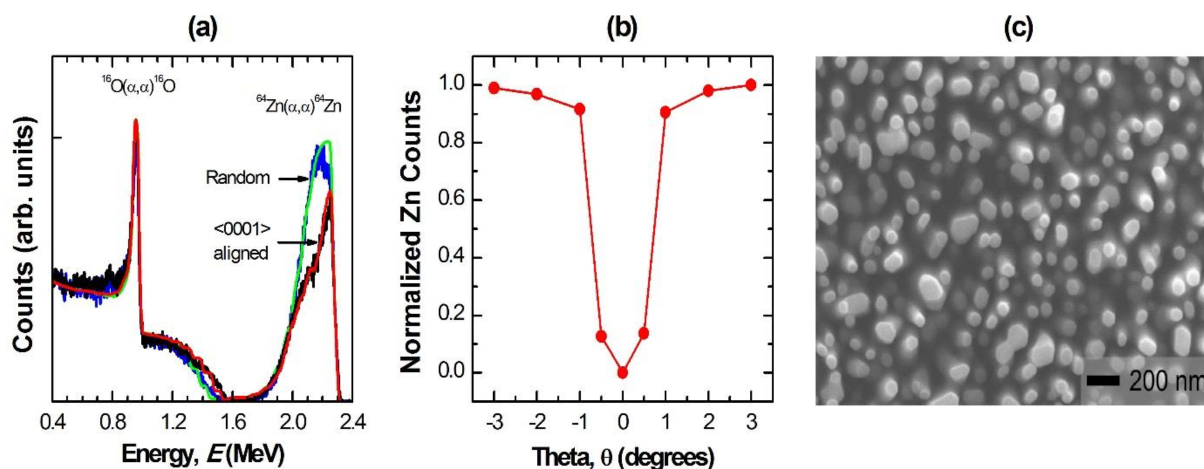

Figure 6.17. (a) RBS <0001> aligned and random measurements, and (b) RBS/C angular scan around <0001> axis of LP ZnO NWs; (c) SEM top-view image of LP ZnO NWs.

According to figure 6.17(a), the high energy edge of Zn signal presents lower intensity in <0001> aligned than in random configuration. In channeling conditions, the high energy edge of Zn signal is defined by incident ions backscattered only from the NW top surface, whereas the rest of the ions directly impact on the substrate surface. In the case of random conditions, as clearly observed in the molecular structure included in figure 6.16(c), there is a higher atom density along the ion beam path which is expected to increase the number of backscattered ions from Zn atoms.

On the other hand, Zn peak bandwidth observed in both spectra is approximately the same, i.e. the low energy edge of Zn signal matches in both configurations. This good agreement between channeling and random results can be explained assuming that the effective Zn layer thickness remains approximately unaltered when NWs are short, NW density is high and the incident angle is low.

The Zn channeling spectrum (figure 6.17(a)) can be interpreted as an overlapping between two peaks called here high and low energy peaks which are centered around the backscattered energies of E = 2.25 MeV and 2.12 MeV, respectively. The backscattered ions coming from the NW top surface experiment lower energy loss in comparison with those backscattered from bottom parts of the NW. In this scenario, the high energy peak presents higher intensity than the lower energy peak.

In random configuration (figure 6.17(a)), the Zn RBS signal is similar than that obtained in a crystalline ZnO thin film. In addition, it is observed that the intensity of the Zn peak increases as the backscattered ion energy decreases. This behaviour can be interpreted as backscattered ions loss an additional energy due to scattering effects at void regions along the ion path.

Al peak coming from the sapphire substrate also presents some differences as function of the RBS configuration. The qualitative analysis of Al peak measured in both configurations points out the energy shift towards higher energies in the case of <0001> aligned spectrum. This effect is due to the existence of incident ions that are directly backscattered by Al atoms at the sample surface. However, this scenario is not found in the random case because superficial Al is buried by ZnO NWs after the sample is tilted 20º.

The analysis and interpretation of the O resonance peak found at 0.95 MeV is hindered because the overlapping between O contributions coming from sapphire and NWs.

A RBS channeling (RBS/C) angular scan has been taken in LP ZnO NW sample in order to analyze the alignment of the NWs (figure 6.17(b)). At an incident angle of θ = 0º, backscattered signal coming from Zn atoms is minimum due to the ion channelling effect through the ZnO structure and along the <0001> direction (figure 6.16(b)). A slight angle change around 0º (δθ ~ 0.5º) leads to the increase of Zn signal caused by the loss of the channelling condition. Therefore, RBS/C results confirm the high crystallinity of LP ZnO NWs and their good alignment along the <0001> crystalline direction of the sapphire.

In figure 6.18(a), RBS <0001> aligned spectra corresponding to HP (figure 6.18(b)) and LP (figure 6.18(c)) ZnO NWs are represented. Analysing Zn peak, the high energy edge of the LP spectrum shows higher intensity comparing to the HP spectrum. As corroborated by SEM images, the void regions observed in the HP sample (figure 6.18(b)) are much larger than LP (figure 6.18(c)), intensifying then the channeling effect. In that respect, the LP spectrum shows a layer-shape peak, i.e. high and low energy edges of Zn peak are approximately abrupt such as occurs in the case of a ZnO thin film. This effect can be explained because in the case of LP sample, the centre-to-centre distance between NWs is very short, which means the NW surface coverage of the LP sample is much larger than the HP sample. Accordingly, it can be assumed that the LP sample is approximately a thin film of ZnO atop a sapphire substrate. In contrast, HP spectrum has not well defined the low energy edge of Zn peak, where an overlapping between Al and Zn peaks is clearly observed.

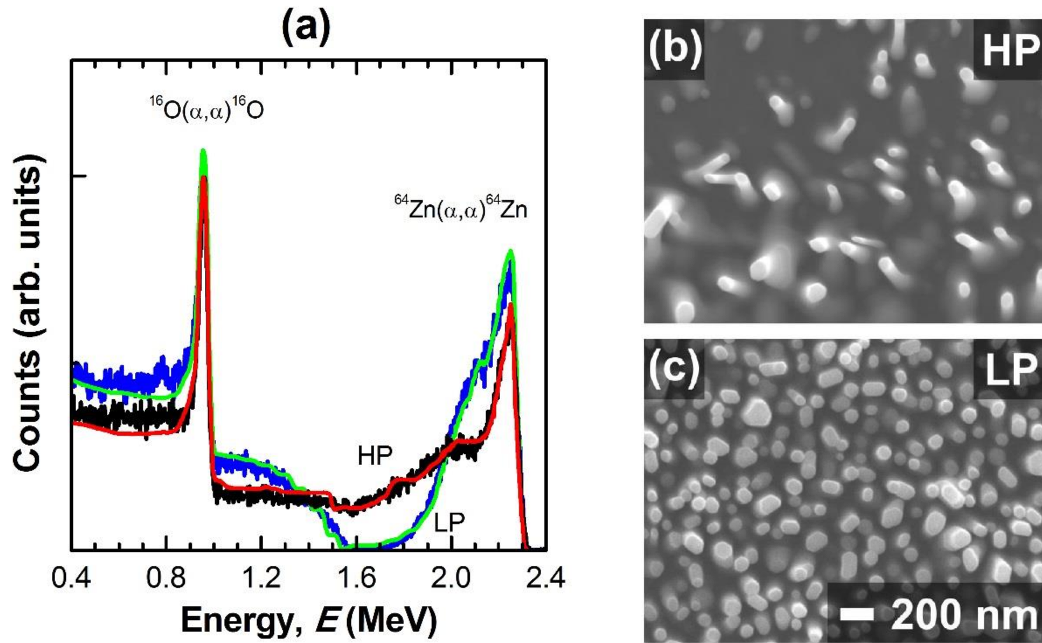

Figure 6.18. (a) RBS <0001> aligned measurements for (b) HP and (c) LP ZnO NWs.

RBS Simulation

A simple model is proposed here to simulate RBS experimental spectra and then to obtain physical parameters of ZnO NWs such as the NW chemical composition and atomic density. In this model, vertically aligned ZnO NWs grown on a sapphire substrate can be interpreted as a ZnO rough layer on top of a Al_2O_3 substrate [24].

The simulation of the RBS measurements is carried out using SIMNRA software. This software allows to simulate the layer roughness by a superposition of N spectra ($N > 50$) with different vertical thicknesses (d_i) around a mean layer thickness of ($\bar{d}$), following a gamma distribution (p) whose standard deviation (σ) depends on the statistical variation of L_{NW} and also on the incident angle of the ion beam. The general equation for a gamma distribution is:

$$p(d) = \frac{\beta^{\alpha}}{\Gamma(\alpha)} d^{\alpha-1} e^{-\beta d} \quad , \tag{6.2}$$

where $\Gamma(\alpha)$ is the gamma function, and the angles α and β are defined as: $\alpha = \bar{d}^2 / \sigma^2$ and $\beta = \bar{d} / \sigma^2$.

As mentioned, RBS experimental data obtained in random configuration show similar spectra than those obtained in ZnO thin films (figure 6.17(a)). In this regard, RBS random spectra measured in both HP and LP samples are simulated by the described two-layer model.

RBS random spectra measured in HP and LP samples are shown in figure 6.19. In this figure, experimental data are represented along with their corresponding best fittings obtained from the two-layer simulations (see figure 6.19 inset). Parameters extracted from simulations, including layer composition, mean

thickness, and roughness (full width at half maximum, FWHM) are used to estimate physical magnitudes such as average L_{NW} and NW atomic density.

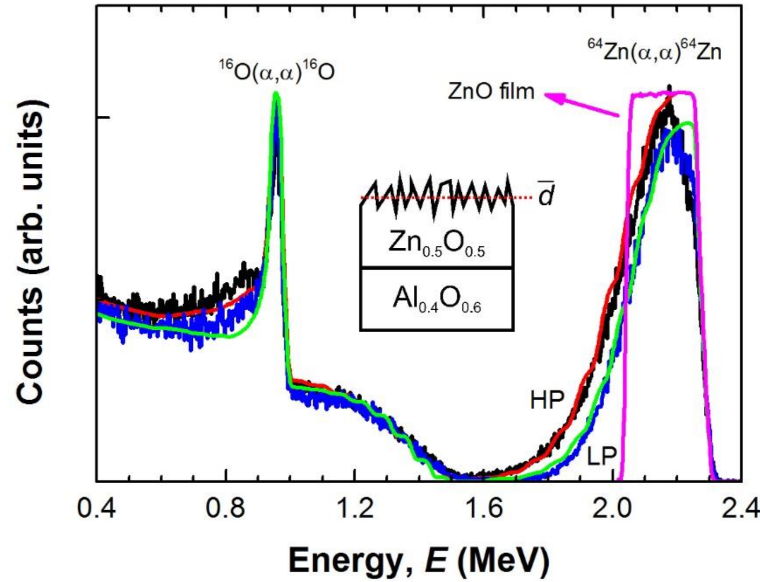

Figure 6.19. RBS random measurements of HP and LP ZnO NWs. Inset: two-layer model used for simulations.

In the RBS spectra of HP and LP samples (figure 6.19), the effect of the layer roughness reduces the low energy edge of the RBS Zn peak and increases its broadening in comparison to the simulated RBS Zn peak obtained in a ZnO thin film (also included in figure 6.19). This result demonstrates the good agreement between experimental data and simulations, and therefore confirms the validity of such simple layer model. In that respect, results obtained from the fitting using the two-layer model show a stoichiometric ZnO layer on top of the Al_2O_3 substrate.

In the low energy part of the spectrum, the signal from the O atoms of the substrate sums up to the O signal from the NWs, hindering the interpretation of the results. Hence, in order to extract information on the NWs, it is necessary to focus the analysis on the Zn signal.

Results obtained from fittings of the Zn peak are summarized in table 6.2, where the $\bar{d}$ and FWHM parameters are shown for HP and LP NWs.

Table 6.2. $\bar{d}$ and FWHM for HP and LP samples measured in random configuration.

ZnO NW sample	Layer mean thickness, $\bar{d}$ ($\times 10^{18}$ atoms cm^{-2})	Layer roughness, FWHM ($\times 10^{18}$ atoms cm^{-2})	SEM NW length, L_{NW} (μm)
HP	4.3	2.2	4.13
LP	3.0	3.0	1.15

From that table, one can observe that $\bar{d}$ is lower in LP NWs comparing to HP NWs. Assuming that $\bar{d}$ is directly related to the average L_{NW}, RBS results confirm SEM observations.

As mentioned, the incidence ion beam sees an effective medium composed by a low concentration of inclusions (voids) surrounded by the ZnO material. This medium can be approximated by a uniform ZnO layer with a lower atomic density than the one measured in a compact layer. Therefore, results obtained from random configuration analysis are used to perform a quantitative calculation of the molecular density (atoms cm^{-3}) in each sample. This magnitude is obtained from equation (6.3):

$$\text{molecular density}\,(\text{atoms cm}^{-3}) = \frac{\bar{d}}{L_{\text{NW}}}\ , \qquad (6.3)$$

where $\bar{d}$ and L_{NW} (the latter estimated from SEM images, figure 6.13(b,d)) are expressed in atoms cm^{-2} and cm, respectively. Molecular density estimated for HP and LP samples results in 1.04×10^{22} and 2.61×10^{22} atoms cm^{-3}, respectively.

6.2.3. Structural Analysis

XRD Analysis

Crystalline structure of vertically aligned ZnO NWs shown in figure 6.13(a,b) is analyzed by means of XRD technique. The characterized NWs were grown in The University of Alabama, whereas the XRD measurements were performed at the SIDI (UAM) facilities. Measurements are taken in two different configurations: θ-2θ (figure 6.20(a)) and grazing incidence (GIXRD) (figure 6.20(b)).

The θ-2θ diffractogram presented in figure 6.20(a) only shows (00l) (where l is an integer number) peaks owing to the alignment of this crystal direction along the normal vector of the substrate surface. The diffractogram shows (002) and (006) peaks which are identified within the ZnO WZ structure, and the Al_2O_3 substrate, respectively, using the International Centre for Diffraction Data (ICDD) Card no. 04-008-81-97 for ZnO and 04-007-5143 for Al_2O_3.

Since GIXRD is more sensitive to details of the sample surface than θ-2θ, mainly because the use of smaller incidence angles, GIXRD diffractogram presents many diffraction peaks (figure 6.20(b)), which are identified within the ZnO WZ structure with lattice parameters of a = 0.325 nm and c = 0.5207 nm using the above ICDD cards. This result confirms the polycrystalline characteristics of the NW sample.

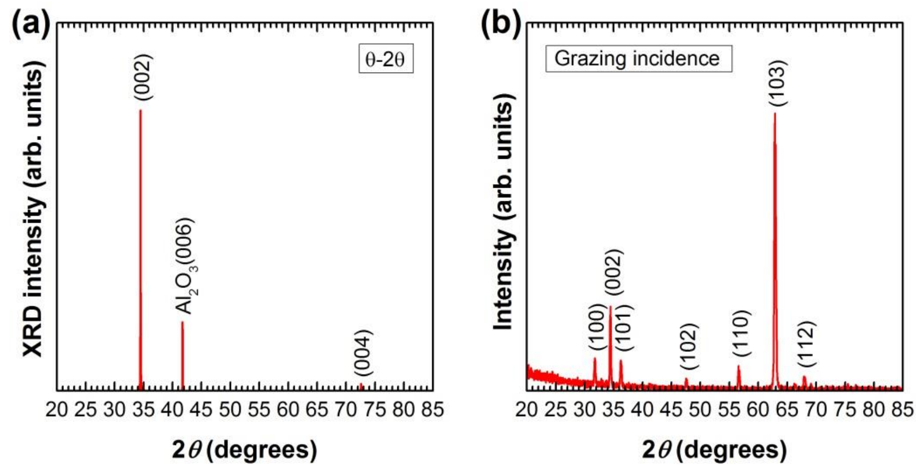

Figure 6.20. XRD spectra of vertically aligned ZnO NWs on sapphire measured in (a) θ-2θ and (b) GIXRD configurations.

Raman Spectroscopy

For a perfect ZnO crystal, only optical phonons at the center of the Brillouin zone (Γ point) are involved in first-order Raman scattering according to the Raman selection rules (chapter 4, section 4.7.2). At the Γ point, group theory predicts the existence of the following phonon modes: $\Gamma = 2 \times (A_1 + B_1 + E_1 + E_2)$. Among these modes, there are acoustical modes with $\Gamma_{aco} = A_1 + E_1$, and optical modes $\Gamma_{opt} = A_1 + 2 \times B_1 + E_1 + 2 \times E_2$ [25]. B_1 modes are silent modes. A_1 and E_1 modes are polar and split into transversal optical (TO) and longitudinal optical (LO) phonons. A_1 and E_1 phonons are polarized perpendicular, and parallel to the *c*-plane, respectively. The E_2 modes have two wave numbers, namely E_2(high) and E_2(low) associated with the motion of O and Zn sublattice, respectively. Strong E_2(high) mode is characteristic of WZ lattice, is commonly observed in ZnO NWs, and nanotubes and indicates good crystallinity [26, 27].

Raman scattering measurements are performed in backscattering geometry and using polarized light source (see system description in chapter 4, section 4.8.2). In this geometry, E_2, A_1(TO), and E_1(TO) modes are allowed when incident radiation is perpendicularly to the *c*-axis of the sample (LO modes are forbidden), whereas E_2, A_1(LO) and E_1(LO) might be observed since incident light is parallel to the *c*-axis [28]. Although each ZnO NW is oriented along its *c*-axis, perpendicularly aligned to the substrate surface, it is possible that some of the NWs are slightly titled respect to *c*-axis of the substrate, such as observed in figure 6.15(a). Accordingly, forbidden modes might show up in the Raman spectrum.

Figure 6.21 shows RT Raman spectrum for ZnO NW sample shown in figure 6.15(a); measurements were carried out using a monochromatic laser light at λ = 532 nm and an optical power of 200 mW. In the Raman spectrum, there are two dominant peaks located at energies of 418 and 438 cm^{-1}. The former is a convolution of two peaks: E_1(TO) and A_{1g} modes of ZnO NWs and sapphire substrate, respectively. The latter is also a convolution of two peaks: E_2 (high) and E_g modes of ZnO NWs and sapphire substrate, respectively. The Raman spectrum also shows a low intensity peak at 332 cm^{-1} related to multiphonon process associated to second order Raman mode $2E_2$(M). The peak at 379 cm^{-1} is assigned to A_1(TO) mode. The peak at 576 cm^{-1}

can be assign to $E_1(LO)$; this mode should not be observed in the Raman spectra due to the geometry of the measurements; however, NWs are slightly tilted away the substrate normal direction, which means the incident light is not perfectly aligned along the NW axis, allowing the observation of forbidden modes such as $E_1(LO)$. $E_1(LO)$ is associated to the presence of O vacancies and Zn interstitial in the ZnO structure [27]. The Raman spectra also show peaks at 657 cm^{-1} (A_1 acoustic overtone), 1096 cm^{-1} (A_1,E_2 acoustic combination), 1151 cm^{-1} ($2E_1(LO)$ optical overtone) associated to ZnO NWs, and at 750 cm^{-1} (E_g) associated to the sapphire substrate.

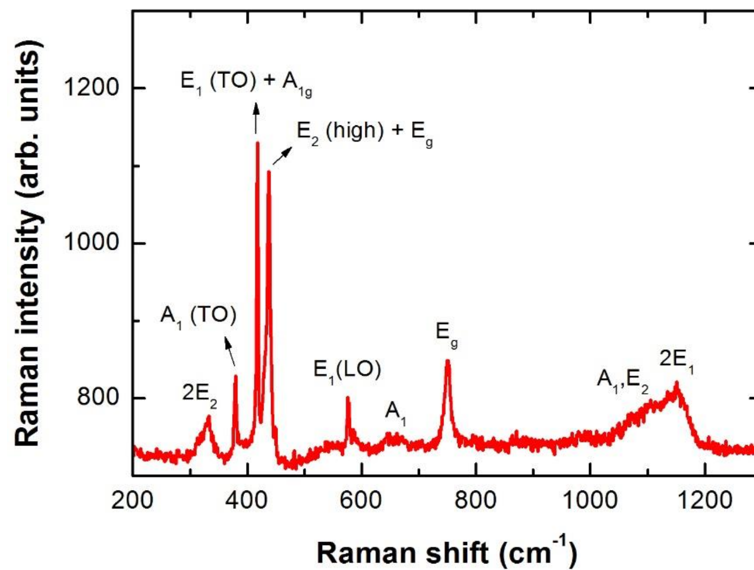

Figure 6.21. RT Raman spectrum of vertically aligned ZnO NWs on sapphire, using monochromatic laser light at λ = 532 nm and an optical power of 200 mW.

Table 6.3 summarizes phonon modes observed in this work, including phonon peaks reported in the literature for other ZnO based structures.

Table 6.3. Phonon modes found in different ZnO based structures along with their wavenumbers.

Phonon Mode	**Peak Position Our ZnO NWs (cm^{-1})**	**Peak Position ZnO bulk (cm^{-1})**	**Peak Position ZnO NWs (cm^{-1})**	**Peak Position ZnO nanotubes (cm^{-1})**
$2E_2(M)$	332	332 [29]	331 [26]	331 [26]
$A_1(TO)$	379	380 [26]	376 [26]	375 [26]
$E_1(TO)$	418	413 [26]	416 [26]	418 [26]
$E_2(high)$	438	444 [26]	438 [26]	437 [26]
$E_1(LO)$	575	574 [29]		
$A_1(LO)$	658	657 [29]	654 [26]	646 [26]
A_1, E_2	1095	1105 [29]		
$2E_1(LO)$	1151	1158 [29]		

6.3. Integration of ZnO NWs in Optoelectronics

6.3.1. NW Suspension Preparation

ZnO NW suspensions are prepared using an organic solvent such as ethanol, and different ZnO NW sources, including ZnO TP powder (section 6.1.1) or ZnO NWs vertically aligned on Si(100) substrates (section 6.1.2).

NW Suspension From ZnO TPs

A mass of 2 mg of ZnO TP powder is solved in 40 ml of ethanol. Resultant suspension is warmed up at a specific temperature below the boiling point of ethanol for 3 minutes and later sonicated for another 3 minutes. These two steps are repeated three times in order to foster the scission of NWs from TPs and to reduce the number of NW clusters. Resultant suspension is centrifuged at 100 rpm using a spinner system. During the spinning step, 20 ml of the solution are transferred to another recipient. This method allows to filter the solution, taking dispersed NWs and discarding bigger structures contained in the solution. Finally, 20 ml of ethanol are added to the solution (total volume of the new solution is 40 ml) in order to reduce NW concentration.

NW Suspension From Vertically Aligned ZnO NWs

A 1×0.5 cm^2 sample with vertically aligned ZnO NWs is dipped in 1.5 ml of ethanol and sonicated for 2 minutes in order to provoke the scission of these NWs from Si substrate. In order to minimize contaminants (nano- and micro-crystals) coming from the Zn seed layer, a 0.5 ml volume is transferred to another recipient during the sonication step and diluted in a volume of 1 ml of absolute ethanol to obtain a final volume of 1.5 ml. The scission process is demonstrated to occur near the NW base (figure 6.22); this method is therefore beneficial for the further integration of NWs in devices because it preserves the entire length of the crystal.

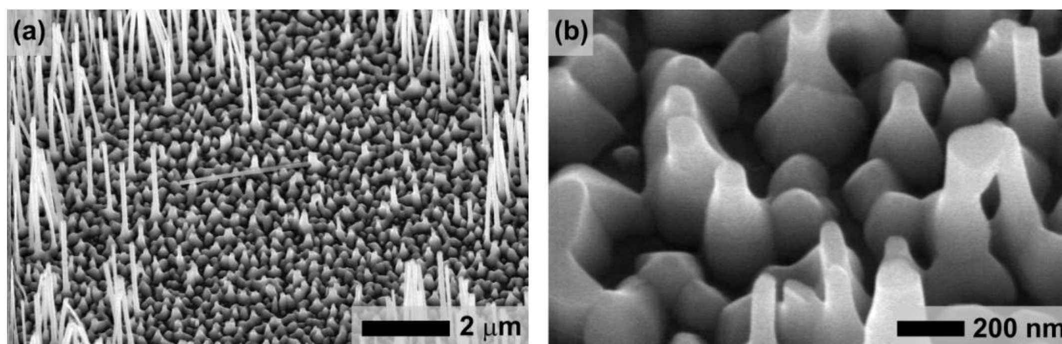

Figure 6.22. SEM image of ZnO NW sample after sonication in ethanol.

After a sonication step of few seconds, the analysis of the sample morphology (figure 6.22(a)) exhibits a NW-free area of about 20% of the total surface; the same sample can be re-used several times to prepare new NW suspensions.

6.3.2. Drop-Casting

Drop-casting is a first approximation to integrate ZnO NWs between pre-defined conductive electrodes. Prior to the NW deposition, AZO electrodes are defined by photolithography and chemical etching processes on SiO_2(300 nm)/Si(100) substrates (figure. 6.23(a)); different series of electrodes have been defined with gap spacings between 2 and 16 μm and a thickness of 50 nm.

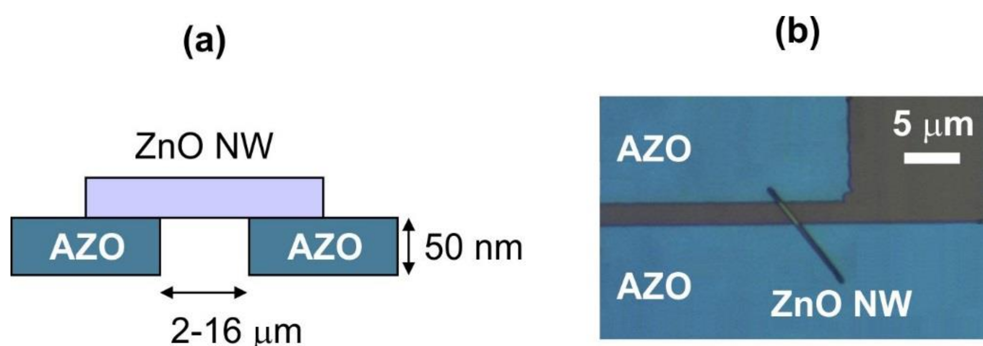

Figure. 6.23. (a) Cross-sectional schematic and (b) optical microscope image of a ZnO NW drop-casted on pre-patterned AZO electrodes.

Drop-casting procedure consists in the deposition of a 2 μl-droplet extracted from a NW suspension (section 6.3.1) on a sample with pre-defined electrodes which is spinning at 200 rpm. Figure. 6.23(b) shows an optical microscope image of a ZnO NW dispersed by drop-casting on AZO electrodes. This figure shows that the placement of a NW occurs without control because the NW is randomly aligned and the contact area of both NW ends on each electrode is totally different. Furthermore, drop-casting process is tedious, ineffective, and slow, presenting thus lower assembling efficiency compared to techniques such as DEP.

6.3.3. Dielectrophoresis

Drop-casting method used in previous section has a low fabrication yield and a lack of performance reproducibility which are two large obstacles for the development of NW based technologies. The present section aims to offer an alternative technique which enables reliable processing of high NW densities in integrated circuits. DEP is a well-known technique which has been used to align NWs [30-32], NPs [33], and CNTs [34] for different applications. This technique relies on AC electric fields to align structures in a given solution at specific sites over large areas, at RT, and without need of expensive tools. DEP can be positive or negative when polarized NWs are driven by the DEP force towards the high or low electric field regions,

respectively. These two behaviours are observed depending on the complex dielectric permittivity of the particle (ε_p) and its surrounding medium (ε_m).

The assembling mechanisms and efficiency of ZnO NWs have been analyzed as a function of:

i) the composition of the electrode (Al, Au, and AZO);
ii) DEP parameters (AC amplitude and frequency);
iii) distance of the NW with respect to the alignment site;
iv) initial alignment of the NW with respect to the electric field.

Effects of Electrode Type on NW Assembling

The number of NWs assembled onto plane-parallel electrodes is taken as a figure of merit to compare different electrode materials. Those materials are deposited by different techniques, Au being thermally evaporated, whereas Al and AZO are deposited by rf-magnetron sputtering. The interest of using AZO is based on its better mechanical resistance and adherence to the substrate than the tested metals. In addition, it can be used on transparent substrates for the precise alignment of NWs in transparent electronic sensors, and for the combination of electrical and optical NW alignment techniques.

Electrodes with a thickness of 100 nm are defined on the oxidized Si substrates (300 nm thick thermal SiO_2 atop the Si substrate surface) by photolithography and chemical etching over a total width and length of 50 μm and 1 cm, respectively. The spacing between them is set at 4 μm, i.e. a distance below the average NW length in the solution (L_{NW} ~ 25 μm).

During a DEP process, a 2 μl droplet extracted from the ZnO NW suspension is deposited on a sample with pre-defined electrodes using a root-mean-square voltage (V_{rms}) of 5 V and an AC frequency (f) of 100 kHz. Figure. 6.24 show SEM images of the resultant devices consisting of ZnO NWs assembled by DEP between Au (a), Al (b) and AZO (c) electrodes. NWs are marked in white in order to highlight their position.

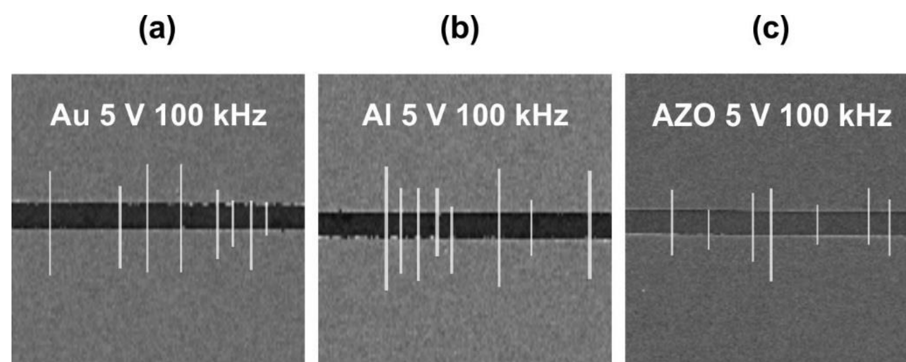

Figure. 6.24. SEM images of ZnO NWs assembled by DEP between (a) Au, (b) Al, and (c) AZO electrodes with a separation gap of 4 μm.

Analysing the NW linear density, i.e. number of NWs per μm, it is observed that for AZO electrodes NW linear density is almost as large as that for metals (Au and Al: 0.16 NWs/μm; AZO: 0.14 NWs/μm). The

semiconductor nature of AZO and its higher resistivity (ρ_{Hall} = 4×10^{-3} Ω·cm) in comparison to metals (ρ_{Au} = 2.2×10^{-6} Ω·cm and ρ_{Al} = 2.8×10^{-6} Ω·cm) may lower the effective V_{rms} around the inter-electrode gap during the DEP process but the resultant linear density seems to validate its use for NW DEP.

It is important to notice that the reduction of the AZO electrode thickness below 100 nm is observed to strongly reduce the DEP efficiency in comparison to metals. However, the high mechanical stability of AZO in comparison with both Al and Au, along with the assembling efficiency found, make this compound very attractive for the fabrication of ZnO NW based PDs.

Dielectrophoretic Force

To understand the influence of DEP parameters, i.e. V_{rms} and f, on the number of assembled NWs, it is necessary to analyze the dielectrophoretic force (F_{DEP}) which is responsible to trap and align those NWs onto a pair of electrodes. In this process, NWs are assembled between electrodes, making electrical contact with the electrodes at both NW ends.

The F_{DEP} associated to a spheroidal particle [35] is given by the equation

$$F_{DEP} = c\varepsilon_m \,\mathrm{Re}[f_{cm}]\nabla E^2, \tag{6.4}$$

where c depends on the volume of the particle, f_{cm} is the Clausius-Mossotti factor and E is the electric field. Equation (6.4) is also valid for NWs because they can be seen as cylindrical particles with a high aspect ratio [36]. For NWs, $c = 1/2\, r_{NW}^2 L_{NW}$.

F$_{DEP}$ vs Frequency

The Clausius-Mossotti factor is defined as the strength of the effective dipole formed along the NW induced by the electric field through the solvent

$$f_{cm} = \frac{\varepsilon_p^* - \varepsilon_m^*}{\varepsilon_m^* + L_i\left(\varepsilon_p^* - \varepsilon_m^*\right)}, \tag{6.5}$$

where ε_p^* and ε_m^* are the complex permittivity ($\varepsilon^* = \varepsilon - \mathrm{j}\,(\sigma/\omega)$, where σ is the electrical conductivity and ω is the angular frequency) of the NW and the medium, respectively. This factor also depends on the NW dimensions (r_{NW} and L_{NW}) and the relative orientation of the NW with the electric field through the depolarization factor (L_i):

$$L_i = \frac{r_{NW}^2\, L_{NW}}{2} \int_0^{\infty} \frac{ds}{\left(s + r_i^2\right)\sqrt{\left(s + r_{NW}^2\right)^2 \left(s + L_{NW}^2\right)}} \,, \tag{6.6}$$

where $r_i = r_{NW}$ or $L_{NW}/2$ when the electric field is perpendicular or parallel to the NW axis, respectively.

In order to see the dependence of the F_{DEP} with f, equation (6.4) has been used to calculate F_{DEP} for a ZnO NW ($\varepsilon_{ZnO} = 10\varepsilon_0$ and $\sigma_{ZnO} = 1$ S/m) with dimensions of $r_{NW} = 50$ nm and $L_{NW} = 10$ μm. For the sake of simplicity, the NW is assumed to be initially aligned along the electrical field direction ($r_i = L_{NW}/2$, resulting in $L_i = 0$). NWs are suspended in ethanol whose ε_{EtOH} and σ_{EtOH} are $24.3\varepsilon_0$ (where ε_0 is the vacuum permittivity), and 10^{-5} S/m, respectively. In addition, the spacing between electrodes is 4 μm. The calculation of $F_{DEP}(f)$ at a V_{rms} of 7.5 V was carried out using Comsol Multiphysics software [37], resulting in the curve shown in figure 6.25.

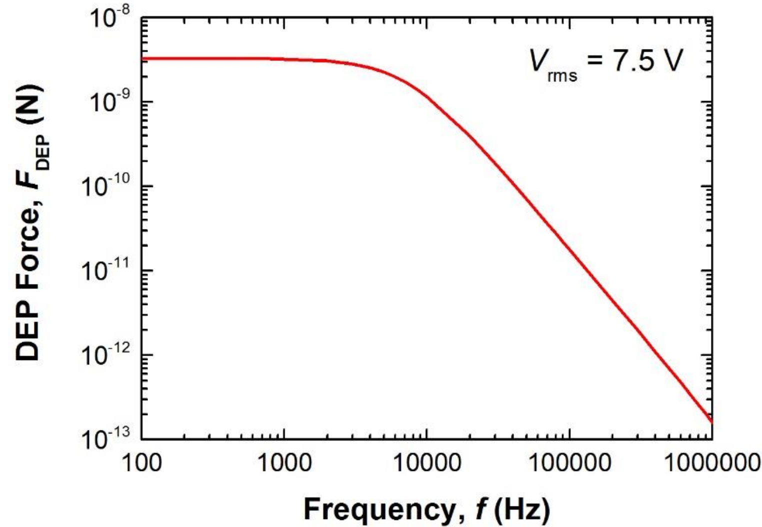

Figure 6.25. Calculated F_{DEP} for a ZnO NW in an AC electric field as a function of frequency.

From the figure above, one can distinguish two different regions: i) a constant F_{DEP} region below 10 kHz, ii) and a decreasing F_{DEP} region above 10 kHz. From that result one can expect different NW trapping efficiencies as a function of f. In order to clarify this point, we now analyze the number of assembled ZnO NWs as a function of f which is varied between 10 and 1000 kHz. The effect of f on the NW assembling rate (at V_{rms} = 7.4 V) shows a maximum value at around f = 100 kHz (figure 6.26(b)). On one hand, frequencies above 1 MHz might hinder the polarization of the NWs due to the reduction of the f_{cm}, lowering the F_{DEP}, and therefore reducing the trapping of NWs. On the other hand, the use of frequencies below 10 kHz produces electrolysis of the liquid solvent at V_{rms} = 7.5 V, hindering the assembling of NWs between electrodes.

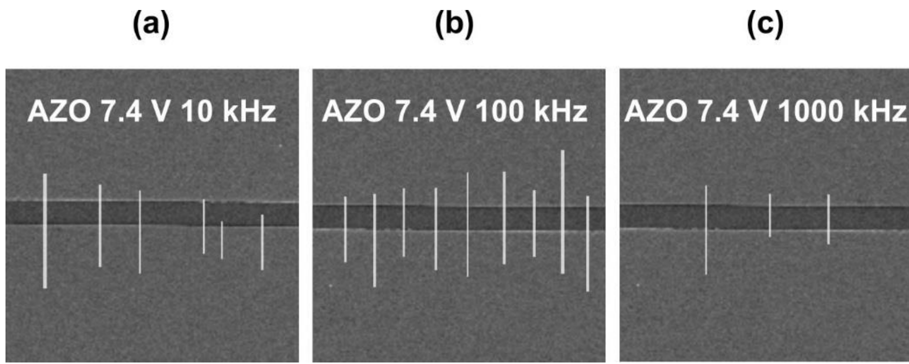

Figure 6.26. SEM images of ZnO NWs assembled by DEP at different AC frequencies.

F_{DEP} vs V_{rms}

The square of the electric field gradient (∇E^2) is an important factor in equation (6.4), having an important impact on the F_{DEP}. In the case of plane-parallel electrodes shown in SEM images (figure. 6.24 and figure 6.26), E is uniform at the inter-electrode gap and then ∇E^2 is zero along the plane (xy). However, ∇E^2 differs from zero along the perpendicular direction (z-axis) to that plane. Equation (6.4) can be easily expressed in terms of V_{rms}. For the sake of simplicity, we have taken into account only the z component of the ∇E^2, and expressed E as a function of the V_{rms}, resulting in

$$F_{DEP} = c\varepsilon_m \operatorname{Re}[f_{cm}]\nabla \left| \frac{dV_{rms}}{dz} \nabla_z \left(\frac{dV_{rms}}{dz} \right) \right| \tag{6.7}$$

Using the previous equation, the F_{DEP} exerted on a ZnO NW with dimensions of r_{NW} = 50 nm and a L_{NW} = 10 µm, initially aligned along the electrical field, 10 µm above the gap, and subjected to an AC electric field with a f = 100 kHz and different V_{rms}, is represented in the figure below:

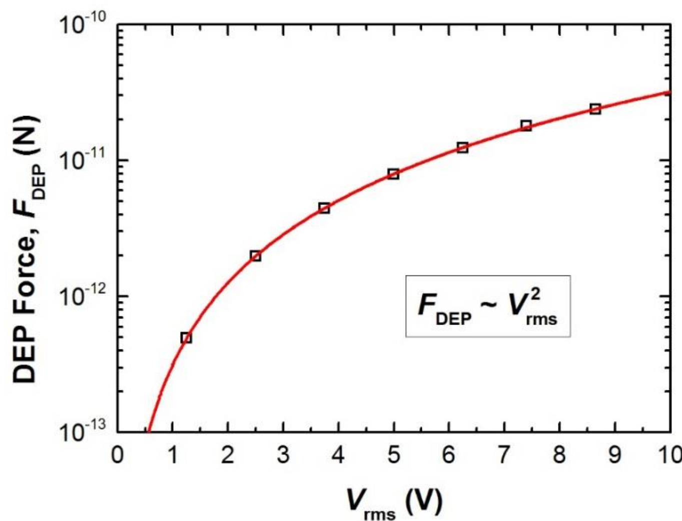

Figure 6.27. F_{DEP} vs V_{rms} at f = 100 kHz.

From that figure, one can conclude that the NW is subjected to a F_{DEP} with a magnitude between 0.1-30 pN that tends to increase with the square of the V_{rms} as points out the fitting line represented along with the calculated data (black squares).

Experiments carried out using different V_{rms} (figure 6.28(a-c)) justify the increase of the assembled NW linear density from 0.1 to 0.18 NWs/µm when V_{rms} increases from 2.5 to 7.4 V.

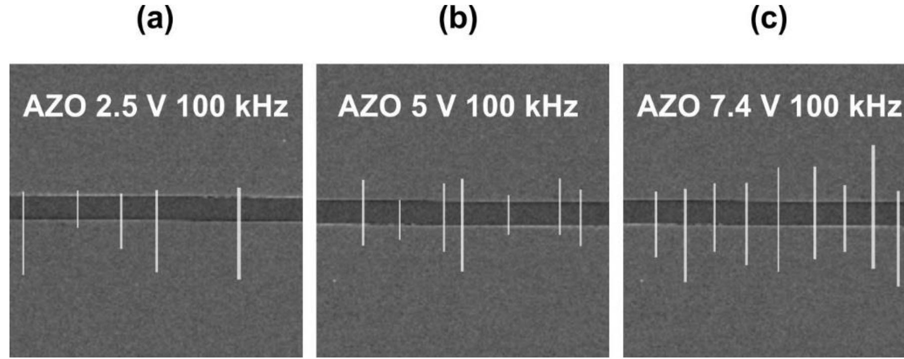

Figure 6.28. SEM images of ZnO NWs assembled by DEP at different V_{rms}.

NW linear density assembled by DEP using different electrode materials, and DEP conditions is summarized in table 6.4.

Table 6.4. NW linear density of devices fabricated using different electrode materials and DEP conditions.

Electrode material	DEP conditions		NW linear density (NWs/µm)
	V_{rms} (V)	f (kHz)	
AZO	2.5	100	0.10
Au	5	100	0.16
Al	5	100	0.16
AZO	5	100	0.14
AZO	7.4	10	0.12
AZO	7.4	100	0.18
AZO	7.4	1000	0.06

F_{DEP} vs NW Position

The F_{DEP} exerted on a ZnO NW suspended in ethanol changes with the distance between the NW and the electrodes gap. Assuming a ZnO NW with the same dimensions and relative orientation than those used in the f and V_{rms} studies, the F_{DEP} was calculated as a function of the distance along the z-axis (z = 0 is taken at the electrodes gap) for f = 100 kHz and three different V_{rms} (figure 6.29).

Figure 6.29 represents results of the simulations along with their best fittings. As can be deduced from equation (6.7), the F_{DEP} depends on the distance to the electrodes gap following a ~ z^{-3} power law.

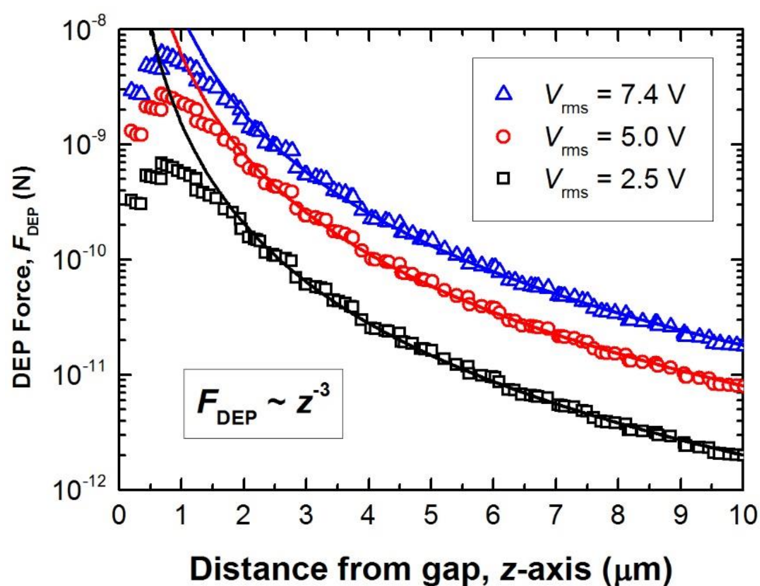

Figure 6.29. F_{DEP} vs NW distance above the electrodes gap (z-axis) at different V_{rms}.

F_{DEP} vs NW Orientation

In the suspension, NWs are distributed randomly in terms of the angle formed with the electric field lines. However, this angle has a strong impact on the F_{DEP} through the f_{cm}. Although the initial alignment of the NWs cannot be controlled, it is interesting to study the variation of F_{DEP} as a function of the NW orientation. Using equation (6.7), the F_{DEP} has been calculated for a ZnO NW forming different angles with the electric field lines. For these calculations, we assume a NW at a 10 μm distance above the gap, and DEP conditions of V_{rms} = 7.5 V and f = 10 kHz. Figure 6.30 shows calculated values of F_{DEP} as a function of the relative angle

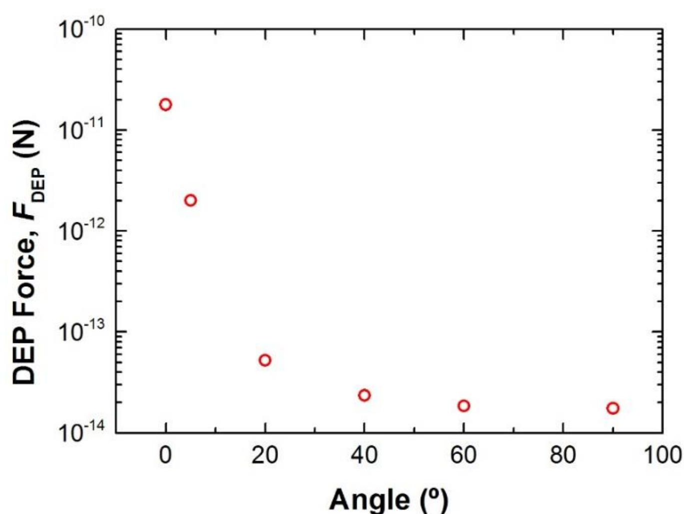

Figure 6.30. F_{DEP} exerted on a NW as a function of the angle between the NW and the electric field.

formed between the NW and the electric field. In that figure, it is observed that the maximum force is exerted on the NW when it is aligned parallel to the electric field, whereas this force decreases sharply as the angle increases. For angles above 20º, F_{DEP} reaches very low values around 10^{-14} N range. Thus, NWs unaligned with the electric field have lower chances to be trapped by DEP.

NW Assembling Path

DEP processes are monitored in real-time using a video camera (10 frames per second) integrated in an optical microscope system in order to study the alignment mechanism of NWs over time. Figure 6.31 shows a representative image of a NW typical assembling path where the NW is marked in dark in order to highlight its position in each recorded frame of the total sequence.

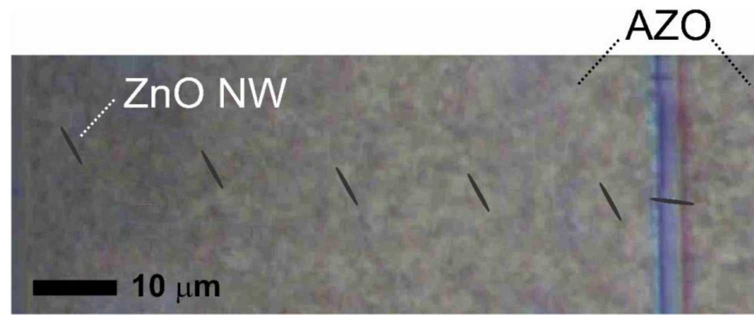

Figure 6.31. Optical microscope sequence of a typical NW trapping path.

This figure shows a NW whose orientation does not change during the approaching to the alignment site, and that is moving along the horizontal plane (hundreds of μm), reaching a velocity (v) around 400 μm/s. When the NW is far from the alignment site there is no torque induced by the electric field and then does not change its relative orientation along the whole path. In addition, NW velocity is estimated to be constant along the whole examined path which means the F_{DEP} is completely balanced by the viscous force (F_{vis})

$$F_{DEP} = F_{vis} = 3\pi\eta \, L_{NW} D v \ , \tag{6.8}$$

where η is the viscous coefficient (for ethanol $\eta = 10^{-3}$ Pa·s), D is the shape factor (0.18 can be used for NWs). Therefore, the F_{DEP} exerted on a NW with a L_{NW} of 10 μm which is responsible to its attraction to the alignment site, takes values in the pN range which is in good agreement with the F_{DEP} calculated from equation (6.4).

Finally, when the NW is close to the inter-electrode gap, the electric field is capable to induce a dipolar moment ($\vec{p}$) along the NW, creating a torque equivalent to $1/2\,\vec{p} \times \vec{E}$, which leads to the alignment of the NW along the electric field.

NW Alignment

During the DEP assembling of NWs, different alignment modes can be observed. We analyze those in depth during the alignment of ZnO NWs between Au electrodes. An array consisting of 100-nm thick Au electrodes are fabricated using optical lithography and chemical etching. This electrode array comprises two bus bars separated 46 μm between each other, and contains a set of 160 alignment sites. Each alignment site has two squared fingers (20×20 μm^2) with a minimum distance of 6.1 μm between their corners (figure 6.32(a-b)).

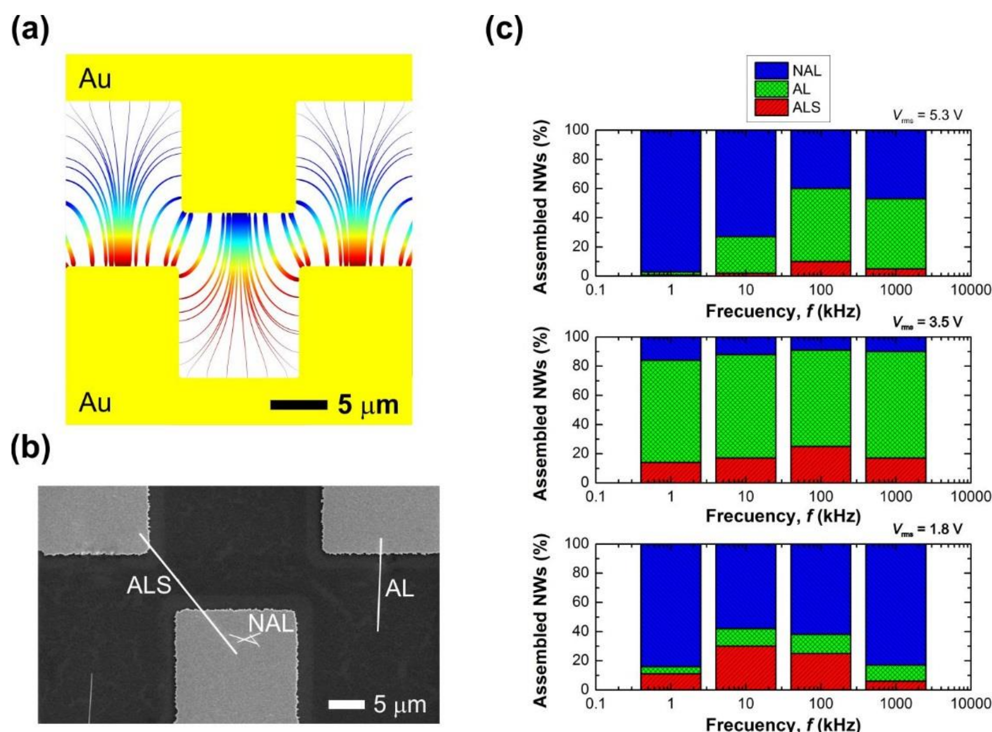

Figure 6.32. (a) Electric field vector (streamlines) and module (line thickness), and electric potential (line color) simulated for the Au electrodes array; (b) SEM image after a DEP experiment performed at V_{rms} = 5 V and f = 100 kHz; (c) statistic of ALS, AL, and NAL NWs as a function of the DEP conditions.

The electric field lines are represented in figure 6.32(a) where the thickness and color correspond to the module of the electric field and the electric potential, respectively. ∇E^2 direction can be determined using either the spacing or the thickness of the E field lines. Starting from the gap region where E is maximum, as represented with low spaced thick lines, the ∇E^2 is directed towards the region with larger spaced narrow lines. Thus, NWs follow this gradient direction and are attracted to the gap between electrodes because, there, E is maximum (positive DEP). After the deposition of a 2 μl volume droplet taken from a ZnO NW suspension, NWs with different dimensions are deposited and distributed in different sites along the area covered by the droplet. From SEM images, both, the assembling sites and dimensions of trapped NWs are analyzed as a function of the DEP conditions.

Trapped NWs can be classified in three different groups, depending on their deposition site and alignment state: i) aligned inside the gap (ALS), ii) aligned outside the gap (AL), and iii) non-aligned (NAL).

Figure 6.32(b) shows a SEM image with representative examples of ALS, AL, and NAL NWs. Depending on the DEP conditions, the per cent of each NW type changes as shown in figure 6.32(c); in all the cases, it was observed that an intermediate frequency between 1 and 1000 kHz exhibits the highest density of ALS NWs. In the V_{rms} = 3.5 and 5.3 V cases, this optimized frequency is 100 kHz, whereas if V_{rms} is lowered down to 1.8 V, there is a shift of the optimized frequency downwards to 10 kHz. As discussed in the case of plane-parallel electrodes (figure 6.26), the assembling efficiency increases with the frequency and enhances the NW assembling process, improving the amount of both ALS and AL NWs, thus lowering the NAL (figure 6.32(c)). Furthermore, a high frequency signal (~1000 kHz) hinders the polarization of the NWs due to the reduction of the f_{cm}, producing the decrease of the percentages of AL and especially ALS NWs.

A maximum value of ALS NWs around 30% is obtained at V_{rms} = 1.8 V and f = 10 kHz, however, the number of NAL NWs is also increased in comparison to higher V_{rms}. The increase of V_{rms} leads to the reduction of NAL per cent due to the increase of the AL NWs and helps to prevent the random distribution of disoriented NWs in the gap between electrodes.

Comparing AZO plane-parallel with Au array electrodes, the latter geometry allows the optimization of the ALS NWs by lowering the NAL NWs and controlling the deposition of single NWs in the gap site by increasing the AL NWs and reducing the probability to assemble more than one NW between a pair of electrodes.

In summary, a V_{rms} = 3.5 V and f = 100 kHz are considered the best DEP conditions to manage the deposition of a single ZnO NW between electrodes.

Aligned NW Dimensions

The radius distribution of the ZnO NW dispersion is obtained by depositing a 2 μl droplet taken from the NW suspension on a Si piece of wafer (called as reference in figure 6.33). After solvent is completely evaporated, sample is analyzed by SEM and the radius distribution is compared with that distribution of ALS NWs assembled by DEP carried out at V_{rms} = 5 V and different frequencies. Distributions follow a Gaussian function whose center is shifted toward lower radius in the case of ALS NWs. The most common radius found in the NW solution is around 130 nm, whereas ALS NWs show that DEP tends to trap NWs with lower radius. In addition, the radius of the trapped NWs decreases with the DEP frequency showing the lowest values (r_{NW} = 80 nm) at f = 1 kHz.

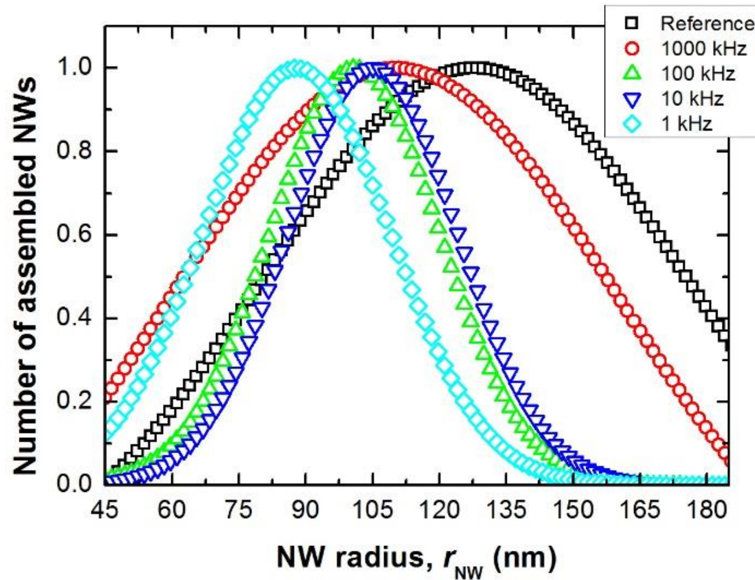

Figure 6.33. NW radius distribution of ALS NWs deposited by DEP carried out at V_{rms} = 5 V and different frequencies.

From figure above, one can conclude that the DEP process is selective to the NW dimensions, showing preferential NW dimensions, as a function of the DEP conditions.

As it will be discussed in section 6.4.1, NWs with lower radius are desirable for sensors due to the larger surface-to-volume ratio, and therefore, DEP can be considered as a potential technique to design improved NW based devices by controlling dimensions of assembled NWs.

Fabrication of a Single NW Device

Electrodes geometry is also an important key, affecting to the DEP assembling efficiency. In this case, AZO tip-ended electrodes with a thickness of 100 nm, are fabricated following the same procedure previously described for plane-parallel electrodes. For those electrodes, figure 6.34(a) shows the electric field lines distributed on the sample surface. The color of the lines represents the electric potential whereas its thickness is proportional to the electric field module ($|\vec{E}|^2 = E^2$). ∇E^2 can be seen as both the spacing of the electric field lines (the larger the spacing, the larger ∇E^2) or through the variation of the line thickness. As E^2 is maximum (a critical point for ∇E^2) in the inter-electrode gap, F_{DEP} will drift the NW in the direction perpendicular to the gap up to reaching the equilibrium point at the alignment site, in which the F_{DEP} becomes zero. Thus, F_{DEP} presents a strong component perpendicular to the inter-electrode gap at both sides of the site enabling NW trapping (arrows drawn in figure 6.32(a)). Once a NW is trapped, the electric field profile changes drastically around the site. In particular, ∇E^2 presents a singularity in the perpendicular direction to the gap that provokes an important reduction of the F_{DEP} which prevents the alignment of a second NW at the same site.

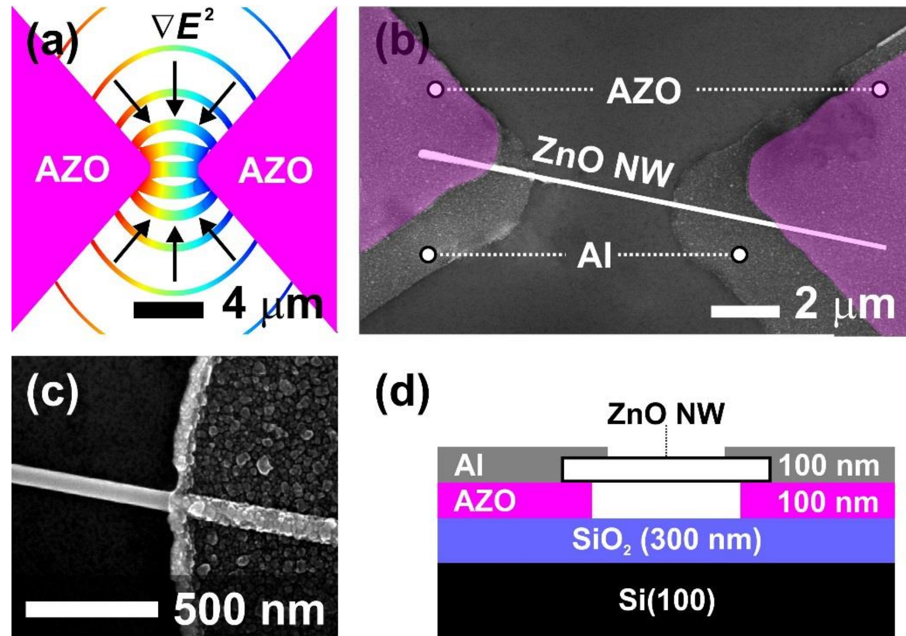

Figure 6.34. (a) Electric field lines (thickness and color represent E^2 and electric potential, respectively) and ∇E^2 arrows for AZO electrodes; (b) SEM image of single ZnO NW device whose ends are covered with Al (c) as detailed in the schematic (d).

After a single ZnO NW is deposited between a conductive pair of electrodes using DEP a second lithographic step is carried out to cover the NW ends with a 100-nm thick Al film by RT DC-sputtering, followed by a lift-off process (figure 6.34(b-d)). Al coating is expected to significantly reduce the noise in the *I*/*V* characteristics and to improve the contact linearity and performance reproducibility. Figure 6.34(d) shows the final device structure, including the layer sequence and its corresponding thickness. The device presented in that figure constitutes an original structure which combines the use of AZO electrodes and Al to integrate single ZnO NWs.

6.4. ZnO NW Based PDs

6.4.1. *I-V* Characteristics

Following the same procedure described for the fabrication of the device presented in figure 6.34, three different devices are fabricated, consisting of single ZnO NWs with r_{NW} of 50, 120 and 260 nm, and L_{NW} of 4.0, 6.2, and 7.5 µm, respectively. *I/V* characteristics of these devices are measured in a probe station in dark and under UV illumination.

Figure 6.35 shows *I*/*V* characteristics, represented in logarithmic (a) and linear (b) scales, of ZnO NWs with different r_{NW} measured in dark conditions at voltages between -5 and 5V. The current values measured in dark (I_{dark}) increase with the r_{NW} due to the enhancement of the conductive volume along the NW axis. In addition, figure 6.35(b) shows symmetric and non-linear *I*/*V* characteristics due to the contact formed between the ZnO NW and Al metal electrodes.

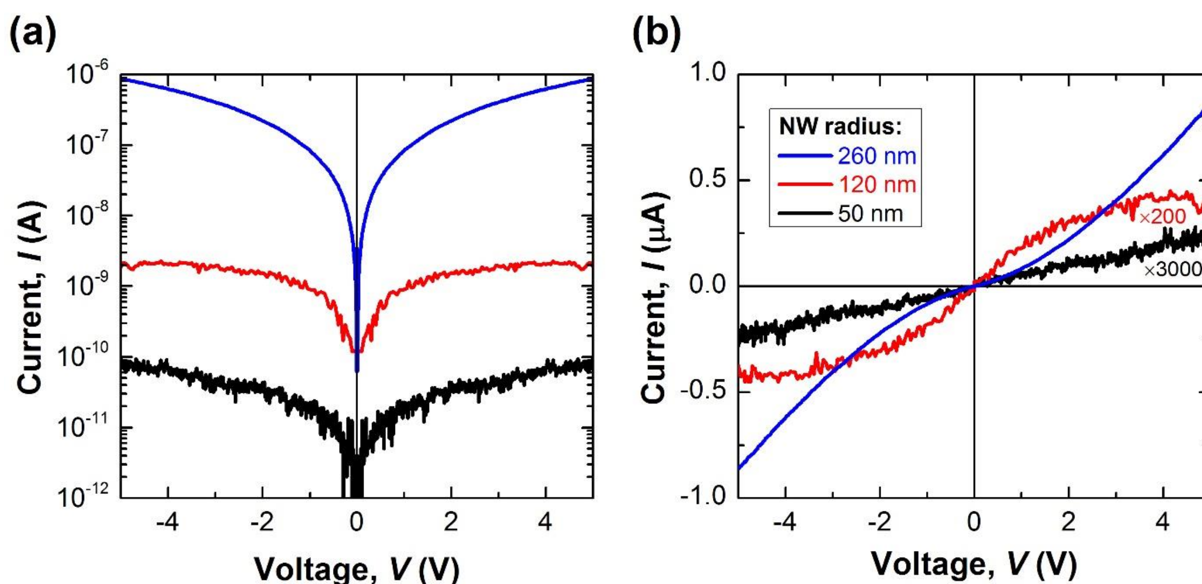

Figure 6.35. *I*/*V* characteristics measured in dark for single ZnO NWs with different radii, and represented in (a) logarithmic and (b) linear scales.

The experimental evidences obtained during the characterization of a single ZnO NW based devices can be explained using the band structure diagram shown in figure 6.36. ZnO NW surface is highly reactive to the O species contained in the ambient. Different studies in the literature confirm the adsorption of O_2 molecules by trapping electrons from the conductive volume and modifying electrical properties of the NW [38]. In that respect, O species tend to trap electrons at the NW surface at energy states located inside the band gap of ZnO (figure 6.36). The origin of this surface traps is still unknown and is commonly associated to O vacancies [39, 40]. These defects are n-type donor defects and then increase the free charge in the NW bulk. Since a free surface state is filled by an electron coming from the NW bulk, there is a band bending (BB) of

the conduction (CB) and valence bands (VB), generating a region at the surface of the NW called surface charge region (SCR) with a low electrical conduction (figure 6.36). Depending on r_{NW}, the SCR can affect in different ways the conductive volume of the NW. The axial electrical conduction in NWs with thick radius is weakly affected by the SCR, showing high I_{dark} (figure 6.36(a)). In contrast, the thickness of the SCR affects more the electrical conduction of NWs with narrower radius as observed in the *I*/*V* measurements carried out in dark. As shown in figure 6.36(b), the narrow region associated to the conductive volume is highly confined by the SCR and for that reason I_{dark} is lowered.

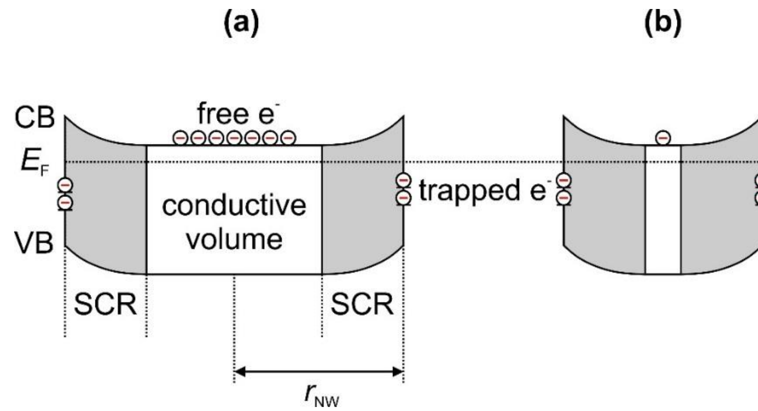

Figure 6.36. Electronic band structure of two NWs with different r_{NW}.

Figure 6.37 represents the device resistance measured in dark as a function of the inverse NW radius squared (r_{NW}^{-2}), which is a proportional magnitude to the NW cross-sectional area. Although the displayed resistance is taken at 5 V, the variation of this parameter over the analyzed voltage range (-5 to 5 V) is around 100%. The resistance increases superlinearly with the cross-sectional area, indicating that the conductive

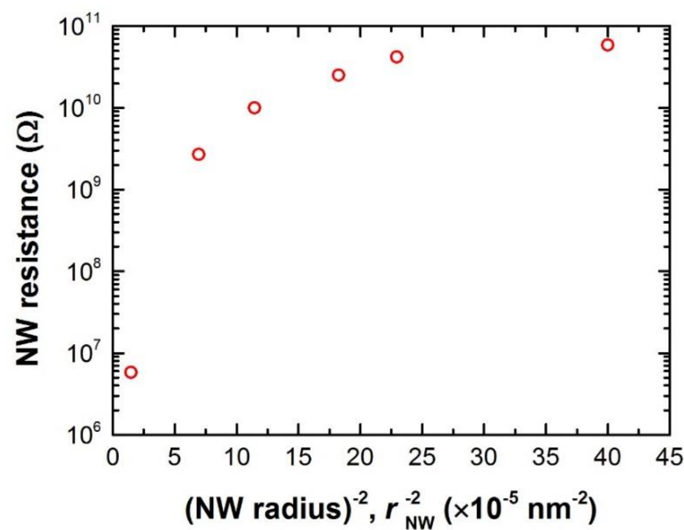

Figure 6.37. NW resistance obtained at 5 V as a function of the inverse NW radius squared (r_{NW}^{-2}).

volume diminishes more markedly than expected from the NW radius reduction mainly because the existence of the SCR. Interestingly, the resistance saturates for the thinnest NWs. A resistance value of about 50 GΩ is obtained when the radius is lower than a critical value of 65 nm ($r_{NW,c}$). This anomaly indicates that when the SCR thickness is in the order of the NW radius, the NW is nearly depleted, i.e. the conductive volume is almost empty of free charge.

Assuming a donor concentration (N_d) and taking into account the area ($A_{NW} = 6\, r_{NW}\, L_{NW}$) and volume ($V_{NW} = \sqrt{27/4}\, r_{NW}^2\, L_{NW}$) of a hexagonal prism shape NW, the surface charge (N_{ss}) necessary to deplete completely the volume would be given by

$$N_{ss} A_{NW} = N_d V_{NW} \tag{6.9}$$

$$N_{ss} = \frac{\sqrt{3}}{4} r_{NW,c}\, N_d \tag{6.10}$$

Equation (6.9) accounts for the completely migration of electrons from bulk towards NW surface. For a typical donor concentration of 10^{18} cm^{-3} [41], equation (6.10) yields a N_{ss} of 2.8×10^{12} cm^{-2}. Considering O vacancies as a possible site to chemisorb O species [39, 40], N_{ss} is less than a hundredth of the total O surface concentration in the $\{10\bar{1}0\}$ planes (NW facets). Thus, this finding suggests that O adsorption produces less than 1% coverage of the NW surface but, thanks to the semiconductor properties of the NW, is large enough to affect significantly the electrical properties.

In addition, it can be inferred that the surface coverage would be even lower for smaller radius than $r_{NW,c}$, mainly limited by the total free charge in the NW volume. In those nearly depleted NWs, the conduction mechanism is strongly influenced by the surface states and their carrier emission and capture times. The current level, carrier mobility, transit time, and residual resistance would be limited by these surface generation-recombination processes. This conduction mechanism is a minor contribution to the drift through the conducting core in thicker NWs, for which the *I/V* characteristics are only limited by the cross-sectional conducting area.

The photoconductivity of devices based on a single ZnO NW with radius r_{NW} = 50, 120 and 260 nm is analyzed. Figure 6.34 shows *I/V* characteristics of these devices measured in dark and under UV illumination using a Xenon lamp (power density of 5.51 W/cm); the lamp is coupled to a monochromator in order to select a specific wavelength (λ) above the ZnO band gap energy (λ = 370 nm).

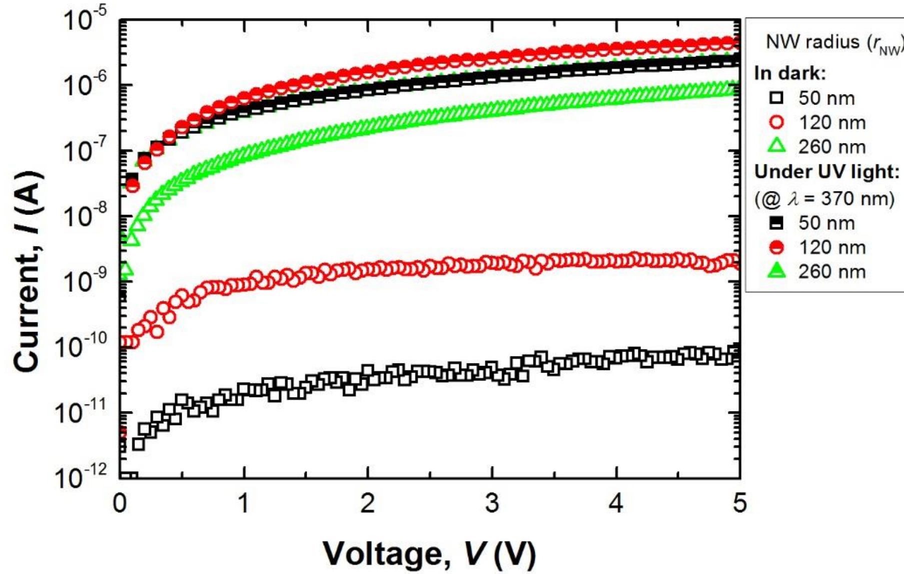

Figure 6.38. *I/V* characteristics measured in dark and under UV illumination for single ZnO NWs with different radii.

The current values under illumination (I_{light}) increase up to the mA range independently on r_{NW} (figure 6.38). In the case of r_{NW} = 50 nm, I_{light} exhibits values four orders of magnitude higher than the I_{dark} (at the incident power used). On the other hand, in the thickest NW (r_{NW} = 260 nm), this variation is just a factor ten mainly due to its high I_{dark}. From the photocurrent ($I_{photo} = I_{light} - I_{dark}$) values, the narrowest NW (r_{NW} = 50 nm) presents much higher dynamic range. Therefore, from a practical point of view, the integration of thinner ZnO NWs through the adjustment of parameters during NW synthesis and processing can lead to the fabrication photoconductor structures with higher signal-to-noise ratio (SNR).

These variations of the ZnO NW photoconductivity are mainly governed by adsorption/desorption mechanisms of O species along the NW surface. During the illumination of the NW with UV light, electron-hole pairs are photogenerated. Photogenerated holes travel from the ZnO NW bulk to the surface recombining there with trapped electrons and then desorbing oxygen species attached to the NW surface and releasing electrons to the NW bulk. The accumulation of negative charge along the NW surface induces an electric field in the transverse direction of the NW. This electric field is the main responsible for the quickly drift of carriers from surface to the conductive volume through the SCR. Therefore, the UV illumination empties the surface states of electrons and leads to a flattening of the BB, reducing the SCR thickness and therefore increasing of the conductive volume in the NW. In this scenario, the conduction mechanism resembles the conduction in thicker NWs and differs from the surface generation-recombination mechanism described in darkness for the thinnest NWs. The main consequence is the high I_{photo} obtained in the thinnest NWs.

The photoresponse, also called responsivity (R_{photo}), is calculated using

$$R_{photo} = \frac{I_{photo}}{P} \quad , \tag{6.11}$$

where P is the lamp power absorbed by the NW and is expressed as

$$P = P^{*} \frac{A_{\mathrm{NW}}}{A_{\mathrm{beam}}} , \qquad (6.12)$$

where P^{*} is the lamp power measured using a power meter placed in the equivalent position of the device; A_{beam} is the area of the circular spot (beam radius, r_{beam} = 5 mm) produced by the optical fiber coupled to the monochromator output on the sample surface; A_{NW} is the area of the NW irradiated by the light beam. The calculation of P is based on the highly uniform optical density, which presents peak-to-valley power fluctuations lower than 5% of the average power density throughout the beam area.

Figure 6.39(a) shows the collection of R_{photo} curves measured at different voltages ranging between 1 and 5 V, for a r_{NW} of 65 nm. R_{photo} up to 10^{8} A/W are obtained at 5 V and above the cut-off wavelength (λ_{c}), observing UV/VIS contrasts as high as 10^{4}. These R_{photo} values are similar than the record values reported in

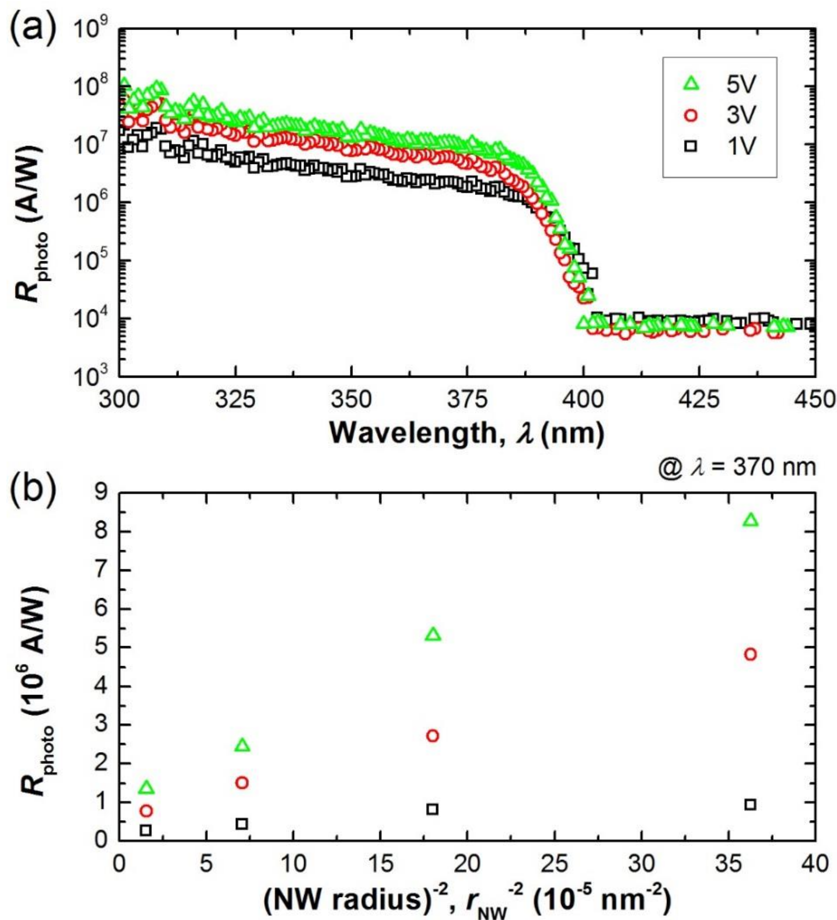

Figure 6.39. Responsivity represented as a function of (a) photon wavelength and (b) inverse radius square for different bias voltages.

the literature for single ZnO NW based UV PDs [42, 43]. Furthermore, these responsivities are comparable to those found in avalanche photodiodes working in Geiger operation mode, illustrating the high sensitivity of these devices. NW responsivity to the VIS range ($\lambda > 400$ nm) is attributed to the photoemission of trapped electrons from the surface to the conductive volume due to the existence of the electric field already described. The responsivity and the UV/VIS contrast increases with the bias voltage as shown in figure 6.39(b), where R_{photo} measured at $\lambda = 370$ nm is plotted as a function of r_{NW}^{-2} for different voltages. In addition, it can be noticed that R_{photo} also increases as r_{NW} decreases which confirms the enhancement of the photosensitivity for narrow NWs.

The photoconductive gain (G_{photo}) is estimated from the relationship with R_{photo} by

$$G_{photo} = R_{photo} \frac{h\nu}{q\eta} , \tag{6.13}$$

where $h\nu$ is the photon energy, q is the elementary charge and η is the quantum efficiency which is assumed to be 1 for simplicity. The G_{photo} values are estimated to be ranged between 10^7 and 10^8 as shown in figure 6.40. The high values obtained for G_{photo} are attributed to the SCR modulation as a result of O desorption from surface states during NW illumination such as discussed above and in good agreement with other authors [30, 42]. These results show that G_{photo} values steadily increase as the NW radius decreases, confirming the important role of the surface in the device responsivity and yielding values near 10^8 for the smallest NW radius characterized (r_{NW} = 50 nm). In addition, G_{photo} also increases with bias voltage due to the reduction of the

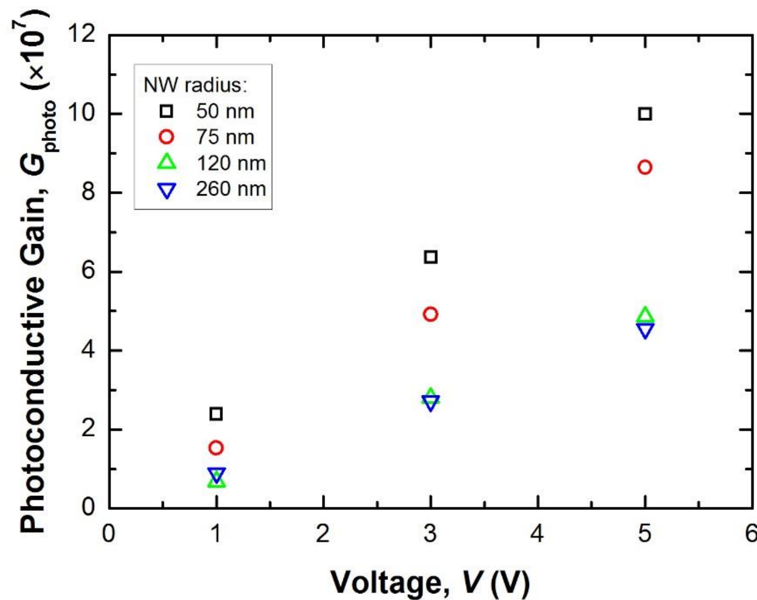

Figure 6.40. G_{photo} represented as a function of the voltage for different r_{NW}.

transit time across the micrometric inter-electrode distance which enhances the quotient between carrier recombination time and transit time, and consequently, the gain mechanism [44].

From the photocurrent measurements, the λ_c is extracted for NWs with different radii. This parameter is defined as the wavelength at which the photocurrent drops 3 dBs from its maximum value. The analysis of λ_c as a function of r_{NW} (figure 6.41) shows that λ_c monotonously reduces (energy blue shift) as the r_{NW} decreases. In the narrowest NW, λ_c reduces down to 363 nm at 1 V. This shift could be associated to band structure changes in the surface region due to the large O concentration. Additional experiments will be needed to elucidate the origin of the shift.

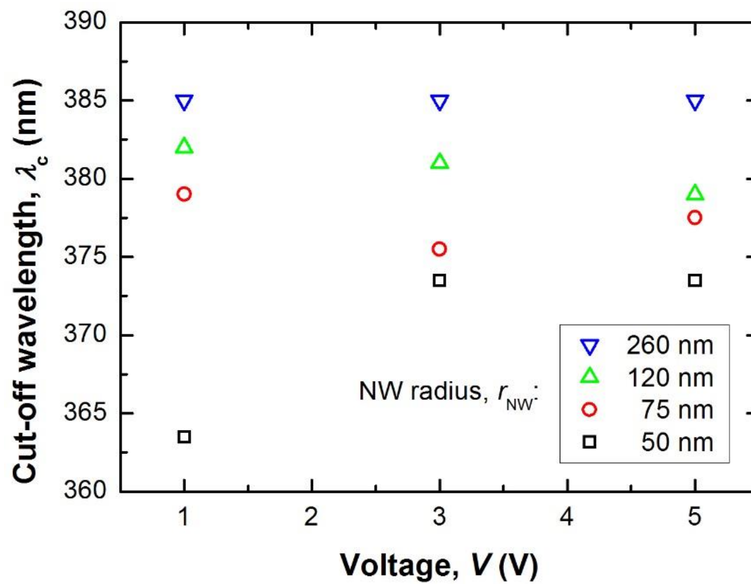

Figure 6.41. Cut-off wavelength as a function of the voltage for different r_{NW}.

From results presented above, it can be noticed that the high R_{photo} of ZnO NW based UV PDs is mainly attributed to the adsorption/desorption mechanisms of O species along the NW surface. However, those mechanisms (specially the re-adsorption of O) are confirmed to be slow and therefore limit the response time of these devices. ZnO NW size can also affect the excitation and relaxation times during UV light exposure measurements. In order to further analyze the effect of the NW dimensions on the device time response, transient photoresponse experiments were performed for devices based on a single NWs with different radii.

Figure 6.42 shows I_{photo} measured over time in two devices fabricated through DEP technique in order to control the assembling process of a single NW. Resultant devices are based on a NW with a r_{NW} of 260 (device A) and 50 nm (device B), aiming to analyze the effect of the NW dimensions on the time response. According to the previous discussion, both devices should be differently depleted.

I_{photo} is obtained biasing the NW at a constant voltage of 3 V. After a few seconds in darkness (~ 30 s), the NW is exposed to monochromatic light (at $\lambda = 370$ nm) for 5 min to study the rise time (τ_{rise}). After that, the light is turned off during another 5 min in order to measure the decay time (τ_{decay}). Solid lines represented in figure 6.42 are the best fitting to the experimental data by using sum of exponential functions

$$I_{\text{photo}}(t) \sim \sum_{i=1}^{N} A_i \exp(-t/\tau_i) \ , \tag{6.14}$$

where N is the number of exponential terms, and A_i and τ_i are the fitting parameters for each one.

Device A exhibits an abrupt increment of I_{photo} which corresponds to a $\tau_{\text{rise}} < 1$ s. After that, the I_{photo} continue increasing but is governed by a slower process that increases the τ_{rise} up to 78 s. The relaxation region presents also two different regions: the first one shows a faster decay time ($\tau_{\text{decay}}^{\text{I}}$) around 15 s whereas the second one is much slower ($\tau_{\text{decay}}^{\text{II}} = 356\text{s}$).

Device B does not show a fast rise time component, presenting only an exponential function with a τ_{rise} of about 89 s. The surface generation-recombination mechanism described above seems to limit the response speed in the nearly depleted NW bulk. This mechanism also arises in device A after the fast component with a τ_{rise} of 78 s. This result indicates that the fast component is directly related to the existence of a neutral region in the core of the NW and that its presence provides a fast channel for carrier flow after emission from the surface.

In the relaxation process, device B also shows two exponential terms with a first constant $\tau_{\text{decay}}^{\text{I}} = 17\text{s}$, whose value is similar to that observed in device A, and a second one $\tau_{\text{decay}}^{\text{II}} = 152\text{s}$ lower than that observed in device A.

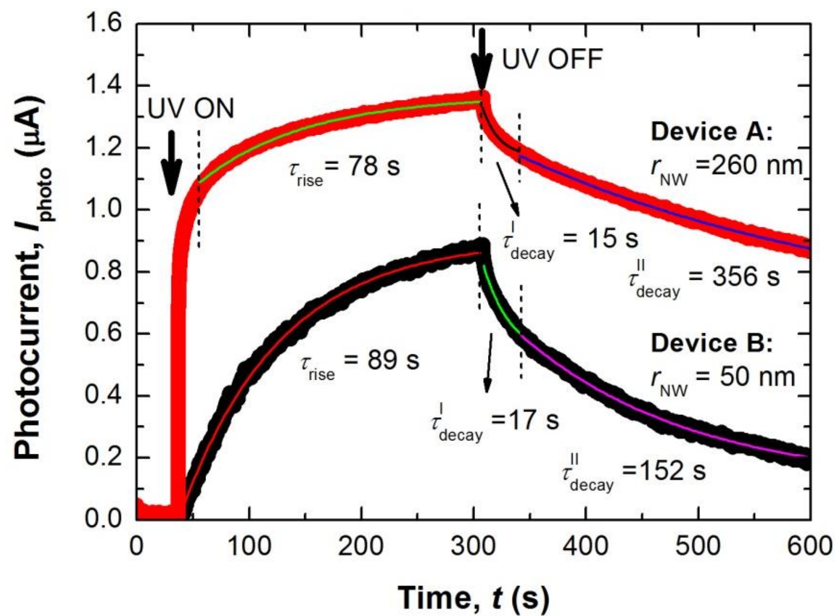

Figure 6.42. Response time of single NW with different r_{NW} (bias voltage of 3 V).

All the calculated times for both devices are included in table 6.5. From their analysis, it seems that relaxation times are slightly reduced in NW devices with smaller r_{NW}. Thus, although optimization of the rise time requires the increase of the conductive volume by increasing the NW size, radius reduction impacts positively on the decay time. We suppose that the reduction of the adsorbed O density in the nearly depleted structure (device B) could enhance the recovery time after illumination. The study of time response in single NW device can also be helpful in gas sensing applications, a major research area of this kind of structures [45].

Table 6.5. Rise and decay times measured in devices A and B based on a single NW with 260 and 50 nm in radius.

	τ_{rise}(s)	τ^{I}_{decay}(s)	τ^{II}_{decay}(s)
Device A (r_{NW} = 260 nm)	78	15	356
Device B (r_{NW} = 50 nm)	89	17	152

6.5. Chemical Modification of ZnO NW Surface

In this work, ZnO NW surface is analyzed by different techniques, including contact angle measurements, SEM, AFM, XPS, CPD, SPV, and *I*/*V* measurements. Properties of these NWs are analyzed after different surface treatments, comprising hydroxylation and silanization with amino-propyldiethoxymethylsilane (APDEMS). For the sake of comparison, a high purity a-plane ZnO bulk crystal is used as reference sample in both contact angle measurements and XPS.

The effects of both chemical modifications on the surface BB of the NWs are analyzed by CPD and SPV. In addition, *I*/*V* characteristics of a single ZnO NW, assembled between electrodes by DEP, are studied after each surface modification in order to analyze the effects of BB variations on the NW electrical conduction.

6.5.1. Hydroxylation and Silanization of ZnO NWs

Hydroxylation

For the hydroxylation of m-plane (NW sidewall) and a-plane (bulk crystal used as reference sample) ZnO surfaces, both samples are sequentially dipped in hot ethanol, acetone, and ethanol for 5 min, dried in N_2 flow and finally transferred to an O plasma system (100-E TePla). Once the samples are loaded into the plasma chamber, it is pumped to 0.1 mbar to reduce the influence of contaminants; then, the O_2 gas valve is opened, increasing the pressure up to 1.4 mbar. Finally, a power plasma of 200 W is turned on for 5 min.

Plasma treatment removes surface organic leftovers and also promotes the formation of a uniform and stable coverage of hydroxyl groups (-OH) on the ZnO NW surface. The hydroxyl ions near the ZnO NW surface originate mainly from the chemical adsorption of water molecules when the sample is exposed to the air after the plasma treatment. An O rich NW surface with induced surface defects after an O plasma treatment could enhance the dissociative adsorption of water molecules in ambient air, forming therefore a uniform -OH group coverage.

Silanization

The silanization of ZnO surfaces is carried out after the hydroxylation process described above. The silanization of hydroxylated ZnO is based on the displacement of alkoxy groups in the silane molecule by -OH, forming Si-O-Si covalent bonds along the ZnO surface [46].

The silanization process is performed in a glovebox under Ar ambient (O_2 < 1ppm, and H_2O < 2 ppm) to prevent the oligomerization of APDEMS molecules due to the ambient exposure [47]. Once the samples are transferred to the glovebox, they are dipped in an APDEMS solution (0.02 M APDEMS in toluene) and stored in there for 90 min. After that, samples are rinsed in toluene and isopropanol, and dried in N_2 flow.

6.5.2. Characterization of ZnO NW Surfaces

Contact Angle Measurements

A 3 µl droplet of DI water is drop-casted on top of the a-plane ZnO bulk crystal reference sample and the vertically aligned ZnO NWs sample after hydroxylation and silanization. Figure 6.43(a,b) show contact angle images after hydroxylation, presenting values of ~5º and ~15º for the bulk crystal and the NW sample, respectively. These images reveal a strong hydrophilic behaviour in both samples which is in good agreement with previous works performed in ZnO NWs [48].

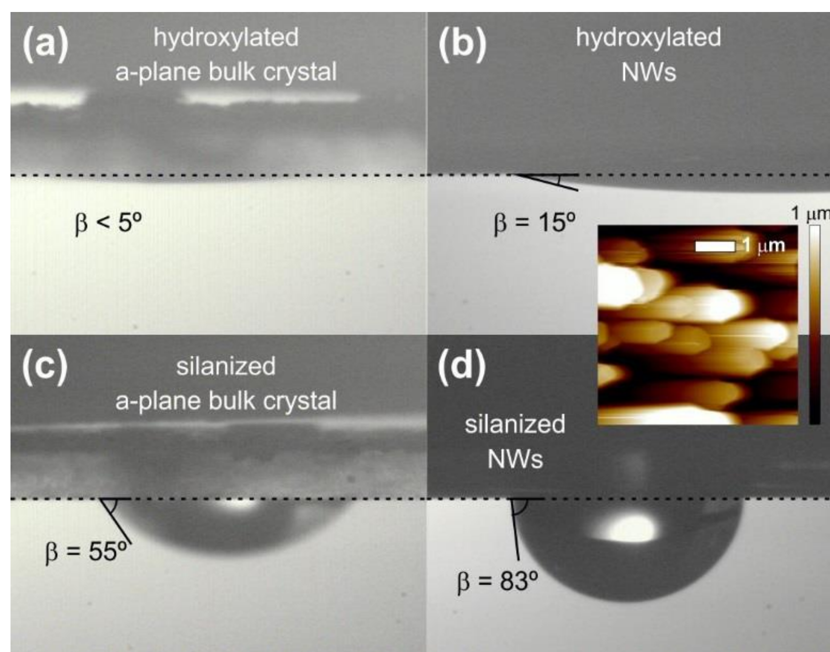

Figure 6.43. Contact angle measurements of a-plane ZnO bulk crystal and ZnO NW surface after (a,b) hydroxylation, and (c,d) silanization. Inset: AFM image of vertically aligned ZnO NWs grown on a Si(100) substrate.

After silanization (figure 6.43(c,d)), the surface turns hydrophobic, exhibiting an increase of the contact angles up to 55º, in the a-plane bulk crystal, and 83º, in the NW sample. The contact angle obtained for silanized a-plane bulk crystal is close to that value measured in SiC surfaces functionalized by APDEMS [49]. In addition, the higher contact angle observed in the NW sample is associated with the nanostructured morphology of the surface, on which, according to the Cassie's model [50], the droplets can stand, forming a high contact angle.

XPS Characterization

XPS spectra corresponding to N 1s, C 1s, Zn 2p3/2, and surface/bulk O 1s core levels were measured in both a-plane ZnO bulk crystal and ZnO NW samples after their hydroxylation and silanization. In comparison to the a-plane reference sample (not shown), it is worth noticing that the binding energies (BE) for all these elements in the NW sample are shifted about 3 eV towards larger values due to the geometry of the surface, which induces an extra stopping power when electrons from deeper atoms in the NW are photoemitted.

Figure 6.44(a) shows XPS survey and figure 6.44(b-d) show core levels of ZnO NW sample after its hydroxylation (black) and silanization (red). First evidence of the silanization is the presence of a N peak (figure 6.44(b)), coming from the amine terminal group, and the increase of the C 1s peak intensity (figure 6.44(c)), produced by the hydrocarbon groups in the APDEMS self-assembled monolayer (SAM). The origin of the C 1s signal in the hydroxylated sample is likely due to the unintentional C contamination of the ZnO bulk sample during the growth process (section 6.1.2). After silanization, the C 1s peak increases and shifts 350 meV towards lower binding energies. These variations provide another evidence of the presence of the SAM on the ZnO surface associated to the increase of the C molar fraction and the change in the chemical environment of the C atoms.

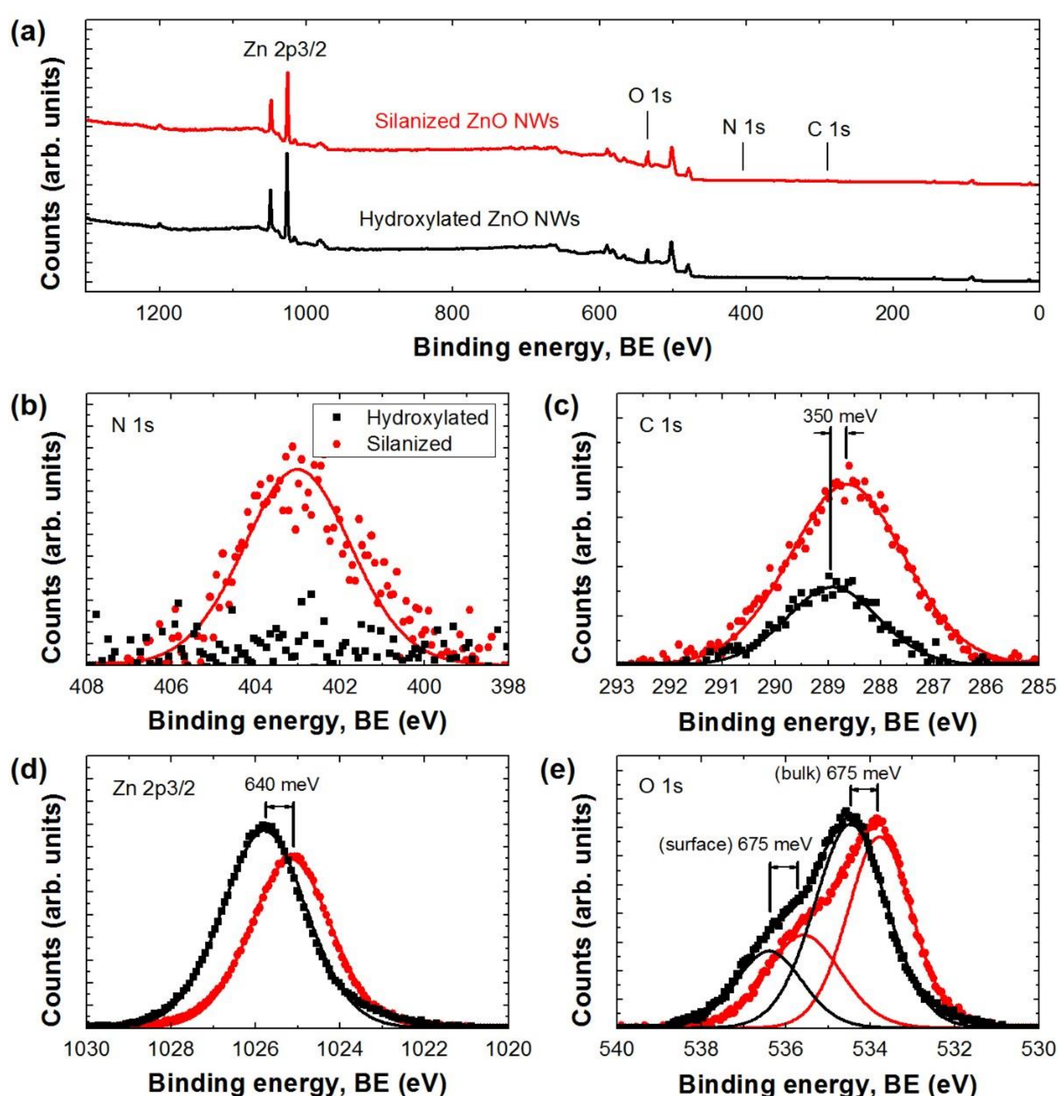

Figure 6.44. (a) XPS survey spectra of hydroxylated (black) and silanized (red) ZnO NW surfaces. (b) N 1s, (c) C 1s, (d) Zn 2p3/2, and (e) O 1 s XPS core level spectra for Zn NW surfaces after hydroxylation (black) and silanization (red). Solid lines represent the Gaussian-Lorentzian functions used to fit the signal of each element.

The attenuation of the Zn photoemission peak observed in figure 6.44(d) is another sign of the SAM formation atop the ZnO surface. Such attenuation can be used to determine the surface coverage and the SAM thickness (d_{SAM}) [51]; the latter is estimated following the equation

$$d_{\mathrm{SAM}} = -\lambda_{\mathrm{n}} \ln\left(\frac{I_{\mathrm{SAM}}}{I_0}\right) , \tag{6.15}$$

where λ_{n} is the photon wavelength at the center of the peak, and I_0 and I_{SAM} are the photoelectron intensity after hydroxylation and silanization, respectively. Equation (6.15) is used to determine the d_{SAM} in the NW and a-plane bulk crystal samples, yielding values of 0.37 and 0.58 nm, respectively. Surface coverage is calculated from those values, using the equation

$$\Gamma\left(\mathrm{molecules/cm^2}\right) = \frac{d_{\mathrm{SAM}}\, \rho_{\mathrm{APDEMS}}\, N_{\mathrm{A}}}{M_{\mathrm{APDEMS}}} , \tag{6.16}$$

where ρ_{APDEMS} and M_{APDEMS} are the density and molar mass of APDEMS, respectively, and N_{A} is the Avogadro constant. From equation (6.16), the surface coverage after silanization is calculated to be 8.0×10^{13} molecules/cm^2 in the NW sample and 12.6×10^{13} molecules/cm^2 in the a-plane bulk crystal sample. Comparing with the total achievable surface coverage for an a-plane ZnO surface (6.82×10^{14} molecules/cm^2), the resultant surface concentrations correspond to coverages of 11.7% (NWs) and 18.5% (bulk crystal).

After using the R.S.F., given in chapter 4, in Zn (figure 6.44(d)) and O bulk (figure 6.44(e)) signals, the O(bulk):Zn ratio calculated for the non-silanized sample is 1.03, confirming the stoichiometric characteristics of the NWs. After silanization, this factor remains near 1, suggesting that there are no significant changes in the atomic distribution of the bulk caused by the SAM formation.

Figure 6.44(e) shows the surface and the bulk O peaks for the NW sample after its hydroxylation and silanization. We have first focused on the variation of the surface O. The integral to the Gaussian-Lorentzian fit under the surface O peak is calculated and corrected by both the R.S.F. and the molar factors. For the hydroxylated surface, it must be taken into account that -OH groups bind to the Zn atom under a stoichiometric ratio of 2:1 to form $Zn(OH)_2$ (figure 6.45(a)); therefore, the molar factor is 2. In contrast, silanized samples have APDEMS molecules attached to the ZnO surface (figure 6.45(b)), resulting in a stoichiometric ratio of O:Zn=3:1, and yielding an effective molar factor of 3. The ratio between the surface O signals in silanized and hydroxylated samples results in 0.9; using this ratio and the surface coverage calculated for APDEMS (8.0×10^{13} molecules/cm^2), the surface coverage of hydroxylated NWs is expected to be around 8.9×10^{13} molecules/cm^2. This result points out the efficiency of the initial -OH coverage to promote the attachment of the APDEMS molecules, indicating that most of the -OH groups should be nearly replaced by APDEMS molecules along the ZnO surface.

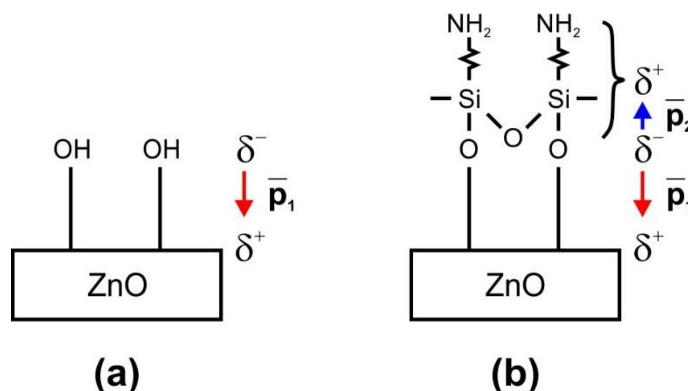

Figure 6.45. ZnO surface dipole formed after (a) hydroxylation, and (b) silanization.

The successful formation of the SAM on the ZnO surface can be also demonstrated by analyzing the energy shift of the XPS peaks. Figure 6.44(d) presents a strong energy shift (640 meV) of the Zn peak towards lower binding energies after the silanization step. This behaviour can be attributed to the attenuation of the negative surface dipole, formed after hydroxylation (figure 6.45(a)), by the charges in the APDEMS molecules (figure 6.45(b)). In the hydroxylated samples, the kinetic energy of the photoemitted electrons from the ZnO bulk is reduced due to the influence of the negative surface dipole. Finally, the evidence of the presence of a surface dipole change is also observed in both the O bulk and surface signals which present a binding energy shift of approximately 675 meV towards lower binding energies (figure 6.44(e)).

Surface BB Determination

CPD measurements are taken in order to find out changes in the surface work function of the NW sample due to the formation of the different surface dipoles after hydroxylation or silanization. Those dipoles can affect the surface BB of the energy bands, which determines the space charge region width (w_{SCR}) and the transverse conduction volume along the NW.

Following the hydroxylation treatment, ZnO NW samples exhibited a dark CPD value of eV_{CPD} = +0.32 eV (CPD energy plateau observed in the black curve of figure 6.46 for times ranged between 0 and 7 min), which corresponds to the energy necessary to nullify the difference between the Au work function (Φ_{Au} = 4.7 eV) and the surface work function (Φ), defined as the sum of the ZnO work function (Φ_{ZnO}), the surface BB (Φ_s) and the energy step associated to the negative surface dipole induced by the hydroxyl group (Φ_{OH}) (figure 6.47(a)). Therefore, the surface work function of the hydroxylated ZnO NW surface is estimated to be $\Phi = eV_{CPD} + \Phi_{Au} = 5.02$ eV.

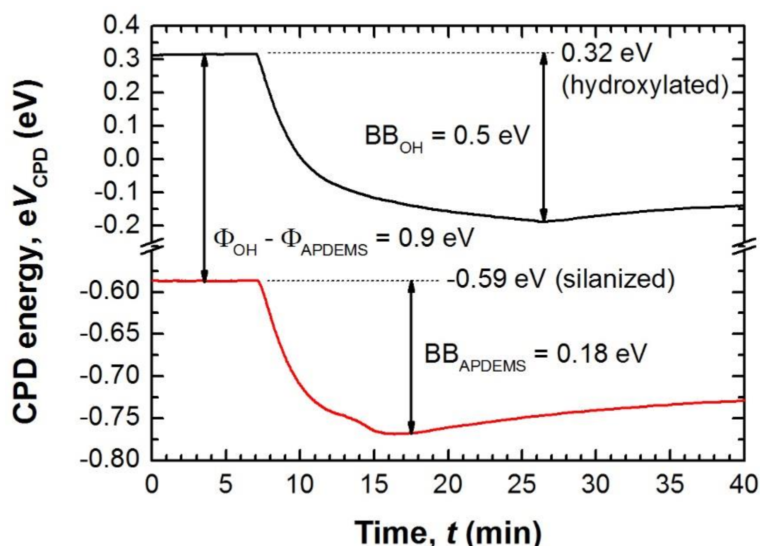

Figure 6.46. CPD and SPV energies measured for hydroxylated (black) and silanized (red) ZnO NW samples.

For silanized surfaces, the dark CPD values decreases down to -0.59 eV (CPD energy plateau observed in the red curve of figure 6.46 for times ranged between 0 and 7 min), which means that the local vacuum level is lowered by a negative energy step induced by the reduction of the surface dipole, due to the charge distribution in the adlayer (Φ_{APDEMS}) (figure 6.47(b)). Then, the surface work function of the silanized ZnO NW surface is calculated to be $\Phi = eV_{CPD} + \Phi_{Au} = 4.11$ eV. As eV_{CPD} is negative in this case, the work function of the silanized surface is lower than the Au work function. This is a direct consequence of surface dipole reduction after silanization also observed in the XPS analysis of the O peak [47].

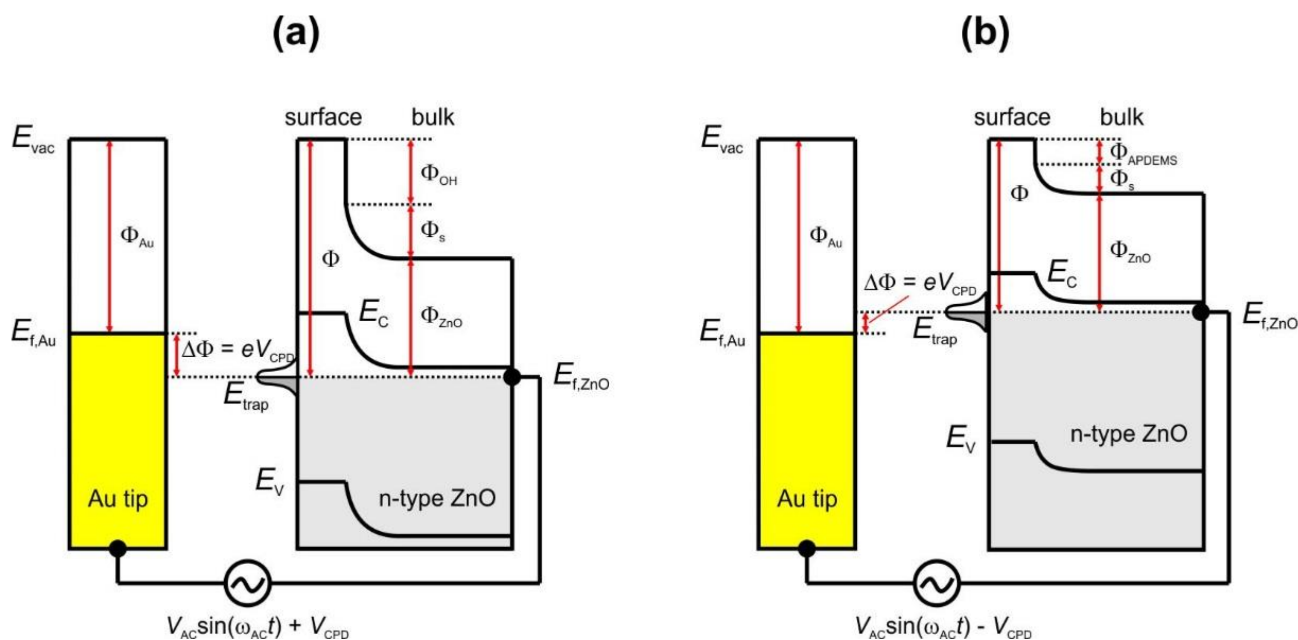

Figure 6.47. Electronic band structure of (a) hydroxylated, and (b) silanized ZnO NW surface for CPD measurements

During the SPV measurements, the use of a strong illumination above the band gap energy of ZnO produces BB flattening in hydroxylated and silanized samples which allows determining Φ_s. The Φ_s value obtained for hydroxylated and silanized ZnO NW surfaces are found to be 0.5 and 0.18 eV, respectively. Using Φ_s and Φ values obtained from SPV and CPD studies, respectively, and the ZnO work function reported in the literature for as-deposited ZnO (Φ_{ZnO} = 3.74 eV) [52], one can determine the surface dipoles Φ_{OH} and Φ_{APDEMS}, resulting in 0.78 and 0.19 eV, respectively, being in good agreement with XPS results.

Solving the Poisson's equation, in thermal equilibrium, for a n-type semiconductor with a single set of discrete surface states of acceptor type, it is possible to obtain the density of surface states (N_{ss}) from the Φ_s equation [53]:

$$\Phi_s = \frac{(e\,N_{ss})^2}{2\,\varepsilon_{ZnO}\,\varepsilon_0\,N_d} \quad , \tag{6.17}$$

where N_d is the donor density, ε_{ZnO} is the relative permittivity for ZnO ($11\varepsilon_0$), ε_0 is the vacuum permittivity (8.85×10^{-12} C/V·m), and e is the electron charge (1.602×10^{-19} C). Assuming a N_d of 10^{17} cm^{-3} for CVT ZnO NWs [54, 55], the N_{ss} can be estimated for hydroxylated and silanized samples using equation (6.17) and obtained Φ_s values from CPD and SPV measurements (called BB_{OH} and BB_{APDEMS} in figure 6.46), resulting in 7.8×10^{11} and 4.7×10^{11} cm^{-2}, respectively. Therefore, the decrease of the BB obtained after silanization is the result of a reduction in N_{ss} of around 3.1×10^{11} cm^{-2} upon attachment of the organic adlayer.

Electrical Conductivity

The surface studies discussed above are completed with the characterization of the electrical conductivity in a single ZnO NW. For that purpose, single ZnO NW devices were fabricated by DEP and photolithography, following the fabrication steps described in section 6.3.3 (figure 6.34).

Once the NW devices are fabricated, the NW surface is first hydroxylated and later silanized as described above. *I*/*V* characteristics of the resultant devices are measured, in dark conditions, at every surface treatment step, aiming to observe variations produced by –OH and APDEMS surface coverages on the electrical conduction of the ZnO NW.

Figure 6.48 shows a layer schematic and a SEM image of a resultant device. In figure 6.48(a), it is represented the SAM covering the ZnO NW surface. On the other hand, the SEM image (figure 6.48(b)) uses dashed lines to highlight electrodes composed by Al and AZO.

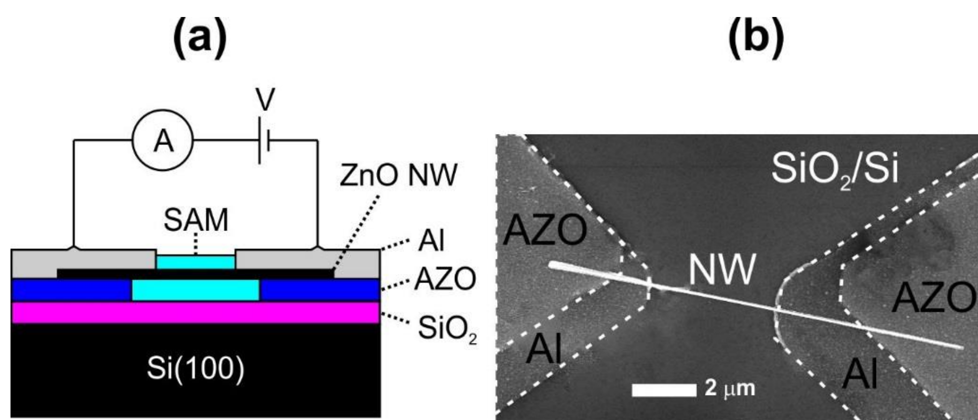

Figure 6.48. (a) Layer schematic, and (b) SEM image of the single NW device.

I/*V* characteristics of the fabricated devices are measured after every surface treatment (figure 6.49). After hydroxylation (black curves), the device presents a current of 0.4 nA at 5 V which is much lower than those currents measured in the NW devices before any surface treatment (blue curves); in addition, both *I*/*V* curves (before and after hydroxylation) are also represented in linear scale (figure 6.49(a)), exhibiting a non-linear behaviour that will be analyzed in depth later on.

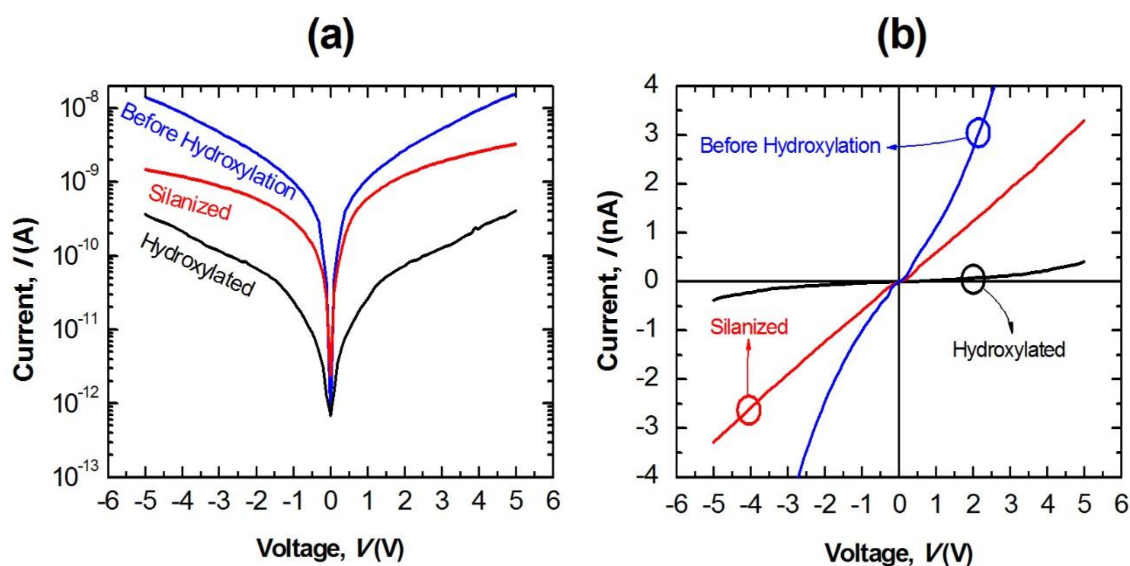

Figure 6.49. *I-V* characteristics, (a) in logarithmic and (b) linear scales, of a single NW measured before (blue) and after hydroxylation (black), and after silanization (red).

Comparing both hydroxylated and silanized devices, the latter (red curves) presents higher current levels (3 nA at 5V). In order to understand this change of the current, the w_{SCR} value is calculated at every step from the BB magnitude (Φ_s) obtained in SPV measurements (figure 6.46), and using the following equation [56]:

$$\Phi_s = \frac{e^2}{2\varepsilon_{ZnO}\varepsilon_0} N_d w_{SCR} \ , \tag{6.18}$$

The values obtained for w_{SCR} are 78 and 47 nm for hydroxylated and silanized devices, respectively. From figure 6.48(b), the r_{NW} and L_{NW} are estimated to be around 60 nm and 4 μm, respectively. Subtracting w_{SCR} from r_{NW}, the hydroxylated device is expected to be nearly depleted ($w_{SCR} > r_{NW}$), while the silanized device has a $w_{SCR} < r_{NW}$. Therefore, that higher current levels measured in the silanized device (or even higher in untreated ZnO NW based devices) are suggested to be a direct consequence of the SCR narrowing, which means an increase of the conductive volume. Similar results have been observed in section 6.4.1 (figure 6.35 and figure 6.36) where current levels of devices with the same geometry were demonstrated to be directly related by r_{NW} of the ZnO NW [57].

The increase of the NW conductive volume is also suggested to have a positive effect on the contact linearly such as observed in figure 6.49(b), where the *I*/*V* curve changes from non-linear to linear after silanization. Although the free charge emission mainly occurs from the naked surface of the NW, the increase of the free charge density inside the NW can enhance tunneling transport through the contact built-in voltage [58]. Quantum theory predicts that the increase of the carrier density in the NW enhances the transmission probability through a potential barrier. From the results obtained after silanization, it seems that the increase of the free charge inside the volume of a nearly-depleted NW through the passivation of surface states can also provoke the improvement of the contact linearity.

CONCLUSIONS

In this work, both ZnO TPs and vertically aligned ZnO NWs have been grown by CVT technique using Zn and O as gas sources and Ar as carrier gas. For the TP growth, Zn gas is obtained by the direct thermal evaporation of Zn powder at temperatures above 700ºC; whereas for the NW growth, Zn gas is obtained by carbo-thermal reduction of ZnO powder at 900 ºC. The NW growth is carried out on Si(100) substrates with a 7-nm thick Zn seed layer, resulting NWs with dimensions of r_{NW} = 45-435 nm, and L_{NW} up to 10.5 μm. Resultant NWs have been characterized by different techniques, including transmission spectrophotometry, PL, XRD, and IBA (RBS, non-RBS and NRA). Channeling and random RBS measurements have been demonstrated to be an effective tool to determine composition, molecular density, surface coverage, and tilt angle of vertically aligned ZnO NWs.

ZnO NWs have been used for the fabrication of UV PDs based on a single NW. Their long length allowed NW assembling between pairs of electrodes with micrometric inter-electrode distances by positive DEP. AZO electrodes have been introduced and tested, showing high mechanical strength and adherence to the oxidized Si substrates. DEP parameters such as voltage amplitude and frequency have been studied for the deposition of ZnO NWs, analyzing the effect of the dielectrophoretic force on the NW alignment. Using optimized DEP conditions, a single NW device has been implemented following a scheme fully compatible with CMOS technology. The optoelectronic properties of a single NW photoconductor with different radius have been studied. A critical NW radius of 65 nm is found to nearly deplete the NW volume. Surface generation-recombination processes are proposed to account for the residual electrical resistance. Increasing photoconductive gains are observed as the NW radius reduces, reaching values near 10^8 for nearly depleted NWs. Blue-shifted cut-off wavelengths are also measured in these devices. Time response has also been analyzed at large time scales. Rise and decay times presented an opposite behavior as a function of the NW radius. Whereas the increase of the NW radius tends to speed up the device response upon illumination it also tends to slow down device recovery.

ZnO NWs have been successfully functionalized with APDEMS as demonstrated by different techniques such as contact angle measurements, CPD, SPV, and XPS. Silanization makes the surfaces hydrophobic in comparison to the hydrophilic properties shown in the hydroxylated surfaces. The XPS spectra confirmed the attachment of the APDEMS molecules through the presence of N 1s and C 1s peaks, belonging to amine and hydrocarbon groups. The spectra also show a binding energy redshift of both peaks Zn 2p3/2 (640 meV) and O 1s (675 meV) compared to those of the hydroxylated ZnO, evidencing a change in the surface dipole formed atop the ZnO surface. This change of the surface dipole also produces a reduction of the ZnO work function from 5.02 eV (hydroxylation) to 4.11 eV (silanization) as determined by CPD. On the other hand, comparing the width of the surface BB obtained from SPV measurements with the NW axial dimensions, it can be concluded that the hydroxylated NWs are nearly depleted. The *I*/*V* characteristics of a single NW are measured integrating the NW between a pair of Al electrodes using DEP. The silanized NW shows larger currents than the hydroxylated NW due to the enlargement of the conductive volume. Finally, it is observed

that the NW silanization improves the linear characteristic of the contact formed between the NW and the Al electrode mainly due to the increase of the total free charge in the NW, which can benefit the output parameters of ion-gated FET.

REFERENCES

[1] C. García Núñez, A. Redondo Cubero, M. Cervera, S. Gang, P. Kung, and J. L. Pau, "Ion beam analysis of vertically aligned ZnO nanowires," *Nuclear Instruments and Methods in Physics Research Section B: Beam Interactions with Materials and Atoms,* (in preparation) 2015.

[2] C. García Núñez, J. L. Pau, E. Ruíz, A. García Marín, B. J. García, J. Piqueras*, et al.*, "Enhanced fabrication process of zinc oxide nanowires for optoelectronics," *Thin Solid Films,* vol. 555, pp. 42-47, 2014.

[3] C. García Núñez, A. García Marín, P. Nanterne, J. Piqueras, P. Kung, and J. L. Pau, "Conducting properties of nearly depleted ZnO nanowire UV sensors fabricated by dielectrophoresis," *Nanotechnology,* vol. 24, p. 415702, 2013.

[4] C. García Núñez, M. Sachsenhauser, B. Blashcke, A. García Marín, J. A. Garrido, and J. L. Pau, "Effects of Hydroxylation and Silanization on the Surface Properties of ZnO Nanowires," *ACS applied materials & interfaces,* vol. 7, pp. 5331-5337, 2015.

[5] M. H. Huang, Y. Wu, H. Feick, N. Tran, E. Weber, and P. Yang, "Catalytic growth of zinc oxide nanowires by vapor transport," *Advanced Materials,* vol. 13, pp. 113-116, 2001.

[6] J. Nowalk, "Growth of Zinc Oxide Nanobelts," in *APS March Meeting Abstracts*, 2013, p. 1122.

[7] Y. Dai, Y. Zhang, Q. Li, and C. Nan, "Synthesis and optical properties of tetrapod-like zinc oxide nanorods," *Chemical Physics Letters,* vol. 358, pp. 83-86, 2002.

[8] B.-B. Wang, J.-J. Xie, Q. Yuan, and Y.-P. Zhao, "Growth mechanism and joint structure of ZnO tetrapods," *Journal of Physics D: Applied Physics,* vol. 41, p. 102005, 2008.

[9] C. Ronning, N. G. Shang, I. Gerhards, H. Hofsäss, and M. Seibt, "Nucleation mechanism of the seed of tetrapod ZnO nanostructures," *Journal of Applied Physics,* vol. 98, p. 034307, 2005.

[10] M. Shiojiri and C. Kaito, "Structure and growth of ZnO smoke particles prepared by gas evaporation technique," *Journal of Crystal Growth,* vol. 52, pp. 173-177, 1981.

[11] K. Nishio, T. Isshiki, M. Kitano, and M. Shiojiri, "Structure and growth mechanism of tetrapod-like ZnO particles," *Philosophical Magazine A,* vol. 76, pp. 889-904, 1997.

[12] Y. Wang, L. Zhang, G. Wang, X. Peng, Z. Chu, and C. Liang, "Catalytic growth of semiconducting zinc oxide nanowires and their photoluminescence properties," *Journal of Crystal Growth,* vol. 234, pp. 171-175, 2002.

[13] J. Pau, C. Bayram, P. Giedraitis, R. McClintock, and M. Razeghi, "GaN nanostructured pin photodiodes," *Applied Physics Letters,* vol. 93, pp. 221104-221104-3, 2008.

[14] D. C. Reynolds, D. C. Look, B. Jogai, J. E. Hoelscher, R. E. Sherriff, M. T. Harris*, et al.*, "Time-resolved photoluminescence lifetime measurements of the Γ5 and Γ6 free excitons in ZnO," *Journal of Applied Physics,* vol. 88, pp. 2152-2153, 2000.

[15] B. Guo, Z. R. Qiu, and K. S. Wong, "Intensity dependence and transient dynamics of donor–acceptor pair recombination in ZnO thin films grown on (001) silicon," *Applied Physics Letters,* vol. 82, pp. 2290-2292, 2003.

[16] A. Kohan, G. Ceder, D. Morgan, and C. G. Van de Walle, "First-principles study of native point defects in ZnO," *Physical Review B,* vol. 61, p. 15019, 2000.

[17] M. Liu, A. Kitai, and P. Mascher, "Point defects and luminescence centres in zinc oxide and zinc oxide doped with manganese," *Journal of Luminescence,* vol. 54, pp. 35-42, 1992.

[18] Ü. Özgür, Y. I. Alivov, C. Liu, A. Teke, M. A. Reshchikov, S. Doğan*, et al.*, "A comprehensive review of ZnO materials and devices," *Journal of Applied Physics,* vol. 98, p. 041301, 2005.

[19] T. Schmidt, K. Lischka, and W. Zulehner, "Excitation-power dependence of the near-band-edge photoluminescence of semiconductors," *Physical Review B,* vol. 45, p. 8989, 1992.

[20] L. Bergman, X.-B. Chen, J. L. Morrison, J. Huso, and A. P. Purdy, "Photoluminescence dynamics in ensembles of wide-band-gap nanocrystallites and powders," *Journal of applied physics,* vol. 96, pp. 675-682, 2004.

[21] V. A. Fonoberov, K. A. Alim, A. A. Balandin, F. Xiu, and J. Liu, "Photoluminescence investigation of the carrier recombination processes in ZnO quantum dots and nanocrystals," *Physical review B,* vol. 73, p. 165317, 2006.

[22] G. Shen, N. Dawahre, J. Waters, S. M. Kim, and P. Kung, "Growth, doping, and characterization of ZnO nanowire arrays," *Journal of Vacuum Science & Technology B,* vol. 31, p. 041803, 2013.

[23] A. Mohanta, J. G. Simmons, H. O. Everitt, G. Shen, S. M. Kim, and P. Kung, "Effect of pressure and Al doping on structural and optical properties of ZnO nanowires synthesized by chemical vapor deposition," *Journal of Luminescence,* vol. 146, pp. 470-474, 2014.

[24] M. Mayer, "SIMNRA user's guide," 1997.

[25] X. Zhang, Y. Liu, and S. Chen, "A novel method for measuring distribution of orientation of one-dimensional ZnO using resonance Raman spectroscopy," *Journal of Raman Spectroscopy,* vol. 36, pp. 1101-1105, 2005.

[26] M. Soosen Samoel, J. Koshy, A. Chandram, and K. George, "Optical phonon confinement in ZnO nanorods and nanotubes," *Indian Journal of Pure & Applied Physics,* vol. 48, pp. 703-708, 2010.

[27] C. Arguello, D. Rousseau, and S. P. d. S. Porto, "First-order Raman effect in wurtzite-type crystals," *Physical Review,* vol. 181, p. 1351, 1969.

[28] F. Decremps, J. Pellicer-Porres, A. M. Saitta, J.-C. Chervin, and A. Polian, "High-pressure Raman spectroscopy study of wurtzite ZnO," *Physical Review B,* vol. 65, p. 092101, 2002.

[29] R. Cuscó, E. Alarcón-Lladó, J. Ibanez, L. Artús, J. Jiménez, B. Wang*, et al.*, "Temperature dependence of Raman scattering in ZnO," *Physical Review B,* vol. 75, p. 165202, 2007.

[30] Q. Li, Q. Wan, Y. Liang, and T. Wang, "Electronic transport through individual ZnO nanowires," *Applied Physics Letters,* vol. 84, pp. 4556-4558, 2004.

[31] J. Suehiro, N. Nakagawa, S.-i. Hidaka, M. Ueda, K. Imasaka, M. Higashihata, *et al.*, "Dielectrophoretic fabrication and characterization of a ZnO nanowire-based UV photosensor," *Nanotechnology,* vol. 17, p. 2567, 2006.

[32] A. Jamshidi, P. J. Pauzauskie, P. J. Schuck, A. T. Ohta, P.-Y. Chiou, J. Chou, *et al.*, "Dynamic manipulation and separation of individual semiconducting and metallic nanowires," *Nature Photonics,* vol. 2, pp. 86-89, 2008.

[33] R. J. Barsotti, M. D. Vahey, R. Wartena, Y. M. Chiang, J. Voldman, and F. Stellacci, "Assembly of metal nanoparticles into nanogaps," *small,* vol. 3, pp. 488-499, 2007.

[34] J. Suehiro, G. Zhou, and M. Hara, "Fabrication of a carbon nanotube-based gas sensor using dielectrophoresis and its application for ammonia detection by impedance spectroscopy," *Journal of Physics D: Applied Physics,* vol. 36, p. L109, 2003.

[35] T. B. Jones and T. B. Jones, *Electromechanics of particles*: Cambridge University Press, 2005.

[36] J. Venermo and A. Sihvola, "Dielectric polarizability of circular cylinder," *Journal of electrostatics,* vol. 63, pp. 101-117, 2005.

[37] C. Multiphysics, "COMSOL multiphysics user guide (Version 4.3 a)," *COMSOL, AB,* 2012.

[38] T. Barry and F. Stone, "The reactions of oxygen at dark and irradiated zinc oxide surface," *Proceedings of the Royal Society of London. Series A. Mathematical and Physical Sciences,* vol. 255, pp. 124-144, 1960.

[39] G. Li, T. Hu, G. Pan, T. Yan, X. Gao, and H. Zhu, "Morphology− function relationship of ZnO: polar planes, oxygen vacancies, and activity," *The Journal of Physical Chemistry C,* vol. 112, pp. 11859-11864, 2008.

[40] K. M. Wong, S. Alay-e-Abbas, Y. Fang, A. Shaukat, and Y. Lei, "Spatial distribution of neutral oxygen vacancies on ZnO nanowire surfaces: An investigation combining confocal microscopy and first principles calculations," *Journal of Applied Physics,* vol. 114, p. 034901, 2013.

[41] I. Mora-Seró, F. Fabregat-Santiago, B. Denier, J. Bisquert, R. Tena-Zaera, J. Elias, *et al.*, "Determination of carrier density of ZnO nanowires by electrochemical techniques," *Applied physics letters,* vol. 89, p. 203117, 2006.

[42] C. Soci, A. Zhang, B. Xiang, S. A. Dayeh, D. Aplin, J. Park, *et al.*, "ZnO nanowire UV photodetectors with high internal gain," *Nano letters,* vol. 7, pp. 1003-1009, 2007.

[43] J. He, P. Chang, C. Chen, and K. Tsai, "Electrical and optoelectronic characterization of a ZnO nanowire contacted by focused-ion-beam-deposited Pt," *Nanotechnology,* vol. 20, p. 135701, 2009.

[44] R. H. Bube, "Photoconductivity of Solids," *New York, Krieger,* 1978.

[45] Q. Wan, Q. H. Li, Y. J. Chen, T. H. Wang, X. L. He, J. P. Li, *et al.*, "Fabrication and ethanol sensing characteristics of ZnO nanowire gas sensors," *Applied Physics Letters,* vol. 84, pp. 3654-3656, 2004.

[46] C. Allen, D. Baker, J. Albin, H. Oertli, D. Gillaspie, D. Olson, *et al.*, "Surface modification of ZnO using triethoxysilane-based molecules," *Langmuir,* vol. 24, pp. 13393-13398, 2008.

[47] S. E. Saddow, *Silicon carbide biotechnology: a biocompatible semiconductor for advanced biomedical devices and applications*: Elsevier, 2011.

[48] X. Meng, D. Zhao, J. Zhang, D. Shen, Y. Lu, L. Dong, *et al.*, "Wettability conversion on ZnO nanowire arrays surface modified by oxygen plasma treatment and annealing," *Chemical physics letters,* vol. 413, pp. 450-453, 2005.

[49] S. J. Schoell, M. Sachsenhauser, A. Oliveros, J. Howgate, M. Stutzmann, M. S. Brandt, *et al.*, "Organic functionalization of 3C-SiC surfaces," *ACS applied materials & interfaces,* vol. 5, pp. 1393-1399, 2013.

[50] A. Cassie and S. Baxter, "Wettability of porous surfaces," *Transactions of the Faraday Society,* vol. 40, pp. 546-551, 1944.

[51] E. Johansson and L. Nyborg, "XPS study of carboxylic acid layers on oxidized metals with reference to particulate materials," *Surface and interface analysis,* vol. 35, pp. 375-381, 2003.

[52] F.-L. Kuo, Y. Li, M. Solomon, J. Du, and N. D. Shepherd, "Workfunction tuning of zinc oxide films by argon sputtering and oxygen plasma: An experimental and computational study," *Journal of Physics D: Applied Physics,* vol. 45, p. 065301, 2012.

[53] W. Mönch, *Semiconductor surfaces and interfaces* vol. 26: Springer Science & Business Media, 2001.

[54] Q. Li, Y. Liang, Q. Wan, and T. Wang, "Oxygen sensing characteristics of individual ZnO nanowire transistors," *Applied Physics Letters,* vol. 85, pp. 6389-6391, 2004.

[55] P.-C. Chang, Z. Fan, D. Wang, W.-Y. Tseng, W.-A. Chiou, J. Hong, *et al.*, "ZnO nanowires synthesized by vapor trapping CVD method," *Chemistry of materials,* vol. 16, pp. 5133-5137, 2004.

[56] Z. L. Wang, "Zinc oxide nanostructures: growth, properties and applications," *Journal of Physics: Condensed Matter,* vol. 16, p. R829, 2004.

[57] C. G. Núñez, A. G. Marín, P. Nanterne, J. Piqueras, P. Kung, and J. L. Pau, "Conducting properties of nearly depleted ZnO nanowire UV sensors fabricated by dielectrophoresis," *Nanotechnology,* vol. 24, p. 415702, 2013.

[58] S. M. Sze and K. K. Ng, *Physics of semiconductor devices*: John Wiley & Sons, 2006.

7. Gallium Arsenide Nanowires

This chapter describes the growth of GaAs NWs by Ga-assisted CBE on oxidized Si(111) substrates, using TEGa and TBAs as metalorganic precursors of Ga and As, respectively. The growth kinetics of these NWs has been analyzed as a function of the growth conditions (T_s, V/III flux ratio, …). The influence of growth conditions on the resultant morphological, structural, and optical properties has been studied by means of SEM, RHEED, TEM, and Raman spectroscopy [1-3]. TEM and Raman spectroscopy measurements were carried out in The University of Alabama.

The growth of GaAs NWs through Ga-assisted VLS conditions requires a careful and controlled preparation of the Si(111) surface oxide (thickness, roughness, and composition) in order to enable the formation of Ga droplets using TEGa. Different substrate preparations have been developed in this work, allowing for Ga droplet formation, and then enabling the VLS growth of the GaAs NWs [1-3].

In this work, we have also analyzed the effect of the Ga droplet on the resultant NW crystalline structure. During the VLS growth, this droplet might bury partially or completely the GaAs NW front, showing important changes in the NW structural purity [1].

A thorough study of the Raman phonon modes in GaAs NWs has been also included in this chapter. The analysis of the longitudinal and transversal optical phonon modes in GaAs NWs allows to estimate the density of defects in a single NW. In addition, the possible oxidation or the existence of surface defects along GaAs NW sidewalls enable the observation of surface optical phonons. Analyzing in depth the energy shift of this phonon, NW surface roughness can be also determined [4].

Finally, the integration of single GaAs NWs between conductive electrodes has been studied as a function of the DEP conditions, allowing for the characterization of the NW optoelectronic properties. The assembling procedure has analyzed as a function of the DEP conditions, including the control over the assembled NWs, their alignment, and critical trapping distances [5].

7.1. Growth of GaAs NWs by Ga-assisted CBE

The growth of GaAs NWs is carried out by means of Ga-assisted VLS procedure, consisting in a homo-PAG growth mechanism previously described in chapter 2 (figure 2.12(a)). Under Ga-assisted VLS conditions, the self-formation of Ga droplets is necessary to enable the growth of GaAs NWs mainly because these droplets have a double role, acting as traps for Ga and As elements (nucleation sites), and also assisting the GaAs NW growth along a preferential direction, as determined by the substrate crystalline orientation. The successful growth of GaAs NWs by Ga-assisted VLS mechanisms is even more challenging in the case of CBE, because the use of metalorganic precursors for Ga and As instead of solid sources.

This section presents different surface treatments of Si(111) substrates that allow for the formation of Ga droplets from the TEGa precursor. The section also includes a description of a standard Ga-assisted growth procedure of GaAs NWs on oxidized Si(111) substrates by CBE. Finally, it will present the analysis of GaAs NW growth kinetics under different growth conditions.

7.1.1. Si(111) Substrate Preparation

The epitaxial growth of GaAs NWs is very sensitive to the substrate surface chemical and crystalline structural properties. For this reason not only the type of substrate, but also its preparation should be carefully studied in order to further understand the NW growth mechanisms.

As mentioned in chapter 2 (section 2.3.1), Si(111) is commonly chosen as substrate to carry out the synthesis of GaAs NWs by means of Ga-assisted VLS due to many advantages. In this regard, Si(111) substrates have been successfully used for Ga-assisted VLS growth by techniques such as MBE [6]; however, in the case of CBE, the use of metalorganic precursors makes the preparation of the Si(111) substrate surface even more critical for this kind of growth. The cracking efficiency of a metalorganic precursor on the oxidized surface of the Si(111) substrate is strongly influenced by factors such as SiO_x surface thickness, roughness and chemical properties such as the T_s and the metalorganic precursor type.

The study of the Si(111) substrate preparation is therefore important because of the necessity to find a reproducible way to grow GaAs NWs under specific CBE conditions, obtaining NWs with the same properties.

Substrate Etching Protocols

Substrates used in this work consist in pieces of Si(111) wafers manufactured by Virginia Semiconductor. The cleavage of the wafer is carried out along the perpendicular direction to the wafer flat, and also along other directions rotated 60º degrees with respect to the first cleavage, which correspond to {-211} planes. Resultant substrates are typically triangular-shaped whose sides are therefore {-211} planes. The use of this kind of substrates allows us later to an easy identification of GaAs NW crystalline planes.

Table 7.1 summarizes six different protocols followed in this work to prepare Si(111) substrate surface, involving the use of buffered solutions to clean and later to oxidize the Si(111) surface, controlling the resultant oxide properties.

Table 7.1. Description of different protocols used to prepare Si(111) substrates.

Protocol (1)	**Protocol (2)**	**Protocol (3)**
1) HF:EtOH (1:9) for 5 min 2) Rinsed in DI H_2O 3) Dried in N_2 flow 4) Hot plate for 5 min*	1) HF:EtOH (1:9) for 5 min 2) Rinsed in DI H_2O 3) Dried in N_2 flow 4) Hot plate for 5 min* 5) HF:EtOH (1:9) for 5 min 6) Rinsed in DI H_2O 7) Dried in N_2 flow	Original wafer (without etching)
Protocol (4)	**Protocol (5)**	**Protocol (6)**
1) HF:H_2O (1:9) for 5 min 2) Rinsed in DI H_2O 3) Dried in N_2 flow 4) Hot plate for 5 min*	1) HF:H_2O (1:9) for 5 min 2) Rinsed in DI H_2O 3) Dried in N_2 flow 4) Hot plate for 5 min* 5) HF:H_2O (1:9) for 5 min 6) Rinsed in DI H_2O 7) Dried in N_2 flow	1) HF:H_2O (1:9) for 5 min 2) Rinsed in DI H_2O 3) Dried in N_2 flow 4) Hot plate for 5 min* 5) HF:H_2O (1:9) for 5 min 6) Rinsed in DI H_2O 7) Dried in N_2 flow 8) Dipped in H_2O_2 (30%) for 1 min 9) Rinsed in DI H_2O 10) Dried in N_2 flow

* Hot plate step means the bonding of the substrate on the molyblock surface using In at around 200 ºC.
HF = Hydrofluoric acid; DI = Deionized; EtOH = Ethanol; H_2O_2 = Hydrogen Peroxide

In protocol (1), a Si(111) substrate is firstly dipped in a 1:9 buffered solution of HF:EtOH for 5 minutes in order to remove the SiO_x native layer, and also to clean of the surface from contaminants. The substrate is then extracted from the solution, immediately rinsed in DI H_2O, and dried in N_2 flow before bonding to a molyblock using In. Bonding process is carried out on a hot plate at a temperature above the In melting point (~ 157 ºC), taking around 5 minutes. After the substrate bonding, the molyblock is rapidly transferred to the CBE system.

In protocol (2), after the Si(111) substrate is bonded on the molyblock, its surface is re-etched in the same buffered solution for 5 minutes to remove any possible SiO_x layer grown during In-bonding; then it is rinsed in DI water, dried in N_2 flow and finally transferred to the CBE system.

In protocol (3), the substrate surface is not treated at all, that means, the substrate is transferred to the CBE system with the native SiO_x layer as it is extracted from the manufactures box.

Protocols (4) and (5) are the same as (1) and (2) respectively, but using DI H_2O instead of EtOH. The use of different solvents in the buffer solution aims to study the effect of different passivation layers formed

on top of the Si surface whose main role is to preserve a clean Si surface during sample transfer to the CBE system.

Protocol (6) is based on protocol (5), but including three additional steps. During second etching (step #7) the SiO_x at the substrate surface should be completely removed; the substrate is then dipped in a H_2O_2:H_2O (3:10) solution for 1 minute, rinsed in DI H_2O, dried in N_2 flow, and transferred to the CBE system. The main role of this extra procedure is the growth of a rough and thin SiO_x layer.

SiO_x Characterization

The use of different surface preparations aims to understand the importance of SiO_x properties, morphology and thickness on the growth of GaAs NWs by CBE. For that reason, resultant surface properties of Si(111) substrates after their chemical treatment (table 7.1) are analyzed by means of FTIR, ATR and SE. The latter is used to determine both oxide thickness and roughness, whereas FTIR and ATR techniques are employed to study the chemical structure of SiO_x after the application of the different protocols (1-6).

The chemical composition of the resultant Si(111) surface oxide after the application of different etching protocols (1-6) is analyzed by FTIR (figure 7.1(a)) and ATR (figure 7.1(b)). FTIR measurements show a diffuse reflectance signal with two main peaks centered around 1100 and 1250 cm^{-1} which are related to interstitial O (Si-O-Si) and stoichiometric SiO_2, respectively [7].

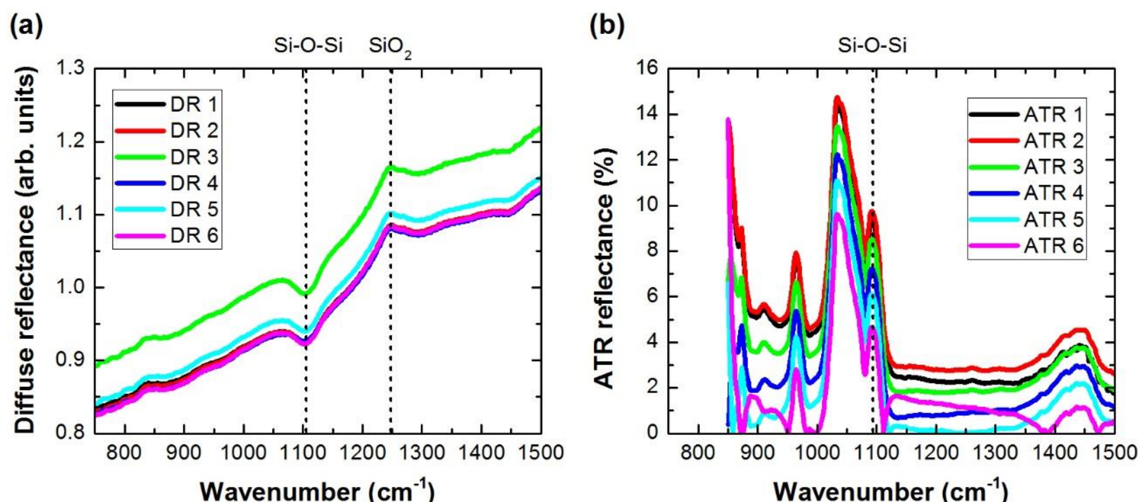

Figure 7.1. (a) FTIR and (b) ATR measurements for Si(111) substrates prepared using protocols described in table 7.1.

On the other hand, ATR spectra confirm the existence of the peak associated to Si-O-Si bond, but does not show any evidence of SiO_2. The absence of the latter peak in the ATR spectrum is attributed to the thin thickness of the surface oxide [7].

From FTIR and ATR results, it can be concluded that there are not big differences among all used protocols, that is, from a chemical point of view, all Si surface oxides present similar characteristics. The existence of the Si-O-Si peak has been previously considered in the literature as important for the Ga-

assisted growth of GaAs NWs on Si(111) substrates [7]. In this regard, the observation of this peak is a good indication of the surface treatments developed in this work.

Surface oxide has been also analyzed by means of SE after each of the six etching protocols, where ellipsometric angles (Ψ, Δ) are measured in the energy range between 1.5 and 4.5 eV. Using a simple two layer model (consisting of a SiO_2 rough thin film over a Si substrate) the experimental data are simulated. In this model, layer roughness is simulated by means of a smooth surface layer with a distribution of voids, the content of voids being proportional to the layer surface roughness. Simulated Ψ and Δ angles are fitted to the measured angles by varying both layer thickness and void density through an iterative process that minimizes the chi-square error (χ^2). The thorough description of the method used to extract physical parameters from SE was previously explained in chapter 4 (section 4.7.1).

Figure 7.2 shows an example of Ψ and Δ obtained from a Si substrate etched by protocol (3). The line in figure 7.2 represents the fitting curves to the experimental data.

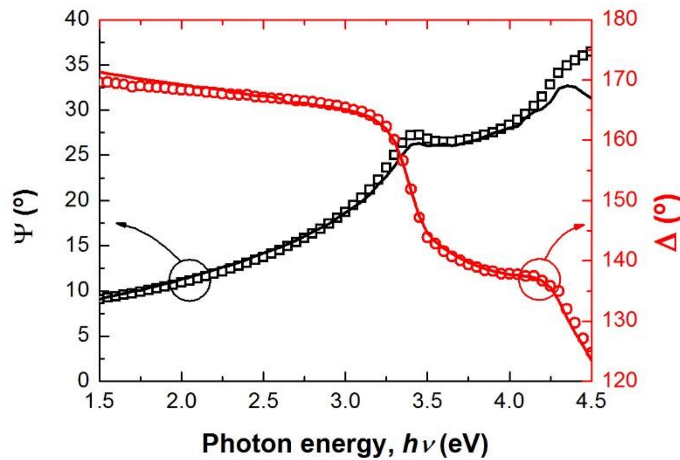

Figure 7.2. SE measurements of SiO_x/Si(111) sample after protocol (3) etching, and fitting curves of the two-layer model.

Table 7.2 summarizes the resultant oxide thickness and void density calculated from the simulation, including χ^2.

Table 7.2. Resultant thickness and void density in SiO_x surface layer formed after different etching protocols of Si(111) substrate.

Protocol number	SiO_2 thickness (nm)	SiO_2 voids density (%)	χ^2
(1)	1.45	1.2	0.8
(2)	0.63	4.5	0.6
(3)	0.13	8.8	0.6
(4)	0.80	4.3	0.4
(5)	0.09	30.9	1.0
(6)	0.30	14.8	0.7

In protocols (1) and (2), the oxide thickness reduction from 1.45 to 0.63 nm, and the increase of the void density from 1.2 to 4.5 indicate the increase of the surface roughness, which is caused by the double etching process using the buffered solution of HF:EtOH. Similar results are obtained using DI H_2O instead of EtOH as solvent in the buffered solution in protocols (4) and (5), exhibiting even thinner oxide thickness and higher roughness than protocols (1) and (2).

7.1.2. Principles of Ga-Assisted GaAs NW Growth

After Si(111) substrate preparation following the protocols described in table 7.1, the molybdenum sample holder with the In bonded substrate, is transferred to the CBE system. The NW growth procedure consists in four steps: substrate annealing, Ga pre-deposition, stabilization, and (Ga,As) deposition. After the annealing of the substrate, the standard growth conditions used in this work consist in:

i) Ga pre-deposition at T_s = 580 ºC, using a $P_{cam,TEGa}$ = 0.63 Torr (BEP_{TEGa} = 3.9×10^{-6} Torr);

ii) stabilization step at T_s = 580 ºC, and without gas flux;

iii) (Ga,As) deposition at T_s = 580 ºC, using a:

- $P_{cam,TEGa}$ = 0.63 Torr
- $P_{cam,TBAs}$ = 1.40 Torr (BEP_{TBAs} = 3.1×10^{-6} Torr).

Substrate Annealing

T_s is slowly increased from RT up to 650 ºC (~20ºC/min). During temperature ramp, the observed RHEED pattern consists of vertical diffuse lines, corresponding to the Si (1×1) surface reconstruction (figure 7.3). A ring-shaped and more diffuse region is also observed, and related to a thin amorphous surface oxide over Si(111) substrate. For T_s > 450 ºC, the diffuse ring vanishes, indicating a rearrangement of the surface oxide layer. The annealing of the sample is carried out at T_s around 650 ºC for times between 1 and 5 min in order to clean and to desorb impurities, and probably also to promote the formation or arrangement of pinholes on the SiO_x surface.

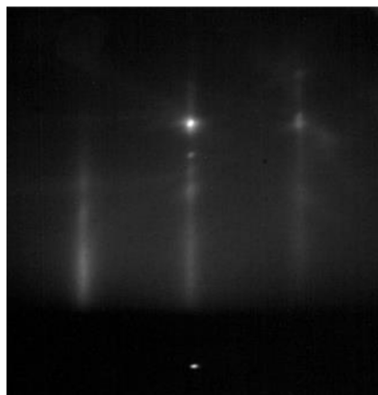

Figure 7.3. Characteristic RHEED diagram observed during the annealing of Si(111) at T_s = 650 ºC.

Ga Pre-Deposition

After substrate annealing, T_s is lowered down to 580 ºC to deposit Ga droplets along the Si(111) surface; this process is called here "Ga pre-deposition". At this temperature, TEGa valve is opened, and precursor molecules can be thermally cracked on the oxidized Si(111) surface, resulting in Ga atoms that diffuse along the Si surface (see mechanism (1) in figure 7.4) to nucleate Ga droplets; for substrates with extremely thin surface oxides, droplet Ga atoms might react with SiO_x at some pinholes, forming the contact between the Ga droplet and the substrate surface through a nanometric pore (figure 7.4). On the other hand, thermal cracking of the TEGa molecules can also occur directly on the Ga droplet (mechanism (2) in figure 7.4). Finally, there is a certain probability to desorb uncracked TEGa molecules (mechanism (3) in figure 7.4) from the sample surface.

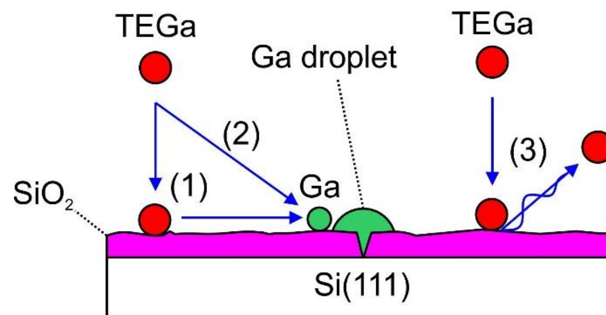

Figure 7.4. Ga droplet formation on oxidized Si(111) substrate using TEGa.

Ga droplets are deposited for different times (t_{pre}), and using the same equivalent Ga flow than used for the growth of GaAs(100) layers (0.5 monolayers per second) as calibrated by RHEED during the growth of GaAs layers on GaAs(100) substrates. Using this deposition rate, Ga droplet pre-deposition is carried out for different times (15, 30, and 60 s) on Si(111) substrates prepared by protocol (5); the resulting Ga droplets are seen in the SEM images shown in figure 7.5. It can be also noticed the increase of the t_{pre} from 15 to 60 s produces a decrease of the droplet density from 2.4 to 0.16 droplets per μm^2. The main explanation for this evidence is the increase of the droplet size at expense of the droplet density reduction due to Ga surface diffusion.

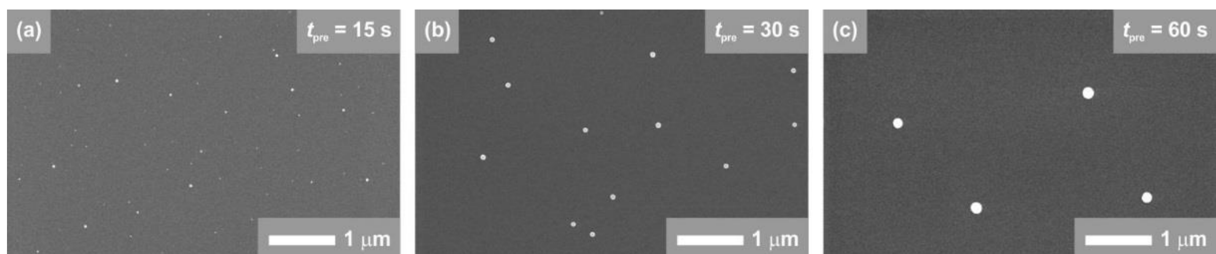

Figure 7.5. Ga droplets pre-deposited for different times.

Stabilization

After Ga droplet pre-deposition, T_s is kept constant at 580 ºC during different stabilization times (t_s) in order to analyze its effect both on the resultant density of droplets, and on their size. Ga droplets obtained after a t_{pre} = 15 s on Si(111) substrates prepared by protocol (5) (figure 7.5(a)), were stabilized for different times (0, 90, and 180 s) and later observed by SEM (figure 7.6).

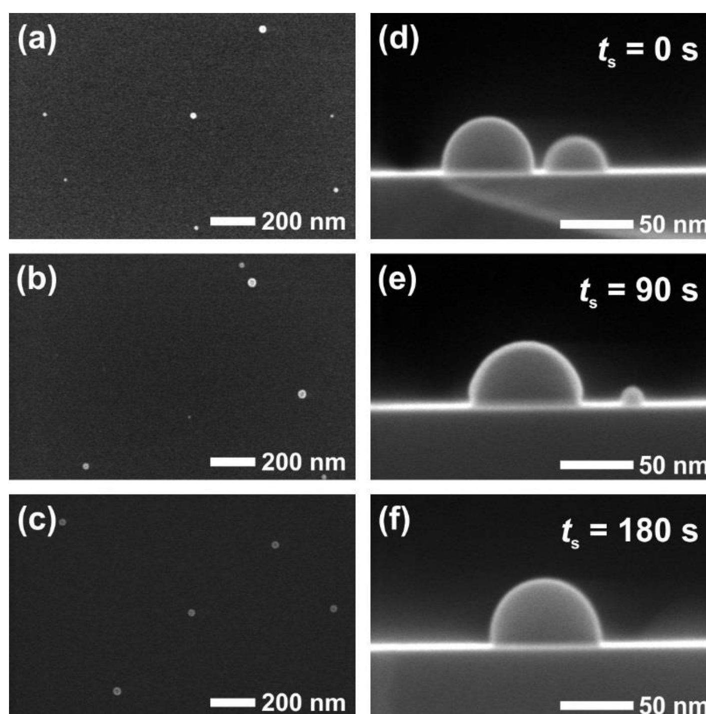

Figure 7.6. SEM images of Ga droplets stabilized during times.

The droplet density can be roughly estimated from SEM images taken at 0º (figure 7.6(a-c)) with respect to the sample normal direction; whereas the average droplet volume can be calculated from SEM images taken at 90º from the sample normal direction (figure 7.6(d-f)). Both magnitudes allow to study the effective Ga incorporation from the Ga total dose. For this purpose, we analyzed 10 droplets in samples with a near uniform distribution of diameters, whose lateral views are shown in figure 7.6(d-f). In order to calculate the average surface density of Ga atoms, we first determine the actual volume of each droplet, which in the case of figure 7.6(d), is 1.0×10^{-17} cm^3. Then, the number of atoms per droplet is calculated through the solid Ga specific gravity (5.91 g/cm^3), resulting in about 5.2×10^5 atoms/droplet. On the other hand, as previously stated from GaAs 2D-growth conditions, the pre-deposited Ga density corresponds to 4.7×10^{15} atoms/cm^2; the expected density of same-sized droplets should be 9×10^9 droplets/cm^2. SEM observations found around 0.3×10^9 droplets/cm^2 which represents only a 3% of the expected value. Following the same procedure for droplets shown in figure 7.6 (e) and (f), the results also show an effective incorporation of Ga around 3%. This demonstrates the low cracking efficiency of TEGa molecules on the oxidized Si(111) surface, which extremely reduces the effective number of Ga atoms during the pre-

deposition and/or stabilization processes. Ga atom re-evaporation during both the pre-deposition and stabilization steps can also partially contribute to the low Ga incorporation efficiency.

(Ga,As) Deposition

After the stabilization step, T_s was rapidly changed to the specific growth temperature (580, 600 or 620 ºC). Growth was started by opening both TEGa and TBAs valves for different growth times ranged between 1 min and 1 h. The Ga flux used during growth is the same than previously used for Ga pre-deposition, while different V/III flux ratios around 1 were studied. The evolution of the NW growth was monitored by RHEED while the resultant morphology was observed by SEM. Once the NW growth is finished, T_s was lowered down to RT at the fastest rate allowed by the system natural cooling down response.

Since TBAs valve is opened, then As atoms are solved in Ga droplets (pre-deposited on the Si(111) substrate and pinned at its surface pinholes), forming a (Ga,As) alloy (figure 7.7(a)). This alloy is continuously fed with Ga and As atoms from cracked/uncracked precursor fluxes as described in figure 7.7(a), corresponding to thermal cracking of TEGa precursor and AsH_x radicals directly impinging on the substrate surface or directly over the droplet alloy.

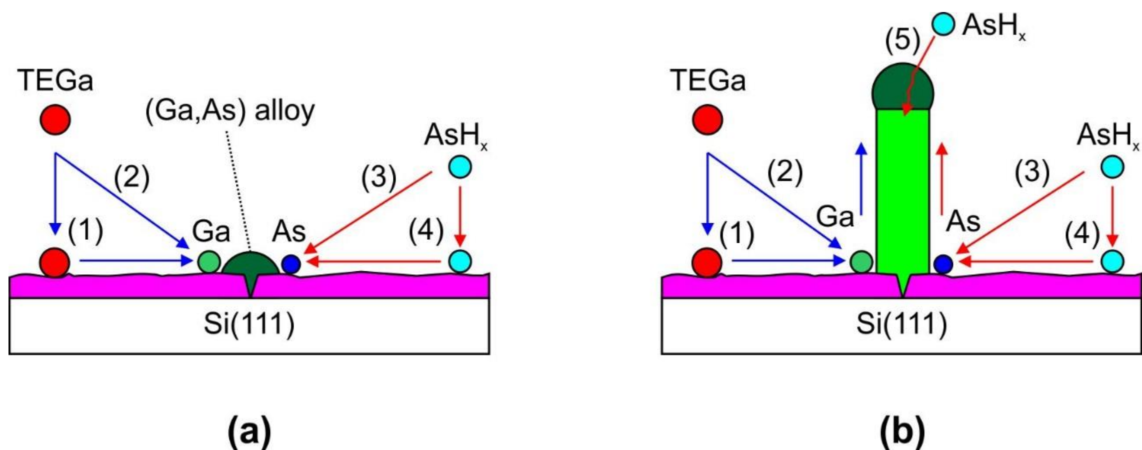

Figure 7.7. Schematic of the Ga-assisted growth of GaAs NWs by CBE.

As the concentration of As atoms increases inside the Ga droplet, the As solubility limit can be reached; the As-saturation of the droplet inducing GaAs precipitation at the liquid-solid interface formed between the Ga droplet and the substrate, in a sort of liquid phase epitaxy. The grown GaAs crystal must accumulate the strain due to the mismatch to the Si substrate in order to allow for the coherent growth of a vertical NW with a small footprint, as it is usually observed (figure 7.7(b)).

It is worth to note the role of Ga flow supplied to the droplet, to compensate the Ga losses due to the NW growth process. If a dynamical equilibrium is reached, the diameter of the droplet, and then the NW cross section, will be preserved over time. During the GaAs NW growth, there are at least three possible paths for Ga atoms to reach the droplet:

i) After the TEGa molecule is thermally cracked on the substrate surface, Ga atoms can diffuse along the oxidized substrate surface (due to the Ga high mobility) until they reach a GaAs NW base, where they can finally diffuse along the NW sidewalls towards the (Ga,As) droplet (mechanism (1) in figure 7.7(b)).

ii) The TEGa molecule could also impact on the NW sidewalls, where it could be also cracked and Ga atoms could diffuse along the NW sidewalls towards the (Ga,As) droplet (mechanism (2) in figure 7.7(b)).

iii) The TEGa molecule could also impact on the droplet, where it could be also cracked and Ga directly incorporated in the droplet.

The relative importance of the above mechanisms is therefore highly influenced by the NW length because long NWs could shadow the substrate surface, hindering the deposition of new Ga atoms. Long NWs can also difficult Ga diffusion from the NW base towards the droplet when the NW length is larger than the typical Ga diffusion length. Thus, there is a critical NW length above that supplied Ga atom flux is not enough to compensate the catalyst Ga losses, leading to a progressive droplet reduction until the NW growth interruption is achieved.

Similar paths can be expected for AsH_x radicals arriving to the sample surface from TBAs cracked in the high temperature cell at T_{HT} = 820 ºC. These radicals can be impinged either on the substrate surface (mechanism (4) in figure 7.7(b)), directly on NW side (mechanism (3) in figure 7.7(b)), or directly on the (Ga,As) droplet (mechanism (5) in figure 7.7(b)), supplying As atoms that contribute to the GaAs growth and to maintain the dynamic equilibrium between Ga and As contents in the (Ga,As) droplet.

7.1.3. Study of GaAs NW Growth

Once the standard growth of GaAs NWs carried out by Ga-assisted CBE has been described, the influence of substrate preparation and growth parameters, such as T_s, growth time, and V/III flux ratio on the morphological and structural properties of GaAs NWs were studied by SEM and RHEED.

Influence of the Substrate Preparation

For this study, Si(111) substrates were prepared using the protocols previously described and listed in table 7.1. Once the substrate is prepared by following one of these protocols, it is annealed at T_s = 650 ºC for 1 minute. Assuming standard growth conditions (previously described in section 7.1.2), Ga droplets were deposited for 15 s (which is equivalent to 7.5 monolayers of Ga), and stabilized for 0 s. Then, (Ga,As) deposition was carried out for 15 min.

When following protocols (1) and (2), which use a HF:EtOH (1:9) solution to carry out a single or double, respectively, etching of the Si surface, the formed passivated layer prevents the oxidation of the substrate surface even for long exposure times (~ 30 min) in air ambient conditions, but the growth of GaAs NWs over these type of surfaces was not achieved; instead, the growth of a polycrystalline-like layer of

GaAs is observed by SEM (figure 7.8(a)). Surface structure of these layers is confirmed by RHEED patterns observed during growth, consisting of diffuse concentric ring-shaped pattern (figure 7.8(b)) characteristic of volume diffraction through polycrystals. The ring intensity in the observed RHEED pattern is not constant in all directions, being reinforced near some points corresponding to the same diffraction spots in monocrystalline GaAs NWs, as it will be later described, suggesting these layers have a preferential orientation induced by the substrate. For this reason this layer will be referred as nanocrystalline.

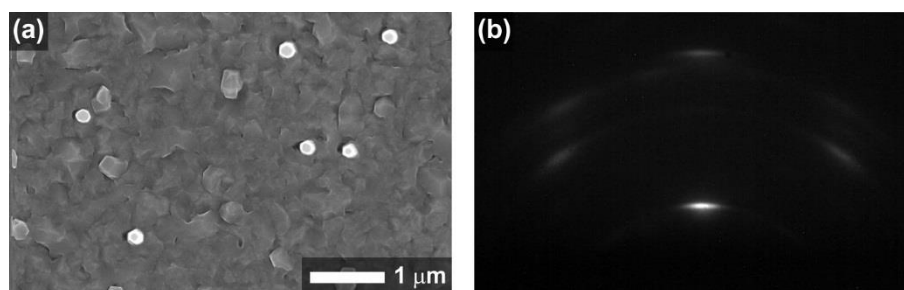

Figure 7.8. (a) SEM image and (b) RHEED pattern of GaAs polycrystalline layer.

Similar results have been obtained using Si(111) substrates prepared by protocol (6). This protocol uses H_2O_2 after the second etching process, in order to form a rough surface oxide. The formation of large pinholes generated by the final H_2O_2 dipping could cause the growth of nanocrystals along the whole Si surface.

The use of Si substrates either with the native oxide (protocol (3)), or after a single cleaning using a HF:H_2O buffered solution (protocol (4)), inhibits the growth GaAs NWs, as demonstrated by SEM. This behaviour could be attributed to Ga droplet nucleation inhibition by a thick SiO_2 layer. Figure 7.9(a) shows a representative SEM image of Ga droplets pre-deposited on Si(111) substrates prepared under protocols (3) or (4). It is therefore evident the lack of Ga droplets along the substrate surface, observing two-dimensional marks along the substrate surface related to those regions where the Ga atoms attended to contact to the Si surface.

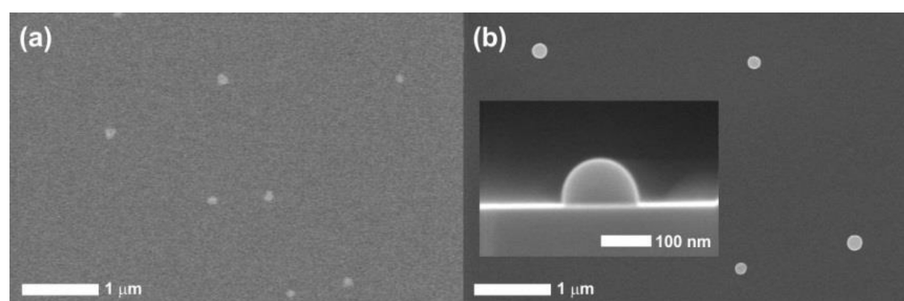

Figure 7.9. Ga droplets pre-deposited on Si(111) substrates etched under (a) protocols (3 or 4), and (b) protocol (5). Inset: Magnification of a droplet taken at 90º tilted away the substrate normal direction.

The last surface preparation protocol (5), consisting in the double etching of the Si(111) substrate using a HF:H_2O (1:9) buffered solution, shows the successful growth of GaAs NWs, only when exposing the substrate surface to the ambient air during a critical window of time, about 5 min, right after the second cleaning. This short oxidation time promotes the formation of a thin SiO_x layer on top of the substrate, which is crucial for the nucleation of GaAs NWs; much longer air exposure times inhibit the growth of NWs, probably due to the formation a thicker oxide layer, whereas the use of much shorter times leads again to the formation of a GaAs polycrystalline layer. This optimum time is observed to be strongly dependent on the Si wafer origin. During this work, two different sets of Si(111) wafers have been used. The optimum time calibrated for the second set of Si(111) wafers is determined to be close to 15 min instead of 5 min.

The growth of GaAs NWs on Si(111) substrates prepared by protocol (5) has been confirmed *in-situ* and *ex-situ* by RHEED and SEM, respectively.

RHEED pattern changes from streaky (figure 7.3) to spotty (figure 7.10) during the growth of GaAs NWs. The central region of RHEED pattern exhibits six horizontal bars corresponding to NWs and spots underneath each bar which are attributed to GaAs traces. These traces are nanostructures of GaAs that grow along the Si substrate surface from a Ga droplet which is not able to lift-off from the sample surface, leaving a crystal trace as it moves following one of three equivalent directions on the surface. This traces show high symmetry planes linked to the Si crystal structure, as NW do, but they are not able to grow along the vertical direction with respect to the substrate surface.

Figure 7.10. RHEED diffraction pattern observed during the growth of GaAs NWs.

SEM images confirm the existence of GaAs NWs, as well as the presence of traces and nanocrystals (figure 7.11). The crystalline structure of these traces and nanocrystals is clearly observed in figure 7.11(b). The diameter of the Ga droplet on top of the GaAs NW is around 140 nm; droplets with larger diameters (> 200 nm) formed on the Si surface are not able to start a vertical growth on the Si surface, then droplets move along the substrate surface forming crystalline traces of GaAs. On the other hand, the nucleation of GaAs directly on the Si(111) surface is also observed as nanocrystals with a pyramidal shape characteristic of the GaAs nucleation of Si(111). Therefore, the use of an extremely thin oxide is the main responsible for the nucleation of both traces and nanocrystals which are usually not desirable, at least for the scope of this study.

The reduction of the SiO_x thickness prior to the NW growth is crucial for the development of VLS growth in CBE. As mentioned before, because cracking of TEGa molecules occurs on the substrate surface,

it is expected to be more efficient on a reactive nude Si surface than on a passivated SiO_x layer, and therefore it could seem more interesting from the NW growth point of view to completely remove the SiO_x native oxide before growth process. However, this etching can promote the formation of undesired nanostructures, such as traces and nanocrystals along the Si surface. Parameters such as V/III ratio and T_s, as well as the use of lithographically defined patterns should be studied in order to reduce the number of these parasitic nanostructures.

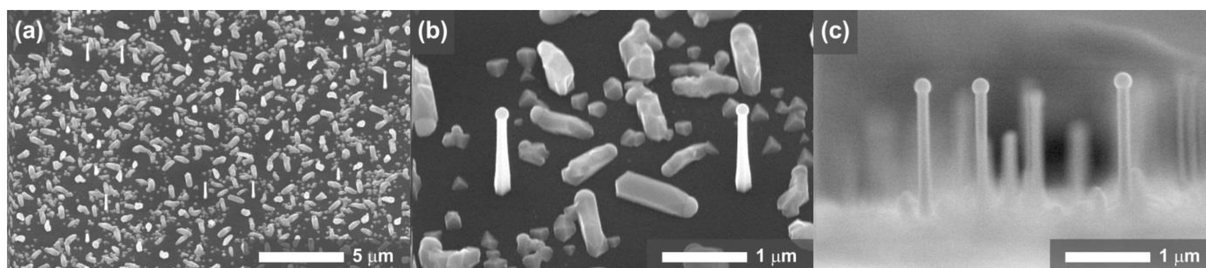

Figure 7.11. SEM images taken at different magnifications and tilted (a,b) 30º and (c) 90º away from the sample normal direction.

The analysis of the SEM image taken at angle 90º titled away the substrate normal direction (figure 7.11(c)) shows an average NW length and diameter of around 1.6 μm and 130 nm, respectively, corresponding to a NW growth rate of 6.4 μm/h which is approximately 13 times faster than the expected growth rate for a GaAs/GaAs(100) layer under same growth conditions.

Summarizing the results obtained on the growth of GaAs NWs on Si(111) under the same growth conditions, but with substrates prepared using different protocols, it can be concluded that protocol (5) shows the only successful growth of GaAs NWs with excellent structural and morphological properties, as confirmed by RHEED and SEM images. In the following, we will refer to GaAs NWs grown under different conditions but always on Si(111) substrates prepared by protocol (5).

Influence of the Substrate Annealing Step

Prior to Ga pre-deposition, Si(111) substrates are subjected to an annealing process aiming to promote the formation and/or arrangement of pinholes, and also to desorb surface impurities. In order to study the effect of substrate annealing on the resultant NW morphology, four different annealing treatments have been studied: (A) at T_s = 650 ºC for 1 min, (B) at T_s = 650 ºC for 5 min, (C) at T_s = 675 ºC for 1 min, and (D) at T_s = 675 ºC for 5 min.

Figure 7.12 show SEM images of resultant GaAs NWs grown on substrates annealed using procedures (A), (B), and (C); NWs were grown under standard growth conditions, comprising a Ga pre-deposition of 15 s, a stabilization step of 0 s, and a (Ga,As) deposition of 15 min.

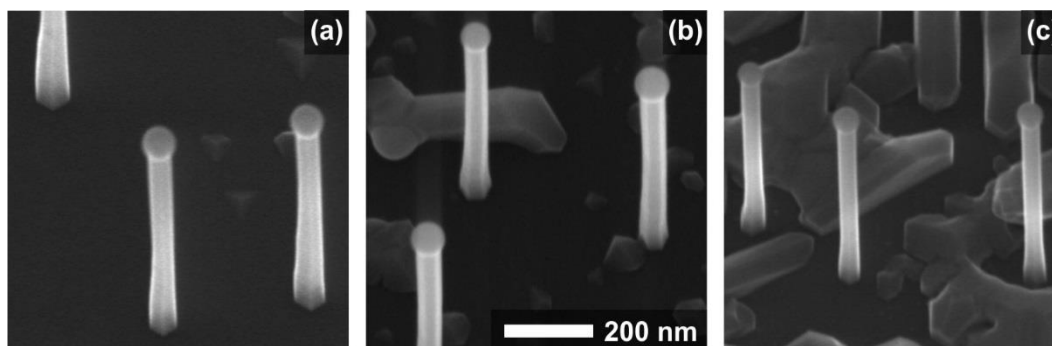

Figure 7.12. SEM images of GaAs NWs grown after different annealing treatments of the Si(111) substrate.

The annealing step helps to the formation and/or rearrangement of nucleation sites, called here pinholes, where NWs can preferentially grow (figure 7.12(a)); the omission of this annealing step, even for thin surface oxides, has been demonstrated to inhibit NW nucleation due to the absence of pinholes on the surface oxide. When increasing the annealing time the formation of pinholes is promoted, leading to the nucleation not only of NWs, but also traces and nanocrystals (figure 7.12(b)). An increase on the annealing temperature can further increase pinhole density, improving the nucleation of polycrystals on the substrate surface and, also affecting the GaAs NW aspect ratio (figure 7.12(c)). The excess of annealing treatment (T_s = 675 ºC for 5 min), not shown in the above figure, leads to the growth of a polycrystalline GaAs layer; the growth of this layer totally inhibits again the formation of GaAs NWs.

In the following, we will refer to GaAs NWs grown on Si(111) substrates after the annealing procedure (A), i.e. the annealing step performed at T_s = 650 ºC for 1 min.

Influence of the Stabilization Step

The stabilization step after Ga pre-deposition strongly influences both the NW length and diameter. The use of different stabilization times leads to a different density of Ga droplets with different sizes (figure 7.6). Assuming standard growth conditions, this study analyzes resultant NWs grown using a Ga pre-deposition of 15 s, different t_s of 0, 90, and 180 s, and a (Ga,As) deposition of 5 min.

In the case of t_s = 0 s, i.e. no stabilization, Ga droplets have a spread distribution of diameters, and a critical minimum diameter for NW growth is observed. Figure 7.13(a) shows the described scenario, where a Ga droplet with a diameter of around 100 nm exhibits a GaAs NW grown under the droplet, whereas the Ga droplet with a smaller diameter below 100 nm does not have enough strain to assist the growth of the NW.

For longer stabilization times, such as t_s = 90 s, the observed Ga droplet size distribution is reduced but it shows still NWs with different lengths (figure 7.13(b)). Finally, for the largest stabilization time used (t_s = 180 s), NW lengths and Ga droplets on top of NWs are near uniform in size (figure 7.13(b)), which is mainly caused by the initial uniform distribution of Ga droplets size after a long stabilization time (figure 7.6(c)).

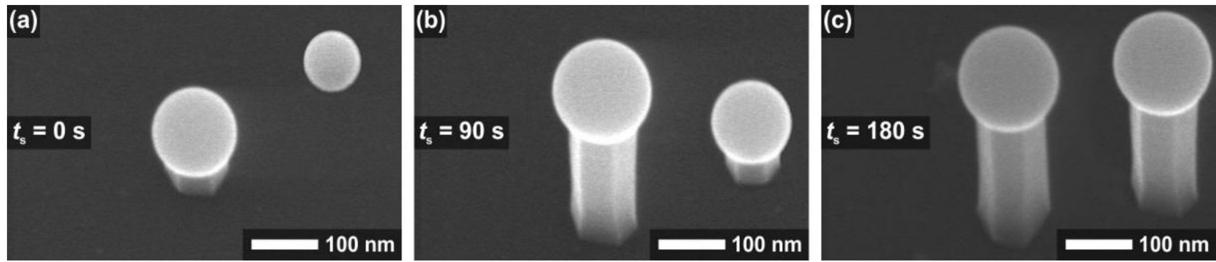

Figure 7.13. SEM images of GaAs NWs grown using different stabilization times after the Ga pre-deposition.

It should be noticed that since TEGa and TBAs flux are turned on to start the NWs growth after Ga droplet nucleation, new Ga droplets could also be nucleated on the substrate surface, contributing to the delayed growth of new NWs with shorter lengths, contributing to the broadening of NW length and diameter distributions.

The incubation time (t_0), defined as the time delay between the simultaneous TEGa and TBAs initial supply and the time at which NW growth is initiated, has been observed to be strongly influenced by the stabilization time. The NW length, as estimated from SEM images is represented as a function of the growth time in figure 7.14 for some runs with stabilization times. The extrapolation of the plots to $L_{NW} = 0$ gives the value for t_0, as pointed out with arrows in figure 7.14 taking values around 210, 90 and 30 s, for t_s values of 0, 90 and 180 s, respectively. As a result, the increase of t_s leads to a decrease of t_0, which can be explained in terms of the Ga droplet initial size; for $t_s = 180$ s, the initial droplet size is estimated to be around 80-100 nm, being sufficient large to assist the growth of the GaAs NWs along the vertical direction. In absence of stabilization ($t_s = 0$ s) Ga droplets need to be further fed with more Ga atoms in order to increase their size up to reach critical values (~ 100 nm).

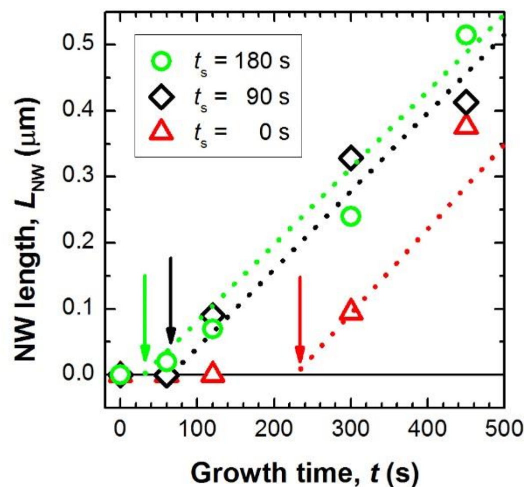

Figure 7.14. NW length vs growth time. Incubation times for each run family are pointed out with arrows.

Influence of the Growth Time

Growth parameters such as Ga droplet pre-deposition and stabilization times, T_s and V/III flux ratio are responsible for the equilibrium between the Ga and As atomic species in the droplet, which are consumed at the NW/droplet interface, and the supplied Ga and As precursor gases refreshing its Ga and As contents. Once this equilibrium is achieved, the coherent growth of the NW can occur with a uniform diameter along its stem. However, as the NW length increases, Ga and As atoms must diffuse through longer paths from the substrate surface along the NW facets to reach the interface between the Ga droplet and the NW front, which modifies the equilibrium conditions. In that scenario, the Ga droplet size could change, contributing to the change of the NW diameter. Then, the NW diameter and length, as well as the growth rate could be consequently be affected by the growth time.

The NW length increases with growth time, as it can be observed by comparing SEM images shown in figure 7.15(a,b), corresponding to samples grown at T_s = 600 ºC during 450 and 900 s, respectively (samples in both images are tilted by 90º from the surface normal).

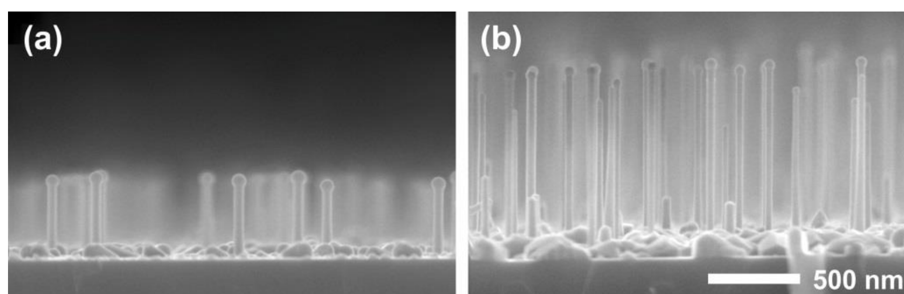

Figure 7.15. SEM images of GaAs NWs grown at T_s = 600 ºC during 450 and 900 s. Images are taken at 90º respect to the substrate surface normal.

However, the analysis of the average NW length shows that both parameters, NW length and growth time are not exactly proportional. When doubling the growth time from 450 (figure 7.15 (a)) to 900 s (figure 7.15 (b)), the average NW length increases from 440 to 1050 nm, the latter being 20% larger than expected from a simple linear extrapolation. The corresponding average NW growth rates can be then calculated as 3.5 and 4.1 μm/h, respectively. However, the lack of linearity could be related to contribution of the NW incubation time; in fact, the calculation of the growth time without taking into account t_0 could lead to an underestimation of the real growth rate. It is important to notice that obtained values for NW growth rate are about 7-8 times larger than the expected equivalent 2D-growth rate, indicating that NW growth is fed by the species arriving to the substrate surface in the NW neighbourhood, which diffuse until they reach the NW base to later migrate through its facets up to the NW end.

A further study of the growth rate has been carried out by analyzing a wide number of growth times. In this study we used standard growth conditions, i.e. Ga pre-deposition (7.5 monolayers), stabilization (90 s), during the growth a T_s = 580 ºC and V/III flux ratio close to 1. Figure 7.16 shows SEM images of GaAs NWs from samples grown with different growth times ranging from 1 to 40 min.

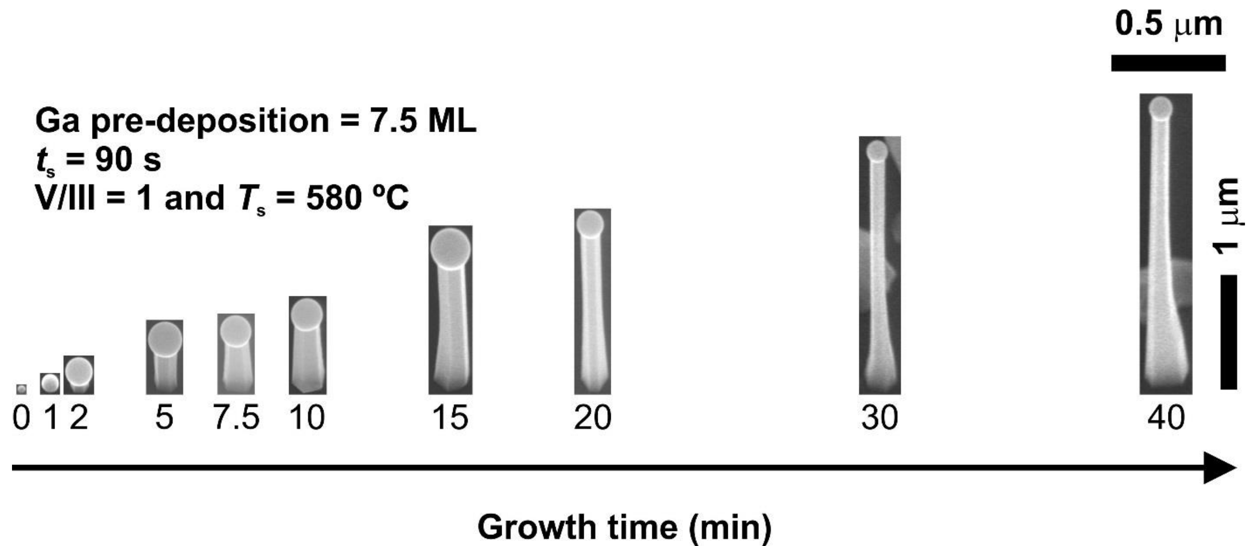

Figure 7.16. SEM images corresponding to a sequence of growths different deposition times.

It is important to notice that horizontal and vertical scales in the above figure are not the same, corresponding to 0.5 μm and 1 μm, respectively, as the SEM images are taken at 30º away from the substrate surface normal direction, the apparent vertical dimensions are reduced by a factor of sin 30º = 0.5, so the real scale has to be multiplied by a factor of 2 allowing to estimate the NW length directly from figure 7.16. In addition, the above figure positions the NWs in the horizontal scale according to their growth time.

In figure 7.16, every NW image corresponds to the average NW found for every the sample, being representative of the observed NW population. Thereafter the stabilization step, it can be observed Ga droplets have a size around 50 nm (t = 0 s). Once both TEGa and TBAs flux are opened, the size of the droplet increases up to around 100 nm in absence of any NW stem, that is, the GaAs NW structure is not observed for growth times below 1 minute. This observation has been confirmed by RHEED observations, where the diffraction pattern changes from the initial streaks to spotty for growth times larger than 1 min and 30 seconds.

As soon as the NW starts to grow, the observed L_{NW} is proportional to the growth time, with a r_g around 5.4 μm/h (figure 7.17). The linear proportionality region for L_{NW} on the growth time is observed for times ranging between 5 and 30 min. For growth times larger than 30 min, L_{NW} exhibits a sub-linear increase with growth time. This change on the r_g tendency can be explained considering the flow of Ga atoms diffusing along the NW facets towards the NW/droplet interface is reduced as the L_{NW} increases. The parasitic growth of structures on the substrate surface such as traces and nanocrystals surrounding NWs also reduces the effective flux of Ga and As species available for the NW growth.

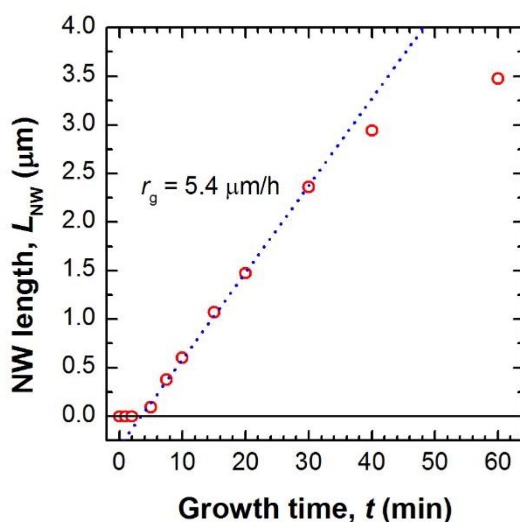

Figure 7.17. NW length vs growth time. The fitting line corresponds to r_g = 5.4 μm/h.

The growth of GaAs NWs has been carried out using growth times up to 1 h. Figure. 7.18(a) shows a SEM lateral-view of a GaAs NW with a length of 3.5 μm. Resulting NWs do not exhibit a Ga droplet on top of their tips (figure. 7.18(b)), but a pyramidal formed by three equivalent facets is observed instead. Ga droplet extinction could be produced by the incorporation of Ga and As species at the polycrystalline layer developed surrounding the NWs.

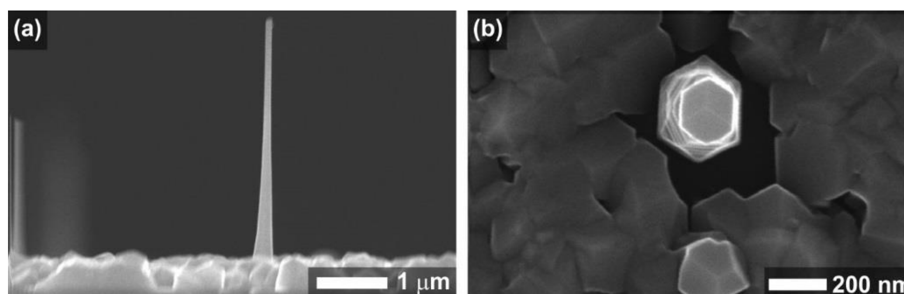

Figure. 7.18. SEM images of GaAs NWs grown for 1 h, taken at (a) 90º and (b) 0º away the substrate normal direction.

Although Ga-assisted processes used in CBE for GaAs NW growth require the use of a thin surface oxide covering the Si(111) substrate, it has been observed that for growth times longer than 1 h this thin surface oxide is completely dissolved or covered by a polycrystalline layer of GaAs, thus limiting the growth of GaAs NWs. This layer is responsible for trapping growth species necessary to keep the dynamic equilibrium at the interface between the Ga droplet and the GaAs NW, leading to growth extinction.

In order to overcome this drawback, we have developed the growth of GaAs NWs by using a novel procedure, called “two-steps growth”. Figure 7.19 shows a step-by-step description of this novel procedure. Steps from (a) to (c) involve the one-step growth previously used and described in this section, including substrate annealing, Ga droplet pre-deposition, stabilization, and (Ga,As) growth steps. The first growth step

presented in figure 7.19(c) is called pre-growth in order to distinguish with the second later explained growth.

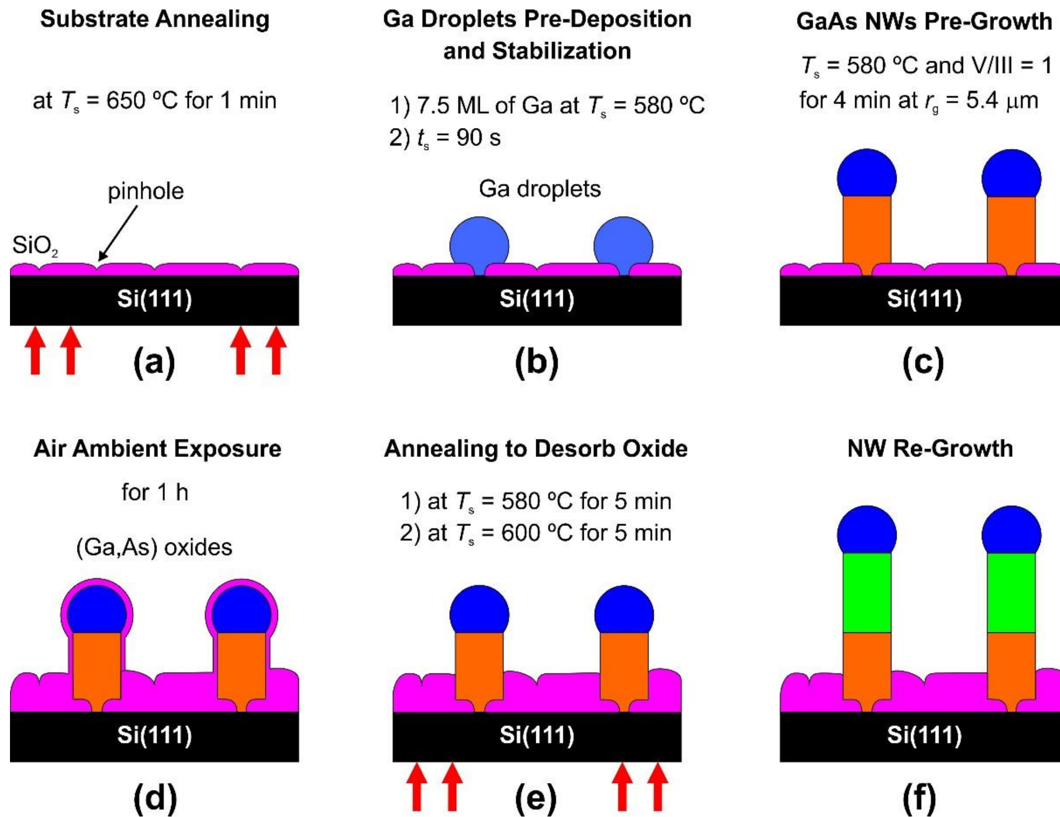

Figure 7.19. Schematic of the two-steps growth, consisting in: (a-c) one-step growth, (d) air exposure, (e) annealing, and (f) re-growth.

After a pre-growth of 4 min at r_g of 5.4 µm/h, the sample is taken out of the CBE system and exposed to the ambient air for 1 hour to grow a thicker oxide layer; pre-growth is carried out for only 4 min in order to ensure the growth of short GaAs NWs, preventing the nucleation of parasitic species such as traces and nanocrystals along the substrate surface. The 4 min value for the pre-growth time has been calibrated using RHEED, prior to observe spotty patterns characteristic of these impurities. Once the sample has been exposed for 1 h to the ambient air, the thickness of the surface oxide covering not only the Si substrate, but also NWs and their Ga droplets, should increase (figure 7.19(d)).

After this oxidation step, samples are introduced again in the CBE system and annealed firstly at T_s = 580 ºC for 5 min and later at T_s = 600 ºC for 5 more min (figure 7.19(e)). This annealing step pretends to desorb the surface oxide covering NWs and Ga droplets, but avoiding at the same time SiO_x desorption due to its relatively low T_s; the substrate oxide layer should then remain to help during the next NW growth step.

Finally, under the same growth conditions used for the pre-growth, the NW growth is resumed (figure 7.19(f)) in a second step, called here "re-growth" carried out for 16 min. Therefore, the total growth time, including pre-growth (4 min) and re-growth (16 min), is equivalent to 20 min.

Comparing obtained GaAs NWs by Ga-assisted CBE growth either by a one- or two-steps growth, both under the same surface preparation, growth conditions, and for a total growth time of 20 min (figure 7.20) we can extract three main conclusions:

i) In the two-steps growth, the nucleation of surface impurities such as traces and nanocrystals is almost completely inhibited (figure 7.20(b)).

ii) In the two-steps growth, the NW r_g increases; comparing figure 7.20(c) and (d) the NW length is enhanced from 1.5 to 2.1 μm. This behaviour is attributed to the absence of GaAs impurities surrounding the NW, so Ga and As trapping at the substrate surface is inhibited.

iii) In the two-steps growth, the NW aspect ratio is improved, with values around 20 for a 30 min NW grown.

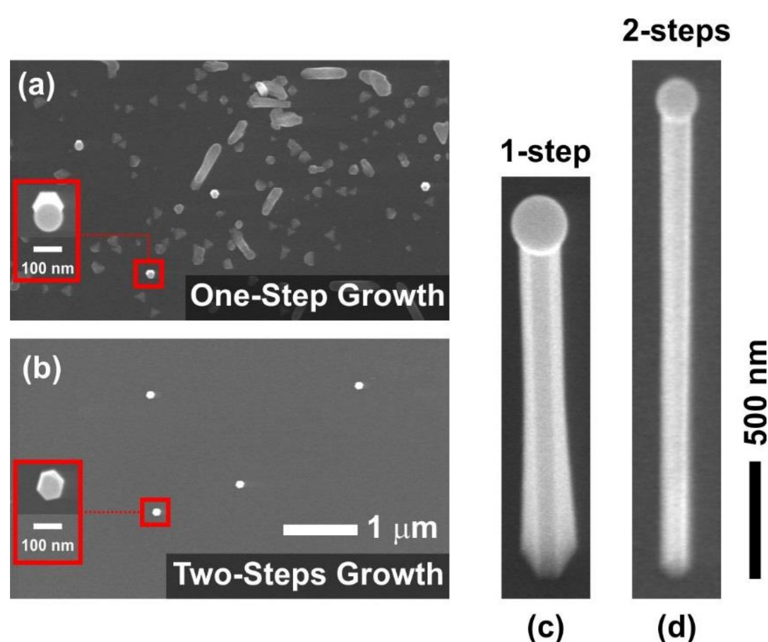

Figure 7.20. SEM images of GaAs NWs grown by (a,c) one- and (b,d) two-steps growth for 20 min. (a,b) and (c,d) images are taken at 0º and 30º away the substrate surface normal direction, respectively. (a,b) insets: magnification view of a NW.

The two-steps growth procedure developed here allows to grow NWs with total lengths larger than the 3.5 μm limiting value obtained by one-step growth. This result facilitates the integration of long GaAs NWs in optoelectronic devices, as it will be shown later in section 7.3.

Influence of the Substrate Temperature

The T_s parameter affects to the TEGa molecule cracking efficiency, to the mobility of the Ga atoms along the substrate surface, and then to the growth of GaAs NWs. Therefore, the study of the resultant morphology of GaAs NWs grown at different T_s has also been performed.

During the growth of GaAs by CBE, the metalorganic precursor for Ga (TEGa) dissociates efficiently on GaAs surfaces for T_s ranging from 400 to 600 ºC [8, 9], but the growth of a GaAs

polycrystalline layer on top of a SiO_2 layer can take place for T_s lower than 560 ºC [10], thus reducing the above temperature window for GaAs NW growth. Therefore, the study on growth temperature will be focused on three different growths carried out for 30 min at standard conditions, and using different T_s of 580, 600 and 620 ºC.

The morphology of the obtained NWs is analyzed by SEM as shown in figure 7.21, where (a-c) top and (d-f) 30° tilted from sample normal direction view images are presented. From these images one can observe that there are important changes in the sample morphology related to T_s, including the reduction of GaAs nanocrystals and NWs as T_s is increased.

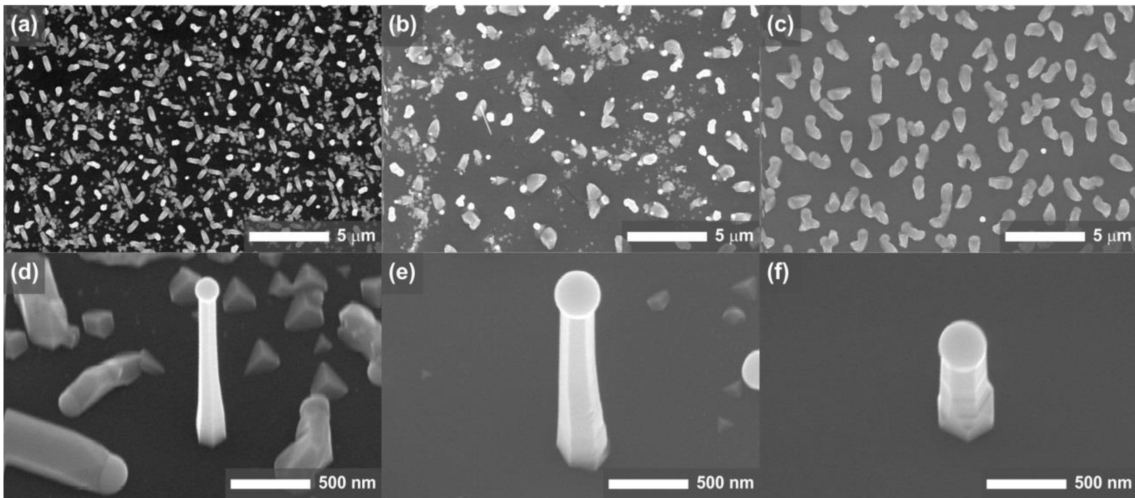

Figure 7.21. SEM images of GaAs NWs grown at T_s of (a,d) 580 ºC, (b,e) 600 ºC and (c,f) 620 ºC for 30 minutes using standard conditions. Images are taken (a-c) along and (d-f) 30° tilted away the sample normal direction.

On the other hand, figure 7.21(d-f) allow us to analyze NW morphology by performing physical measurements on d_{NW}, L_{NW}, NW aspect ratio, etc. as a function of T_s.

For T_s = 580 ºC, the resultant average d_{NW} and L_{NW} obtained from SEM images are 95±2 nm and 2.2±0.1 μm, respectively (figure 7.21(d)). This value of d_{NW} is below the limit reported by Cirlin et al. for the coherent growth of GaAs NWs [11]. The aspect ratio observed on these NWs only shows some tapering effect in the region close to the NW base, associated to changes in the Ga droplet size during the NW growth. Ga droplet size is progressively reduced until reaching equilibrium between the amount of Ga lost by the droplet at the growth front and the amount of Ga supplied by the TEGa gas source. This equilibrium mainly depends on the V/III flux ratio and T_s parameters, being also influenced by surface diffusion. In this regard, the initial droplet size could be tuned by changing the TEGa pre-deposition time and flux, as well as the stabilization time, in order to achieve the ideal droplet size for a specific V/III flux ratio. Under these refined conditions, it is expected to obtain a NW without tapering effects.

Increasing T_s up to 600 ºC, d_{NW} also increases (133±2 nm), while L_{NW} decreases (2.0±0.1 μm). This reduction on L_{NW} can be explained as due to either the reduction of the growth rate because of the large NW

cross section, or to the higher desorption rate of Ga and As atoms as a consequence of the higher T_s. The NW diameter is observed to be larger, when comparing to the NW grown at 580 ºC, probably due to a larger initial Ga droplet size associated to the brief and uncontrolled stabilization time existent since T_s is increased from the pre-deposition temperature (580 ºC) up to the growth temperature (600 ºC). In this case, the NW shows tapering along the whole NW stem, indicating the excess of T_s modifies the effective V/III flux ratio, resulting in a progressive reduction of the Ga droplet over the growth. For larger growth times, these growth conditions can cause the total consumption of the Ga droplet, then finishing the NW growth. In figure 7.21(e) some defects are also observed along the (110) plane corresponding to the NW facet. These defects are assumed to be related to a d_{NW} which is larger than the predicted maximum value for the coherent growth of GaAs NWs (110 nm) [11].

Finally, for T_s = 620 ºC, d_{NW} presents extremely large values around 285 nm which are much larger than for NWs grown at 580 ºC, which is considered the optimum T_s for GaAs NW growth; obtained shorter values L_{NW} (around 0.43 μm) are in good agreement with the increased desorption of Ga and As atoms, as well as to the reduction of the growth rate because of the larger NW cross section. As in the 600 ºC case, tapering, defects along the facets and shorter NWs are also observed, and are assumed to be related to the large value of T_s. In addition, the increase of T_s over the optimum temperature results in a reduction on the surface nanocrystal density as clearly observed in figure 7.21(f); NWs observed in the sample shown in this figure have a particular shape, in which the originally developed NW sidewalls gradually evolve from {112} to the final {110} facets.

Influence of the V/III Flux Ratio

Morphological properties of GaAs NWs were analyzed as a function of the V/III flux ratio. The value of flux ratio can be calculated using equation (3.4) described in chapter 3 (section 3.3).

GaAs NWs were grown for 30 minutes under the same conditions used in the above study on T_s (figure 7.21), i.e. standard conditions, but using V/III flux ratios of: 0.9, 0.8, 0.7, and 0.6. Figure 7.22 shows four representative NWs grown under different V/III flux ratios.

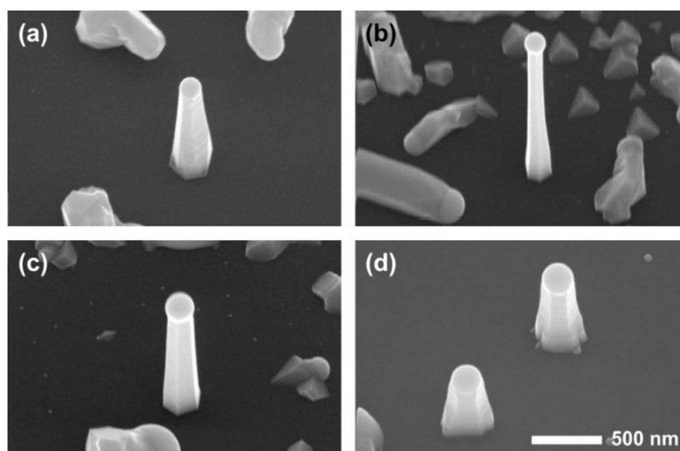

Figure 7.22. SEM images of GaAs NWs grown with different V/III flux ratios: (a) 0.9, (b) 0.8, (c) 0.7, and (d) 0.6.

The best aspect ratio (longest and thinnest NWs) is observed in figure 7.22(b). Figure 7.22(b,c) present smooth and defectless NW facets in comparison with those observed in figure 7.22(a,d). In figure 7.22(a), the reduction of the droplet size is produced by the high As flux, which consumes more Ga than supplied during growth, or, in other words, Ga flux is not sufficient to keep a constant droplet size during the NW growth process. The main reason for a reduction on the Ga flux arriving to the Ga droplet might be the Ga incorporation to GaAs nanocrystals or to GaAs traces nucleated by Ga droplets over the SiO_x/Si surface, as they can be seen in the SEM images of the grown samples. Nanocrystals and traces can act as Ga traps where the Ga atoms are incorporated, leading to the reduction of both, Ga droplet size and NW cross section. Therefore, the nucleation of traces and nanocrystals can be promoted under non-optimized V/III flux ratio conditions, overcoming the nucleation of GaAs NWs.

On the other hand, a reduction of the As flux for V/III < 0.8 (figure 7.22(d)) leads to an increase of the Ga droplet size, inducing a widening of the NW diameter that reduces the NW length.

7.2. Characterization of GaAs NW Properties

7.2.1. Morphological Analysis

NW Morphology, Growth Direction, and Relative Orientation

The lack of inversion symmetry in semiconductors such as GaAs is an important issue when growing over a non-polar substrate with inversion symmetry, such as Si(111). This subtle difference on symmetry properties may leads to the growth of crystals which could locally nucleate with different crystal orientations, giving rise to anti-phase domains and twins separated by defects after lateral coalescence during the growth of 2D layers. The growth of GaAs on the Si(111) surface could lead to either <111> or <-1-1-1> oriented structures which are also referred as <111>A and <111>B, respectively. In the following, we will refer to crystal directions or planes on the Si substrate, but when previously identified, to crystal directions or planes of the GaAs grown structures.

GaAs NW morphology and relative crystal orientation for samples grown under the standard conditions described in previous sections were firstly studied by SEM. After growth, randomly distributed GaAs NWs with hexagonal footprint are observed, as shown in the SEM image of figure 7.23, where hexagonal footprint and the Ga-rich droplet can be clearly observed. Most NWs are aligned to the substrate normal direction, are terminated by a Ga-droplet, and have similar dimensions and the same relative orientation for each individual sample. However, the exact crystal orientation of these NW cannot be univocally asserted only from SEM images; 60º rotationally twinned NWs cannot be distinguished by SEM,

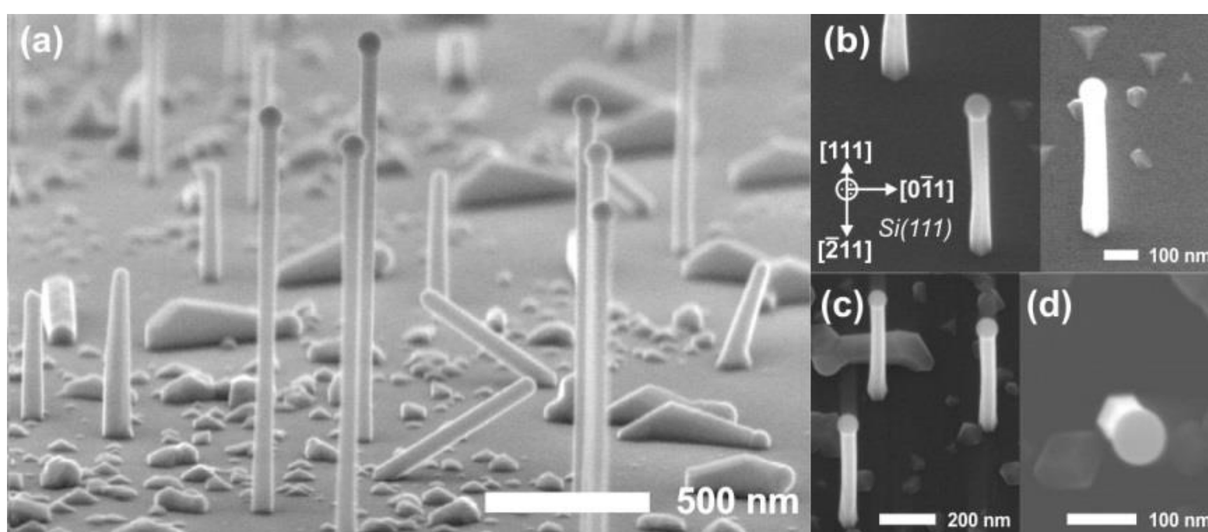

Figure 7.23. SEM images tilted (a) 80º, (b,c) 20º, and (d) 2º towards [2-1-1] direction, showing GaAs NWs and nanocrystals. In (b) three ortogonal Si lattice directions are also drawn (projected on the image); due to the large difference in secondary electron signal collected from NWs and nanocrsystals, different brightness and constrast settings are used at each side of this picture to allow for a detailed view of different structures.

because the external morphology should be the same. Si(111) surface has a threefold symmetry (120º) defined by the projection of the three bonding directions different than the <111> direction of the final Si atom; alternating Si layers show this three bonds rotated by 60º, pointing either towards the substrate or towards the surface. When GaAs NW nucleation takes place on Si(111), the initial layer Ga atoms can take one of two different orientations, depending on the local surface finish of the substrate, then nucleating one of two possible 60º twinned NWs, as it will be later shown in the RHEED patterns.

Traces and Nanocrystals

Figure 7.23 also shows some other structures such as nanocrystals and Ga-terminated horizontal traces which are grown during a standard CBE process. Nanocrystals observed in this figure show a pyramidal shape, characteristic of the GaAs growth on nominal GaAs(111)B substrates [12, 13]. The facets of these pyramids are tilted about 0.5 to 2º away from the (111)B GaAs plane. The small angle of the pyramidal facets can be confirmed in the image shown in figure 7.23(b), where the apex remains close to the triangle centre even when the sample is tilted by 20º away from the Si [111] direction towards [2-1-1] (reference axis in figure 7.23(b) has been identified by the relative orientation of the original Si wafer main flat).

Pyramidal facets have been identified to be tilted towards 3 equivalent [2-1-1] directions on the GaAs(111)B plane [12], their intersecting edges being oriented along the other 3 [-211] equivalent directions. Some pyramids are rotated by 60º, suggesting the GaAs nucleation mechanism could lead to two types of twined crystals. These observations were extracted from figure 7.23(b) but they will be later confirmed in the TEM section considering GaAs nanocrystals are assumed to grow in the [111]B direction over the Si [111] oriented substrate, as it is usually observed by most research groups [14]. Nevertheless, we will refer to the GaAs growth direction as <111>A,B because we were not able to discriminate as being either [111]A or [111]B type.

Based on the relative orientation of the NW facets, pyramids and Si substrate, the 6 NW facet orientations are identified as the 6 planes equivalent to (0-11) which are perpendicular to the (111) surface; this result is in good agreement with previous works [15] identifying NW facets. If some NWs were also twined by 60º as some pyramids did, the set of facet orientations for both NW subsets should be the same, being undistinguishable by SEM imaging. Furthermore, different facet terminations are also observed along the structure of the same NW. Figure 7.21(f) shows an example of a NW with progressively evolving facets giving rise to an apparent rotation of 60º between the base and the droplet regions.

On the other hand, the formation of droplet-terminated traces along the Si surface takes place when the interface energy of the liquid Ga-droplet is lower on the Si substrate than on the GaAs NW [16]. Figure 7.23(a) shows some of those traces with three different orientations along the substrate surface, which are also linked to the substrate crystal orientation.

7.2.2. Structural Analysis

Reflection High-Energy Electron Diffraction

RHEED patterns were monitored during the NW growth process, analyzing <1-10> and <11-2> azimuths (figure 7.24(a-c)). Prior to the Ga pre-deposition, a characteristic streaky Si(111) pattern is observed, indicating a (1×1) Si(111)surface reconstruction, as well as a faint specular spot (γ) due to the specular reflection on the substrate surface (figure 7.24(a)). During Ga pre-deposition (TEGa flux on), the streaky pattern is still observed; however, the intensity of the specular spot tends to decrease as a consequence of Ga droplet formation, partially covering the substrate surface, as it is observed in region I of figure 7.24(d). Thereafter, during the stabilization step (TEGa flux off), the specular spot intensity increases up to the stabilization, probably due to the rearrangement of droplets that partially uncovers more Si surface (region II in figure 7.24(d)).

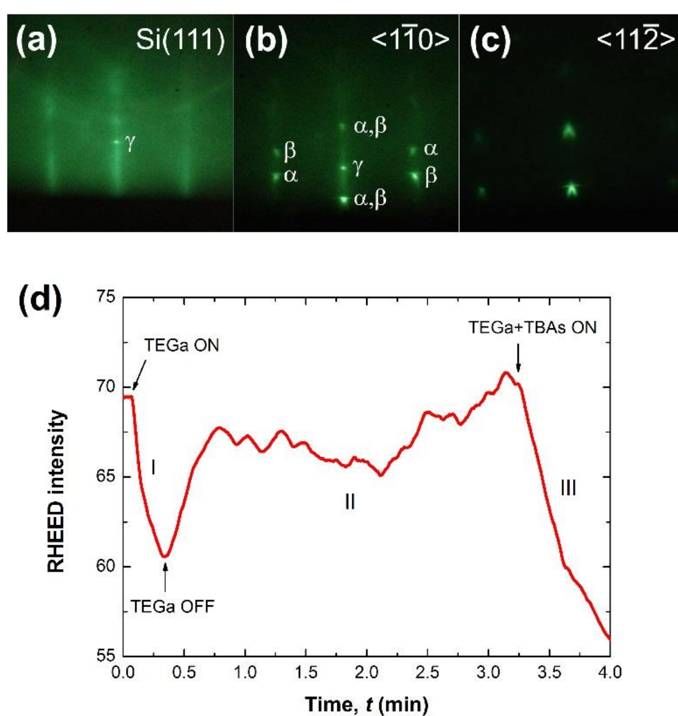

Figure 7.24. (a), (b) and (c) RHEED patterns and (d) intensity of the specular spot monitored during NW growth. Steps I, II, and III correspond to Ga pre-deposition, stabilization and NW growth, respectively.

When both TEGa and TBAs fluxes are turned on, the nucleation of GaAs structures such as NWs, traces, and nanocrystals is rapidly detected by RHEED because the streaky pattern associated to Si(111) surface gradually disappears and the intensity of a new spotty pattern tends to predominate in the RHEED image. Then, the intensity of the specular spot progressively decreases down until the specular spot disappears (region III in figure 7.24(d)) due to an elevated shadowing and coverage of the substrate surface.

The observed spotty pattern depends on the azimuthal angle, as shown in figure 7.24(b) and (c) corresponding to <1-10> and <11-2> azimuths respectively. Analyzing azimuth <1-10> two kinds of spots

are identified (indexed as α and β) which are associated to bulk diffraction by ZB GaAs NW planes and its 60º rotational twin, respectively. The observation of the double set of spots (α and β) suggests that NWs could twinned, as usually observed by different groups [17]. In our case, TEM analysis will show our NWs are twin-free ZB structures [1], because this explanation must be discarded. Instead, two subsets of NWs should be presented on the samples, each twinned by 60º from each other, due to different local nucleation symmetries over the Si(111) substrate, as before explained. As both twinned NW populations are randomly distributed over the sample surface, both sets of RHEED spots have the same intensities on the RHEED screen.

As growth proceeds, a more detailed view of them shows these spots are composed by a horizontal bar over a circular dot placed over the position of the initial Si vertical bar. Circular dots appear after about 1 min of growth, when the nucleation of GaAs NWs and other 3D-structures takes place, after some incubation time. The horizontal bars are suggested to be associated to some kind of electron scattering produced on the NW structure; they are observed in the RHEED pattern under both <1-10> and <11-2> azimuths, when the electron beam is directed to the NW facets and edges, respectively. In addition, these bars are always observed to appear after about 2 min of growth when the NW length is long enough to scatter incident electrons or probably indicating some kind of stress relaxation. Therefore, the existence of those horizontal bars in the RHEED pattern is a good indicative that hexagonal footprint NW growth is taking place. The length of these horizontal bars could be related with the lateral dimensions of the NW, i.e. its diameter. In this regard, thinner NWs should present longer horizontal bars.

EDAX Spectrometry

Figure 7.25 shows the EDAX linear scan taken in scanning transmission electron microscopy (STEM) mode along a 100 nm path from the final droplet to the body of a NW grown at standard conditions (T_s = 600 ºC, a V/III = 0.8 and during 15 min) as shown in the inset of the figure superimposed to the high resolution TEM (HRTEM) image.

The small signal related to O, either due to SiO_x layer reduction during Ga-droplet formation or to GaAs NW exposition to ambient conditions for a long time interval between growth and EDAX measurements has been removed from the plot, thus renormalizing the Ga and As signals. As shown in the EDAX profile, the droplet is a solution almost completely composed by Ga and a small amount of As; in such a way that Ga and As are acting as solvent and solute, respectively. The NW body is observed to grow as stoichiometric GaAs. The observed transition region, about 10 to 15 nm thick, between the droplet and the NW body is highlighted in the figure, indicating a concentration gradient at the droplet to NW interface. Due to the high T_s during NW growth (about 600 ºC), and the liquid nature of the final droplet, high diffusion coefficients should be expected for As species inside the Ga droplet, leading to a uniform concentration of As under equilibrium conditions. VLS is a dynamic process, and due to the observed growth rate, about 7-13 times larger than under equivalent 2D growth conditions for GaAs, most of the As and Ga species should

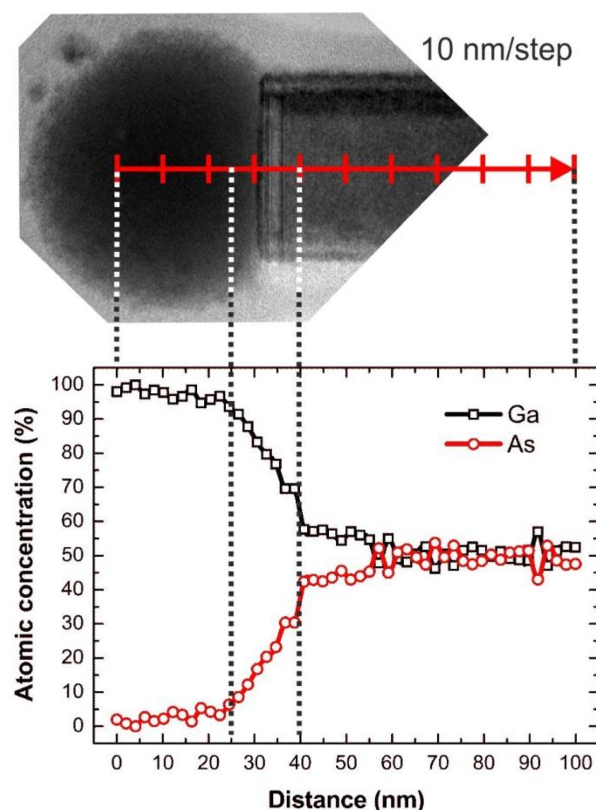

Figure 7.25. EDAX profile showing Ga and As atomic concentration measured from the droplet to the NW stem, as shown in top HRTEM image.

reach the NW growth front by diffusing along the NW facets in the NW stem. This process could explain the existence of an As gradient in the droplet, with an enriched As region under the droplet, near the NW end.

Another possible explanation to the concentration gradient is related to the growth interruption at the end of the growth process, and the subsequent cooling down process. It has been demonstrated that Ga droplets can etch away GaAs surfaces at high T_s and low As fluxes [18], as it is the situation at the beginning of our final cooling down. If liquid Ga droplets should dissolve solid GaAs at the NW to droplet interface, thus incorporating fresh Ga and solving As atoms, even for short exposure times, the existence of an As gradient in the liquid phase near the NW stem could be explained.

A third explanation for the concentration gradient could be related to a non-flat liquid-solid interface, as suggested from SEM and TEM images. GaAs nucleation and growth under the droplet could take place following a different mechanism than the usual Franck-van der Merwe 2D-growth.

Transmission Electron Microscopy

The crystalline structure of single GaAs NWs was analyzed by TEM. Sample preparation for TEM consisted in dipping one portion of the as-grown sample in 1.5 ml of ethanol in an ultrasonic bath for a few seconds in order to remove NWs from the substrate. Bubbles and sound waves produced during this sonication process are responsible for breaking NWs near the interface with the substrate, so the NW length is almost preserved. A micro-droplet of the above solution was deposited on a holey carbon copper grid,

allowing for easy localization of NWs using coordinates edges. Once the solvent is completely evaporated, the grid is loaded into the TEM system for NW characterization. TEM measurements were carried out by using the electron beam aligned perpendicularly to one of the NW facets.

Figure 7.26 shows three representative TEM images corresponding to three different GaAs NWs whose schematics are also drawn; these NWs were grown under the same conditions than described for the NW previously shown in figure 7.25 but using several T_s values, T_s = 600 ºC for figure 7.26(a,c) and T_s = 580 ºC for figure 7.26(b). The different wetting areas, centre positions and shapes of the Ga droplets in each case suggest different VLS growth modes. The contact angle measured in each case is β_A=159º, β_B=174º, β_C=152º as represented in figure 7.26(a), (b) and (c), respectively.

In figure 7.26(a) the Ga-droplet does not wet the NW sidewalls (mechanism called here non-wetting VLS), being bonded to the NW body through a defective region whose width is about 12-nm, as observed in a dark-brightness contrast. The remainder of the NW stem is composed by a uniform ZB phase, as we will analyze in depth later on. Figure 7.26(b) reveals the Ga droplet is wetting NW sidewalls (called here wetting-VLS) because the Ga-GaAs interface remains inside the droplet. Finally, as observed in figure 7.26(c), more than 1/3 of the Ga droplet is covering the NW edge; in this case the Ga droplet shape became more elongated, as predicted by theoretical results [19].

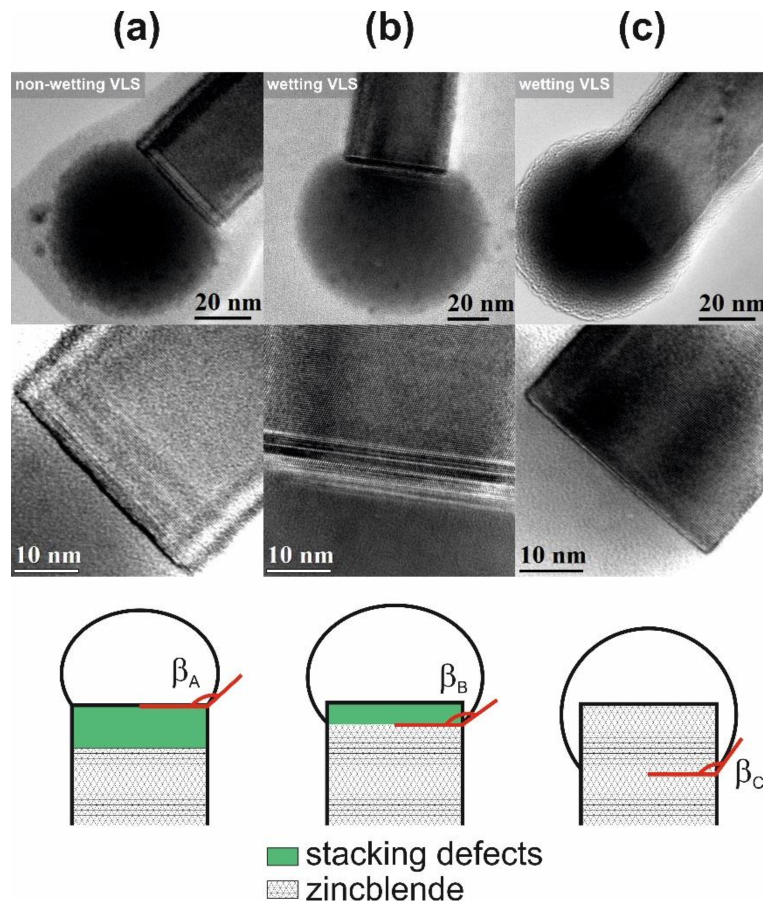

Figure 7.26. TEM images and their corresponding schematics of GaAs NW samples grown at (a,c) T_s = 600 ºC and (b) 580 ºC for 15 min.

The high portion of the NW wall wetted by the Ga droplet in the last case shows a transition region between the droplet and the NW stem which is almost free of defects. Therefore, comparing the transition regions in NWs grown under wetting and non-wetting VLS modes, a crystalline quality improvement is suggested in that region for the wetting case. It should be noted that TEM images in figure 7.26 are essentially 2D projections of 3D configurations, which may not yield a fully exact representation of the Ga droplet characteristics.

It is important to notice that the region including defects is located at the NW termination for all the observed NWs, meaning it was formed at the end of the NW growth, close to time at which TEGa and TBAs fluxes and substrate heater are turned off; the induced sample fast cool down may induce a last stage of GaAs growth fed by the remaining As solved in the Ga droplet, which are not the optimum conditions for the growth of high quality crystalline structures.

Figure 7.27(a) shows an image with atomic resolution for the same NW previously studied in figure 7.26(b), where three low-index crystalline planes are identified: (002), (11-1) and (111), the last one being perpendicular to the <111>A,B growth direction, which we are not able to discriminate as being either [111]A or [111]B type. This result is a good indication of an epitaxial growth along the preferential direction determined by the Si(111) substrate. The measured spacing between (002) planes is 0.289 nm, whereas for (11-1) and (111) planes it is 0.325 nm, in good agreement to the (111) spacing of 0.326 nm for bulk GaAs. The good matching between lattice spacing in bulk GaAs and that measured in our GaAs NWs suggests that GaAs NW lattice is fully relaxed, at least after removal from the Si substrate.

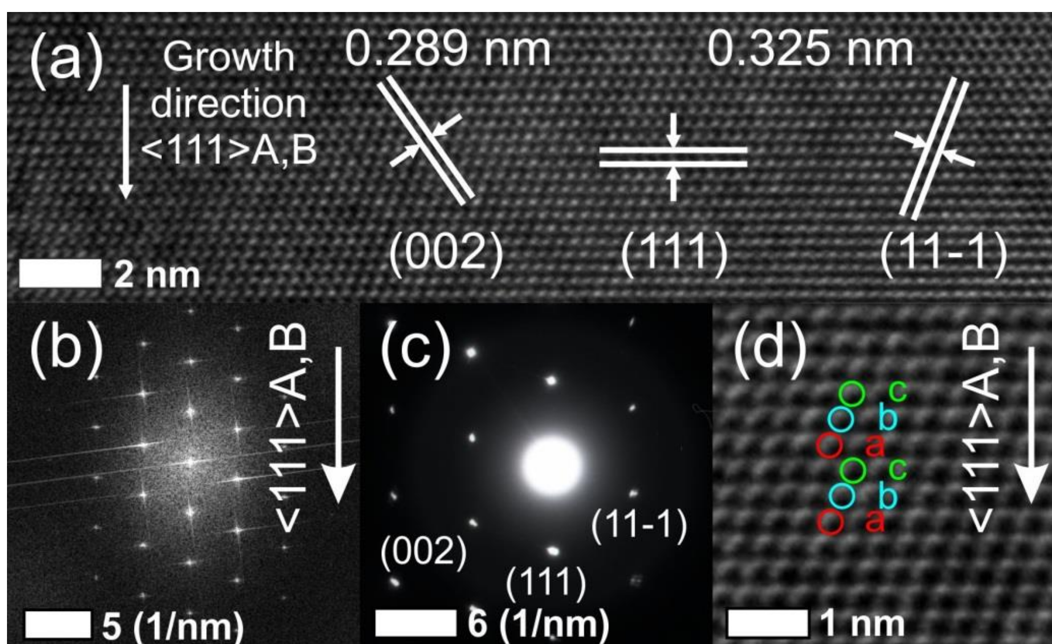

Figure 7.27. Analysis of a GaAs NW facet crystalline structure by TEM. (a) HRTEM image, (b) 2D-FFT, (c) ED diffractogram and (d) ZB *abcabc* stacking sequence along the NW growth direction.

Two complementary studies, TEM image 2D FFT (figure 7.27(b)) and TEM electron diffraction (ED) (figure 7.27(c)) of the NW stem allowed to identify different low-index diffraction spots. Both patterns are equivalents, giving the same information, either by electron diffraction or by Fourier transforming the TEM image. Even more, this patterns must also be equivalent to the diffraction pattern observed by RHEED; in this last, only half of the image (upper part) is seen because of the shadowing effect of the substrate at low incidence angle. Comparing both diffraction patterns, RHEED (figure 7.24(b)) and TEM (figure 7.27(c)), this one only reproduces the set of α spots observed in the RHEED pattern, indicating our NW are free of twins. The observation of both sets of diffraction spots (α and β) in the RHEED pattern with the same intensity can only be explained if the same population of two sets of twined NWs is assumed to be present at the sample surface.

The stacking sequence along the growth direction <111>A,B is identified to be *abcabc* (figure 7.27(d)), characteristic of the ZB structure. TEM measurements performed on a set of NWs, including all the NWs shown in figure 7.26, confirmed our NWs present ZB structure along the whole NW stem, which means the pure ZB phase can be obtained under both VLS growth modes: wetting and non-wetting.

Although the growth of pure ZB GaAs NWs have been proven by both wetting and non-wetting VLS processes, the latter is not able to preserve the NW termination free of defects. A detailed view of the final region of one GaAs NW grown under non-wetting VLS is shown in figure 7.28(a,b). These images are a HRTEM image (a) and its high-magnification (b), corresponding to the NW previously shown in figure 7.26(b). As clearly observed in figure 7.28(b), the ZB *abcabc* stacking sequence is identified up to the NW neck where some defects contribute to diffuse the image, but without any evidence of the characteristic WZ *ababab* stacking sequence.

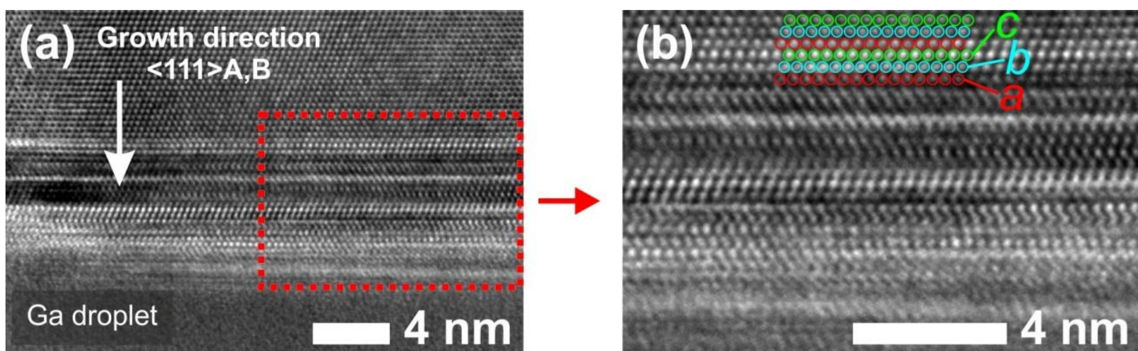

Figure 7.28. (a) HRTEM image and (b) a high-magnification TEM image of the interface formed between GaAs NW and the Ga droplet catalyst.

Raman Spectroscopy

As already mentioned, GaAs NWs grown by means of VLS processes have one major problem related to the presence of structural defects such as twins, voids, or stacking faults, generated around the interface formed between the NW and the catalyst droplet during growth. Raman spectroscopy, as a non-

destructive contactless characterization technique, has been used to analyze surface properties (surface phonon existence), structural quality (NW strain and density of structural defects), thermal and quantum confinement effects, as a function of the NW dimensions [18, 20-22]. Tensile and compressive forces can be identified in Raman spectra as red and blue energy shifts, respectively. The existence of defects in the NW lattice structure leads to a relaxation of the Raman selection rules at the Brillouin zone (BZ) centre (Γ point, wavevector $q = 0$) by a quantity (δq) proportional to the inverse of the NW diameter ($\delta q \sim \pi/d_{NW}$) [23]; this breaking of the selection rules allows not only the observation of forbidden modes in different backscattering geometries, but also peak shifts and asymmetrical broadening of the Raman peak shape. For III-V compound semiconductors with ZB structure, transverse (TO) and longitudinal (LO) optical modes are split at $q \sim 0$ due to the polar nature of the crystal (long range Coulomb forces). TO and LO vibrational modes have been observed in GaAs NW under specific backscattering geometries [15], being strongly affected by lattice defects.

Analyzing in depth the position and shape of the Raman peaks, interesting information about GaAs NWs can be extracted. Tensile and compressive strains generated along the NW are especially observed in polytypism structures formed by both phases ZB and WZ, where strain can be characterized by a peak shift towards lower and higher Raman wavenumbers (cm^{-1}), respectively [15]. Quantum confinement could also lead to a peak shift towards lower energies; as demonstrated by Campbell and Fauchet calculations [24], NWs with diameters below 3 nm are necessary to show a significant peak shift up to 4 cm^{-1}. Furthermore, the excitation laser power can also induce shifts on the TO and LO peaks towards lower energies, due to sample heating [18, 25].

In this section, the crystalline structure quality of GaAs NWs grown under different conditions was analyzed by Raman spectroscopy. This optical characterization was performed in samples with vertically aligned NWs grown on Si(111) substrates and under two different configurations called: backscattering geometry type A and B (see figure 7.29 insets). In type A geometry, the Si(111) substrate cleavage planes are used as references for NW orientation. Assuming the GaAs NW growth direction as [-1-1-1] or [111]B, the NW coordinate system is set with the z axis along the growth direction, the x axis pointing in the [-211] direction (perpendicular to NW edge) and the y axis along the [0-11] direction (NW facet). The configuration for type A in Raman standard notation is then x(y,y)-x, with the incident and scattered electric fields (ε_i and ε_s) linearly polarized along y axis. In type B, the configuration is denoted as -z(xy,xy)z, because no special care was taken to align the polarization vector relative to the NW facets. The resultant spot is a few microns in size, which means that an amount of three or four NWs are analyzed during each measurement.

Raman selection rules allow both TO and LO modes in backscattering from the <-211> and <111> directions [26], which correspond to type A and B geometries described in figure 7.29. Figure 7.29 shows Raman spectra measured under type A and B geometries for GaAs NWs grown for 15 min at T_s = 600 ºC and using a V/III flux ratio around 0.8. Both Raman spectra show three peaks, whose central frequencies are marked in the figure by vertical dotted lines, corresponding to TO and LO vibrational modes, and a third peak inserted between them, probably related to a surface optical (SO) phonon that will be also analyzed in

depth later on. Comparing to the reported frequencies for bulk GaAs, the observed TO and LO modes in NWs appear to be slightly downshifted (NW: $\omega_{TO} = 268.1$ cm^{-1}, bulk: $\omega_{TO} = 269$ cm^{-1}; NW: $\omega_{LO} = 289.6$ cm^{-1}, bulk: $\omega_{LO} = 292.0$ cm^{-1}) which could be related to the strain induced by the lattice mismatch between GaAs and Si.

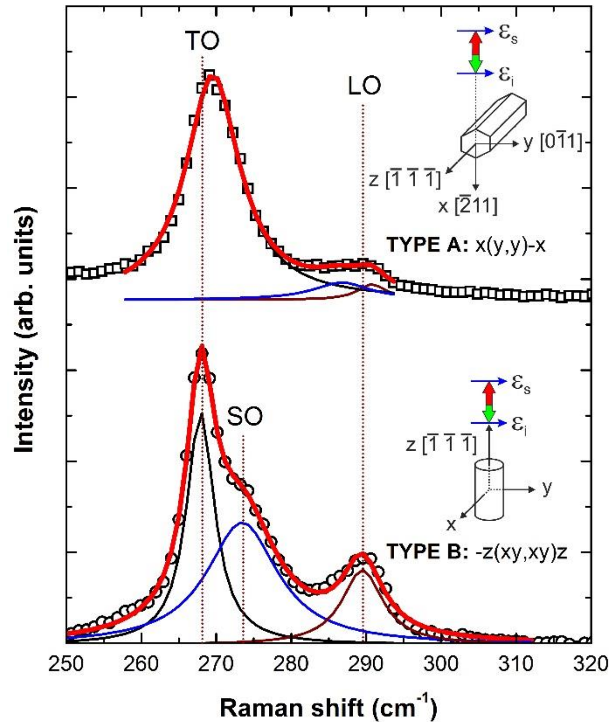

Figure 7.29. Raman spectra of vertically aligned GaAs NWs on Si(111) measured under type A and B geometries. Inset: Schematics of type A and B backscattering geometries.

Peak shift could also be due to the heating effect of the laser excitation [18, 21]. However, because of the low excitation power used in our Raman experiments, TO and LO peak shifts are found to be almost independent on the laser excitation power, as shown in figure 7.30 plot. In addition, the slight spreading observed on peak positions comparing samples grown under the same conditions or even different regions on the same sample, also discards any heating effect due to laser beam power.

TO and LO peaks in spectra shown in figure 7.29 exhibit small full width at half-maximum (FWHM) values, around 5 cm^{-1}, indicating NWs have a high crystal quality. The ratio between the intensity of both peaks (I_{TO}/I_{LO}) is also analyzed for Raman spectra shown in figure 7.29; this ratio usually depends on crystal orientation, measurement geometry and surface electric field [25]. The value for I_{TO}/I_{LO} is found to be close to 1.5, where higher values are usually related to WZ GaAs NWs ($I_{TO}/I_{LO} > 1.5$), while much lower values are found in the case of ZB GaAs epitaxial layers ($I_{TO}/I_{LO} < 0.1$).

The structure of the analyzed NWs is confirmed to be composed by only a pure ZB phase, because GaAs NWs with WZ structure should show, additionally to TO and LO modes, another mode at 259 cm^{-1}

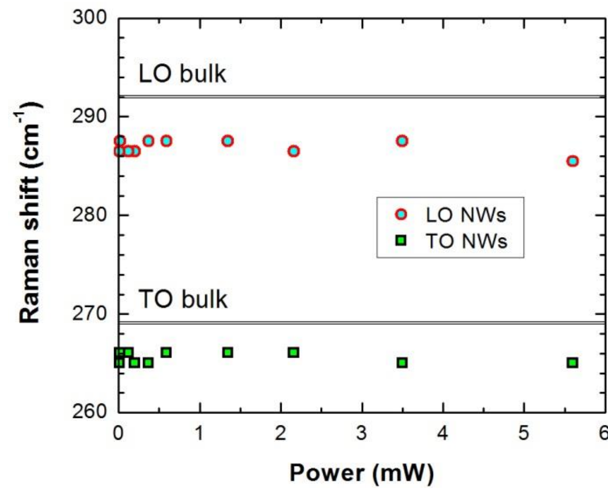

Figure 7.30. TO and LO Raman shift measured as a function of the excitation power in GaAs NW and bulk samples.

called E_2^H which is characteristic for this phase. From spectra shown in figure 7.29, the lack of the E_2^H related peak is evident, in good agreement with the absence of WZ phase in TEM images.

In figure 7.29, simulation of Raman spectra using a sum of Lorentzian curves is shown. However, there is an alternative mathematical method that enables the simulation of the Raman intensity as a function of the Raman shift, extracting information about some important physical magnitudes related to the NW structure, including lattice disorder in the NW structure and low-dimensional effects which can be studied by means of the Raman line-shape analysis using the phonon confinement model (PCM), also known as "special correlation model." This model, first proposed by Richter to account for the observed shift and broadening in microcrystalline Si [27], and further developed by Campbell [24] to be applied to cylindrically-shaped NWs and thin films, has been used to analyze Raman line shapes in NWs composed by different semiconductor materials such as GaP [28], Si [21], InAs or GaAs [18]. This model takes into account the contributions of phonons away from the first BZ which are responsible for the modification of the Raman spectrum line shape. PCM has also been used to study LO modes showing broadening and asymmetric peak-shapes, because the existence of a SO mode close to the LO peak can distort its shape. However, PCM has rarely been used for the TO mode; due to its low dispersion, this peak presents symmetric Lorentzian shape and therefore no structural disorder neither quantum confinement effects can be studied for this vibrational mode. According to PCM, a set of NWs with a given distribution of diameters, but constant along their length, their corresponding Raman intensity can be expressed as

$$I(\omega) \cong \int_{BZ} \frac{|C(q_0, q)|^2}{[\omega - \omega_0(q)]^2 + [\Gamma_0/2]^2} dq^3 \ , \qquad (7.1)$$

where ω is the incident photon frequency, $dq^3 \sim qdq$ for NWs [18], $|C(q_0, q)|^2$ is the Fourier coefficient of a confinement function which could depend on the structure shape and it is a function of the wavevector q

centered at q_0 [25], $1/\Gamma_0$ is the phonon lifetime (Γ_0 represents the natural FWHM of the bulk GaAs phonon and takes a value about 4.5 cm^{-1}), while $\omega_0(q)$ is the phonon dispersion relationship. Although both Γ_0 and $\omega_0(q)$ are functions of the NW temperature, the use of a low laser excitation power allows to discard any temperature dependence.

While equation (7.1) was presented by Richter to analyze LO phonons along the <001> directions, corresponding to the directions connecting the Γ and X points in the first BZ [27], this equation has been used here to accurately fit the line shapes of all three Raman modes (TO, SO, and LO) measured in GaAs NWs samples.

For a primitive cell including two atoms (such as GaAs) bonded by a force C_1 (see figure 7.31(c)), $\omega_0(q)$ can be expressed as [29]

$$\omega_0(q) = C_1\sqrt{\frac{M_1 + M_2 + \sqrt{M_1^2 + M_2^2 + 2M_1M_2\cos(qa)}}{M_1M_2}}\ , \tag{7.2}$$

where M_1 and M_2 are the averaged atomic masses of Ga (69.723 u) and As (74.922 u), respectively, a is the spacing between adjacent planes with the same kind of atoms, and q is the component of the wavevector along the direction perpendicular to these planes. Equation (7.2) can be deduced for waves propagating along a high-symmetry direction for which a single vibrating plane contains only a single type of atom; such directions are <111> in NaCl and <100> in CsCl crystals [30].

Figure 7.31(a,b) show a schematic for the crystal structure of the cross section (NW front) and lateral walls (NW facet) of a hexagonal ZB GaAs NW oriented along the [111]B direction. Figure 7.31(c) represents a phonon wave propagating along one of the <001> directions, the {010} family of planes only containing one type of atom (either Ga or As) with a spacing $a = a_0/2 = 0.326$ nm, a_0 being the GaAs lattice parameter; both LO and TO phonons are also represented, depending on the atomic vibration direction with respect to the wavevector. In the case of surface phonons, the SO mode is similar to those observed in bulk layers but with only atoms at the surface contributing to phonon propagation (figure 7.31(d)).

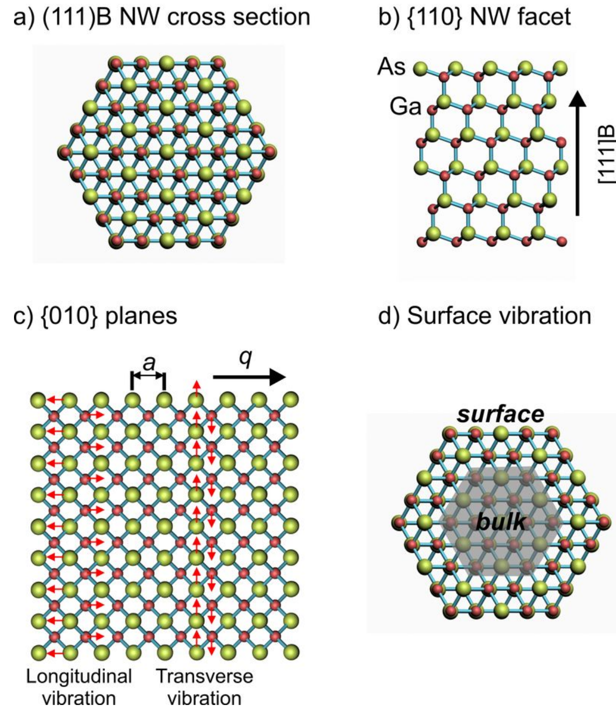

Figure 7.31. Schematics of a single GaAs NW; (a) hexagonal NW front, (b) NW facet, (c) GaAs {010} planes, and (d) atoms at the surface and in the bulk of the NW.

For $q_0 = 0$, Fourier coefficient used in expression (7.1) can be written as

$$|C(0,q)|^2 = C_0 \exp\left[-\frac{1}{2}(qA)^2\right] \tag{7.3}$$

$$A = L / 4\pi \tag{7.4}$$

$$A = d_{\mathrm{NW}} / \alpha \, a_0 \tag{7.5}$$

where C_0 is a fitting parameter. The parameter A has been defined by Campbell and Adu [30] in different ways, as expressed in equations (7.4) and (7.5), respectively. Equation (7.4) uses the fitting parameter L, known as the correlation length (related to the distance between defects and equivalent to the grain size in polycrystals), while equation (7.5) uses both parameters d_{NW} and α, which are the NW diameter and the confinement coefficient, respectively. L gives information about the size of the confinement region formed between two adjacent defects in the NW structure, whereas α sets the confinement scale in the NW due to its diameter size and is characteristic for each material and independent on d_{NW} [31].

The asymmetry, broadening and downshifting of Raman peaks are mainly simulated by the Fourier coefficient (equation (7.3)) using either L or d_{NW} as fitting parameters, while the Raman intensity and peak position are determined by C_1 and C_0, respectively.

Once the theory of the PCM is exposed, we now are able to simulate a Raman spectra measured in samples composed by NWs with a homogenous distribution of diameters. For that study, three different samples were grown at T_s = 620, 600 and 580 ºC, whose average d_{NW} are 57, 54 and 40 nm, respectively. Measured Raman spectra are shown in figure 7.32, which were simulated by the superposition of TO, LO and SO phonon modes, each one fitted by using equation (7.1). The shape of the TO peak is almost a Lorentzian function, whereas in the case of SO and LO, they present some asymmetry and broadening. Because every peak has its own integral given by equation (7.1), every peak has its own set of fitting parameters given by C_0, C_1, L and α, where L and α are obtained from equations (7.4) and (7.5), respectively.

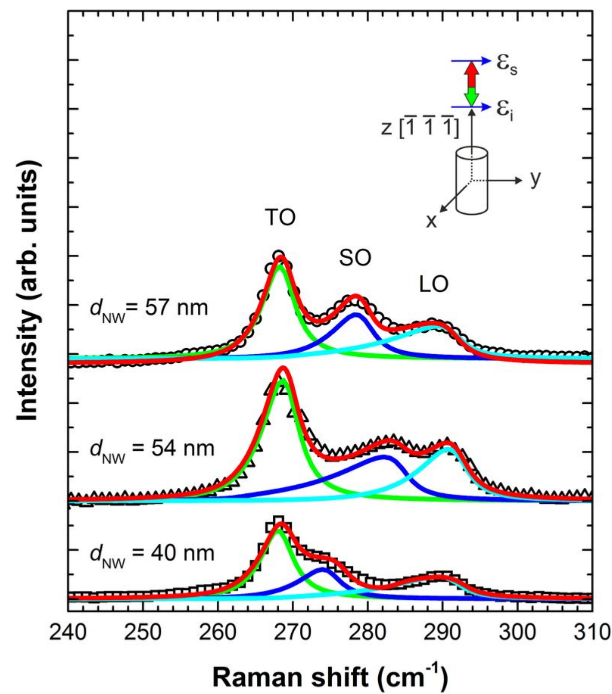

Figure 7.32. Raman spectra corresponding to three GaAs NW samples with different average NW diameters.

The analysis of the LO shape allows us to extract information about the disorder in the NW structure, according to PCM. A similar study has been carried out by Begum et al. [25] by means of a thorough analysis about the Raman line-shape in GaAs and InAs NWs grown by Au-assisted solid source MBE, estimating the density of defects in a single NW by using the parameter L. However, from that study the density of defects in this kind of Au-assisted growth resulted to be too high. Considering that α has been studied in several semiconductor NWs, but not yet in GaAs, the estimation of both parameters α and L for GaAs NWs is promising in order to estimate the crystalline quality of NWs grown by different techniques and conditions.

LO peaks are fitted following the above procedure and using experimental values extracted from SEM images for d_{NW}, obtaining parameters for L and α which are shown in table 7.3. The correlation factor

was obtained to be $r^2 \geq 0.997$ for all fits, indicating that the model can accurately reproduce the LO peak shape.

Table 7.3. Parameters obtained after fitting LO shape (α and L) using equations (7.1) - (7.5) for GaAs NWs with different d_{NW}.

d_{NW} (nm)	α (nm^{-1})	L (nm)	Defect density, 1/L (nm^{-1})
40	23	30	0.033
54	23	40	0.025
57	23	45	0.022

The confinement coefficient value, α, corresponding to GaAs NWs studied in this work is observed to be independent on d_{NW}, taking values around $\alpha = 23$ nm^{-1}, the value of this parameter being characteristic for each material. While it has been previously reported to be $\alpha = 6.3$ nm^{-1} for Si NWs [21], to the best of our knowledge, its value has not been already estimated for GaAs NWs. Therefore, considering α is constant in equation (7.5), the only factor responsible for the variation of A (A changes means variations in the asymmetry and broadening of the Raman peak) is d_{NW}, which has been independently measured from SEM images.

On the other hand, the study of the correlation length, L, shows that L increases with d_{NW}. The density of defects can be estimated as $1/L$. As shown in table 7.3, as d_{NW} increases (from 40 to 57 nm) the defect concentration decreases (from 0.033 to 0.022 nm^{-1}).

Finally, the relationship obtained by combining expressions (7.4) and (7.5): $L = 4\pi d_{NW}/\alpha a_0$, allows to calculate L from simulated α values and vice versa; so obtained calculations differ between 5 and 10% from values shown in table 7.3, which is a good indication that both Fourier coefficients have been properly simulated.

Both, figure 7.29 and figure 7.32 show a third Raman peak at Raman frequencies located between TO and LO peaks, which is usually attributed to a SO phonon. This vibrational mode is first proposed by Fuchs et al. [32] who considered the SO mode as a macroscopic optical phonon whose propagation and penetration depth is connected with a macroscopic electric field. SO phonons can be generated at the interface between different materials, propagating along their interfaces with a wavevector q. Atomic vibrations involved in the propagation of the SO mode have amplitudes which are confined to the near-surface region of the material (figure 7.31(d)). SO modes are generated by the breakdown of the translational symmetry of the surface potential, which in a NW is due to the surface roughness or to different diameters along the NW length. Therefore, this phonon can be actively associated with surface modulation (roughness), cross section shape (hexagonal, cylindrical, or square) and backscattering geometry of the Raman system. There are a few reports about the SO phonons observed in NWs composed of various semiconductor materials such as InGaN/GaN multi-quantum-well nanopillars [33], AlN [31], GaN [34] InN [35], GaP [28] or GaAs [20]. Some of above works show relevant information about the NW structure and surface quality of the NWs extracted from the Raman analysis of the SO peak.

In this part of the Raman study, we investigated the mechanism responsible for the SO phonon generation by the Raman analysis of the length scale parameter (λ) or also called SO wavelength perturbation [28]. This parameter is defined as the distance between two adjacent morphological defects found along the surface of the NW, its value being extracted from the difference between the SO and LO peak frequencies, and later corroborated by TEM images. As NW sidewall oxidation could also produce SO frequency shifts, caused by the propagation of the SO mode through the interface formed by oxide and the NW, the influence of a native oxide layer has been considered.

For the study of the SO peak, the -z(xy,xy)z backscattering configuration (type B in figure 7.29) offers an important advantage over other possible configurations, such as for example y(x,x)-y or x(y,y)-x where one of the {110} NW facets or {211} NW edges, respectively, are illuminated. This advantage consists on the empirical observation of a better defined SO band (figure 7.29) because of the large frequency shift between the LO and SO peaks.

Comparing LO and SO peak positions in figure 7.32, the relative shift observed in the case of LO peak is below the resolution limit of 1 cm^{-1}, while the SO peak position is more sensitive to either the NW diameter d_{NW} (or the correlation length L), showing a relative shift up to 9 cm^{-1}.

From figure 7.32, the SO peak shift dependence on NW diameter is not clear. Previously reported works [20] observed an increasing downshift of ω_{SO} with respect to the ω_{LO} peak position as the NW diameter decreases, in such a way that when the SO extremely downshifts with respect to the LO peak, the latter becomes broad and asymmetric to compensate the lack of SO contribution.

It should be noted that because all NWs suffered a large exposure to ambient air before they were characterized by Raman spectroscopy, their surface could have different oxidation degrees. Then, surface oxidation process can induce changes in the SO frequency position due to the change of the relative permittivity at the GaAs NW surface (GaAs/oxide instead of GaAs/air). In order to better understand this effect, the frequency ω_{SO} was calculated following a simple model which considers NWs as perfect cylinders surrounded by different environments [28]; in this model, the SO frequency is given by equations

$$\omega_{SO}^2 = \omega_{TO}^2 + \frac{\tilde{\omega}_p^2}{\varepsilon_\infty + \varepsilon_m f(qr_{NW})} \tag{7.6}$$

$$f(qr_{NW}) = \frac{[I_0(qr_{NW})K_1(qr_{NW})]}{[I_1(qr_{NW})K_0(qr_{NW})]} \tag{7.7}$$

$$\tilde{\omega}_p^2 = \left(\tilde{\omega}_{LO}^2 - \tilde{\omega}_{TO}^2\right)\varepsilon_\infty \tag{7.8}$$

where ω_{SO}, ω_{TO} and ω_{LO} are again the SO, TO and LO phonon frequencies, respectively, $\tilde{\omega}_p$ is the screened ion plasma frequency, ε_∞ is the high frequency relative permittivity (~10.88), ε_m is the relative permittivity of

the surrounding medium, I_n and K_n are the modified n^{th} Bessel functions, r_{NW} is the NW radius and q is the wavevector which is calculated using the laser wavelength as $q = 4\pi/\lambda = 0.023621$ nm^{-1}. The experimental values for the frequency shift between ω_{LO} and ω_{SO} are represented in figure 7.33 as a function of the average NW diameter obtained from SEM analysis for several samples.

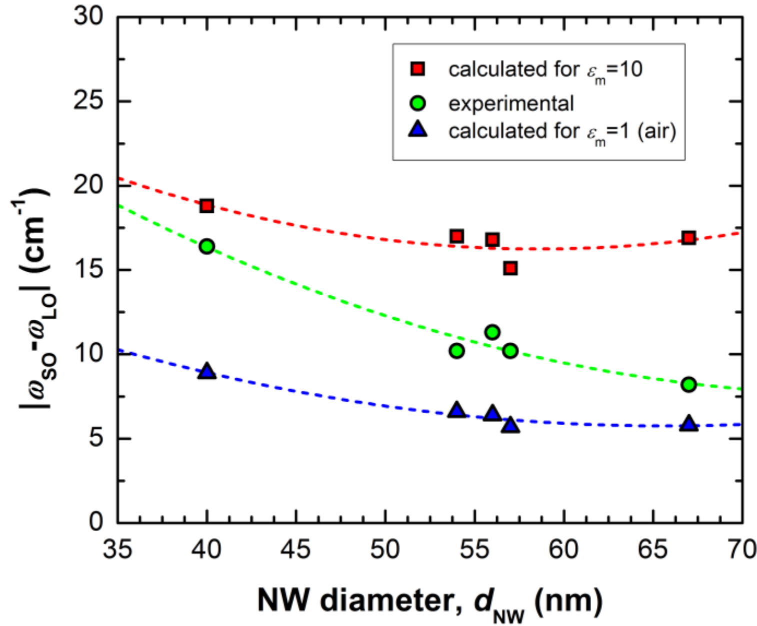

Figure 7.33. SO to LO phonon frequency shifts as a function of the NW diameter and the surrounding environment. Dotted lines are drawn to guide the eye.

Calculated ω_{SO} values (using the set of equations (7.6) - (7.8) for different environments such as air ($\varepsilon_m = 1$) or oxide based compounds (GaO_x, AsO_x, …) whose relative permittivity was assumed to be around $\varepsilon_m = 10$, are also plotted in the same figure. As observed in figure 7.33, experimental data are located between calculated values for both environments, air and oxide, meaning that NWs are probably partially oxidized and capped by with an oxide thin layer. Corresponding ε_m for each NW diameter can be roughly estimated using equations (7.6) - (7.8) to calculate the effective ε_m value to fit experimental ω_{SO}-ω_{LO} values, following the same procedure than used in figure 7.33 for $\varepsilon_m = 1$ and $\varepsilon_m = 10$, and the salient results are recorded in Table 7.4.

Table 7.4. Measured average d_{NW}, L_{NW} and SO Raman shift (ω_{SO}^{exp}) for several samples; effective relative permittivity (ε_m), qr_{NW} value, and length scale (λ) calculated as a function of d_{NW}.

$d_{NW} = 2r_{NW}$ (nm)	L_{NW} (µm)	ω_{SO}^{exp} (cm^{-1})	ε_m	qr_{NW}	λ (µm)
40	1.3	273.2	4.60	0.48	0.52
54	0.4	279.4	2.07	0.64	0.72
56	1.2	277.3	2.69	0.66	0.75
57	0.4	277.3	2.78	0.67	0.76
67	0.3	281.4	1.68	0.79	0.53

Figure 7.33 shows that as NW diameter increases, i.e. larger correlation lengths, the obtained frequency shift between SO and LO phonons decreases, which indicates NWs with larger diameters tend to be less oxidized along their surfaces due to their lower surface-to-volume ratio. Alternatively, different oxide coverage degree for different samples, possibly due to different post-growth storage conditions and ambient exposure times, is not discarded.

The SO mode detection in Raman spectroscopy is enhanced using backscattering configuration type B (–z(xy,xy)z, as described in figure 7.29), because the surface potential perturbation along the NW axis is excited by a high component of the incident wavevector. The values of the wavevector responsible for the observation of the SO mode can be estimated by comparing experimental values of ω_{SO}^{exp} to those calculated using equation (7.6) for NWs with different radii in ambient air. As shown in figure 7.34, corresponding $q^{exp}r_{NW}$ values are extracted from the intersection of ω_{SO}^{exp} (y axis) and calculated ω_{SO} values (plotted curve) for every NW dimensions and effective relative permittivity of the surrounding media, and its extrapolation to the x axis as pointed out by arrows in that figure. The obtained values for $q^{exp}r_{NW}$ (included in table 7.4) are located in a very short interval, in the range 0.5 to 0.8.

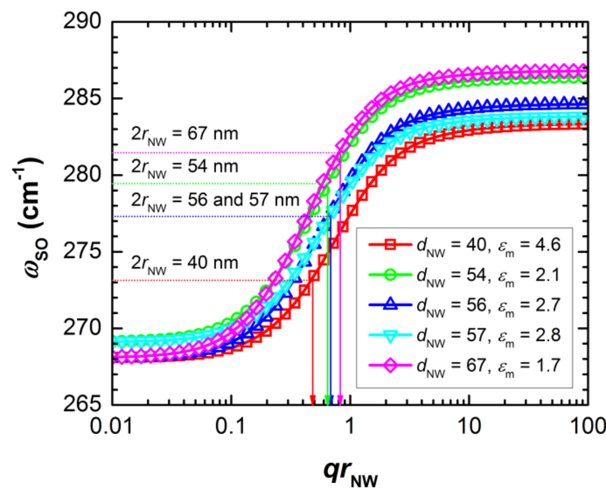

Figure 7.34. Calculated SO Raman shift for single cylindrical GaAs NWs with different diameters and corresponding ε_m values. For a given r_{NW}, $q^{exp}r_{NW}$ values are deduced from measured ω_{SO}^{exp}, following the model described in the text.

Many factors can induce the activation of the SO mode, the main ones being the surface roughness or changes in the NW diameter along the NW stem. Both are typically found in VLS growths due to changes in the catalyst size during growth. Distance between this kind of surface defects can be roughly estimated using the length scale, usually defined as $\lambda = 2\pi\, d_{NW}/q^{exp} r_{NW}$ [28]. Calculated λ values are included within a narrow interval, in the range 0.5 to 0.8 μm, as also shown in table 7.4. This λ value could be interpreted as the distance between steps along the NW surface, as previously reported for AlN NWs [31], where symmetrical breaking responsible for the SO generation is mainly caused by surface roughness modulation.

Figure 7.35 shows TEM overview images and their magnification, corresponding to three different NWs of about 40 nm diameter and 1.3 μm length. In these pictures, they are highlighted both the smooth surface of the NWs, and the reduced number of morphological surface defects. As marked with arrows, the existence of one step (figure 7.35(a)) and waist-style defects (figure 7.35(b,c)) along the whole NW facets are hardly detected in some of the studied NWs.

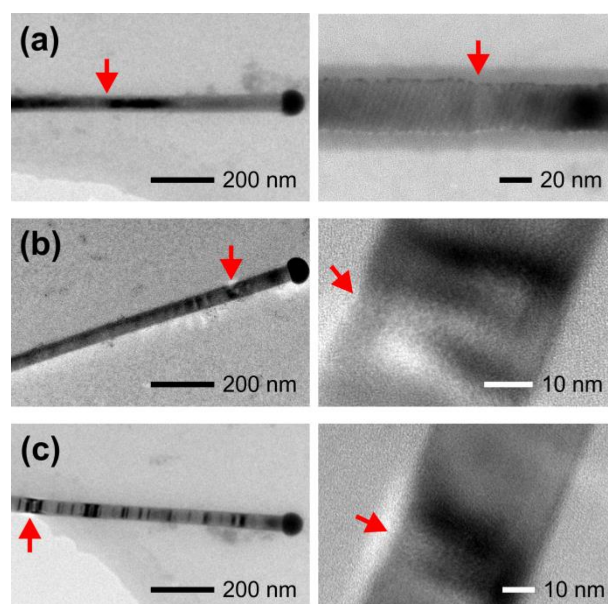

Figure 7.35. TEM images showing (a) one surface step, (b) and (c) waist-style morphological defects found on some NWs.

Therefore, TEM confirms the low density of surface defects in GaAs NWs which is in good agreement with SO Raman results, where λ takes values which are close to those measured by SEM for NW length.

On the other hand, SO line width is analyzed as a function of the NW diameter. There is no significant difference between the FWHM values obtained for NWs with 40 nm of diameter (11.0 cm^{-1}) and those obtained for NW with 67 nm (17 cm^{-1}), thus meaning SO phonons have similar decay channels and their lifetime was approximately in the same range [28].

7.3. Integration of GaAs NWs in Optoelectronics

GaAs NWs can be used as building blocks for high performance VIS PDs. For that purpose, GaAs NWs have been integrated between conductive electrodes by DEP.

DEP processes are analyzed in depth in order to control not only the number of assembled NWs but also their alignment. The effective alignment of GaAs NWs is therefore studied as a function of the DEP conditions. Furthermore, a reproducible way to fabricate single-NW and multi-NW based structures using DEP will be described, allowing to characterize the electrical properties of these structures such as photoconductivity.

7.3.1. GaAs NW Assembled by DEP

In previous section 6.3 positive DEP mechanism has been described and applied to assemble ZnO NWs between conductive electrodes. In this section, the assembling efficiency of GaAs NWs has been analyzed as a function of DEP parameters (such as AC amplitude and frequency), the NW distance to the gap between electrodes, and the initial alignment of the NW with respect to the electric field.

NWs Suspension Preparation

The alignment of NWs by DEP requires to previously prepare a NW suspension in a liquid solvent. In this regard, two different NW suspensions were prepared, consisting in GaAs NWs with and without a Ga droplet on top of their tips. The main purpose of these two kinds of NWs is to analyze the effect of the Ga droplet on the contact quality formed after assembling process.

The suspension containing GaAs NWs with Ga droplets on their tips (figure 7.36(a)) is prepared in a similar way than previously described for TEM analysis. After dipping a 0.5×1.5 cm^2 sample containing NWs in 1.5 ml of ethanol, it is sonicated for a few seconds (~ 10 s), the sonication step producing the scission of GaAs NWs from the substrate near their base, as shown in figure 7.36(b). In order to check the morphological properties of these free standing NWs in the suspension, a 4 μl droplet of as-prepared suspension was deposited over a Si substrate. Figure 7.36(c) shows a SEM image taken after ethanol is completely evaporated, where a GaAs NW is shown with a Ga droplet still on top of its tip.

On the other hand, the suspension containing GaAs NWs without a Ga droplet is prepared by firstly etching a 0.5×1.5 cm^2 NW sample with a buffered solution of HCl:DI H_2O (1:9) for 1 min to completely etching Ga droplets, exhibiting a flat NW front (figure 7.36(d)). After the sonication of the resultant suspension, NWs are removed from the substrate (figure 7.36(e)). Figure 7.36(f) shows a SEM image of a GaAs NW without Ga droplet, deposited on a Si substrate.

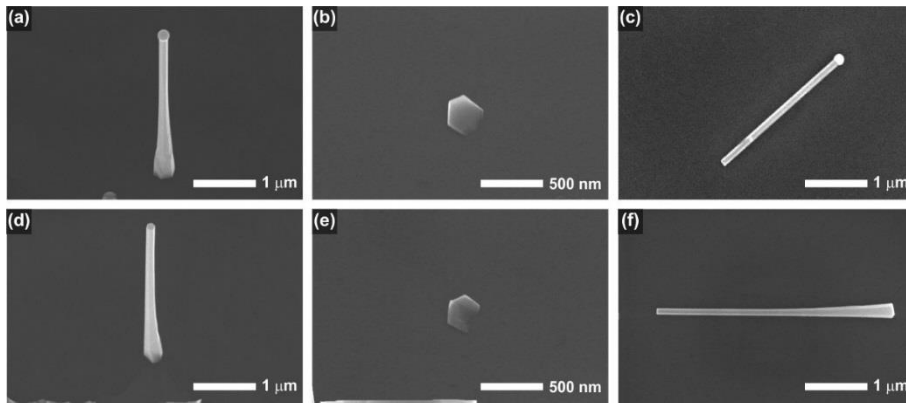

Figure 7.36. SEM images taken at each step of the NW suspension preparation. GaAs NW (a) with and (d) without Ga droplet; (b,e) GaAs NW base after sonication; GaAs NW with (c) and (f) without droplet dispersed on a Si substrate.

Conductive Electrodes

We have grown GaAs NWs by Ga-assisted CBE with L_{NW} up to 5 μm. The gap spacing between electrodes should therefore be limited to less than 5 μm in order to assemble NW. For this purpose, 200-nm thick Al electrodes have been deposited on glass substrates, their geometry was later defined by combining photolithography and chemical etching to obtain a gap spacing from 2 to 4 μm between them.

Figure 7.37 shows both, a schematic of a lateral view of structure, and a SEM top view after assembling of a single GaAs NW between a pair of Al electrodes. Gap spacing and the layer thickness are indicated in (a), while the SEM image in (b) shows a GaAs NW without droplet assembled by DEP between a pair of Al electrodes with a gap spacing around 3.5 μm.

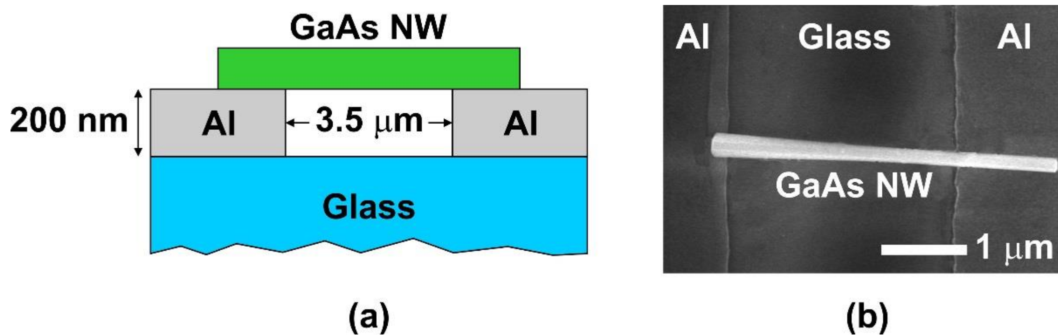

Figure 7.37. (a) Layer schematic and (b) SEM image of a single GaAs NW connecting a pair of Al electrodes.

Dielectrophoretic Force

As already mentioned in chapter 6, the F_{DEP} exerted on a NW subjected to a non-uniform electric field (equation 6.4) depends on the AC frequency through the f_{cm} coefficient (equation 6.5), on the V_{rms} value through the $\nabla|E|^2$ (equation 6.7), on the electrical properties of both NW and surrounding medium also through the f_{cm} coefficient, and finally on the NW dimensions and its relative orientation with respect to the electric field through the L_i factor (equation 6.6). For this reason the F_{DEP} exerted on the GaAs NWs is in

principle different to the force exerted on ZnO NWs because the electrical properties and also the aspect ratio of both kinds of NWs are radically different. In this regard, assembling of GaAs NWs has been carried out under different DEP conditions, analysing the resulting geometries by SEM.

The following studies were carried out taking into account an idealized GaAs NW whose dimensions are r_{NW} = 50 nm and a L_{NW} = 4.5 μm, with electrical properties given as $\varepsilon_{GaAs} = 10.89\varepsilon_0$ and σ_{GaAs} = 6000 S/m, suspended in ethanol ($\varepsilon_{EtOH} = 24.3\varepsilon_0$ and $\sigma_{EtOH} = 10^{-5}$ S/m).

F_{DEP} vs Frequency

We first calculated F_{DEP} as a function of the AC frequency using equation (6.4), assuming a NW initially aligned to the electric field (L_i = 0), separated a distance of 10 μm away the electrodes gap, while applying an AC voltage of V_{rms} = 7.5 V. Obtained $F_{DEP}(f)$ curve shown in figure 7.38 exhibits a low-pass response, where two different regions are observed; an initial constant force region for f < 100 Hz to later decrease as $F_{DEP} \sim 1/f^2$ for larger frequency values.

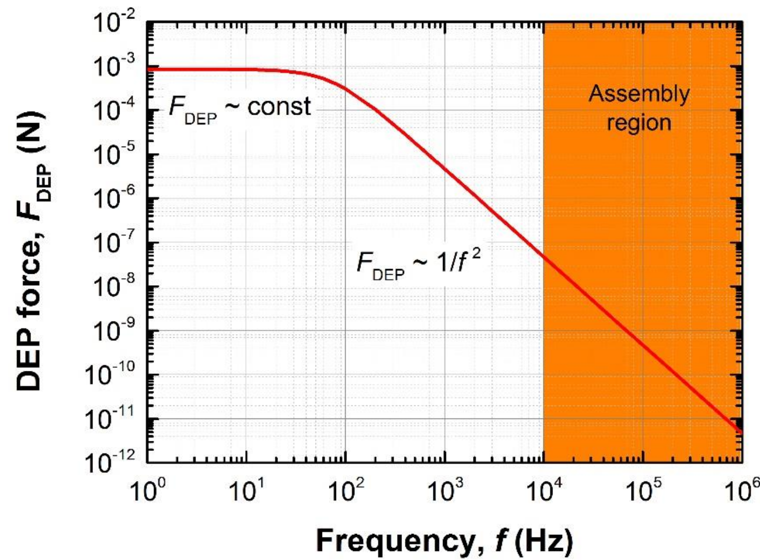

Figure 7.38. F_{DEP} exerted on a GaAs NW subjected to an AC electric field, as a function of the AC frequency.

At a first sight, it could be deduced from this figure that low frequencies are better to assemble GaAs NW due to the large force values obtained in this region, but experiments shows the opposite result. In order to observe the effects of frequency on the NW assembling, DEP processes were carried out by using f values up to 1 MHz. After DEP process, samples were observed by SEM as shown in figure 7.39. The successful trapping of GaAs NWs is observed only for f values above 10 kHz, involving F_{DEP} in the pN and nN ranges, as it is highlighted in figure 7.38 and called here assembling region. In the assembly region, NWs can reach a better alignment with the electric field lines when f is increased, mainly because the assembling process of the NW is carried out under a lower F_{DEP}, resulting in slower and softer than for low frequencies. In this regard, figure 7.39 shows NWs forming an angle with respect to the electric field lines of 5.2°, 3.1° and 1.2°

for DEP processes developed at 10 kHz, 100 kHz, and 1 MHz; demonstrating the improvement of the NW alignment with increasing *f*.

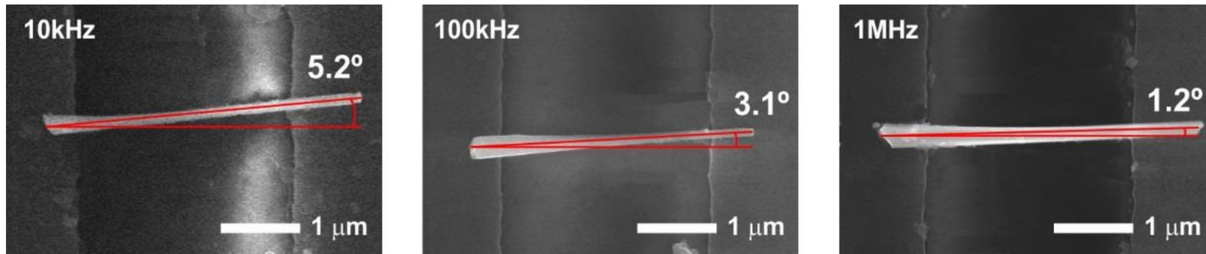

Figure 7.39. SEM images of DEP experiments carried out at different AC frequencies.

F_{DEP} vs V_{rms}

F_{DEP} applied to a GaAs NW as a function of the applied V_{rms} value can be calculated using equation (6.7). Considering a typical situation involving a GaAs NW initially aligned along the electric field ($L_i = 0$), separated by a distance of 10 μm from the electrodes gap, using an assembling frequency $f = 100$ kHz, the obtained F_{DEP} for different V_{rms} values up to 7 V is plotted in figure 7.40.

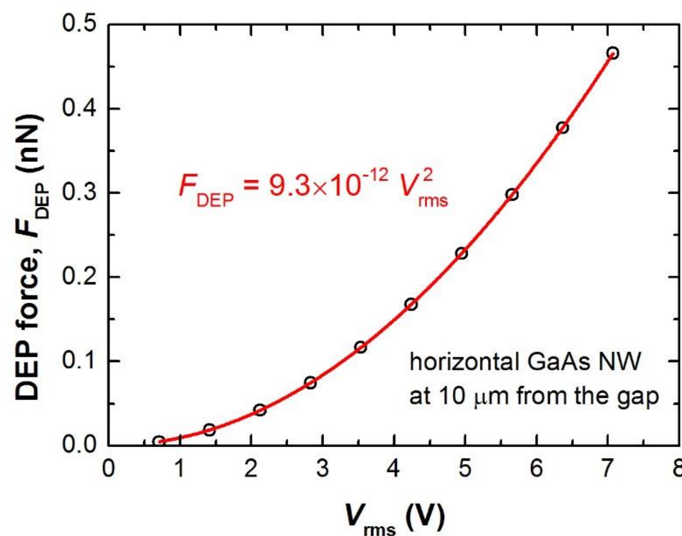

Figure 7.40. F_{DEP} exerted on a GaAs NW as a function of the V_{rms}.

From this figure, GaAs NWs are subjected to a F_{DEP} whose magnitude tends to increase as the squared value of the applied V_{rms}, as indicated by the fitting line represented along with the calculated data (black circles), reaching values up to 0.5 nN for $V_{rms} = 7$ V.

In order to test the above model, DEP experiments were also carried out using different V_{rms} values, whose SEM images are shown in figure 7.41. In addition, the length of the electrodes gap region is 100 μm, allowing the assembly of multiple NWs interconnecting both electrodes.

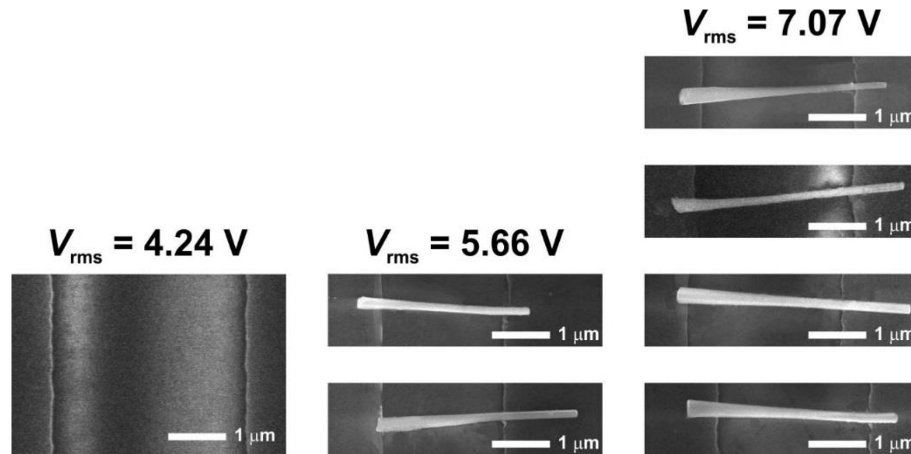

Figure 7.41. SEM images of three DEP experiments carried out at different V_{rms}. Sets of NWs shown below each V_{rms} conditions were assembled along the same electrode gap (100 μm gap length).

From above SEM images, it is noticeable that a V_{rms} value of 4.24 V is not enough to trap any GaAs NW; from figure 7.40, this V_{rms} produces F_{DEP} = 0.15 nN which is not sufficiently high to overcome the drag force in the fluid (see equation (6.7)). For large V_{rms} values, such as 5.66 V and 7.07 V, F_{DEP} is capable to successfully trap NWs between the electrodes gap, obtaining NW densities of 0.02 and 0.08 NW/μm. The observed increase on the assembled NW density with increasing V_{rms}, is in good agreement with the tendency predicted in figure 7.40.

F_{DEP} vs NW Position

The force exerted on a GaAs NW has been also calculated as a function of the distance between the NW and the electrodes gap. DEP calculations have been performed using previously obtained optimum values of f = 100 kHz and V_{rms} = 7.07 V, assuming a NW initially aligned along the electric field (L_i = 0) and using 2 μm of electrode spacing. For the sake of simplicity, the distance between the NW and the electrodes is calculated along the sample normal direction (z axis) such as represented in the left vertical axis of figure 7.42. This figure represents the F_{DEP} calculated amplitude values using constant magnitude arrows to represent its direction; the figure also includes a color scale to represent the F_{DEP} magnitude, which is very sensitive to the distance. The exerted dielectrophoretic force, as seen in this figure, is pointing to the electrode gap, allowing for NW trapping.

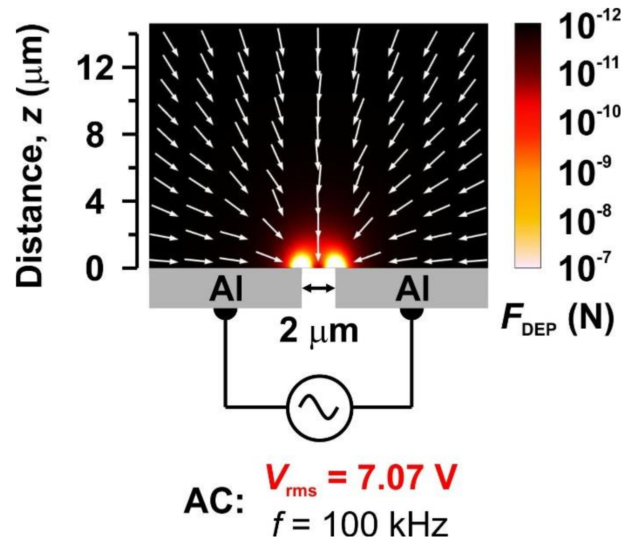

Figure 7.42. Simulation of F_{DEP} field as a function of distance.

The F_{DEP} dependence on the distance (z) along a vertical line starting on one electrode corner (see figure 7.42), is plotted in figure 7.43 showing a fast decrease of F_{DEP} as z increases, following a negative power law (z^{-3}) for distance values larger than the electrode separation. Pethig et al. [36] estimated that producing a significant F_{DEP} requires $\nabla|E|^2$ values in the range of 10^{-5} V^2 μm^{-3} or even larger. In our calculations$\nabla|E|^2$ produces F_{DEP} in the pN range, while the above threshold value is reached at 30 μm indicating NWs could be trapped at distances up to 30 μm.

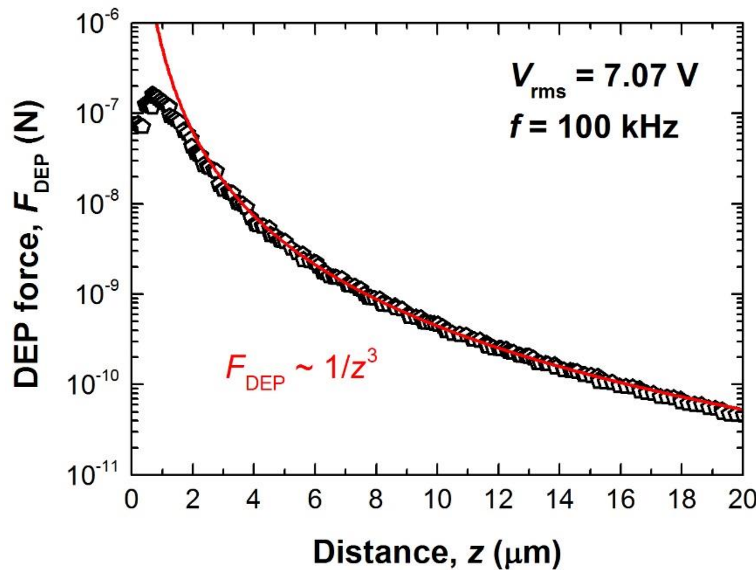

Figure 7.43. F_{DEP} exerted on a GaAs NW as a function of its distance to the electrodes gap.

7.3.2. GaAs NW Photoconductivity

As DEP technique allowed us to assemble a single GaAs NW between a pair of Al electrodes under specific conditions, the photoconductivity of a GaAs NW could be characterized by measuring the *I*/*V* characteristic curve both under dark conditions and under VIS illumination.

As explained in section 7.3.1, two different NW suspensions were prepared, consisting of GaAs NWs with and without a Ga droplet on top of the NW tip. A 4 μl droplet extracted from each NW suspension was deposited on two different glass substrates with previously defined Al electrodes. DEP processes were carried for 30 s using V_{rms} = 7.07 V and f = 100 kHz; time was limited only because of ethanol solvent evaporation.

GaAs NW without Ga Droplet

The layer schematic and a SEM image of the structure consisting of a GaAs NW without droplet connecting two Al electrodes have been previously shown in figure 7.37. As observed in that figure, the NW exhibits tapering along its stem, with a larger diameter at the base than at the tip. All the devices based on NWs without droplet show asymmetric NW overlapping regions at each electrode. DEP assembling mechanism should be the main responsible for this phenomenon.

I/*V* characteristic curve of the GaAs NW contacting both electrodes was measured in a Karl Suss probe station under dark conditions. Figure 7.44(a) shows measured $|I_{dark}|$ in the voltage range between -2 and 2 V, observing only a noisy result in the 0.1-1 pA range. The same result is obtained under the microscope lamp illumination. This figure also includes the current density (J) calculated by assuming that the NW in figure 7.37 has an average diameter of 200 nm. The low current level exhibited by this NW is attributed to the existence of two SB contacts in opposition, as indicated in figure 7.44(b) [37]. That figure also shows a series resistance associated to the GaAs NW and defined here as R_{NW}.

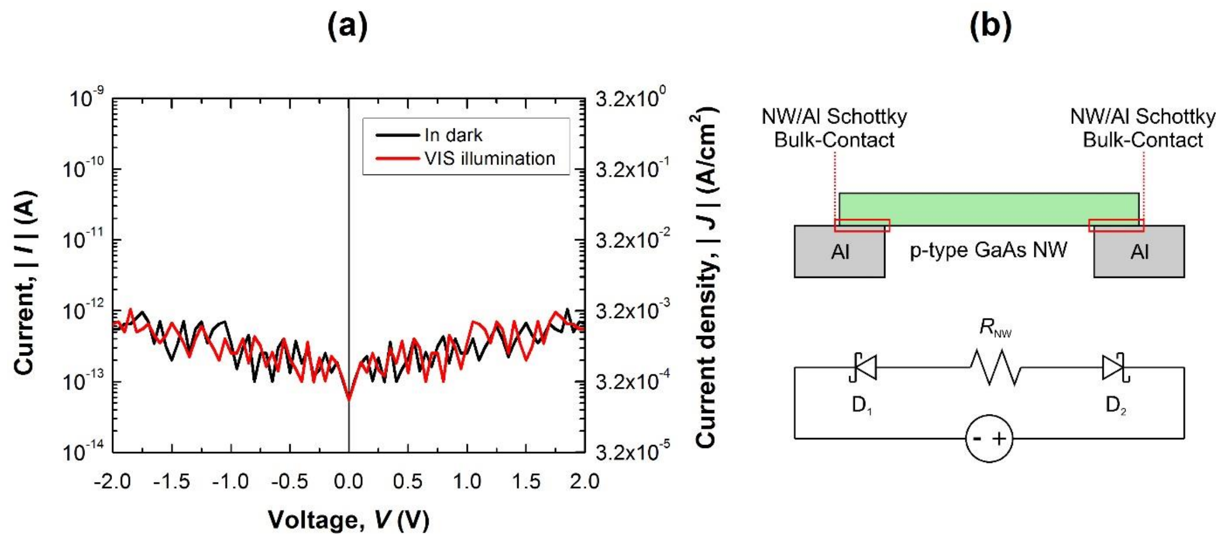

Figure 7.44. (a) *I*/*V* characteristics of a single GaAs NW shown in figure 7.37, and (b) its equivalent circuit.

GaAs NW with Ga Droplet

Figure 7.45(a) shows a SEM image of a GaAs NW with L_{NW} = 4.7 µm and d_{NW} = 200 nm integrated between a pair of AZO electrodes. Figure 7.45(b) and (c) present magnification views of the contact formed with electrodes at NW ends; as clearly observed in figure 7.45(b), one of the NW ends has traces of a Ga droplet, whereas the other end is freely suspended over the electrode (figure 7.45(c)).

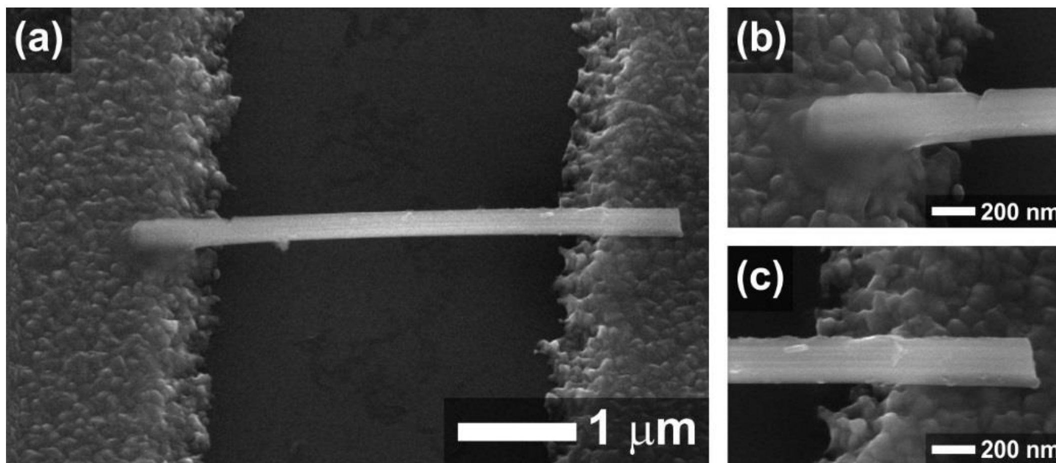

Figure 7.45. (a) SEM image of a GaAs NW assembled between a pair of electrodes. (b,c) Magnification views of contacts formed between the NW ends and the electrodes.

I/*V* characteristic curves of the structure shown in figure 7.45 were also measured in the voltage range between -2 and 2 V, under both, dark conditions and VIS illumination, being plotted in figure 7.46(a). This GaAs NW exhibits a non-symmetrical *I*/*V* curve, with a diode-like aspect. $|I_{dark}|$ reaches values up to 2 nA for a bias of +2 V, while $|I_{dark}|$ decreases by three orders of magnitudes when voltage is reversed. The series resistance of the NW (R_{NW}) could be responsible for the current saturation level in forward bias region.

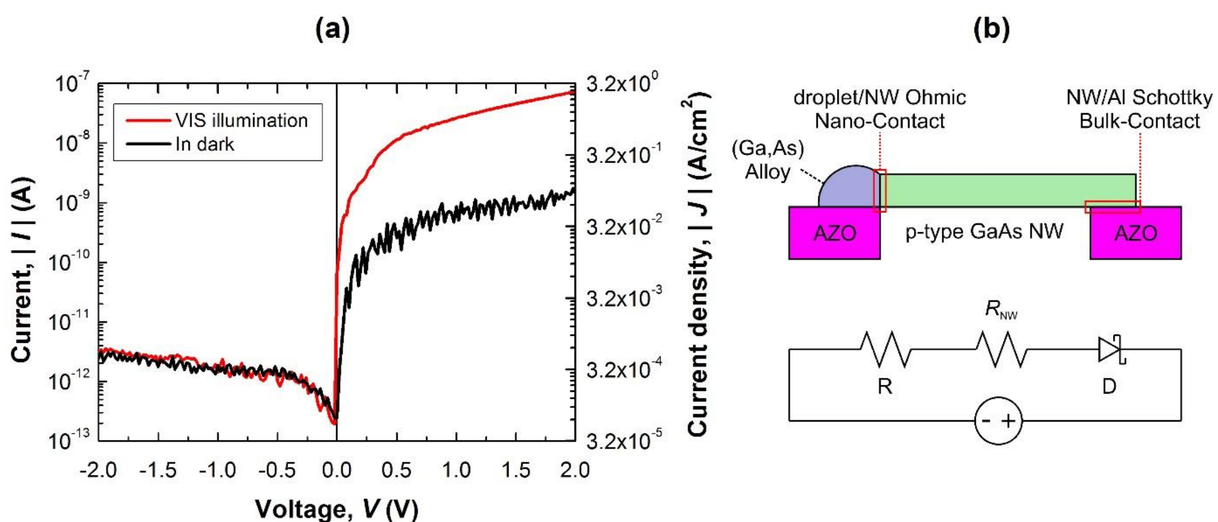

Figure 7.46. (a) *I*/*V* characteristics of the single GaAs NW shown in figure 7.45, and (b) its equivalent circuit.

This asymmetric conductance of this device could be explained due to the formation of an ohmic contact between the droplet and the NW (resistance, R) and a SB contact between the NW and the electrode (diode, D), such as represented by the equivalent circuit drawn in figure 7.46(b).

The growth of GaAs NWs by Ga-assisted VLS mechanism forms a built-in contact between the (Ga,As) alloy droplet and the NW, which might minimize interface state density [38]. During the VLS growth, precursor atoms diffuse through the Ga droplet, inducing NW formation at the droplet/NW interface; therefore, chemical bonds are formed in this abrupt junction, yielding a nanoscale metal-semiconductor contact, which is different than "bulk-contacts" formed after growth between deposited metal electrodes and NWs. The formation of these nanoscale contacts might alleviate the well-known Fermi-level pinning to achieve the effective formation of an intimate ohmic contact at one of the NW ends. The other NW end forms a bulk-contact with the Al electrode, behaving as a Schottky junction.

I/V characteristics present a high sensitivity to the VIS illumination even for the microscope lamp illumination, showing near two-orders of magnitude increase when comparing to the I_{dark} level (figure 7.46(a)). The most significant difference between I/V curves under dark and illumination is observed in the high current or forward region on the right side of the plot, while the reverse saturation current on the left side seems to be very similar under both illumination conditions, indicating a low generated photocurrent. The above observed difference on the dark and illuminated I/V characteristics could be related only to the R_{NW}, which should decrease under illumination, allowing for large currents. The reduction in R_{NW} could then be explained as due to carrier photo-generation in the NW bulk, reducing the space charge region (SCR), thus increasing the conductive section and the NW conductance.

On the other hand, the low or near-null generated photocurrent could be related to the large surface-to-volume ratio of the NW and to the large density of surface states present in non-passivated GaAs surface.

Therefore, the existence of a Ga droplet on top of the GaAs NWs could be a cost-effective and easy of development alternative to other techniques commonly used to fabricate SB based PDs, such as FIB.

CONCLUSIONS

GaAs NWs have been grown by Ga-assisted CBE on Si(111) substrates, and characterized by SEM, RHEED, and TEM. A novel procedure has been developed in order to prepare Si(111) surface oxide, enabling the NW growth in CBE. During the preparation of the Si(111) substrates, it was found that after etching of the native SiO_x, substrate should be exposed to the ambient air for around 5 min in order to grow an oxide with thickness of 0.5 nm. SEM study shows clear evidences that confirm the NW growth is catalyzed by Ga droplets formed after the effective cracking of the TEGa molecules on the prepared surface.

The method to grow GaAs NWs consists in a pre-deposition of TEGa at T_s = 580 ºC, followed by a stabilization step and finally the NW growth takes place when fluxes of TBAs and TEGa are turned simultaneously on. The morphological analysis of the so obtained NWs for different growth times shows typical incubations times ranging between 30-210 s depending on the stabilization time. Furthermore, the stabilization time is demonstrated to be directly related to the initial Ga droplet size which will affect not only the NW growth rate but also the resultant NW diameter. Each growth step was monitored by RHEED, enabling to confirm the formation of pure ZB phase along the whole NW structure. The growth conditions of this method have been optimized showing best results in terms of NW aspect ratio and growth rate for T_s = 580 ºC and V/III ratio = 0.8, and using 7.5 ML of Ga during the pre-deposition step and 90 s of stabilization time. Furthermore, it was found that in Ga-assisted CBE, NW growth is almost interrupted for growth times larger than 1 h because of the formation of a polycrystalline GaAs layer over the Si substrate which reduces the effective incorporation of Ga and As to the NW. In order to overcome this drawback, an alternative growth procedure has been developed to prevent the formation of the above GaAs surface structures; this procedure includes a two-step growth, inserting a self-aligned native Si oxide layer after the first growth step. Resulting NWs have a better aspect ratio and longer NW lengths with respect to those NWs grown through a one-step growth. In addition, the parasitic growth of nanocrystals and nanotraces is demonstrated to be strongly reduced under the two-step growth conditions, which is a promising procedure for device fabrication.

Crystalline structure of GaAs NWs has been thoroughly analyzed by TEM. A ZB structure free of twins was obtained along the NW stem, even at the Ga-droplet/GaAs-NW transition region (except for some stacking defects due to a fast cooling after growth interruption) under specific growth conditions. Different VLS growth modes have been experimentally demonstrated by TEM, showing that Ga-droplet partially wet NW sidewalls during the growth, which was considered to be responsible for the crystal quality improvement of the resultant NWs. In addition, Raman measurements performed at different backscattering configurations did not show any peak at the characteristic frequencies related to phonons in the WZ structure, confirming the TEM observations.

Raman spectroscopy measurements of GaAs NWs grown in this work, also evidenced the presence of SO phonon mode located in between TO and LO modes, whose frequency depends either on the NW diameter or on the oxide coverage. The frequencies of SO mode shifted downwards as NW diameter decreased and/or NW oxide thickness increased. Wavevector responsible for the SO activation in NWs was

calculated in the case of ambient air, showing length scales between 0.5 and 0.8 μm, which are similar to the NW length, and indicating the high uniformity of the cross section size during the NW growth. In addition, LO shape was analyzed by the PCM, allowing to obtain the value for the confinement coefficient of GaAs NWs, taking values around $\alpha = 23\ \text{nm}^{-1}$, characteristic for this material.

VIS PDs based on single GaAs NWs have been also fabricated by DEP. DEP conditions were optimized in order to trap a single GaAs NW between conductive electrodes, allowing us to characterize its *I*/*V* characteristics. Results show currents in the nA range and photoresponse to VIS illumination under forward bias, whereas reversed bias presents near-null currents (< pA) under both dark conditions and VIS illumination; this behaviour is attributed to the formation of a SB contact between NW-base/electrode, whereas the NW-tip/electrode contact is expected to be ohmic. The latter is mainly due to chemical bonds formed between the Ga droplet and the NW during growth which improve one of the electrical contact of the device. Changes in SCR of the NW govern the current levels observed under different illumination conditions, and allow to obtain I_{photo} two orders of magnitudes higher than I_{dark}.

REFERENCES

[1] C. García Núñez, A. Braña, J. Pau, D. Ghita, B. García, G. Shen, *et al.*, "Pure zincblende GaAs nanowires grown by Ga-assisted chemical beam epitaxy," *Journal of crystal growth,* vol. 372, pp. 205-212, 2013.

[2] C. García Núñez, A. F. Braña, N. López, and B. J. García, "GaAs Nanowires Grown by Ga-assisted Chemical Beam Epitaxy: Substrate Preparation and Growth Kinetics," *Journal of Crystal Growth (submitted),* 2015.

[3] C. García Núñez, A. F. Braña, N. López, and B. J. García, "On the growth mechanisms of GaAs nanowires by Ga-assisted chemical beam epitaxy," *IEEExplore (submitted),* 2015.

[4] C. García Núñez, A. F. Braña, J. L. Pau, D. Ghita, B. J. García, G. Shen, *et al.*, "Surface optical phonons in GaAs nanowires grown by Ga-assisted chemical beam epitaxy," *Journal of Applied Physics,* vol. 115, p. 034307, 2014.

[5] C. García Núñez, A. F. Braña, N. López, J. L. Pau, and B. J. García, "Integration of GaAs Nanowires on Electronic Devices by Dielectrophoresis," *18th European Molecular Beam Epitaxy Workshop,* 2015.

[6] C. Colombo, D. Spirkoska, M. Frimmer, G. Abstreiter, and A. F. i Morral, "Ga-assisted catalyst-free growth mechanism of GaAs nanowires by molecular beam epitaxy," *Physical Review B,* vol. 77, p. 155326, 2008.

[7] F. Matteini, G. Tutuncuoglu, D. Rüffer, E. Alarcon-Llado, and A. Morral, "Untangling the role of oxide in Ga-assisted growth of GaAs nanowires on Si substrates," *arXiv preprint arXiv:1307.6113,* 2013.

[8] D. Ghita, J. Plaza, M. Sánchez, A. Climent-Font, and B. García, "Ga and In incorporation rates in Ga 1− x In x As growth by chemical beam epitaxy," *Journal of Crystal Growth,* vol. 314, pp. 48-52, 2011.

[9] D. Wildt, J. Castano, J. Piqueras, and C. Pastor, "Chemical beam epitaxial growth of GaAs 1-x P x on GaAs (100) substrates," *Journal of Vacuum Science & Technology B: Microelectronics and Nanometer Structures,* vol. 16, pp. 1804-1807, 1998.

[10] P. Pernas, E. Ruíz, J. Garrido, J. Castaño, and B. García, "Channel waveguides grown by selective area chemical beam epitaxy," *Optical Materials,* vol. 17, pp. 259-262, 2001.

[11] G. E. Cirlin, V. G. Dubrovskii, I. P. Soshnikov, N. V. Sibirev, Y. B. Samsonenko, A. D. Bouravleuv, *et al.*, "Critical diameters and temperature domains for MBE growth of III–V nanowires on lattice mismatched substrates," *physica status solidi (RRL) – Rapid Research Letters,* vol. 3, pp. 112-114, 2009.

[12] L. J. Schowalter, K. Yang, and T. Thundat, "Atomic step organization in homoepitaxial growth on GaAs (111) B substrates," *Journal of Vacuum Science & Technology B,* vol. 12, pp. 2579-2583, 1994.

[13] B. Garcia, C. Fontaine, and A. Muñoz-Yagüe, "Molecular beam epitaxial growth and optical characterization of GaAs/AlxGa1− xAs quantum wells on nominally oriented (111) B GaAs substrates," *Applied physics letters,* vol. 63, pp. 2691-2693, 1993.

[14] G. Cirlin, V. Dubrovskii, Y. B. Samsonenko, A. Bouravleuv, K. Durose, Y. Y. Proskuryakov*, et al.*, "Self-catalyzed, pure zincblende GaAs nanowires grown on Si (111) by molecular beam epitaxy," *Physical Review B,* vol. 82, p. 035302, 2010.

[15] I. Zardo, S. Conesa-Boj, F. Peiro, J. Morante, J. Arbiol, E. Uccelli*, et al.*, "Raman spectroscopy of wurtzite and zinc-blende GaAs nanowires: polarization dependence, selection rules, and strain effects," *Physical Review B,* vol. 80, p. 245324, 2009.

[16] S. Breuer, M. Hilse, A. Trampert, L. Geelhaar, and H. Riechert, "Vapor-liquid-solid nucleation of GaAs on Si (111): Growth evolution from traces to nanowires," *Physical Review B,* vol. 82, p. 075406, 2010.

[17] D. Spirkoska, J. Arbiol, A. Gustafsson, S. Conesa-Boj, F. Glas, I. Zardo*, et al.*, "Structural and optical properties of high quality zinc-blende/wurtzite GaAs nanowire heterostructures," *Physical Review B,* vol. 80, p. 245325, 2009.

[18] S. Piscanec, M. Cantoro, A. Ferrari, J. Zapien, Y. Lifshitz, S. Lee*, et al.*, "Raman spectroscopy of silicon nanowires," *Physical Review B,* vol. 68, p. 241312, 2003.

[19] V. Dubrovskii, G. Cirlin, N. Sibirev, F. Jabeen, J. Harmand, and P. Werner, "New mode of vapor− liquid− solid nanowire growth," *Nano letters,* vol. 11, pp. 1247-1253, 2011.

[20] D. Spirkoska, G. Abstreiter, and A. F. i Morral, "Size and environment dependence of surface phonon modes of gallium arsenide nanowires as measured by Raman spectroscopy," *Nanotechnology,* vol. 19, p. 435704, 2008.

[21] K. Adu, H. Gutierrez, U. Kim, G. Sumanasekera, and P. Eklund, "Confined phonons in Si nanowires," *Nano letters,* vol. 5, pp. 409-414, 2005.

[22] K. Adu, Q. Xiong, H. Gutierrez, G. Chen, and P. Eklund, "Raman scattering as a probe of phonon confinement and surface optical modes in semiconducting nanowires," *Applied Physics A,* vol. 85, pp. 287-297, 2006.

[23] K. Tiong, P. Amirtharaj, F. Pollak, and D. Aspnes, "Effects of As+ ion implantation on the Raman spectra of GaAs:‘‘Spatial correlation’’interpretation," *Applied Physics Letters,* vol. 44, pp. 122-124, 1984.

[24] I. Campbell and P. M. Fauchet, "The effects of microcrystal size and shape on the one phonon Raman spectra of crystalline semiconductors," *Solid State Communications,* vol. 58, pp. 739-741, 1986.

[25] N. Begum, M. Piccin, F. Jabeen, G. Bais, S. Rubini, F. Martelli*, et al.*, "Structural characterization of GaAs and InAs nanowires by means of Raman spectroscopy," *Journal of Applied Physics,* vol. 104, p. 104311, 2008.

[26] T. Li, L. Gao, W. Lei, L. Guo, T. Yang, Y. Chen, *et al.*, "Raman study on zinc-blende single InAs nanowire grown on Si (111) substrate," *Nanoscale research letters,* vol. 8, pp. 1-7, 2013.

[27] H. Richter, Z. Wang, and L. Ley, "The one phonon Raman spectrum in microcrystalline silicon," *Solid State Communications,* vol. 39, pp. 625-629, 1981.

[28] R. Gupta, Q. Xiong, G. Mahan, and P. Eklund, "Surface optical phonons in gallium phosphide nanowires," *Nano Letters,* vol. 3, pp. 1745-1750, 2003.

[29] C. Kittel, "Introduction to Solid State Physics," *Wiley (New York) 7th ed., Chapt. 4,* 2003.

[30] K. Adu, H. Gutiérrez, U. Kim, and P. Eklund, "Inhomogeneous laser heating and phonon confinement in silicon nanowires: a micro-Raman scattering study," *Physical Review B,* vol. 73, p. 155333, 2006.

[31] S. Sahoo, S. Dhara, A. Arora, R. Krishnan, P. Chandramohan, and M. Srinivasan, "Raman scattering from surface optical phonon in diameter modulated AlN nanotips," *Applied Physics Letters,* vol. 96, pp. 103113-103113-3, 2010.

[32] R. Fuchs and K. Kliewer, "Optical modes of vibration in an ionic crystal slab," *Physical Review,* vol. 140, p. A2076, 1965.

[33] S. E. Wu, S. Dhara, T. H. Hsueh, Y. F. Lai, C. Y. Wang, and C. P. Liu, "Surface optical phonon modes in ternary aligned crystalline InGaN/GaN multi-quantum-well nanopillar arrays," *Journal of Raman Spectroscopy,* vol. 40, pp. 2044-2049, 2009.

[34] P. Sahoo, S. Dhara, S. Dash, A. Tyagi, B. Raj, C. Das, *et al.*, "Surface optical modes in GaN nanowires," *International Journal of Nanotechnology,* vol. 7, pp. 823-832, 2010.

[35] S. Sahoo, M. Hu, C. Hsu, C. Wu, K. Chen, L. Chen, *et al.*, "Surface optical Raman modes in InN nanostructures," *Applied Physics Letters,* vol. 93, p. 233116, 2008.

[36] R. Pethig and G. H. Markx, "Applications of dielectrophoresis in biotechnology," *Trends in biotechnology,* vol. 15, pp. 426-432, 1997.

[37] E. Ramayya, D. Vasileska, S. Goodnick, and I. Knezevic, "Electron transport in silicon nanowires: The role of acoustic phonon confinement and surface roughness scattering," *Journal of Applied Physics,* vol. 104, p. 063711, 2008.

[38] N. Han, F. Wang, S. Yip, J. J. Hou, F. Xiu, X. Shi, *et al.*, "GaAs nanowire Schottky barrier photovoltaics utilizing Au–Ga alloy catalytic tips," *Applied Physics Letters,* vol. 101, p. 013105, 2012.

[39] F. Léonard and A. A. Talin, "Electrical contacts to one-and two-dimensional nanomaterials," *Nature nanotechnology,* vol. 6, pp. 773-783, 2011.

8. Conclusions and Future Work

8.1. Conclusions

This section summarizes the main results obtained in this thesis work about the synthesis and characterization of Zn_3N_2 thin films, ZnO NWs, and GaAs NWs, and their application in electronic devices.

8.1.1. Zn_3N_2 Thin Films

Properties of Zn_3N_2 layers grown by rf-magnetron sputtering have been analyzed as a function of growth conditions. The study shows that Zn_3N_2 properties are strongly dependent on the growth rate and the substrate temperature.

The growth of Zn_3N_2 layers at high growth rates ($r_g > 50$ nm/min) by using high rf-powers (~ 200 W) was observed to prevent the unintentional incorporation of O into the Zn_3N_2 sublattice; in that respect, IBA measurements confirm the growth of high purity and stoichiometric Zn_3N_2 layers. SEM and XRD show that resulting layers are polycrystalline and have more oriented grains as T_s decreases. Optical characterization shows a direct band gap semiconductor behaviour, and E_g values between 1.25 and 1.46 eV, depending on T_s; in this regard, E_g shifts to higher energies as T_s decreases mainly because a better grain orientation of analyzed nitride layers. These structural changes with T_s also affect the resistivity of layers, showing low values around 10^{-3} $\Omega \cdot$cm at $T_s = 423$ K, which are one of the lowest values ever reported in the literature for this material.

The growth of Zn_3N_2 at low growth rates (r_g ~ 4.4 nm/min) results in layers with less defined grain boundaries which benefits the electrical transport between grains, and then enhances the electron mobility up to reaching values around 100 $cm^2/V\cdot s$, and also yields carrier concentrations of 3.2×10^{18} cm^{-3}.

The metastability of pure and stoichiometric Zn_3N_2 layers stored in air ambient conditions has been analyzed in depth by different techniques, including IBA, SE, and spectrophotometry. The study reveals the surface oxidation of nitride layers, showing O-rich oxide atop the nitride layer, whose stoichiometry is determined to be close to that of ZnO. The thickness of that ZnO layer increases without saturation over time; the oxidation of nitride layers has been estimated by SE, resulting in 36 and 20 nm/day for layers grown at T_s of 298 and 473 K, respectively; accordingly, nitride layers grown at higher T_s show better stability in ambient air. On the other hand, it was demonstrated that the oxidation of Zn_3N_2 can be prevented by growing a ZnO layer atop of that.

The effects of both, surface oxidation and O incorporation during growth, on the optical properties of Zn_3N_2 have been taken into account in order to estimate magnitudes such as optical constants (n and k) and E_g. In this regard, optical constants of pure Zn_3N_2 layers grown at high growth rates (r_g > 50 nm/min) have been measured by SE right after their deposition in order to prevent surface oxidation; results show n = 2.8−2.0 and k = 0.6−1.0 for photon energies between 1.5 and 4.5 eV. On the other hand, the effect produced by the formation of ZnO on the nitride surface has also observed to shift the transmission edge towards higher energies over time. The transient region formed between both layers (ZnO and Zn_3N_2) could be composed by a ternary compositional gradient layer ($Zn_xN_yO_z$) that might widen the E_g and then shifts the transmission edge.

Zn_3N_2 layers have been patterned using electrical discharge lithography through a micrometric tip. The study reveals that the areas scanned at low voltages present a lower resistivity due to the removal of the native oxide; this procedure would allow to determine true optoelectronic properties of Zn_3N_2 due to the removal of the surface oxide. At larger voltages, arc discharge produces deep trenches with high electrical resistance properties. That treatment also induces strong compositional changes at the central part of the scan, yielding ZnO:N submicron structures from the Zn_3N_2 crystal grains. The dimensions, surface density and chemical composition of resulting crystals could be used as seeds to grow ZnO NWs.

Zn_3N_2 has been also used as active layer in bottom-gate TFTs and photo-transistors. As mentioned, a ZnO capping layer was deposited on top of the nitride surface in order to prevent its oxidation, improving the device stability in air ambient conditions. Bottom-gate TFTs present transistor characteristics in n-channel enhancement-mode, and without the need of an annealing process. In addition, the drain current presents sensitivity to the IR/VIS light illumination, showing increasing photosensitivity with V_{GS}. On the other hand, photo-transistors have been fully fabricated by photolithography. The growth of Zn_3N_2 channel under optimized conditions, as well as the reduction of the device dimensions contribute to enhance transistor photoresponse, presenting R_{photo} values up to 3.5×10^6 A/W.

8.1.2. ZnO NWs

ZnO NWs have been synthesized on Si(100) substrates by CVT in an oxidizing ambient at temperatures about 700–900 ºC. The use of a seed layer consisting of a Zn thin (~ 10 nm) film deposited on the Si(100) substrate prior to the CVT process, was demonstrated to assist the NW growth along the substrate normal direction. Resulting NWs show aspect ratios about 10–15, and diameters between 90 and 870 nm. On the other hand, CVT processes carried out on Si(100) substrates without Zn seed layer result in a mesh of ZnO TPs consisting of hexagonal-shape crystals from which NWs grow in lengths larger than 10 μm; the diameter of the NWs from these TPs varies between 100 and 300 nm, presenting aspect ratios larger than 100 in many cases.

ZnO NWs have been used for the fabrication of UV PDs. The long length of these NWs (> 10 μm) simplifies their assembly between a pair of electrodes with micrometric inter-electrode distances. AZO electrodes have been introduced and tested, showing high mechanical strength and adherence to the oxidized Si substrates. The assembly of the NWs between AZO electrodes was successfully carried out by positive DEP. DEP parameters such as voltage amplitude and frequency have been studied for the deposition of ZnO NWs, analyzing the effect of both f_{CM} or ∇E^2 on the NW alignment efficiency. The study shows that F_{DEP} exerted on the NWs increases with V_{rms} and decreases at high f; showing the highest alignment efficiencies at V_{rms} = 7 V and f = 100 kHz. AZO electrodes with a specific geometry have been used to promote the assembly of a single NW using described DEP conditions. Since a single NW connects AZO electrodes, NW ends were covered with a 100-nm thick Al film in order to reduce the noise of I/V characteristics and to improve the performance reproducibility. Resulting device constitutes an original structure which combines the use of AZO and Al electrodes to integrate single ZnO NWs in the current Si based CMOS technology.

The optoelectronic properties of single ZnO NW photoconductors with different radii have been studied. In dark conditions, a critical r_{NW} of 65 nm is found to nearly deplete the NW conductive volume. In nearly depleted NWs (r_{NW} < 65 nm), the conduction mechanism is strongly influenced by the surface states and their carrier emission and capture times. On the other hand, this conduction mechanism is a minor contribution to the drift through the conducting core in thicker NWs (r_{NW} >> 65 nm), for which the I/V characteristics are only limited by the cross-sectional conducting area.

Under UV illumination (λ < 370 nm) the conduction mechanism through the NW resembles the conduction in thicker NWs and differs from the surface generation-recombination mechanism described in darkness for the thinnest NWs. The main consequence is the strong difference between I_{light} and I_{dark}. Increasing R_{photo} and G_{photo} are observed as the r_{NW} reduces, reaching values near 10^8 A/W and 10^8, respectively in a PD based on a NW with a r_{NW} of 50 nm. In addition, it was found that the cut-off wavelength depends on r_{NW}, presenting a clear blue-shift as r_{NW} decreases. The origin of this phenomenon is still not clear and needs to be further investigated.

Transient photoresponse studies show that nearly depleted NWs (r_{NW} = 50 nm) have long rise times mainly because the generation-recombination mechanism limits the response speed. This mechanism arises in thicker NWs (r_{NW} = 260 nm) after a fast component, indicating that these NWs have a neutral region in the core that provides a fast channel for carrier flow after emission from the surface. During the relaxation process, thinner NWs exhibit faster decay times than those measured in thicker NWs; it is likely that the reduction of the adsorbed O density in nearly depleted NWs could enhance the decay time after UV illumination.

Electrical and surface properties of ZnO NWs have been analyzed after different surface treatments, involving hydroxylation and silanization with APDEMS. The study was carried out by different techniques, including contact angle measurements, CPD, SPV, and XPS. Silanization makes ZnO NW surface hydrophobic with respect to the hydrophilic properties shown in the hydroxylated surfaces. The XPS spectra proved the attachment of the APDEMS molecules through the presence of both peaks N 1s and C 1s, belonging to amine and hydrocarbon groups. The spectra also show a binding energy red-shift of both peaks Zn 2p3/2 (640 meV) and O 1s (675 meV) compared to those of the hydroxylated ZnO, evidencing a change in the surface dipole formed atop ZnO surface. This change of the surface dipole also produces a reduction of the ZnO work function from 5.02 eV (after hydroxylation) to 4.11 eV (after silanization) as determined by CPD. On the other hand, comparing the width of the surface BB obtained from SPV measurements with r_{NW}, one can conclude that the hydroxylated NWs are nearly depleted. The *I*/*V* characteristics of a single NW have been analyzed after each surface treatment. The silanized NW shows larger currents than the hydroxylated NW due to the enlargement of the conductive volume. Therefore, one can conclude that current levels presented in these NWs are also governed by the SCR width as occurs in NWs with different r_{NW}. Finally, it is observed that the NW silanization improves the linear characteristics of the contact formed between the NW and the Al electrode mainly due to the increase of the total free charge in the NW, which can benefit the output parameters of ion-gated FETs.

8.1.3. GaAs NWs

GaAs NWs have been synthesized by Ga-assisted CBE on oxidized Si(111) substrates. SEM study shows clear evidences that confirm the NW growth is catalyzed by Ga droplets formed after the effective cracking of the TEGa molecules on the prepared surface oxide; in this regard, the preparation of substrate surface is critical to allow the formation of Ga droplets. We have developed a novel substrate preparation procedure which consists in the etching of the substrate native oxide using a HF:H_2O buffer solution followed by an air exposure step for 5 min, promoting the formation of a 0.5-nm thick SiO_x. This procedure leads to the formation of a random distribution of pinholes along the oxide surface, which are essential for the formation of Ga nanodroplets.

Prior to the GaAs NW growth, Ga droplets are pre-deposited at T_s = 580 ºC and later stabilized. Since both TBAs and TEGa flows are turned on the NW growth takes place. Growth parameters, including

T_s, V/III ratio, Ga pre-deposition and stabilization times have been optimized in order to obtain NWs with high crystal quality and aspect ratio. Best results have been observed for T_s = 580 ºC and V/III ratio = 0.8 (pre-depositing 7.5 Ga monolayers and stabilizing for 90 s). The formation of a polycrystalline GaAs layer on top of the Si substrate surface during the NW growth is the main responsible for the reduction of Ga and As effective incorporation to the NW, then limiting the maximum NW length (L_{NW} ~ 3.5 µm). In order to overcome this issue, we have developed a two-step growth to preserve the substrate surface free of parasitic GaAs structures. Accordingly, GaAs NWs are grown in two steps, called pre-growth and re-growth, introducing an air exposure step for 1 h between both growth steps. Comparing the observed morphology of resulting NWs grown under one- and two-step conditions, the latter show a clear improvement of the NW aspect ratio, a higher growth rate, and a substrate surface free of parasitic structures. Two-step growth allows to grow GaAs NWs with lengths up to 5 µm which is nearly a 40% higher than the maximum length obtained in one-step growth.

GaAs NW crystal structure was analyzed by RHEED and TEM, showing pure ZB structure free of any WZ evidence. From HRTEM images one can observe that Ga droplet is partially wetting NW sidewalls; this fact could be responsible for the lack of polytypisms, i.e. mixture of ZB and WZ phases, along the NW structure. Raman spectroscopy measurements confirm the absence of peaks at characteristic frequencies related to phonons in WZ structure. In addition, the analysis of LO peak shape using PCM allows us to determine a confinement coefficient of α = 23 nm^{-1} which is characteristic of GaAs. Surface properties, including roughness and oxide were analyzed through the study of SO Raman frequency shift, evidencing the high uniformity of the cross-sectional size obtained during the GaAs NW growth.

Finally, VIS PDs based on single GaAs NWs have been fabricated by DEP. As in the ZnO NW case, DEP conditions were optimized in order to trap a single GaAs NW between conductive electrodes, allowing us to characterize its *I*/*V* characteristic. Two different types of GaAs NWs have been integrated between conductive electrodes, comprising NWs with and without a Ga droplet. Devices based on a NW without droplet present noisy currents about 1 pA (at 2 V) in dark and under VIS illumination; this result could be explained due to the formation of two SB contacts, at both NW ends, in opposition which hinders the electrical current. On the other hand, devices based on a NW with droplet exhibit asymmetrical *I*/*V* curves, showing currents about 2 pA and 2 nA at -2 and +2 V, respectively. At reverse voltages, the device is not sensitive to the VIS light, while under forward voltages the device presents currents around 1 order of magnitude higher than those measured in dark conditions. This behaviour could be attributed to the formation of a SB contact between NW-base/electrode, and an ohmic contact between the Ga-droplet/electrode. The contact resistance associated to Ga-droplet/NW is expected to be very low due to the formation of chemical bonds during the NW growth.

8.2. Future Work

This section includes possible future research lines related to the work presented here. Furthermore, new ideas are proposed in order to guide new researchers to proceed with the investigations around the advanced materials analyzed in this thesis work, giving continuity to efforts already done. Therefore, this section presents promising future works around Zn_3N_2 thin films (section 8.2.1), ZnO NWs (section 8.2.2) and GaAs NWs (section 8.2.3), including the optimization of their properties, and interesting applications. Finally, section 8.2.4 proposes the fabrication of advanced optoelectronic devices taking advantage of DEP technique.

8.2.1. Zn_3N_2 Thin Films

Channel mobility of a TFT is one of the most important electrical parameters, evaluating the semiconductor compound performance as channel layer. The high mobility of Zn_3N_2 thin films grown in this work was obtained at low growth rates and without annealing treatments; resulting layers presented less defined grain boundaries which could improve the electrical transport between grains. This property makes Zn_3N_2 attractive for the development of high mobility TFTs. In this regard, the optimization of Zn_3N_2 TFT fabrication procedure is proposed as a promising way to obtain high field effect mobilities equaling or even improving mobility values obtained in existing TFTs, with potential applications in integrated circuits and active-matrix liquid-crystal displays.

Zn_3N_2 exhibited continuous oxidation rates about 20 and 36 nm/day which means that nitride thin films can be fully transformed into ZnO after a few days in an oxidizing ambient. The possibility to obtain p-type ZnO from the oxidation of Zn_3N_2, makes the latter attractive for the development of p-n ZnO homojunctions. In this regard, the use of homojunctions rather than heterojunctions could reduce the density of defects induced by the mismatch between lattice parameters at the heterojunction. This kind of technology could be integrated in solar cell applications. The excellent optical properties of the Zn_3N_2 thin films observed before, during, and after their total conversion in to ZnO, make this compound very attractive for the development of solar cells with a tunable absorption edge in the UV/VIS spectral range, depending on the nitride composition.

The high reactivity of Zn_3N_2 surface to O species contained in the ambient air, makes this compound very attractive for the development of gas sensors. Furthermore, surface functionalization of passivated Zn_3N_2, i.e. Zn_3N_2 with a capping layer of ZnO, is also an interesting research line that would allow to fabricate biosensors such as ion-gate FETs with different sensitivities to chemical agents and biomolecules.

8.2.2. ZnO NWs

ZnO NWs have been grown on Si substrates using a Zn seed layer to assist the NW growth along the substrate normal direction and at random positions. Since the NWs are randomly positioned, each NW will

have a different surrounding during growth, resulting in a variation in their properties that could subsequently affect device performance. The NW aspect ratio, position, and surface density can be further enhanced via pre-patterned substrates; in this regard, Zn seed layer can be prepared prior to the NW growth by lithographic methods in order to define well-ordered Zn island arrays. The Zn island height, diameter, and inter-island center spacing are key parameters for the optimization of the growth mechanism. Since the growth of well-ordered NW arrays is obtained, the fabrication of metal electrodes directly on this sample, i.e. without the manipulation of NWs, would prevent NW damage, and allows to a direct integration of these NWs with Si technology.

ZnO NW based UV PDs have been fabricated, exhibiting photoresponsivities about 10^7–10^8 A/W. The high photoresponsivity and photoconductive gain presented by these devices are mainly attributed to both the high surface-to-volume ratio and reduced dimensions of the conductive volume. In this work, single NW based PDs showed cut-off wavelengths between 364 and 385 nm depending on the NW diameter. The combination of ZnO with Mg and Cd allows to further extend the detection spectral range between 210 and 450 nm. The growth of ZnMgO and ZnCdO NWs is proposed to fabricate tunable PDs in that spectral range.

Sensitivity and response time of ZnO NW based UV PDs can be improved through different methods, comprising NW surface decoration with NPs, NW surface coverage with UV sensitive polymers, and the fabrication of SB contacts.

i) Since ZnO NWs are decorated with Au NPs, the formation of SB regions at the NP/NW interface might deplete, locally, surface charge carriers of the NW, lowering the dark current. On the other hand, the enhancement of photocurrent to dark current ratio and the reduction of the decay time with respect to bare ZnO NWs, are still not well understood and thus the effects of NPs on the excitation/relaxation mechanisms need to be further investigated.

ii) The use of polymers to cover ZnO NW surface is proposed as a suitable method to enhance NW photoresponse. The role of these polymers is similar than O_2 molecules in bare NWs, i.e. to trap free electrons from the NW bulk at the positively charged NW surface, resulting in lower dark currents. In the case of polymers with UV absorption, the generation of electron-hole pair during illumination might be assisted by absorption of photons in the polymer, contributing to enhance the resultant photocurrent. However, the role of ground and excited states in the polymer and their contribution to the charge transfer under UV illumination need to be clarified.

Although ZnO NWs are highly sensitive to the UV light, persistent current after illumination leads to long recovery times, limiting their application in commercial devices. The fabrication of PDs based on SB contacts formed between ZnO NW and metal electrodes is proposed as a promising way to speed up the recovery time of PDs while the sensitivity is preserved.

The surface functionalization of ZnO NWs has been demonstrated in this work. The possibility to form an organic SAM covering ZnO NW surface, as well as the high surface-to-volume ratio of NWs, make

these nanostructures suitable for the development of biosensors. An attractive feature of such chemically sensitive FETs is that binding of species to the surface of a functionalized NW can be monitored by a direct change of their electrical conductivity through the variation of the NW conductive volume. This property enhances the sensitivity of the biosensor and would allow approaching to a few molecule detection regime. On the other hand, surface functionalization of ZnO NW arrays directly grown on Si substrates is expected to further improve the sensitivity of the device, and therefore is also proposed as a promising structure for high performance biosensors.

Since the ZnO NW conductivity is mainly governed by the surface, the high surface-to-volume ratio of these structures makes ZnO NW based gas sensors highly sensitive to low concentrations of gas. In addition, these sensors present different behaviours in presence of reductive or oxidizing gases. Reductive gases, such as ethanol, react with oxygen adsorbed along the NW surface, releasing electrons to the NW bulk, and then increasing its conductivity. On the other hand, oxidizing gas, such as NO_2, increases the density of adsorbed O_2 along the NW by trapping free electrons from the NW bulk; the depletion region is extended from the surface, reducing the NW conductivity. The fabrication of gas sensors based on ZnO multi-NW junctions is proposed as a promising way to improve existing device performance.

8.2.3. GaAs NWs

The successful growth of GaAs NWs by Ga-assisted CBE is strongly influenced by the preparation of Si(111) substrate surface and the growth conditions (T_s, V/III flux ratio, etc.). In this regard, this work has shown a feasible and reproducible way to grow GaAs NWs, controlling their aspect ratio, and reducing the parasitic growth of GaAs nanocrystals. Using this knowledge, complex structures based on GaAs NWs are proposed to be grown by Ga-assisted CBE. To the best of our knowledge, structures proposed below have not been grown in CBE yet, which supposes a challenge that can open interesting research lines.

i) Well-ordered GaAs NW arrays on lithographed substrates. Nanoholes pre-defined on the surface oxide of Si(111) substrates are expected to limit the nucleation sites, reducing the density of parasitic growth. These substrates have been successfully used in MBE processes, showing a high control over the NW surface density via the hole-to-hole spacing and hole size. However, the use of these substrates in CBE is not straightforward due to the narrow range of oxide thickness which allows for the NWs growth.

ii) GaAs/AlGaAs core-shell NWs, where GaAs and AlGaAs are the core and the shell of the heterostructure, respectively. Bare GaAs NWs have a large density of surface states that can act as non-radiative carrier traps and increase the surface scattering, hindering NW electrical properties (low carrier mobility, …); the use of bare GaAs NWs in applications such as photoconductors or LEDs could hinder the resultant device performance. In order to overcome this issue, the conformal coating of the GaAs NWs with a semiconductor shell such as AlGaAs has been proposed in order to passivate the core surface, decreasing non-

radiative carrier traps. The enhancement of properties such as radiative emission and the photocurrent to dark current ratio, makes GaAs/AlGaAs core-shell NWs suitable for the development of high performance optoelectronic devices.

iii) The growth of GaP NWs by Ga-assisted CBE is expected to be straightforward by using similar conditions than those used to grow GaAs NWs. Furthermore, the growth of NWs based on the ternary compound $GaAs_{1-x}P_x$ allows to tune the E_g from 2.25 (pure GaP) to 1.43 eV (pure GaAs). This enables to change the band gap by controlling the composition of the material with promising applications in optoelectronics, including PDs at different spectral ranges. On the other hand, by introducing a GaAsP segment (direct band gap) into a GaP NW (indirect band gap), i.e. $GaP/GaAs_{1-x}P_x/GaP$, this segment could act as an optical active element, which could emit light at different wavelengths, depending on the segment composition. In this regard, inserting several segments with different compositions along the NW body, they can serve as multi-wavelength fluorescent labels, enabling the use of these structures in biomedical analysis systems.

iv) Dilute nitrides, such as $GaAs_{1-x}N_x$, show band gap energies well below 1.4 eV for N contents in the range $0<x<0.2$. The possibility to tune the band gap energy of this material allows to extend the light detection towards the IR range. The incorporation of N into the alloy could induce three-dimensional growth during GaAsN epitaxy rather than planar growth. Taking advantage of this favorable behaviour, Ga(As,N) NWs are proposed to be grown by CBE through Ga-assisted VLS process.

8.2.4. Integration of Nanostructures

During this work, DEP has been used to assemble both ZnO and GaAs NWs between electrodes in order to fabricate single NW based PDs sensitive to different spectral ranges. DEP conditions and electrode geometry were optimized in order to control the number of assembled NWs, having a degree of control over the trapped NW size. However, the use of this assembly technique can be further extended to fabricate complex structures.

i) The fabrication of electrode arrays would allow to a large-scale assemble of NWs in a single DEP procedure. The massive trapping of NWs at specific sites, i.e. connecting pairs of electrodes, enables the fabrication of large-area gas sensors, biosensors and photodetectors.

ii) The integration of different types of NWs, for example ZnO and GaAs NWs, in the same device is also an attractive idea that enables to fabricate PDs with high sensitivity in different spectral ranges. The use of hierarchical DEP to assemble both ZnO and GaAs NWs, one after each other, on pre-patterned electrodes is a suitable way to fabricate PDs sensitive to a wide spectral ranges from UV to NIR.

iii) The use of a specific electrode geometry would allow to make a contact between NWs of different types via DEP. A possible idea is to define four electrodes forming a cross-like structure. First, a NW can be assembled between one pair of counterpart-electrodes, then a second NW can be trapped between the other pair of electrodes. This hierarchical process would allow to make a vertical contact between two NWs of different types which is promising for the development of different nano-diodes, including LEDs, photodiodes…

iv) Since the integration of NWs between electrodes has been successfully carried out by DEP, we expect that the alignment of flakes consisting of bidimensional materials such as graphene, MoS_2, WS_2, $MoSe_2$, $MoTe_2$, $TaSe_2$, … should be straightforward. Furthermore, using similar hierarchical methods described above to integrate different types of NWs, the combination of both structures, i.e. NWs and bidimensional flakes, could improve optoelectronic properties of existing technology.

8.3. Conclusiones

En esta sección se resumen los resultados más relevantes obtenidos durante ésta tesis doctoral, relacionados con la síntesis y caracterización de láminas delgadas de Zn_3N_2, nanohilos de ZnO, y nanohilos de GaAs, así como su aplicación en dispositivos electrónicos.

8.3.1. Láminas Delgadas de Zn_3N_2

En este trabajo se han analizado las principales propiedades de capas de Zn_3N_2 crecidas mediante pulverización catódica de radio frecuencia. A partir de estos estudios se puede concluir que las propiedades del Zn_3N_2 dependen de las condiciones de depósito, principalmente del ritmo de crecimiento y temperatura del sustrato (T_s), usadas durante el crecimiento de las capas.

Las capas de Zn_3N_2 crecidas a ritmos de crecimiento altos (r_g > 50 nm/min), utilizado potencias de radio frecuencia altas (~ 200 W), tienen una incorporación despreciable de oxígeno en su estructura, según se ha demostrado por IBA. Por otro lado, los estudios de SEM y XRD muestran que las capas resultantes son policristalinas; sus granos cristalinos presentan una mayor orientación para T_s menores. La caracterización óptica de estas capas, muestra que el Zn_3N_2 se comporta como un semiconductor de tipo directo, y tiene una banda prohibida con una energía (E_g) entre 1.25 y 1.46 eV dependiendo de T_s. Este estudio también muestra un corrimiento de E_g hacia mayores energías a medida que T_s disminuye, debido fundamentalmente a una mayor orientación de los granos. Estos cambios en la estructura con respecto a T_s, también afectan a la resistividad de las capas, mostrado valores mínimos alrededor de 10^{-3} Ω·cm para T_s = 423 K; estos valores de resistividad son los más bajos medidos en este material hasta el momento.

El crecimiento de capas de Zn_3N_2 a ritmos de crecimiento bajos (r_g < 4.4 nm/min) produce capas con las fronteras de grano menos definidas, lo que beneficia el trasporte eléctrico entre granos, y aumenta la movilidad de electrones hasta alcanzar valores alrededor de 100 cm^2/V·s, para concentraciones de carga de 3.2×10^{18} cm^{-3}.

La metaestabilidad de una capa pura y estequiométrica de Zn_3N_2 se ha analizado por IBA, SE y espectrofotometría después de su exposición al aire. Los estudios revelan una oxidación superficial del Zn_3N_2, mostrando la formación de una capa rica en oxígeno sobre la superficie del nitruro, cuya estequiometría parece corresponder a ZnO. El espesor de dicha capa incrementa a lo largo del tiempo, sin llegar a saturar, lo que conlleva que la capa de Zn_3N_2 tienda a transformarse completamente en ZnO después de un tiempo suficiente de exposición al aire. El ritmo de oxidación ha sido determinado por SE, mostrando valores de 36 nm/día y 20 nm/día para capas crecidas a T_s de 298 y 473 K, respectivamente. A partir de estos resultados, es evidente que las capas crecidas a mayor T_s, presentan una mayor estabilidad en ambientes oxidantes. Por otro lado, se ha demostrado que la oxidación progresiva del Zn_3N_2 puede prevenirse utilizando una capa protectora de ZnO evaporada sobre el nitruro inmediatamente después de su depósito, es decir, antes de exponer el nitruro al aire.

La oxidación superficie del Zn_3N_2 y la incorporación inintencionada de oxígeno durante el crecimiento, pueden alterar las propiedades ópticas de la capa. Teniendo en cuenta ambos efectos, las constantes ópticas (n y k) y el E_g del Zn_3N_2 han sido determinados. Se han realizado medidas de elipsometría espectroscópica (SE) en capas de Zn_3N_2 crecidas a $r_g > 50$ nm/min y justo después de su depósito, para determinar n y k, previniendo la oxidación superficial y asegurando la pureza del nitruro. Los resultados muestran $n = 2.8-2.0$ y $k = 0.6-1.0$ para fotones con una energía entre 1.5 y 4.5 eV. Por otro lado, las medidas de espectrofotometría de transmisión realizadas en capas de Zn_3N_2 parcialmente oxidadas, es decir, con una capa de ZnO superficial, muestran un desplazamiento del borde de transmisión hacia mayores energías; este desplazamiento incrementa con el tiempo de exposición de la capa al aire. La región intermedia entre ambas capas (ZnO y Zn_3N_2) podría estar compuesta por una capa con una composición incremental ($Zn_xN_yO_z$) que podría ensanchar la energía de la banda prohibida y por lo tanto movería el borde de trasmisión.

En este trabajo se han realizado patrones de tamaño micrométrico sobre capas de Zn_3N_2, utilizando procesos litográficos basados en descargas eléctricas aplicadas a través de una punta micrométrica. El estudio revela que las áreas afectadas por la descarga producida a voltajes bajos, presentan una resistividad menor, fundamentalmente por la eliminación del óxido nativo superficial del nitruro; este proceso facilitaría la determinación de las propiedades optoelectrónicas del Zn_3N_2, mediante la eliminación de su óxido superficial. Para procesos llevados a cabo a voltajes altos, la descarga produce zanjas profundas con una resistencia eléctrica alta. Este tratamiento también induce importantes cambios en la composición en la parte central de la zanja, que resulta estar formada por estructuras de tamaño micrométrico compuestas de ZnO:N. Las dimensiones, densidad superficial y composición química de los cristales resultantes, son estructuras interesantes para ser usadas como semillas (catalizadores) en crecimientos, por ejemplo, de nanohilos de ZnO.

El Zn_3N_2 ha sido también usado como capa activa en transistores de lámina delgada (TFT) y foto-transistores. Como ya se ha comentado, el recubrimiento del nitruro con una capa de ZnO es conveniente para prevenir la oxidación de este material, mejorando su estabilidad de los TFTs. Los TFTs fabricados, presentan características de transistor tipo-n, en modo enriquecimiento, y sin necesidad de aplicar ningún tratamiento térmico. Además, la corriente de drenador muestra sensibilidad a la luz IR/VIS; dicha foto-sensibilidad se ha observado que aumenta con el voltaje aplicado entre la puerta y la fuente del TFT. La fabricación del foto-transistor fue completamente realizada utilizando procesos fotolitográficos. En estos transistores, el crecimiento de la capa de Zn_3N_2 (canal), se realizó utilizado las condiciones de crecimiento optimizadas, con el objetivo de maximizar la movilidad de los electrones en la capa. La combinación de una movilidad alta en el canal, con la reducción de las dimensiones del dispositivo, ha contribuido a mejorar la fotorespuesta (R_{photo}) del foto-transistor hasta alcanzar R_{photo} máximas de 3.5×10^6 A/W.

8.3.2. Nanohilos de ZnO

En este trabajo se han sintetizado con éxito nanohilos de ZnO sobre sustratos de Si(100), mediante transporte químico en fase vapor (CVT), en un ambiente oxidante, y a temperaturas de 700−900 ºC. Para ello, se ha utilizado una lámina delgada de Zn (~ 10 nm) como semilla, cuyo papel fundamental es el de asistir el crecimiento de los nanohilos de ZnO a lo largo de la dirección normal a la superficie del sustrato. Los nanohilos resultantes muestran relaciones de aspecto de 10−15, y diámetros entre 90 y 870 nm. Por otro lado, el producto resultante de los procesos CVT llevados a cabo sobre sustratos de Si(100) sin la capa semilla, está compuesto por una mezcla de tetrápodos (TPs) de ZnO; dichos TPs son cristales con forma hexagonal de cuyas caras emergen nanohilos de hasta 10 μm de longitud. El diámetro de estos nanohilos varía ente 100 y 300 nm, y sus relaciones de aspecto pueden alcanzar valores superiores a 100.

Los nanohilos de ZnO fueron utilizados para fabricar fotodetectores de luz UV. La gran longitud de estos nanohilos (>10 μm) ha facilitado su ensamblaje e integración entre electrodos conductores separados distancias micrométricas. Para la fabricación de estos dispositivos se han utilizado electrodos de óxido de zinc dopado con aluminio (AZO); estos electrodos muestran una gran resistencia mecánica y una gran adherencia a los sustratos Si con una capa aislante superficial. El ensamblaje de los nanohilos se ha llevado a cabo utilizando dielectroforesis (DEP). Los parámetros característicos de la DEP, tales como la amplitud y la frecuencia de la señal alterna aplicada entre los electrodos, han sido estudiados con el objetivo de optimizar el ensamblaje de nanohilos de ZnO. Para ello se han analizado los efectos del factor de Classius-Mossotti (f_{CM}) y el gradiente del módulo al cuadrado del campo eléctrico (∇E^2) sobre la eficiencia de atrapamiento de los nanohilos. Los resultados muestran que la fuerza dielectroforética (F_{DEP}) ejercida sobre los nanohilos, incrementa con el voltaje promedio (V_{rms}) aplicado y tiende a disminuir a altas frecuencias (f). Las mayores eficiencias de alineamiento se observan para V_{rms} = 7 V y f = 100 kHz. El diseño de electrodos de AZO con una geometría específica, ha permitido el ensamblaje de un único nanohilo entre los electrodos, utilizando las condiciones de DEP descritas. Después del atrapamiento de un nanohilo de ZnO entre un par de electrodos de AZO, los extremos del nanohilo fueron recubiertos con una capa fina de Al (100 nm) para reducir el ruido de las características I/V y mejorar la reproducibilidad del proceso. El dispositivo resultante constituye una estructura totalmente original que combina el uso de electrodos de AZO y Al para integrar nanohilos de ZnO en la tecnología CMOS actual basada en Si.

Las propiedades optoelectrónicas de fotoconductores basados en un único nanohilo de ZnO han sido estudiadas en función del radio del nanohilo (r_{NW}). En condiciones de oscuridad, los nanohilos con un r_{NW} inferior a 65 nm muestran un volumen conductivo prácticamente deplexado (vaciado de portadores de carga). Los mecanismos de conducción que presentan estos nanohilos, están fundamentalmente influenciados por los estados de superficie, y los tiempos de emisión/captura de electrones desde estos estados superficiales. Por otro lado, el mecanismo de conducción en nanohilos de mayor r_{NW} ocurre fundamentalmente a través del núcleo del nanohilo y está limitado por la sección transversal de conducción.

Bajo iluminación UV ($\lambda < 370$ nm), el mecanismo de conducción a través de los nanohilos es similar al descrito para el caso de nanohilos gruesos; este mecanismo difiere, por lo tanto, de los mecanismos de generación-recombinación descritos para nanohilos finos en condiciones de oscuridad. La principal consecuencia es la fuerte diferencia entre la corriente bajo iluminación y en oscuridad. La R_{photo} y ganancia fotoconductora (G_{photo}) incrementan a medida que r_{NW} disminuye, alcanzado valores máximos de 10^8 A/W y 10^8, respectivamente, en fotodetectores basados en un nanohilo con un r_{NW} de 50 nm. Además, la longitud de onda de corte se ha demostrado que depende con r_{NW}, y presenta un claro corrimiento hacia el azul (mayores energías) a medida que r_{NW} disminuye. El origen de este fenómeno es todavía incierto y por lo tanto necesita ser estudiado en profundidad.

Estudios de la fotorespuesta en función del tiempo muestran que los nanohilos prácticamente deplexados (r_{NW} = 50 nm) tienen unos tiempos de excitación mayores debido a que el mecanismo de generación-recombinación limita la velocidad de respuesta del nanohilo. Los nanohilos gruesos (r_{NW} = 260 nm) también presentan esta respuesta lenta después de una primera respuesta rápida, indicando que tienen una región neutral en el núcleo que proporciona un canal rápido para el flujo de carga después de la emisión de electrones desde la superficie. Durante el proceso de relajación (después de la iluminación), los nanohilos más finos exhiben tiempos de decaída más rápidos que los medidos en nanohilos gruesos; este comportamiento puede explicarse debido a la reducción de la densidad de oxígenos adsorbidos en los nanohilos finos, que podría mejorar el tiempo de decaída de estos dispositivos después de su iluminación.

Las propiedades eléctricas y superficiales de los nanohilos de ZnO han sido analizadas después de diferentes tratamientos superficiales, que involucran la hidroxilación y silanización con APDEMS. El estudio fue llevado a cabo mediante diferentes técnicas: ángulo de contacto, CPD, SPV, y XPS. La superficie silanizada de los nanohilos de ZnO muestra un comportamiento hidrofóbico, mientras que la superficie hidroxilada presenta un comportamiento hidrofílico. Los espectros de XPS confirman la formación con éxito de la capa auto-ensamblada de APDEMS sobre la superficie de los nanohilos, mediante la presencia de los picos N 1s y C1s pertenecientes a los grupos amina e hidrocarburo, respectivamente. Los espectros también muestran un corrimiento hacia el rojo (menores energías) de la energía de enlace de los picos Zn 2p3/2 (640 meV) y O 1s (675 meV) en comparación con la superficie hidroxilada de ZnO, lo que evidencia un cambio en la magnitud del dipolo superficial formado sobre la superficie del ZnO. Este cambio en el dipolo superficial también produce una reducción de la función de trabajo del ZnO desde 5.02 eV (después de la hidroxilación) hasta 4.11 eV (después de la silanización) según se determinó mediante CPD. Por otro lado, comparando la anchura del doblaje de bandas superficial obtenido a partir de las medidas de SPV, se puede concluir que los nanohilos hidroxilados están prácticamente deplexados. Las características I/V de un único nanohilo de ZnO también han sido analizadas después de cada tratamiento superficial. Los nanohilos silanizados muestran mayores corrientes que los hidroxilados debido a un ensanchamiento del volumen conductivo. Por lo tanto, se puede concluir que los niveles de corriente mostrados por estos nanohilos están gobernados por la anchura de la región de carga espacial, tal y como ocurren en los nanohilos con diferentes r_{NW}. Finalmente, se ha observado que la silanización mejora las linealidad de la características del contacto

formado entre el nanohilo y electrodo de Al; este efecto puede estar relacionado con el incremento de carga libre en el nanohilo, lo que beneficiaría los parámetros de salida de transistores de efecto campo.

8.3.3. Nanohilos de GaAs

En este trabajo se han sintetizado nanohilos de GaAs mediante epitaxia de haces químicos (CBE) asistida por Ga, sobre sustratos Si(111) convenientemente oxidados. El estudio de SEM muestra evidencias claras que confirman el crecimiento de estos nanohilos a partir de gotas de Ga, es decir, las gotas de Ga ejercen un papel de catalizador del crecimiento; la ruptura de las moléculas de TEGa sobre la superficie oxidada del sustrato permite la formación de estas gotas. La preparación de la superficie del sustrato es crítica para permitir la formación de dicha gotas. Esta preparación consiste en un primer ataque del óxido nativo utilizando una solución ácida de HF:H_2O, seguido de una exposición al aire durante 5 min para permitir la formación de un óxido superficial (SiO_x) de aproximadamente 0.5 nm de espesor. Este proceso promueve la formación de agujeros en el óxido superficial distribuidos de manera aleatoria; la formación de gotas de Ga se produce de manera preferencial en estos agujeros, limitando el número de centros de nucleación de nanohilos.

Antes del crecimiento de los nanohilos de GaAs, las gotas de Ga son pre-depositadas a T_s = 580 ºC; después del pre-depósito, se espera un tiempo denominado de estabilización, para permitir el reordenamiento de las gotas sobre la superficie del sustrato. El crecimiento de los nanohilos ocurre cuando los flujos de TBAs y TEGa son abiertos. Los parámetros de crecimiento (T_s, relación de flujos V/III, tiempos de pre-depósito de Ga y estabilización, ...) han sido optimizados con el objetivo de obtener nanohilos con una alta calidad cristalina y relación de aspecto. Los mejores resultados han sido obtenidos para T_s = 580 ºC y una relación de flujos V/III = 0.8 (pre-depositando 7.5 monocapas de Ga y estabilizando durante 90 s). Durante el crecimiento de los nanohilos, se ha observado la formación de una capa policristalina de GaAs sobre la superficie del sustrato; esta capa reduce la incorporación efectiva tanto de Ga como de As al nanohilo, lo que limita la longitud máxima de los nanohilos (L_{NW} ~ 3.5 μm). Con el objetivo de superar esta longitud límite, se ha desarrollado un proceso denominado crecimiento en dos pasos, que pretende preservar la superficie del sustrato limpia de estructuras parásitas de GaAs. En este proceso, los nanohilos de GaAs son pre-crecidos durante 4 min, después la muestra es expuesta al aire durante 1 h, y finalmente se continúa con el crecimiento durante el tiempo deseado (re-crecimiento). Comparando la morfología de los nanohilos crecidos en un paso o en dos pasos, el crecimiento en dos pasos presenta una clara mejora en la relación de aspecto y longitud máxima de los nanohilos, así como una menor densidad de impurezas de GaAs sobre la superficie del sustrato.

La estructura cristalina de los nanohilos de GaAs ha sido analizada por RHEED y TEM, mostrando una estructura pura zinc blenda (ZB), y sin ninguna evidencia de wurtzita (WZ). A partir de las imágenes de HRTEM, se ha observado que durante el crecimiento, las gotas de Ga pueden parcialmente las paredes laterales de los nanohilos; este fenómeno podría ser el responsable de la buena calidad cristalina exhibida por

los nanohilos, incluso en la región de transición existente entre el nanohilo y la gota de Ga. Por lo tanto, este tipo de crecimiento podría prevenir la formación de mezclas entre fases ZB y WZ a lo largo del cuerpo del nanohilo.

Las medidas de espectroscopía Raman confirman la ausencia de picos relacionados con la estructura WZ en los nanohilos de GaAs. Además, el análisis de la forma del pico asociado al fonón óptico longitudinal (LO), se ha llevado a cabo utilizando el modelo de confinamiento de fonones (PCM), permitió la determinación del coeficiente de confinamiento α = 23 nm^{-1} característico del GaAs. Las propiedades superficiales (rugosidad y oxidación superficial) de los nanohilos de GaAs, fueron analizadas estudiando el corrimiento de pico Raman asociado a los fonones ópticos superficiales (SO). Los resultados del estudio mostraron una gran uniformidad en el diámetro del nanohilo a lo largo de todo su cuerpo.

Finalmente, se han fabricado mediante DEP fotodetectores de luz VIS basados en nanohilos únicos de GaAs. Como ocurría en el caso de los nanohilos de ZnO, las condiciones de DEP fueron optimizadas con el objetivo de atrapar un nanohilo entre electrodos conductores, permitiendo su posterior caracterización eléctrica. Dos tipos diferentes de nanohilos se han integrado, con y sin gota en uno de los extremos del nanohilo. Los dispositivos basados en nanohilos sin gota, presentan corrientes muy bajas en el rango de los pA (a 2 V) tanto en oscuridad como bajo iluminación VIS. La formación de dos contactos Schottky en oposición podría ser la explicación de tales corrientes. Por otro lado, los dispositivos basados en nanohilos con la gota de Ga, presentan características *I*/*V* asimétricas, mostrando corrientes de 2 pA y 2 nA para -2 y +2 V, respectivamente. En polarización inversa, el dispositivo no es sensible a la luz VIS, mientras que bajo polarización directa, la corriente medida es aproximadamente un orden de magnitud mayor que la medida en oscuridad. Este comportamiento podría ser atribuido a la formación de un contacto Schottky en una de las uniones nanohilo/electrodo, y un contacto óhmico entre la gota de Ga y el otro electrodo. La resistencia constante asociada a este último contacto es muy baja fundamentalmente por la formación de enlaces químicos (nano-contactos) entre la gota y el nanohilo durante su crecimiento.

8.4. Trabajo Futuro

Esta sección incluye posibles líneas de investigación futuras relacionadas con el trabajo presentado en esta tesis. Además, se proponen nuevas ideas con el objetivo de guiar a nuevos investigadores en formación para continuar con las investigaciones sobre los materiales avanzados analizados en este trabajo, dando continuidad a los esfuerzos realizados hasta el momento. La sección contiene posibles trabajos futuros relacionados con láminas delgadas de Zn_3N_2 (sección 8.4.1), los nanohilos de ZnO (sección 8.4.2), los nanohilos de GaAs (sección 8.4.3), incluyendo la optimización de sus propiedades y su integración en diferentes aplicaciones. Finalmente, la sección 8.4.4 propone la fabricación de nuevos dispositivos avanzados utilizando DEP.

8.4.1. Láminas Delgadas de Zn_3N_2

La movilidad de portadores de carga es uno de los parámetros eléctricos más importantes para evaluar el rendimiento de un semiconductor como canal de un TFT. En este trabajo, se han crecido capas de Zn_3N_2 a ritmos de crecimiento bajos, obteniéndose movilidades de electrones altas, y sin necesidad de aplicar tratamientos térmicos; estas capas presentan fronteras de grano poco definidas, lo que podría contribuir a mejorar el transporte eléctrico entre granos. Esta propiedad convierte al Zn_3N_2 en un material muy atractivo para el desarrollo de TFTs de alta movilidad. Se propone la optimización de los procesos de fabricación de estos dispositivos, como una posible vía para igualar o incluso superar los valores de movilidad de efecto campo mostrados por los TFTs existentes; la integración de estos TFTs en circuitos integrados y pantallas de cristal líquido, son algunas de las potenciales aplicaciones de estos dispositivos.

Debido a su metaestabilidad, el Zn_3N_2 tiende a oxidarse de manera progresiva (20−36 nm/día) lo que significa que la capa tiende a convertirse completamente en ZnO, después de un tiempo suficiente de exposición al aire. La posibilidad de obtener ZnO tipo-p a partir de la oxidación del Zn_3N_2, convierte al Zn_3N_2 en un material muy interesante para el desarrollo de homo-uniones p-n de ZnO. El uso de homo-uniones en lugar de hetero-uniones, podría reducir la densidad de defectos inducidos por el desajuste de red en la intercara formada entre los dos materiales. Uno de los posibles campos en los que se podría integrar este tipo de tecnología, es el relacionado con las células solares. Las buenas propiedades ópticas observadas en láminas de Zn_3N_2 antes, durante, y después de su total conversión en ZnO, hacen que este material sea atractivo para el desarrollo de células solares, con diferentes bordes de absorción en el rango UV/VIS dependiendo de la composición de la nitruro.

Otra posible aplicación del Zn_3N_2, es en sensores de gas, debido a su alta reactividad superficial a las especies de oxígeno contenidas en el aire. Además, la posibilidad de funcionalizar superficies pasivadas de Zn_3N_2, es decir, con una capa protectora de ZnO sobre la capa de nitruro, permitiría abrir nuevas líneas de investigación relacionadas con la fabricación de biosensores, como transistores de efecto campo modulados

por líquido electrolítico; este tipo de dispositivos permitiría detectar diferentes concentraciones de biomoléculas y agentes químicos disueltos en la solución líquida donde esté sumergido el biosensor.

8.4.2. Nanohilos de ZnO

El crecimiento de nanohilos de ZnO se ha realizado sobre sustratos de Si, utilizando una capa semilla de Zn para asistir el crecimiento de los nanohilos a lo largo de la dirección normal a la superficie del sustrato. Sin embargo, este tipo de crecimiento produce una distribución aleatoria de los nanohilos sobre la superficie del sustrato, es decir, cada nanohilo tiene un entorno diferente a su alrededor, lo que podría afectar al rendimiento de un dispositivo. La relación de aspecto, y la densidad superficial de nanohilos, pueden ser mejoradas utilizando sustratos convenientemente preparados. En este sentido, antes del crecimiento de los nanohilos, la capa semilla de Zn puede ser previamente tratada mediante métodos litográficos, para definir un conjunto ordenado de islas de Zn a lo largo de la superficie del sustrato. La altura, diámetro, y separación entre islas, son parámetros clave para la optimización de los mecanismos que gobiernan el crecimiento. Una vez conseguido el crecimiento ordenado de nanohilos sobre la superficie del sustrato, la fabricación de electrodos directamente sobre los nanohilos (utilizando el sustrato como contra electrodo), podría permitir la integración directa de estos nanohilos en la tecnología del Si.

Los fotodetectores de luz UV basados en nanohilos de ZnO, muestran R_{photo} entre 10^7–10^8 A/W. Estos valores tan elevados se deben fundamentalmente a la alta relación superficie volumen, y al reducido volumen conductor de los nanohilos. Además, estos fotodetectores muestran longitudes de onda de corte variable entre 364 y 385 nm, dependiendo del r_{NW}. La combinación de ZnO con Mg y Cd, permite extender el rango de detección espectral entre 210 y 450 nm. Se propone, por lo tanto, el crecimiento de nanohilos de ZnMgO y ZnCdO, y su posterior integración en fotodetectores con bordes de absorción en el rango espectral mencionado.

La sensibilidad y tiempo de respuesta de los fotodetectores de UV basados en nanohilos de ZnO, pueden ser mejorados utilizando diferentes métodos, tales como, la decoración de la superficie de los nanohilos con nanopartículas, el recubrimiento de la superficie del nanohilo con polímeros con absorción a la luz UV, y la fabricación de contactos Schottky.

i) Si los nanohilos de ZnO son decorados con nanopartículas de Au, se pueden crear localmente regiones Schottky en la intercara formada por la nanopartícula y el nanohilo; estás regiones deplexarían el nanohilo y reducirían, por tanto, la corriente en oscuridad. Por otro lado, la mejora del cociente entre la fotocorriente y la corriente en oscuridad, así como la reducción del tiempo de relajación con respecto a nanohilos sin nanopartículas, son efectos que no están claros y deben ser investigados.

ii) El uso de polímeros para recubrir la superficie de los nanohilos de ZnO, podría mejorar la fotorespuesta de los fotodetectores basados en estas estructuras. El principal papel del polímero es similar al que desempeña el oxígeno en nanohilos sin recubrimiento, es decir, el

atrapamiento de electrones libres desde el volumen del nanohilo hacia la superficie positivamente cargada; el resultado es una reducción de la corriente de oscuridad debido a la disminución del volumen conductor. En el caso especial de polímeros que tengan una cierta absorción a la luz UV, la iluminación de los nanohilos recubiertos con este tipo de polímero, permitiría la generación de pares electrón-hueco en el nanohilo durante la iluminación, asistida por la absorción de fotones en el polímero en los niveles fundamentales. Esta contribución adicional, podría mejorar la fotocorriente alcanzada. Sin embargo, el papel que juegan el estado fundamental y el excitado del polímero en el proceso de absorción de fotones y la trasferencia de carga entre el nanohilo y el polímero son todavía cuestiones que no están resueltas.

Aunque se ha demostrado que los nanohilos de ZnO son altamente sensibles a la luz UV, la corriente persistente después de la iluminación, conlleva tiempos de recuperación muy largos, lo que limita el uso de estas estructuras en dispositivos comerciales. La fabricación de fotodetectores basados en contactos Schottky formados entre el nanohilo de ZnO y los electrodos metálicos, se propone como una alternativa prometedora para acelerar el tiempo de respuesta del dispositivo, mientras se conserva su sensibilidad.

En este trabajo, se ha demostrado que la funcionalización superficial de los nanohilos de ZnO es posible. La posibilidad de formar capas orgánicas auto-ensambladas sobre la superficie de los nanohilos de ZnO, así como su alta relación superficie-volumen, son características muy prometedoras para el desarrollo de biosensores. Como ejemplo de biosensor, se propone la fabricación de un transistor de efecto campo, utilizando como elemento activo nanohilos de ZnO funcionalizados. La sensibilidad química de este tipo de dispositivos, está basada en el cambio de la conductividad eléctrica del nanohilo funcionalizado cuando una especie (molécula, …) se enlaza sobre su superficie. Este tipo de dispositivos, por lo tanto, podrían mejorar la sensibilidad de los biosensores actuales, permitiendo alcanzar el régimen de detección de unas pocas moléculas. Además, la funcionalización de nanohilos de ZnO verticalmente alineados sobre sustratos de Si, podría mejorar la sensibilidad del biosensor, facilitado la integración de los nanohilos en el dispositivo y aumentado el área activa de detección.

Como la conductividad de los nanohilos de ZnO está fundamentalmente gobernada por efectos de la superficie, la alta relación superficie-volumen de estas estructuras hace que los nanohilos de ZnO sean unos candidatos muy prometedores para el desarrollo de sensores de gas. Debido a las propiedades de la superficie del ZnO, este tipo de sensores presenta diferentes comportamientos dependiendo de la naturaleza del gas (reductivo u oxidante). Los gases reductivos como el etanol, reaccionan con el oxígeno adsorbido sobre la superficie del nanohilo de ZnO, liberando electrones hacia el volumen del nanohilo, e incrementado el volumen conductor. Por otro lado, un gas oxidante como el NO_2, incrementa la densidad de especies de oxígeno adsorbidas sobre la superficie del nanohilo mediante el atrapamiento de electrones libres, produciendo un ensanchamiento de la región de carga espacial que reduciría el volumen conductor del nanohilo. Por lo tanto, los sensores de gas basados en nanohilos de ZnO podrían detectar pequeñas

concentraciones de gas gracias a su gran superficie activa, y tener cierto grado de selectividad. Además, la unión entre dos nanohilos de ZnO es una arquitectura prometedora, que podría ayudar a mejorar las propiedades optoelectrónicas del sensor de gas.

8.4.3. Nanohilos de GaAs

Según se ha observado, el crecimiento de nanohilos de GaAs mediante CBE asistido por Ga, está fuertemente influenciado por la preparación previa de la superficie del sustrato de Si(111) y las condiciones de crecimiento (T_s, relación de flujos V/III, etc.). En este trabajo se ha desarrollado un método fiable y reproducible para preparar dichos sustratos, que permite conseguir el crecimiento de nanohilos de GaAs; además, la optimización de las condiciones de crecimiento, ha permitido controlar las propiedades morfológicas de los nanohilos, reduciendo el crecimiento inintencionado de nano-cristales de GaAs sobre la superficie del sustrato. Utilizando este método, se propone el crecimiento de estructuras más completas basadas en nanohilos de GaAs. El crecimiento de estas estructuras en CBE, supone un verdadero reto, y por lo tanto ofrece la posibilidad de abrir nuevas líneas de investigación.

i) Crecimiento ordenado de nanohilos de GaAs sobre sustratos previamente litografiados. La definición de agujeros sobre la superficie oxidada de los sustratos de Si(111), debería limitar los sitios de nucleación, reduciendo el crecimiento de estructuras parásitas de GaAs sobre su superficie. Este tipo de sustratos se ha utilizado con éxito en procesos llevados cabo mediante epitaxia por haces moleculares (MBE), mostrado un control elevado sobre la densidad de nanohilos y sus dimensiones a través del espaciado entre los agujeros y su tamaño. Sin embargo, el uso de este tipo de sustratos en CBE no es trivial, ya que la ventana de espesores de óxido que permite el crecimiento de nanohilos es muy estrecha.

ii) Crecimiento de nanohilos de GaAs recubiertos por una capa de AlGaAs. Los nanohilos de GaAs tienen una densidad de estados de superficie elevada, que pueden actuar como centros de recombinación no-radiativa, e incrementar la dispersión superficial, empeorando las propiedades optoelectrónicas de los nanohilos (baja movilidad de los portadores, …); por lo tanto, el uso de nanohilos de GaAs en aplicaciones tales como fotodetectores, o diodos emisores de luz (LED), podría empeorar el rendimiento de estos dispositivos. El recubrimiento de estos nanohilos con una capa de AlGaAs, pretende pasivar la superficie del GaAs, disminuyendo los estados de superficie. Propiedades tales como la emisión radiativa, y el cociente entre la fotocorriente y la corriente de oscuridad, pueden verse mejoradas en este tipo de estructuras. Por lo tanto, se propone la fabricación de este tipo de estructuras para el desarrollo de dispositivos optoelectrónicos de alto rendimiento.

iii) Los mecanismos de crecimiento de los nanohilos de GaP mediante CBE asistido por Ga, deberían ser similares a los observados en los nanohilos de GaAs; esto significa que su crecimiento podría realizarse utilizando condiciones similares a las usadas para los nanohilos

de GaAs (preparación del sustrato, pre-depósito de Ga, …). Además, el crecimiento de nanohilos basados en un compuesto ternario de $GaAs_{1-x}P_x$ permitiría modular el E_g del material desde 2.5 eV para el GaP puro, hasta 1.43 eV del GaAs puro. La posibilidad de cambiar E_g controlando la composición del nanohilo, tiene aplicaciones muy prometedoras en el campo de la optoelectrónica, incluyendo la fabricación de fotodetectores que detecten luz en distintos rangos espectrales. Por otro lado, el crecimiento de segmentos de GaAsP (semiconductor de tipo directo) en nanohilos de GaP, formando estructuras del tipo $GaP/GaAs_{1-x}P_x/GaP$, permitiría la emisión de luz en diferentes longitudes de onda dependiendo de la composición del segmento. El intercalado de segmentos con diferentes composiciones a lo largo del cuerpo del nanohilo, serviría para la fabricación de etiquetas fluorescentes para sistemas de análisis biomédicos.

iv) Los nitruros diluidos tales como el $GaAs_{1-x}N_x$, muestran valores de E_g por debajo de 1.4 eV para concentraciones de N en el rango $0<x<0.2$. La posibilidad de variar E_g en este material permite extender el rango de detección hacia el IR. La incorporación de N en el aleado de GaAsN, promueve el crecimiento tridimensional durante la epitaxia en lugar de un crecimiento bidimensional. Este comportamiento es favorable para la nucleación de nanohilos de Ga(As,N), por lo tanto se propone el crecimiento de este tipo de nanohilos mediante CBE asistido por Ga.

8.4.4. Integración de Nanoestructuras

Durante este trabajo, la técnica DEP ha sido utilizada para llevar a cabo el ensamblaje de nanohilos de ZnO y GaAs entre electrodos, con el objetivo de fabricar fotodetectores de luz en distintos rangos espectrales. Las condiciones de DEP y la geometría de los electrodos, fueron optimizadas con el objetivo de controlar el número de nanohilos atrapado, teniendo también un cierto control sobre las dimensiones de dichos nanohilos. Sin embargo, el gran potencial de esta técnica podría permitir fabricar estructuras más complejas.

i) La fabricación de matrices con pares de electrodos enfrentados, permitiría llevar a cabo el ensamblaje de nanohilos a gran escala, a través de un único proceso de DEP. El atrapamiento masivo de nanohilos en sitios específicos de la muestra, es decir, creando una conexión entre un par de electrodos enfrentados, es un método muy prometedor para la fabricación de dispositivos con una gran superficie activa, muy interesante para el desarrollo de aplicaciones como sensores de gas, biosensores y fotodetectores.

ii) La integración de diferentes tipos de nanohilos en el mismo dispositivo, por ejemplo, combinado los dos tipos de nanohilos estudiados en este trabajo: ZnO y GaAs, es una propuesta atractiva que permitiría la fabricación de fotodetectores con alta sensibilidad en

diferentes rangos del espectro electromagnético. El uso de procesos jerárquicos de DEP para el ensamblaje de nanohilos de ZnO y GaAs (de manera secuencial) sobre electrodos pre-definidos, es un método novedoso para fabricar fotodetectores sensibles tanto al rango UV como al NIR.

iii) También se propone el desarrollar una geometría específica para los electrodos que permitiera hacer un contacto entre diferentes tipos de nanohilos mediante DEP. La idea consiste en definir cuatro electrodos enfrentados dos a dos (formando una cruz), de manera que una vez se hayan atrapado dos nanohilos conectando cada par de electrodos, ambos nanohilos formen un contacto. Este tipo de proceso permitiría la formación de contactos verticales entre nanohilos de diferentes tipos, y el posterior desarrollo de nano-diodos tales como LEDs o fotodiodos.

La técnica DEP también podría ser usada para llevar a cabo la integración de las tecnologías basadas en nanohilos y en materiales bidimensionales tales como grafeno, MoS_2, WS_2, $MoSe_2$, $MoTe_2$, $TaSe_2$, … Utilizando procesos jerárquicos similares a los descritos, se podrían fabricar dispositivos electrónicos basados nanohilos y materiales bidimensionales, con el objetivo de mejorar las propiedades optoelectrónicas de la tecnología existente.

Appendix A

Publications and Conference Contributions

This appendix includes all the publications and conference contributions resulting from this research.

Publications

1. **C. García Núñez**, A.F. Braña, N. Lopez, and B.J. García, "GaAs Nanowires Grown by Ga-assisted Chemical Beam Epitaxy: Substrate Preparation and Growth Kinetics", Journal of Crystal Growth (Accepted 2015).
2. **C. García Núñez**, A.F. Braña, N. Lopez, and B.J. García, "On the Growth Mechanisms of GaAs Nanowires by Ga-assisted Chemical Beam Epitaxy", IEEExplore (2015).
3. **C. García Núñez**, M. Sachsenhauser, B. Blashcke, A. García Marín, J.A. Garrido, and J.L. Pau, "Effects of Hydroxylation and Silanization on the Surface Properties of ZnO Nanowires", ACS Applied Materials and Interfaces 7 (2015) 5331.
4. **C. García Núñez**, A.F. Braña, J.L. Pau, D. Ghita, B.J. García, G. Shen, D.S. Wilbert, S.M. Kim, and P. Kung, "Surface Optical Phonons in GaAs Nanowires Grown by Ga-assisted Chemical Beam Epitaxy", Journal of Applied Physics 115 (2014) 034307.
5. **C. García Núñez**, J.L. Pau, E. Ruiz, A. García Marín, B.J. García, J. Piqueras, G. Shen, D.S. Wilbert, S.M. Kim, and P. Kung, "Enhanced Fabrication Process of Zinc Oxide Nanowires for Optoelectronics", Thin Solid Films 555 (2014) 42.
6. **C. García Núñez**, A. García Marín, P. Nanterne, J. Piqueras, P. Kung, and J.L. Pau, "Conducting Properties of Nearly-Depleted ZnO Nanowire UV Sensors Fabricated by Dielectrophoresis", Nanotechnology 24 (2013) 415702.
7. **C. García Núñez**, J. Jiménez-Trillo, M. García Vélez, J. Piqueras, J.L. Pau, C. Coya, and A.L. Álvarez, "Sub-micron ZnO:N Particles Fabricated by Low Voltage Electrical Discharge Lithography on Zn_3N_2 Sputtered Films", Applied Surface Science 285 (2013) 783.
8. **C. García Núñez**, A.F. Braña, J.L. Pau, D. Ghita, B.J. García, G. Shen, D.S. Wilbert, S.M. Kim, and P. Kung, "Pure Zincblende GaAs Nanowires Grown by Ga-assisted Chemical Beam Epitaxy", Journal of Crystal Growth 372 (2013) 205.
9. **C. García Núñez**, J.L. Pau, E. Ruiz, and J. Piqueras, "Thin Film Transistors Based on Zinc Nitride as a Channel Layer for Optoelectronic Devices", Applied Physics Letters 101 (2012) 253501.
10. **C. García Núñez**, J.L. Pau, M.J. Hernández, M. Cervera, E. Ruiz and J. Piqueras, "Influence of Air Exposure on the Compositional Nature of Zn_3N_2 Thin Films", Thin Solid Films 522 (2012) 208.

11. **C. García Núñez**, J.L. Pau, M.J. Hernández, M. Cervera, E. Ruiz, and J. Piqueras, "On the Zinc Nitride Properties and the Unintentional Incorporation of Oxygen", Thin Solid Films 520 (2012) 1924.
12. **C. García Núñez**, J.L. Pau, M.J. Hernández, M. Cervera, and J. Piqueras, "On the True Optical Constants of Zinc Nitride", Applied Physics Letters 99 (2011) 232112.
13. A. García Marín, **C. García Núñez**, P. Rodríguez, G. Shen, S.M. Kim, P. Kung, J. Piqueras, and J.L. Pau, "Continuous-Flow System and Monitoring Tools for the Dielectrophoretic Integration of Nanowires in Light Sensor Arrays", Nanotechnology 26 (2015) 115502.
14. J.L. Pau, **C. García Núñez**, A. García Marín, C. Guerrero, P. Rodríguez, S. Borromeo, and J. Piqueras, "Contact Properties and Surface Reaction Kinetics of Single ZnO Nanowire Devices Fabricated by Dielectrophoresis", SPIE 8987 (2014) 8987Q.
15. A. García Marín, **C. García Núñez**, E. Ruiz, J. Piqueras, and J.L. Pau, "Fast Response ZnO:Al/CuO Nanowire/ZnO:Al Heterostructure Light Sensors Fabricated by Dielectrophoresis" Applied Physics Letters 102 (2013) 232105.
16. J.L. Pau, **C. García Núñez**, A. García Marín, E. Ruiz, and J. Piqueras, "Metal Oxide Nanowires as Building Blocks for Light Detectors, Gas Sensors, and Biosensors", IEEExplore 102 (2013) 232105.

Conference Contributions

1. **C. García Núñez**, A.F. Braña, N. López, J.L. Pau, and B.J. García, "Integration of GaAs Nanowires on Electronic Devices by Dielectrophoresis", 18th European Molecular Beam Epitaxy (E-MBE), Canazei (Italy), 15-18 Mar 2015, oral presentation.
2. **C. García Núñez**, A.F. Braña, N. López, and B.J. García, "On the Growth Mechanisms of GaAs by Ga-assisted Chemical Beam Epitaxy", 10th Spanish Conference on Electron Devices (CDE), Aranjuez (Spain), 11-13 Feb 2015, oral presentation.
3. **C. García Núñez**, A.F. Braña, J.L. Pau, D. Ghita, B.J. García, G. Shen, D.S. Wilbert, S.M. Kim, and P. Kung "Pure Zincblende Ga(As,P) Nanowires Grown by Ga-assisted Chemical Beam Epitaxy", 7th Nanowire Growth Workshop, Lausanne (Switzerland) 10-12 Jun 2013, poster presentation.
4. **C. García Núñez**, A.F. Braña, J.L. Pau, D. Ghita, B.J. García, G. Shen, D.S. Wilbert, S.M. Kim, and P. Kung, "Pure Zincblende GaAs Nanowires Grown by Ga-assisted Chemical Beam Epitaxy", 17th European Molecular Beam Epitaxy (E-MBE), Levi (Finland), 10-13 Mar 2013, poster presentation.
5. **C. García Núñez**, J.L. Pau, E. Ruiz, A. García Marín, B.J. García and J. Piqueras, "Enhanced Fabrication Process of Zinc Oxide Nanowires for Optoelectronics", 4th International Symposium on Transparent Conductive Materials (TCOs), Crete (Greece), 21-26 Oct 2012, oral presentation.
6. **C. García Núñez**, J.L. Pau, E. Ruiz, B.J. García, and J. Piqueras, "Zinc Oxide and Gallium Doped Zinc Oxide Nanowires for Optoelectronics", 9th NanoSpain, Santander (Spain), 26-01 Mar 2012, poster presentation.

7. **C. García Núñez**, J.L. Pau, E. Ruiz, M.J. Hernández, M. Cervera, and J. Piqueras, "Hight Mobility n-type Zn_3N_2 Thin Films as Channel for Thin Films Transistors", XIV Jornada de Jóvenes Científicos del Instituto de Ciencia de Materiales Nicolás Cabrera (INC), 11 Dec 2011, oral presentation.
8. **C. García Núñez**, J.L. Pau, M.J. Hernández, M. Cervera, E. Ruiz and J. Piqueras, "High Mobility n-type Zn_3N_2 Thin Films as Channel for Thin Film Transistors", 35th Workshop on Compound Semiconductor Devices (WOCSDICE), Catania (Italy), 29-01 Jun 2011, oral presentation.
9. **C. García Núñez**, J.L. Pau, M.J. Hernández, M. Cervera, E. Ruiz, and J. Piqueras, "High Mobility n-type Zn_3N_2 Thin Film Transistors for Sensing and Biosensing Applications", 1st Annual Meeting of the AVANSENS Group, Madrid (Spain), 23-27 Jun 2011, oral presentation.
10. **C. García Núñez**, D. Ghita, and B.J. García, "Sn Doped GaAs by CBE using Tetramethyltin", 16th European Molecular Beam Epitaxy Workshop (E-MBE), Alpe d'Huez (France), 20-23 Mar 2011, poster presentation.
11. **C. García Núñez**, J.L. Pau, M.J. Hernández, M. Cervera, and J. Piqueras, "Effect of the Deposition Temperature on the Properties of Zn_3N_2 Layers Grown by rf Magnetron Sputtering", 8th Spanish Conference on Electron Devices (CDE), Palma de Mallorca (Spain), 8-11 Feb 2011, poster presentation.
12. **C. García Núñez**, D. Ghita, and B.J. García, "Sn doped GaAs by CBE using Tetramethyltin", 8th Spanish Conference on Electron Devices (CDE), Palma de Mallorca (Spain), 8-11 Feb 2011, poster presentation.
13. J.L. Pau, **C. García Núñez**, A. García Marín, C. Guerrero, P. Rodríguez, S. Borromeo, and J. Piqueras, "Contact Properties and Surface Reaction Kinetics of Single ZnO Nanowire Devices Fabricated by Dielectrophoresis", (SPIE), San Francisco (USA), 2-5 Feb 2014, oral presentation.
14. J.L. Pau, **C. García Núñez**, A. García Marín, E. Ruiz, and J. Piqueras "Optical Sensors Based on Metal Oxide Nanowires for UV/IR Detection", Optics+Optoelectronics (SPIE), Praga (Czech Republic), Apr 2013, oral presentation.
15. J.L. Pau, **C. García Núñez**, A. García Marín, E. Ruiz, and J. Piqueras, "Metal Oxide Nanowires as Building Blocks for Light Detectors, Gas Sensors and Biosensors", 9th Spanish Conference on Electron Devices (CDE), Valladolid (Spain), 12-14 Feb 2013, oral presentation.
16. A. García Marín, **C. García Núñez**, E. Ruiz, J. Piqueras, and J.L. Pau, "p-type CuO NWs Based Photodetectors", Nanoportugal, Oporto (Portugal), 13-15 Feb 2013, poster presentation.
17. A. García Marín, **C. García Núñez**, E. Ruiz, J. Piqueras, and J.L. Pau, "WO_3 Nanoparticle-Functionalized Nanowires for NO_x Sensing" Nanoportugal, Oporto (Portugal), 13-15 Feb 2013, poster presentation.
18. J.L. Pau, A. García Marín, **C. García Núñez**, E. Ruiz, and J. Piqueras, "NO Sensors for Disease Control and Medication Monitoring in Asthmatic Patients", 9th Spanish Conference on Electron Devices, Valladolid (Spain), 12-14 Feb 2013, poster presentation.

19. J.L. Pau, J.M. Abaz, M.J. Hernández, M. Cervera, E. Ruiz, **C. García Núñez**, E. Lorenzo, and J. Piqueras "Investigation of Surface Plasmon Resonance in Au Nanoparticles Deposited on ZnO:Al Thin Films", 8th Spanish Conference on Electron Devices (CDE), Palma de Mallorca (Spain), 8-11 Feb 2011, oral presentation.